UNIVERSITY OF SOUTHAMPTON

FACULTY OF ENGINEERING AND THE ENVIRONMENT

School of Engineering Sciences

High–Pressure Torsion Processing of AZ91 Magnesium Alloy

By

Ahmed Sattar Jabbar Al–Zubaydi

Thesis for the degree of Doctor of Philosophy

November – 2015

UNIVERSITY OF SOUTHAMPTON

ABSTRACT

FACULTY OF ENGINEERING AND THE ENVIRONMENT

School of Engineering Sciences

Thesis for the degree of Doctor of Philosophy

HIGH–PRESSURE TORSION PROCESSING OF AZ91 MAGNESIUM ALLOY

Ahmed Sattar Jabbar Al–Zubaydi

AZ91 magnesium alloy has been successfully processed at room temperature by high–pressure torsion as well as at elevated temperatures. Ultrafine grains and nano–sized particles of β–phase have developed with increasing number of turns. The hydrostatic pressure, the geometry of the processing zone and the unidirectional nature of torsional straining during the HPT processing have facilitated processing of AZ91 alloy at room temperature. Extensive grain refinement and twinning segmentation of the coarse grains have been observed in the microstructures processed at room temperature and elevated temperatures, respectively. The twins have been observed at all processing temperatures during processing and their distribution was proportional to the processing temperature and number of turns. The morphology and distribution of the β–phase have altered during processing, with fragmentation of coarse clusters of the β–phase into nano–sized particles and the alignment of these particles in the direction of torsional strain being observed. Microstructural homogeneity has gradually developed at a relatively low number of turns using the lower processing temperature and continued with increasing number of turns. A significant improvement in the strength of the alloy has been found after HPT processing at all processing temperatures. The dislocation density has developed significantly for the alloy processed at room temperature rather than at elevated temperatures with increasing number of turns. An experimental Hall–Petch relationship has emphasized a significant dependence of the strength on grain size for the alloy processed at room temperature. The high–strain rate superplasticity, low–temperature superplasticity, and thermal stability of the processed alloy have been observed and attributed to the ultrafine–grained microstructures produced by HPT at room temperature and the dispersion of nano–sized β–phase particles. Grain–boundary sliding was the main deformation mechanism during the high–strain rate superplasticity regime. Glide–dislocation creep accommodated by grain–boundary sliding was the deformation mechanism operating during the low–temperature superplasticity regime. At high temperature and slow strain rate grain–boundary sliding was accommodated by a diffusion creep mechanism.

TABLE OF CONTENTS

LIST OF FIGURES

LIST OF TABLES

LIST OF SYMBOLS AND ABBREVIATIONS

HCP	Hexagonal close–packed
FCC	Face centred cubic
BCC	Body centred cubic
a, c	Short and long lattice constants in HCP structure
a_1, a_2, a_3	Lattice axes in HCP structure
wt. %	Weight percent
ASTM	American Society for Testing and Materials
α– Mg	Mg–Al Solid solution in AZ91 alloy
β– phase	Intermetallic compound in AZ91 alloy
L	liquid phase (in Figure 2.3)
T– 6	Solution treatment at (400–420) °C for (16–24) hours, then ageing at (180–210) °C for (8–16) hours (in Table 2.1)
HB	Brinell hardness (in Table 2.1)
$El.$	Elongation
CRSS	Critical resolved shear stress
SPD	Severe plastic deformation
UFG	Ultrafine–grained
HAGB	High–angle grain boundaries
σ	Strength in Hall–Petch equation (in Eq. 1.1)
d	Grain size
σ_0 , k	Constants in Hall–Petch equation (in Eq. 1.1)
ECAP	Equal–channel angular pressing
ARB	Accumulative rolling–bonding
HPT	High–pressure torsion
FSP	Friction stir processing
T	Absolute temperature
T_m	Absolute melting point
γ_{SFE}	Stacking fault energy
Φ	Channel angle in ECAP die (in Eq. 1.2 and Figure 2.11)
Ψ	Curvature angle in ECAP die (in Eq. 1.2 and Figure 2.11)
n	Number of cycles (in Eq. 1.3)
TE	Twist extrusion
β	Angle of twist (in Eq. 1.4 and Figure 2.14)

CG	Coarse–grained
σ	True stress or flow stress (in Eq. 1.5 and Eq. 1.6)
ε	True strain (in Eq. 1.5)
K	Strength coefficient (in Eq. 1.6)
n	Strain–hardening exponent (in Eq. 1.6)
$\dot{\varepsilon}$	Steady–state strain rate (in Eq. 1.6 and Eq. 1.8)
A	Dimensionless constant (in Eq. 1.6)
D	Diffusion coefficient (in Eq. 1.6)
D_o	Pre–exponential complex constant
Q	Activation energy
R	Gas constant (in Eq. 1.6)
G	Dynamic shear modulus (in Eq. 1.6)
$\boldsymbol{b}$	Burgers vector (in Eq. 1.6 and Eq. 3.2)
k	Boltzmann's constant (in Eq. 1.6)
T	Absolute melting point (in Eq. 1.6)
p	Exponents of the inverse grain size (in Eq. 1.6 and Eq. 1.8)
n	Exponents of the normalized stress (in Eq. 1.6)
m	Strain–rate sensitivity (in Eq. 1.7)
$\mathrm{d}_1, \mathrm{d}_2, \mathrm{T}_1, \mathrm{T}_2$	Values for grain sizes and temperatures (in Figure 2.19)
Q_L	Activation energy for lattice diffusion (in Figure 2.23)
Q_{gb}	Activation energy for grain–boundary diffusion (in Figure 2.23)
Q_s	Activation energy for solute atom diffusion in alloy (in Figure 2.23)
γ	Shear strain (in Eq. 1.9)
N	Number of passes or turns (in Eq. 1.2 and Eq. 1.9)
r	Distance from the centre of the disk (in Eq. 1.9)
ε_{eq}	Equivalent von Mises strain
ε_{true}	True strain imposed by HPT (in Eq. 1.10)
h_0, h	Initial and final thicknesses of the HPT disk (in Eq. 1.11)
Hv	Vickers microhardness
TEM	Transmission electron microscopy
H_0	Initial microhardness (in Figure 2.33)
H_s	Saturation microhardness (in Figure 2.33)
P	Applied pressure
LAGB	Low–angle grain boundaries
GND	Geometrically necessary dislocations

SSD	Statistically stored dislocations
ABE	Accumulative back extrusion
EDS	Energy–dispersive spectroscopy
OM	Optical microscope
SEM	Scanning electron microscope
XRD	X-ray diffractometry
RT	Room temperature
2θ	Bragg angle
λ	Wave length of x–ray source
ΔK_{FWHM}	Breadth of the profile in XRD
ρ	Density of dislocations (in Eq. 3.2)
ε	Microstrain (in Eq. 3.2)
$< d_c >_v$	Apparent volume-weighted crystallite size (in Eq. 3.2)
$< d_c >_l$	apparent linear crystallite diameter
d_{sp}	Inter–spacing distance between the atomic planes (in Eq. 4.1)
$h\ k\ l$	Miller indices
t	Testing time in the tensile test (in Figure 4.82)
Hv	Vickers microhardness
k_H	Microhardness's constant in the Hall–Petch relationship for the hardness measurement
D_p	Particle diameter (in Figure 4.30)
EBSD	Electron back–scattered diffraction
σ_{ss}	Strengthening by solid solution in the equation $\sigma_{ss} \cong k_s c^{2/3}$
k_s	Constant in the equation $\sigma_{ss} \cong k_s c^{2/3}$
c	Atomic concentration of solute in the equation $\sigma_{ss} \cong k_s c^{2/3}$

DECLARATION OF AUTHORSHIP

I, **Ahmed Sattar Jabbar Al–Zubaydi**, declare that this thesis and the work presented in it are my own and has been generated by me as the result of my own original research.

HIGH–PRESSURE TORSION PROCESSING OF AZ91 MAGNESIUM ALLOY

I confirm that:

1. This work was done wholly or mainly while in candidature for a research degree at this University;
2. Where any part of this thesis has previously been submitted for a degree or any other qualification at this University or any other institution, this has been clearly stated;
3. Where I have consulted the published work of others, this is always clearly attributed;
4. Where I have quoted from the work of others, the source is always given. With the exception of such quotations, this thesis is entirely my own work;
5. I have acknowledged all main sources of help;
6. Where the thesis is based on work done by myself jointly with others, I have made clear exactly what was done by others and what I have contributed myself;
7. Either none of this work has been published before submission, or parts of this work have been published as:

- **Structural and hardness inhomogeneities in Mg–Al–Zn alloys processed by high-pressure torsion**. A. Al-Zubaydi, R.B. Figueiredo, Y. Huang, T.G. Langdon, *Journal of Materials Science*, 48 (2013) 4661–4670.
- **An overview of flow patterns development on disc lower surfaces when processing by high-pressure**. Y. Huang, A. Al-Zubaydi, M. Kawasaki, T.G. Langdon, *Journal of Materials Research and Technology*, 3 (2014) 303–310.
- **Effect of anvil roughness on the flow patterns and hardness development in high-pressure torsion**. Y. Huang, M. Kawasaki, A. Al-Zubaydi, T.G. Langdon, *Journal of Materials Science*, 49 (2014) 6517–6528.
- **Superplastic behaviour of AZ91 magnesium alloy processed by high–pressure torsion**. Ahmed S.J. Al–Zubaydi, Alexander P. Zhilyaev, Shun C. Wang, Philippa A.S. Reed, *Materials Science and Engineering A*, 637 (2015) 1 – 11.
- **Evolution of microstructure in AZ91 alloy processed by high-pressure torsion**. Al-Zubaydi, Ahmed S.J. Al–Zubaydi, Alexander P. Zhilyaev, Shun C. Wang, Pawee Kucita, Philippa A.S. Reed, *Journal of Materials Science*, 51 (2016) 3380–3389.

Signed: ……

Date: ……

ACKNOWLEDGEMENTS

I would like to thank my supervisors: Professor Philippa A.S. Reed, Dr. Alexander P. Zhilyaev and Dr. Shun C. Wang, for their support, patience, guidance along my study. I also very grateful to Professor Philippa A.S. Reed for her kindness and creative co-operation during my work and writing this thesis. My thanks also go for Dr. Andrew J. Chipperfield, Professor Martyn Hill, staff of the graduate school, the administrative staff and the technical staff in School of Engineering Sciences in Faculty of Engineering and the Environment. Thanks for Professor Terence G. Langdon, Dr. Yi Huang, my colleagues and friends in the School of Engineering Sciences for their help. I am very appreciative to the Higher Committee for Education Development (HCED) of the Government of IRAQ for the provision of PhD scholarship. My sincere thanks also go to my family, wife and my kids for their prayers, patience and support throughout my life and study.

Chapter One: Introduction

1. INTRODUCTION

The scientific principles of severe plastic deformation were revealed by Bridgman, when he noticed the increase in strength of a bar under twisting when it was subjected to a compressive loading. Bridgman's work focused on the mechanical behaviour of bulk metals under high pressures. Later, Bridgman invented an apparatus to produce very high pressures and was awarded a Nobel Prize for this work [1]. The effect of grain size on mechanical properties was revealed by Hall and Petch. They showed that the strength of low–carbon steel increased significantly with decreasing grain size, and their work proposed the well–known Hall–Petch relationship, which describes the strengthening due to accumulation of dislocations at grain boundaries [2][3]. Armstrong and Petch extended the Hall–Petch relationship to describe the effect of the grain size on the flow stress in stress–strain behaviour [4]. Further studies were performed by Armstrong to show the effect of grain size on the other mechanical properties of polycrystalline materials such as hardness, fatigue and creep [5]. The above–mentioned works emphasize the effect of grain size on the mechanical properties of polycrystalline materials. It was found that fine grain sizes (< 1 μm) lead to higher strength at room temperature compared to coarser grain sizes (> 100 μm) [6]. Fine–grained materials show a good ductility at room temperature, and a high ductility at elevated temperatures, where high ductility is an important factor in superplastic forming operations [7].

The combination of strength and ductility in fine–grained materials has attracted researchers in the field of materials science to think about possible procedures for producing grain refinement in metals and alloys. Based on Bridgman's work, Kuznetsov and his co–workers from the Institute of Metals Physics in Russia have conducted the first high–pressure torsion (HPT) processing, where torsion and compression are applied simultaneously on a disk–shaped sample for several turns [1]. Segal and his co–workers in the Institute of Minsk introduced equal channel angular pressing (ECAP), where a sample in the form of a billet is pressed several times within a special geometry die [8]. The processing of metals and alloys by very large strains whilst retaining the overall dimensions of the work

piece is called severe plastic deformation (SPD). The HPT and ECAP techniques are used effectively to impose large plastic strains to produce ultrafine–grained microstructures with superior properties [6]. Numerous studies have been conducted on different materials processed by SPD processing techniques to investigate the relation between processing conditions and the evolution in microstructures and the resultant properties [1][6].

Magnesium alloys are widely used in several applications such as transportation, materials–handling, and commercial equipment due to their low density compared to other structural alloys such as steel and aluminium alloys [9]. The main limitation on the use of these alloys is their poor workability at room temperature which makes mechanical processing difficult. The low ductility of magnesium alloys is a result of the hexagonal crystal structure of magnesium [10]. It has been found that severe plastic deformation can improve the strength and ductility of many materials including magnesium alloys [1]. Ultrafine–grained magnesium alloys have the potential to be used in automotive and aerospace applications due to their low density, a high ratio of strength–to–weight, and consequently, reduced fuel consumption [11][12]. Hence, several attempts have been performed to enhance their mechanical properties, but the majority of these experiments were conducted at elevated temperature, where dynamic recrystallization and grain growth also take place [13][14][15].

The development of superplastic behaviour of ultrafine–grained magnesium alloys has been attracting significant consideration in the last decade. Among magnesium alloys, the AZ91 alloy is widely used in industry. This alloy has a good machinability and castability, high strength–to–density ratio, and good corrosion resistance [11][16]. Fine–grained AZ91 alloy has been produced through several severe plastic deformation (SPD) techniques, such as ECAP [10], [13], EX–ECAP [17] and HPT [18]. Fine–grained AZ91 magnesium alloys have shown a wide range of superplasticity depending on microstructure, strain rate and temperature [19]. The earlier work on superplasticity in SPD processed AZ91 alloy has been based on processing of the AZ91 alloy at high temperatures, where the limited ductility and workability of the alloy has been improved by the activation of

additional slip systems and dynamic recrystallization [20]. Up to now, no experiment have reported the development of microstructure and microhardness across horizontal and vertical cross–sections of the AZ91 samples processed by HPT at different processing temperatures, especially at room temperature and no study has been described the superplastic behaviour of the AZ91 alloy processed by HPT at room temperature.

1.1 The Aim of the Work

The first aim of the present research is to study the microstructural evolution of the AZ91 magnesium alloy during high–pressure torsion processing at different processing temperatures, particularly at room temperature, with regards to the α–Mg matrix and β–phase. Microstructural observations have been conducted using optical, scanning electron, transmission electron microscopes and X-ray diffractometry. The second aim of this work is to investigate the mechanical properties of the processed alloy, considering the microstructural evolution of the alloy after processing. The development of microhardness and strengthening has been studied using Vickers microhardness tests across both horizontal and vertical cross–sections and X-ray diffractometry. The superplastic behaviour and the thermal stability have been investigated for the alloy processed at room temperature, and tested over different temperatures and strain rates.

1.2 Thesis Structure

The structure of this thesis is as follows. After this introduction, Chapter 2 comprises a scientific review of magnesium and its alloys, the basics of SPD processing, especially HPT, proposals for the development of homogeneity in HPT–processed materials, properties of the materials processed by SPD and previous studies in the SPD processing of magnesium alloys. Chapter 3 demonstrates the materials used in this study, processing conditions, and preparation of samples for microstructural, microhardness and tensile investigations. Chapter 4 presents the microstructural and microhardness results

across both horizontal and vertical cross–sections of the processed disks, the results of chemical analysis of the alloy before and after processing and tensile properties of the processed samples. Chapter 5 presents a thorough analysis of the results that are shown in chapter four. Chapter 6 summarizes the main outcomes of the current study and indicates the conclusions that can be drawn from the PhD. Chapter 7 outlines proposed future work.

Chapter Two: Literature Review

2. LITERATURE REVIEW

2.1 Magnesium

Magnesium is the lightest metal used in structural alloys. It has the lowest density (1.74 gm/cm^3) among other structural metals such as aluminium (2.7 gm/cm^3), titanium (4.5 gm/cm^3), and iron (7.8 gm/cm^3) [21][22]. It has become an attractive competitor to replace the above–mentioned metals in the transportation industry [11]. However, magnesium possesses a hexagonal close–packed (HCP) structure and a limited number of slip systems, so it has a low ductility and a limited formability at room temperature [13]. Pure magnesium is usually alloyed with different elements such as aluminium, zinc, and manganese to form a variety of magnesium alloys [23].

2.1.1 Crystallography of Magnesium

The crystal structure of magnesium is hexagonal close–packed (HCP) with a primitive unit cell consisting of two axes ($a \neq c$) as shown in Figure 2.1, with a corresponding inter-axial angle of 120° separating the axes a_1, a_2 and a_3. The HCP structure consists of top and bottom layers consisting of six atoms in the form of hexagons, with a central atom in each hexagon as labelled by C and G in Figure 2.1 (a). In addition to that, three atoms exist as an atomic mid–plane between the top and bottom hexagons. Therefore, six equivalent atoms are present in the HCP crystal structure with the stacking sequence of $ABABAB$ as shown in Figure 2.2. Magnesium, zinc, cadmium and titanium are examples of metals with HCP structure [24][25]. The axial ratio (c/a = 1.624) and atomic diameter (0.320 nm) of magnesium determine its alloying compatibility with different metals through solid solutions [23]. A solid solution is defined as the solid–state solution resulting from the addition of impurity atoms (solute atoms) to the host atoms (solvent atoms) [23]. The formation of magnesium solid solution alloys depends on the following factors [26]:

1. The favourable atomic size of alloying elements must be within the range ± 15 % of the atomic diameter of magnesium. This ratio is 15 % and 1 % for Al and

Zn respectively; which allows these elements to form solid solutions with magnesium.

2. Crystal structure compatibility leads to a substitutional solid solution in the case of the presence of Zn (HCP), or Al (FCC); otherwise, the interstitial solid solution can be formed with Mn (BCC).
3. The high electropositivity of Mg (1.2) tends to form stable intermetallic compounds of Mg_2(Si, Pb) with Si and Pb of electronegativity 1.8 and 2.2, respectively, instead of the formation of a substitutional solid solution.
4. Magnesium tends to form solid solutions with metals of similar valences such as Al, Zn.

2.1.2 Magnesium Alloys

Magnesium alloys exhibit a good machinability and castability, high strength/ density ratio, and good corrosion resistance. These alloys also show a limited toughness and poor workability at room temperature; and limited strength, corrosion, and creep resistance at high temperatures [11][16]. Magnesium alloys are designated internationally using ASTM International nomenclature, by which each alloy is coded by the two letters of the major alloying elements followed by their weight percentage [16][23]. For example, AZ91 consists of 9 wt.% Al and 1 wt.% Zn, and the AZ31 alloy consists of 3 wt.% Al and 1 wt.% Zn [9]. Table 2.1 shows the compositions and mechanical properties for pure magnesium and some of its common alloys [21][23] [27][28].

Table 2.1: Mechanical properties of the pure magnesium and its alloys at room temperature.

Material	**Condition**	**Al wt.%**	**Zn wt.%**	**Mn wt.%**	**Other wt.%**	σ_y **(MPa)**	σ_{UTS} **(MPa)**	$El.$ **%**	**HB**
Mg [21]	Extruded	–	–	–	–	70	185	4	40
AZ91 [23]	As cast	9.0	0.7	0.3	–	125	200	7	55
AZ91 [28]	T–6	8.1–9.3	0.4–1.0	0.17–0.35	–	170	270	5	65
AM60 [27]	As cast	6.0	–	0.13		130	240	13	65
AS41 [27]	As cast	4.2	–	0.2	1.0 Si	140	240	15	60
AZ31 [21]	Extruded	3.0	1.0	0.2	–	180	250	15	50
AZ61 [21]	Extruded	6.0	1.0	0.3		220	300	12	55
ZK60 [21]	Extruded	–	5.5	–	0.5 Zr	260	340	11	90

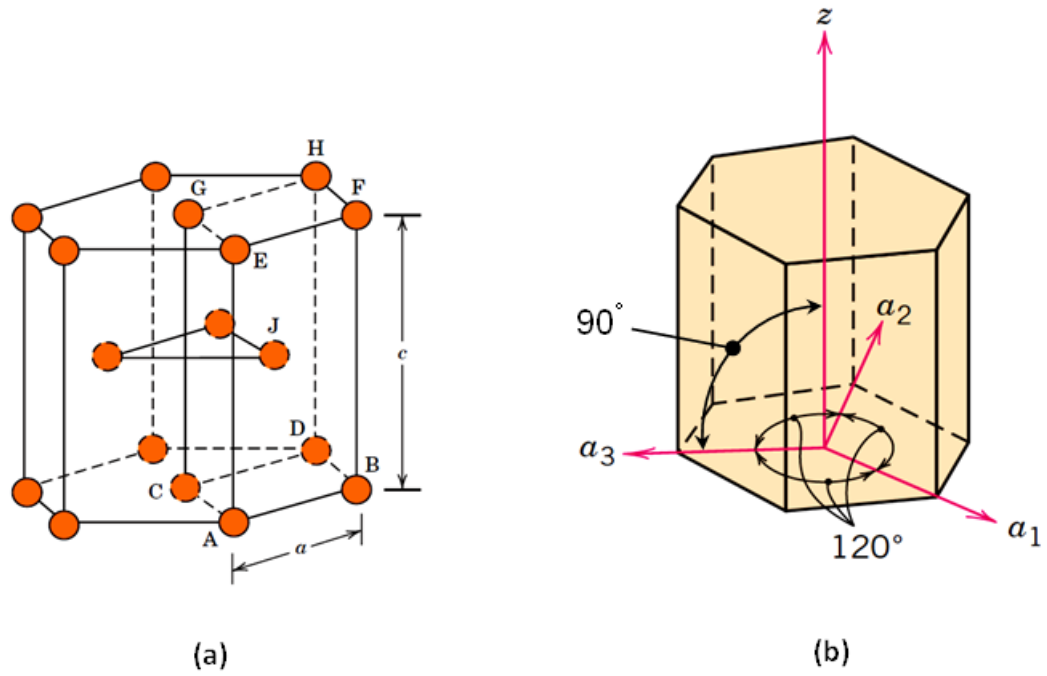

Figure 2.1: (a) Hexagonal close–packed crystal structure shows the primitive unit cell indicated by letters A to H, whereas the letter J refers to one of three atoms that lie in mid–plane inside the crystal structure and C and G represent the central atoms in the top and bottom hexagons. The short and long edge lengths are represented by labels a and c, respectively. (b) Coordinate axis system of the hexagonal crystal structure illustrates the angular relationship between axes ($\boldsymbol{a_1}$, $\boldsymbol{a_2}$, $\boldsymbol{a_3}$, $\boldsymbol{z}$) [24].

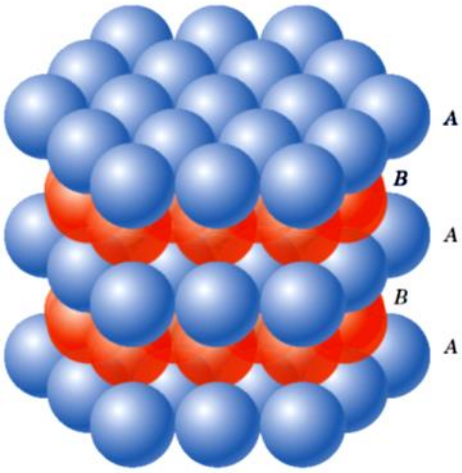

Figure 2.2: Stacking sequence for the hexagonal close–packed structure as labeled by ***ABABAB*** [24].

2.1.3 Main Alloying Elements in Magnesium Alloys

Addition of different alloying elements can alter the properties of magnesium alloys through solid–solution hardening and/or precipitation hardening. The solid–solution hardening mechanism is based on the available substitutional and interstitial atoms of the alloying element, while the precipitation hardening mechanism depends on the solubility of the atoms of alloying element, temperature of application, and the formation of intermetallic phases [16]. Aluminium represents the main alloying element in magnesium alloys. It forms a eutectic system at 437 °C that enhances castability and increases strength and hardness [9][16]. The addition of zinc enhances the castability and strengthens the magnesium alloy [16]. The magnesium–aluminium eutectic separates completely within the alloy system due to the addition of zinc [9][29]. The solid solubility of aluminium in magnesium can be reduced by the addition of zinc to the alloy system, and the latter can slightly increase the strength of the alloy [23]. Addition of 0.2 wt.% of manganese improves the corrosion resistance, grain refinement, and tensile strength [16].

2.1.4 Magnesium–Aluminium System

Magnesium alloys can be classified into two types according to the amount of aluminium content [30][31]:

1. Mg–Al–Zn–Mn and Mg–Al–Mn alloys that consist of 2–10 wt.% Al as well as small amounts of Zn and Mn. These alloys are characterised by the low cost of production, good corrosion resistance, and limited mechanical properties at elevated temperatures.
2. Mg–Zr–Zn, Mg–RE–Zr, Mg–Ag–RE–Zr, Mg–Y–RE–Zr alloys, in which aluminium is replaced by a variety of elements like rare earths, Zr, Ag, and Si. The high cost of production and the stability at elevated temperatures are the main features of these alloys.

The high content of aluminium 3–9 wt.% in magnesium–aluminium system produces alloys with a good castability, good mechanical properties and corrosion resistance at room temperature [16]. The AZ91 alloy (Mg–9wt.%Al–1wt.%Zn–0.3wt.%Mn) is a common alloy in the Mg–Al–Zn family. This alloy has the following features [32]:

1. Ease of production and machining as cast alloys due to high aluminium content.
2. Good strength–to–density ratio (200 MPa / 1.8 gm/cm^3).
3. Good corrosion resistance due to low levels of contaminants (Fe, Cu, Ni).

The microstructure of AZ91 alloy principally consists of a matrix of α–Mg solid solution and β–phase ($Mg_{17}Al_{12}$). The maximum solid solubility of aluminium in magnesium is 12.7 wt.% at a temperature of 437 °C. This solubility decreases to about 2 wt.% at a temperature of 100 °C as shown in the Mg–Al phase diagram in Figure 2.3 [33]. The β–phase ($Mg_{17}Al_{12}$) is an intermetallic compound of a high aluminium content (43 wt.%), this it is formed due to the high reactivity of magnesium [23]. The β–phase exists around grain boundaries and acts as a strengthening phase at room temperature [34], since it obstructs dislocation movements during deformation by pinning their climb and cross–slip. Its higher hardness compared to the matrix can also contribute to the overall strengthening [35]. Generally, the mechanical properties of AZ91 alloy decrease with increasing

temperature over 120–130 °C [16]. This can be attributed to the softening of β–phase, which allows grain boundary sliding to occur [23].

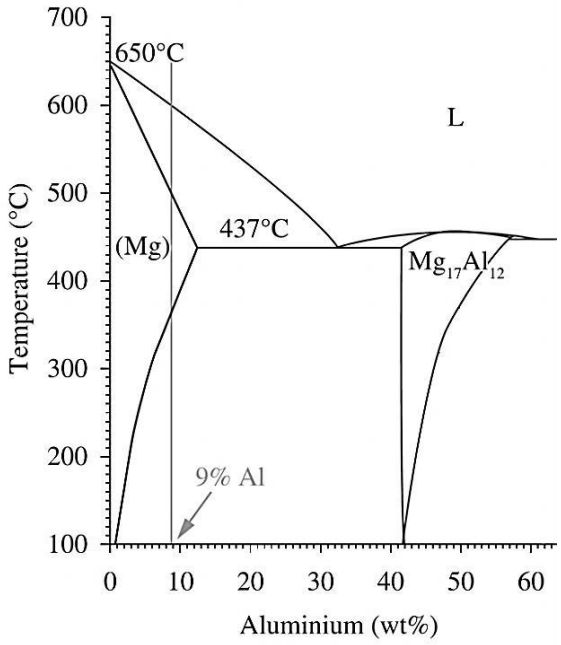

Figure 2.3: A part of Mg–Al phase diagram [33].

2.1.5 Deformation Mechanisms in Magnesium and its Alloys

2.1.5.1 Deformation by Slip

Slip systems are defined as planes with preferred crystallographic directions along which dislocation movement occurs during plastic deformation. These planes and directions tend to have the highest atomic planar and linear densities, respectively [24]. Face–centred cubic (FCC) and body–centred cubic (BCC) metals have a higher number of slip systems compared with hexagonal close–packed metals (HCP) as illustrated in Table 2.2. Therefore, the FCC and BCC metals are ductile whereas the HCP metals are brittle [25]. Magnesium as HCP metal has the following set of crystallographic slip systems that operate at room temperature and elevated temperatures, which are represented schematically in Figure 2.4 [36]:

1. Basal $< a >$: $\{0001\}$ <$11\bar{2}0$>.
2. Prismatic $< a >$: $\{10\bar{1}0\}$ <$11\bar{2}0$>.

3. Pyramidal (Twinning) $< a >$: $\{10\bar{1}1\}$ <$11\bar{2}0$>.
4. 1st order pyramidal $< c + a >$: $\{10\bar{1}1\}$ <$11\bar{2}3$>.
5. 2nd order pyramidal $< c + a >$: $\{11\bar{2}2\}$ <$11\bar{2}3$>.

Slip initiates when the applied shear stress exceeds a critical value called the critical resolved shear stress (CRSS). This value generally depends on the value of applied shear stress, type of crystal structure, and temperature [25]. The values of CRSS for basal slip $\{0001\}$ <$11\bar{2}0$> and twinning $\{10\bar{1}1\}$ <$11\bar{2}0$> are 0.5 and 3 MPa, respectively, which are both lower than that for prismatic and 1st & 2nd pyramidal plane (40 MPa). Hence, basal slip and twinning deformations can occur instead of slip by prismatic and pyramidal systems at room temperature. Therefore, basal slip and twinning are considered as the dominant deformation modes at ambient temperature [36].

However, the crystal structure must be restored (without a change in volume) after the slip process due to the translation symmetry of the crystal lattice, which requires five independent slip systems according to the von Mises criteria to achieve a homogeneous deformation in polycrystalline material without failure [27]. Therefore, since HCP magnesium has only two independent slip systems for basal slip plane (0001) <$11\bar{2}0$> at room temperature, this causes brittleness and limited ductility [37]. The presence of additional non–basal slip systems (at a temperature of 250 °C) such as 1st order prismatic and 2nd pyramidal slip systems can enhance the plasticity of magnesium and its alloys [38]. The activation of these slip systems depends on their critical resolved shear stress, which in turn, depends on temperature, solute atoms and precipitation state [32].

Table 2.2: Slip systems in FCC, BCC and HCP metals [24].

Metals	*Slip Plane*	*Slip Direction*	*Number of Slip Systems*
	Face-Centered Cubic		
Cu, Al, Ni, Ag, Au	{111}	$\langle 1\bar{1}0 \rangle$	12
	Body-Centered Cubic		
α-Fe, W, Mo	{110}	$\langle \bar{1}11 \rangle$	12
α-Fe,W	{211}	$\langle \bar{1}11 \rangle$	12
α-Fe, K	{321}	$\langle \bar{1}11 \rangle$	24
	Hexagonal Close-Packed		
Cd, Zn, Mg, Ti, Be	{0001}	$\langle 11\bar{2}0 \rangle$	3
Ti, Mg, Zr	$\{10\bar{1}0\}$	$\langle 11\bar{2}0 \rangle$	3
Ti, Mg	$\{10\bar{1}1\}$	$\langle 11\bar{2}0 \rangle$	6

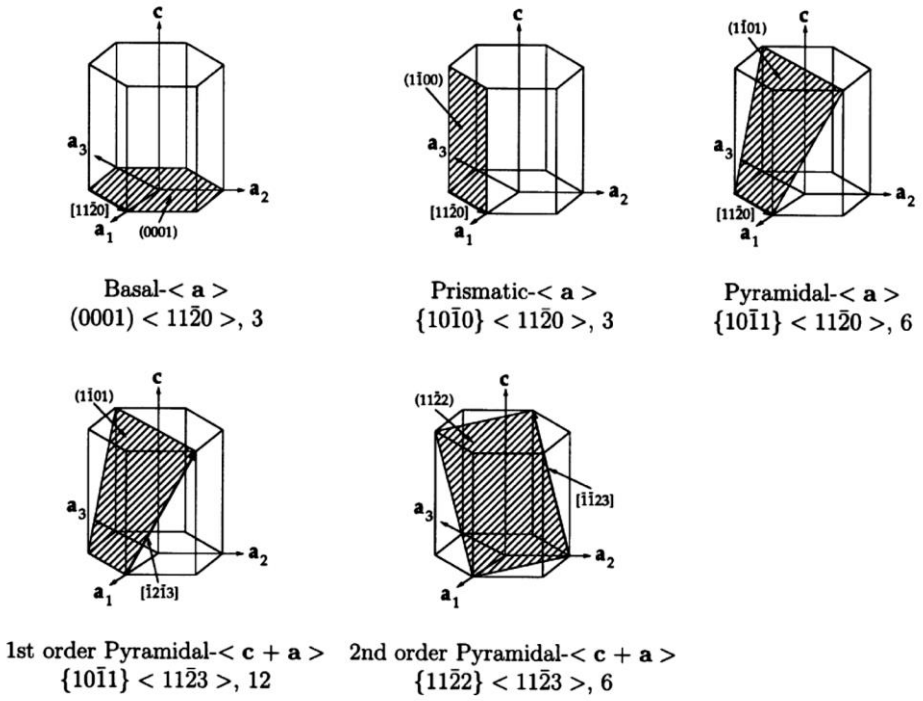

Figure 2.4: Slip systems in HCP metals [38][36].

2.1.5.2 Deformation by Twinning

Deformation by twinning results from atomic displacements under an applied shear stress, in which the atoms on both sides of the twinning plane (twin boundary) become a mirror image of each other [24]. Twinning is accomplished by atomic displacements that are less than the interatomic separation and it leads to

a difference in orientation across the twinning plane [25]. Twinning in metals can be classified into two types: mechanical twinning and annealing twinning. Mechanical twinning occurs as a result of mechanical deformation in HCP metals at low temperature where deformation by slip is restricted, or at high rates of stresses, or when the critical resolved shear stress of twinning is lower than that for the slip [25]. The other type of twinning, annealing twinning, occurs during the annealing process in FCC metals. However, the amount of plastic deformation produced by twinning is smaller than by slip deformation and its importance is highlighted most in the deformation of HCP metals where only a few slip systems are operative [26].

Twinning in HCP metals can be further classified into two types according to the ratio (c/a); The first type is tension twinning $\{10\bar{1}2\}$ <$\bar{1}011$> that appears when the (c/a) < 1.732, and the second one is compression twinning $\{10\bar{1}1\}$ <$\bar{1}012$> that appears when the (c/a) > 1.732, as shown in Figure 2.5 [39]. Deformation by twinning takes place in the initial stages of plastic deformation, when both temperature and strains are low. It has been found that poorly orientated grains can be re–orientated for easy slip due to the occurrence of twinning [40].

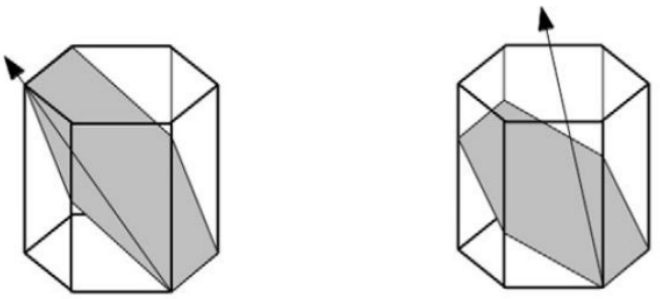

Figure 2.5: Tension twinning and compression twinning in magnesium [40][41].

2.1.6 Stacking Faults

Stacking faults are defined as planar defects of atomic stacking interruptions existing in close–packed crystal structures due to slip or twin deformation [25].

There are three basal stacking faults in HCP magnesium: two intrinsic stacking faults with stacking sequence $ABAB\boldsymbol{C}B\boldsymbol{C}B$ and $AB\boldsymbol{CACAC}$, and one extrinsic stacking fault with stacking sequence $ABAB\boldsymbol{C}ABAB$. These faults have an energy known as the stacking fault energy (γ_{SFE}), which affects the value of critical resolved shear stress, and hence influences the mechanical behaviour and deformation mechanisms in metals and alloys [42].

The separation between the partial dislocations is determined by the stacking fault energy as shown in Figure 2.6. The mobility of dislocations during plastic deformation is influenced by the stacking fault energy. A lower stacking fault energy allows a wider separation between the partial dislocations and thus a wider stacking fault. The latter inhibits cross–slip of dislocations and produces planar arrays of dislocations, resulting in a fast rate of strain hardening and a low rate of dynamic recovery during plastic deformation [43]. On the other hand, a high stacking fault energy leads to a narrow separation between partial dislocations and this leads to a narrow stacking fault that facilitates the cross–slip process. The latter process results in formation of substructures consisting of three dimensional dislocation structures such as cells (subgrains), which leads to a slow rate of strain hardening and a high rate of dynamic recovery during plastic deformation [44]. Stacking faults in FCC metals are simpler compared to those in HCP metals since slip can take place more easily in FCC metals than that in HCP metals [45].

It has been shown that dynamic recovery can be affected by the presence of solute atoms, which can restrict the movement and mobility of dislocations. Thus dynamic recovery can be inhibited by the pinning effect on dislocations by these solute atoms [46]. The increase in the alloying elements also decreases the stacking fault energy and then in turn decreases grain size during SPD deformation by means of the respective effects on twinning and shear banding. Stacking fault energies for many metals and their alloys are shown in Table 2.3 [20][47][48][49][50]. It was found that the fragmentation of the original grains occurs by means of the twin boundaries in materials with low stacking fault energies. Twinning and twin fragmentation in the materials with low stacking fault energies may result in a microstructural refinement down to smaller grain sizes

than that seen in materials with high stacking fault energies that may be refined by the subdivision of dislocation cells [51][52].

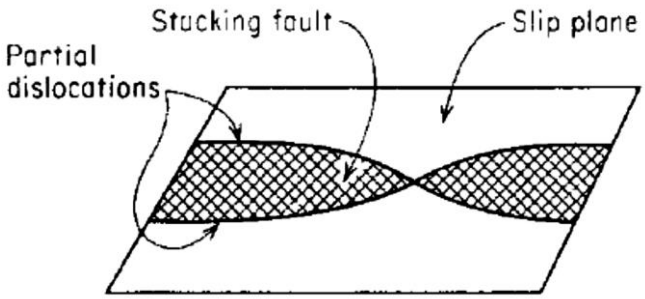

Figure 2.6: An illustration shows the relation between stacking fault and partial dislocations [25].

Table 2.3: Values of the stacking fault energies for different metals and their alloys.

Material	γ_{SFE} **(mJm^{-2})**
Mg	125 [20]
Mg–3wt.%Al	27 [47]
Mg–6wt.%Al	16 [47]
Mg–9wt.%Al	6 [47]
Al	200 [48]
Al–0.7wt.%Mg	130 [48]
Al–1.1wt.%Mg	87 [49]
Cu	78 [50]
Cu–10wt.%Zn	35 [50]
Cu–30wt.%Zn	14 [50]

2.1.7 Dynamic Recovery in Magnesium

The plastic deformation of a metal introduces several changes in the microstructure such as changes in shapes and sizes of grains, strain hardening, and modified properties [25]. The changes in the microstructure and properties can be restored to the pre–cold–worked state by employing an appropriate heat treatment at appropriate temperatures. Recovery and recrystallization can be used

as heat treatment processes to revert the metal back to pre–deformation stage [53]. However, most of the deformation energy is dissipated as heat, and only a minor part of this energy is internally stored in the deformed metal. The major fraction of this energy is associated with dislocations as strain fields [54]. Part of this energy is relieved during recovery through the partial annihilation and/or rearrangement of dislocations, and producing structures with lower energies through formation of low–angle grain boundaries (LAGB) as shown in Figure 2.7 [55].

Reduction in the stored strain energy is the driving force for the migration of dislocations, which leads to partial annihilation and rearrangement of dislocations during static recovery [24]. The annihilation of dislocations with opposite signs can occur by dislocation glide, cross–slip or by climb [53]. An unequal number of opposite–sign dislocations leads to incomplete annihilation and results in the arrangement of these dislocations in the form of dislocation walls as shown in Figure 2.8 [55], and such arrangements lead to release of part of the stored strain energy which works as the driving force for the aforementioned process [56]. The recovery process that occurs in the absence of external applied stress is called static recovery, whereas it is called dynamic recovery if it occurs during the hot deformation processes (T > 0.4 T_m) such as hot rolling and extrusion [25].

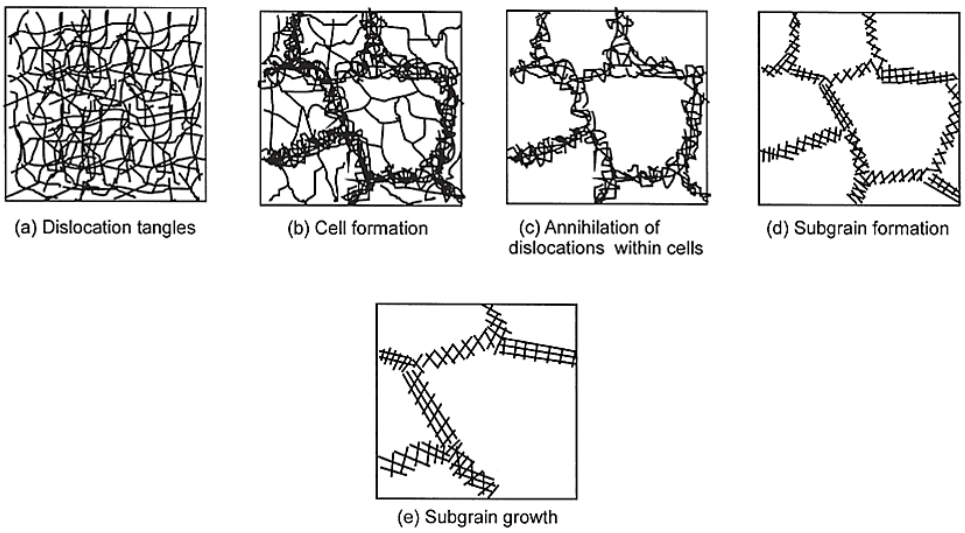

Figure 2.7: An illustration of the formation of low–angle grain boundaries during recovery process [55].

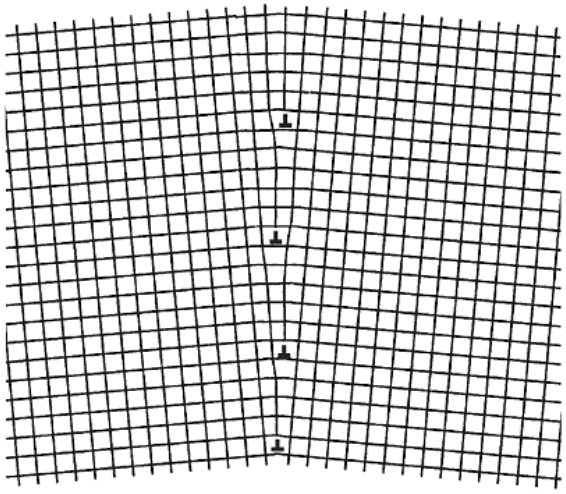

Figure 2.8: An illustration of the of tilt grain boundaries [55].

Dynamic recovery leads to a softening effect by lowering the flow stress of the metal as illustrated in Figure 2.9, which facilitates the forming process [54]. It has been shown that the additional slip systems that are activated during the hot deformation of magnesium can provide extra paths for dislocations and decrease work–hardening rate, which facilitates the effect of softening (dynamic recovery) [46][57]. It was found that the presence of aluminium solute atoms can reduce the stacking fault energy of magnesium by solute–dislocation interactions, which reduces the mobility of these dislocations during hot deformation [20].

It is note worth that the stacking fault energy of deformed metal can influence the rate of dynamic recovery. The stacking fault energy controls the dissociation process of dislocations into partial dislocations [56]. A low value of stacking fault energy promotes the dissociation of dislocations, and blocks the climb and cross–slip of dislocations, leading to a slow rate of dynamic recovery. In contrast, climb and cross–slip can happen easily in a metal with high stacking fault energy resulting in a fast rate of dynamic recovery [55].

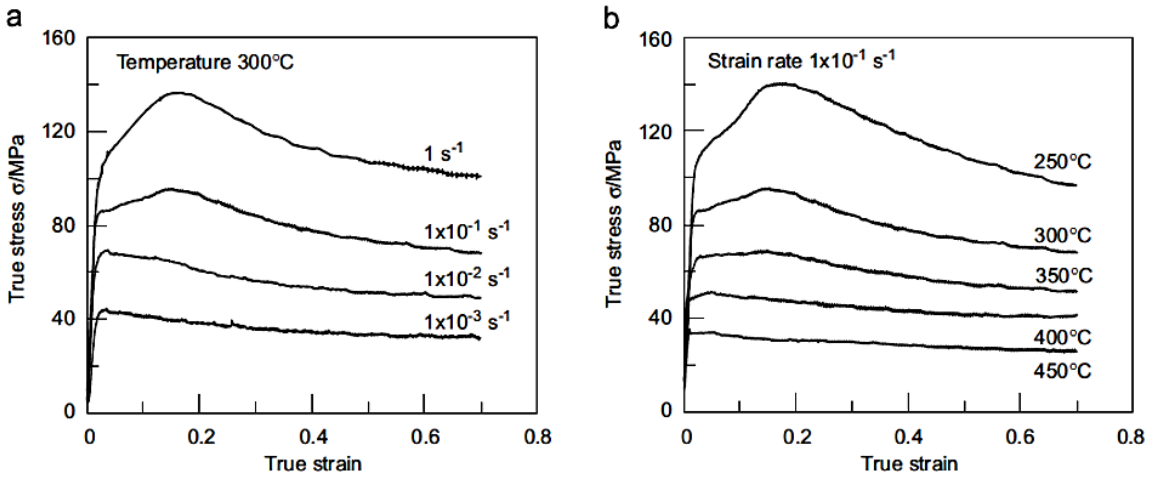

Figure 2.9: The effect of dynamic recovery (softening) on the flow stress of AZ61 magnesium alloy under compression test for: (a) different strain rates and (b) different testing temperatures [57].

2.2 Severe Plastic Deformation Processing (SPD)

Imposing a large plastic deformation into a solid material leads to formation of an ultrafine–grained microstructure with grain sizes less than 1 μm [58]. This microstructure can be produced by means of severe plastic deformation at relatively low temperatures, where the overall dimensions of the sample before the processing are retained by the geometry of processing tool [6]. A high plastic strain is required to form a homogeneous refined microstructure of equiaxed grains with high–angle grain boundaries [7]. An ultrafine microstructure of metals and alloys processed by SPD may contain nano–crystalline structures, nano–twins, and nano–sized particles [6][59]. The main objective of severe plastic deformation processing is a fabrication of materials with a combination of high strength and moderate plasticity. It was found that the strength of the fine–grained materials is larger than that of their coarse–grained counterparts, as expressed by the Hall–Petch relationship [2][3]:

$$\sigma = \sigma_0 + kd^{-1/2} \tag{1.1}$$

where σ is the strength, d is the grain size, σ_0 and k are constants. Ultrafine–grained materials can be considered environmentally clean, since elemental additions are not required for introducing an increment in strength [60].

2.2.1 Grain refinement mechanisms

Microstructural evolution at room temperature during unidirectional metal processing such as in HPT and ECAP (without rotation of the billet) is basically similar to that which occurs during rolling processes. The grain refinement process that occurs has been suggested to follow these steps [61]. Slip occurs in a single slip plane where the dislocations easily glide without any significant obstruction resulting in little initial strain hardening. As deformation proceeds, the grains start to rotate and thus slip occurs on many slip systems, leading to the multiplication of dislocations [56]. The grains fragment into deformation bands of different misorientations as shown in Figure 2.10 [55]. The deformation bands consist of many bands of incidental dislocation boundaries (IDBs) of relatively low misorientation (~ 1°). The incidental dislocation boundaries contain aligned cell blocks as shown in Figure 2.10 [61][55]. Shear bands can form when the deformation bands extend over many grains as shown in Figure 2.10 [55]. The shear bands form due to alignment of the deformation bands across many grains with relatively similar orientations and sizes of aligned cell blocks [56]. These bands occur due to shear localization or plastic instability when the microstructure has second phase particles, precipitation, twins and / or an insufficient number of slip systems for homogeneous deformation [61][56].

The increase in the imposed strain (ε_e ~ 2) leads to an increase in the misorientations between some cell blocks resulting in the formation of high–angle grain boundaries (HAGBs) with misorientations of < 30°. A fibrous structure develops and the fraction of the HAGBs increases as deformation proceeds (ε_{eq}~ 4) resulting in lamella HAGB structures [61][62]. The spacing between the lamella boundaries decreases with further strain (ε_{eq}~ 5) leading to ribbon grains with a width of one subgrain (< 1 µm) [63]. These fibrous or ribbon structures will be fragmented into submicrometre grains by interaction with the existing shear bands,

the second phase particles and the existing low–angle grain boundaries (LAGBs) which increase their misorientations with further straining [61]. It should be noted that in materials with high stacking fault energies, the evolution of dislocation tangles and then cell structures will occur with increasing imposed strain and thus the grain refinement will occur by the dislocation subdivision [64]. In materials with low stacking fault energies, the dislocations arrange in the form of arrays of dislocations. Extensive twinning, twin fragmentation and shear bands are expected to occur at high strains of deformation in materials with low stacking fault energies [52].

Thus grain refinement will happen by twin fragmentation and shear banding in materials with low stacking fault energies [52][56]. The rate of strain hardening and the subsequent grain refinement will be relatively faster in the initial stages of deformation in materials with high stacking fault energies due to the existence of more active slip systems *cf.* materials with low stacking fault energies. However, the final achievable grain size may be finer in materials with low stacking fault energies *cf*. materials with high stacking fault energies due to their higher rates of dynamic recovery processes [51][52].

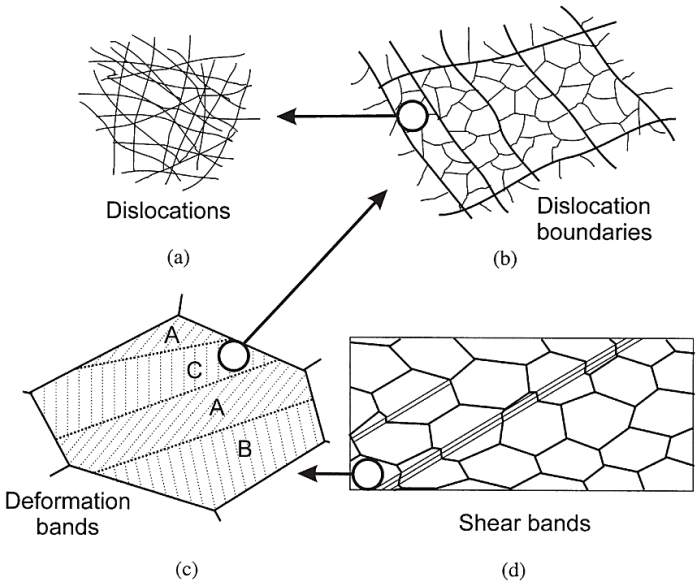

Figure 2.10: The microstructural evolution in a metal under slip deformation: (a) Tangling of accumulated dislocations, (b) Structure of dislocation boundaries that separate low dislocation density regions, (c) Structure of deformation bands and (d) Structure of shear bands [55].

2.2.2 Essential Rules for Microstructure Refinement

Several factors control the formation of ultrafine–grained microstructure using SPD. These “rules” comprise the conditions of processing and the nature of the material under processing. A short description of these rules is presented below based on [60][61][65][66][67][68][69]:

1. Processing at relatively low temperatures ($T < 0.4\,T_m$) is recommended to achieve a high dislocation density. Processing at elevated temperatures results in a reduction in the dislocation density and the concomitant occurrence of grain growth.
2. A high imposed strain is required to produce a homogeneous refined microstructure and to introduce a considerable fraction of high–angle grain boundaries.
3. Considerable hydrostatic pressure is required to enhance the workability of the material under processing and to introduce high densities of lattice defects.
4. The stacking fault energy influences the mechanical behaviour of the material under processing. A material with low stacking fault energy allows the dislocations to dissociate easily into partials and thus prevents easy cross–slip and climb processes. This leads to a slower rate of dynamic recovery and thus a faster rate of grain refinement and strain hardening compared to material with a high stacking fault energy.
5. The strain path has an effect on the rate of grain refinement and formation of equiaxed grains during the HPT and ECAP. Reversed or cyclic straining leads to lower rates of grain refinement and strain hardening due to generation and annihilation of opposite–sign dislocations. An equiaxed microstructure is expected to occur at a faster rate during reversed deformation where the shear strain is redundant and the grain restored their equiaxed shapes.
6. The presence of second phase particles may enhance the rate of grain refinement and strain hardening. The matrix areas around these particles are usually highly deformed zones containing significant strain gradients. This results in reduction in the lengths of deformation bands and lamella structures at relatively low strains and thus produces an earlier evolution of fine microstructures during SPD.

2.2.3 SPD Techniques

A number of different SPD techniques have been introduced to impose very high strains on metallic materials that result in production of ultrafine–grained microstructures. The equal–channel angular pressing (ECAP), high–pressure torsion (HPT), accumulative roll bonding (ARB), and twist extrusion (TE) are examples of SPD techniques. The following section presents briefly some of these SPD techniques, apart from HPT which is reviewed in greater detail in section 2.2.5. These techniques employ different routes during processing and have a common feature that the grain refinement in processed work pieces reaches down to the submicrometre–nanometre level [60].

Equal–channel angular pressing (ECAP) has been used frequently in the field of SPD and it can be summarised as pressing a sample in the form of a rod–shaped billet through a solid die having an internal hallow channel with an equal cross section [60][70]. The high plastic strain imparted to the sample when it passes through the bending area is illustrated in Figure 2.11 [71]. During ECAP processing, the overall cross–sectional dimensions of the sample are unchanged, and thus a high shear strain can be imposed into the sample by repetitive pressing of the billet through the intersection volume between the two parts of the channel [72]. The ECAP process is a repetitive process whereby the same billet can be pressed through several passes. The equivalent strain (ε_{eq}) passed into the ECAP sample depends on the values of the channel angle (Φ), the angle of curvature (Ψ) and number of passes (N), the equivalent strain in ECAP is given by the following expression [73]:

$$\varepsilon_{eq} = \frac{N}{\sqrt{3}}\left[2\cot\left\{\left(\frac{\Phi}{2}\right)+\left(\frac{\Psi}{2}\right)\right\}+\Psi\csc\left\{\left(\frac{\Phi}{2}\right)+\left(\frac{\Psi}{2}\right)\right\}\right] \tag{1.2}$$

Rotation of the billet in ECAP processing along its longitudinal axis results in activation of different slip systems, thus four processing routes A, B_A, B_C, C have been identified. In route A, the billet is pressed without any rotation. In route B_A, the billet is rotated in alternative directions by 90° between each pressing. In route B_C, the billet is rotated in the same directions by 90° between each pressing. In

route C, the billet is rotated by 180° and all these routes are schematically illustrated in Figure 2.12 [74]. In practice, route B_C is preferred as it produces homogeneous and equiaxed microstructures with high–angle grain boundaries [72].

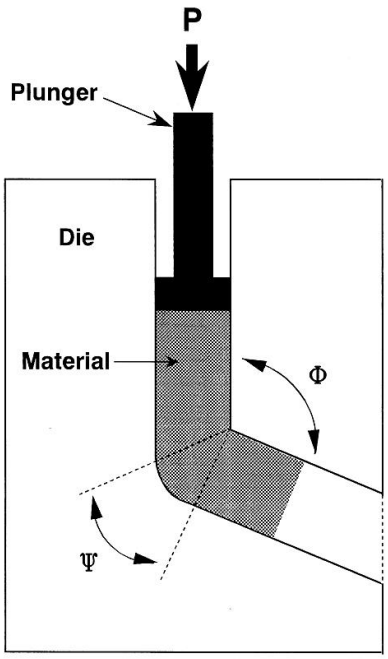

Figure 2.11: Schematic illustration of ECAP facility; (Φ) and (Ψ) represent the channel angle and the angle of curvature, respectively [71].

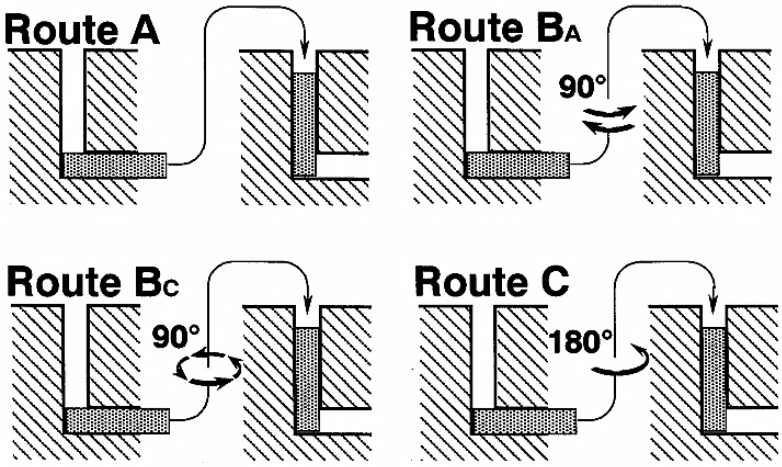

Figure 2.12: Schematic illustration of the four routes in ECAP processing [74].

Accumulative roll bonding (ARB) has been developed from conventional rolling for continuous production of ultrafine grained materials. In this technique, a sheet is rolled to a half of its original thickness and then the rolled sheet cut into two segments. The resultant two sheets or segments are degreased and wired brushed at their contact or bonding surfaces and then these sheets stacked together and rolled again to one–half thickness as shown in Figure 2.13 [75]. Lamellar fine microstructures are usually produced in the ARB due to the nature of this process. A large accumulative strain can be imposed into the material during the ARB by repeating the steps of rolling, cutting, brushing and stacking many cycles. The equivalent strain in ARB for a specific number of cycles (n) is given by the following expression [76]:

$$\varepsilon_{eq} = 0.80\, n \tag{1.3}$$

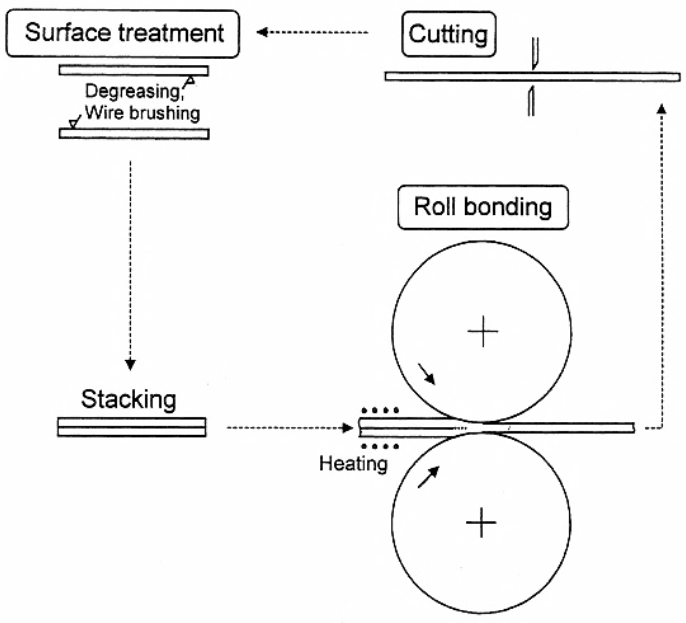

Figure 2.13: Schematic illustration of the ARB processing [75].

Twist extrusion has been introduced as a tool for grain refinement and it is similar in principal to ECAP, where a sample is extruded through a die with constant dimensions and shape at the entrance and exit channels [77]. The sample is twisted along its longitudinal axis in the midway of the extrusion channel as shown

in Figure 2.14. As a result of tool shape, the extruded sample restores its pre–extruded shape after each pass [78]. The equivalent strain in TE for a specific angle of twist (β) is given by the following expression [79]:

$$\varepsilon_{eq} = \frac{2}{\sqrt{3}} \tan \beta \tag{1.4}$$

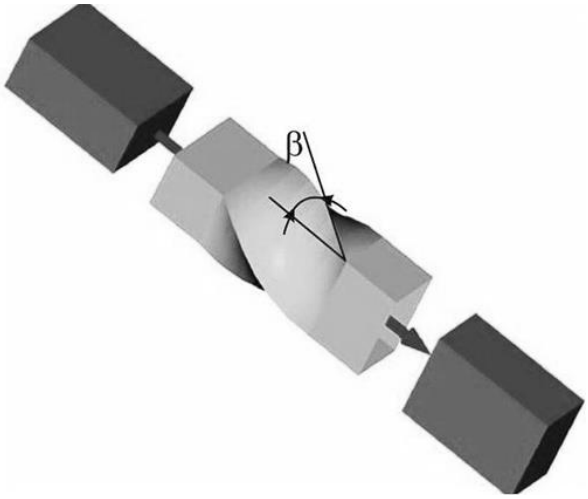

Figure 2.14: Schematic illustration of the twist extrusion [78].

2.2.4 Properties of the materials processed by SPD

2.2.4.1 Mechanical properties at room temperature

The mechanical properties of materials are controlled by several factors such as the grain size, texture, loading conditions, thermal history and environmental conditions [24]. The strength of the material at room temperature and the occurrence of superplastic behaviour at elevated temperatures are affected significantly by its grain size as expressed by the Hall–Petch relationship [2][3] and the constitutive superplastic law [6], respectively. It has been concluded that reduction in grain size leads to a considerable improvement in the strength and significant superplastic properties, and this consequence has been noticed clearly in materials processed by severe plastic deformation techniques [80].

Tensile testing can be used to show the difference in strength of the UFG materials and their coarse grained (CG) counterparts as shown for example in Figure 2.15. It can be concluded that the UFG material shows higher tensile strength and lower ductility than its CG counterpart at room temperature [81]. Hardness measurement can be used also to assess the effect of grain refinement on the strength of the UFG material as illustrated in Figure 2.16, where the reduction in grain size from 50 μm to 100 nm resulted in a considerable increase in strength (as indicated by hardness measurements). The strength of UFG materials can be higher than predicted by the Hall–Petch relationship, and this has been attributed to the formation of nanostructures such as non–equilibrium grain boundaries, nanotwins, and nano–sized particles [6]. The strengthening contributions from these nanostructures and by the grain refinement results in the overall strength of the UFG materials [59][81].

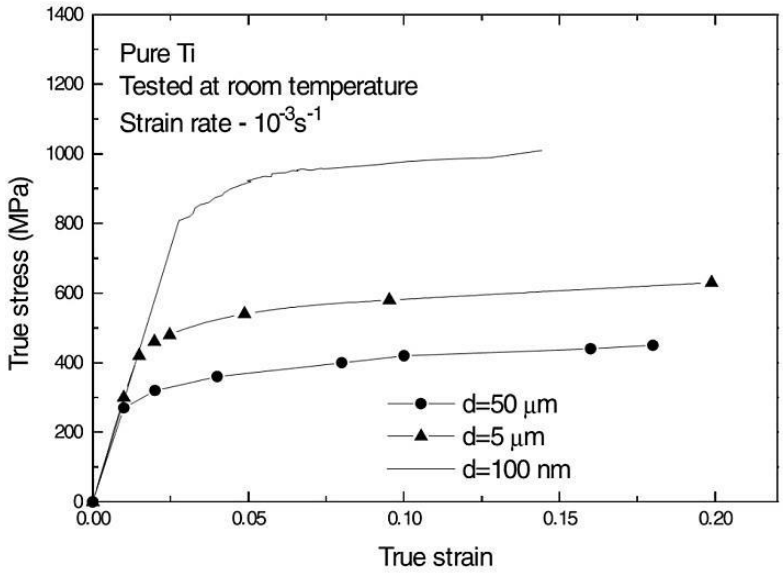

Figure 2.15: True stress–strain curve for commercial purity Ti processed at room temperature in HPT and then tested in tension at room temperature [82][83].

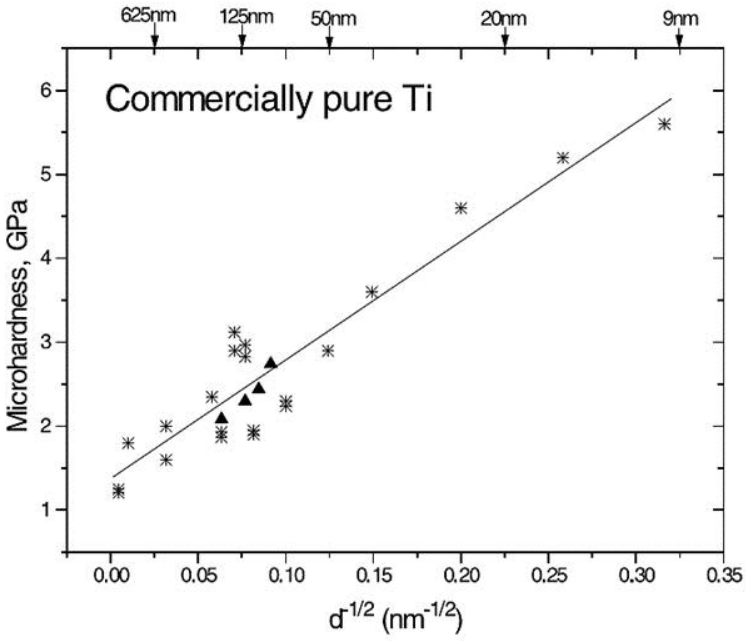

Figure 2.16: The relationship between microhardness and grain size at room temperature for commercial purity Ti processed at room temperature in HPT [82][84][85][86][87].

2.2.4.2 Mechanical properties at elevated temperatures: Superplasticity

The phenomenon of superplasticity is defined as the ability of a material to undergo an extensive elongation prior to fracture without any significant necking [88]. This phenomenon is measured usually under a tension deformation mode and the measured superplasticity in general reaches about 400 % [89]. The benefit of superplasticity lies in the possibilities of superplastic forming in which sheets of metals and alloys can be manufactured into complex-shaped parts for (amongst others) transportation and aerospace applications [90]. At relatively low temperature ($T < 0.4\,T_m$) and in tension, the polycrystalline material strain hardens and flows plastically. The mechanical behaviour of the material in the plastic region of deformation can be described by [25]:

$$\sigma = K\varepsilon^n \tag{1.5}$$

where σ is the true stress or flow stress, ε is the true strain, K is the strength coefficient and n is the strain–hardening exponent. This expression describes the stable behaviour of the material from the point at which the plastic flow occurs until the point of the maximum load at which the material starts to neck or becomes plastically unstable [88]. At elevated temperatures ($T > 0.5\,T_m$), the strain hardening decreases and the material steadily flows without necking. Thus the material exhibits superplastic behaviour at such temperatures prior to fracture [91]. The steady–state behaviour of the material at elevated temperatures can be expressed by [92]:

$$\dot{\varepsilon} = A\frac{DG\boldsymbol{b}}{kT}\left(\frac{\boldsymbol{b}}{d}\right)^{p}\left(\frac{\sigma}{G}\right)^{n} \tag{1.6}$$

where $\dot{\varepsilon}$ is the steady–state strain rate, A is a dimensionless constant, D is the appropriate diffusion coefficient $D = D_o exp(-Q/RT)$, D_o is the pre–exponential complex constant, Q is the activation energy, R is gas constant, G is the dynamic shear modulus, $\boldsymbol{b}$ is the Burgers vector, k is Boltzmann's constant, T is the absolute melting point, d is the grain size, σ is the applied stress (or flow stress), p and n are the exponents of the inverse grain size and normalized stress, respectively. This constitutive relationship describes the development of superplasticity during hot deformation with finer grain sizes [93]. The relation between the flow stress and strain rate can be realized through the strain–rate sensitivity (m), which defines as the variation in the flow stress with the variation in the strain rate at a specific temperature and it is given by [94]:

$$m = \frac{\partial ln\sigma}{\partial ln\dot{\varepsilon}} \tag{1.7}$$

The value of strain–rate sensitivity can be determined from the slope of the logarithmic plot of the flow stress versus the strain rate as shown schematically in Figure 2.17 [94]. Three distinctive regions have been identified from Figure 2.17 [94], which are region I, II and III and these regions have different values of flow stress and strain–rate sensitivity [94]. In the first and third regions, a change in the

shape of grains occurred where the elongation of grains is found along the direction of tension. The low values of strain–rate sensitivity, $m \approx 0.2$, that have been obtained indicate the occurrence of non–superplastic behaviour [88]. In the second region, the grains had equiaxed shapes with a fine grain size. The value of strain–rate sensitivity was higher than in the first and third regions, $m \approx 0.5$, with occurrence of superplastic elongations [95].

The difference in these three regions with regard to elongation can be seen in Figure 2.18 [96], where the regions I, II and III are depicted. A high elongation has been found in the second region, which is consistent with the high value of strain–rate sensitivity, whereas the first and third regions are characterized by lower elongations associated with low values of strain–rate sensitivity [97]. The effect of temperature is obvious in prompting the superplasticity at fast and moderate strain rates in the second and third region, whilst the superplasticity is decreased in the first region where some grain growth happened at slow strain rates [96]. There are many prerequisites for achieving superplastic elongations in metallic materials as follows:

1. Grain size:

The grain size of the material must be fine and equiaxed, typically less than 10 μm. Equiaxed–shaped fine grains can experience gliding over each other more easily than elongated grains [88]. It has also been found that decreasing the grain size leads to an increase in the optimum strain rate for superplastic deformation. Therefore, for a material with finer grain size and at a specific strain rate, the flow stress required would be lower which is advantageous in the superplastic forming industry. The dependency of strain rate $(\dot{\varepsilon})$ on grain size (d) can be described by the following relation [91]:

$$\dot{\varepsilon} \propto d^{-p} \tag{1.8}$$

where p is the exponent of grain size and it equals 2 or 3. The effect of grain size on the strain rate is illustrated in Figure 2.19 [98] and Figure 2.20 [19]. The effect of grain size reduction and the increase in temperature result in occurrence of the superplastic behaviour at higher strain rates [97].

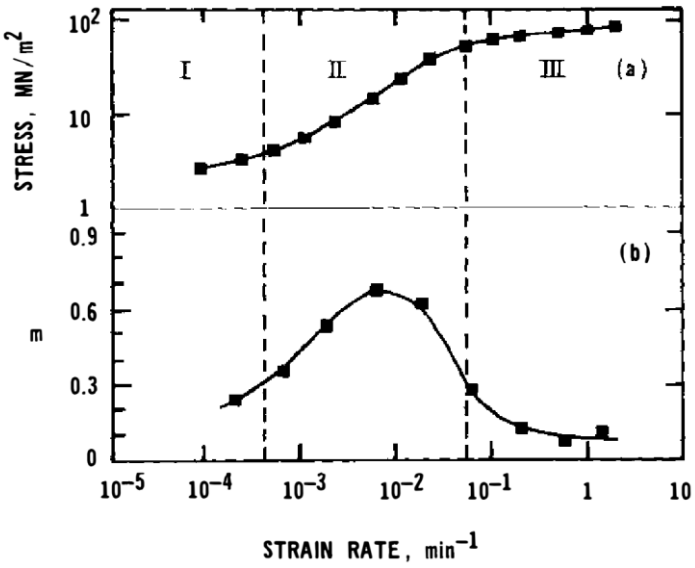

Figure 2.17: The variation in (a) flow stress–strain rate curve and (b) strain–rate sensitivity (m) versus the strain rate for 66.8wt.%Mg–33.6wt.%Al eutectic alloy [94].

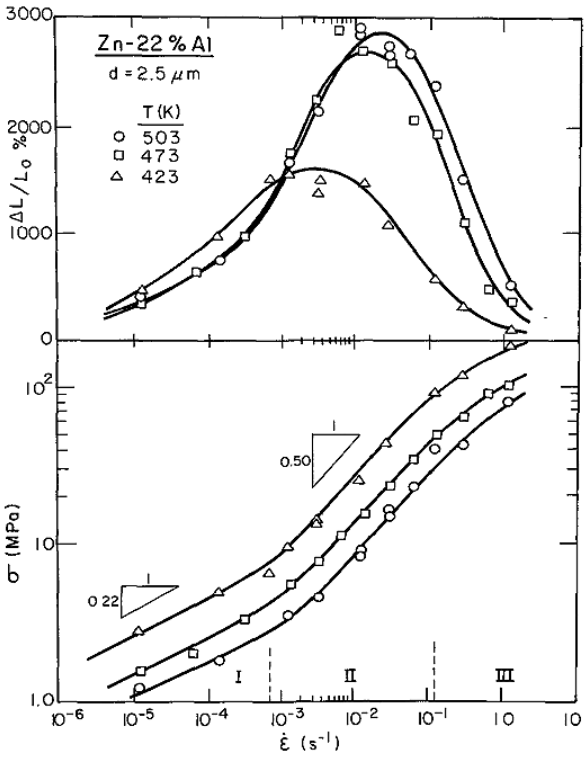

Figure 2.18: The variation in elongation–to–fracture (top) and flow stress (bottom) versus the strain rate for Zn–22%Al alloy at different temperatures [96].

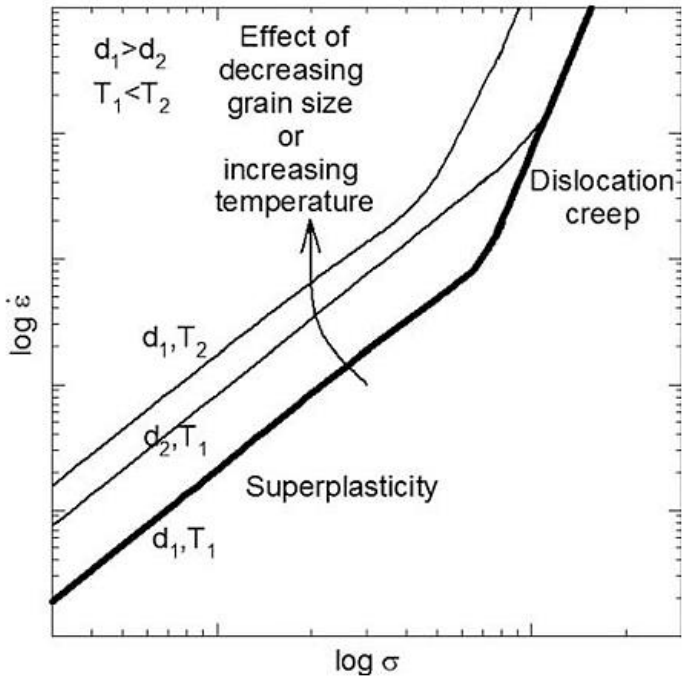

Figure 2.19: Schematic illustration showing the effect of grain size reduction and temperature on the strain rate and flow stress [98].

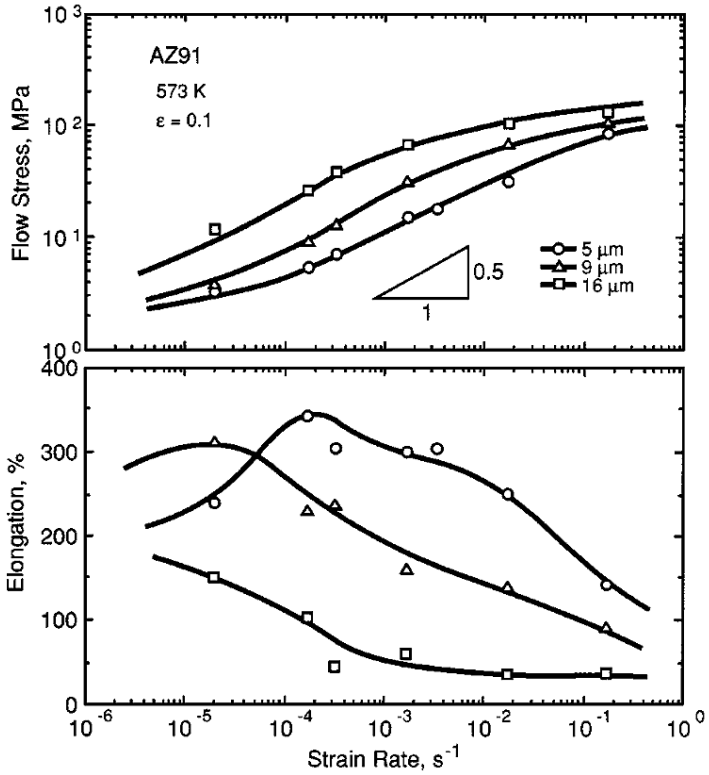

Figure 2.20: Variation in flow stress and elongation as a function of strain rate and grain size at 573 K for extruded AZ91 magnesium alloy [19].

2. Testing temperature:

The temperature of deformation should exceed half that of the absolute melting temperature of the material, to promote the superplastic flow of the material. Figure 2.21 [99] shows the effect of testing temperature on the superplastic behaviour of the AZ61 alloy, where an increase in temperature above 0.5 T_m leads to significant superplasticity especially at fast strain rates. However, the effect of temperature on the superplasticity is detrimental at the slowest strain rates due to the occurrence of grain growth [96].

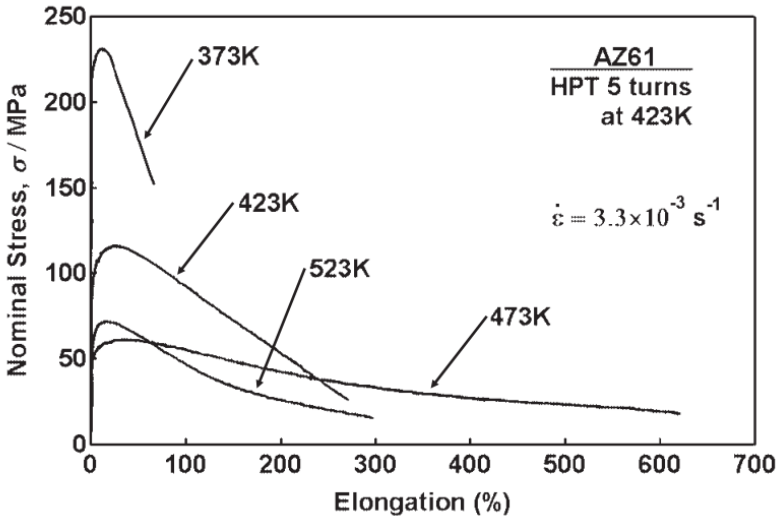

Figure 2.21: The effect of testing temperature on the elongation for the AZ61 magnesium alloy processed by HPT at 423 K for 5 turns and then tested in tension at a strain rate of 3.3×10-3 s-1 [99].

3. Existence of secondary phases:

Single–phase materials with fine grains tend not to exhibit significant superplasticity compared to their counterparts containing secondary phases, because of the rapid grain growth that happens at elevated temperatures [95]. The presence of second–phase particles at the grain boundaries aids retention of the fine grain size in the matrix material and thus increases the range of superplastic deformation. Fine grains and a homogenous distribution of second–phase particles are necessary for inhibition of grain growth and can enhance grain–boundary sliding [97]. The effect of the presence of these second phases on the

thermal stability of fine–grained aluminium alloys processed by ECAP can be seen in Figure 2.22 [100][101][102][103], where the microstructural stability has been enhanced due to formation of fine precipitates that retarded the grain growth at elevated temperatures [96].

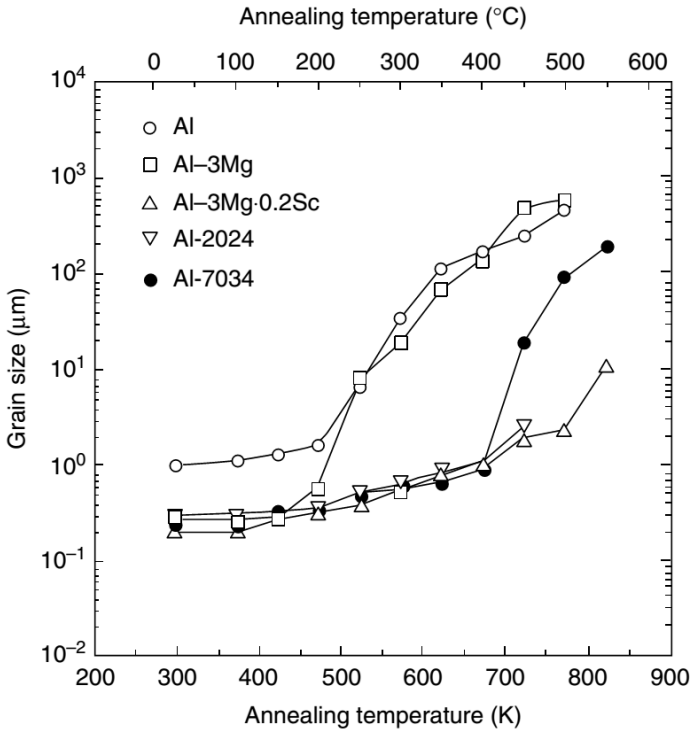

Figure 2.22: The variation in grain size with temperature after annealing for 1 hr for ECAP processed pure aluminium, Al–3% Mg alloy [100], Al–3% Mg–0.2% Sc alloy [101], Al–2024 alloy [102], Al–7034 alloy [103].

4. Nature of grain boundaries:

High–angle grain boundaries (HAGB) promote grain–boundary sliding more than low–angle grain boundaries (LAGB) [91]. It has been found that the misorientation in materials processed by SPD techniques increases with increasing imposed plastic strain. Therefore, a high fraction of HAGB volumes is anticipated in these ultrafine–grained materials and superplastic elongations are expected through the increased degree of grain–boundary sliding [89].

2.2.4.3 Mechanisms of Superplasticity

A number of mechanisms for superplastic behaviour have been proposed to explain the variation in superplasticity with the grain size, temperature and strain rate [88][95]. There are three distinctive regions in Figure 2.17 [94] and Figure 2.18 [96], with different values for elongation and strain–rate sensitivity as a consequence of variation in the flow stress, strain rates, grain size and temperature [95][104]. Diffusion creep, grain–boundary sliding and dislocation creep have been proposed as deformation mechanisms for superplasticity as illustrated in Figure 2.23 [105]. It has been suggested that the deformation in each region is controlled by one or more mechanisms [93][106]. Each mechanism is reviewed in the following section according to the increase in flow stress as illustrated in Figure 2.23 [105].

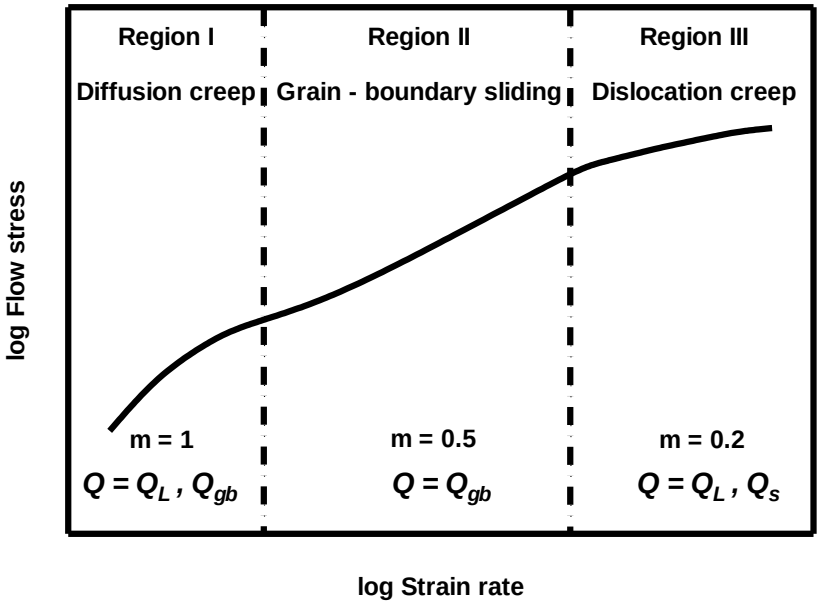

Figure 2.23: Schematic illustration of different mechanisms of superplasticity with their corresponding values of the strain–rate sensitivity and activation energies [105].

2.2.4.3.1 Diffusion Creep

This mechanism dominates during the low flow stress regime with a corresponding value of $m \approx 1$, i.e. region I, as illustrated in Figure 2.17 [94] and Figure 2.23 [105]. Diffusion within the material occurs during deformation at high temperatures

($T \approx 0.9\,T_m$) by diffusional transportation of atoms along the grain boundaries or through the grains [88]. The atomic flow in diffusion is driven by the applied stress and it arises from compression sites to tension sites. Two forms of diffusional creep have been proposed: Nabarro–Herring creep and Coble creep [107].

In Nabarro–Herring creep, the diffusional flow occurs through the grain as illustrated schematically in Figure 2.24 (a) [91]. This flow includes the movement of vacancies under the tension stress from the grain boundaries existing perpendicular to the direction of the tension towards the grain boundaries lying parallel to direction of tension [108]. Therefore, the flow of vacancies moves through the grain as shown in Figure 2.24 (a) [91], which causes elongation of the grain in the direction of stress. The gradient in the concentration of vacancies is the driving force for transportation of atoms under the applied stress. It should be noted that the flow of vacancies is opposite to the flow of atoms [109]. The mechanism of Coble creep supposes the occurrence of diffusion along the grain boundaries instead of within the grains as illustrated schematically in Figure 2.24 (b) [91]. Therefore, diffusional flow happens rapidly through the grain boundaries rather than the interior of grains [110].

Diffusion through the interior of grains requires higher energy than for Coble creep. Therefore, Nabarro–Herring creep occurs at relatively higher temperatures than for Coble creep [95]. Thus, Nabarro–Herring creep has an activation energy for lattice diffusion (Q_L) that is higher than the activation energy for grain–boundary diffusion (Q_{gb}) for Coble creep [91]. Nabarro–Herring creep also has a lesser grain size dependence than for Coble creep, where the reduction in grain size leads to an increase in the proportion of grain boundaries and hence enhances the diffusional Coble creep along the grain boundaries [107].

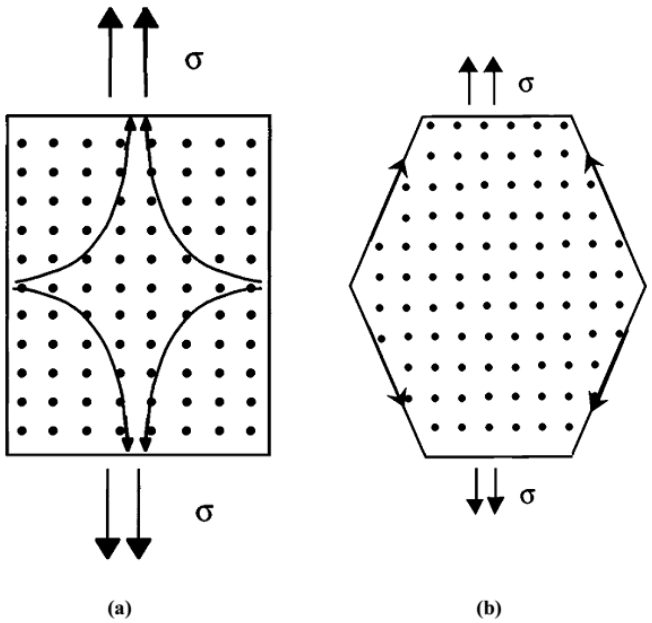

Figure 2.24: Schematic illustration of (a) Nabarro–Herring creep and (b) Coble creep [91].

2.2.4.3.2 Grain–Boundary Sliding

This mechanism dominates during the moderate regime of the flow stress with a corresponding value of $m \approx 0.5$, i.e. region II, as illustrated in Figure 2.17 [94] and Figure 2.23 [105], where the activation energy is the activation energy for grain–boundary diffusion (Q_{gb}). Grain–boundary sliding (GBS) refers to the displacement of grains over each other under the influence of the external stress, and this sliding occurs usually along their grain boundaries [111][112][113][114]. Grain–boundary sliding has been proposed as the dominant mechanism for superplasticity at elevated temperatures and under large strains [115].

There are two types of grain–boundary sliding, Rachinger sliding [111][112] and Lifshitz sliding [116]. Rachinger sliding is represented as pure grain–boundary sliding where the grains retain their equiaxed shapes during superplastic deformation with an increase in the number of sliding grains along the axis of applied stress [107]. This type of grain–boundary sliding leads to superior superplastic ductilities in fine–grained materials, where the formation of cavities is less likely in these materials with no need for an accommodation process [106]. In Lifshitz sliding, the grain–boundary sliding acts as accommodation process for the

diffusion creep. According to this mechanism, there is no change in the number of grains along the along the axis of applied stress and it leads to the occurrence of elongated grains [117].

It has been proposed that grain–boundary sliding requires an accommodation mechanism to maintain itself and to minimize cavitation under high–temperature deformation [93]. This need has arisen due to the presence of grains with either an inconsistent orientation for sliding and/or microstructure irregularities such as grain–boundary ledges and triple junctions [95]. Diffusional accommodation and dislocation accommodation have been proposed as accommodation mechanisms for this grain–boundary sliding [88][95][114].

2.2.4.3.2.1 GBS accommodated by dislocation motion

Several models have been proposed to explain the accommodation of grain–boundary sliding with dislocation movement during the superplastic regime, some of which are reviewed in this section. The mechanism of sliding of grains as one ensemble during superplastic regime has been proposed by Ball and Hutchison [118]. The presence of a grain which is unsuitably oriented for sliding can obstruct the movement of other sliding grains as illustrated in Figure 2.25 [119]. This obstruction leads to the occurrence of a stress concentration at the blocking grain, which generates dislocations in the blocking grain as illustrated in Figure 2.25 [119]. The accumulation of these dislocations at the opposite grain boundary produces a back stress that opposes the motion of additional dislocations until it stops the generation of dislocations and stops the sliding of the grains. Dislocation climb will occur at the head of the pile up into and along the grain boundaries into annihilation sites. Then further sliding will occur again by continuous replacement of these dislocations, and grain boundary diffusion controls the dislocation climb [118].

A modification to the Ball–Hutchison model has been proposed by Mukherjee, where it has been assumed that the grains can rotate and slide individually instead of their sliding as a group as in the Ball–Hutchison model. The ledges and

protrusions of grain boundaries act as sources for dislocations under the effect of sliding shear, which move through the grain and pile up at the grain boundaries and later climb into the grain boundary. The rate of dislocation climb into annihilation sites that are located at the grain boundary will control the sliding of grains [120]. Another mechanism proposed to accommodate grain–boundary sliding has been proposed by Gifkins and it is based on grain–boundary dislocations. The pile up of these dislocations at the triple points results in a stress concentration, which is relaxed by the dissociation of these new grain–boundary dislocations [114]. The new dislocations have the ability to move along the grain boundary and / or within the grains. Annihilation or combination of the new grain–boundary dislocations with each other during their climbing or gliding along the grain boundary generates different grain–boundary dislocations as illustrated in Figure 2.26 [90]. Gifkins's model has been called a core and mantle theory, where the grain is considered as a non–deforming core and the motion of the dislocations (climb and glide) in the mantle region or the periphery of grain can accommodate the grain–boundary sliding. In this model, grain rotation has been suggested through the material flow in the mantle region, and therefore, the movement of grains is introduced [121] as illustrated schematically in Figure 2.27 [91][122].

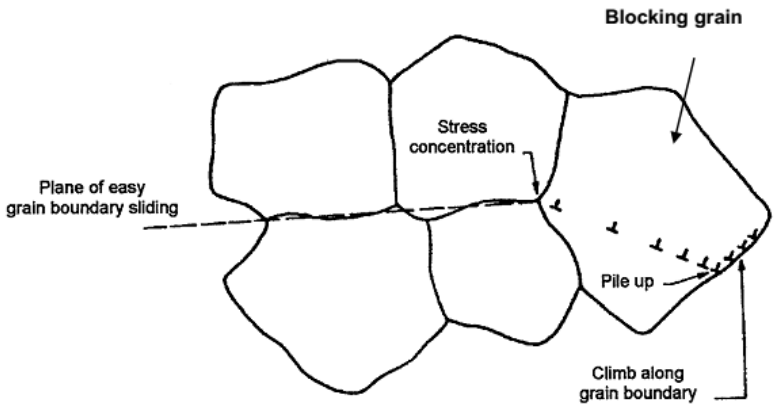

Figure 2.25: Schematic illustration of Ball–Hutchison model for grain–boundary sliding accommodated by dislocation motion [119].

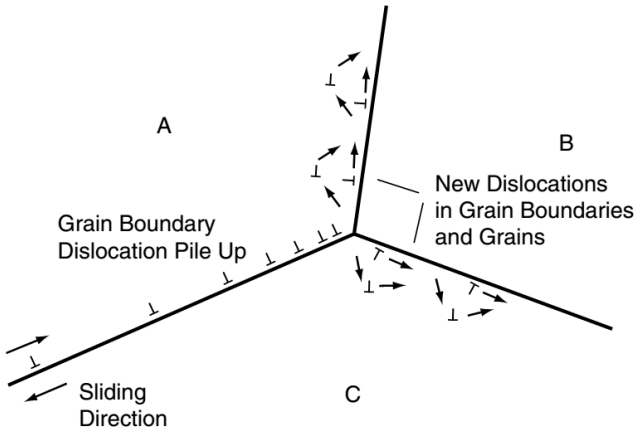

Figure 2.26: Schematic illustration of Gifkins's model for grain–boundary sliding accommodated by dislocation motion [90].

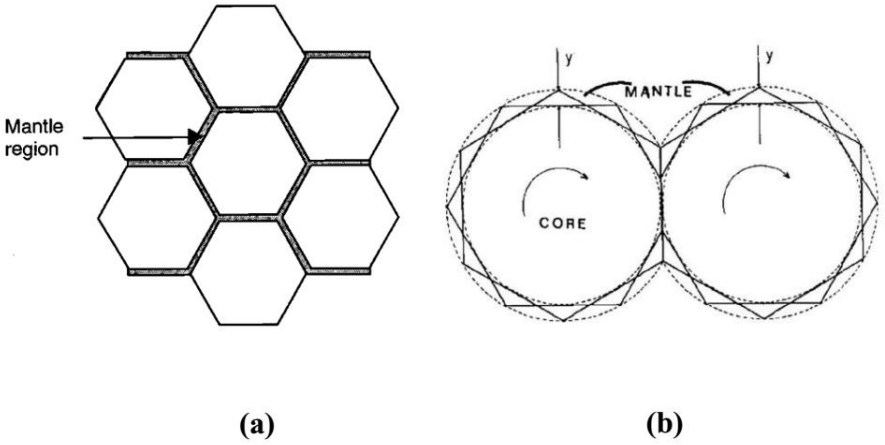

Figure 2.27: Schematic illustration of (a) the core (grain) and mantle regions (peripheries of grains) [91], and (b) The flow of material along the mantle region and rotation of the cores (grains) [122].

2.2.4.3.2.2 GBS accommodated by diffusion

This mechanism has been proposed by Ashby and Verrall in which grain–boundary sliding is accommodated by diffusional flow. In this model, grain switching occurs in a group of grains to avoid elongation of grains under the applied stress [123]. Figure 2.28 illustrates a cluster of four grains which change their shapes temporarily during sliding under the tensile stress. To maintain the continuity during the deformation, a diffusional flow occurs across the grain boundary and equiaxed grains are restored [119].

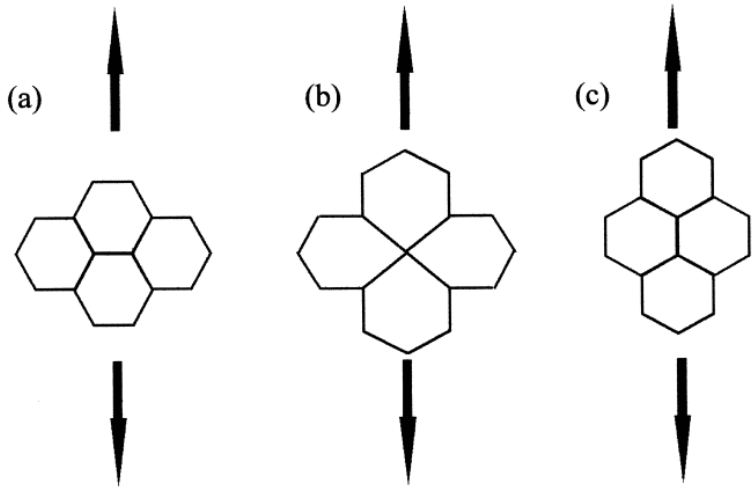

Figure 2.28: Schematic illustration of Ashby–Verrall model for grain–boundary sliding accommodated by diffusional flow and grain switching [119][123].

2.2.4.3.3 Dislocation Creep

This mechanism dominates during the high regime of the flow stress with a corresponding value of $m \approx 0.2$, i.e. region III, as illustrated in Figure 2.17 [94] and Figure 2.23 [105]. The dislocation slip in the grains controls the activity of the dislocation creep as illustrated in Figure 2.29 [91], where dislocation slip occurs by the glide of dislocations on slip planes and their climb over obstacles such as solute atoms and precipitations. The deformation in region III is characterized by the formation of dislocation tangles, elongated grains and the flow stress is less sensitive to the grain size and strain rate than observed in region II or superplastic region [105]. Activation of extra slip systems occurs with increasing temperature that promotes the gliding of dislocations. When gliding dislocations are blocked by an obstacle, as illustrated in Figure 2.29, they pile up against that obstacle until their concentration increases [25]. Therefore, a back stress occurs at the head of dislocation pile up and thermal activation at elevated temperatures, the blocked dislocation can climb by diffusion to another slip plane. This process can repeat in this sequence to produce a dislocation creep through glide and climb of dislocations [124].

Dislocation creep occurs at both high temperature and stress as the gliding of dislocations becomes more complicated with increasing density of intersected dislocations on different slip planes [25], as well as the climb process of the gliding dislocation being a diffusion controlled process that is activated at elevated temperatures. Interaction of the gliding dislocations with the solute atoms or any other obstacles results in reduction in the rate of gliding [119]. Therefore, the glide process will be slower than the climb process and solute drag creep or dislocation glide controlled creep will occur with an activation energy equal to Q_S. The domination of the solute drag creep mechanism requires a high concentration of solute atoms, significant difference in the lattice parameters and a low diffusivity of solute atoms [125].

The climb controlled dislocation creep was proposed by Weertman [126]. In this model the piled up dislocations at a slip barrier leads to hindrance of their motion and the occurrence of strain hardening. Climb of these dislocations under thermal excitation results in their escaping away from the pile up location and annihilation [25]. When the rate of strain hardening equals the rate of recovery, a steady state will occur, and the rate of creep is controlled by the rate of dislocation climb with activation energy equals to Q_L [107]. At elevated temperatures and in the presence of compression and tension regions ahead of the slip direction leads to sequential absorption and creation of vacancies that increases the rate of dislocation climb [127].

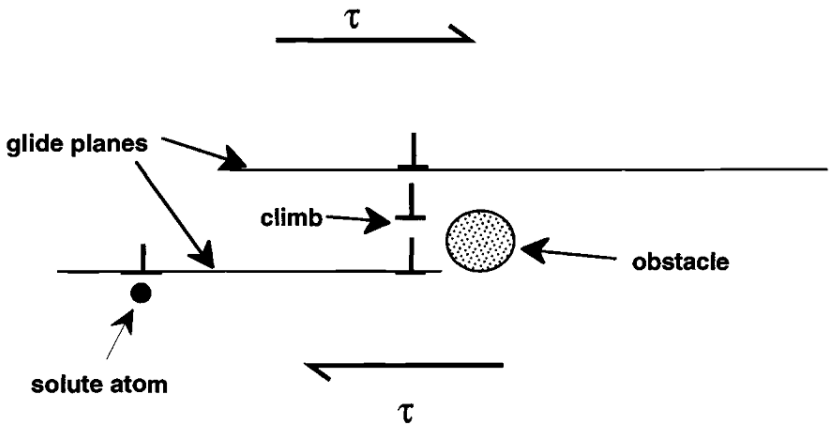

Figure 2.29: Schematic illustration of glide and climb processes during dislocation creep [91].

2.2.5 High–Pressure Torsion (HPT)

High–pressure torsion is one of the SPD techniques that is used for fabrication of bulk nanostructured microstructure with a grain size of 100 nm or less [1]. A schematic illustration of HPT processing is shown in Figure 2.30 [128]. The disk–shaped sample is located in a small depression between the two anvils, and compressive pressure and rotation are applied to the sample simultaneously [129]. High–pressure torsion is performed at room temperature and/or at elevated temperatures using an applied pressure of several GPa. The plastic torsional strain is imposed into the sample by the rotation of the lower anvil. Due to the rotation of the lower anvil during the processing, the sample deforms plastically through surface frictional forces [1][6].

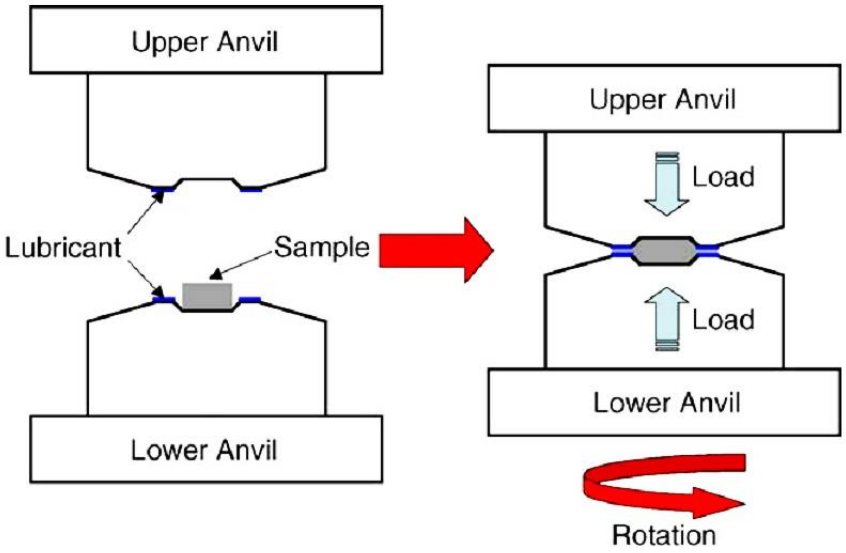

Figure 2.30: Schematic illustration of the HPT setup before and after application of loading [128].

2.2.5.1 The Imposed Strain by HPT

The shear strain that is imposed during HPT can be calculated by the following relation [6][130]:

$$\gamma = \frac{2\pi N r}{h} \tag{1.9}$$

where h is the thickness of disk, N is the number of turns and r is the distance from the centre of the disk. The equivalent von Mises strain ($\varepsilon_{eq} = \gamma/\sqrt{3}$) [131] was used to compare the value of shear strain in Eq. (1.9) with other deformation modes in rolling, drawing or extension. Therefore, the true strain imposed by HPT becomes [132][133]:

$$\varepsilon_{true} = \frac{2\pi Nr}{h\sqrt{3}} \tag{1.10}$$

Practically, the compressive pressure leads to a decrease in the thickness of the disk during HPT processing, thus the true strain becomes [60][134]:

$$\varepsilon_{true} = ln\left(\frac{2\pi Nrh_0}{h^2}\right) \tag{1.11}$$

where h_0 and h represent the initial and the final thicknesses of the HPT disk, respectively. In practice, the number of turns is used to predict the imposed strain on the disk during HPT processing [1][60].

2.2.5.2 The Configurations of HPT

Three types of configurations of HPT processing are available as illustrated schematically in Figure 2.31, which are the unconstrained, constrained, and quasi–constrained HPT [135]. In the unconstrained HPT as shown in Figure 2.31 (a), the material of the disk flows freely out of the anvils during processing. [135][136]. In the constrained HPT that is shown in Figure 2.31 (b), the disk fits into a depression located on the lower anvil. This setup leads to no outward flow and introduces an effective back pressure into the processing zone [135]. Practically, the idealised constrained condition is hard to achieve, so it is common to perform the HPT processing under a quasi–constrained condition as illustrated in Figure 2.31 (c), where the material under processing undergoes a limited flow out of the depression [137]. This type of HPT was used in the current study.

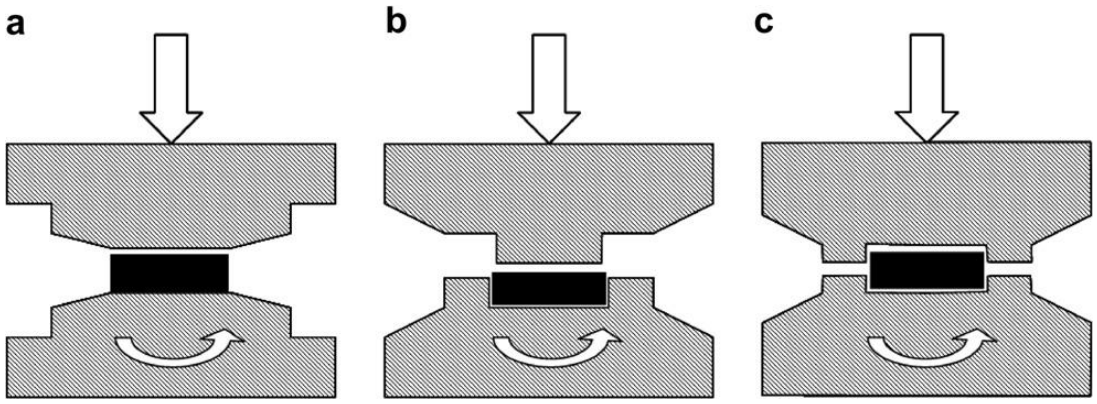

Figure 2.31: An illustration of HPT setups for (a) unconstrained, (b) constrained, and (c) quasi–constrained HPT [135].

2.2.5.3 Microstructural Inhomogeneity by HPT Processing

The existence of microstructural inhomogeneity in UFG materials processed by HPT is important because the resulting properties significantly depend on the microstructure after processing [138]. A variation in the imposed strain was found in the disk, and this strain decreases to almost zero at the centre of the disk, as predicted by Eq. (1.10). Therefore, this variation in the strain distribution through the sample leads to an inhomogeneous microstructure after HPT processing [139]. Measurements of local microhardness and microstructural microscopy were used to investigate the microstructural homogeneity / heterogeneity of the processed material [1][131]. It has been shown that the measurements of the microhardness after HPT processing along the disk's diameter give a reasonable indication of the microstructural evolution [140][141].

It has been shown that the hardness increases significantly in the initial stage of processing at the edge regions, whereas a lower hardness appears in the centre region (although it is still higher than that of the as–received material). A further straining was found to increase the hardness at the centre region, so that it becomes close to the values of hardness at the edge regions [1]. This trend has been found in many materials processed using HPT such as Al–3wt.%Mg–0.4wt.%Cu alloy [132], austenitic steel [138], pure nickel [141], Al–3wt.%Mg–0.2wt.%Sc alloy [142], Mg–9wt.%Al alloy [18]. Examples of this trend are shown by Figure 2.32 and Figure 2.33 for nickel [141] and austenitic steel [138],

respectively. This trend reveals the microstructural heterogeneity that is introduced in the initial stage of HPT processing, whereas the microstructure at the edge regions is finer than that at the centre regions, as shown in Figure 2.34 and Figure 2.35 for nickel [141] and austenitic steel [138], respectively.

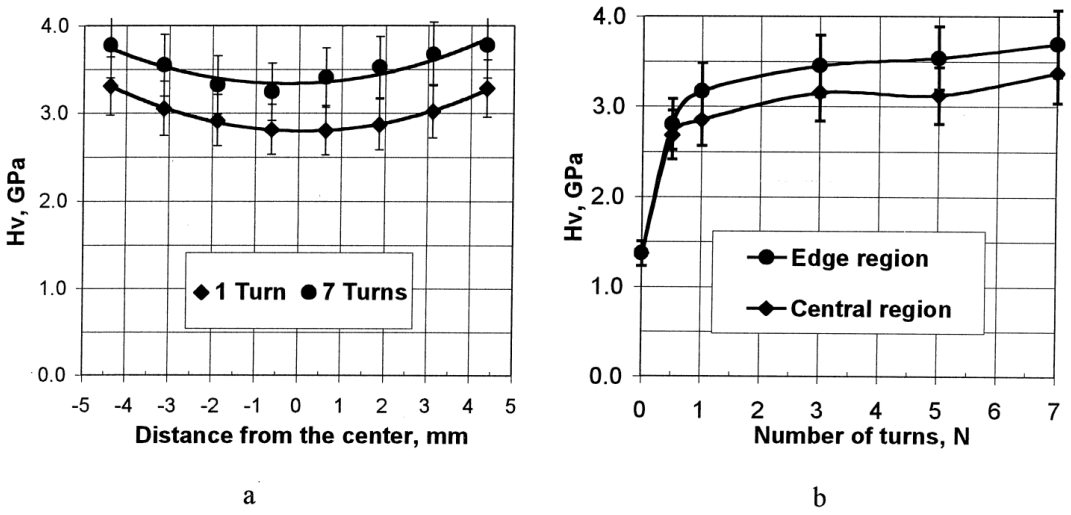

Figure 2.32: Distribution of microhardness for nickel processed by HPT using an applied pressure of 6.0 GPa at room temperature: (a) along the diameter of the disk for two different number of turns and (b) as a function of the number of turns at the edge and centre regions [141].

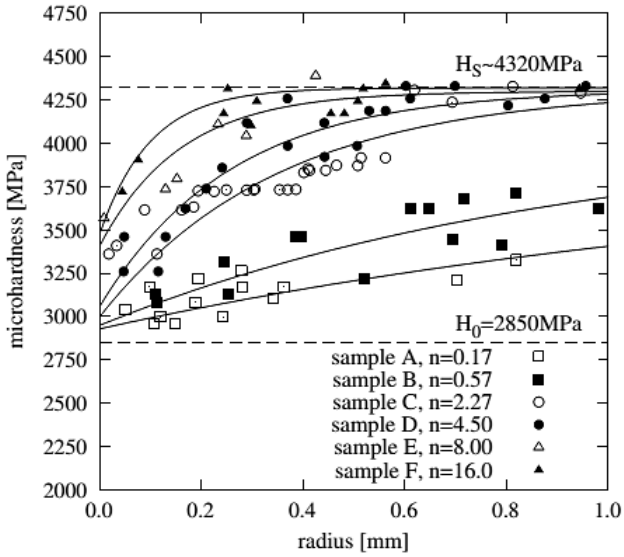

Figure 2.33: Distribution of microhardness after HPT processing for the austenitic steel disks for different numbers of turns [138] (The Figure above contains an error in the axis of radius, where the microhardness values were plotted against a fraction of the radius instead of the whole radius (0 – 5 mm)).

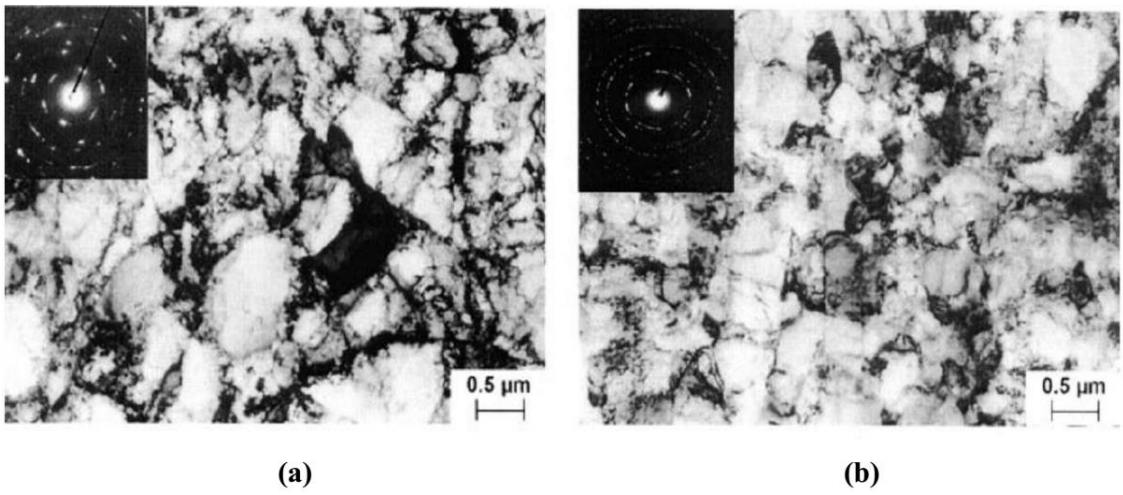

Figure 2.34: Microstructure observation for nickel processed by HPT for 5 turns using an applied pressure of 1.0 GPa at room temperature at (a) the centre region and (b) the edge region [141].

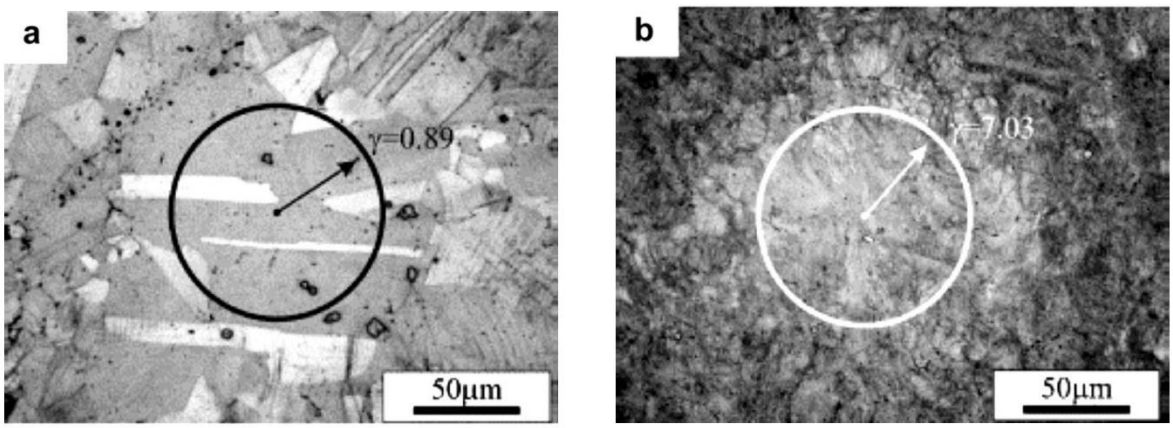

Figure 2.35 Microstructure observations of austenitic steel disk processed by HPT at the centre region for: (a) 2.27 turns and (b) 16 turns [138].

Further studies were conducted to evaluate the homogeneity and/or heterogeneity of microstructure after HPT processing by inspecting the values of microhardness over the entire horizontal cross–sections of the processed disk. The microhardness values were taken by following a rectilinear grid across the horizontal cross–sections of the disk [139]. The variations in distribution of microhardness over the horizontal cross–sections were represented using colour–

coded maps. These measurements provide a comprehensive representation of variations in the microhardness at different locations on the surface of the processed disk for different conditions of HPT processing [143]. The colour–coded maps were used to inspect the distribution of hardness after HPT processing for many materials such as high–purity Al (99.99%) [139], Al–1wt.%Mg alloy [144], Zn–22wt.%Al alloy [145], Al–9.4wt.%Zn–2.5wt.%Mg–2.5wt.%Cu alloy [146], and Cu–0.1wt.%Zr alloy [147].

The aforementioned studies revealed two phenomena: first, the presence of inhomogeneity in microstructures at the initial stages of processing, since fine grains were found at the centre regions and relatively large grains at the edge regions. Therefore, the higher values of hardness existed at the centres than at the edge regions of processed disks. It was shown that the subsequent processing resulted in a decrease in the microstructural heterogeneity and microhardness values at the centre regions, in addition to stability in the hardness distribution across the entire horizontal cross–sections of processed disks. An example of the latter behaviour is shown in Figure 2.36 for pure aluminium [139][143].

Second, an increase in microhardness from the edge regions towards the centre regions was observed at the initial stages of processing, which is symmetric with a gradual microstructural evolution from the edges towards the centres of the processed disks. The subsequent deformation resulted in a reasonable homogeneity in both microstructure and microhardness after a sufficient number of turns, since the microstructure became uniformly finer and homogeneous [14]. Examples of the latter behaviour are shown in Figure 2.37 and Figure 2.38**,** for Al–1wt.% Mg alloy [144] and Cu–0.1wt.%Zr alloy, respectively [147].

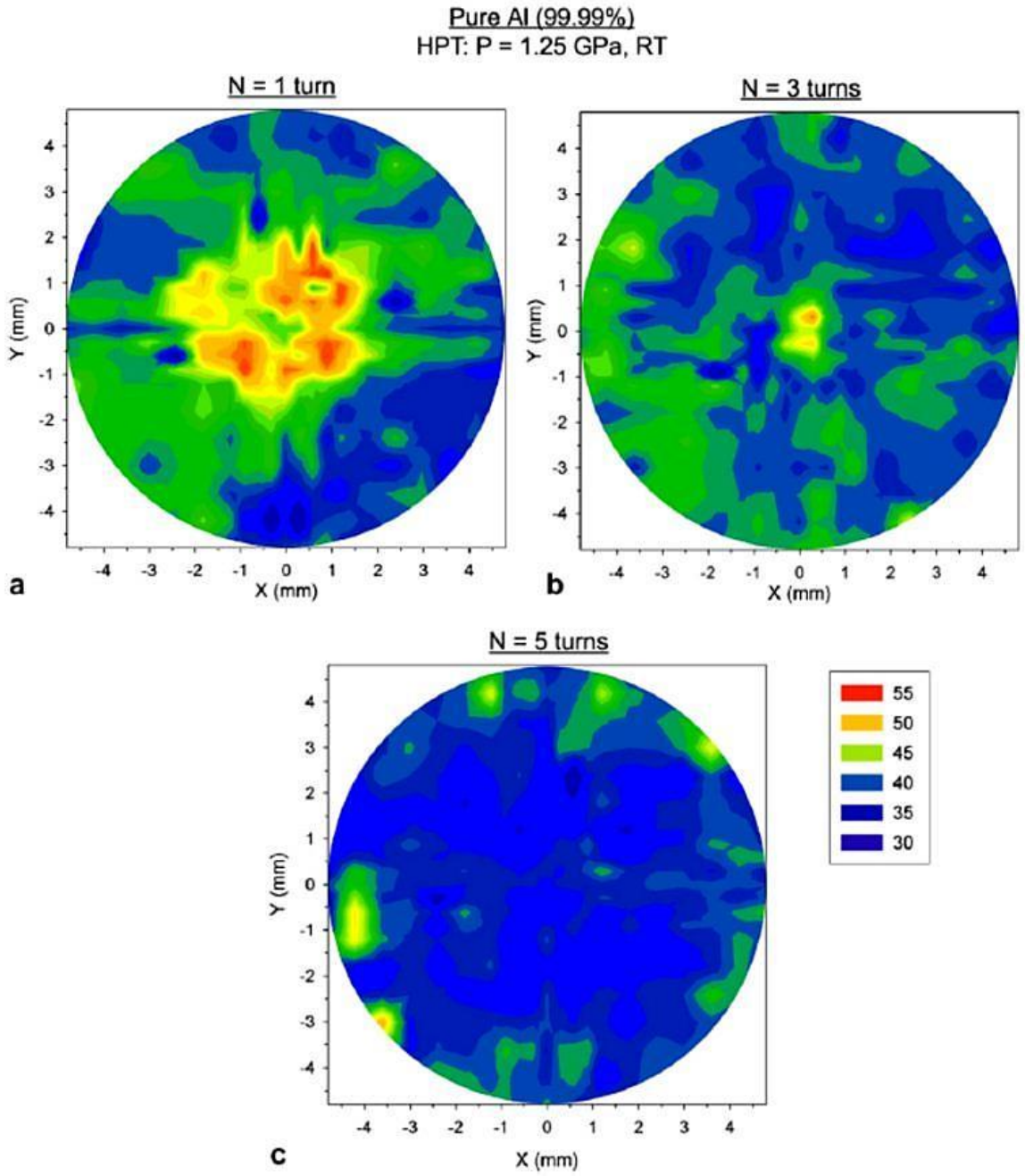

Figure 2.36: Vickers microhardness maps for pure aluminium (99.99%) processed by HPT at room temperature and a pressure of 1.25 GPa for: (a) 1 turn, (b) 3 turns and (c) 5 turns [139].

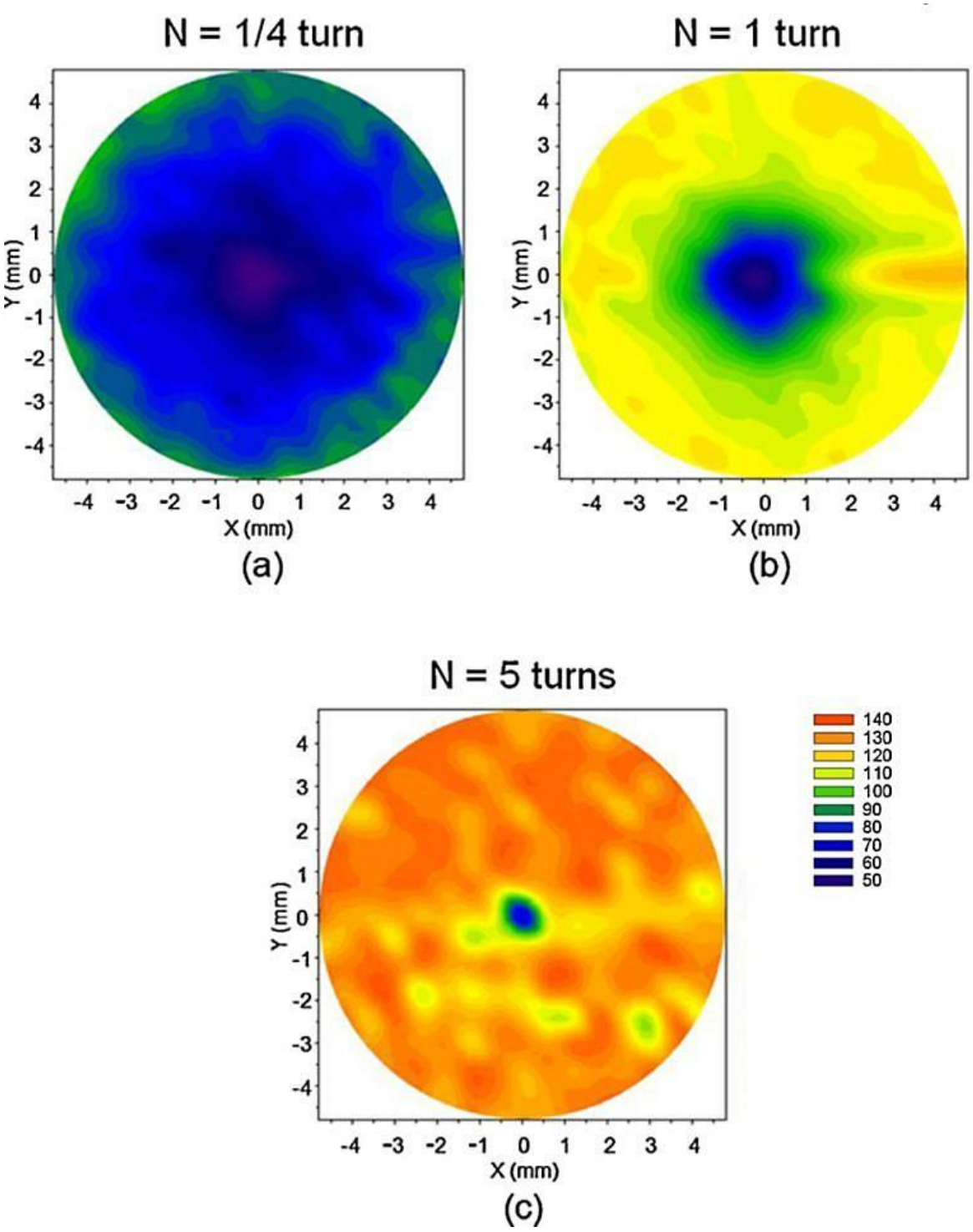

Figure 2.37: Vickers microhardness maps for Al–1wt.%Mg alloy processed by HPT at room temperature and at a pressure of 6.0 GPa for: (a) 1/4 turn, (b) 1 turn and (c) 5 turns [144].

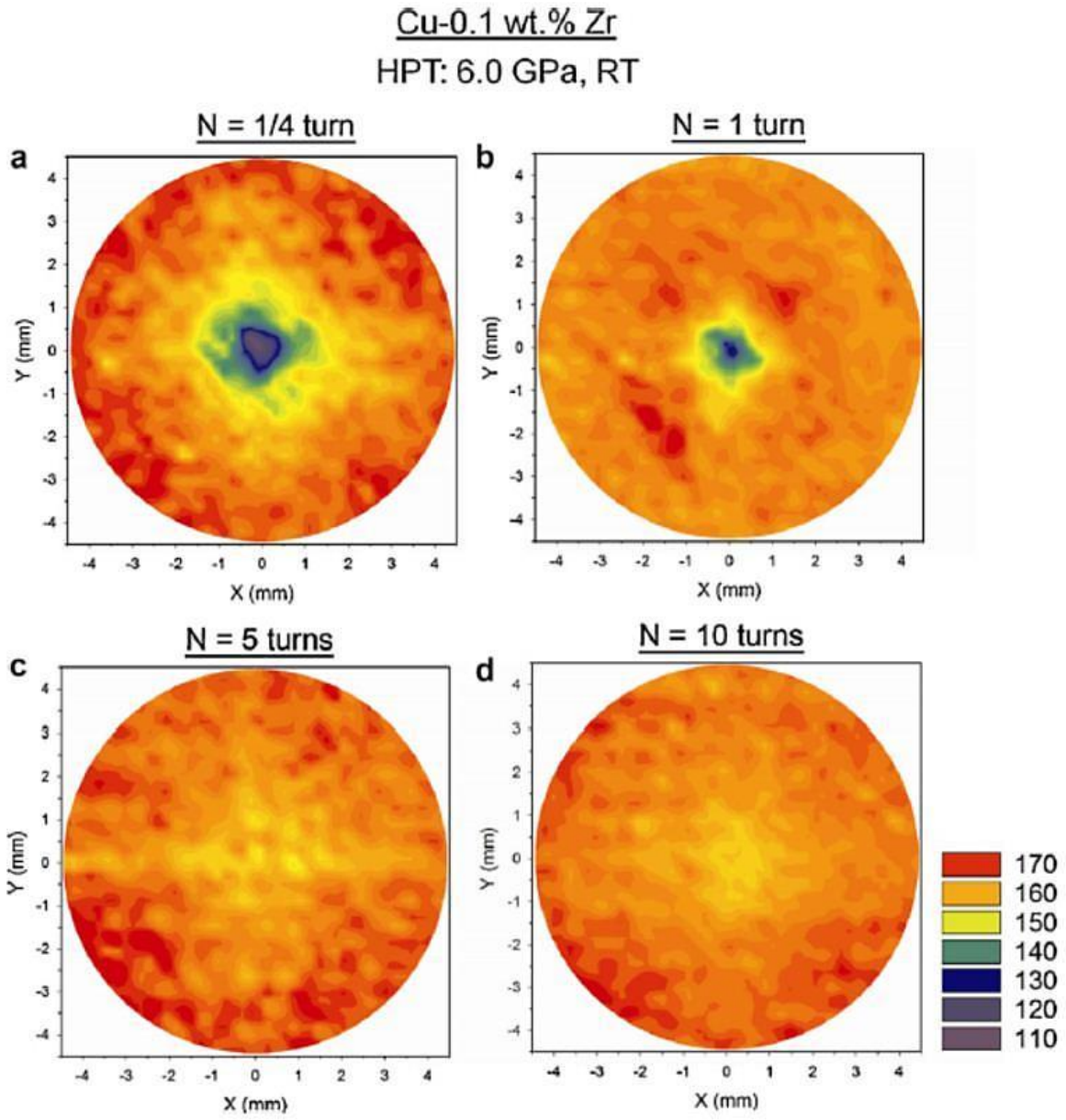

Figure 2.38: Vickers microhardness maps for Cu–0.1wt.%Zr alloy processed by HPT at room temperature and at a pressure of 6.0 GPa for: (a) 1/4 turn, (b) 1 turn, (c) 5 turns and (d) 10 turns [147].

2.2.6 The Basic Factors in HPT Processing

2.2.6.1 Role of the Applied Pressure in HPT processing

The effect of the applied pressure on the microhardness is shown in Figure 2.39 [141]. Nickel disks were processed by HPT at room temperature for 5 turns under pressures of 1.0 and 9.0 GPa. The microhardness at the edge regions of the disk was larger than that at the centre region using the lower applied pressure (1.0 GPa). Increasing the applied pressure resulted in an increase in the microhardness with a reasonable uniform distribution along the diameter of the disk. It was found that the increase in the applied pressure leads to a greater grain refinement as shown in Figure 2.40 [141]. The role of the hydrostatic compression stress is to enhance the fracture strain of the material under processing, and thus improves the deformability of the material under processing [6]. Moreover, the high hydrostatic pressure prevents the sliding between the anvils and the top and bottom surfaces of the disk under processing. The high hydrostatic pressure is important for microstructural refinement by means of introducing a large amount of dislocations into the processed microstructure [138].

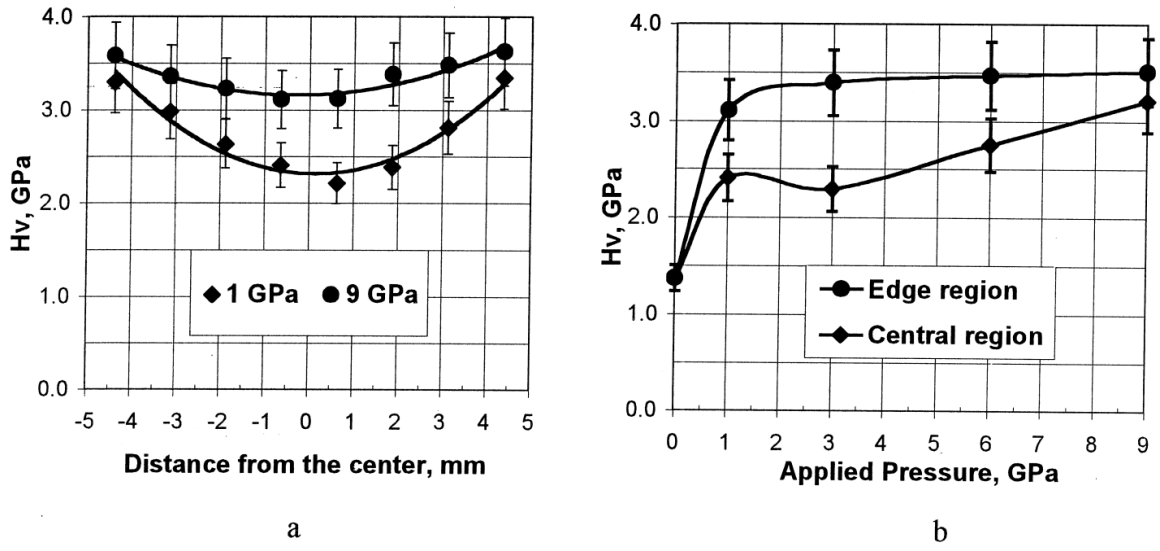

Figure 2.39: Microhardness distribution for nickel processed by HPT at room temperature: (a) along the diameter of disk using for two different applied pressures, and (b) as a function of applied pressure at the edge and centre regions [141].

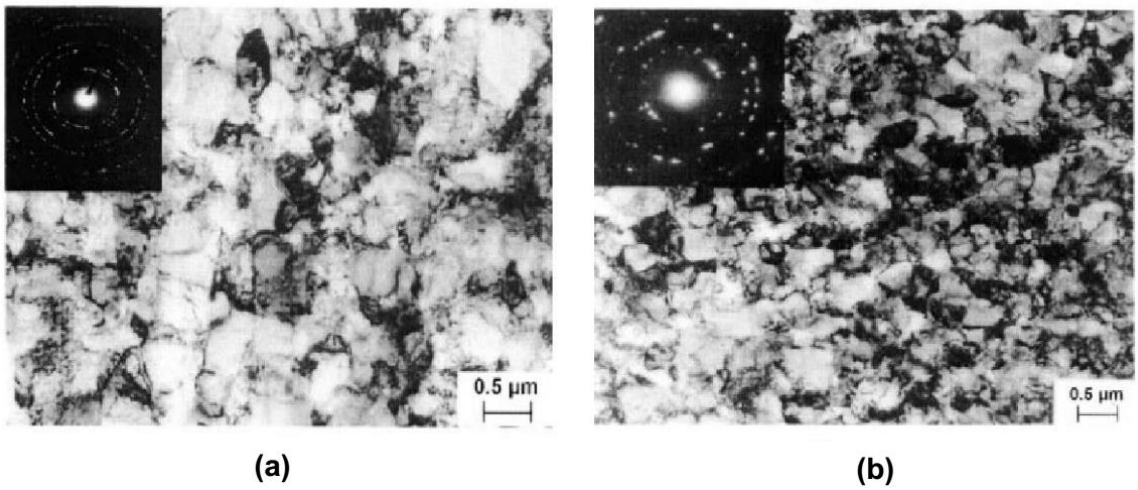

Figure 2.40: Microstructure observations for nickel processed by HPT for *N* = 5 turns at room temperature at the edge region using: (a) 1.0 GPa and (b) 6.0 GPa [141].

2.2.6.2 Role of the Number of Turns in HPT processing

The number of turns determines the total imposed strain into the disk, as shown by Eq. (1.10). The influence of the number of turns on the microhardness and microstructure is shown in Figure 2.41 and Figure 2.32, respectively, for nickel disks processed by HPT at room temperature under an applied pressure of 6.0 GPa for different number of turns [141]. The microhardness increased after one turn at the edge, where the centre of the disk exhibits a lower hardness than the edge. The latter behaviour is attributed to the difference in grain refinement at the edge and centre regions, where the microstructure was finer at the edges than that at the centre as shown in Figure 2.32. Increasing the number of turns resulted in an overall increase in microhardness with a reasonable homogeneous distribution across the diameter of the disk. It was found that the high number of turns leads to a considerable grain refinement in the processed microstructure, which results in a significant homogeneity in the distribution of microhardness [136]. The latter behaviour was also shown for Cu–0.1wt.%Zr alloy processed by HPT at room temperature for 1 turn and 5 turns as shown in Figure 2.41 [147].

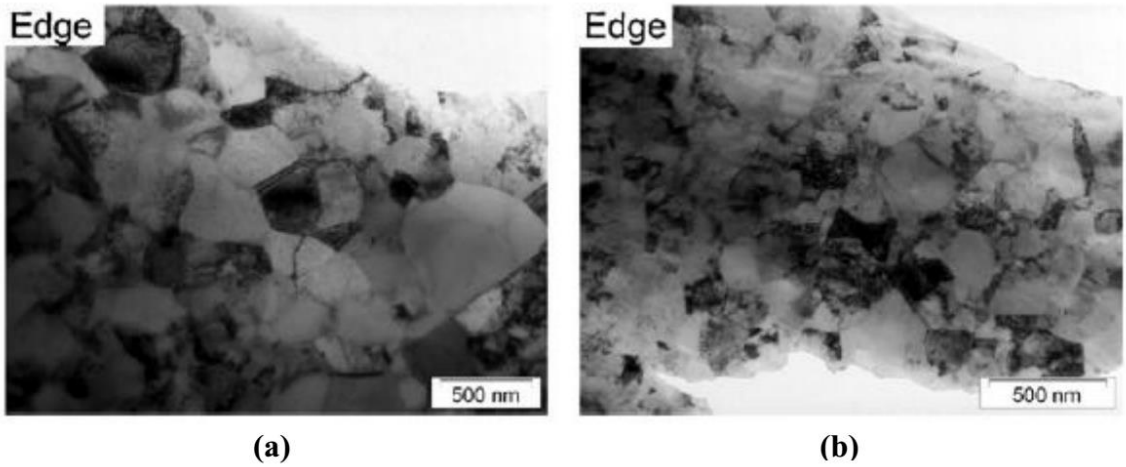

Figure 2.41: Microstructure observations for Cu–0.1wt.%Zr alloy processed by HPT at room temperature and at a pressure of 6.0 GPa for: (a) 1 turn, and (b) 5 turns [147].

2.2.6.3 Proposals to Explain the Development of Homogeneity during HPT Processing

The radial distribution of shear deformation as expressed by Eq. (1.10), reveals that HPT introduces a heterogeneity in the microstructure due to a higher imposed strain at the edge regions and a lower imposed strain at the centre [14]. However, the trend of gradual evolution to a reasonable homogeneous microstructure has been revealed in many reports using a sufficient number of turns and / or applied pressure [138][141].

Two approaches were used to explain the development of homogeneity during HPT processing. The first approach was proposed by Zhilyaev *et al.* [136], and it is based on the transfer mechanism of the shear deformation, where the deformation develops during HPT processing in a repetitive undulating manner. The mechanism suggests that the localisation of high friction at a certain point results in the presence of shearing at that point. Therefore, local hardening is introduced due to the shearing, and then it shifts to an adjacent location as a result of reduction in friction forces at that point. By combining this approach with the physical explanation of Eq. (1.10), and using enough turns, the deformation develops in a repetitive manner, as shown by the undulation in the distribution of microhardness in Figure 2.37 and Figure 2.38. It is obvious that the deformation

occurs at the edge regions and then extends towards the centre region of the disk according to Eq. (1.10), thus producing a reasonable homogeneous microstructure at a high number of turns.

The second approach was suggested by Estrin *et. al.* [148] and it is based on the strain gradient plasticity theory [149]. It was found that the uniformity in the microstructure processed by HPT processing resulted from the strain gradient effects [148]. When a polycrystalline material deforms, each grain tries to deform homogeneously with respect to the total deformation of the whole material. Because of the constraints imposed by the required continuity of the deformation, a strain gradient occurs between the centres of grains and regions near the grain boundaries [25].

Therefore, voids and overlaps will be introduced between the adjacent grains as shown in Figure 2.42. The spaces and superposition can be corrected by refitting the grains together again by introducing geometrically necessary dislocations (GNDs), thus providing a compatibility for deformation of neighbouring grains and in the whole deformed material [53]. The dislocations generated during the deformation of material can provide a hardening effect through storing, accumulating and trapping each other during deformation. These dislocations are normally called statistically stored dislocations (SSDs) and they occur when there is no strain gradient [149]. These statistically stored dislocations are different from the geometrically necessary dislocations (GNDs) that occur as a result of the presence of plastic strain gradients, which, in turn appear due to inhomogeneous plastic deformation of the material [150]. It was found that the geometrically necessary dislocations can provide an extra hardening contribution during deformation [132].

Strain gradient plasticity modelling of the HPT process for pure copper showed a reasonable consistency with experimental data. These data showed a considerable increase in accumulation of plastic strain in the initial stage of torsion at the edge regions of the processed disks, and a relatively low strain at the centre region as shown in Figure 2.43 [148]. It can be seen that the increase in the number of turns leads to a reduction in strain gradient, starting from the edge regions towards the centre regions through the mid–way regions, which is

consistent with earlier reports on microhardness data for austenitic steel [138], commercial purity aluminium [140] and copper [151]. The evolution of strain distribution and strain gradient are related to the variation in the density of the generated dislocations. The low density of geometrically necessary dislocations at the edge regions corresponds to the low strain gradient at these regions. In contrast, the high density of geometrically necessary dislocations occurs as a result of a high strain gradient at the centre region [148].

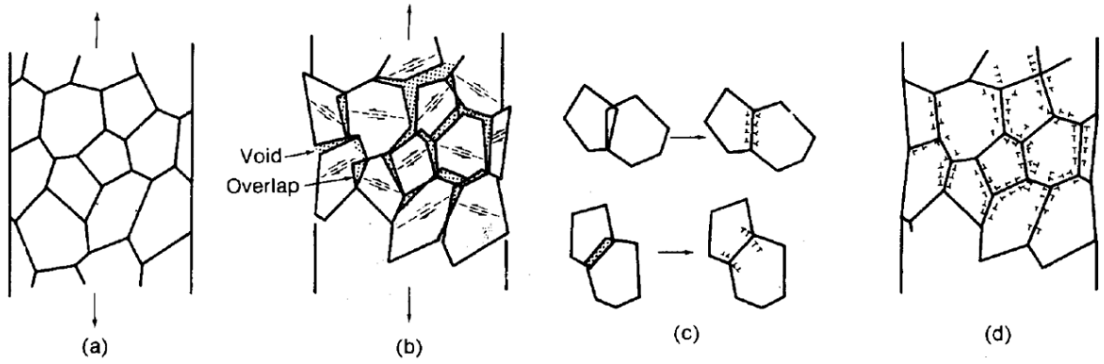

Figure 2.42: An illustration for the generation of geometrically necessary dislocations in a polycrystalline material showing: (a) Beginning of deformation, (b) Formation of voids and overlap between deformed grains, (c) Introduction of geometrically necessary dislocations to correct the former situation and (d) Grains refitted together again to achieve an integrity in the deformation process [25].

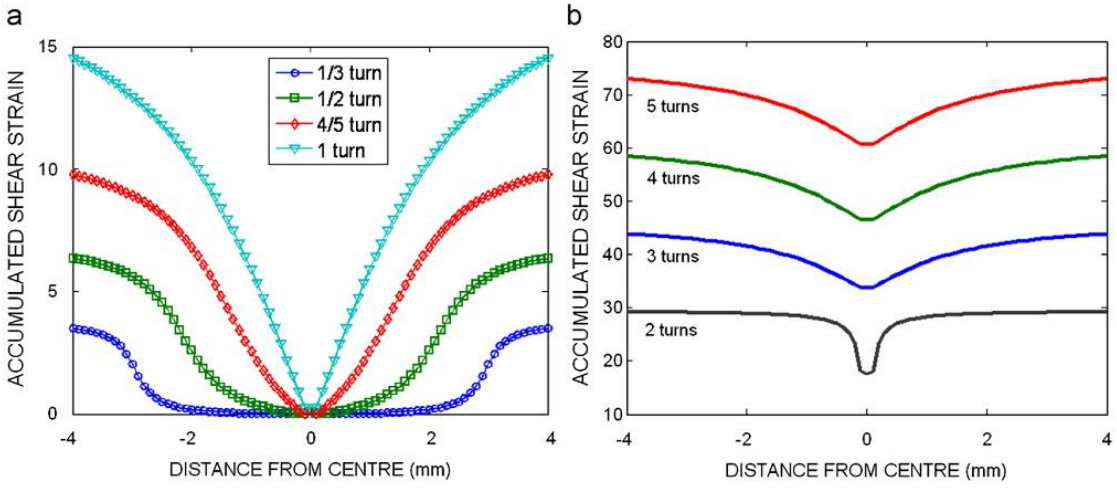

Figure 2.43: The variation in the accumulated equivalent strain imposed by HPT across the diameter for: (a) 1/3 to 1 turn and (b) 2 to 5 turns [148].

2.2.7 SPD Processing of Magnesium Alloys

The grain refinement of magnesium alloys has a great influence on their microstructures, and in turn, their mechanical properties, since they characterized by a limited ductility and workability at room temperatures. The majority of early reports on the bulk ultrafine–grained magnesium alloys had focused on different SPD processing at elevated temperatures, where the dynamic recrystallization and grain growth were present [19][152]. The review below summarizes the results of SPD processing of the common magnesium alloys.

2.2.7.1 AZ31 Magnesium Alloy

An extruded AZ31 alloy (Mg–3wt.%Al–1wt.%Zn) has been processed in ECAP in the route B_C using a 90° die with the variation of processing temperatures (473–593 K) with the number of passes for enhancing the grain refinement and deformability of the processed alloy being assessed. The processing temperature reduced with increasing number of passes. Fine and homogeneous microstructure of average grain size of 2 μm was obtained by increasing the number of passes. The hardness tested at room temperature of the ECAP processed alloy were improved by decreasing the grain size. The tensile yield strength of the processed alloy was lower than for the unprocessed one with a reasonable increase in tensile elongation at room temperature, which was attributed to the modification in texture for the alloy during the ECAP processing [153]. The superplastic behaviour was investigated for the AZ31 alloy processed by EX–ECAP in the route B_C using 110° die at 473 K for 8 passes. A grain reduction was achieved from 75 μm for the as–received alloy to about 0.7 μm after 8 passes at 473 K. A maximum ductility of 460 % was achieved for the EX–ECAP processed alloy at testing temperature of 423 K using a strain rate of 1×10^{-4} s^{-1}. This achieved elongation lies within the regime of low temperature superplasticity and it has been attributed to the effect of strong texture for easy slip that was gained through the extrusion and subsequent EACP processing [22].

The ECAP processing of extruded AZ31 alloy has been successfully achieved at a relatively low temperature of 373 K using a back pressure and using the route B_C and 90° die. A bimodal microstructure consisting of fine and coarse grains was found in the initial stage of processing. By increasing the number of passes, a fine–grained microstructure was produced with an average grain size of 1 μm, whereas the initial grain size was about 15 – 22 μm. It was found that the back–pressure suppresses the dynamic recrystallization and grain growth during processing. The absence of the back pressure resulted in cracking during ECAP processing of the magnesium alloy at 473 K. The hardness and elongation tested at room temperature were improved by increasing the number of passes because of the grain size being decreased. The initial decrease and subsequent increase in the strength at room temperature was attributed to the texture development after ECAP processing and during tensile testing [15]. A significant grain refinement was found for the AZ31 processed for 6 passes in the route B_C using 90° die at 423 K in ECAP with increasing back–pressure used during the processing. The high elongation of 1210 % was achieved using a strain rate of 1×10^{-4} s^{-1} that was attributed to the highest value of the back–pressure. The role of the back–pressure was in producing a bimodal microstructure at relatively lower processing temperature in ECAP, which resulted in a significant superplastic elongation through the grain–boundary sliding accommodated by slip [154].

HPT processing of AZ31 alloy was conducted to study the effect of strain rate imposed by HPT processing on the produced microstructure. A heterogeneous microstructure is expected at the centres of processed disks and a homogeneous microstructure far away from the centres using different rotation rates. Therefore, heterogeneous and homogeneous distributions of hardness were found in the centre region and the remaining regions over the disk surfaces, respectively. The grain refinement was somewhat proportional to the rotation speeds due to the large amount of imposed strain by HPT at fast strain rates [14]. Structural observations and microhardness measurements were conducted on the vertical cross sections of disks of AZ31 magnesium alloy that were processed by HPT at 463 K. It was found that the deformation was heterogeneous in the through–thickness directions, due to the grain size variation at different regions across the vertical planes of processed disks, and due to the formation of shear bands. These

bands were aligned in the nonparallel direction of the vertical cross–sections of the disks. A heterogeneous distribution of hardness was found along the vertical cross section due to the heterogeneity in microstructure [155].

The effect of processing temperature during HPT processing has been studied for the AZ31 alloy over different processing temperatures (296 K to 473 K) up to 5 turns. It was found that the ultrafine–grained microstructure was obtained at 296 K and 373 K, and a relatively coarser microstructure was found at 473 K due to the occurrence of grain growth. Heterogeneous and homogeneous distributions of recorded hardness were found for the alloy processed at 296 K and 473 K, respectively. Hardness data were significantly higher for the alloy processed at 296 K rather than 473 K due to the absence of dynamic recrystallization and grain growth at the relatively lower processing temperature [156]. The mechanical properties, hardness and tensile behaviour, were studied across the longitudinal cross sections for AZ31 alloy processed in ECAP using the route B_C and a 110° die. Small circular disk samples were cut perpendicular to the pressing direction of ECAP for subsequent tests. A homogeneous fine microstructure of 1 μm after 8 passes at 473 K was found, with increasing hardness across the disk surfaces with the number of passes. Tensile elongations for the processed alloy were increased at all testing temperatures (296, 423, 473) K and with increasing the number of passes compared to the unprocessed alloy. The maximum recorded elongation was 192 % which is much lower than the common elongation values seen for superplasticity (400 %). This was attributed to the relatively small scale of the tensile samples and the subsequent behaviour under testing [157].

The superplastic behaviour of AZ31 alloy was conducted at elevated temperatures after ECAP processing. The alloy was processed in ECAP in the route B_C using 135° die for 6 passes, and the processing temperature decreased gradually in two successive passes from 473 K to 413 K. A homogeneous fine microstructure was obtained of an average grain size of μm. The maximum elongation of 1200 % was achieved at testing temperature of 623 K using a strain rate of 1×10^{-4} s^{-1}. The grain–boundary sliding was the deformation mechanism during the superplastic behaviour with strain–rate sensitivity of 0.5, and fracture after the maximum elongation was due to the cavity interlinkage [158]. A recent study has been

conducted on the AZ31 alloy processed in HPT at room temperature. An extreme grain refinement down to 150–200 nm was obtained for samples in the form of 20 mm in diameter disks processed up to 15 turns. Development in hardness towards from heterogeneity to homogeneity was found with increasing the number of turns. The crystallite size and density of dislocation were decreased and increased, respectively, during the HPT processing until saturation occurred at high number of turns [159].

2.2.7.2 AZ91 Magnesium Alloy

The SPD processing of AZ91 magnesium alloy was achieved by equal channel angular pressing at a temperature of 448 K. Fine equiaxed grains of 1 μm were obtained after processing, and a maximum elongation of 661 % was achieved at a testing temperature of 473 K using a strain rate of 6.2×10^{-5} s^{-1}. Microstructural observation indicated that the grain–boundary sliding was assumed as the deformation mechanism during the superplastic behaviour showed a strain–rate sensitivity of 0.3. It was found that the elongation–to–fracture depends mainly on the grain size of the material under tensile tests [10].

Pure magnesium and Mg–9wt.%Al alloy were processed by ECAP using the route B_C and 90° die in the temperature range of (473 – 673) K for different number of passes. The grain size was reduced from 100 μm to 17 μm after processing at 473 K, and the higher processing temperatures resulted in the occurrence of grain growth during processing. It was found that the tensile strength and ductility at room temperature were improved after processing due to the homogeneous equiaxed microstructure that was obtained by the dynamic recrystallization during processing. The tensile properties of this magnesium alloy were better than for pure magnesium due to the presence of Al content within the microstructure of alloy [13].

A two–step EX–ECAP process comprising of an extrusion step followed by ECAP processing was conducted for the Mg–9wt.%Al alloy that was alloyed from high–purity magnesium and aluminium. The extrusion was conducted at 623 K and

followed by ECAP processing at a temperature of 473 K using the route B_C and 90° die. The grain refinement reached down to 0.7 μm after EX–ECAP. The study showed the possibility of pressing magnesium alloys easily and without cracking using an extrusion step prior to ECAP processing. A maximum elongation of 840% was achieved in the processed alloy due to the relative thermal stability of the fine–grained microstructure of the alloy produced by the EX–ECAP. It was found that the fine β–phase particles prevented the grain growth during ECAP processing at the elevated temperatures [17]. A high–temperature extrusion was conducted in a temperature range of (608 – 688) K for investigating the microstructural changes in the AZ91 alloy. A fine–grained microstructure of 4 μm was produced at the lower processing temperature by dynamic recrystallization. It was shown that aluminium solute atoms can hinder the dynamic recovery of magnesium in the alloy through lowering its stacking fault energy [20].

The influence of β–phase on the mechanical properties was studied for a hot extruded AZ91 alloy. The extrusion was conducted at 543 K and the resultant grain refinement was about 4 μm. It was found that the β–phase in the extruded alloy elongated and broke during processing and distributed as fine particles with grain sizes of (0.3 – 0.8) μm along the recrystallized grain boundaries. This phase prevented the grain growth of the dynamically recrystallized microstructure, and thus produced a fine–grained microstructure by the hot extrusion. The tensile strength at room temperature was improved due to the existence of the β–phase particles at the grain boundaries. These fine particles act as a barrier for the motion of dislocations during deformation, and at the same time, the existence of some elongated particles of the β–phase lying parallel to the extrusion direction enhanced the ductility [160].

The microstructure and mechanical properties were studied for AZ91 alloy processed by ECAP at different temperatures and at different numbers of passes. It was found that the two–step ECAP including pressing at 498 K followed by pressing at 453 K resulted in a homogeneous microstructure of grain size of 2 μm. The two–step ECAP processing is described as pressing of a sample through two sequential routes, where each route is conducted at a different number of passes and a specific processing temperature. After the two–step ECAP, a homogeneous

and recrystallized microstructure was found with widely distributed and fine particles of the β–phase. A high tensile strength and good ductility at room temperature were achieved after two–step ECAP due to the development of a homogeneous fine microstructure with fine particles of the β–phase distributed within the processed microstructure [161].

The Mg–9wt.%Al alloy was processed at 296 K and 423 K in the HPT and for a different number of turns. This alloy was prepared by alloying of high–purity magnesium and aluminium. An ultrafine–grained microstructure with grain size of 0.15 μm and 0.37 μm after 5 turns in HPT at room temperature and 423 K, respectively. It was found that the level of grain refinement in HPT is much better than ECAP for this alloy. The hardness and ductility were significantly improved as a result of the ultrafine–grained microstructure produced by HPT processing. A maximum elongation of 810 % was achieved for the alloy processed in HPT at processing temperature of 423 K and then tested in tension at testing temperature of 473 K using a strain rate of 5×10^{-4} s^{-1}. It was found that the hydrostatic pressure used in the HPT retained the solidity of the magnesium alloys during the processing at room temperature, which was not applicable in the case of ECAP processing [18].

In summary, the majority of the earlier work of SPD processing of magnesium alloys (especially for AZ91 alloy) was conducted at elevated temperatures, where the dynamic recrystallization, dissolution and change in morphology of β–phase are seen. Two studies revealed the possibility of HPT processing at room temperature for the magnesium alloys to achieve a homogeneous ultrafine–grained microstructure. One of them focused on the Mg–9wt.%Al alloy. The HPT processing were conducted on this alloy at 296 K and at 423 K [18]. Another study was conducted on the AZ31 magnesium alloy at 296 K [159]. Both of the aforementioned studies revealed the formation of ultrafine–grained microstructures with grain sizes within (150 – 250) nm and the maximum superplastic elongation reached was 810% for the Mg–9wt.%Al alloy processed in HPT at 423 K.

Chapter Three: Experimental Work

3. EXPERIMENTAL WORK

3.1 Material

An extruded rod of AZ91 magnesium alloy was used in this study, which was supplied by Magnesium Elektron Company (Manchester, UK). The starting material was solutionised for 24 hours at a temperature of 420 °C, then cooled in air. Subsequent ageing was applied for 16 hours at a temperature of 210 °C. The purpose of this heat treatment is to increase the yield strength and hardness through precipitation hardening [28]. The chemical composition of the as–received AZ91 alloy as analysed using energy–dispersive spectroscopy (EDS) is shown in the Table 3.1.

Table 3.1: The measured chemical composition of the as–received AZ91 magnesium alloy.

Element	**Mg**	**Al**	**Zn**	**Mn**
Content wt.%	88.74	9.57	1.11	0.58

3.1.1 Metallographic preparation

The AZ91 samples were prepared for microstructural examination prior to high–pressure torsion processing using the following procedure:

1. Sectioning: An abrasive cut–off wheel was used to cut disk–shaped samples from the AZ91 rod. Water was used as a coolant to minimise the thermal damage generated during the cutting process for the samples.
2. Mounting: A cold–mounting method was used for sample mounting due to the low heat generated during polymerisation. Moulds were sprayed with spray separator to ensure a feasible extraction of the mounted samples and to keep the moulds clean for subsequent use.
3. Grinding: Rigid–disk grinding with a series of SiC abrasive papers P800, P1200, and P4000 were used to remove all scratches from previous grinding stages on the surfaces of the mounted samples (generated from sectioning) and to produce flat surfaces and regular edges for the mounted samples. Grinding with the above–mentioned papers was conducted under a load of 22.25 N and a

wheel rotation of 200 rpm. An automatic grinding machine and water (as a coolant) were used during this process.

4. Polishing: was performed in two stages. In the first stage, a diamond paste of 1 µm and a short nap pad were used under a load of 22.25 N with a wheel rotation of 150 rpm. The use of water was avoided during this process and an oil lubricant was used as a coolant. In the second stage a colloidal alumina of 0.05 µm and a napless elastomer pad were used for the final polishing. The polishing with the colloidal alumina was applied under a load of 11.12 N with a wheel rotation of 120 rpm. An automatic polisher machine was used for this process and water was also avoided during this stage.
5. Etching: An acetic–picral solution (5 ml acetic acid, 3.6 ml picric acid, 10 ml H2O, 100 ml Ethanol) was used as an immersant etchant for 10 sec. The etched samples were washed with alcohol, and then dried using compressed air.

3.1.2 HPT processing conditions

HPT processing was conducted at room temperature and elevated temperature using the HPT facility shown in Figure 3.1. This facility consists of upper and lower anvils, with a circular depression of 0.25 mm in depth and 10 mm in diameter that is located centrally in both anvils, as shown in Figure 3.2 [162]. The samples were cut from the AZ91 alloy rod in the form of disks of 10 mm in diameter and 1 mm in thickness. Later, an abrasive paper was used to reduce the thickness of each disk to about 0.82 mm. A small heater was located around both upper and lower anvils as shown in Figure 3.3, this heater surrounds both anvils to achieve homogeneous heating during processing. A thermocouple positioned within the upper anvil was used to measure the temperature continuously. Prior to HPT processing, the anvils were heated to the required processing temperature (± 5 °C) and the temperature held for 10 minutes. Then, the sample was placed in the cavity of the lower anvil and held for 5 minutes at the required processing temperature, thereafter HPT processing was started. HPT processing was conducted under a quasi–constrained condition at a speed of 1 rpm using the conditions mentioned in Table 3.2.

Table 3.2: Conditions for HPT processing used in this study.

P (GPa)	Processing temperature (K)	*N* (turns)	Duration of processing (minute)
3.0	296	0, 1/4 , 1/2 , 3/4 , 1 , 3 , 5 , 10	1, 0.25, 0.5, 0.75, 1, 3, 5, 10
	423	1/2 , 1 , 5 , 10	0.5, 1, 5, 10
	473	1/2 , 1 , 5 , 10	0.5, 1, 5, 10
6.0	296	0 , 1/2 , 1 , 3 , 5 , 10	1, 0.5, 1, 5, 10

The applied pressure in the HPT facility has been calculated as follows: the applied loads by the hydraulic press in HPT facility were 24 tonnes (24000 Kg) and 47 tonnes (47000 Kg) corresponding to applied pressures of 3.0 GPa and 6.0 GPa, respectively. The area under pressure was calculated from the circular area of the HPT disk as $A = \pi r^2$, where r is the radius of the disk equal to 5 mm. Thus, for the applied load of 24 ton, the applied pressure is:

$$\text{Applied Force} = \frac{24000\ \text{Kg}}{0.102\ \text{Kg/N}} = 235294.11\ \text{N}$$

$$\text{A} = \pi\,\text{r}^2 = \pi \times (5 \times 10^{-3})^2 = 7.85 \times 10^{-5}\ \text{m}^{-2}$$

$$\text{Pressure} = \frac{\text{Force}}{\text{Area}} = \frac{235294.11\ \text{N}}{7.85 \times 10^{-5}\ \text{m}^{-2}} = 3.0 \times 10^{9}\ \text{Pa} = 3.0\ \text{GPa}$$

(the same relationships above can be used to show the corresponding applied pressure for the applied load of 47 tonnes is 6.0 GPa). In addition, pressing of disks without torsion was conducted for 1 minute using both above–mentioned pressures and these samples were labelled as *N* = 0, in the microhardness plots. The outer rim of each depression was lubricated with oil before HPT processing to avoid any possible damage to these areas by means of friction. For the disks processed by HPT using an applied pressure of 3.0 GPa, microstructural and microhardness observations were conducted over the horizontal and vertical cross–sections as shown schematically in Figure 3.4 (a,b). A comparison between the distributions of microhardness along the diameters of the disks was carried out for the disks processed in HPT using the applied pressures of 3.0 and 6.0 GPa. After HPT processing, the disks were prepared metallographically using the same steps detailed in the section 3.1.1 over the horizontal and vertical cross–sections

of the processed disks as illustrated schematically in Figure 3.4. The vertical cross–section was produced by cutting the disk (see Figure 3.4 (a)) along the diameter and through its centre to produce two equal halves. An illustration of a one–half segment of the vertical cross–section of the disk is shown in Figure 3.4 (b).

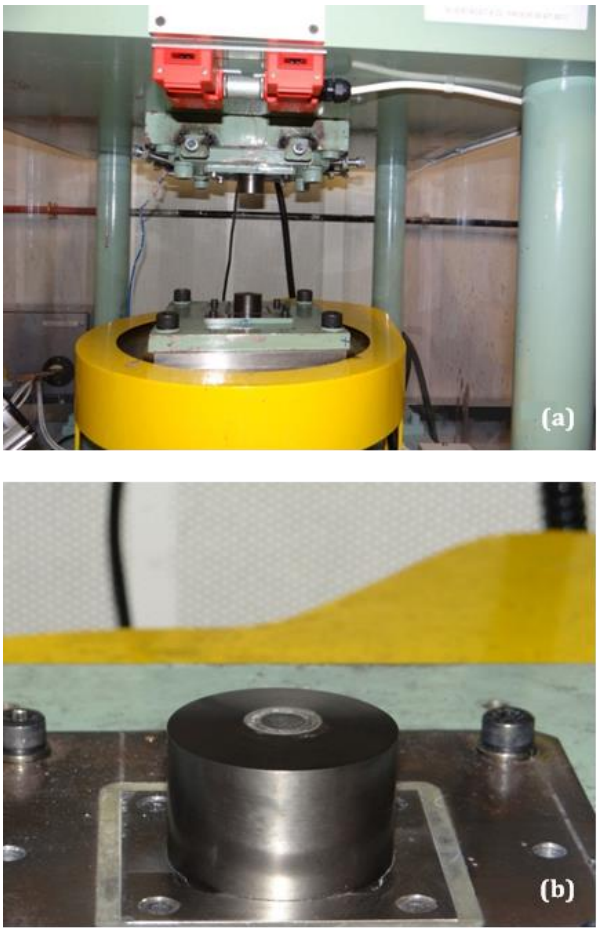

Figure 3.1: (a) The high–pressure torsion facility used in this study, and (b) Configuration of the lower anvil.

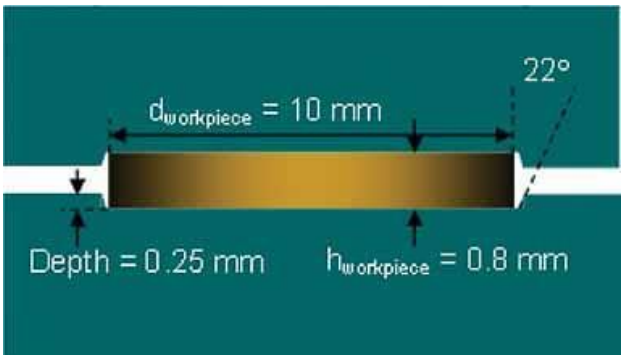

Figure 3.2: An illustration of the anvil configuration in the HPT facility shows the position of the sample in the depression between the anvils [162].

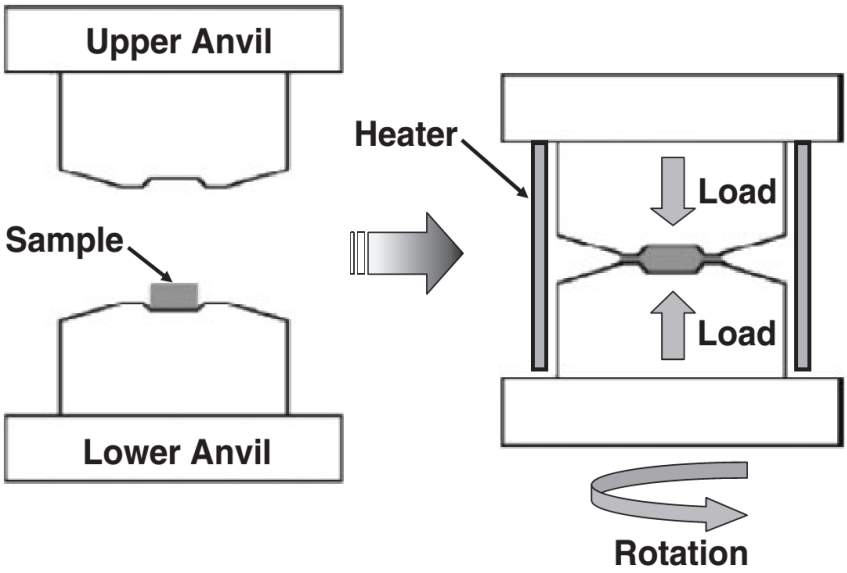

Figure 3.3: Schematic illustration of the heating furnace used during HPT processing [99].

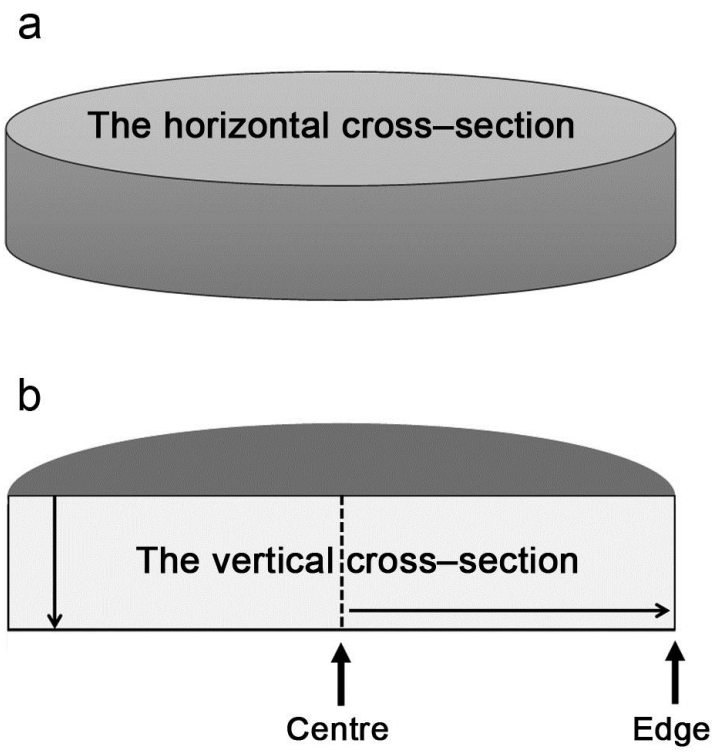

Figure 3.4: An illustration of a HPT disk shows: (a) The horizontal upper cross–section, and (b) The vertical cross–section. These cross–sections were used in the microstructural and microhardness observations. The arrow from the centre to the edge refers to the longitudinal (radial) direction, while the arrow from the upper surface to lower surface refers to the through–thickness direction.

3.2 Microscopy Characterisation

3.2.1 Optical microscopy

By using the optical microscope (OLYMPUS–BX51, Japan) shown in Figure 3.5, microstructural observations were made on the etched cross–sections of the processed disks, prepared as shown in section 3.1.1. The average grain size prior to HPT processing was determined by means of the linear intercept method on optical micrographs.

3.2.2 Scanning electron microscopy

The scanning electron microscope (JEOL JSM–6500F, Japan), shown in Figure 3.5 was used in this study to reveal more details on the morphology of as–received and processed microstructures, and the detailed morphology of the β–phase. The chemical analysis of the as–received and processed microstructures was carried out using energy–dispersive spectroscopy (EDS) attached to the SEM. Samples for SEM inspection were prepared metallographically using the steps mentioned in section 3.1.1.

Figure 3.5: Left: the optical microscope (OLYMPUS–BX51, Japan) and right: the SEM microscope (JEOL JSM–6500F, Japan) facilities used in this study.

3.2.3 The size distribution, area fraction and average size of the β-phase particles

These data have been estimated using *ImageJ* image analysis software (http://imagej.nih.gov/ij/) and using a point count technique [163] on the horizontal cross–sections of the disks for the as–received alloy and the processed alloy in HPT at room temperature using an applied pressure of 3.0 GPa for N = 1/2, 1, 5 and 10 turns. The analysis has been conducted on several SEM micrographs at the same magnification. Three micrographs of each etched microstructure have been selected for analysis at random locations on the relevant horizontal cross–sections of the disks. The micrographs ("field areas") have been transformed into black and white images via contrast control in order to enhance the contrast between the grains and β–phase particles. The area fraction has then been calculated using the following relation [163]:

$$\text{Area fraction of particles } \% = \frac{\text{Total No. of particles} \times \text{Average area of the particle}}{\text{Field area}} * 100\% \qquad (3.1)$$

where the total no. of particles and the average area of the particles have been estimated from the selected field under analysis in terms of black and white pixel assignations by the operator. The field area is the area of the SEM micrograph under analysis. The area fraction of the β–phase particles has been estimated for each of the three selected fields and plotted with associated error bars against the number of turns at which the alloy was processed in HPT at room temperature using an applied pressure of 3.0 GPa as well as for the as–received alloy. The distribution of particle sizes has been estimated and plotted against the particle diameter for the aforementioned conditions of the processed alloy and the as–received alloy. This simple methodology of estimation of the size distribution, area fraction and average size of the β-phase particles has been adopted in several other studies using this standard *ImageJ* image analysis software [164][165][166][167]. The methodology mentioned above is clearly an estimation and the estimated data are affected by the choice of field area under analysis, the accuracy of the count for the finer particles and contrast–colour enhancement between the grains and the β–phase particles, which partly depends on the type of

etchant solution that used in the metallographic preparation of the samples as well as the choice of contrast levels during image analysis.

3.2.4 Transmission electron microscopy

The transmission electron microscope (JEOL JEM–3010, Japan), shown in Figure 3.6 was used in this study to observe the microstructure of the processed alloy down to nanometre scale and in determining the grain size after HPT processing. Samples for TEM inspection were prepared in the form of thin disks of 3 mm in diameter and about 150 μm thickness. These disks were cut from the HPT disks using a punch machine and then mechanically ground using abrasive paper P4000 and methanol as a coolant during grinding process. Later, these disks were subjected to additional thinning to produce thin foils using a twin–jet electro–polishing facility and a solution consisting of with a solution of 15 ml perchloric acid, 15 ml glycerol, and 70 ml ethanol under a voltage of 20 volt for 1 minute.

3.2.5 X-ray diffraction analysis

X–ray diffraction (XRD) analysis was used to determine the crystallite size and density of dislocations in the as–received and processed alloy using the XRD facility (D2 Phaser, Germany) as shown in Figure 3.6. The test was conducted at a step size of 0.02° from 2θ = 25° to 80° using a Cu Kα source of wavelength of 0.154 nm. X–ray diffraction analysis is an indirect and alternative technique for investigating ultrafine–grained materials. The crystallite size and density of dislocations can be estimated using X–ray diffraction analysis [60]. Advantages of X–ray diffraction (XRD) analysis over transmission electron microscopy (TEM) are the relatively larger area that can be analysed, quicker inspection times and less critical sample preparations steps than those are required in TEM [168]. However, a difference has been found between the size (usually called the crystallite size) measured by X–ray diffraction analysis and the grain size measured by TEM observations. This difference reflects the existence of different microstructural elements in the UFG material such as grains, subgrains, cell blocks, dislocation cells and twins [169].

Figure 3.6: Left: the TEM microscope (JEOL JEM–3010, Japan) and right: the XRD facility (D2 Phaser, Germany) facilities used in this study.

The crystallite size has therefore been found to be usually smaller than the grain size measured by TEM in SPD–processed materials, as the grains in these materials are made up of subgrains and / or dislocation cells [170]. Thus coherent scattering in the X-ray diffraction analysis from these substructures represents the (smaller) mean crystallite size rather than the grains which can be more easily observed in TEM [170]. Therefore, both XRD analysis and TEM analysis are preferred (when possible) to allow better microstructural investigation in terms of grain size reduction and the resultant density of dislocations [169]. When crystals are perfect in a material, the diffraction patterns will be uniform and symmetrical as shown in Figure 3.7 (a). However, when the crystals became deformed or imperfect (as would be expected in SPD materials) the diffraction patterns will be shifted and / or broadened as shown in Figure 3.7 (b, c) [60][171]. The shift in X–ray peaks occurs due to internal stresses, stacking faults and twinning [60]. The broadening of X–ray peaks is due to the smallness of the crystallites (< 1 µm) and the lattice distortions [172].

Profile analysis of the X–ray diffraction results has been achieved by two standard methods. The first one is based on the full widths at half maximum intensity (FWHM) method and the second one is the whole–profile fitting (WPF) method [60]. In the FWHM method, the breadth of the profile ($\Delta K_{FWHM} = \beta \cos\theta \, \lambda$) on the y–axis is plotted against $K = 2sin\theta/\lambda$ on the x–axis as shown in Figure 3.8, where β is the full width at half maximum intensity, θ is the Bragg angle and λ is the wave length of x–ray source. The intercept of the extrapolated line with y–axis gives the

inverse value of the apparent crystallite size. This procedure has been suggested by Williamson and Hall [173]. However, a modification has been applied later to the Williamson and Hall method to avoid the scattering of plotted data as a result of strain anisotropy by the elastic fields of dislocations as shown in Figure 3.8 [174]. The whole–profile fitting (WPF) of x–ray peaks has been suggested by Rietveld [175], in which the peaks are refined and reconstructed using the patterns of the ideal random powder of the same sample. Figure 3.8 shows an example for XRD patterns that have been analysed using whole–profile fitting procedure [176][177]. In the current research, the whole–profile fitting procedure has been employed and using Maud XRD software analysis as reported by previous researchers [178][179][180][181]. The density of dislocations has been calculated using the following relationship [1]:

$$\rho = \frac{2\sqrt{3\varepsilon}}{< d_c >_v \boldsymbol{b}} \tag{3.2}$$

where ρ is the density of disloactions, ε is the microstrain, d_c is the apparent crystallite size and $\boldsymbol{b}$ is the value of Burgers vector. The apparent crystallite size and microstrain have been estimated using the whole–profile fitting procedure and Maud XRD software analysis. It should be noted that the crystallites have been assumed to be spherical and their sizes represent the apparent volume-weighted crystallite sizes ($< d_c >_v$) that have been obtained using the relation from [182]: $< d_c >_v = (4/3) < d_c >_l$, where $< d_c >_l$ represents the apparent linear crystallite diameter that is measured from the XRD plot.

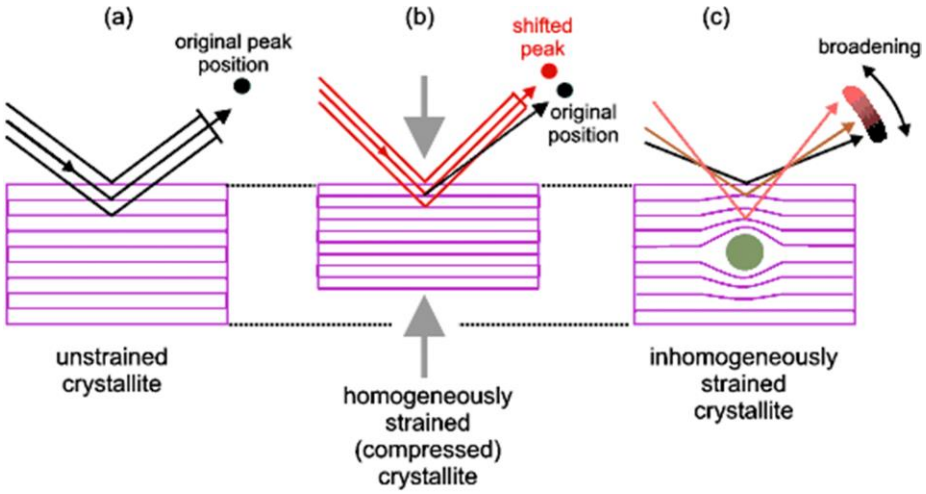

Figure 3.7: Schematic illustration shows the x–ray diffraction from (a) unstrained crystallite, (b) homogeneously strained crystallite and (c) in) homogeneously strained crystallite [171].

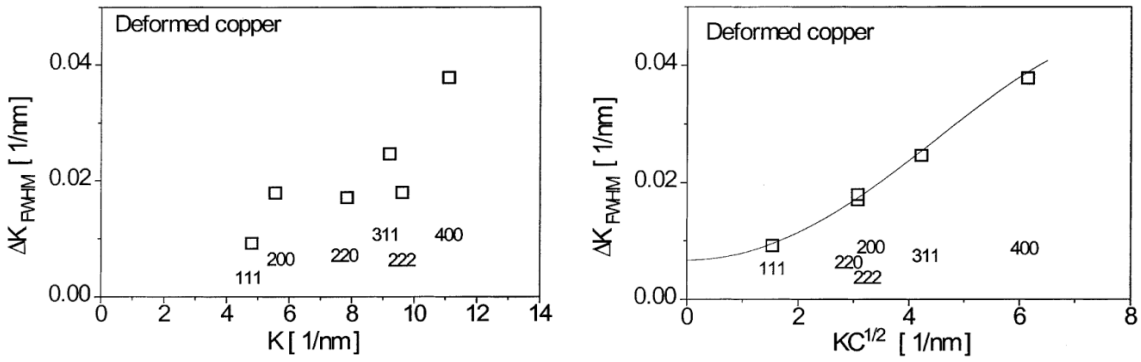

Figure 3.8: The classical (left) and modified (right) Williamson–Hall plot for the Cu processed in ECAP for 12 passes using the route B_c at room temperature [6][183].

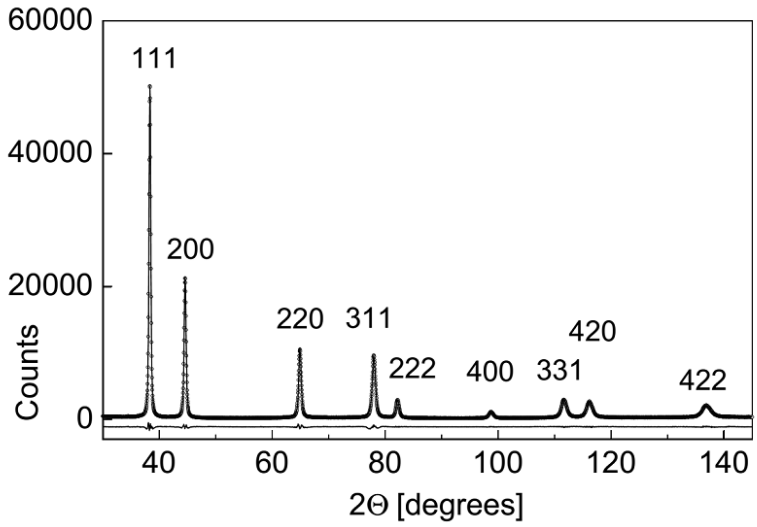

Figure 3.9: The XRD patterns (open circles) for the Al–3% Mg powder milled for 3 hr., where these patterns have been fitted using the whole–profile fitting procedure as shown by the solid line [184].

3.3 Mechanical Tests

3.3.1 Microhardness Test

3.3.1.1 Sample preparation for test

The samples from the microstructure inspection step were re–ground and re–polished using the same steps in section 3.1.1, to get mirror–like finish surfaces for microhardness testing over the horizontal and vertical cross–sections that are shown in Figure 3.4 (b), using the Vickers microhardness tester (FM–300, Japan) as shown in Figure 3.10. The microhardness measurements of the processed disk were conducted using an applied load of 100 gf and a dwell time of 15 sec.

3.3.1.2 Methodology of hardness measurement

Three procedures were adopted to obtain the values of microhardness, as follows:

1. For the microhardness profile along the diameter of the processed disk, the measurements were taken at positions separated by 0.3 mm between two successive indentations in a given horizontal row. An average value of recorded microhardness was obtained for four individual points located around

the selected position. Alternate horizontal rows were offset by 0.15 mm, thus four hardness measurements at a distance of 0.15 mm can be considered to characterise these individual points. An illustration of the locations of these microhardness measurements is shown by the red rectangle in Figure 3.11.

2. For the microhardness distribution over the horizontal cross–section of the processed disk, a rectilinear grid was used to record the microhardness values with a separation of 0.3 mm between each two successive indentations. Colour–coded maps were used to represent the collected data, since these maps provide an indication of the achieved strengthening as a function of processing conditions. The variation in the colours on these maps represents the local variation in microhardness distribution. An illustration of locations for microhardness measurements across one–quarter of the horizontal cross–section is shown by the blue arc in Figure 3.11 [143].
3. For the microhardness distribution over the vertical cross–section of the processed disk, a separation of 0.1 mm was used between each two successive indentations. Colour–coded maps were also used to represent the collected data using a rectilinear grid of recorded values of the microhardness as illustrated in Figure 3.12. The colour–coded map represents the variations of measured microhardness as a function of the positions across the vertical cross–section.

Figure 3.10: Left: The microhardness tester (FM–300, Japan) used in this study and right: Indenter and lens assembly.

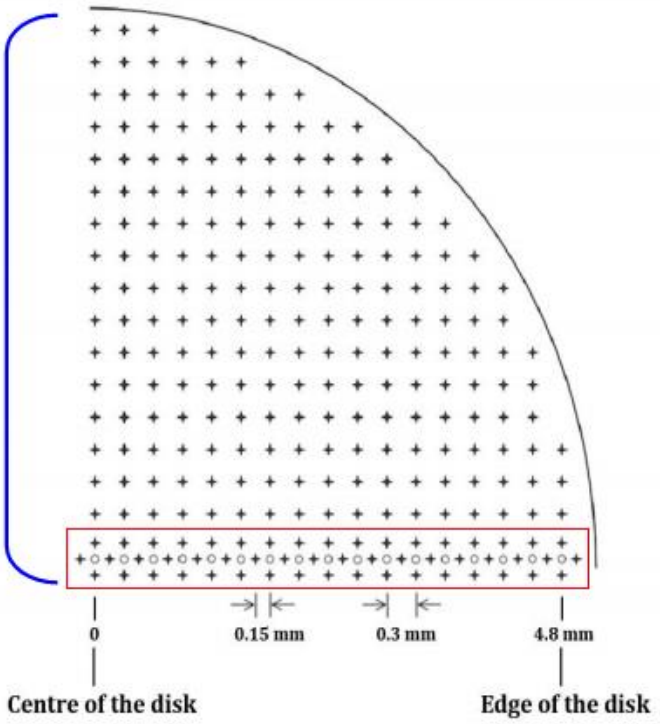

Figure 3.11: An illustration of one–quarter of the horizontal cross–section of HPT disk that illustrated schematically in Figure 3.4 (a), shows the procedure of the microhardness measurement across the diameter of the disk as shown by the red rectangle, where the open circles that are surrounded by four recorded microhardness values represent the selected positions of microhardness profile. The rest of the recorded values, as illustrated by the blue arc, represent the method used in recording the microhardness map over the entire horizontal cross–section of each disk [143].

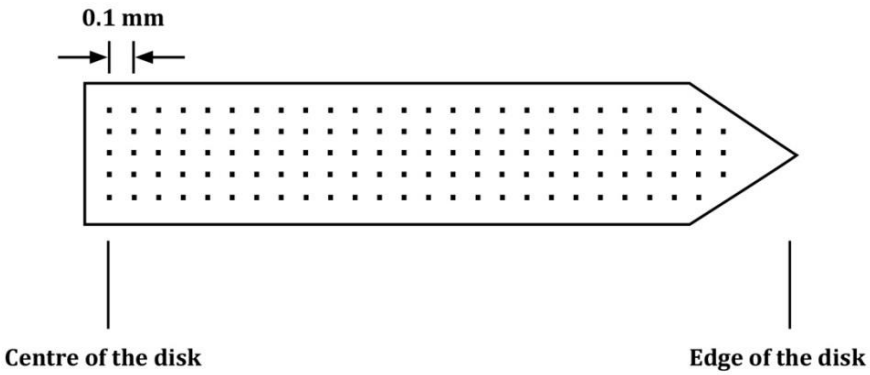

Figure 3.12: An illustration of one–half of the vertical cross–sections of the HPT disk illustrated schematically in Figure 3.4 (a), which shows the locations of the microhardness measurements.

3.3.2 Tensile test

3.3.2.1 Sample preparation for testing

For tensile tests, the processed disks were carefully ground to thicknesses of 0.6 mm using an abrasive paper to prepare them for cutting into micro-tensile samples as illustrated in Figure 3.13 [99]. The method of cutting these micro-tensile samples from the HPT disks is known as the off–centre position method. This method is used to avoid the central region in an HPT disk where structural heterogeneity is anticipated after HPT. This allows production of two miniature tensile samples per HPT disk with dimensions of (1.0×0.9×0.6) mm^3 as measured by the optical microscope.

3.3.2.2 Methodology of tensile test

The tensile test was conducted at initial strain rates between 1×10^{-1} s^{-1} to 1×10^{-4} s^{-1} at each testing temperature of 423, 473, and 573 K, and for tensile samples produced from disks processed for N = 1, 3, 5 and 10 turns. The tensile samples of the as–received alloy were tested at the same range of strain rate and at testing temperatures of 296, 473 and 573 K. The processed alloy was tensile tested at a temperature of 296 K for N = 1 and 3 turns. Each tensile test evaluation of a particular processing condition was conducted using two tensile samples and hence 136 tensile samples were used in this investigation. Tensile testing was carried out using a Zwick/Roell tension (Z030, Germany) machine shown in Figure 3.13 operating at a constant rate of crosshead displacement. The load and displacement data were gathered using testIIXpert testing software in a computer–acquisition system. Curves of engineering stress versus elongation and elongation–to–fracture versus strain rate were plotted. The flow stress versus strain rate curves were plotted to measure the values of strain–rate sensitivity (m). The microstructures of tensile samples after testing were observed at the gauge section surfaces using scanning electron microscopy. In order to investigate the surface morphology in detail, the as–tested samples were observed without any further metallographic preparation. The average grain size was estimated from these SEM images along the gauge lengths of the tested samples using a linear intercept method and then corrected by a factor of 1.74 [185]. This procedure has

been conducted because optical microscopy of tensile samples after testing led to significant smearing in the polished samples after chemical etching, obscuring any grain size measurement. Additional steps of grinding and polishing would also have resulted in a detrimental reduction in the thickness of the tensile sample being observed, which is already very thin after testing. Microstructural observations of the gauge length of tensile samples using SEM observation have been adopted in many studies due to these constraints [186][187][188][189].

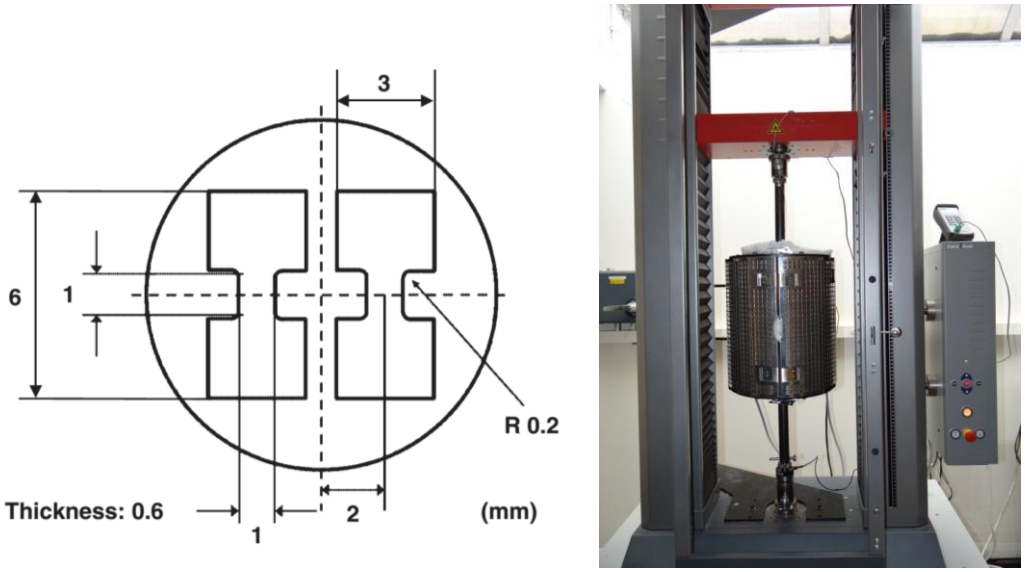

Figure 3.13: *Left*: Schematic illustration for the positions of tensile samples within the HPT disk [99], and *right*: The tensile machine (Z030, Germany) used in in this study.

Chapter Four: Results

4. RESULTS

4.1 Microstructure Observations

4.1.1 Microstructure processed at 296 K across the *horizontal* cross–sections

The as–received AZ91 alloy of an average grain size of 30 µm is shown in Figure 4.1. The microstructure consists of two main phases: α–Mg matrix; and lamellar and agglomerate forms of β–phase with the presence of Al_8Mn_5 particles as shown in Figure 4.1 (b). It is obvious from Figure 4.1 (c) that the grain boundaries between α–Mg grains are covered with the β–phase. The magnesium matrix appears darker than the β–phase, which appears brighter as shown in Figure 4.1. The chemical analyses of the alloy constituents for the as–received alloy and processed alloy for N = 5 turns are shown in Figure 4.2 and Figure 4.3, where the white arrows show the locations of the analyses. The weight fractions of Mg, Al, Zn, and Mn in the matrix, β–phase and Al_8Mn_5 particles are shown in Tables (4.1– 4.2). No significant changes were introduced to the compositions of the alloy before and after processing, as shown by the weight percentages of the alloy constituents.

The microstructures of AZ91 alloy in the case of pressing only (without torsion) are shown in Figures (4.4 – 4.6), where the compression resulted in fragmentation of lamellar and agglomerate β–phase and scattering or spreading of a few β–phase particles to the surrounding areas. The microstructures of AZ91 alloy as observed by SEM and TEM after HPT processing for N = 1/2, 1, 3, 5 and 10 turns at the centre and the edge of the processed disks are shown in Figures (4.7 – 4.29, 4.31), where the grain refinement of the microstructure occurred significantly at the edges in the earlier stage of processing. The grain boundaries became ill–defined as seen by SEM gradually with increasing the number of turns up to N = 10 turns, as shown in Figures (4.13, 4.15, 4.17) for the sample processed for N = 1 turn, Figures (4.18, 4.19) for the sample processed for N = 3 turns, Figures (4.20, 4.22, 4.23, 4.31) for the sample processed for N = 5 turns and Figures (4.26 – 4.29) for the sample processed for N = 10 turns.

The morphology and distribution of the β–phase altered after HPT processing as shown in Figures (4.8, 4.10, 4.11) for the sample processed for N = 1/2 turn,

Figures (4.13, 4.14, 4.15) for the sample processed for *N* = 1 turn, Figures (4.18, 4.19) for the sample processed for *N* = 3 turns, Figures (4.20 – 4.24) for the sample processed for *N* = 5 turns, and Figures (4.26 – 4.28) for the sample processed for *N* = 10 turns. The fragmentation of the β–phase into small particles occurred during processing as revealed in Figures (4.8 – 4.10) for the sample processed for *N* = 1/2 turn, Figures (4.13 – 4.17) for the sample processed for *N* = 1 turn, and Figures (4.18, 4.19) for the sample processed for *N* = 3 turns. The break–up of the β–phase was associated with the scattering or spreading of these particles to the surrounding areas as shown in Figure 4.11 for the sample processed for *N* = 1/2 turn, and Figure 4.17 for the sample processed for *N* = 1 turn. The fine particles of β–phase were aligned in the form of bands as shown in Figure 4.15 for the sample processed for *N* = 1 turn, Figures (4.18, 4.19) for the sample processed for *N* = 3 turns, Figures (4.20 – 4.22, 4.24) for the sample processed for *N* = 5 turns and Figures (4.26 – 4.29) for the sample processed for *N* = 10 turns. A close look at the aligned bands of the β–phase showed well–distributed particles with nanometre sizes, as shown in Figure 4.25 for the sample processed for *N* = 5 turns and Figure 4.29 for the sample processed for *N* = 10 turns. The size distribution, area fraction and average size of β–phase are illustrated in Figure 4.30, for the as–received alloy and processed alloy for different number of turns after HPT processing at 296 K. The AZ91 alloy was inspected using TEM for samples processed at room temperature for *N* = 1/2 and 1 turn in HPT using an applied pressure of 3.0 GPa as presented in Figure 4.31. The microstructure of the alloy at this low number of turns (*N* = 1/2) revealed the occurrence of the grain refinement with grain sizes in the range of (200 – 1000) nm as shown in Figure 4.31 (a). The alloy exhibited a strong degree of grain refinement down to 50 nm after just *N* = 1 turn as exhibited in Figure 4.31 (b) and the grain boundaries after *N* = 5 turns were ill–defined as shown in Figure 4.31 (c).

4.1.2 Microstructure processed at 296 K across the vertical cross–sections

The microstructures of the vertical cross–sections of the disks processed at room temperature, for *N* = 1/4, 1 and 5 turns, using an applied pressure of 3.0 GPa, are

presented in Figure 4.32. The microstructure of the as–received alloy is also shown in Figure 4.32. These images represent the centre, mid–radius and edge regions of the vertical planes of disks. The apparent variation in microstructures can be seen in the through–thickness and radial directions. The as–received alloy showed a matrix of α–Mg solid solution and β–phase along the grain boundaries, without no apparent alignment of either phase, as exhibited in Figure 4.32 (a – c) and Figure 4.33 (a). The processed disks exhibited elongated microstructure, shear bands decorated by β–phase and twinning, all distributed along the vertical cross–sections as presented in Figure 4.32 (d – l) and Figure 4.33 (b – d). The microstructure seems slightly deformed, and tends to be elongated in the direction of torsion straining at the centre region along the vertical cross–sections as exhibited in Figure 4.32 (d) for N = 1/4 turn, which is associated with the presence of the shear bands decorated by β–phase and twinning as shown in Figure 4.32 (d) and Figure 4.33 (b). It can be seen that more shear bands appeared at mid–radius and edge areas as shown in Figure 4.32 (e, f). The elongated microstructure showed an increase in the alignment in the direction of torsion straining as shown in Figure 4.32 (f).

After processing for N = 1 turn, the microstructure was more elongated at the centre region and was associated with the aligned β–phase near the top and bottom surfaces as shown in Figure 4.32 (g). The microstructure exhibited areas containing shear bands decorated by β–phase aligned in random directions, but the major direction of these bands tends to be parallel to the vertical cross–section of the processed disk at mid–radius and edge areas as shown in Figure 4.32 (h, i). Further straining up to N = 5 turns resulted in the formation of a main shear band in the centre area, which consisted of many secondary shear bands aligned at 45° with respect to the main shear band along the vertical cross–section of the processed disk as shown in Figure 4.32 (j). The width of the main shear band increased in the mid–radius region and it was associated with secondary shear bands that aligned along the vertical cross–section of the processed disk as shown in Figure 4.32 (k). It was found that the microstructures in both mid–radius and edge regions consist of severely deformed microstructures aligned parallel to the vertical cross–section as shown in Figure 4.32 (l, i) for N = 1 and N = 5 turns, respectively.

4.1.3 Microstructure processed at 423 K and 473 K across the *horizontal* cross–sections

The microstructure of the AZ91 alloy processed at 423 K using an applied pressure of 3.0 GPa for *N* = 1/2, 1 and 5 turns are shown in Figures (4.34 – 4.36), respectively. The samples showed twinning across the processed microstructures and this evolution of twinning increased and spread gradually with increasing number of turns especially at the edge regions of the processed disks. The microstructures at the centre regions showed a slower rate of twinning evolution as shown in Figure 4.34 (a), Figure 4.35 (a) and Figure 4.36 (a) compared to that at the edge regions. The level of grain refinement at the centre regions occurred at a slower rate than at edge regions. It can be seen that the microstructures at the edge regions were refined effectively through the segmentation of the coarse grains by twinning as shown in Figure 4.34 (b), Figure 4.35 (b) and Figure 4.36 (b). The microstructure of the AZ91 alloy processed at 473 K using an applied pressure of 3.0 GPa for *N* = 1/2, 1 and 5 turns are shown in Figure 4.37. The activity of twinning at the centre regions of the processed disks was increased with increasing number of turns. For samples processed for *N* = 1/2 and 1 turn, the twins were resulted in the segmentation of grains as shown in Figure 4.37 (a, b) similarly for samples processed at 423 K. Grain growth was found in the sample processed for *N* = 5 turns as shown in Figure 4.37 (c).

4.1.4 XRD results

The XRD diffraction patterns were recorded for the as–received alloy and processed alloy at 296 K in HPT using an applied pressure of 3.0 GPa for *N* = 1/2, 1, 5 and 10 turns and the results are plotted as shown in Figure 4.38 (a – e). Recorded peaks belong to the α–Mg matrix, where prismatic planes $(10\bar{1}0)$ and $(20\bar{2}0)$, basal plane (0002) and pyramidal planes $(10\bar{1}1)$, $(10\bar{1}2)$, $(11\bar{2}0)$ and $(10\bar{1}3)$ were detected as shown in Figure 4.38 for all tested samples. The whole–profile fitting procedure for the recorded peaks is shown in Figure 4.38 (f – g) for as–received alloy and processed alloy at 296 K in HPT using

an applied pressure of 3.0 GPa for *N* = 10 turns. The prismatic plane $(10\bar{1}0)$ dominated before HPT processing in the as–received alloy, while after processing the pyramidal plane $(10\bar{1}1)$ was more dominant. Furthermore, two pyramidal planes $(10\bar{1}2)$ and $(10\bar{1}3)$ were detected after processing and these planes were not detected in the as–received alloy. The lattice parameters were calculated for the processed alloy using the following relation [190]:

$$\frac{1}{d_{sp}^2} = \frac{4}{3}\left(\frac{h^2 + hk + k^2}{a^2}\right) + \frac{l^2}{c^2} \tag{4.1}$$

where d_{sp} is the inter–spacing distance between the atomic planes, $h\ k\ l$ are Miller indices and a, c are the short and long lattice constants in the HCP structure. The values of constants a and c of the AZ91 alloy were about 0.317 nm and 0.550 nm, respectively, which are slightly different from their counterparts for pure magnesium that are quoted as 0.320 nm and 0.520 nm for the constants a and c, respectively [191]. The variation in the crystallite size of the processed alloy with the number of turns in HPT processing at 296 K is plotted in Figure 4.39. A significant reduction in the crystallite size was achieved with increasing the number of turns in HPT at 296 K, which emphasizes the advantage of HPT processing at room temperature rather than processing at elevated temperatures. Another direct observation of the effect of processing at room temperature will be shown later through the microhardness results in the next section.

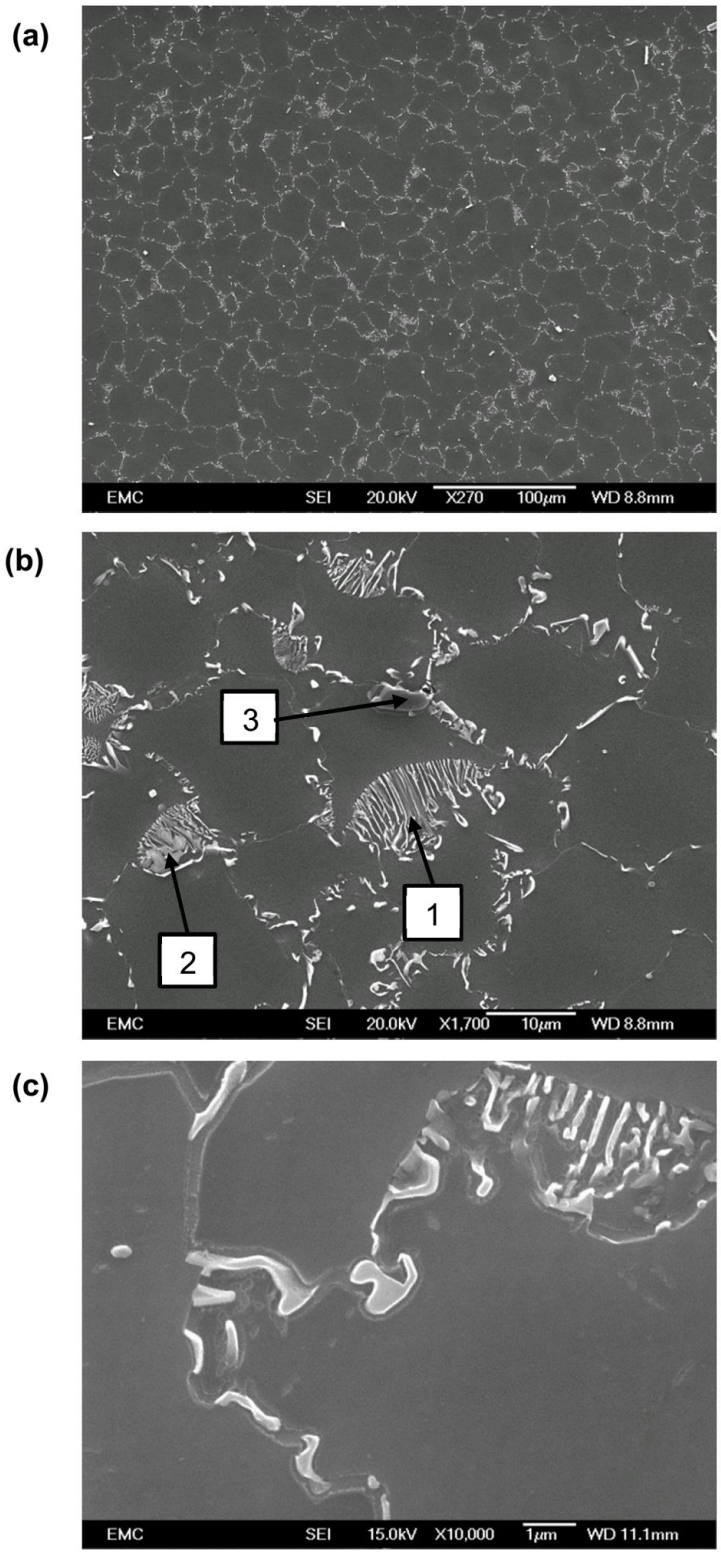

Figure 4.1: (a) The microstructure of the as–received AZ91 magnesium alloy on the horizontal cross–section of the disk, (b) A magnified view of the as–received microstructure shows the presence of lamellar (arrow–1) and agglomerate (arrow–2) forms of β–phase and Al8Mn5 compound (arrow–3), and (c) A magnified view of the as–received microstructure shows the presence of β–phase along the grain boundaries.

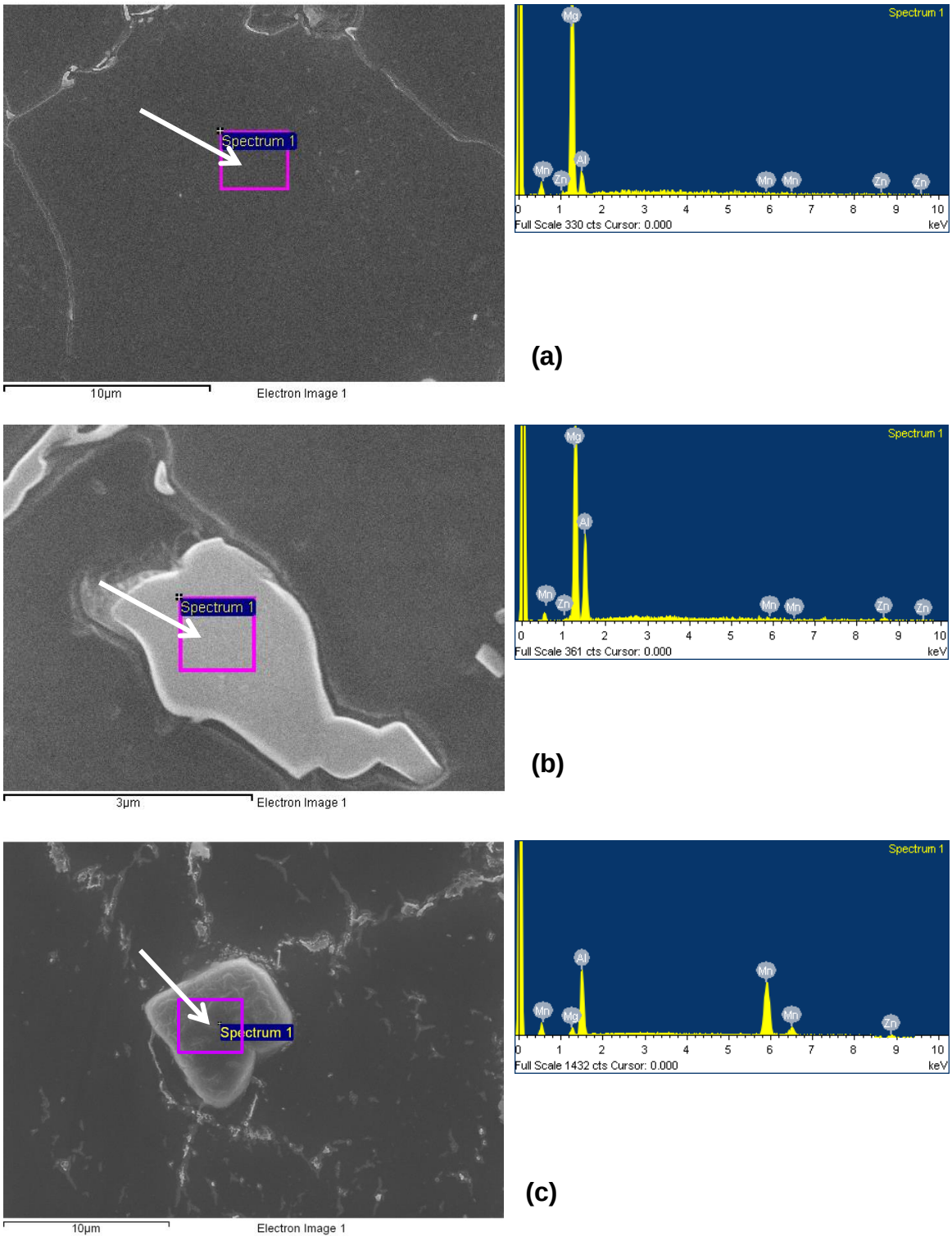

Figure 4.2: The chemical analysis of as–received AZ91 magnesium alloy on the horizontal cross–section of the disk shows: (a) α–matrix, (b) β–phase ($Mg_{17}Al_{12}$ intermetallic compound) and (c) Al_8Mn_5 intermetallic compound. The white arrows show the locations of the chemical analyses.

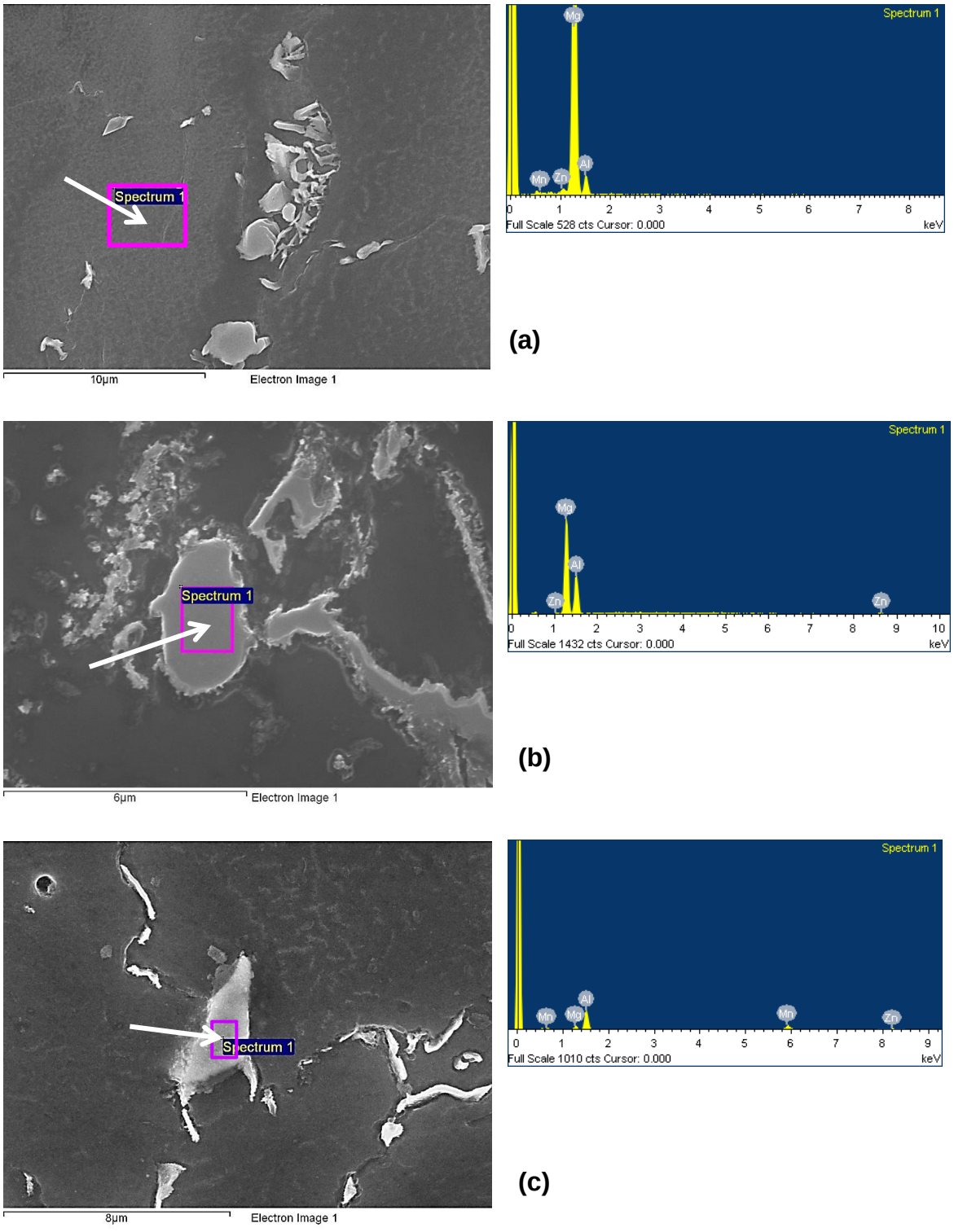

Figure 4.3: The chemical analysis on the horizontal cross–section of the AZ91 disk processed by HPT after N = 5 turns for: (a) α–matrix, (b) β–phase ($Mg_{17}Al_{12}$ intermetallic compound) and (c) Al_8Mn_5 intermetallic compound. The white arrows show the locations of the chemical analyses.

Table 4.1: The chemical compositions on selected locations in Figure 4.2 for the as–received AZ91 magnesium alloy for: (a) α–matrix, (b) β–phase ($Mg_{17}Al_{12}$ intermetallic compound) and (c) Al_8Mn_5 intermetallic compound.

(a) α–matrix		**(b) β–phase ($Mg_{17}Al_{12}$)**		**(c) Al_8Mn_5 compound**	
Element	**wt.%**	**Element**	**wt.%**	**Element**	**wt.%**
Mg	88.74	Mg	55.14	Mg	4.44
Al	9.57	Al	43.13	Al	43.10
Zn	1.11	Zn	0.94	Zn	0.45
Mn	0.58	Mn	0.79	Mn	51.95

Table 4.2: The chemical compositions on selected locations in Figure 4.3 for the AZ91 magnesium alloy processed by HPT after N = 5 turns at 296 K using an applied pressure of 3.0 GPa for: (a) α–matrix, (b) β–phase ($Mg_{17}Al_{12}$ intermetallic compound) and (c) Al_8Mn_5 intermetallic compound.

(a) α–matrix		**(b) β–phase (Mg17Al12)**		**(c) Al8Mn5 compound**	
Element	**wt.%**	**Element**	**wt.%**	**Element**	**wt.%**
Mg	87.74	Mg	58.22	Mg	6.10
Al	10.53	Al	40.20	Al	42.10
Zn	1.31	Zn	0.91	Zn	0.65
Mn	0.42	Mn	0.67	Mn	51.15

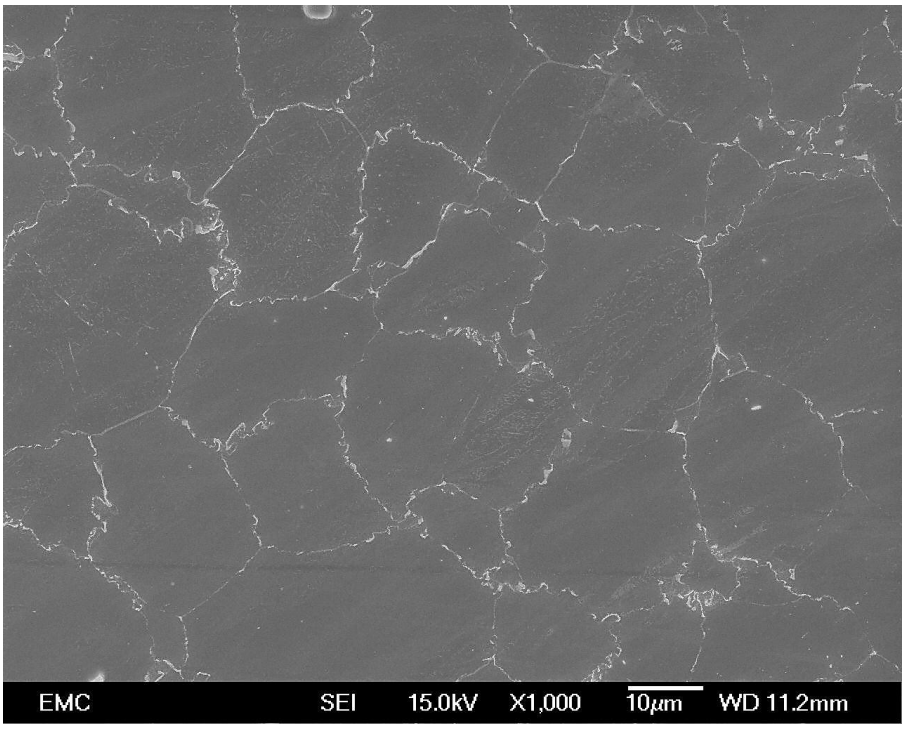

Figure 4.4: The microstructure on the horizontal cross–section at the centre region for the pressed disk without torsion (*N* = 0) at 296 K using an applied pressure of 3.0 GPa.

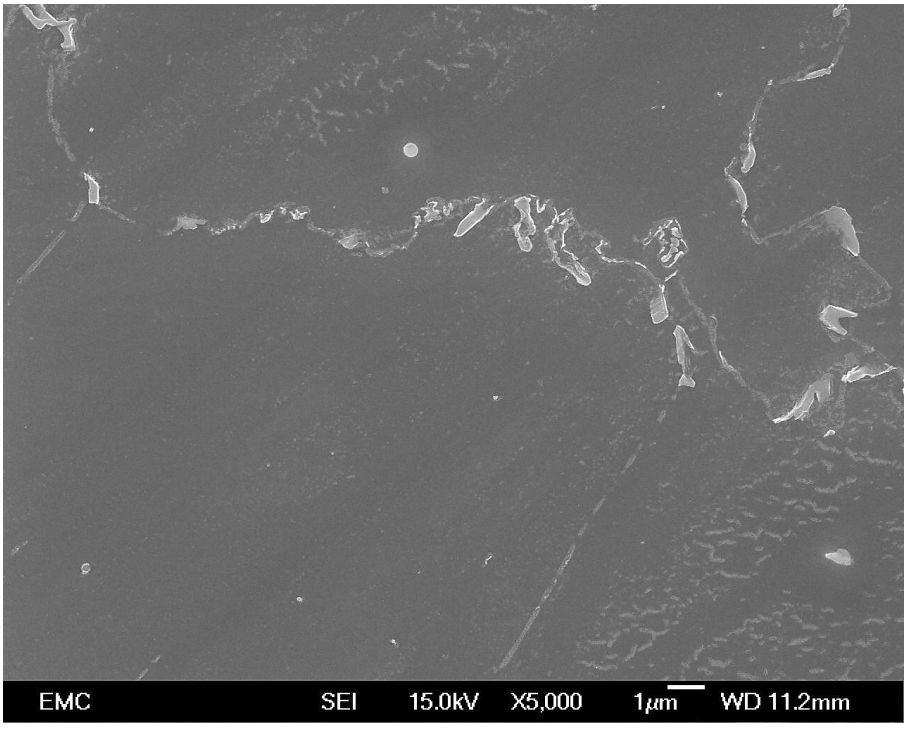

Figure 4.5: A magnified view of the microstructure on the horizontal cross–section at the centre region of the pressed disk without torsion (*N* = 0) at 296 K using an applied pressure of 3.0 GPa, shows the fragmentation of lamellar and agglomerate β–phase.

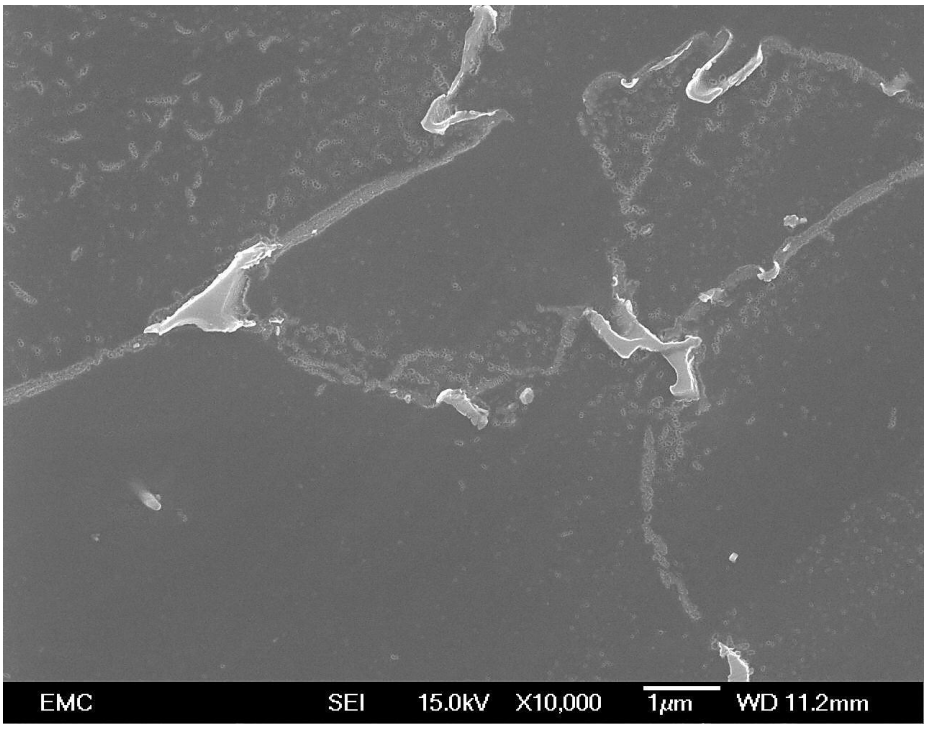

Figure 4.6: A magnified view of the microstructure on the horizontal cross–section at the centre region of the pressed disk without torsion (N = 0) at 296 K using an applied pressure of 3.0 GPa, shows the scattering of β–phase particles.

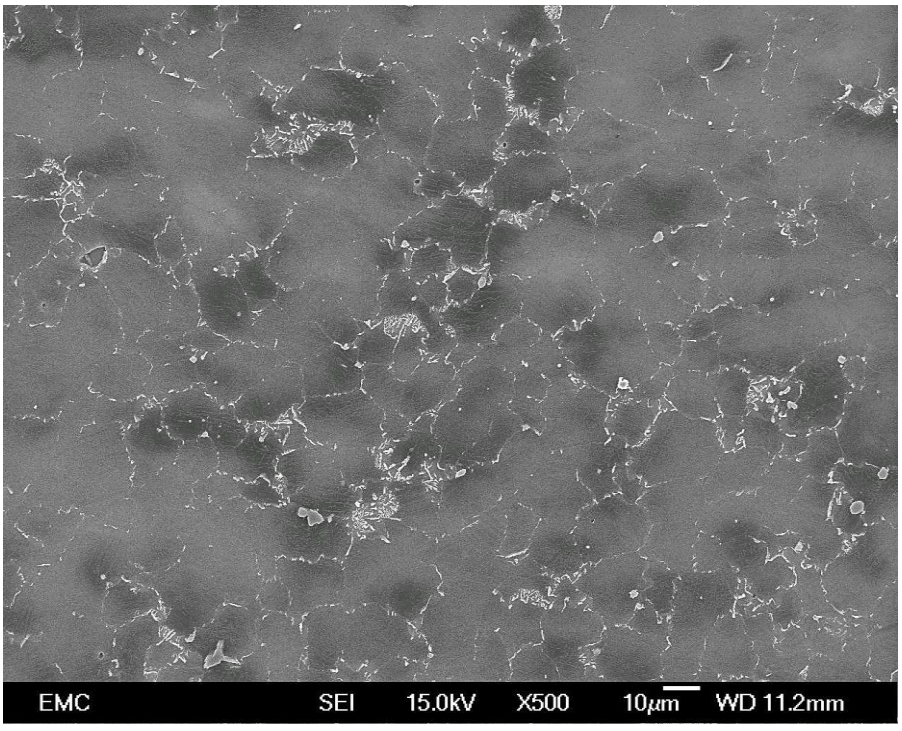

Figure 4.7: The microstructure on the horizontal cross–section at the centre region after HPT processing for N = 1/2 turn at 296 K using an applied pressure of 3.0 GPa.

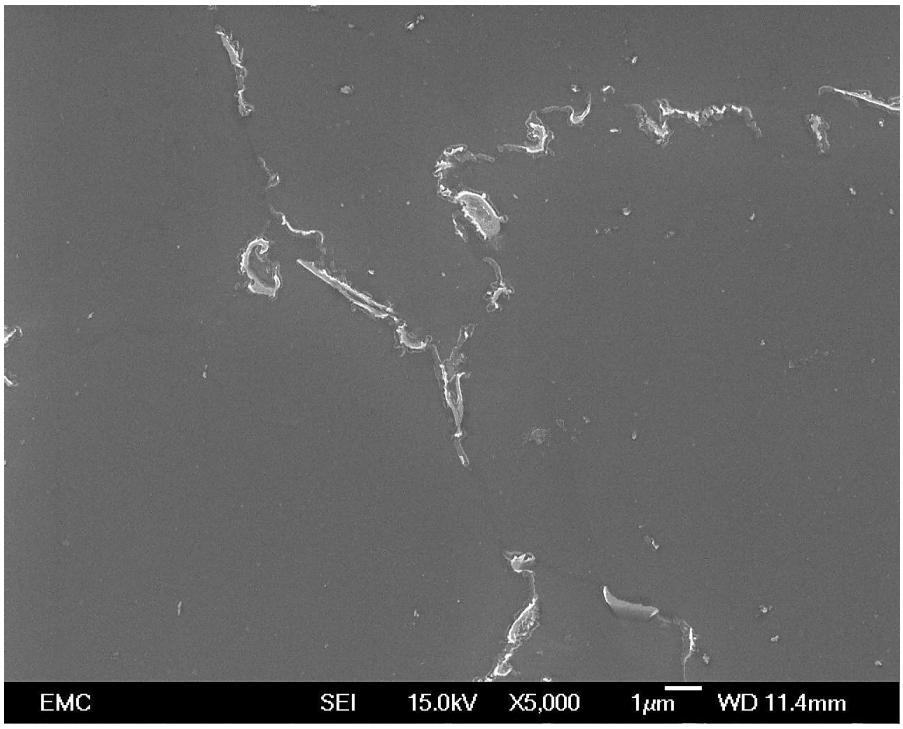

Figure 4.8: The microstructure on the horizontal cross–section at the centre region after HPT processing for *N* = 1/2 turn at 296 K using an applied pressure of 3.0 GPa shows the fragmentation of β–phase.

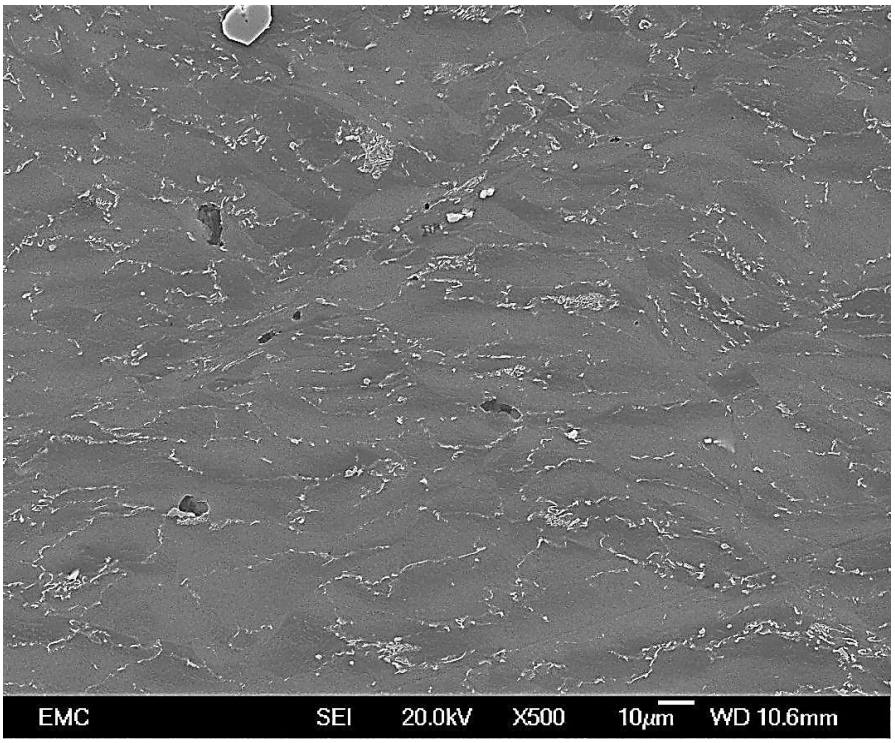

Figure 4.9: The microstructure on the horizontal cross–section at the edge region after HPT processing for *N* = 1/2 turn at 296 K using an applied pressure of 3.0 GPa.

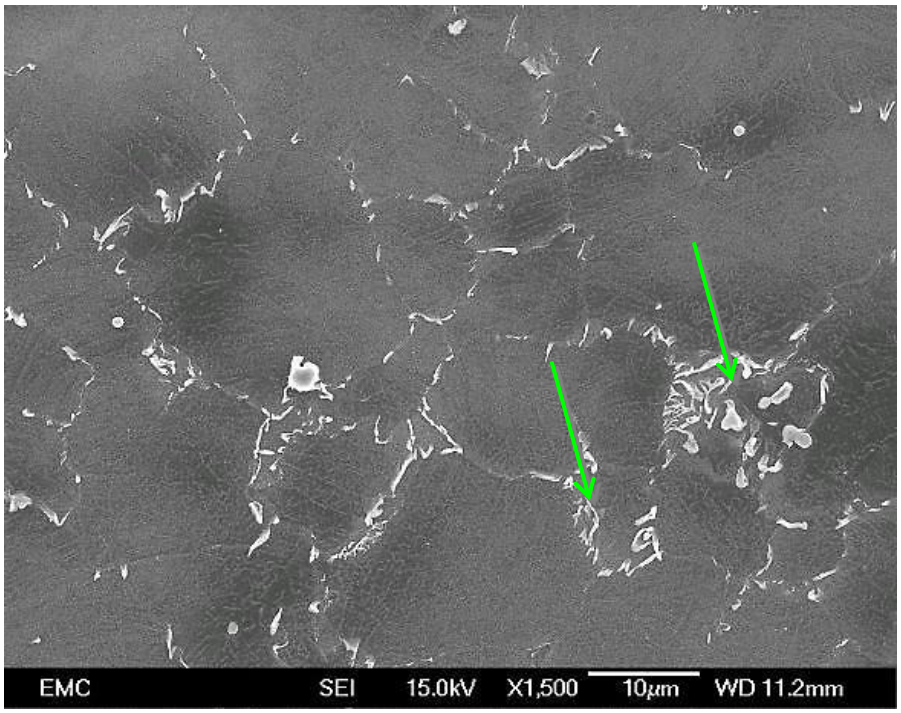

Figure 4.10: The microstructure on the horizontal cross–section at the edge region after HPT processing for *N* = 1/2 turn at 296 K using an applied pressure of 3.0 GPa shows the fragmentation of β–phase as shown by the green arrows.

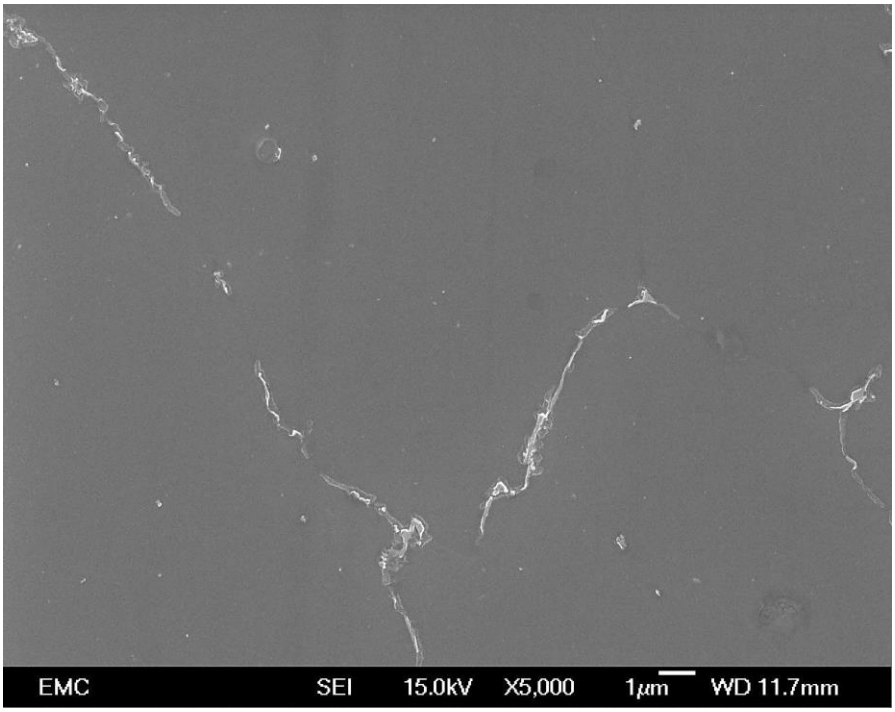

Figure 4.11: A magnified view of the microstructure on the horizontal cross–section at the edge region after HPT processing for *N* = 1/2 turn at 296 K using an applied pressure of 3.0 GPa shows the fragmentation and scattering of β–phase particles.

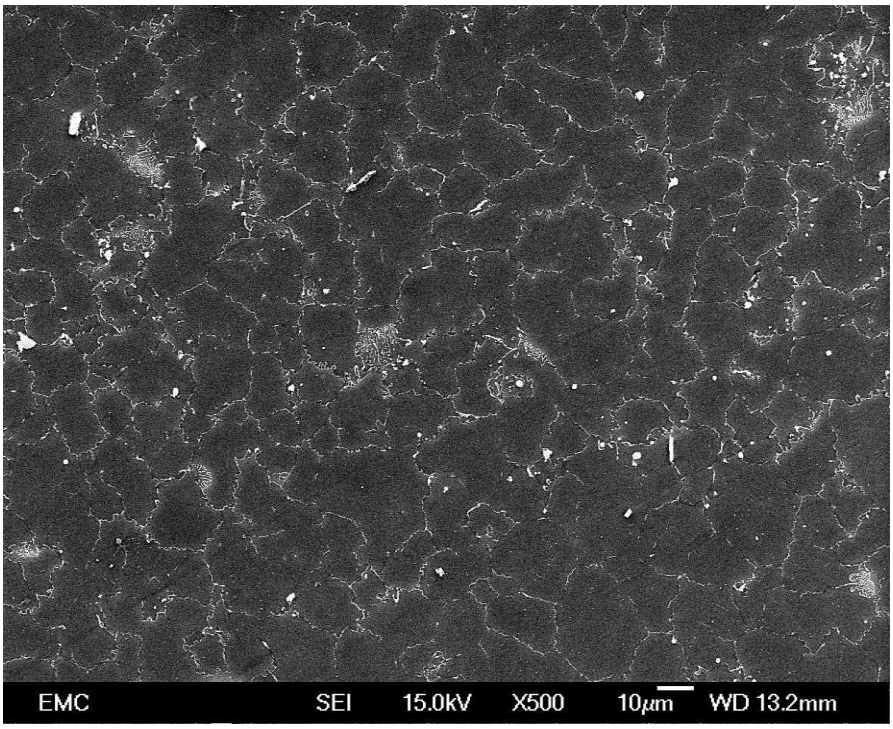

Figure 4.12: The microstructure on the horizontal cross–section at the centre region after HPT processing for *N* = 1 turn at 296 K using an applied pressure of 3.0 GPa.

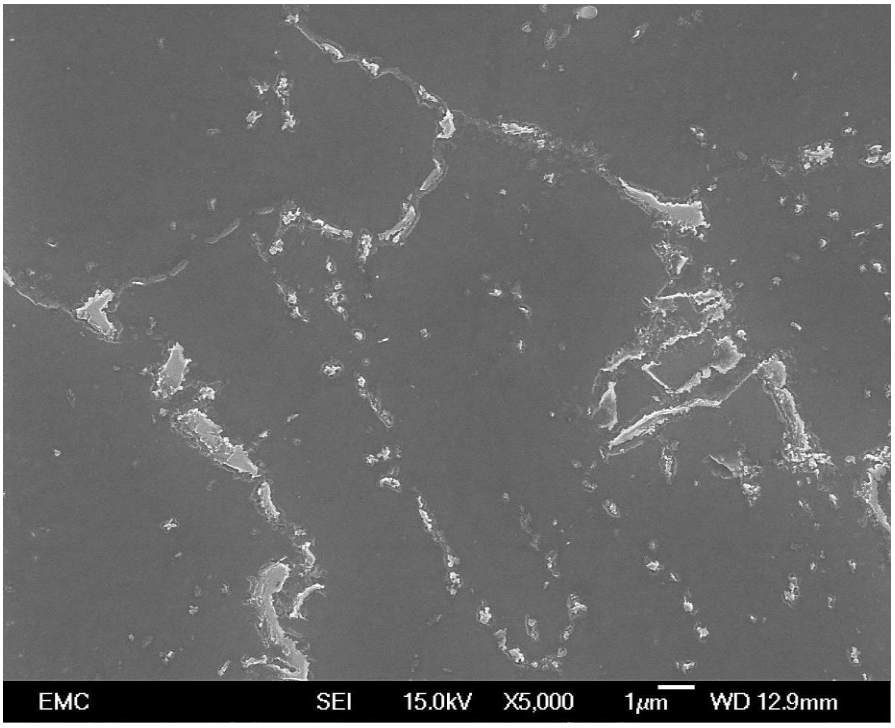

Figure 4.13: The microstructure on the horizontal cross–section at the centre region after HPT processing for *N* = 1 turn at 296 K using an applied pressure 3.0 GPa shows the β–phase fragmentation.

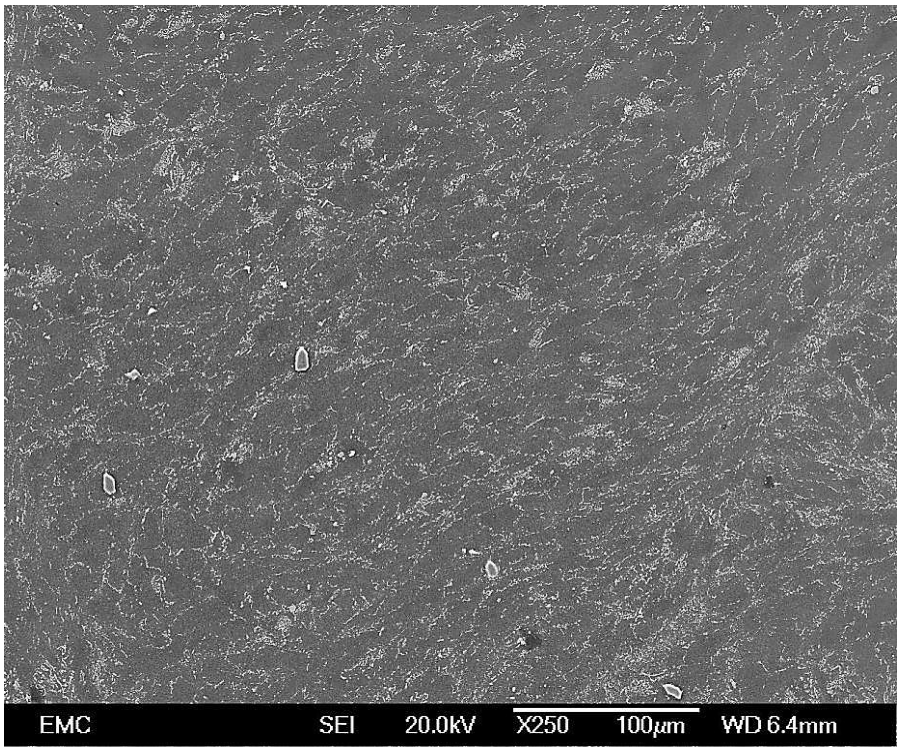

Figure 4.14: The microstructure on the horizontal cross–section at the edge region after HPT processing for *N* = 1 turn at 296 K usning an applied pressure of 3.0 GPa.

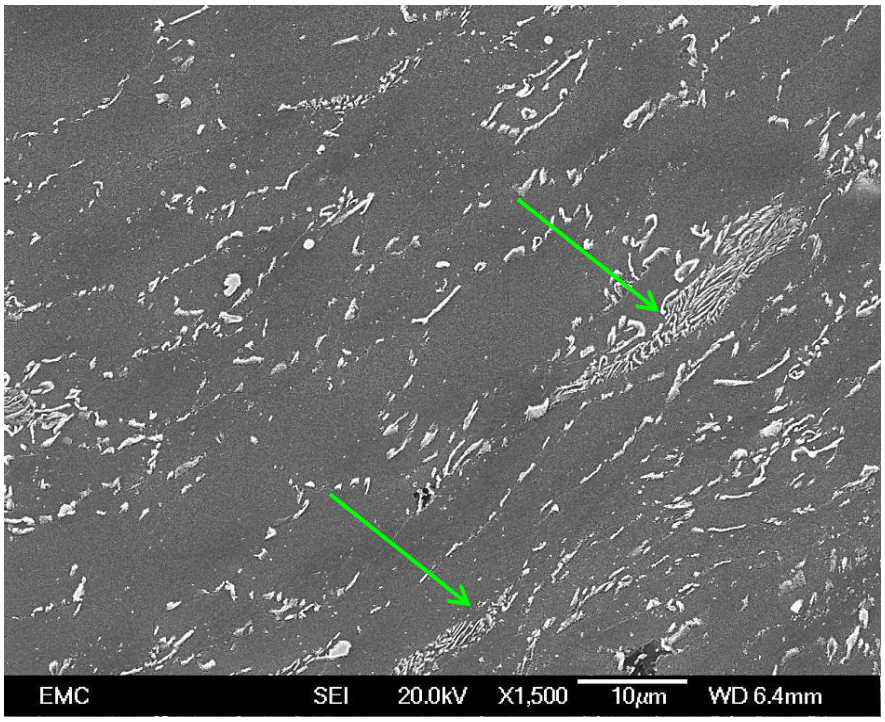

Figure 4.15: The microstructure on the horizontal cross–section at the edge region after HPT processing for *N* = 1 turn at 296 K using an applied pressure of 3.0 GPa shows the alignment of β–phase as indicated by the green arrows.

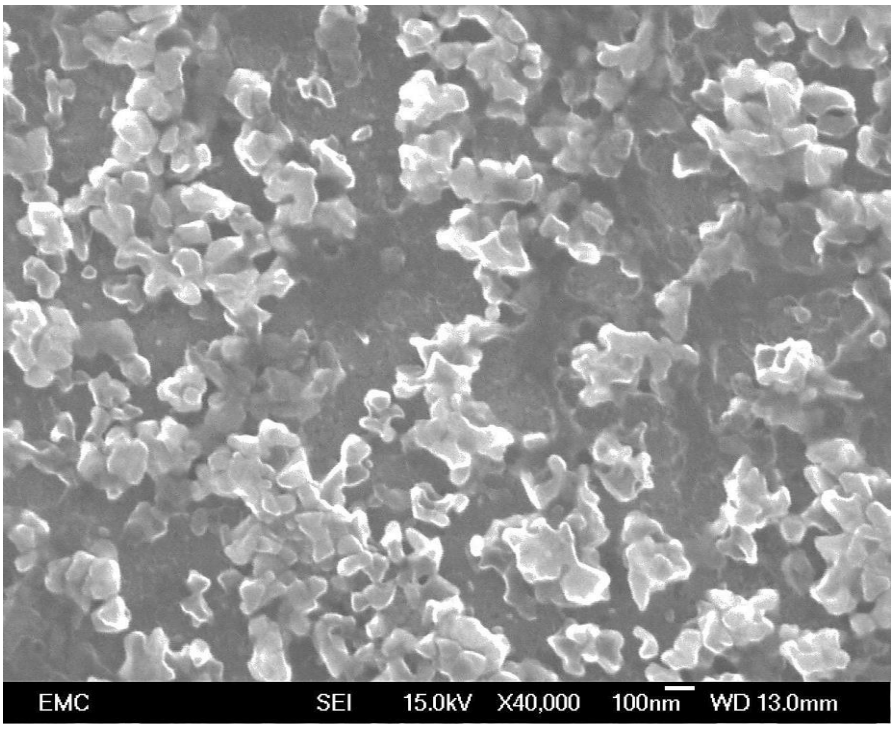

Figure 4.16: A magnified view of the microstructure on the horizontal cross–section at the edge region after HPT processing for *N* = 1 turn at 296 K using an applied pressure of 3.0 GPa shows the nano–sized particles of the aligned β–phase.

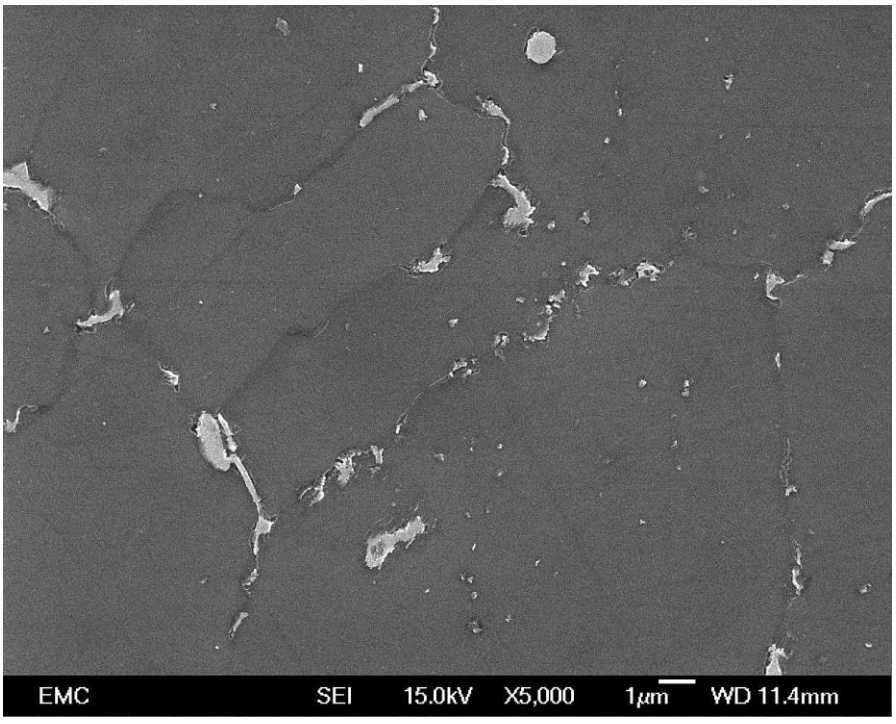

Figure 4.17: A magnified view of the microstructure on the horizontal cross–section at the edge region after HPT processing for *N* = 1 turn at 296 K using an applied pressure of 3.0 GPa shows the grain boundaries became ill–defined and the fragmentation and scattering of β–phase particles.

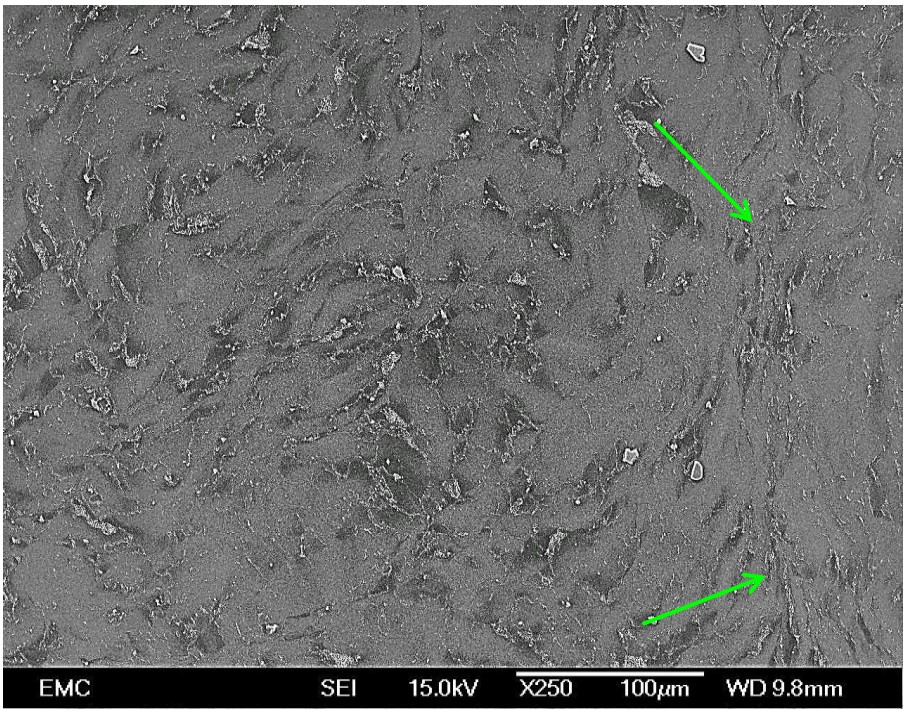

Figure 4.18: The microstructure on the horizontal cross–section at the centre region after HPT processing for *N* = 3 turns at 296 K using an applied pressure of 3.0 GPa shows the alignment of β–phase near the centre region as indicated by the green arrows.

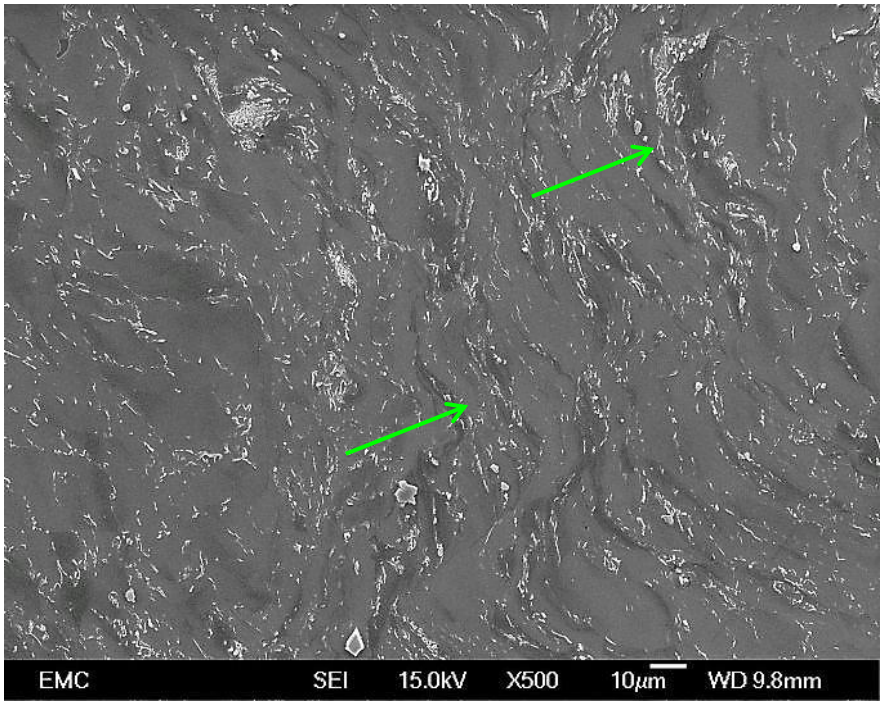

Figure 4.19: The microstructure on the horizontal cross–section at the edge region after HPT processing for *N* = 3 turns at 296 K using an applied pressure of 3.0 GPa shows the grain boundaries became ill–defined and the fragmentation of aligned β–phase as indicated by the green arrows.

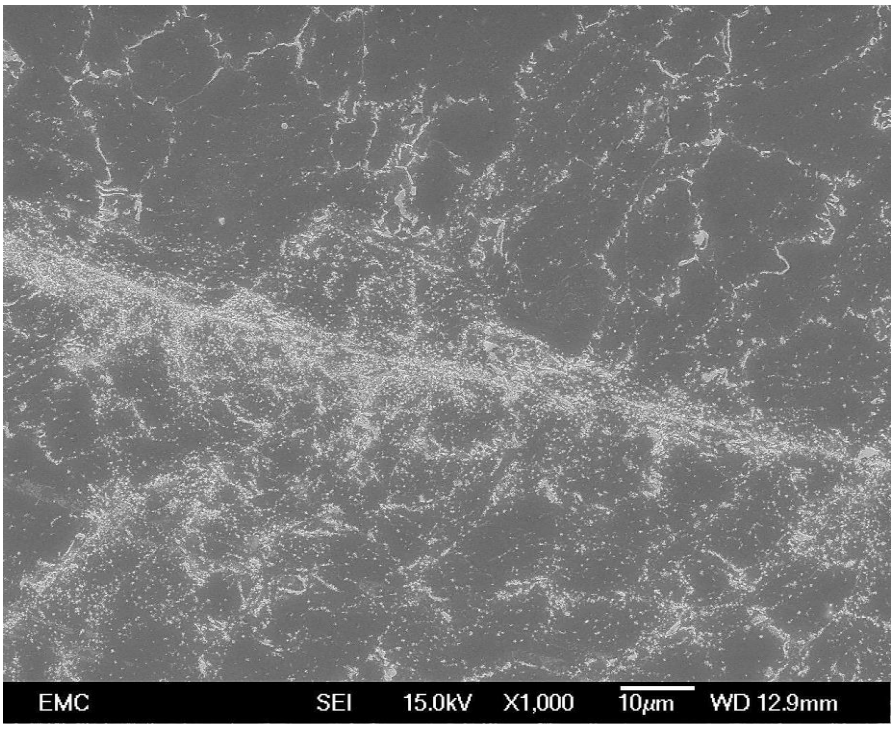

Figure 4.20: The microstructure on the horizontal cross–section at the centre region after HPT processing for *N* = 5 turns at 296 K using an applied pressure of 3.0 GPa shows no distinct grain boundaries and the alignment and distribution of β–phase particles.

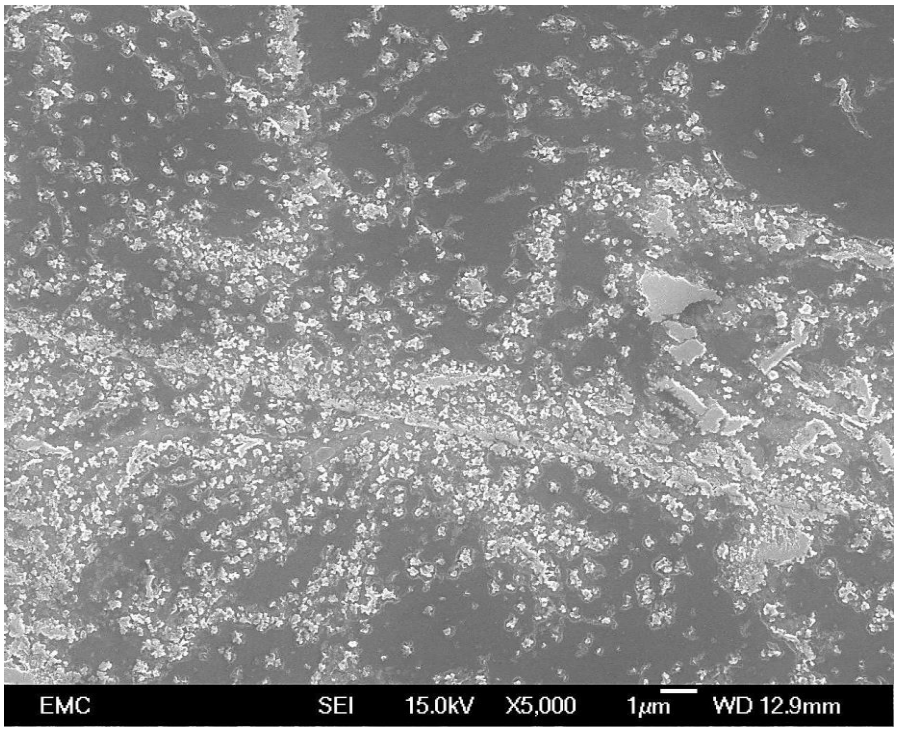

Figure 4.21: The microstructure on the horizontal cross–section at the centre region after HPT processing for *N* = 5 turns at 296 K using an applied pressure of 3.0 GPa shows the alignment of β–phase particles.

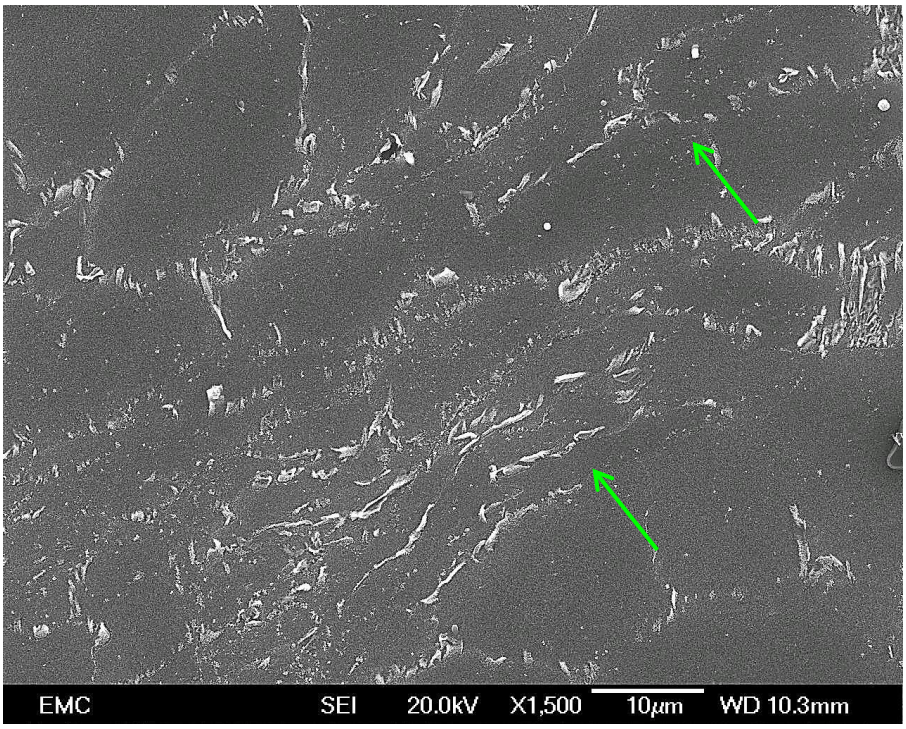

Figure 4.22: The microstructure on the horizontal cross–section at the centre region after HPT processing for *N* = 5 at 296 K using an applied pressure of 3.0 GPa turns shows the fragmentation of aligned β–phase as shown by the green arrows.

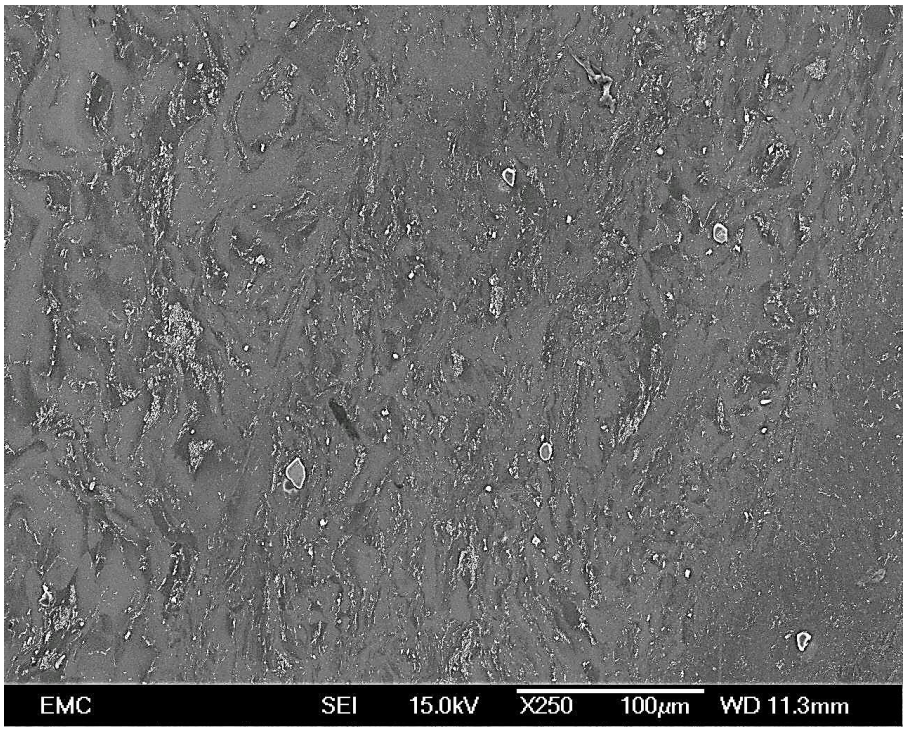

Figure 4.23: The microstructure on the horizontal cross–section at the edge region after HPT processing for *N* = 5 turns at 296 K using an applied pressure of 3.0 GPa shows the distribution of β–phase particles with no distinct grain boundaries.

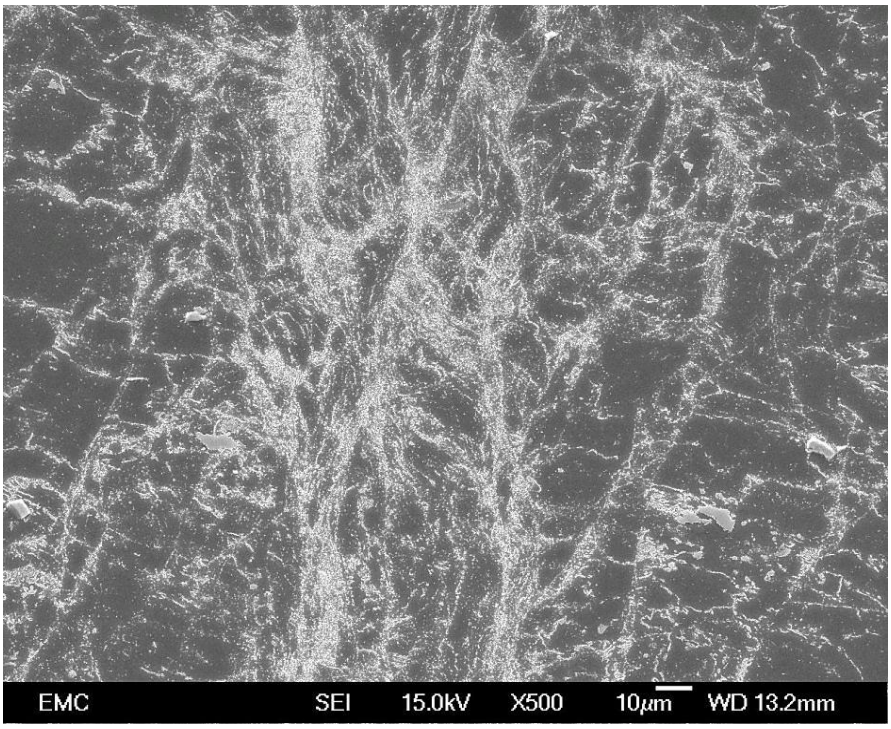

Figure 4.24: The microstructure on the horizontal cross–section at the edge region after HPT processing for *N* = 5 turns at 296 K using an applied pressure of 3.0 GPa.

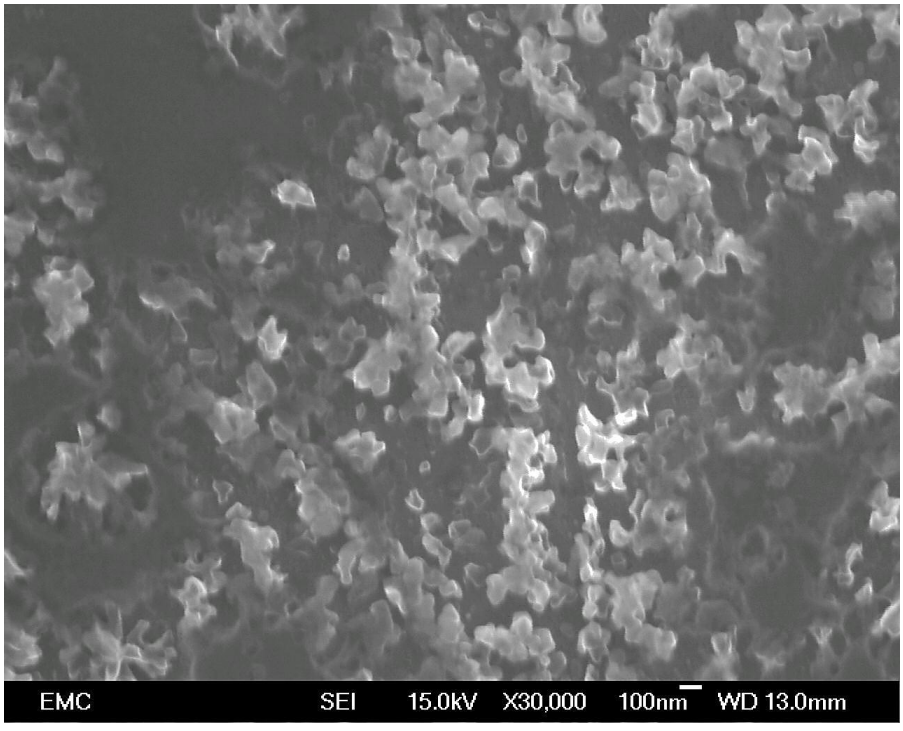

Figure 4.25: A magnified view of the microstructure on the horizontal cross–section at the edge region after HPT processing for *N* = 5 turns at 296 K using an applied pressure of 3.0 GPa shows the nano–sized particles of the aligned β–phase.

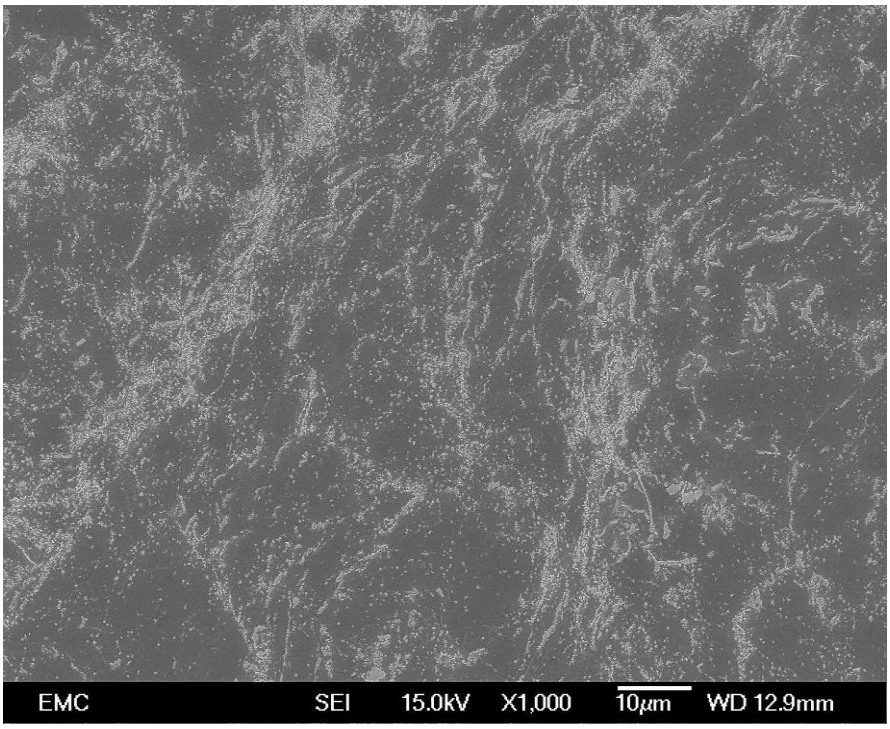

Figure 4.26: The microstructure on the horizontal cross–section at the centre region after HPT processing for *N* = 10 turns at 296 K using an applied pressure of 3.0 GPa shows the alignment of β–phase particles and no distinct grain boundaries.

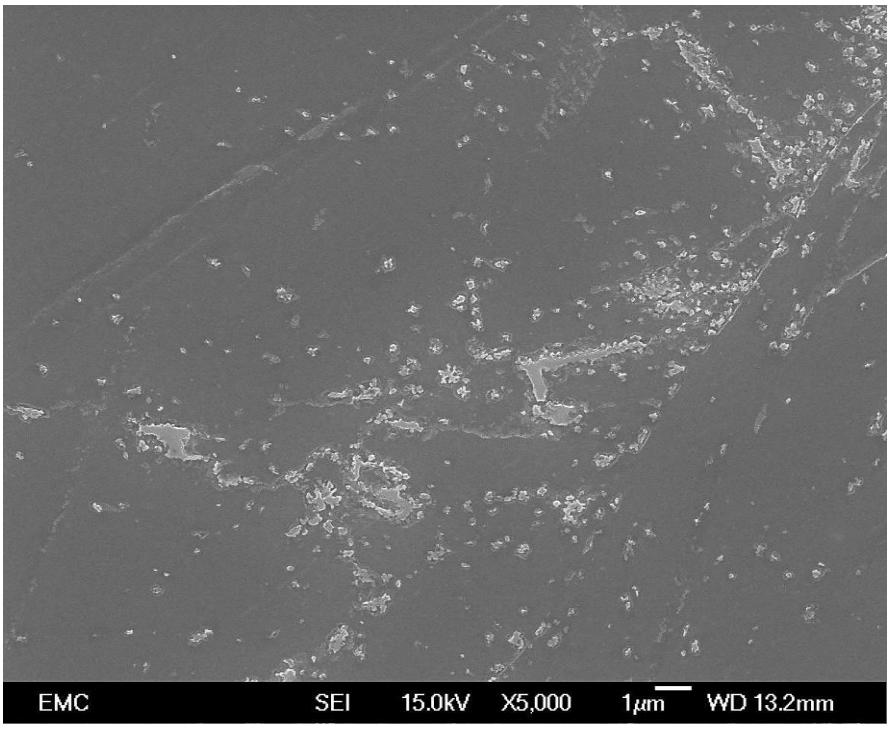

Figure 4.27: The microstructure on the horizontal cross–section at the centre region after HPT processing for *N* = 10 turns at 296 K using an applied pressure of 3.0 GPa shows the fragmentation of β–phase particles and no distinct grain boundaries.

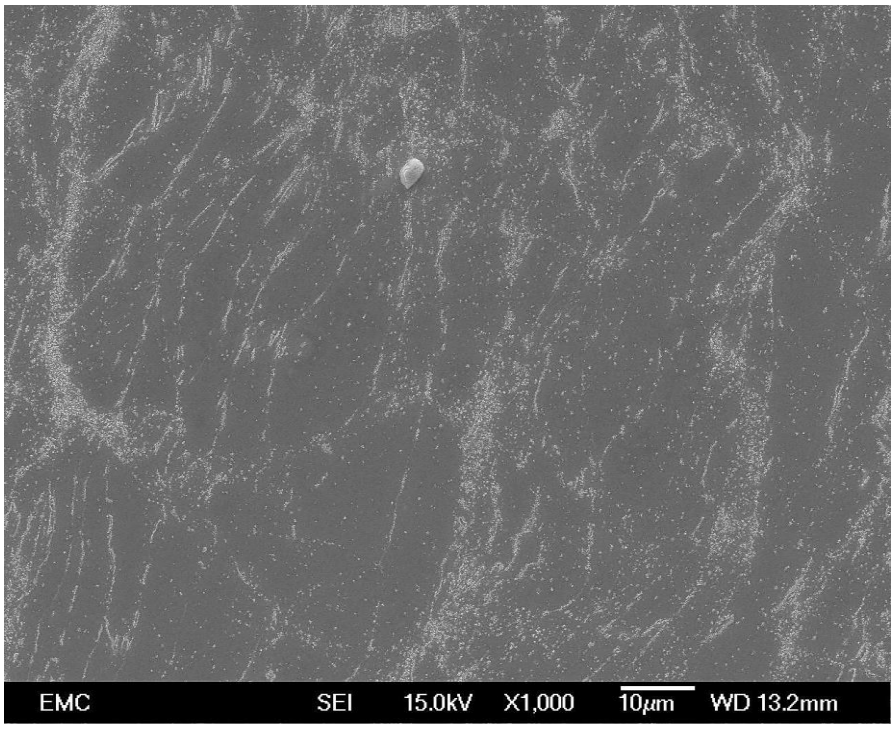

Figure 4.28: The microstructure on the horizontal cross–section at the edge region after HPT processing for *N* = 10 turns at 296 K using an applied pressure of 3.0 GPa shows the alignment of β–phase particles and no distinct grain boundaries.

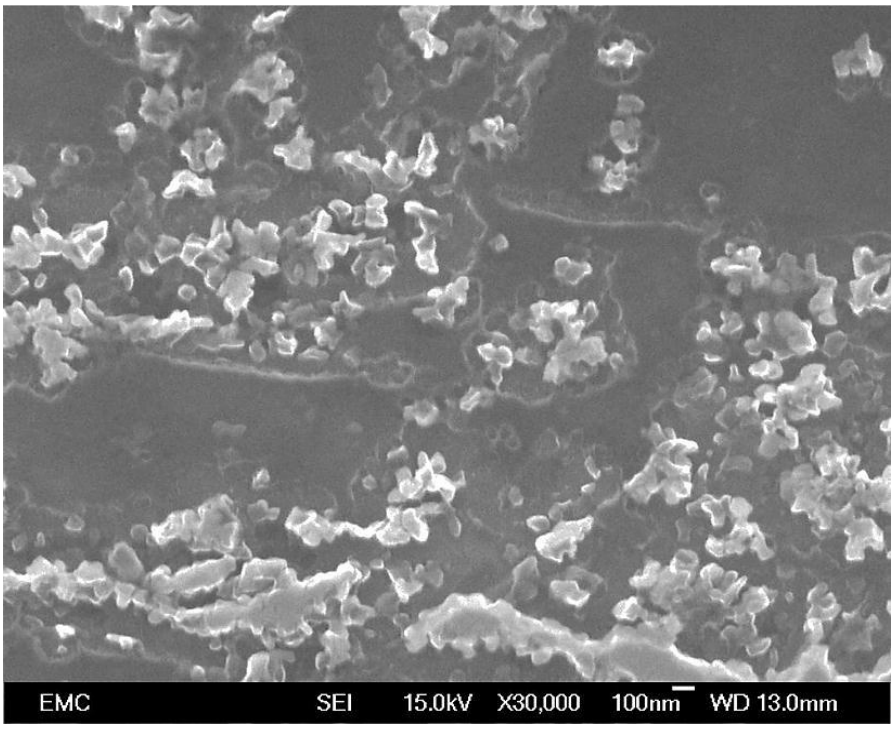

Figure 4.29: The microstructure on the horizontal cross–section at the edge region after HPT processing for *N* = 10 turns at 296 K using an applied pressure of 3.0 GPa shows the nano–sized particles of the aligned β–phase.

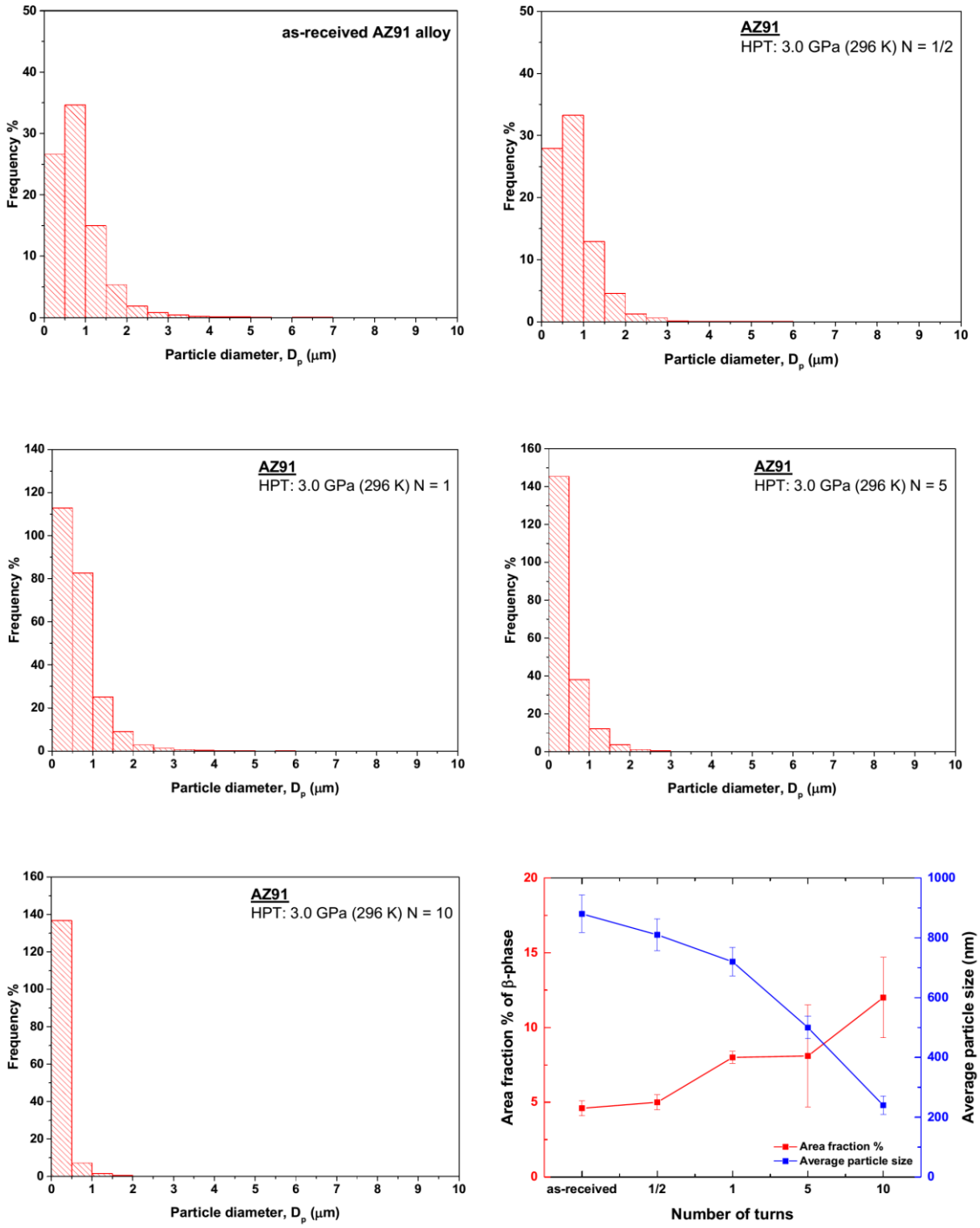

Figure 4.30: The size distribution, area fraction and average size of the β-phase particles in the as–received alloy and processed alloy at 296 K using an applied pressure of 3.0 GPa for different number of turns on the horizontal cross–sections of the processed disks.

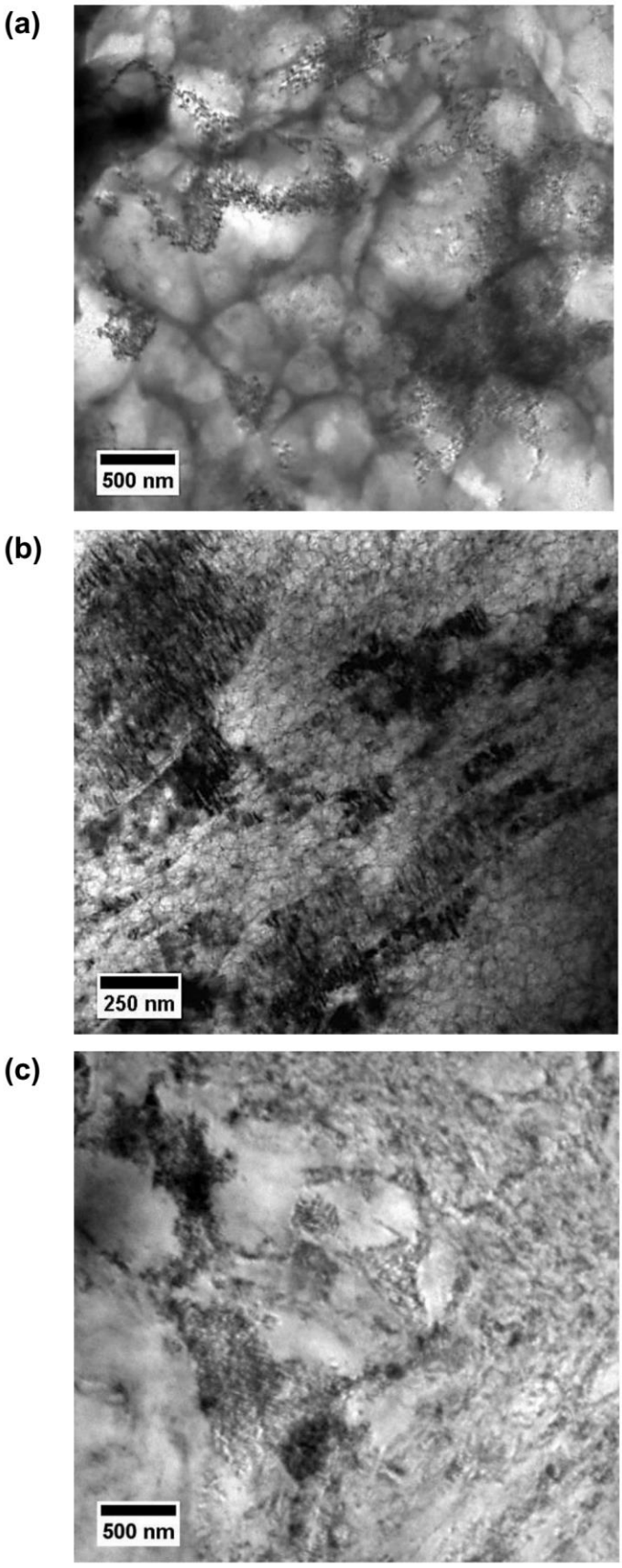

Figure 4.31: Microstructure as observed by TEM of the AZ91 alloy processed in HPT at 296 K using an applied pressure of 3.0 GPa for (a) N = 1/2 turn, (b) N = 1 turn and (c) N = 5 turns on the horizontal cross–sections of the processed disks.

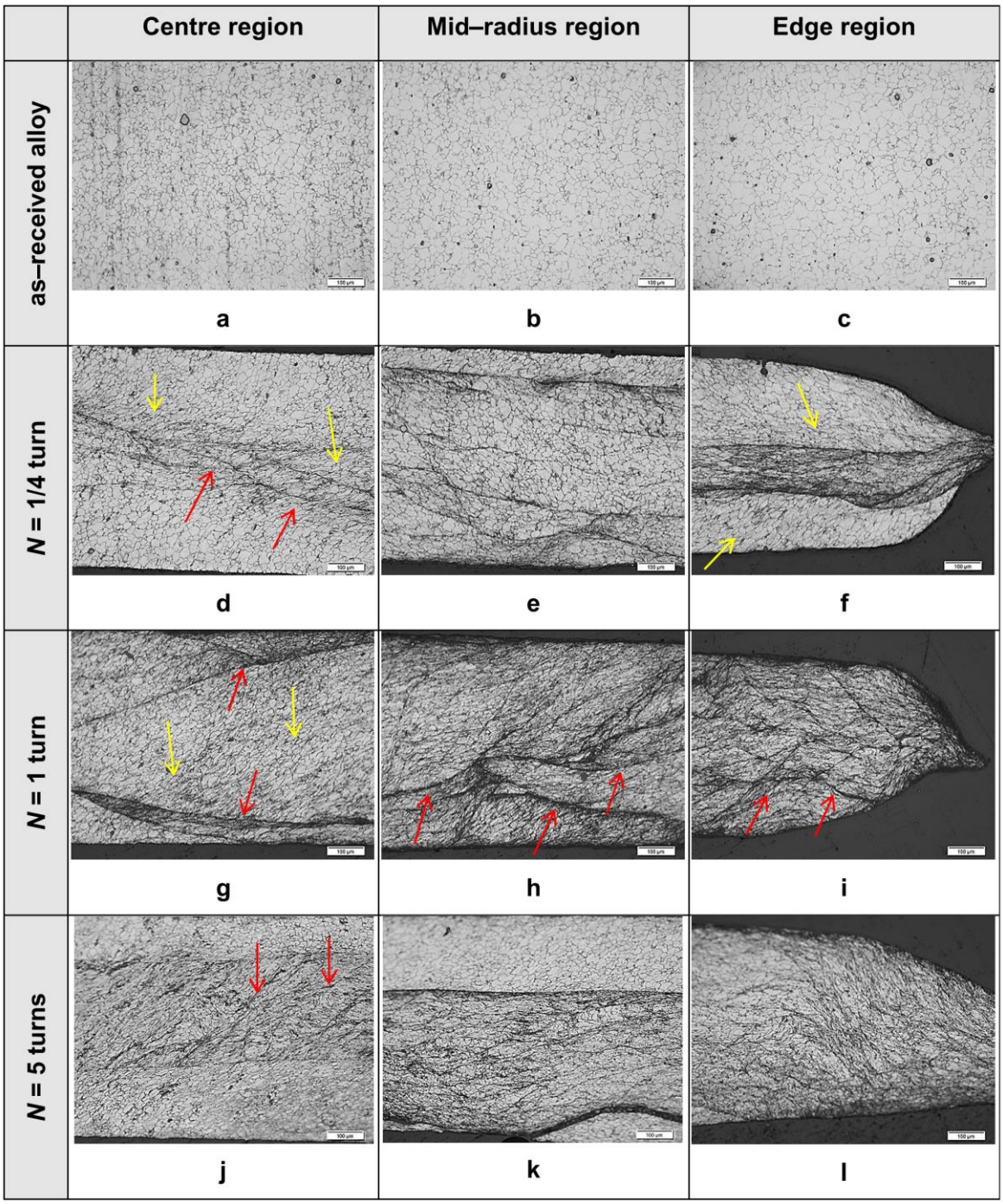

Figure 4.32: The microstructures at the centre, mid–radius, and edge regions across the vertical cross–sections of the as–received and processed disks after different numbers of turns at 296 K using an applied pressure of 3.0 GPa. The yellow and red arrows refer to the elongated microstructure and shear bands decorated by β–phase, respectively. All scales are 100 μm.

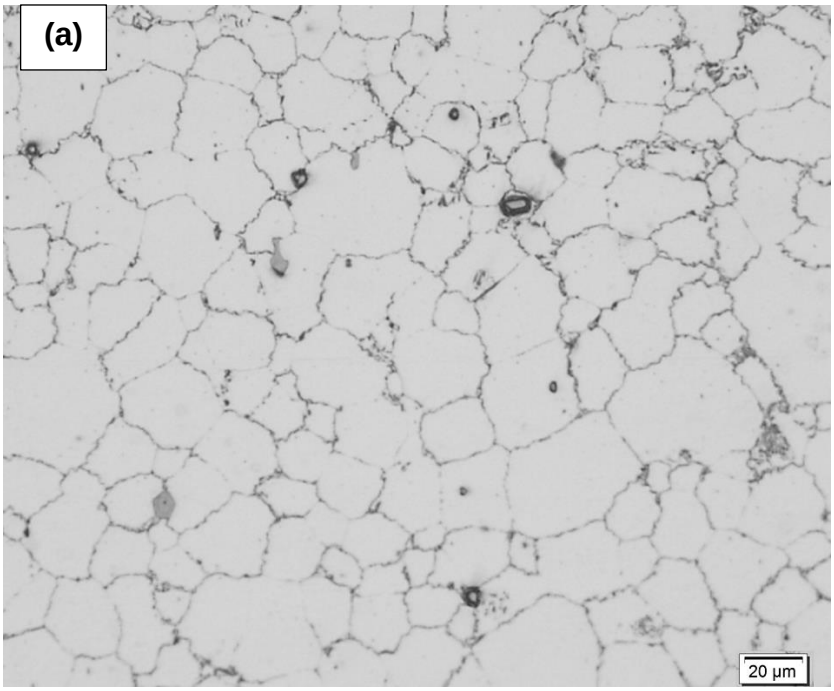
(a)
20 µm

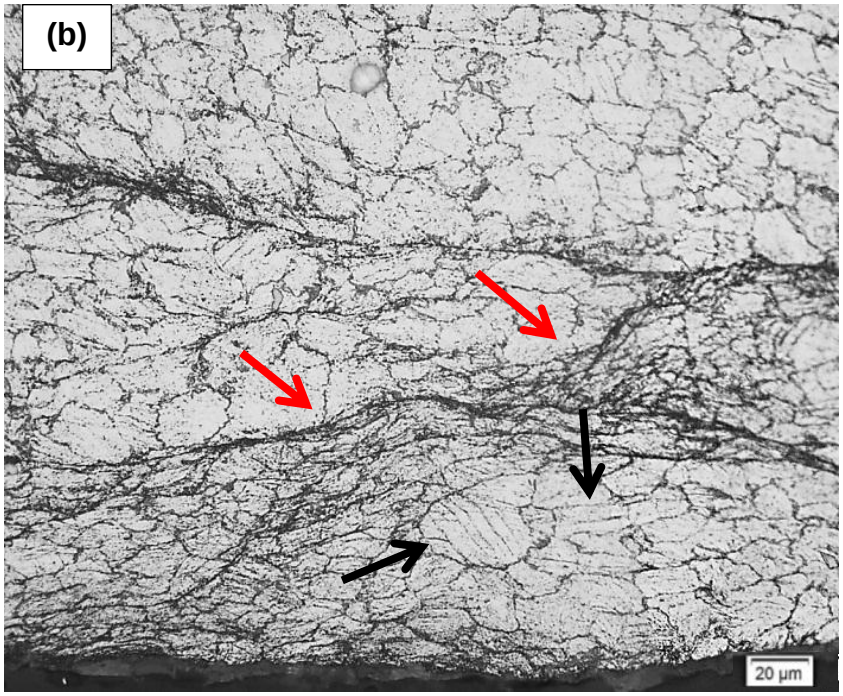
(b)
20 µm

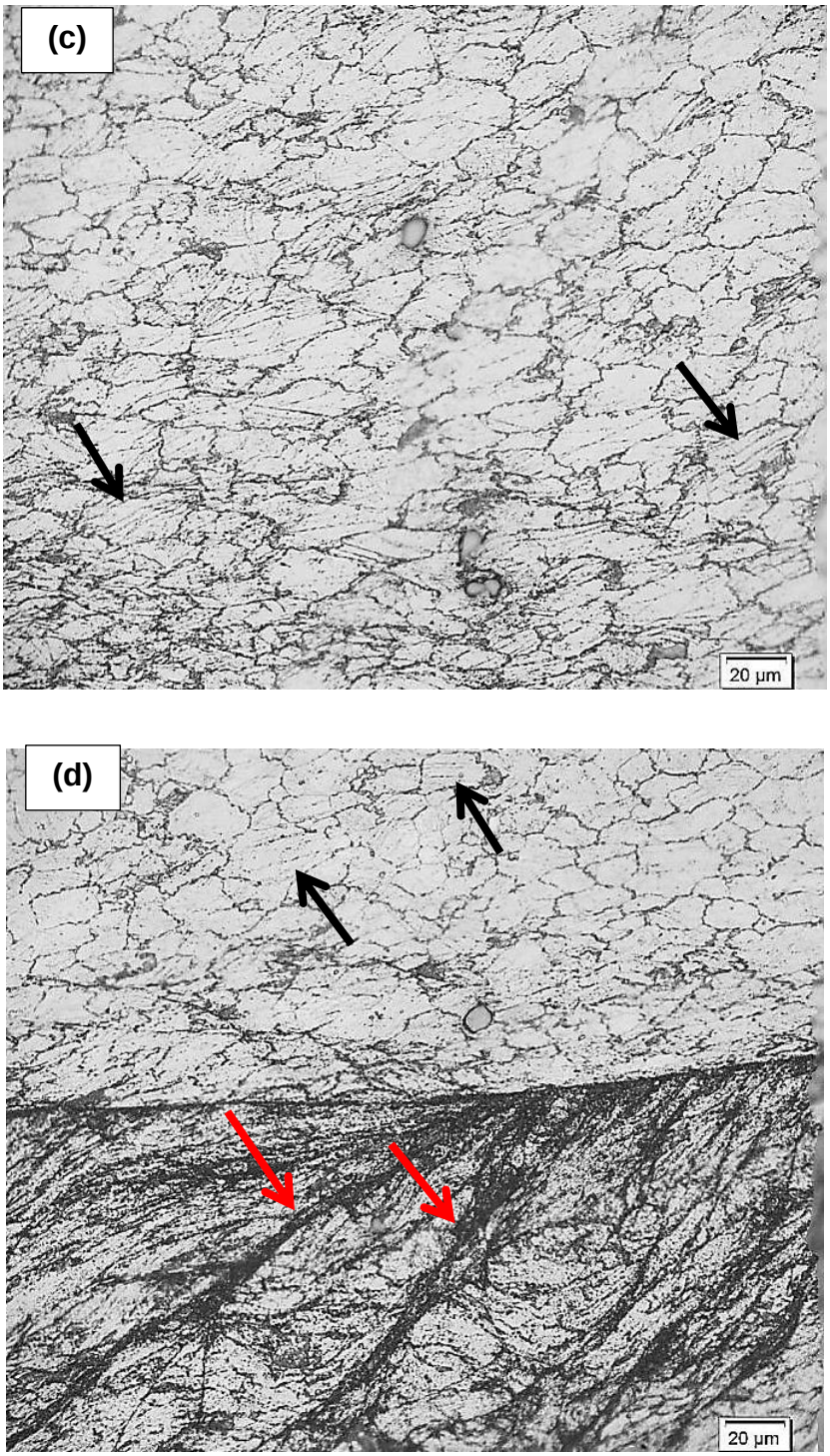

Figure 4.33: Magnified views of the microstructures along the vertical planes as observed by the optical microscope for: (a) the as–received alloy and the disk processed at 296 K using an applied pressure of 3.0 GPa for: (b) *N* = 1/4 turn, (c) *N* = 1 turn and (d) *N* = 5 turns. The black and red arrows refer to the twinning and shear bands decorated by the β–phase, respectively.

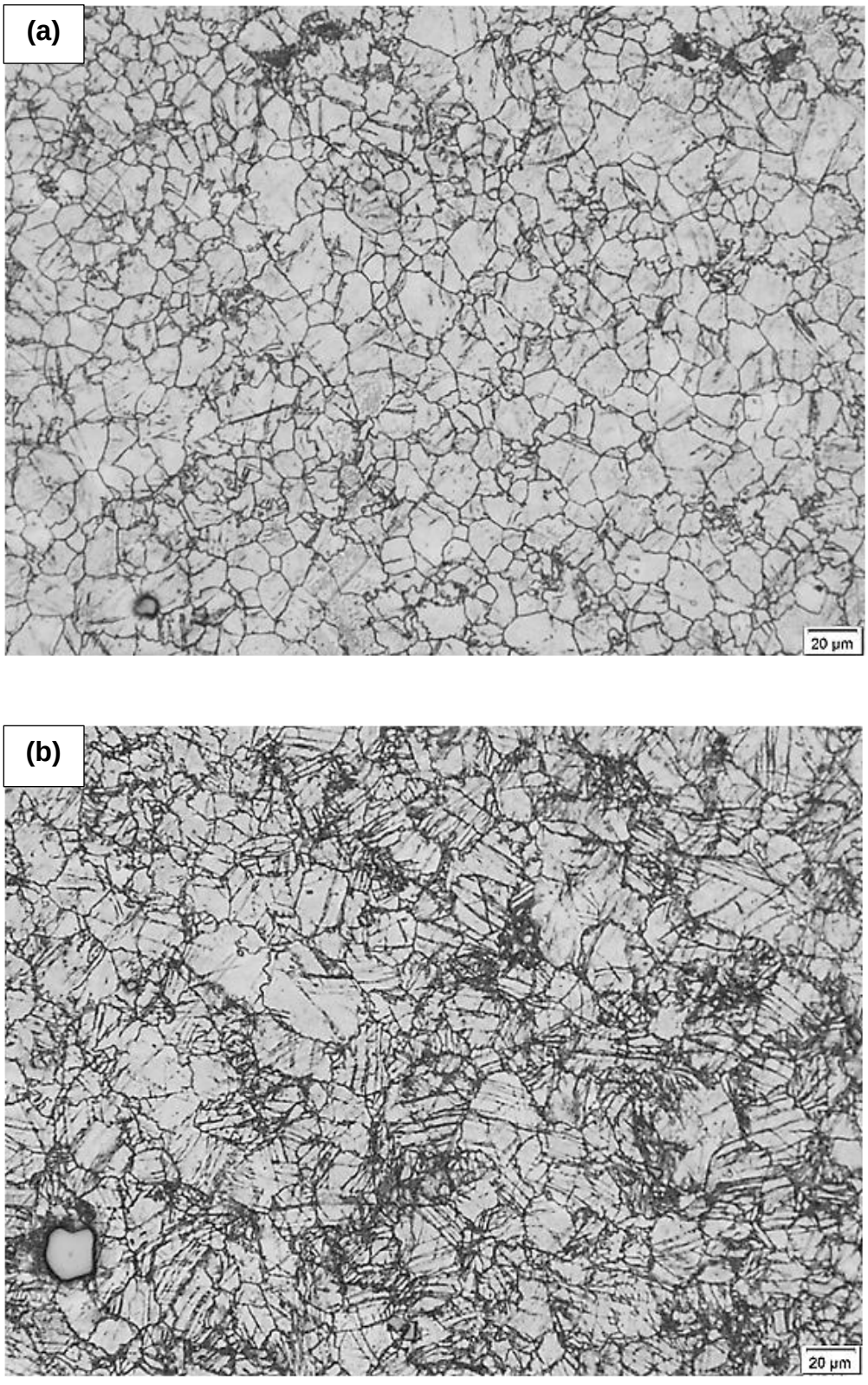

Figure 4.34: Magnified views of the microstructures on the horizontal cross–sections of the disks of the AZ91 alloy processed in HPT at 423 K using an applied pressure of 3.0 GPa for *N* = 1/2 turn at: (a) the centre region and (b) the edge region.

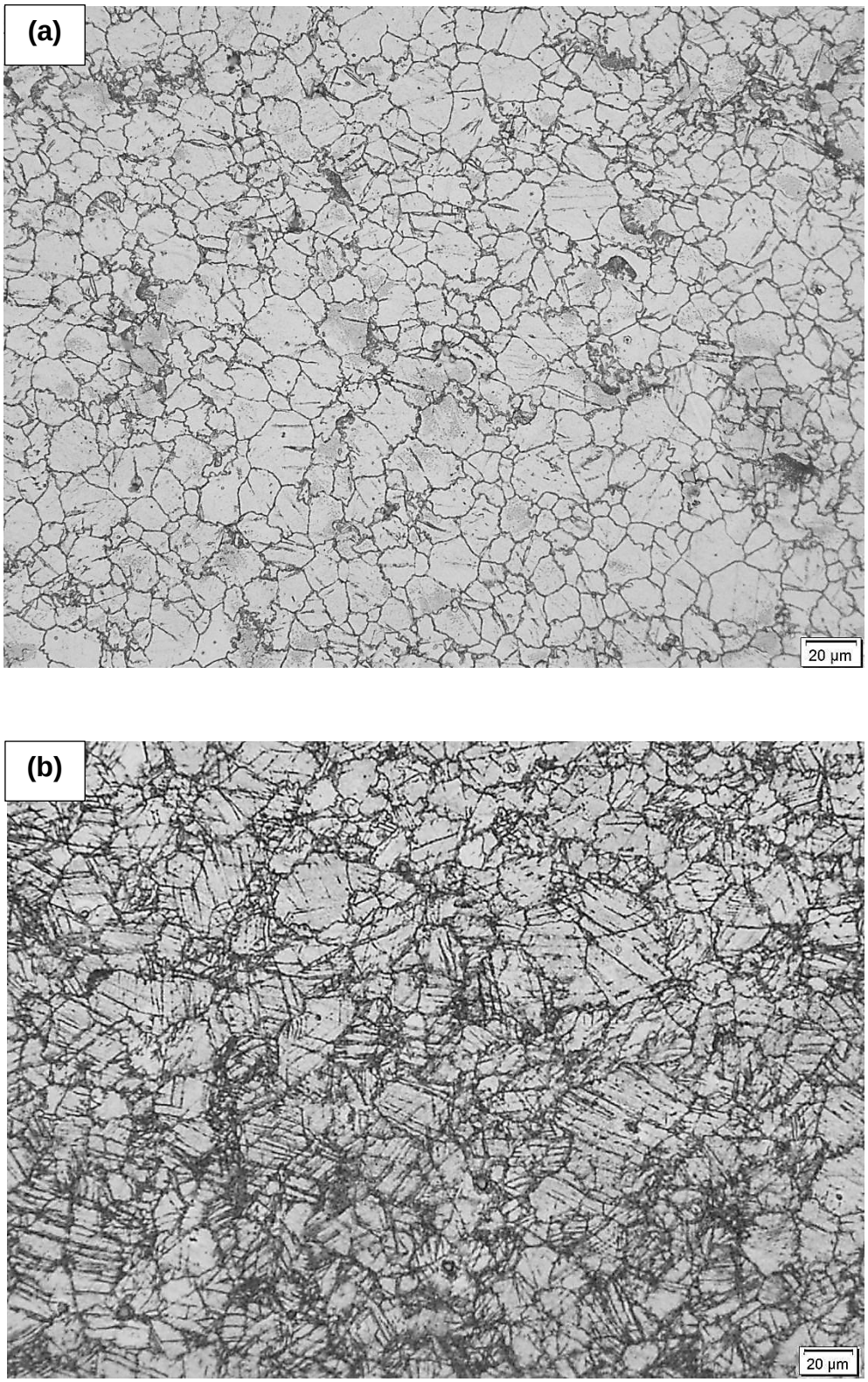

Figure 4.35: Magnified views of the microstructures on the horizontal cross–sections of the disks of the AZ91 alloy processed in HPT at 423 K using an applied pressure of 3.0 GPa for N = 1 turn at: (a) the centre region and (b) the edge region.

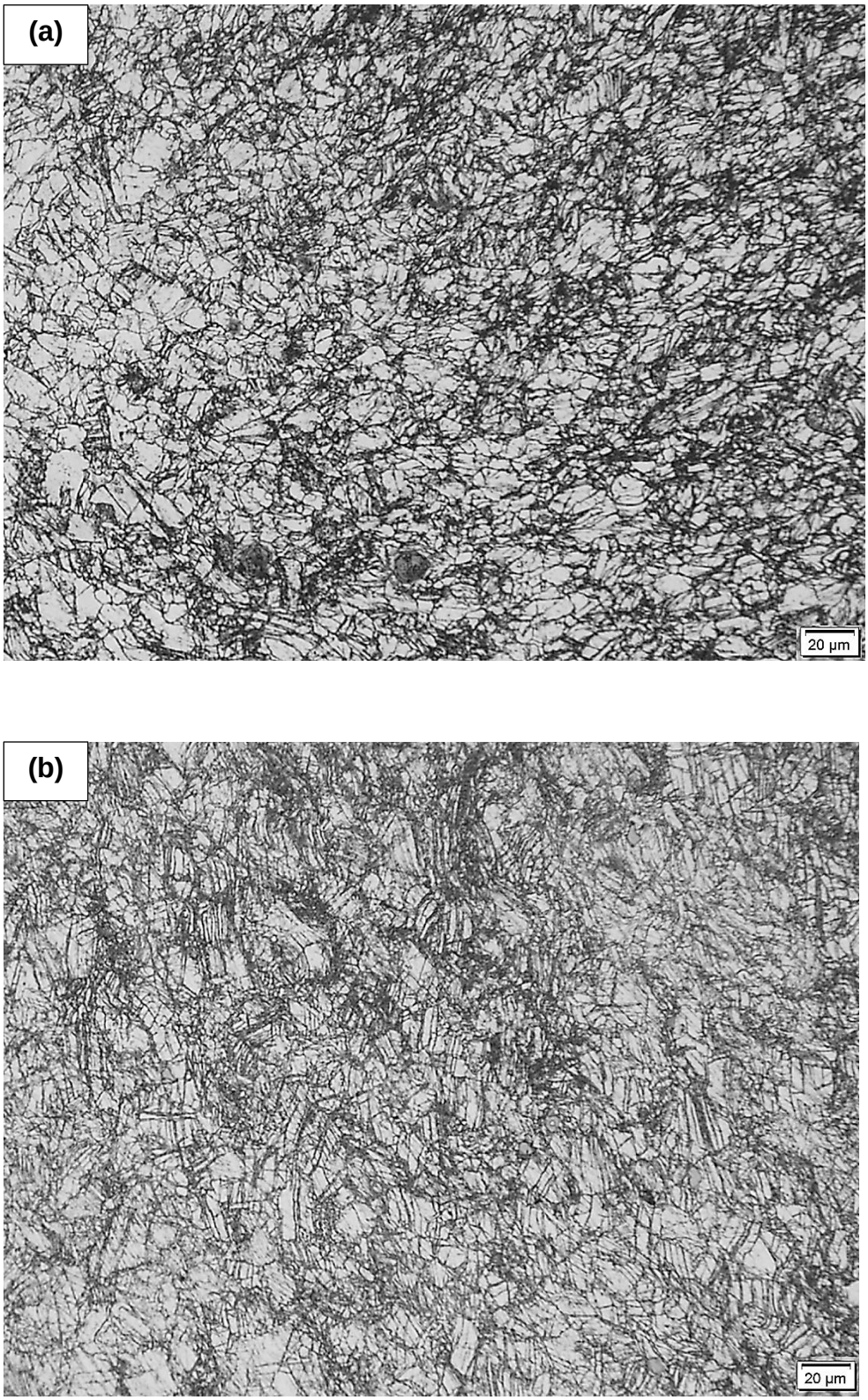

Figure 4.36: Magnified views of the microstructures on the horizontal cross–sections of the disks of the AZ91 alloy processed in HPT at 423 K using an applied pressure of 3.0 GPa for N = 5 turns at: (a) the centre region and (b) the edge region.

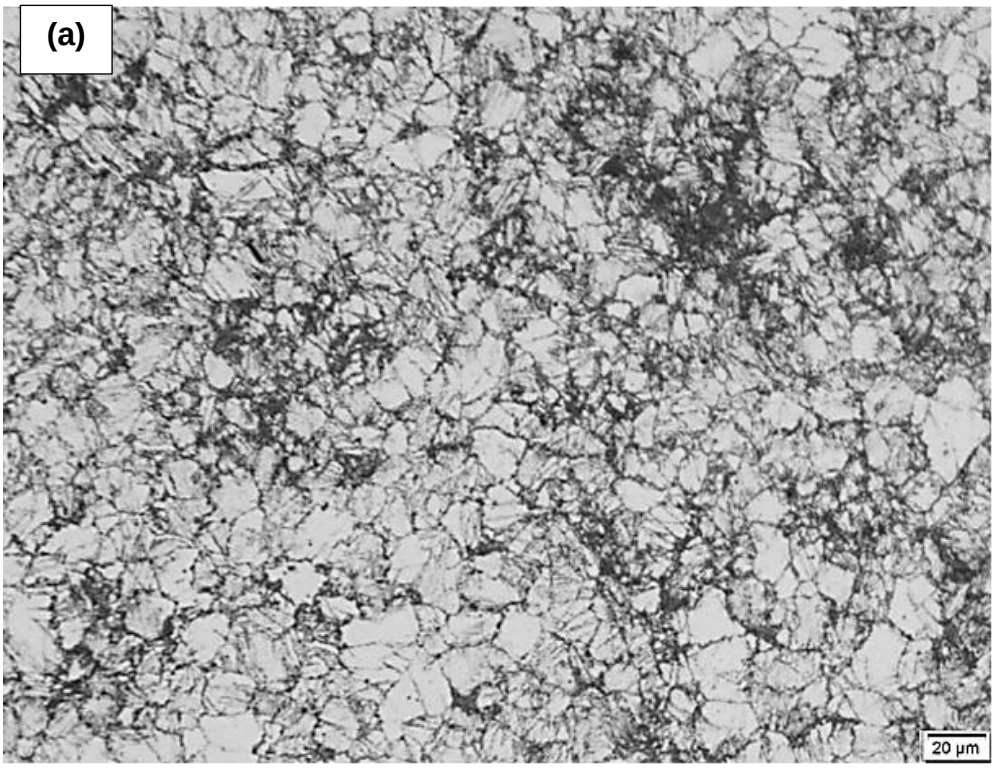
(a)
20 µm

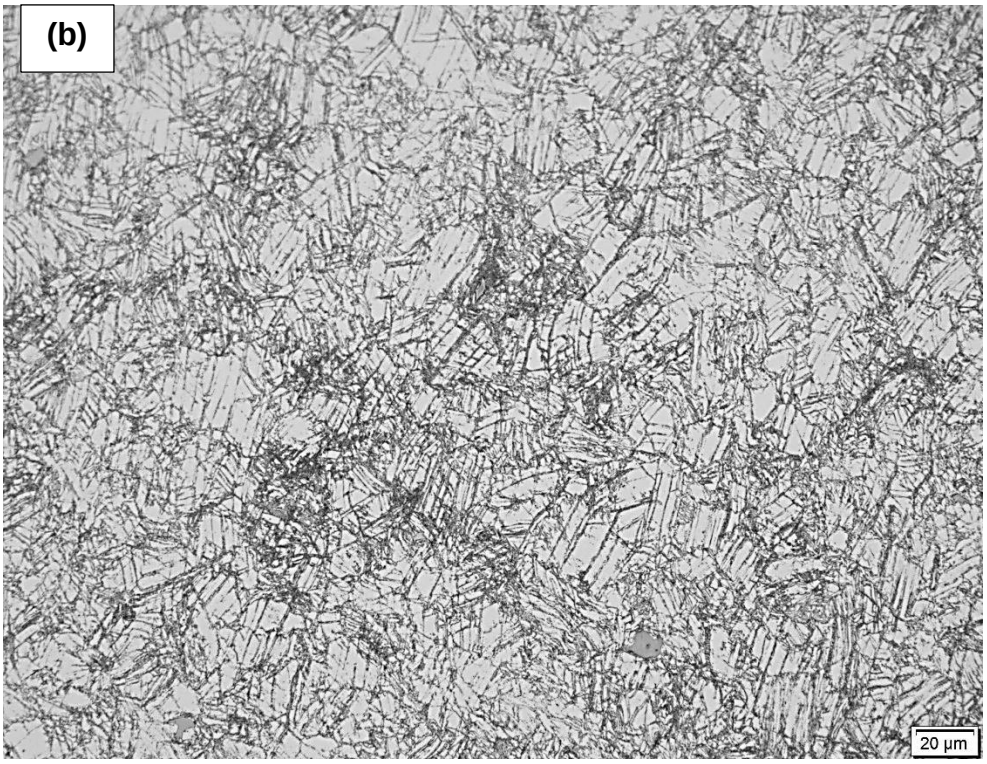
(b)
20 µm

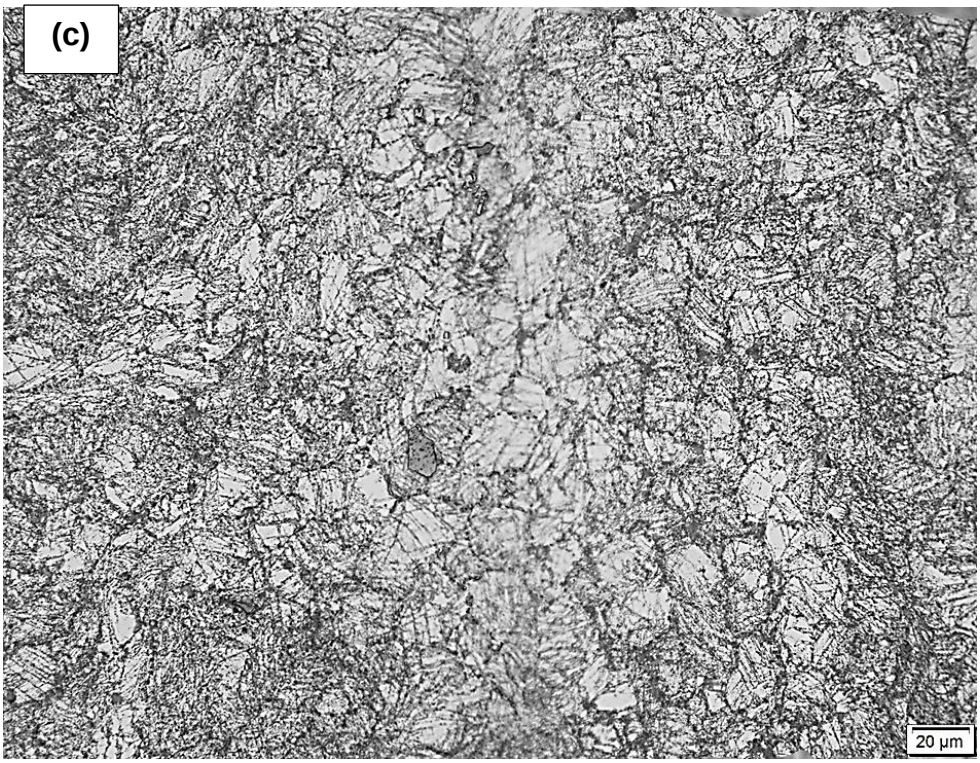

Figure 4.37: Magnified views at the centre regions of the microstructures on the horizontal cross–sections of the disks of the AZ91 alloy processed in HPT at 473 K using an applied pressure of 3.0 GPa for: (a) *N* = 1/2 turn, (b) *N* = 1 turn and (c) *N* = 5 turns.

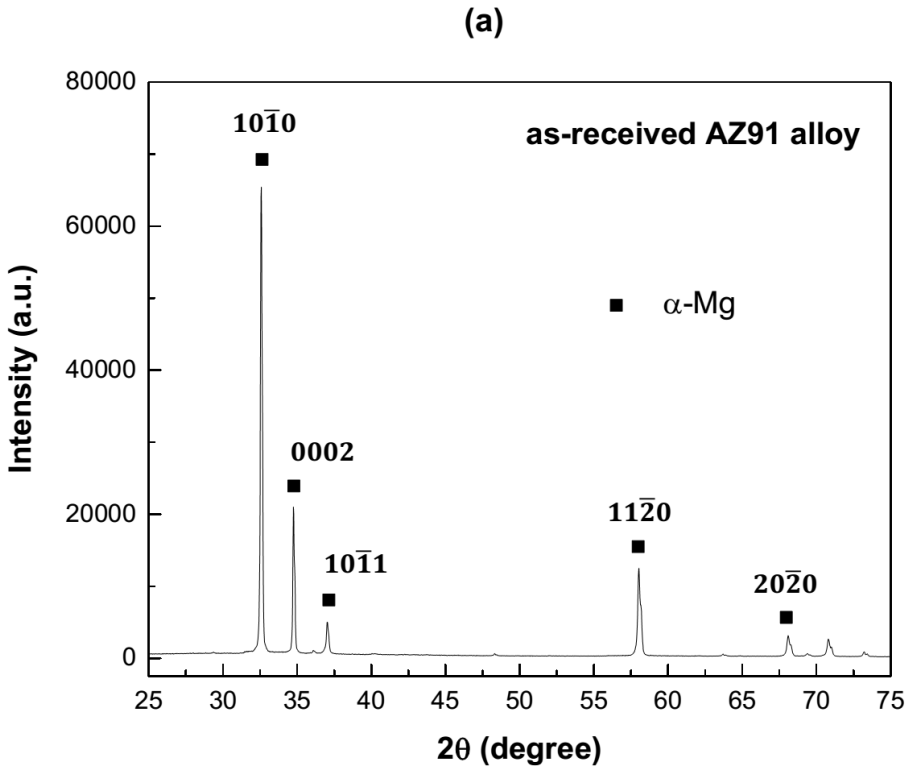

(b)

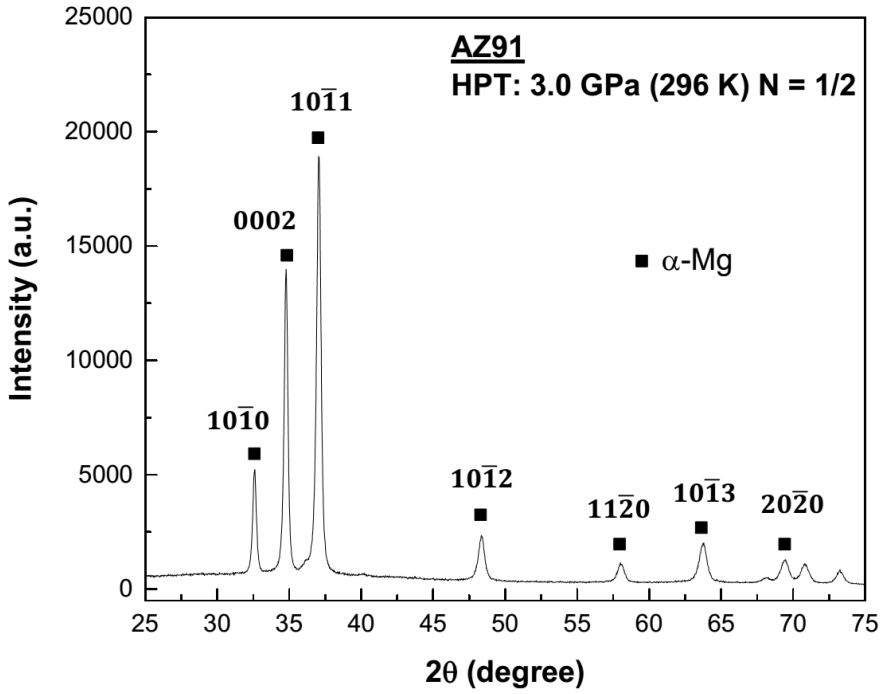
AZ91
HPT: 3.0 GPa (296 K) N = 1/2
Intensity (a.u.)
2θ (degree)
α-Mg
$10\bar{1}1$
0002
$10\bar{1}0$
$10\bar{1}2$
$11\bar{2}0$
$10\bar{1}3$
$20\bar{2}0$

(c)

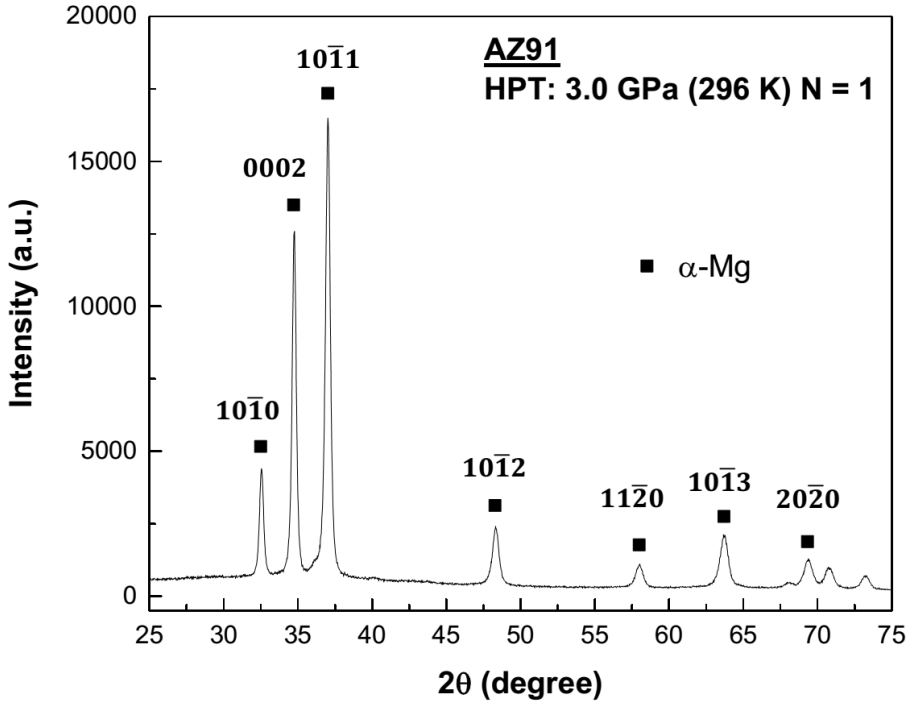
AZ91
HPT: 3.0 GPa (296 K) N = 1
Intensity (a.u.)
2θ (degree)
α-Mg
$10\bar{1}1$
0002
$10\bar{1}0$
$10\bar{1}2$
$11\bar{2}0$
$10\bar{1}3$
$20\bar{2}0$

(d)

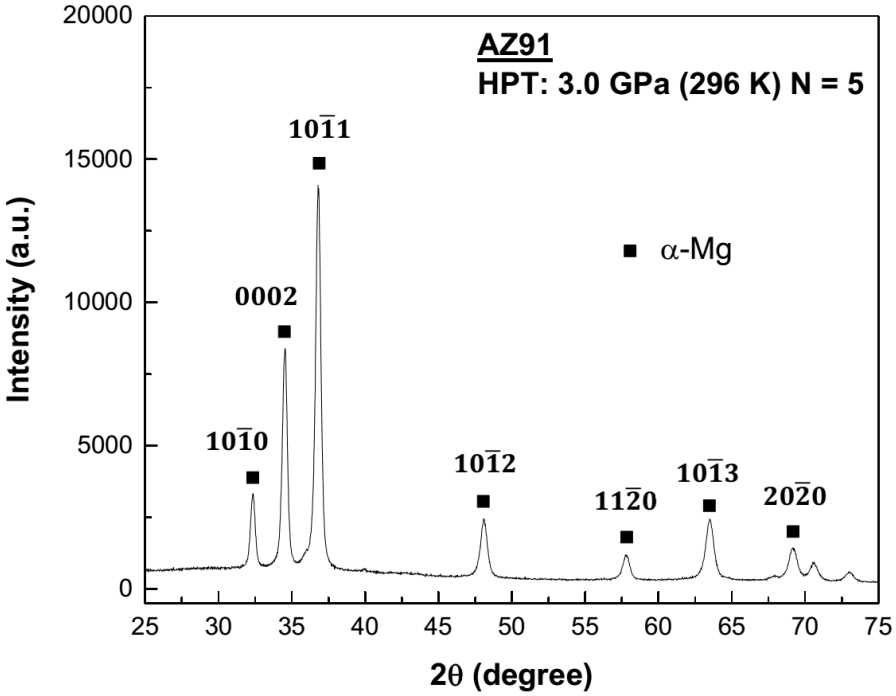
AZ91
HPT: 3.0 GPa (296 K) N = 5
α-Mg
$10\bar{1}1$
0002
$10\bar{1}0$
$10\bar{1}2$
$11\bar{2}0$
$10\bar{1}3$
$20\bar{2}0$
Intensity (a.u.)
2θ (degree)

(e)

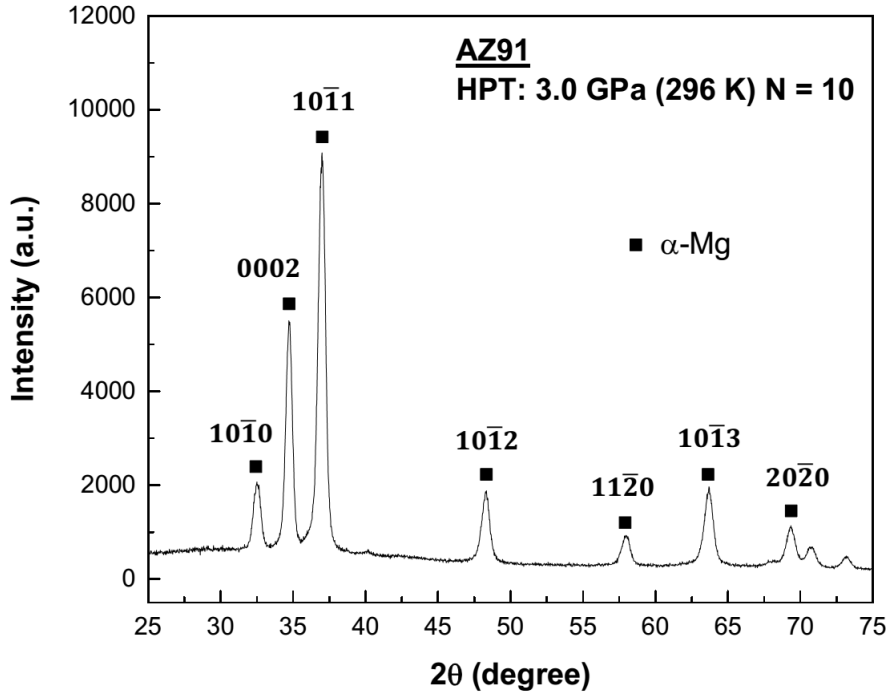
AZ91
HPT: 3.0 GPa (296 K) N = 10
α-Mg
$10\bar{1}1$
0002
$10\bar{1}0$
$10\bar{1}2$
$11\bar{2}0$
$10\bar{1}3$
$20\bar{2}0$
Intensity (a.u.)
2θ (degree)

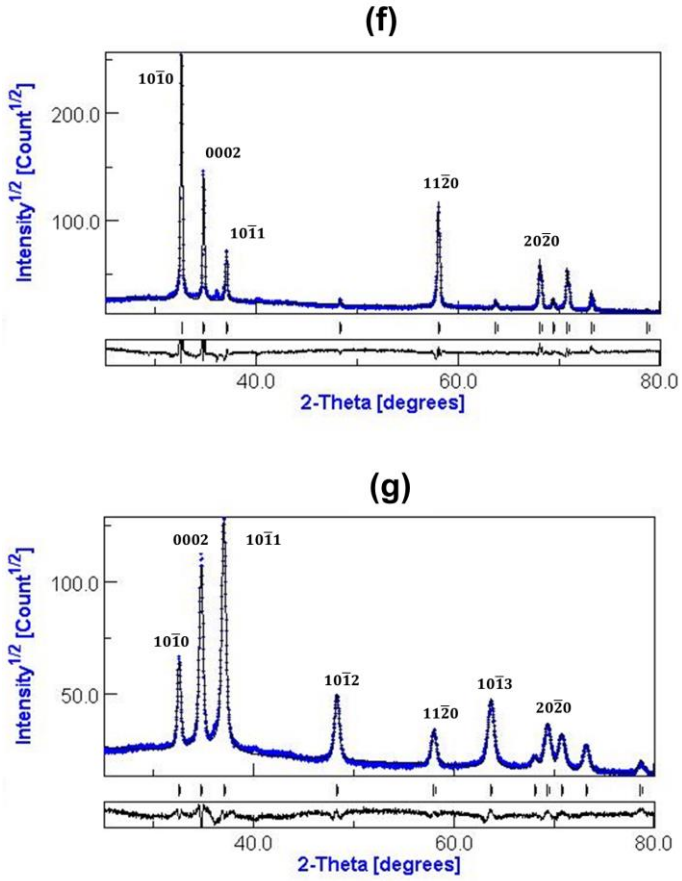

Figure 4.38: XRD diffraction patterns for: (a) the as–received AZ91 alloy and for the AZ91 alloy processed at the edge regions of the disks on the horizontal cross–sections of 296 K using an applied pressure of 3.0 GPa in HPT for: (b) *N* = 1/2 turn, (c) *N* = 1 turn, (d) *N* = 5 turns and (e) *N* = 10 turns. Examples of the fitting for XRD peaks are shown in (f) for the as–received AZ91 alloy and (g) for the AZ91 alloy processed for *N* = 10 turns.

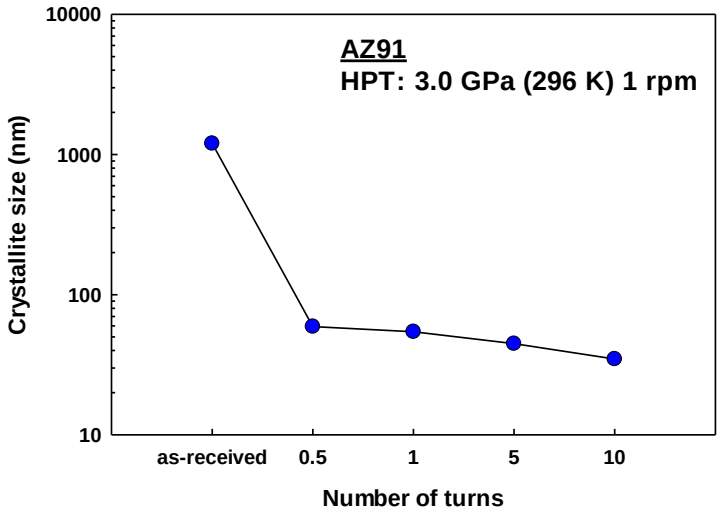

Figure 4.39: The variation in the apparent crystallite size with number of turns for AZ91 alloy processed at 296 K in HPT on the horizontal cross–sections of the as–received alloy and processed alloy.

4.2 Microhardness Results

4.2.1 Distributions of microhardness across the *diameter* after using two different applied pressures in HPT processing

The distributions of microhardness across the diameters are shown in Figure 4.40 for disks of AZ91 magnesium alloy processed by HPT using an applied pressure of 3.0 GPa for N = 0, 1/4, 1/2, 3/4, 1, 5, 10 turns, as well as using an applied pressure of 6.0 GPa for N = 0, 1/2, 1, 3, 5, 10 turns, where N = 0 means the pressed disk for 1 minute without torsion. The grey lines in Figure 4.40 show the average values for the Vickers microhardness of the as–received alloy, which was about 65. After pressing (without torsion) using applied pressures of 3.0 and 6.0 GPa, a gradual increment can be noticed in Vickers microhardness to about 100 in the edge regions, and a smaller increment at the centre region for the pressed disks as shown in Figure 4.40.

After HPT processing using an applied pressure of 3.0 GPa, a gradual increment was found in the microhardness to about 120 for the processed disks for N = 1/4, 1/2, 3/4 and 1 turn at the edge regions, whereas the increment in microhardness was about 100 in the centre regions of the processed disks. No significant differences were found between microhardness distributions for the disks processed along the diameter for N = 1/4, 1/2, 3/4 and 1 turn. By increasing the number of turns, an increment in microhardness to about 130 was found at the centre region of the disk processed for N = 3 turns, with development of stability in the microhardness distribution across the diameter. The microhardness increased to about 135 along the diameter for the disks processed for N = 5 and 10 turns, with no significant difference in microhardness distributions between them.

After HPT processing using an applied pressure of 6.0 GPa and for N = 1/2 turn, a gradual increment was found in the microhardness to about 120 at the edge regions as shown in Figure 4.40, whereas the increment in the microhardness was about 90 at the centre region of the processed disk. By increasing the number of turns to N = 1 and 3 turns, an increment in microhardness distributions was found, where the microhardness increased to about 110 at the centre regions and this increased to about 120 for the rest of the diameters. The microhardness distributions for the disks processed for N = 1 and 3 turns showed no significant

difference along the diameters. The microhardness increased to about 135 along the diameter for the disks processed for *N* = 5 and 10 turns, and no significant difference was noticed in microhardness distributions between them.

The values of microhardness that are listed in Figure 4.40 are illustrated in Table 4.3 and these values are shown for a radius between 0 mm (centre of the disk) and 4.8 mm (edge of the disk) for the disks processed for *N* = 1/2, 1, 3, 5, 10 turns and for the as–received alloy. It was assumed that the values of recorded microhardness are the same along both radii around the centre position (0 mm) of each disk. Each value of microhardness was based on the average of four individual indentations (cross–sign points) taken around an identified position (open circles) as shown schematically by the red rectangle in Figure 3.11 and represented by the column of the distance from the centre in Table 4.3.

Several trends can be concluded from Figure 4.40. First, the highest error bars were found at the centre regions of the disks, and relatively lower error bars were presented in the edge regions. Second, a decrease in the values of the error bars was found at the centre region with increasing number of turns. Third, the edge regions of the processed disks exhibited a bigger increment in the microhardness than that at the centre regions, as shown for the disks processed for *N* = 1/2 and 1 turn. Later, a saturation in the distributions of microhardness was found in the processed disks for *N* = 3, 5 and 10 turns at the centre and edge regions.

A correlation of the microhardness values relative to the imposed equivalent strain during HPT processing is plotted in Figure 4.41. A significant increase in the microhardness was observed with increasing the equivalent strain that imposed during HPT. Another correlation was plotted as shown in Figure 4.42 (a) for the microhardness values and the crystallite size versus the number of turns in HPT for the AZ91 alloy processed at 296 K. It is obvious that the increasing of number of turns is associated with a significant grain refinement and a considerable increase in microhardness. An experimental Hall–Petch relationship was obtained by plotting the values of microhardness and crystallite size obtained in this research as shown in Figure 4.42 (b). The slope of the straight line represents the experimental Hall–Petch relationship for the AZ91 alloy processed in HPT at 296 K for *N* = 1/2, 1, 5, 10 turns. It can be seen there is a significant dependency of

microhardness on the crystallite size for the AZ91 alloy. The dislocation density has calculated for the AZ91 alloy processed at 296 K and plotted versus the crystallite size and Vickers microhardness as shown in Figure 4.43 (a,b). The dislocation density has increased gradually with increasing the number of turns and become relatively saturated at N = 5 and 10 turns, and this behaviour was associated with the decrease in the crystallite size down to nanometre scale as shown in Figure 4.43 (a). The gradual increase in the dislocation density has resulted in a gradual development in microhardness, and the relative saturation in the Vickers microhardness that observed at N = 5 and 10 turns was associated with the relative saturation in the dislocation density shown in Figure 4.43 (b). An experimental Taylor relationship [184][192] was obtained by plotting the values of microhardness versus the dislocation density obtained in this research as shown in Figure 4.44 (a). The trend of strengthening was similar to that obtained by the Hall–Petch relationship and it confirms the effect of dislocation density on the resultant strength as well as the effect of the grain boundaries as illustrated in Figure 4.44 (b).

4.2.2 Distributions of microhardness across the horizontal cross–sections for the alloy processed at 296 K, 423 K and 473 K

The colour–coded maps show comprehensive distributions of the recorded microhardness across the entire horizontal cross–section (see Figures 3.11 (a) and 3.7) with regard to the condition of processing and the location on the horizontal cross–section relative to the centre of the disk. These plots are shown in Figure 4.45 for the disks processed at 296 K using an applied pressure of 3.0 GPa for N = 1/2, 1, 5, and 10 turns. The colours on these maps show the distribution of individual values of the recorded microhardness. A small inset in Figure 4.45 shows the scale of microhardness values with regard to each colour. The distribution of microhardness values for N = 1/2 turn across the horizontal cross–section of the processed disk is shown in Figure 4.45. There are two distinct halves showing an increment in the recorded microhardness. The first half of the processed disk shows a higher value of microhardness within 120 –130, and a few

dots with a relatively lower microhardness of 110. The second half of the disk shows an increment in microhardness of 110 in most of the cross–section area, which is relatively less than their counterparts in the first half of the processed disk, as well as a few dots of a higher microhardness within 120 – 130. Some dots are found in the second half, which contain a relatively lower recorded microhardness of 100, although this is still higher than the initial microhardness of the as–received alloy, which roughly equals to 65. These dots lie at the centre and near the edges in the second half of the processed disk.

The distribution of microhardness values of the disk processed for *N* = 1 turn over the horizontal cross–section of the processed disk is shown in Figure 4.45. Two distinct regions show an increment in the recorded microhardness. The outer area is represented by a higher microhardness in the range 120 – 140, and a few spots of microhardness within 110 – 120. The inner area showed a low microhardness in the centre region with a relatively low microhardness of 100 and an area of a higher microhardness of 110. The distribution of microhardness values for the disk processed for *N* = 5 turns is shown in Figure 4.45 across the horizontal cross–section of the processed disk. The distribution showed a majority of high values of microhardness within 130 – 140, as well as a few spots spread mainly around the edge regions with a microhardness of 110 – 120. The distribution of microhardness of the disk processed for *N* = 10 turns values are shown in Figure 4.45 across the horizontal cross–section of the processed disk. The results showed a high homogeneity in the recorded microhardness with a saturation limit of 135 – 140.

Similar procedures for these microhardness maps were adopted for the alloy processed at 423 K and 473 K in HPT. The Vickers microhardness maps for the disks processed at 423 K in HPT using an applied pressure of 3.0 GPa are shown in Figure 4.46. The distribution of microhardness for the disk processed for *N* = 1/2 turns consists of two regions as shown in Figure 4.46. The inner region has a microhardness of 80 – 90 and this region spread over from the edge towards the centre of the disk. The outer region spreads over a smaller area rather than the inner region. The disk processed for *N* = 1 turn shows a spread of the relatively higher microhardness of 110 starting from the edges of the disk and the relatively lower microhardness is confined to the centre of the disk as shown in Figure 4.46.

Increasing the number of turns in HPT leads to a considerable increase in the microhardness to 120 – 130 over the whole cross–section of the disk processed for N = 5 turns as shown in Figure 4.46, with a relatively small area of lower microhardness at the centre of the disk. Further processing towards N = 10 turns results in a saturation in the distribution of microhardness over the whole cross–section, and this distribution is heterogeneous with the existence of regions of relatively lower microhardness at the centre and the edge of the processed disk as shown in Figure 4.46.

The Vickers microhardness maps for the alloy processed at 473 K in HPT using an applied pressure of 3.0 GPa is shown in Figure 4.47. The level of microhardness is relatively lower than for the alloy processed at 296 K and 423 K. For the disks processed for N = 1/2 and 1 turn, the microhardness is divided into two distinct regions with values of 90 and 110, respectively. A relatively early saturation in microhardness of average value of 110 appears for the disk processed for N = 5 turns associated with regions of relatively lower microhardness. A significant and homogenous decrease in the microhardness is found for the sample processed for N = 10 turns as shown in Figure 4.47.

4.2.3 Distributions of microhardness across the *vertical* cross–sections for the alloy processed at 296 K, 423 K and 473 K

The colour–coded maps were again used to reveal the changes in the microhardness on the vertical cross–sections (see Figure 3.11 (b)) of the processed disks. Figure 4.48 shows the distributions of microhardness relative to the position of measurement in the through–thickness direction (see Figure 3.12). The maps were plotted for whole vertical cross–sections of the disks processed at 296 K using an applied pressure of 3.0 GPa, for N = 1/2, 1, 5 and 10 turns, respectively. Significant differences in the distributions of microhardness can be noticed in different positions in the radial directions for the disks processed for N = 1/2 and 1 turn, and these differences occurred especially at the centres of the disks. A homogeneous distribution of the microhardness was found in the disks processed for N = 5 and 10 turns. The sample processed for N = 10 turns exhibits

relatively higher values of microhardness compared to the sample processed for *N* = 5 turns. The current results show that increasing the numbers of turns results in an increase in homogeneity of microhardness distribution in the vertical cross–sections of the processed disks at room temperature.

The samples processed at 423 K in HPT using an applied pressure of 3.0 GPa are shown in Figure 4.49. The alloy processed at 423 K shows a slower rate of development of microhardness with increasing number of turns in HPT compared to that for the alloy processed at 296 K. The samples processed for *N* = 1/2 and 1 turn exhibit a lower microhardness across the vertical cross–sections especially at the centre region. The samples processed for *N* = 5 and 10 turns show a significant increase in the overall distribution of microhardness with a higher microhardness at the mid-radius and edge regions compared to the centre region. These samples exhibit also heterogeneous distributions of the microhardness across their vertical cross–sections even at high number of turns compared to the homogenous distributions of microhardness found for the samples processed at 296 K.

The samples processed at 473 K in HPT using an applied pressure of 3.0 GPa are shown in Figure 4.50. These samples show significantly lower values of microhardness compared to their counterparts for the samples processed at 296 K and 423 K. The sample processed for *N* = 1/2 turn shows a relatively higher microhardness at the edge regions with a lower microhardness over the rest of the cross–section. A gradual development in the microhardness was found at the edge and near mid–radius regions for the sample processed for *N* = 1 turn. A relatively homogeneous distribution of the microhardness was observed for the sample processed for *N* = 5 turns. Further processing up to *N* = 10 turns results in a relatively homogeneous distribution of the microhardness but lower than for the sample processed for *N* = 5 turns.

The effect of the processing temperature in HPT on the crystallite size, microhardness and dislocation density of the AZ19 alloy is illustrated in Figure 4.51 for samples processed at 296 K, 423 K and 473 K. The crystallite size has increased with increasing the processing temperature. The alloy processed at 296 K and 423 K shows a considerable increase in the microhardness and dislocation

density with increasing number of turns, but the microhardness profile and dislocation density were significantly higher for the alloy processed at 296 K than for the alloy processed at 423 K. An increase in the microhardness and dislocation density were found at a relatively lower number of turns, and then a gradual decrease in the microhardness was found with increasing the processing temperature and increasing the number of turns for the alloy processed at 437 K.

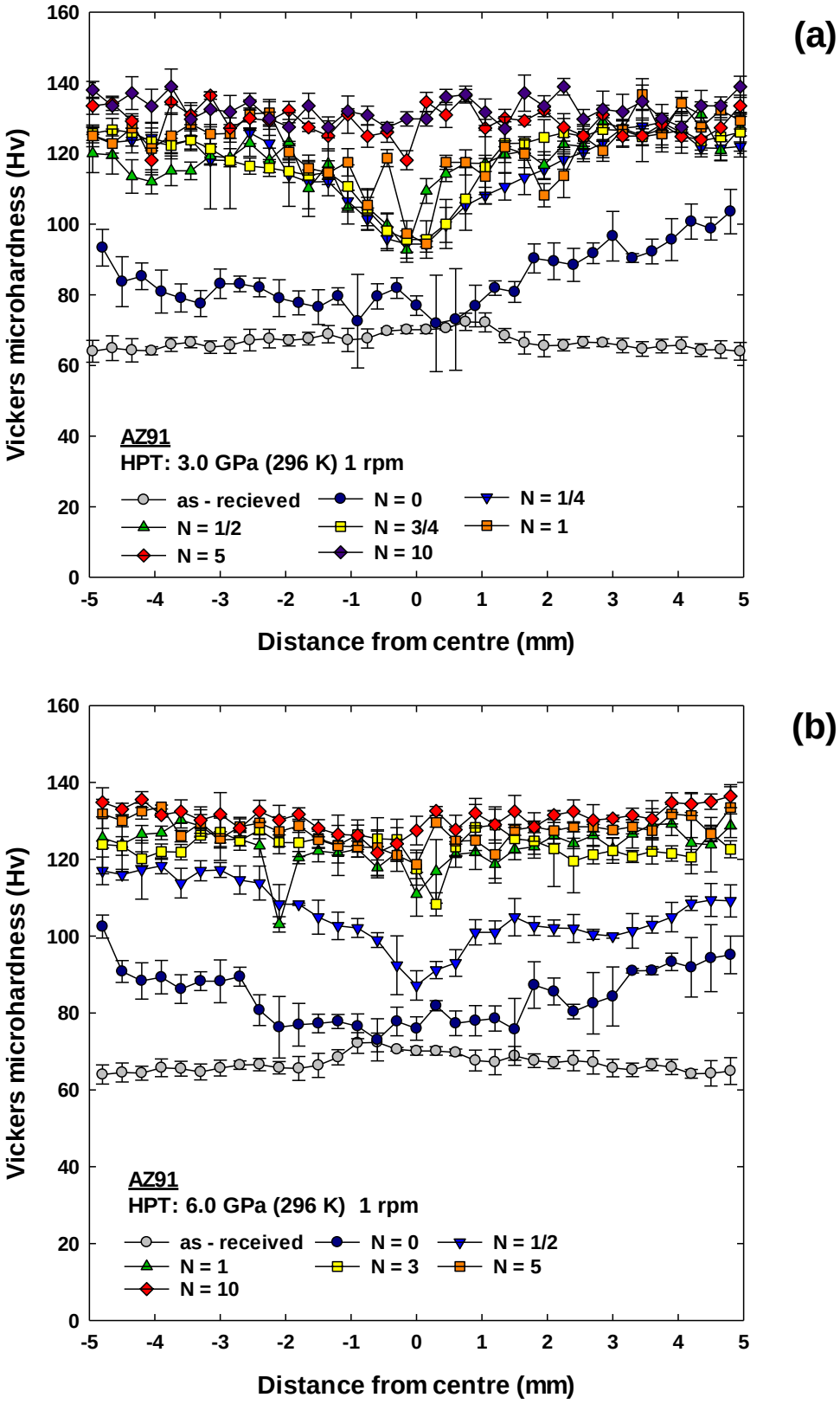

Figure 4.40: The variation in average microhardness along diameters over the horizontal cross–sections of the disks processed at 296 K using applied pressures of: (a) 3.0 GPa and (b) 6.0 GPa, for different numbers of turns.

Table 4.3: The average values of microhardness along diameters over the horizontal cross–sections of the disks processed after HPT processing at 296 K using an applied pressure of 3.0 GPa and for different number of turns.

Distance from centre (mm)	Values of microhardness and their error bars											
	As–received		*N* = 1/2		*N* = 1		*N* = 3		*N* = 5		*N* = 10	
	HV	Err.	HV	Err.	HV	Err.	HV	Err.	HV	Err.	HV	Err.
0	70.1	±1.1	92.7	±3.8	97.3	±3.0	119.0	±2.1	122.1	±1.5	129.8	±1.0
0.3	70.1	±1.1	99.8	±3.3	118.7	±2.8	121.0	±2.4	126.0	±2.0	127.3	±1.5
0.6	69.8	±1.9	104.8	±3.3	105.4	±2.7	121.9	±2.0	124.9	±1.5	130.8	±1.5
0.9	67.7	±2.7	104.8	±3.9	117.5	±3.1	128.0	±2.2	131.0	±1.7	132.0	±1.0
1.2	67.2	±3.3	117.0	±5.0	114.6	±4.2	122.0	±3.3	125.0	±2.2	127.4	±2.0
1.5	68.9	±2.5	110.1	±4.5	115.8	±3.7	124.4	±2.8	127.4	±1.7	133.5	±1.5
1.8	67.6	±1.8	123.1	±3.8	120.4	±3.0	127.0	±2.0	132.2	±2.0	127.5	±2.0
2.1	67.1	±1.6	118.1	±3.3	131.5	±2.5	126.3	±1.6	129.3	±2.0	129.9	±1.0
2.4	67.6	±2.6	122.9	±5.7	131.2	±4.9	127.0	±4.0	130.0	±2.9	134.7	±2.7
2.7	67.2	±3.1	118.8	±4.8	125.7	±4.0	124.2	±3.1	127.2	±2.0	131.8	±1.8
3.0	65.7	±2.3	119.3	±3.0	125.5	±2.2	133.4	±1.5	136.4	±1.3	132.5	±1.3
3.3	65.2	±1.8	115.1	±3.8	128.4	±3.0	127.9	±2.1	130.9	±1.6	129.7	±1.3
3.6	66.6	±1.6	115.1	±3.7	125.0	±2.9	126.0	±2.0	134.6	±1.6	138.9	±0.9
3.9	66.0	±2.0	112.0	±2.3	121.4	±1.5	125.0	±1.6	118.1	±1.6	133.4	±1.1
4.2	64.2	±1.1	113.5	±2.7	127.2	±1.9	126.2	±1.3	129.2	±1.7	137.1	±1.1
4.5	64.3	±3.3	119.6	±2.7	122.8	±1.9	131.2	±1.4	134.2	±1.5	133.5	±0.9
4.8	64.9	±3.5	120.0	±2.6	125.0	±1.8	130.5	±1.5	133.5	±1.4	138.0	±1.0

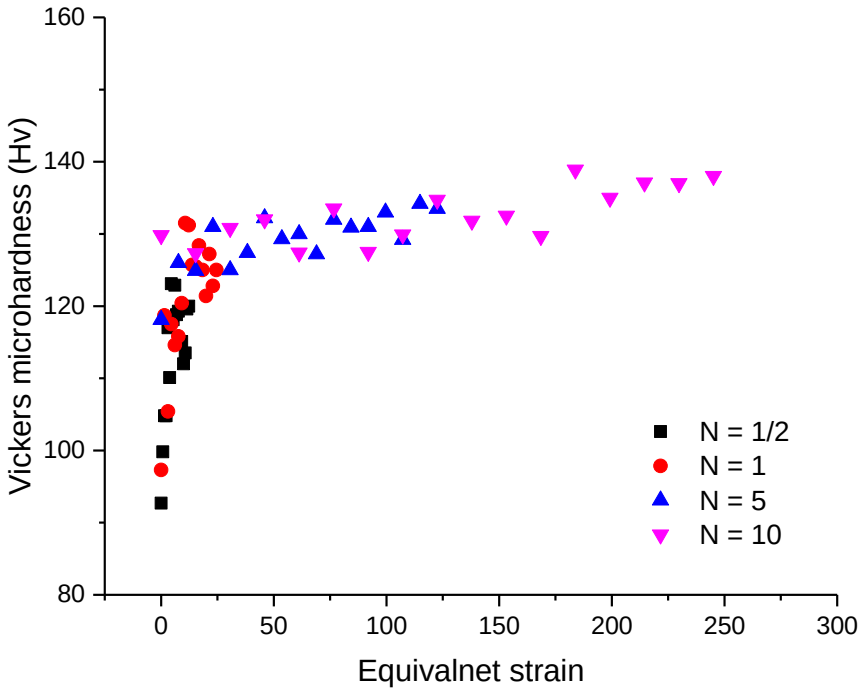

Figure 4.41: Correlation of the measured microhardness with the equivalent strain imposed by HPT along diameters over the horizontal cross–sections of the disks processed at 296 K using an applied pressure of 3.0 GPa and for different number of turns.

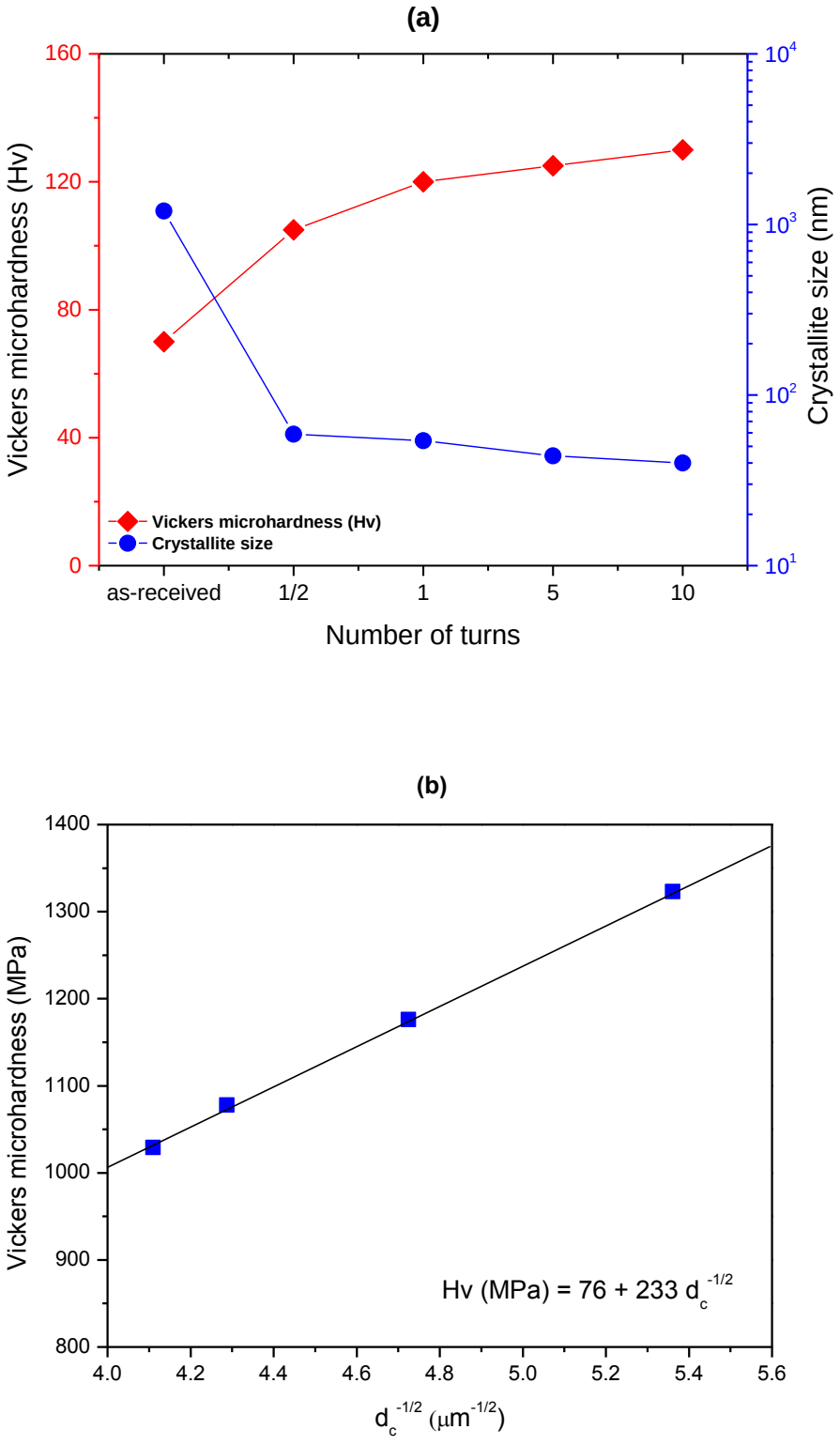

Figure 4.42: (a) The variation in average Vickers microhardness and the average crystallite size with the number of turns in HPT and (b) The variation in Vickers microhardness with the reciprocal square root of the average crystallite size of the AZ91 disks processed at 296 K in HPT. These data have been obtained on the horizontal cross–sections of the disks processed in HPT using an applied pressure of 3.0 GPa at room temperature.

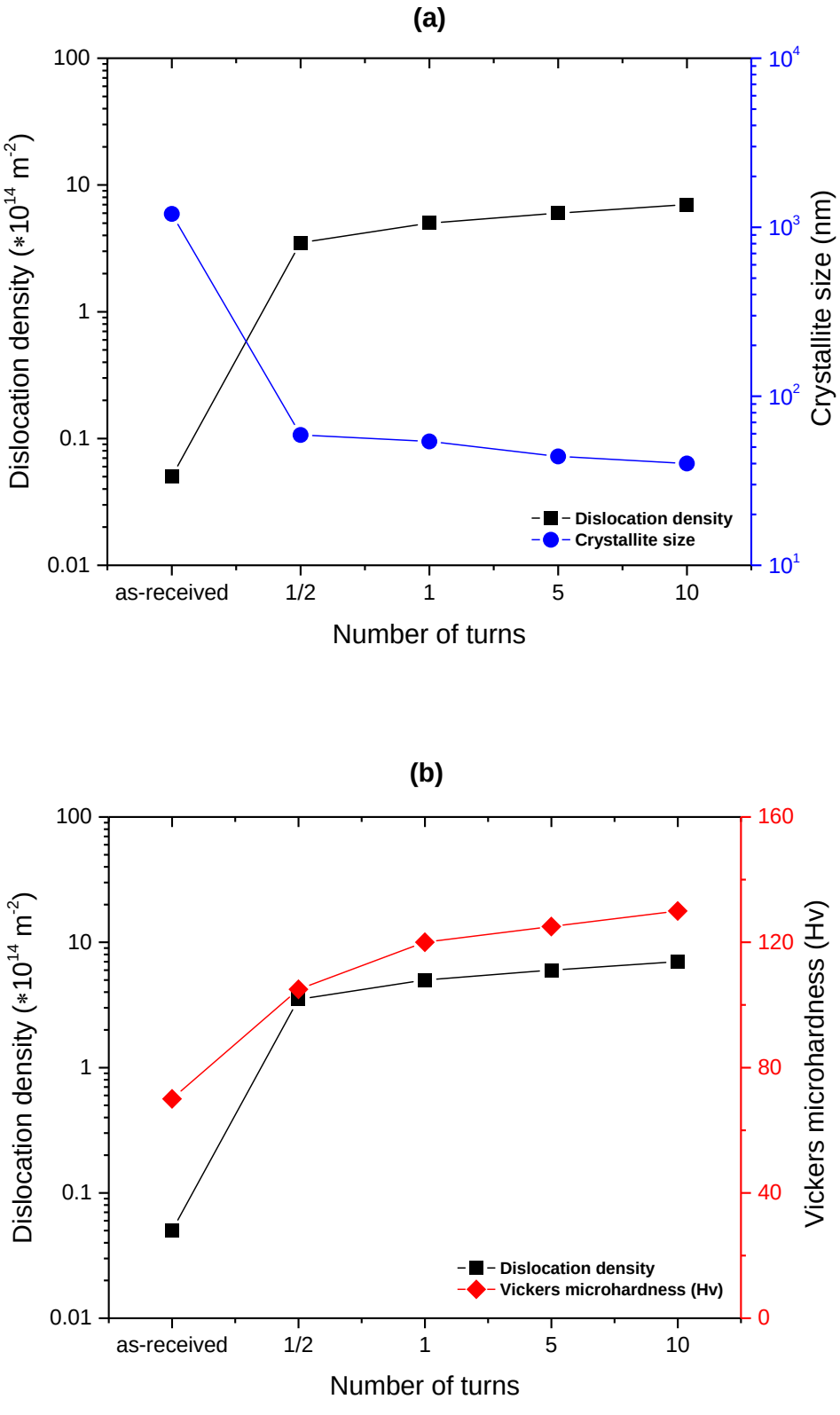

Figure 4.43: The variation in the dislocation density with: (a) the average crystallite size and (b) average Vickers microhardness for the AZ91 alloy processed at 296 K in HPT for different number of turns. These data have been obtained on the horizontal cross–sections of the disks processed in HPT using an applied pressure of 3.0 GPa at room temperature.

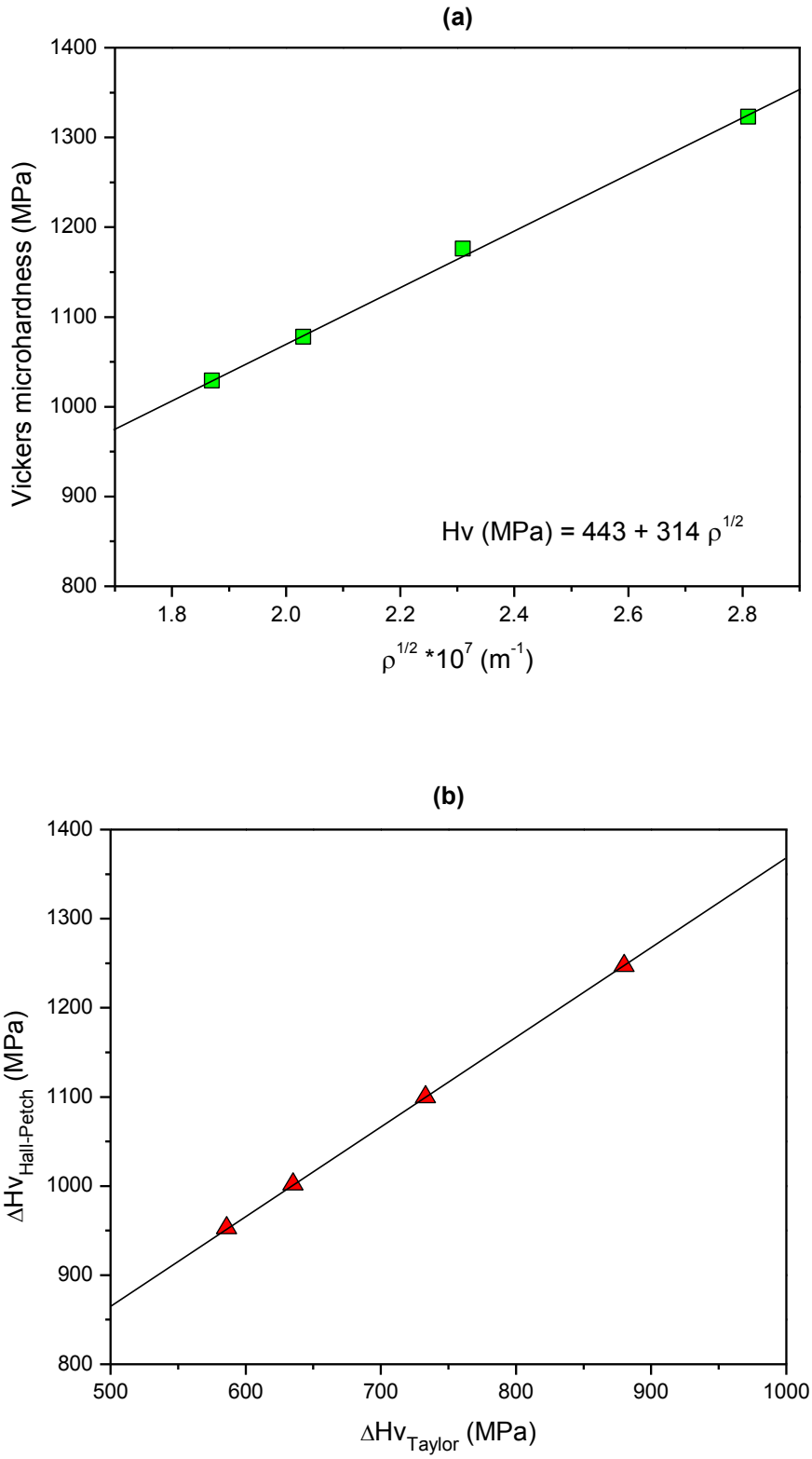

Figure 4.44: (a) The variation in Vickers microhardness with the square root of the dislocation density for the AZ91 disks processed at 296 K in HPT. (b) A comparison between the Hall–Petch and Taylor strengthening. These data have been obtained on the horizontal cross–sections of the disks processed in HPT using an applied pressure of 3.0 GPa at room temperature.

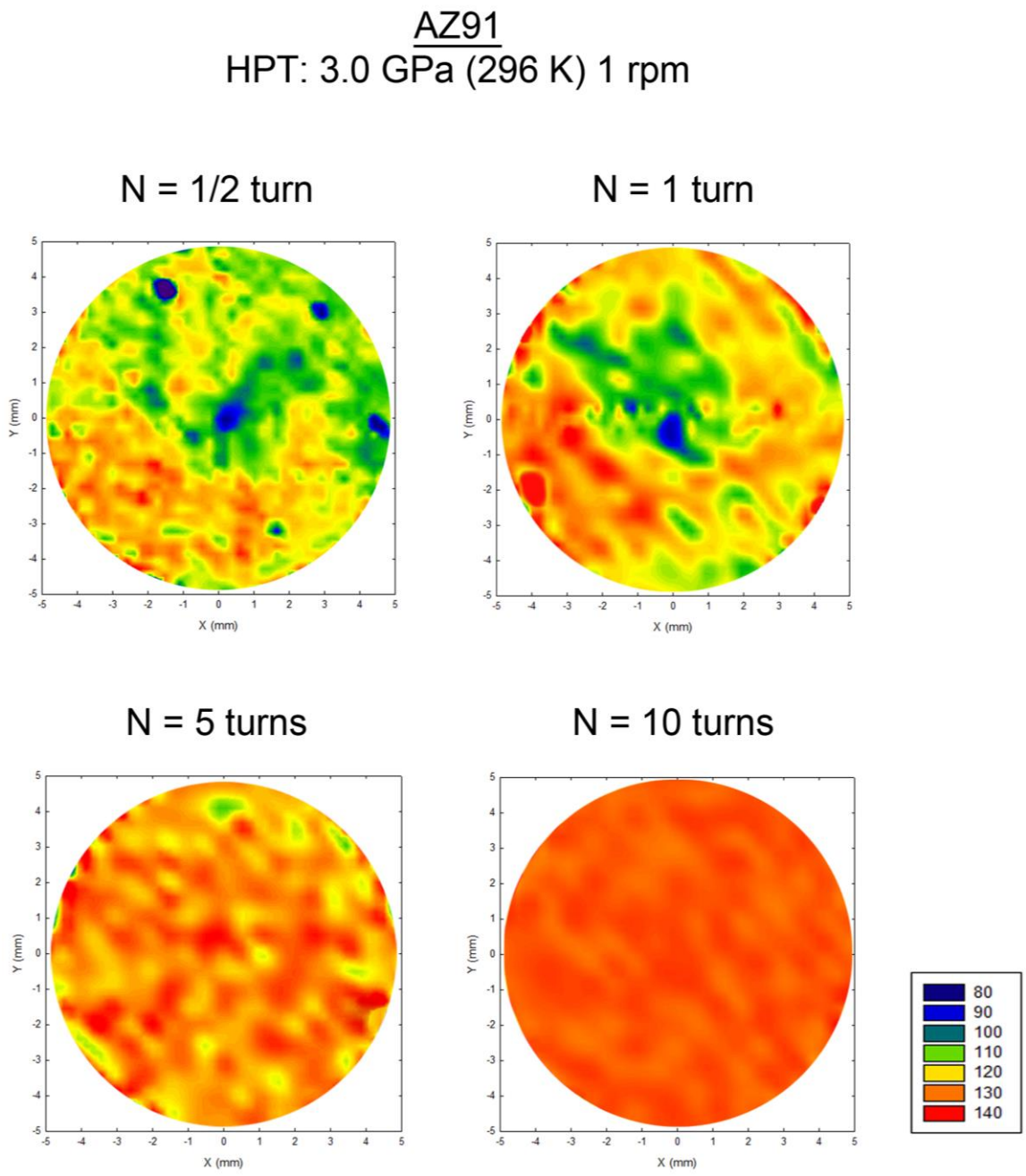

Figure 4.45: The colour–coded maps of the microhardness distributions over the horizontal cross–sections of the AZ91 disks processed by HPT at 296 K and using an applied pressure of 3.0 GPa for *N* = 1/2, 1, 5 and 10 turns. The small inset in the Figure shows the scale of the microhardness (in Kgf/mm^2) in regards of each colour.

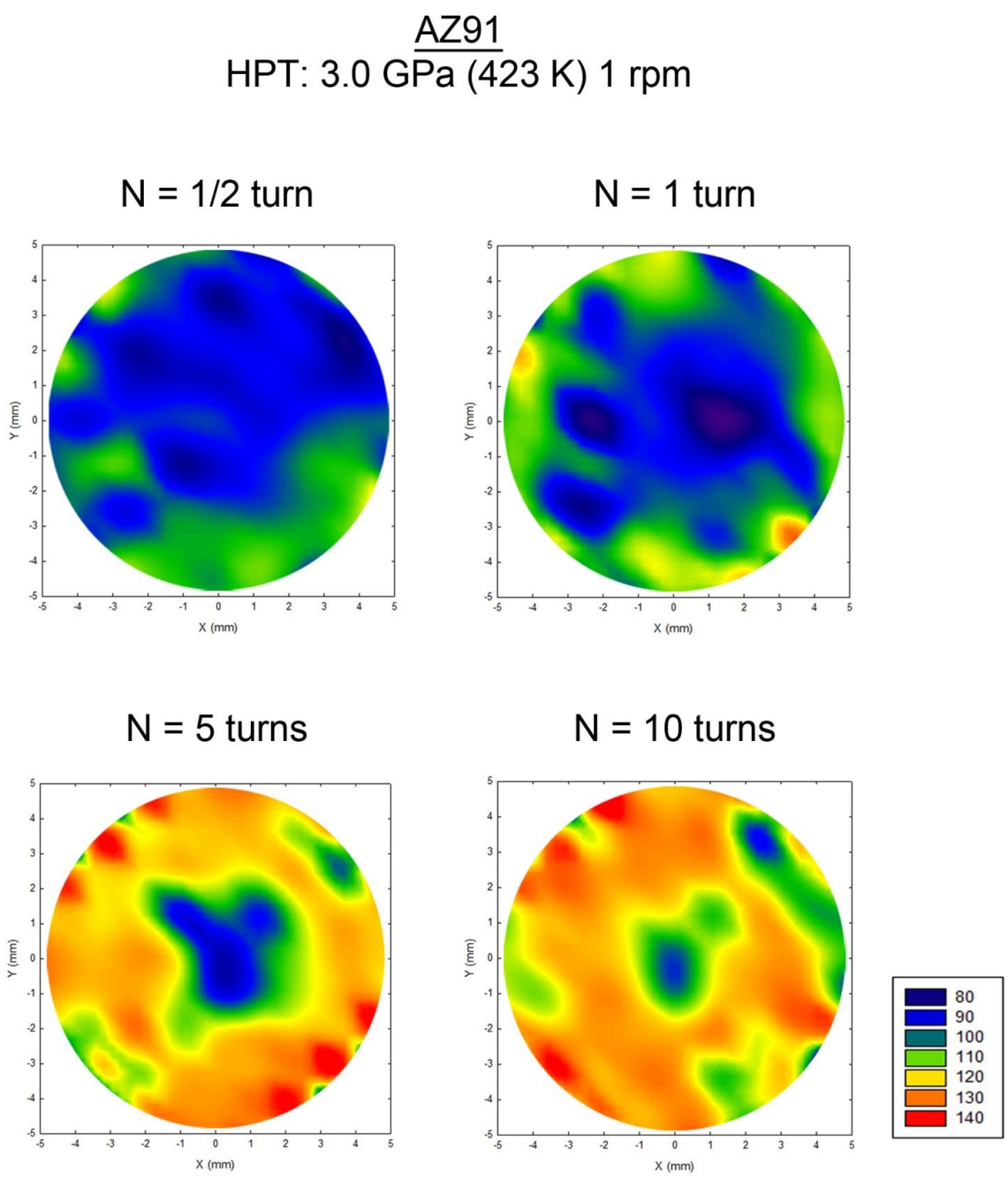

Figure 4.46: The colour–coded maps of the microhardness distributions over the horizontal cross–sections of the AZ91 disks processed by HPT at 423 K and using an applied pressure of 3.0 GPa for *N* = 1/2, 1, 5 and 10 turns. The small inset in the Figure shows the scale of the microhardness (in Kgf/mm^2) in regards of each colour.

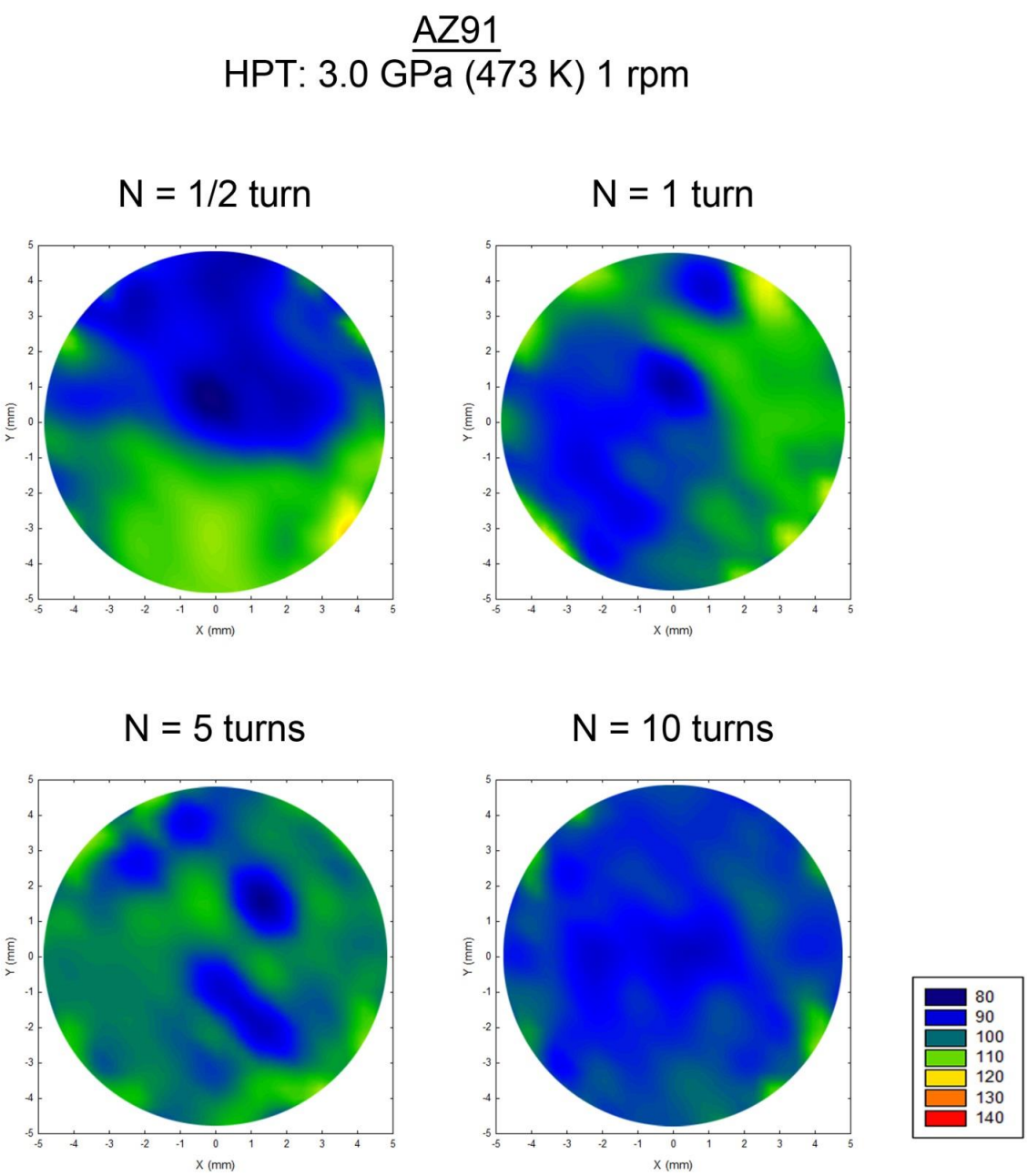

Figure 4.47: The colour–coded maps of the microhardness distributions over the horizontal cross–sections of the AZ91 disks processed by HPT at 473 K and using an applied pressure of 3.0 GPa for *N* = 1/2, 1, 5 and 10 turns. The small inset in the Figure shows the scale of the microhardness (in Kgf/mm^2) in regards of each colour.

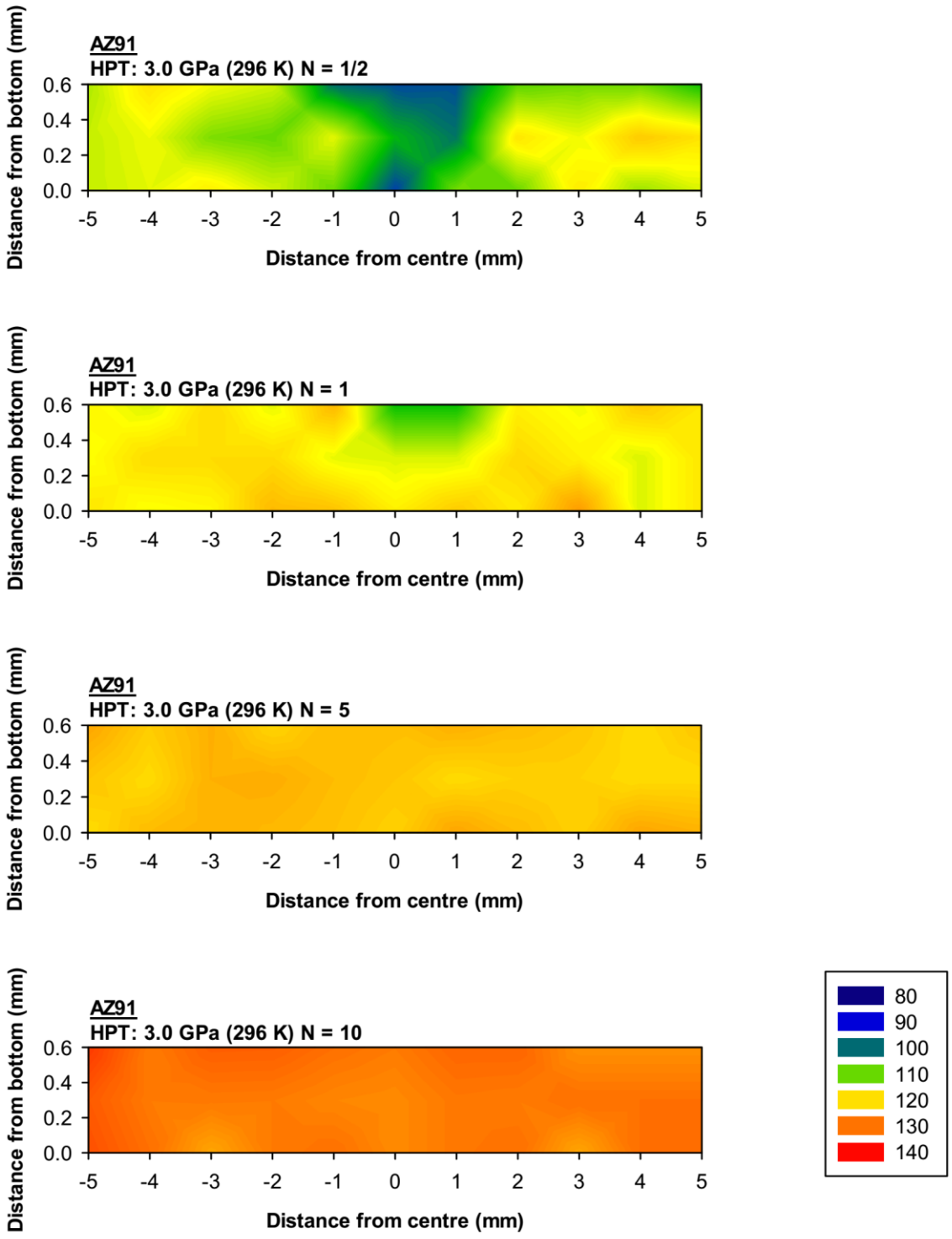

Figure 4.48: The colour–coded maps for the microhardness distributions on the vertical cross–sectional planes of the processed disks after HPT processing at 296 K and using an applied pressure of 3.0 GPa for *N* = 1/2, 1, 5 and 10 turns. The small inset in the Figure shows the scale of the microhardness (in Kgf/mm^2) in regards of each colour.

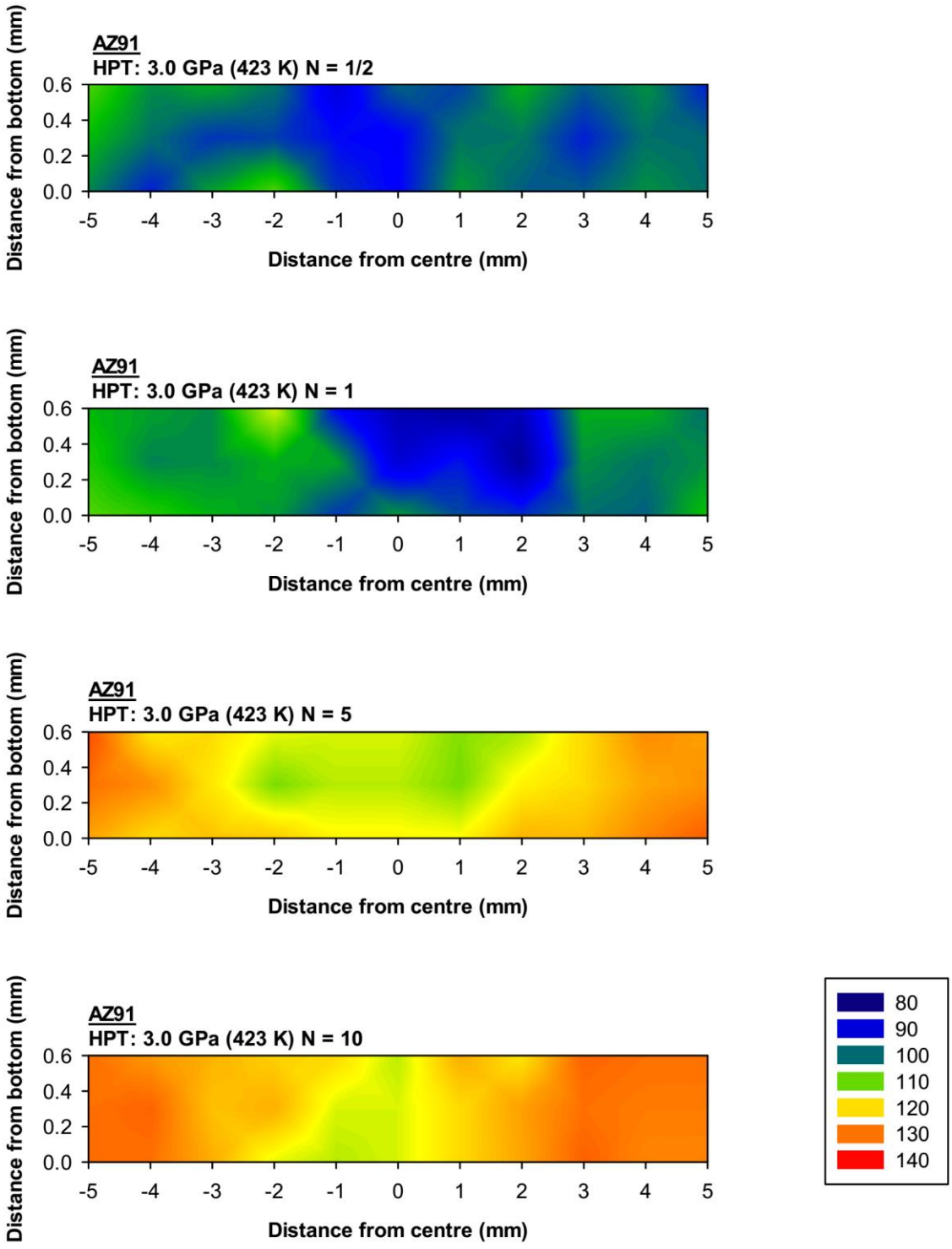

Figure 4.49: The colour–coded maps for the microhardness distributions on the vertical cross–sectional planes of the processed disks after HPT processing at 423 K and using an applied pressure of 3.0 GPa for *N* = 1/2, 1, 5 and 10 turns. The small inset in the Figure shows the scale of the microhardness (in Kgf/mm^2) in regards of each colour.

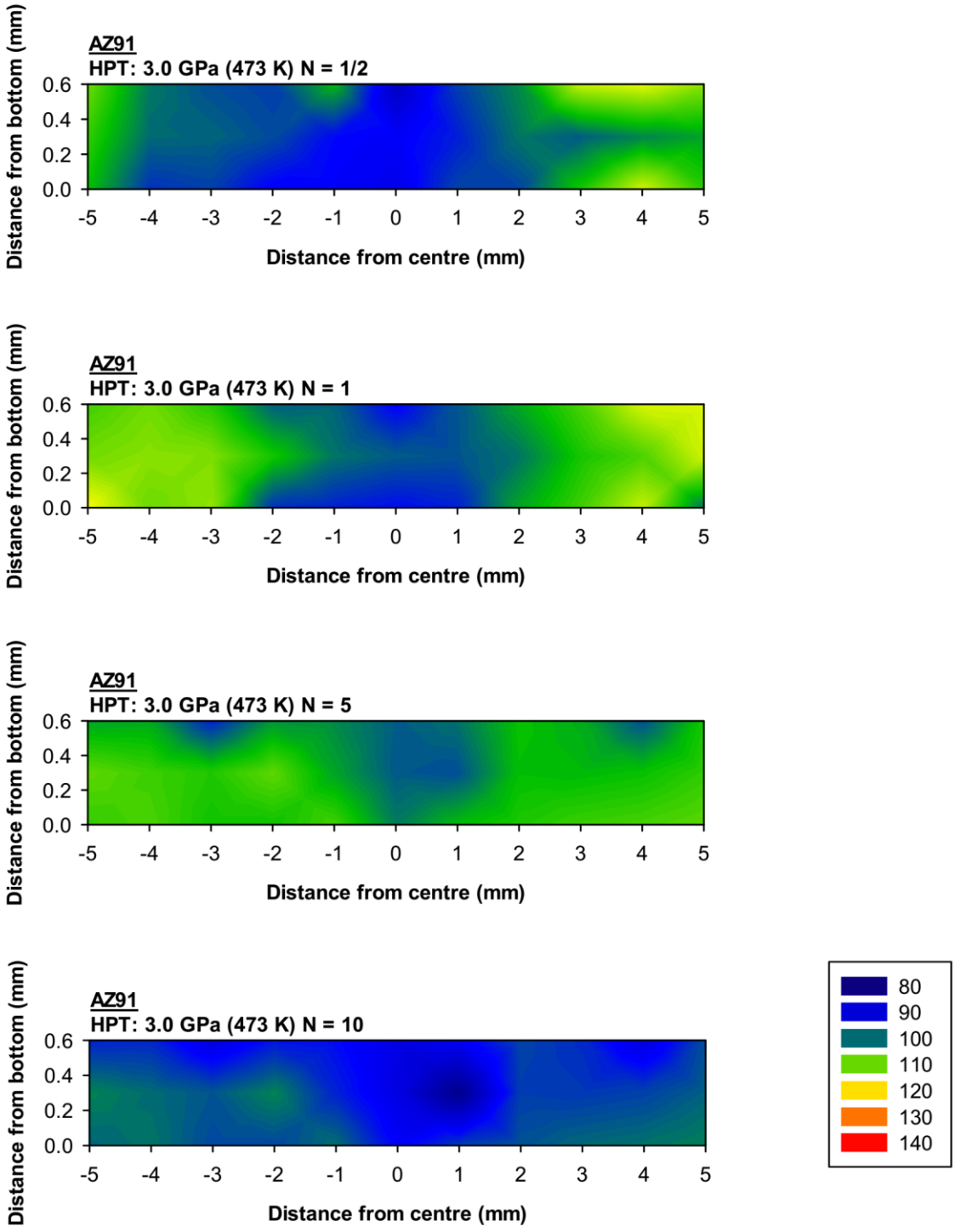

Figure 4.50: The colour–coded maps for the microhardness distributions on the vertical cross–sectional planes of the processed disks after HPT processing at 473 K and using an applied pressure of 3.0 GPa for *N* = 1/2, 1, 5 and 10 turns. The small inset in the Figure shows the scale of the microhardness (in Kgf/mm^2) in regards of each colour.

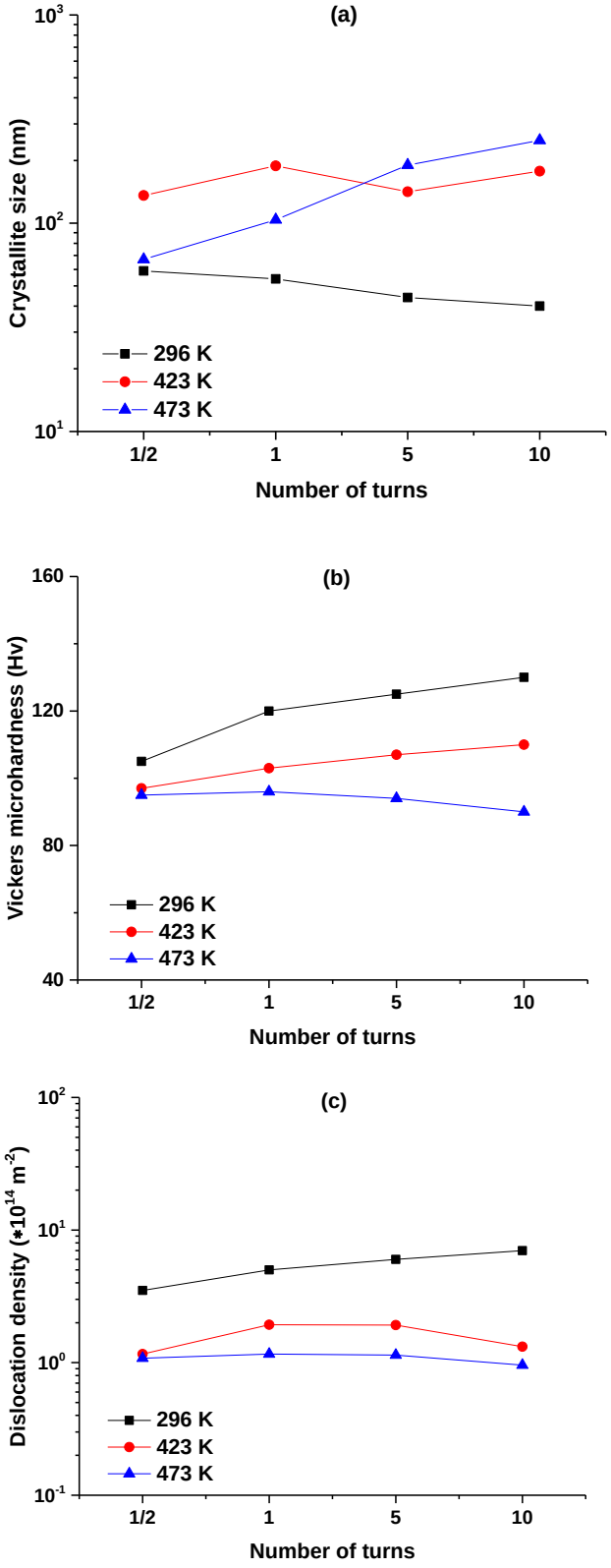

Figure 4.51: The overall variation in the average: (a) crystallite size, (b) dislocation density and (c) microhardness for the AZ91 alloy processed at different processing temperatures in HPT using an applied pressure of 3.0 GPa, where the data were obtained from the horizontal cross–sections of the processed disks.

4.3 Tensile Results

4.3.1 Stress – elongation curves

The tensile properties of the AZ91 alloy processed at 296 K were tested in tension for the samples processed for *N* = 1, 3, 5 and 10 turns are shown in Figures (4.52 – 4.55). These plots represent the engineering stress – engineering strain curves for the alloy tested in tension to fracture at testing temperatures of 423 K, 473 K and 573 K using initial strain rates of 1×10^{-1} s^{-1} to 1×10^{-4} s^{-1}. The testing temperatures used in this investigation corresponded to 0.55 T_m (423 K), 0.61 T_m (473 K) and 0.74 T_m (573 K), where the absolute melting point of the AZ91 alloy is 768 K (495 °C) [191].

These curves show the occurrence of the superplastic elongations with increasing number of turns from *N* = 1 turn to *N* = 10 turns in HPT, with lowering tensile strains from 1×10^{-1} s^{-1} to 1×10^{-4} s^{-1}, as well as with increasing testing temperature from 423 K to 573 K, as illustrated in Figures (4.52 – 4.55). For a sample processed in HPT at a specific number of turns and then tested in tension, the strain hardening behaviour decreased with increasing the testing temperature and decreasing the strain rate in the tensile test. The differences between strain hardening behaviours were insignificant for samples processed at different number of turns and tested at the same temperatures and strain rates.

The engineering stress – engineering strain curves of the as–received AZ91 alloy at testing temperatures of 296 K, 473 K and 573 K are illustrated in Figure 4.56. The strain hardening of the as–received alloy decreased with increasing the testing temperature up to 573 K and decreasing the strain rate down to 1×10^{-4} s^{-1}. The values of the maximum stress decreased with increasing the testing temperature and decreasing the strain rates.

4.3.2 Elongation – strain rate curves and the appearances of fractured samples

The effect of number of turns in HPT, the testing temperature and strain rate in tensile test were concluded from Figures (4.52 – 4.55) and then plotted in Figure

4.57 and Figure 4.58. These Figures represent the variation in the maximum achieved elongation after fracture in tension with different testing temperatures using different strain rates for each sample processed in HPT for a given number of turns as well as for the as–received alloy. Increasing the number of turns in HPT up to *N* = 10 turns resulted in increasing the value of elongation at all strain rates as shown in Figure 4.57. The data of maximum elongations that were achieved in this research are tabulated in Table 4.4. For instance, the maximum elongations for a sample processed for *N* = 1 turn were 277 % and 1014 % using strain rates of 1×10^{-1} s^{-1} and 1×10^{-4} s^{-1}, respectively at testing temperature of 573 K. Whereas for the sample processed for *N* = 10 turns, the maximum elongations were 410 % and 1308 % using strain rates of 1×10^{-1} s^{-1} and 1×10^{-4} s^{-1}, respectively at testing temperature of 573 K.

The effect of testing temperature on the achieved elongation is illustrated by Figure 4.57, where the increase in testing temperature resulted in increasing elongation at all strain rates. For example, for the sample processed in HPT for *N* = 10 turns, the maximum elongations were 760 %, 1164 % and 1308 % at testing temperatures of 423 K, 473 K and 573 K, respectively, using a strain rate of 1×10^{-4} s^{-1}. The role of strain rate on the elongation is shown in Figure 4.57 and Figure 4.58. For a sample processed in HPT for a specific number of turns, the higher strain rates (1×10^{-1} s^{-1} and 1×10^{-2} s^{-1}) caused the occurrence of lower elongations compared to their counterparts, which showed significantly higher values at the slowest strain rates (1×10^{-3} s^{-1} and 1×10^{-4} s^{-1}). For instance, for the sample processed for *N* = 10 turns, the maximum elongations at a testing temperature of 573 K were 410 %, 860 %, 1050 % and 1308 % using strain rates of 1×10^{-1} s^{-1}, 1×10^{-2} s^{-1}, 1×10^{-3} s^{-1}, and 1×10^{-4} s^{-1}, respectively.

For the as–received alloy, the elongations increased slightly for the samples tested at a temperature of 296 K as shown in Figure 4.58 (e). Significant increase in the elongations were observed when samples were tested at temperatures of 473 K and 573 K. The data of the maximum elongations for the as–received alloy is tabulated in Table 4.5. The appearances of fractured samples after reaching the maximum elongations are shown in Figures (4.59 – 4.62) for samples processed in HPT for *N* = 1, 3, 5, and 10 turns, as well as for the as–received alloy. The untested tensile sample is depicted in these images. It can be seen clearly here

the effect of the aforementioned factors on the elongation for the alloy under test. The fractured samples exhibited noticeable elongations associated with relatively uniform deformation across the gauge lengths of tested samples, especially at higher testing temperatures and / or using the lowest strain rates.

4.3.3 Flow stress – strain rate curves and the strain–rate sensitivity results

The flow stress was plotted versus the strain rate for the samples processed in HPT for different numbers of turns and then tested at different testing temperatures using different strain rates. The values of strain–rate sensitivity (m) were obtained from the slopes of the log – log format plots as shown in Figure 4.64. For a given number of turns for the sample processed in HPT and then pulled in tension, the flow stress decreased with decreasing strain rate and testing temperature, which was reflected in the values of the strain-rate sensitivity and in the extent of the elongation–to–fracture.

The values of strain rate sensitivity increased with decreasing the strain rate from 1×10^{-1} to 1×10^{-4} s^{-1} at all testing temperatures. The increase in the values of strain–rate sensitivity are associated with increase in the elongation–to–fracture for the slower strain rates as illustrated in the elongation–strain rate curves in Figure 4.57. Increasing the testing temperature from 423 K to 573 K resulted in an increase in the values of strain rate sensitivity over the strain rate range as illustrated in Figure 4.58. An increase in the values of the strain–rate sensitivity was found also for the as–received alloy with increasing the testing temperature and decreasing the strain rate.

The activation energy (Q) of the superplastic deformation was calculated from the slope of the plot of the variation in the flow stress with the reciprocal of the temperatures from 423 K to 573 K as shown in Figure 4.65 for the tensile sample processed in HPT for N = 10 turns and tested using strain rate 1×10^{-4} s^{-1} over the temperature range (423 – 573) K. The activation energy was calculated using the following equation [3]:

$$Q = \frac{1}{m} R \frac{\Delta \, ln\sigma}{\Delta \, (1/T)} \qquad (4.1)$$

The value of activation energy was 80.34 KJ/mole for the temperature range, which is which is close to the activation energy of grain boundary diffusion of pure magnesium (92 KJ/mol) [193]. The temperature and grain size compensated strain rate versus normalised stress is plotted as shown in Figure 4.66 for the AZ91 alloy processed in HPT for *N* = 10 turns at room temperature and tested in tension at different temperatures and strain rates. The slope of the straight line has a value of the stress exponent of n = 2, and it represents the predicted superplastic strain rate.

4.3.4 Microstructure observations for the fractured samples

The microstructures of tensile samples after the tensile test to fracture were observed along the gauge lengths by SEM as shown in Figures (4.67 – 4.75). These samples were processed in HPT for *N* = 1, 3 and 10 turns and then tested at different testing temperatures and strain rates. These observations revealed that the microstructures after the tensile test have gradually grown with increasing the testing temperature from 423 K to 573 K at all strain rates. For a specific testing temperature, the microstructures were also gradually grown at the slower strain rates (1×10^{-3} s^{-1} and 1×10^{-4} s^{-1}) in a more pronounced way than at the higher strain rates (1×10^{-1} s^{-1} and 1×10^{-2} s^{-1}).

A representative comparison of the grain sizes as observed by SEM along the gauge lengths of the tensile samples tested at different testing temperatures and strain rates is shown in Figure 4.76. These samples were processed in HPT for *N* = 10 turns and then tested in tension at different temperatures and strain rates. At the lower testing temperature, i.e., 423 K, the grain size increased slightly from 0.15 μm to 1.5 μm using strain rates of 1×10^{-1} s^{-1} and 1×10^{-4} s^{-1}, respectively. At the higher testing temperature, i.e., 573 K , the grain size increased moderately from 0.4 μm to 8 μm using strain rates of 1×10^{-1} s^{-1} and 1×10^{-4} s^{-1}, respectively. Another comparison was made between the grain sizes of the samples processed

for *N* = 1 and 10 turns after tensile test as shown in Figure 4.77. The grain sizes for samples processed for *N* = 1 turn are larger than for samples processed for *N* = 10 turns over the range of strain rates and testing temperature. These limited changes in the grain sizes did not influence the extent of superplastic ductilities that have been achieved for the AZ91 alloy in this research.

The microstructure observed along the gauge lengths of the tensile samples for the as–received alloy after tensile testing at 296 K, 473 K and 573 K is also shown in Figures (4.78 – 4.80). These as-received microstructures showed non-superplastic behaviour for all strain rates at all testing temperatures, except at 473 K using a strain rate of 1×10^{-4} s^{-1} and at 573 K using strain rates of 1×10^{-3} s^{-1} and 1×10^{-4} s^{-1} where relatively moderate ductilities were observed. The maximum elongation achieved for the as–received alloy was 332% at 573 K using a strain rate of 1×10^{-4} s^{-1}, and the data of the maximum elongations for the as–received alloy after tensile test to fracture at different testing temperatures and strain rates is illustrated in Table 4.5.

4.3.5 Variation of the grain size with testing temperature and time

The AZ91 alloy processed in HPT at room temperature exhibited significant microstructural stability during the tensile test at elevated temperatures. The microstructures as observed by SEM after tensile test retained their fine grain sizes even at the slowest strain rate (1×10^{-4} s^{-1}) at a testing temperature of 573 K as shown in Figure 4.81 for samples processed in HPT for *N* = 1, 3 and 10 turns. The data of the grain sizes were re-plotted versus the testing temperature and time as shown in Figure 4.82 and Figure 4.75 for the samples processed in HPT for *N* = 1 turn and 10 turns.

The average grain size was about 1.5 μm after testing at 423 K (for 2–1200 minutes) over the strain rate range. After testing at 473 K (for 3–1440 minutes), the microstructures also showed fine grains with only modest grain growth to an average grain size of about 3 μm. Tensile testing at 573 K (for 5–1680 minutes) resulted in the maintenance of a fairly fine microstructure with limited grain growth

up to about 8 μm as shown in Figure 4.77. The samples processed in HPT for *N* = 10 turns exhibited a relatively slower rate of limited grain growth than the samples processed for *N* = 1 turn at the fastest and slowest strain rates, i.e., at 1×10^{-1} s^{-1} and 1×10^{-4} s^{-1}, respectively, as illustrated in Figures (4.82 – 4.75). However, both aforementioned samples revealed considerable thermal stability during tensile testing.

The grains remained equiaxed after testing at 423 K, 473 K and 573 K at different strain rates as observed in Figures (4.67 – 4.76). Some individual grains have developed fibrous morphologies at temperatures of 473 K and 573 K at strain rates of 1×10^{-3} s^{-1} and 1×10^{-4} s^{-1} as shown in Figure 4.77 (b, c, e, f), and at a temperature of 573 K using strain rates of 1×10^{-3} s^{-1} and 1×10^{-4} s^{-1} as shown in Figure 4.77 (k, l). The fibrous or filament structures were observed at the slower strain rates and higher temperatures along the gauge lengths of the tensile samples in the direction of the tension loading. These structures were connected with grains that appear to have separated during the superplastic elongation regimes as observed in Figure 4.81. As a result of the occurrence of these structures, significant elongations were observed as illustrated in Figure 4.81 for samples processed in HPT for *N* = 1, 3 and 10 turns that were tested at 573 K using a strain rate of 1×10^{-4} s^{-1}.

The EDS analysis of these fibrous structures revealed their composition as shown in Figure 4.84, and the analysis was conducted at three locations: grain, grain boundary and filament. It was found that the composition of these filaments consists mostly of β–phase ($Mg_{17}Al_{12}$) as indicated by the relative estimation of the weights of the constituents. It is worth mentioning that the tensile test has been conducted in the air in this research and therefore the surfaces of the samples were oxidized as indicated by the presence of oxygen in the EDS analyses of the tensile samples as illustrated in Figure 4.84.

The oxidation of the alloy appeared as superficial layers on the tested samples at all testing temperatures. At a temperature of 423 K and using high strain rates, i.e., 1×10^{-1} s^{-1} and 1×10^{-2} s^{-1}, the oxidation layer occurred as a fragmented layer as illustrated by the yellow arrows in Figure 4.67 for the sample processed for *N* = 1 turn and as a cracked layer as shown in Figure 4.68 for the sample processed for

N = 3 turns. At temperatures of 473 K and 573 K and / or at slow strain rates, i.e., 1×10^{-3} s^{-1} and 1×10^{-4} s^{-1}, the oxidation layer fragmented into small blocks as shown in Figures (4.67, 4.78 – 4.75). However, the oxidation occurred within the matrix of the alloy as indicated by EDS analyses in Figure 4.84.

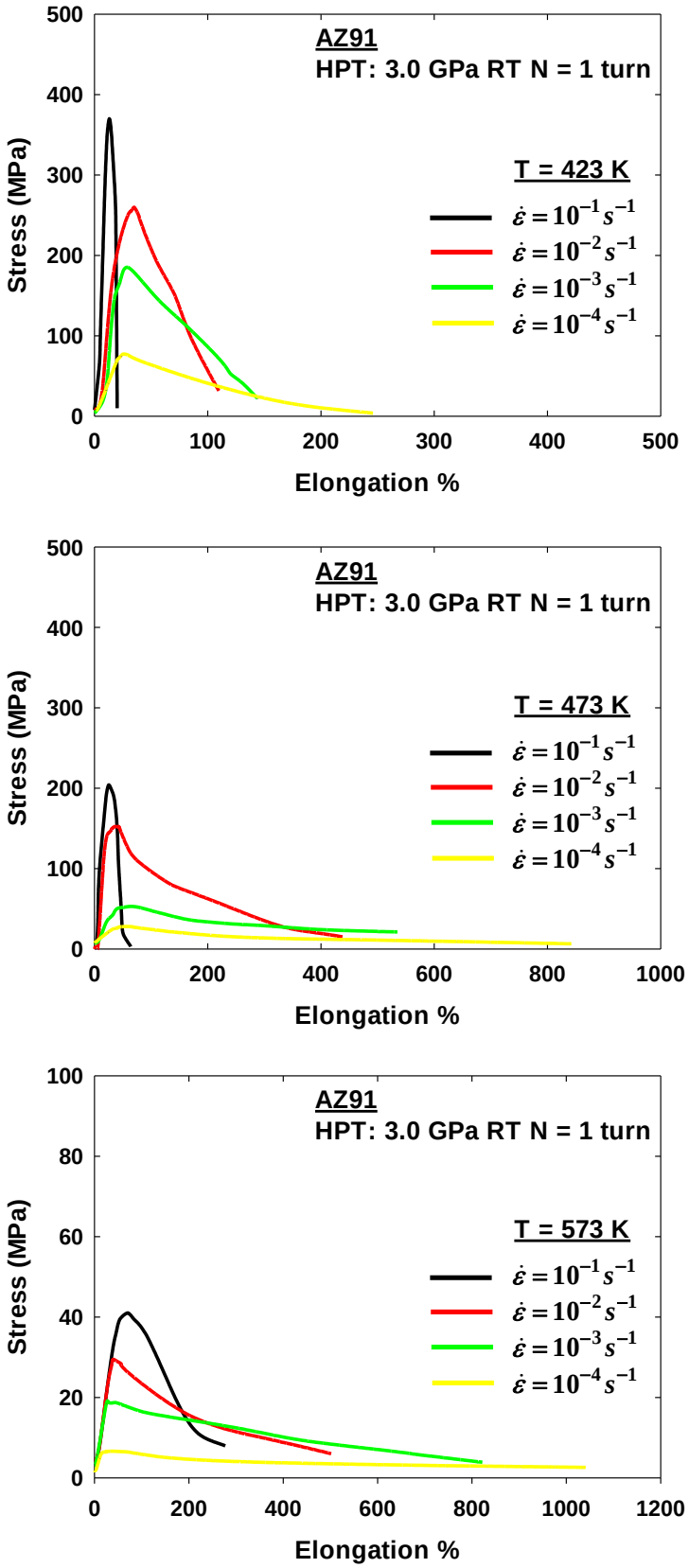

Figure 4.52: Stress–strain curves for the AZ91 alloy processed at room temperature in HPT for *N* = 1 turn using an applied pressure of 3.0 GPa and tested in tension at 423 K, 473 K and 573 K using different strain rates.

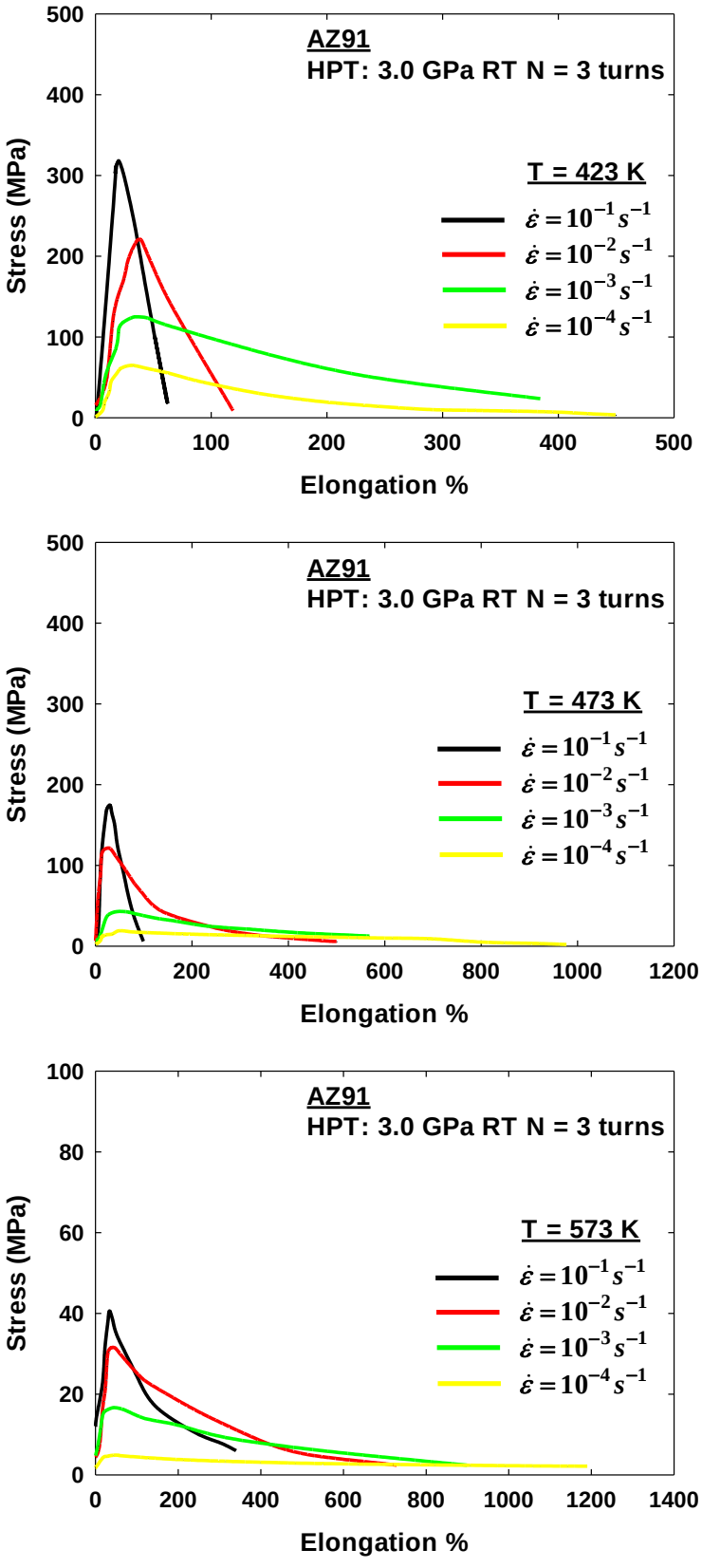

Figure 4.53: Stress–strain curves for the AZ91 alloy processed at room temperature in HPT for *N* = 3 turn using an applied pressure of 3.0 GPa and tested in tension at 423 K, 473 K and 573 K using different strain rates.

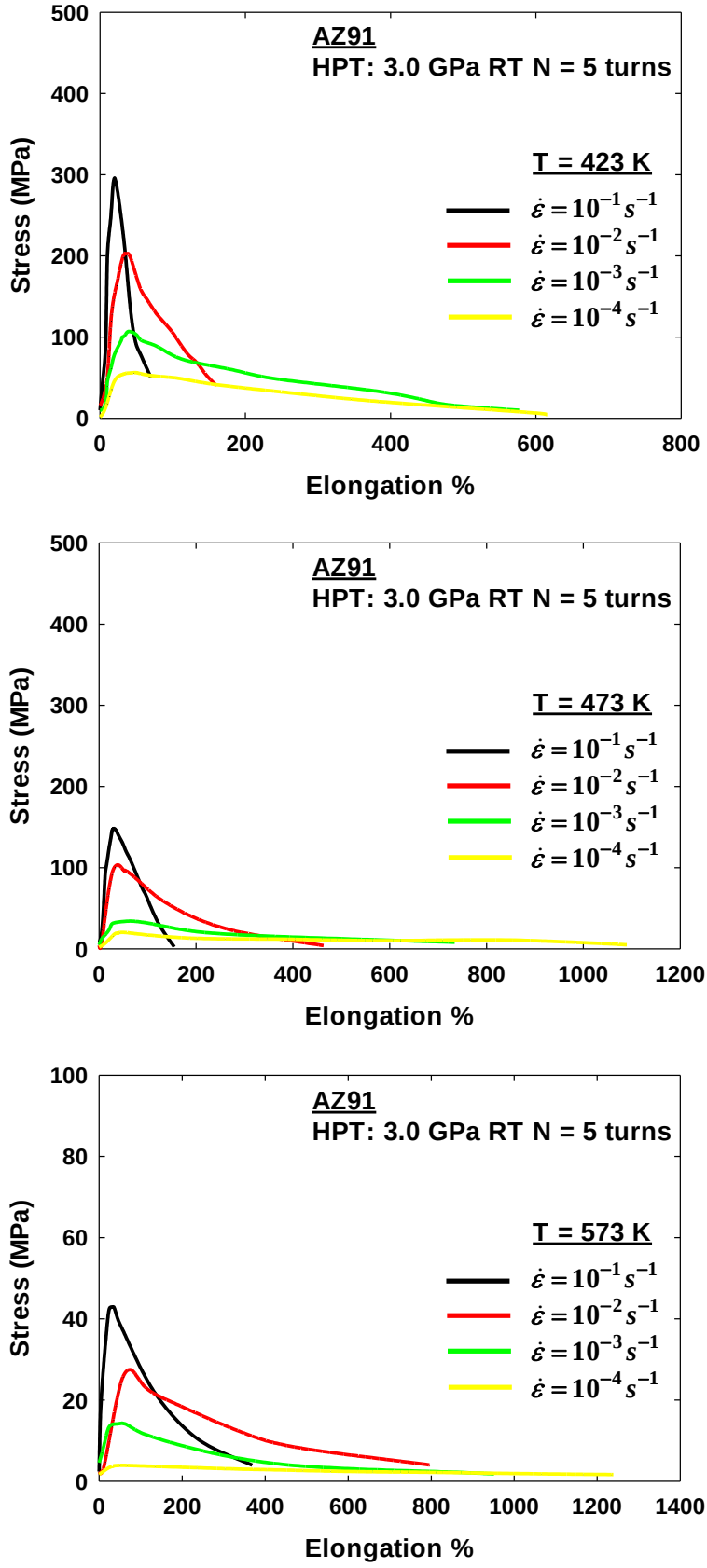

Figure 4.54: Stress–strain curves for the AZ91 alloy processed at room temperature in HPT for *N* = 5 turns using an applied pressure of 3.0 GPa and tested in tension at 423 K, 473 K and 573 K using different strain rates.

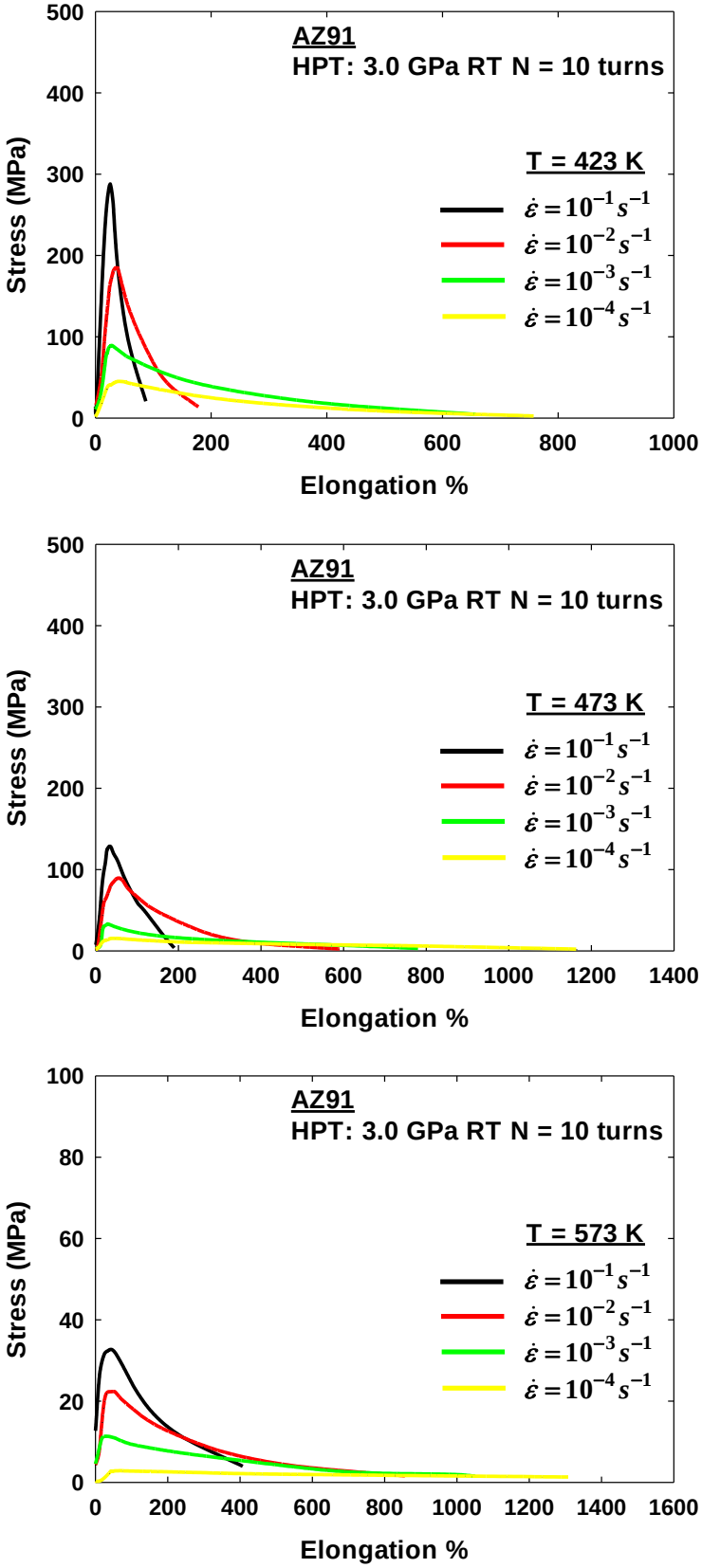

Figure 4.55: Stress–strain curves for the AZ91 alloy processed at room temperature in HPT for *N* = 10 turns using an applied pressure of 3.0 GPa and tested in tension at 423 K, 473 K and 573 K using different strain rates.

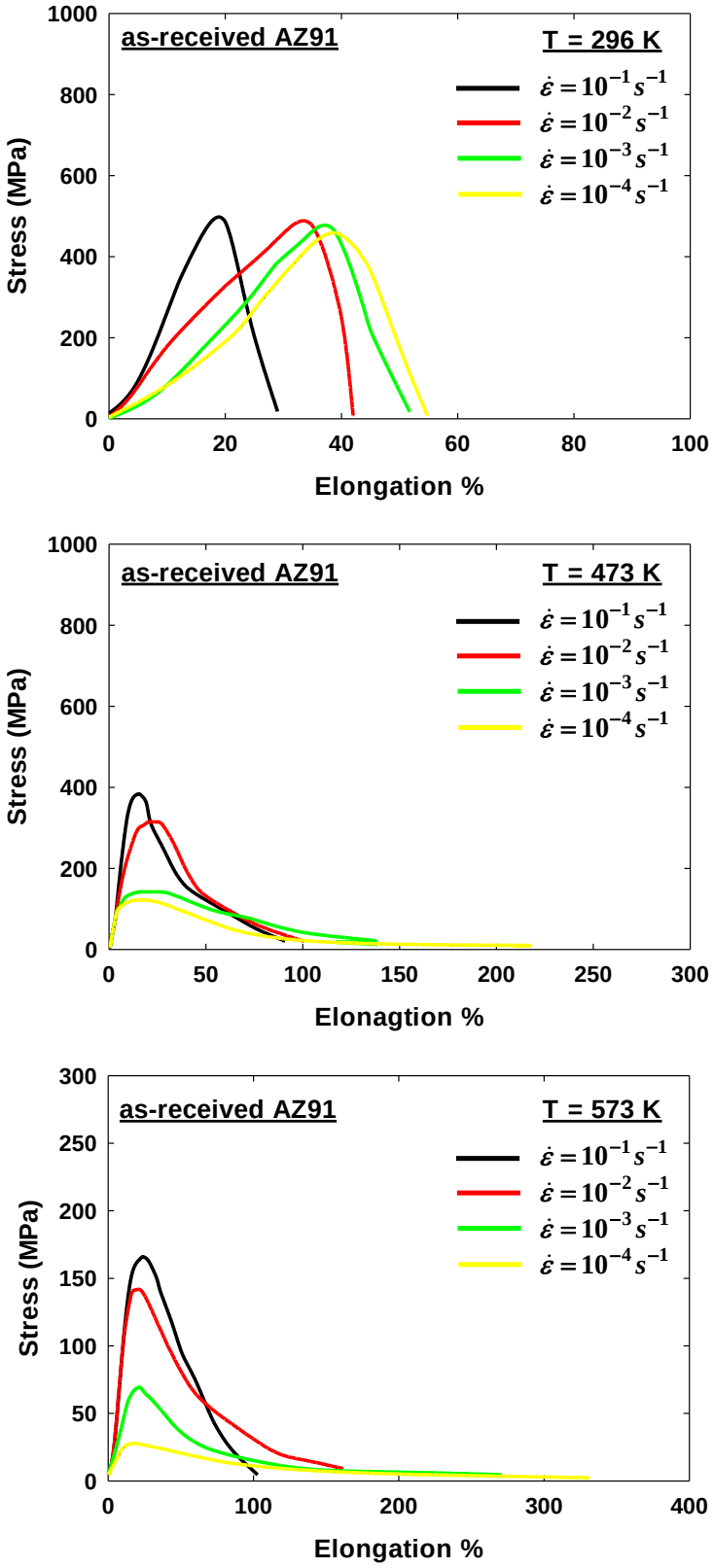

Figure 4.56: Stress–strain curves for the as–received AZ91 alloy and tested in tension at 296 K, 473 K and 573 K using different strain rates.

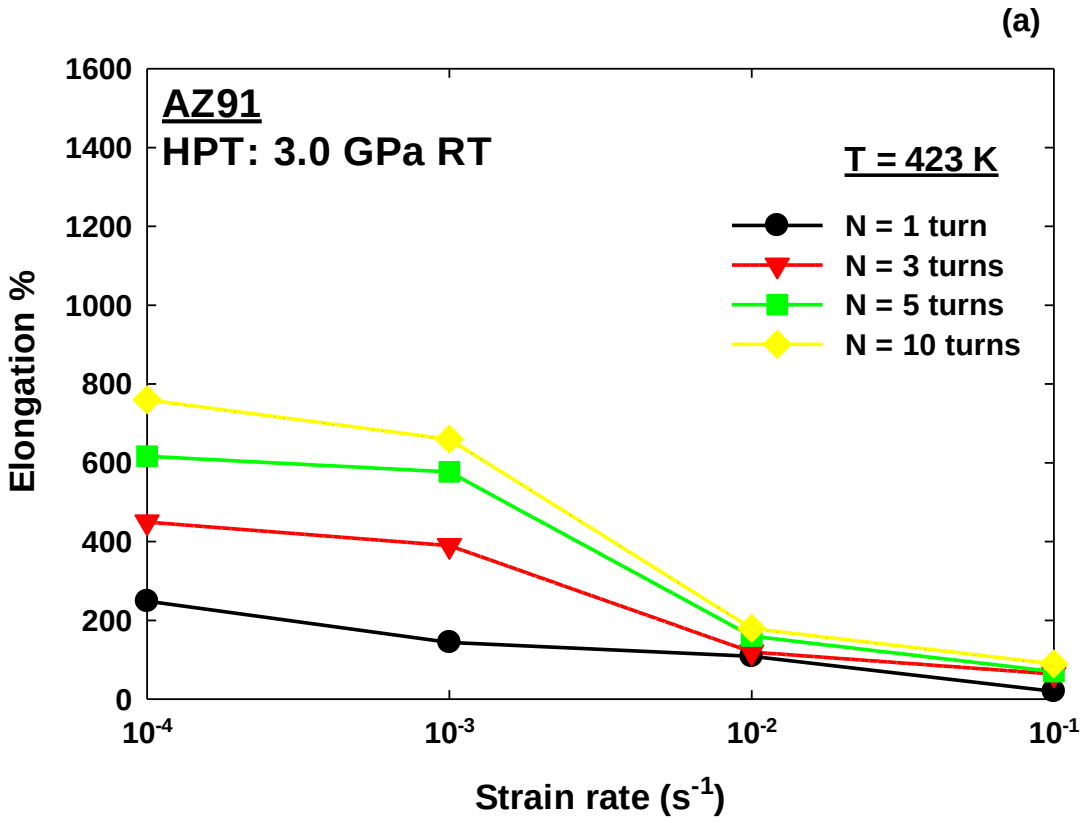
(a)
AZ91
HPT: 3.0 GPa RT
T = 423 K
N = 1 turn
N = 3 turns
N = 5 turns
N = 10 turns
Elongation %
Strain rate (s-1)
0
200
400
600
800
1000
1200
1400
1600
10-4
10-3
10-2
10-1

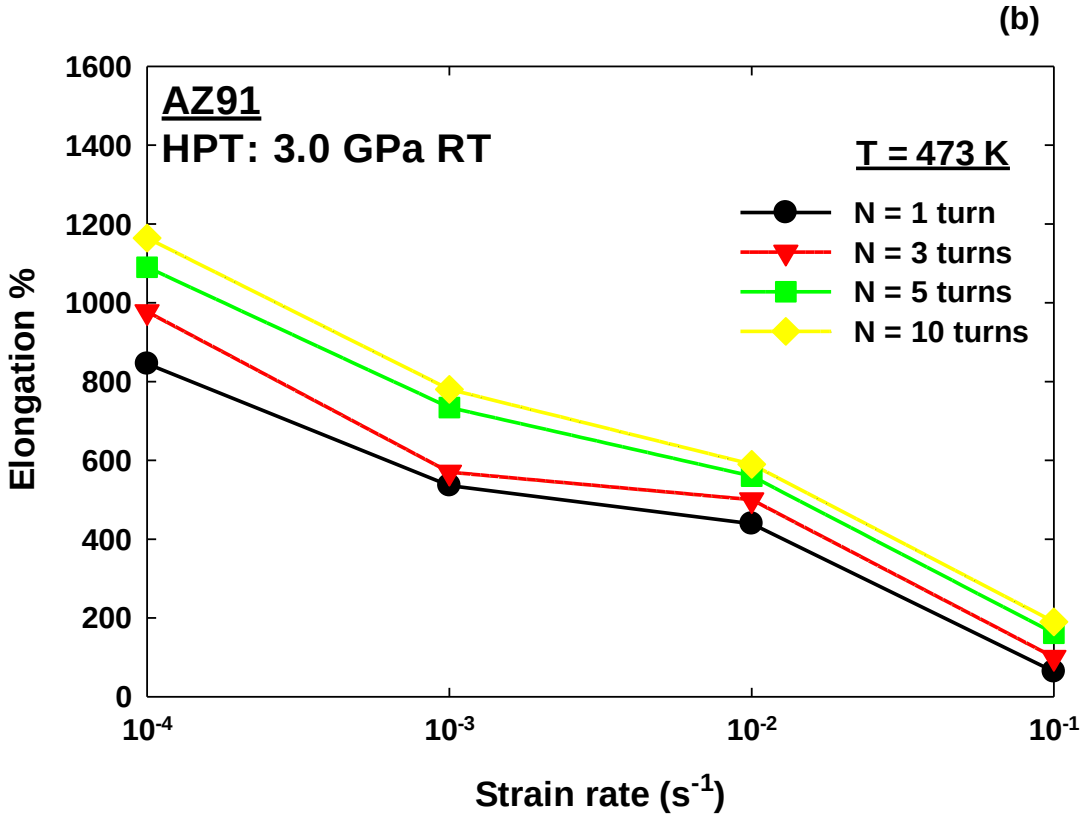
(b)
AZ91
HPT: 3.0 GPa RT
T = 473 K
N = 1 turn
N = 3 turns
N = 5 turns
N = 10 turns
Elongation %
Strain rate (s-1)
0
200
400
600
800
1000
1200
1400
1600
10-4
10-3
10-2
10-1

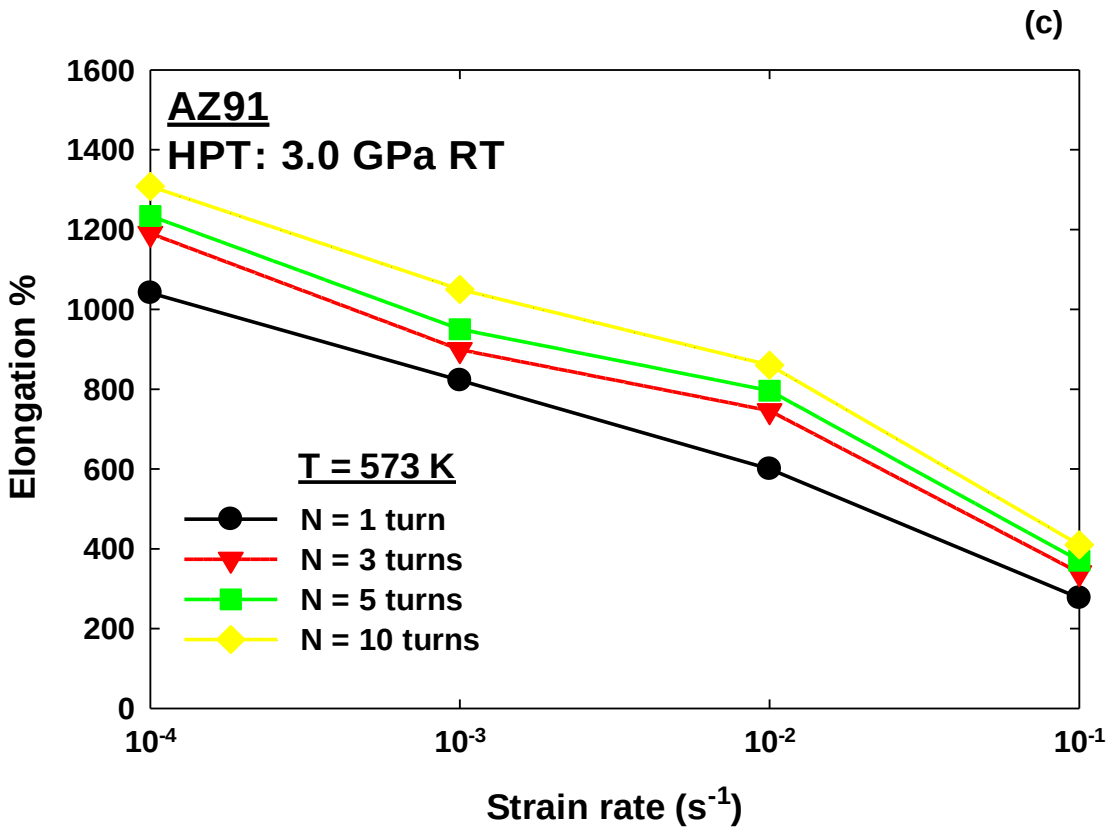

Figure 4.57: Elongation–strain rate curves for the AZ91 alloy processed at room temperature using an applied pressure of 3.0 GPa for different number of turns in HPT and tested in tension at temperatures of: (a) 423 K, (b) 473 K, and (c) 573 K.

Table 4.4: The maximum elongations that achieved in this research for the AZ91 alloy processed in HPT using an applied pressure of 3.0 GPa at room temperature.

N	$T\ (K)$	$\dot{\varepsilon}\ (s^{-1})$	$El.\%$
1	423	1×10^{-1}	20
		1×10^{-2}	109
		1×10^{-3}	144
		1×10^{-4}	249
	473	1×10^{-1}	64
		1×10^{-2}	439
		1×10^{-3}	536
		1×10^{-4}	845
	573	1×10^{-1}	277
		1×10^{-2}	600
		1×10^{-3}	822
		1×10^{-4}	1041
5	423	1×10^{-1}	70
		1×10^{-2}	160
		1×10^{-3}	577
		1×10^{-4}	617
	473	1×10^{-1}	161
		1×10^{-2}	560
		1×10^{-3}	734
		1×10^{-4}	1090
	573	1×10^{-1}	370
		1×10^{-2}	796
		1×10^{-3}	950
		1×10^{-4}	1234

N	$T\ (K)$	$\dot{\varepsilon}\ (s^{-1})$	$El.\%$
3	423	1×10^{-1}	64
		1×10^{-2}	120
		1×10^{-3}	390
		1×10^{-4}	450
	473	1×10^{-1}	100
		1×10^{-2}	500
		1×10^{-3}	570
		1×10^{-4}	977
	573	1×10^{-1}	430
		1×10^{-2}	746
		1×10^{-3}	899
		1×10^{-4}	1190
10	423	1×10^{-1}	90
		1×10^{-2}	180
		1×10^{-3}	660
		1×10^{-4}	760
	473	1×10^{-1}	190
		1×10^{-2}	590
		1×10^{-3}	780
		1×10^{-4}	1164
	573	1×10^{-1}	410
		1×10^{-2}	860
		1×10^{-3}	1050
		1×10^{-4}	1308

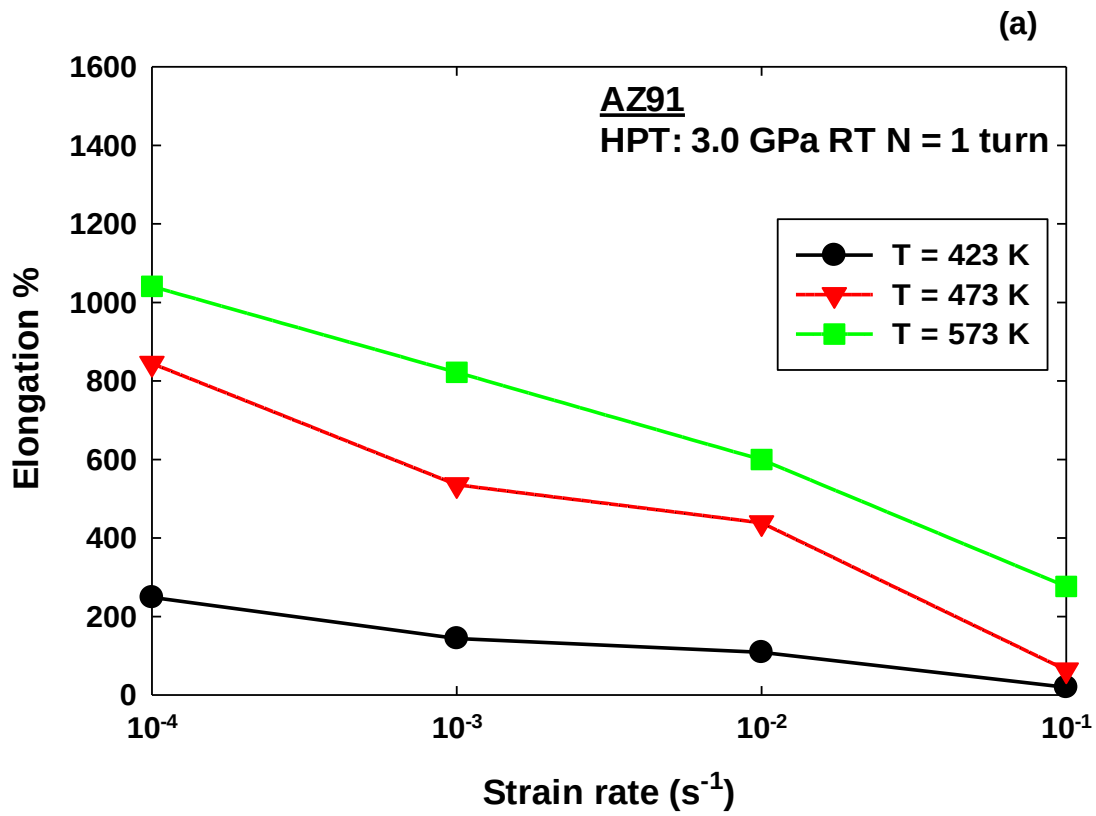
(a)
AZ91
HPT: 3.0 GPa RT N = 1 turn
T = 423 K
T = 473 K
T = 573 K
Elongation %
Strain rate (s-1)
1600
1400
1200
1000
800
600
400
200
0
10-4
10-3
10-2
10-1

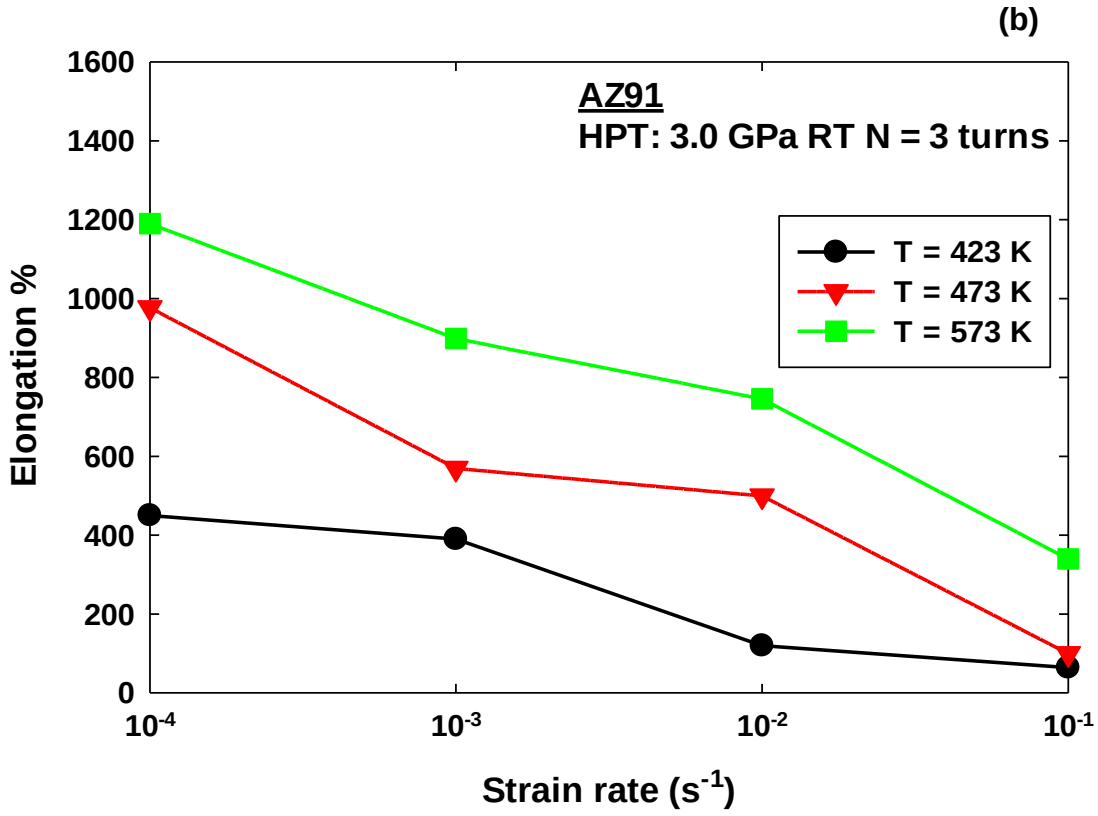
(b)
AZ91
HPT: 3.0 GPa RT N = 3 turns
T = 423 K
T = 473 K
T = 573 K
Elongation %
Strain rate (s-1)
1600
1400
1200
1000
800
600
400
200
0
10-4
10-3
10-2
10-1

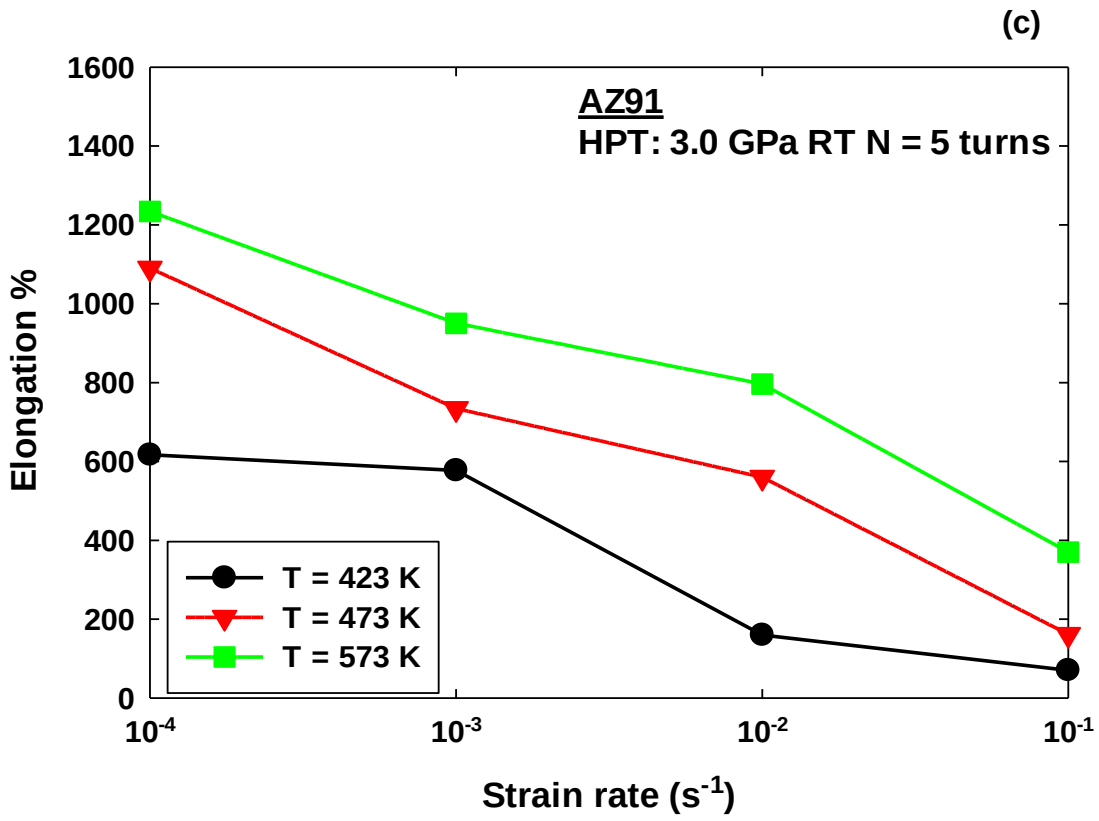
(c)
AZ91
HPT: 3.0 GPa RT N = 5 turns
Elongation %
Strain rate (s-1)
T = 423 K
T = 473 K
T = 573 K
0
200
400
600
800
1000
1200
1400
1600
10-4
10-3
10-2
10-1

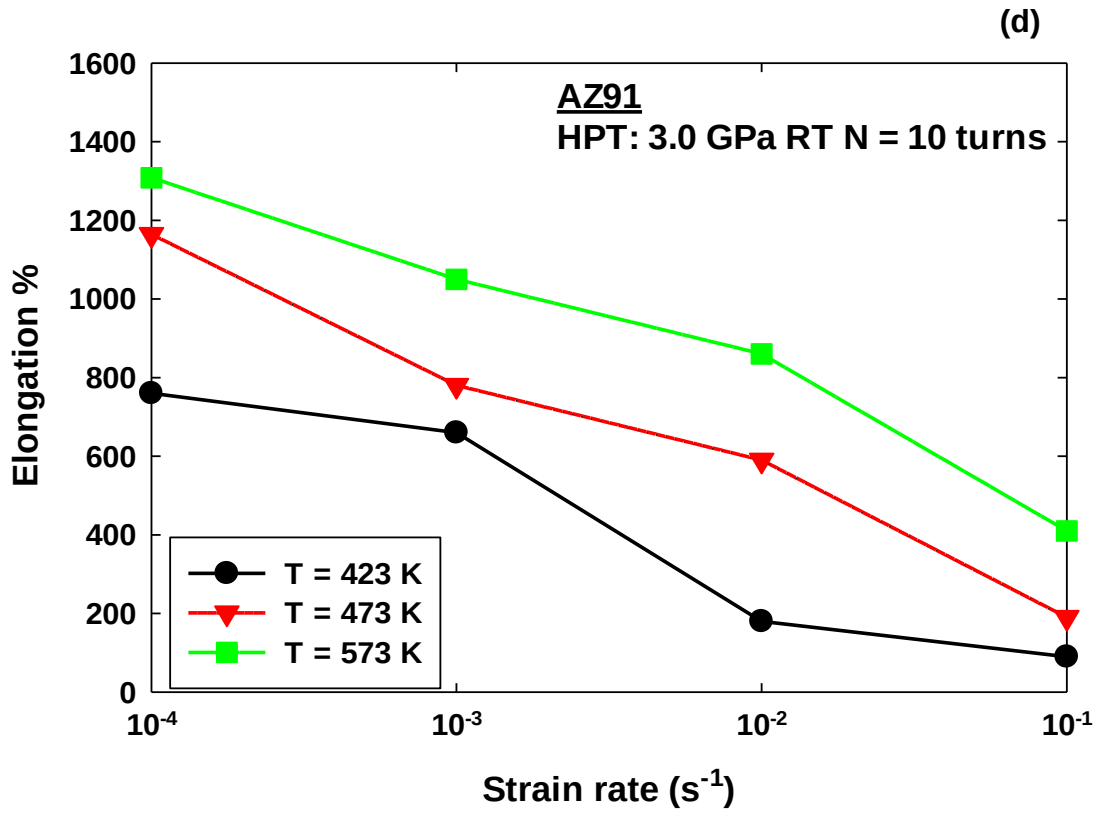
(d)
AZ91
HPT: 3.0 GPa RT N = 10 turns
Elongation %
Strain rate (s-1)
T = 423 K
T = 473 K
T = 573 K
0
200
400
600
800
1000
1200
1400
1600
10-4
10-3
10-2
10-1

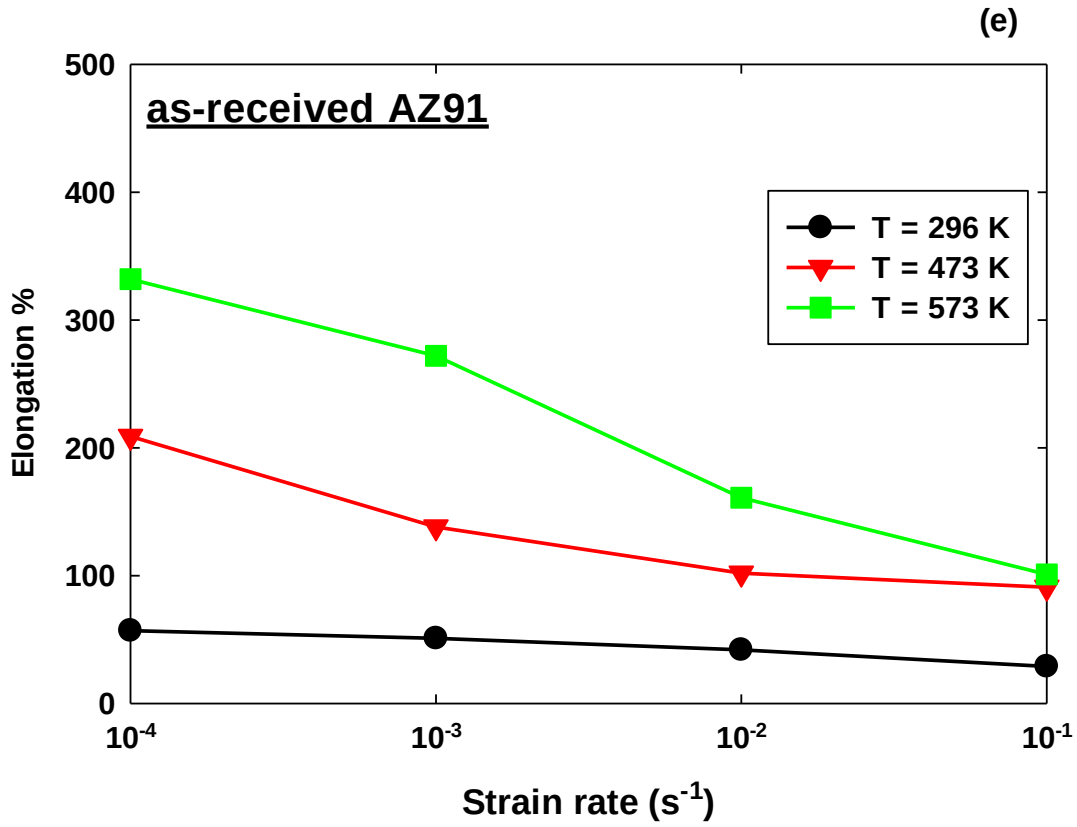

Figure 4.58: Elongation–strain rate curves for the AZ91 alloy processed at room temperature in HPT using an applied pressure of 3.0 GPa for: (a) *N* = 1 turn, (b) *N* = 3 turns, (c) *N* = 5 turns, (d) *N* = 10 turns and (e) as–received alloy and tested in tension at different temperatures.

Table 4.5: The maximum elongations for the as–received AZ91 alloy that obtained in this research.

	T (K)		
$\dot{\varepsilon}\ (s^{-1})$	296	473	573
1×10^{-1}	29	91	101
1×10^{-2}	42	102	161
1×10^{-3}	51	138	272
1×10^{-4}	57	209	332

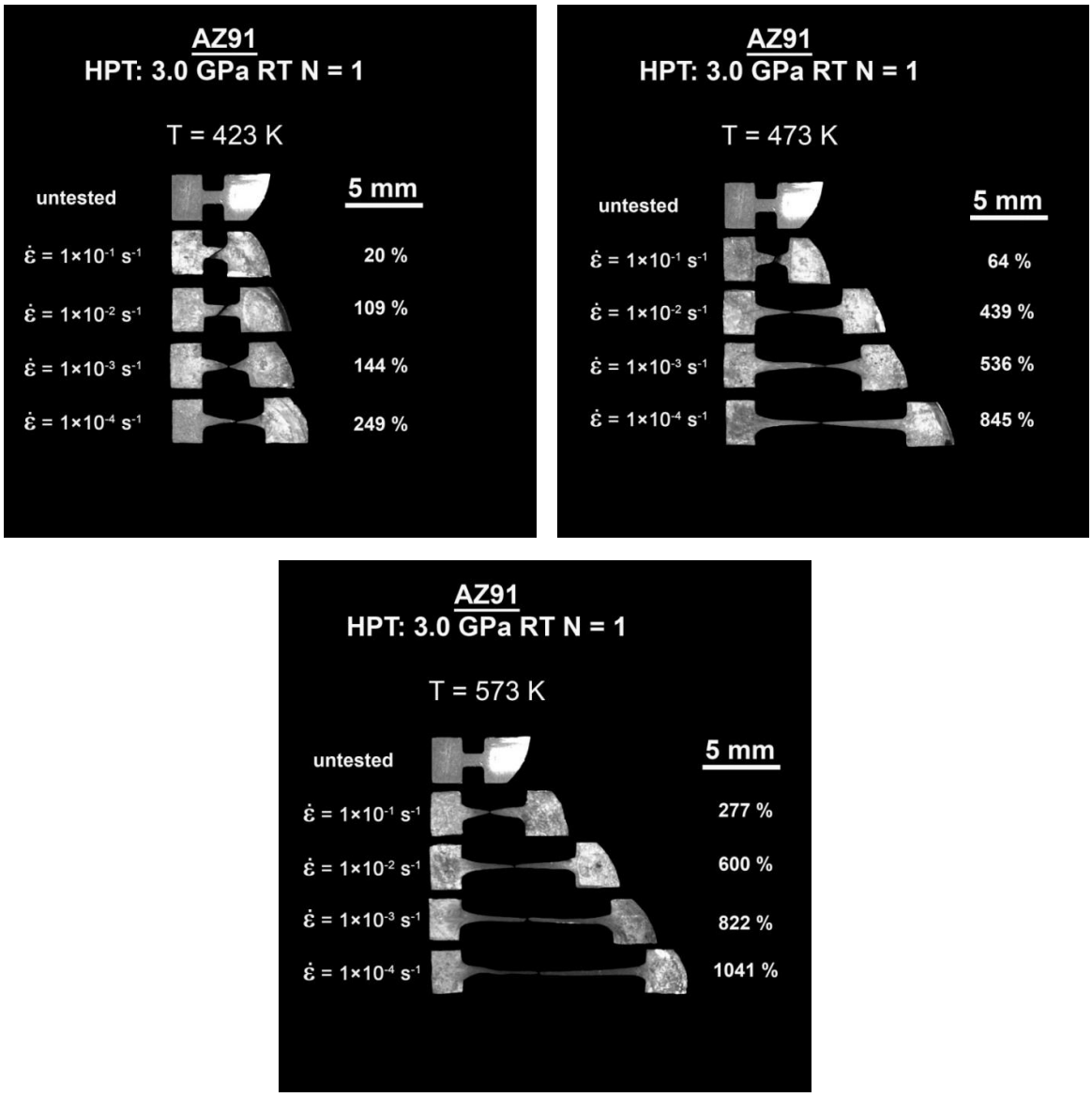

Figure 4.59: Appearance of the AZ91 samples processed by HPT for N = 1 turn using an applied pressure of 3.0 GPa at room temperature after tension to fracture at testing temperatures of 423 K, 473 K, and 573 K using different strain rates. The upper sample represents the untested case.

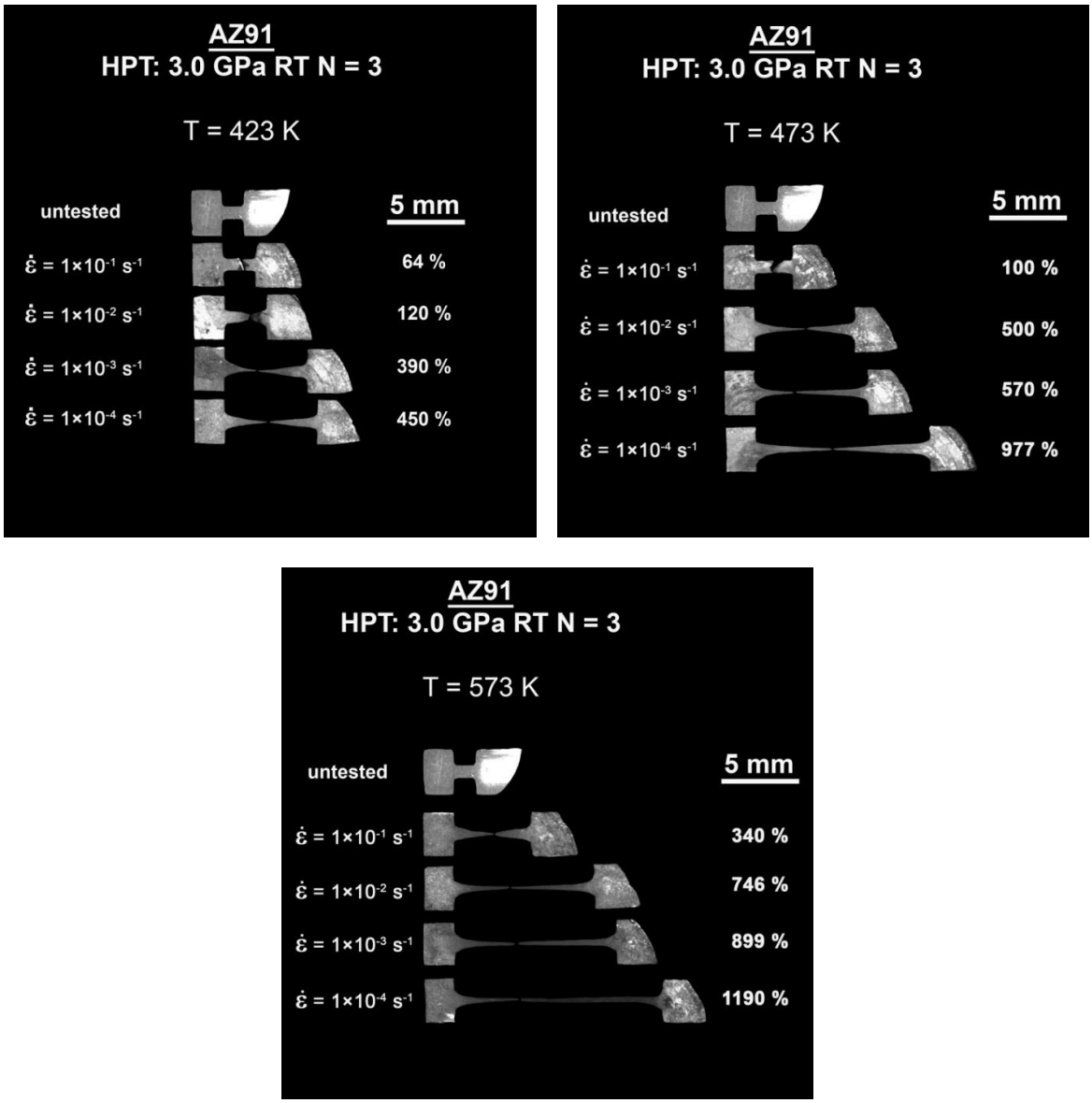

Figure 4.60: Appearance of the AZ91 samples processed by HPT for *N* = 3 turns using an applied pressure of 3.0 GPa at room temperature after tension to fracture at testing temperatures of 423 K, 473 K, and 573 K using different strain rates. The upper sample represents the untested case.

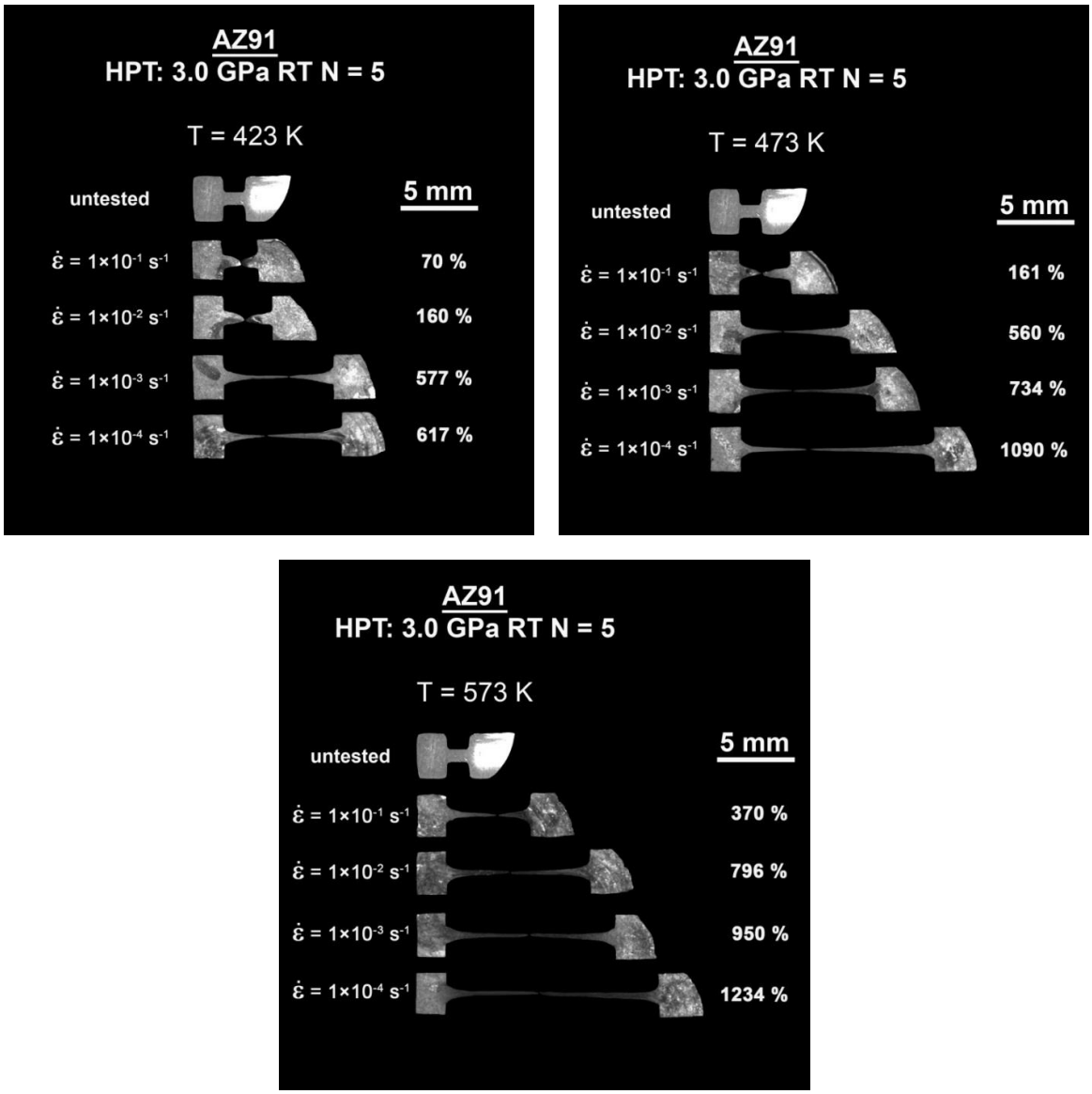

Figure 4.61: Appearance of the AZ91 samples processed by HPT for *N* = 5 turns using an applied pressure of 3.0 GPa at room temperature after tension to fracture at testing temperatures of 423 K, 473 K, and 573 K using different strain rates. The upper sample represents the untested case.

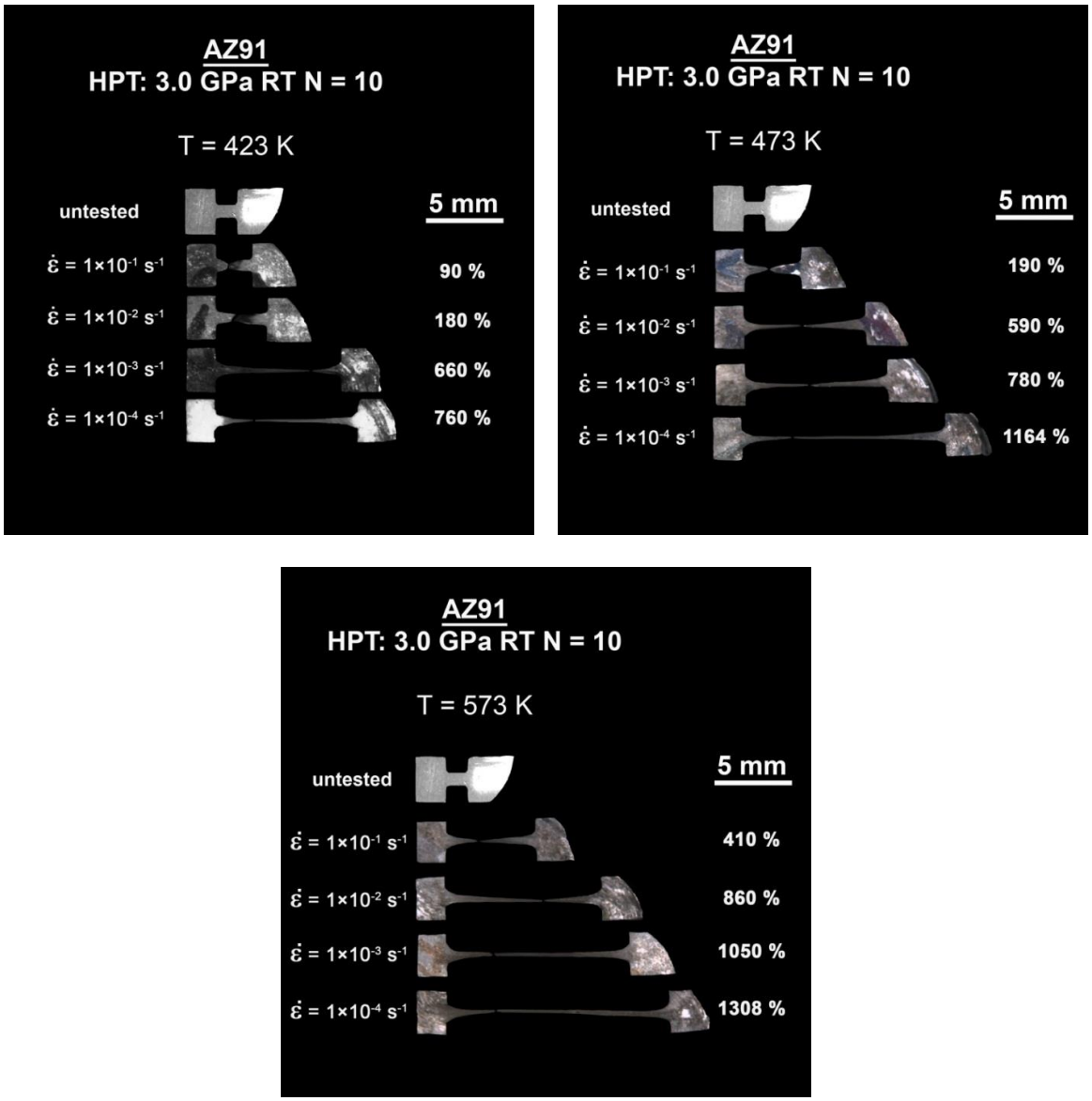

Figure 4.62: Appearance of the AZ91 samples processed by HPT for *N* = 10 turns using an applied pressure of 3.0 GPa at room temperature after tension to fracture at testing temperatures of 423 K, 473 K, and 573 K using different strain rates. The upper sample represents the untested case.

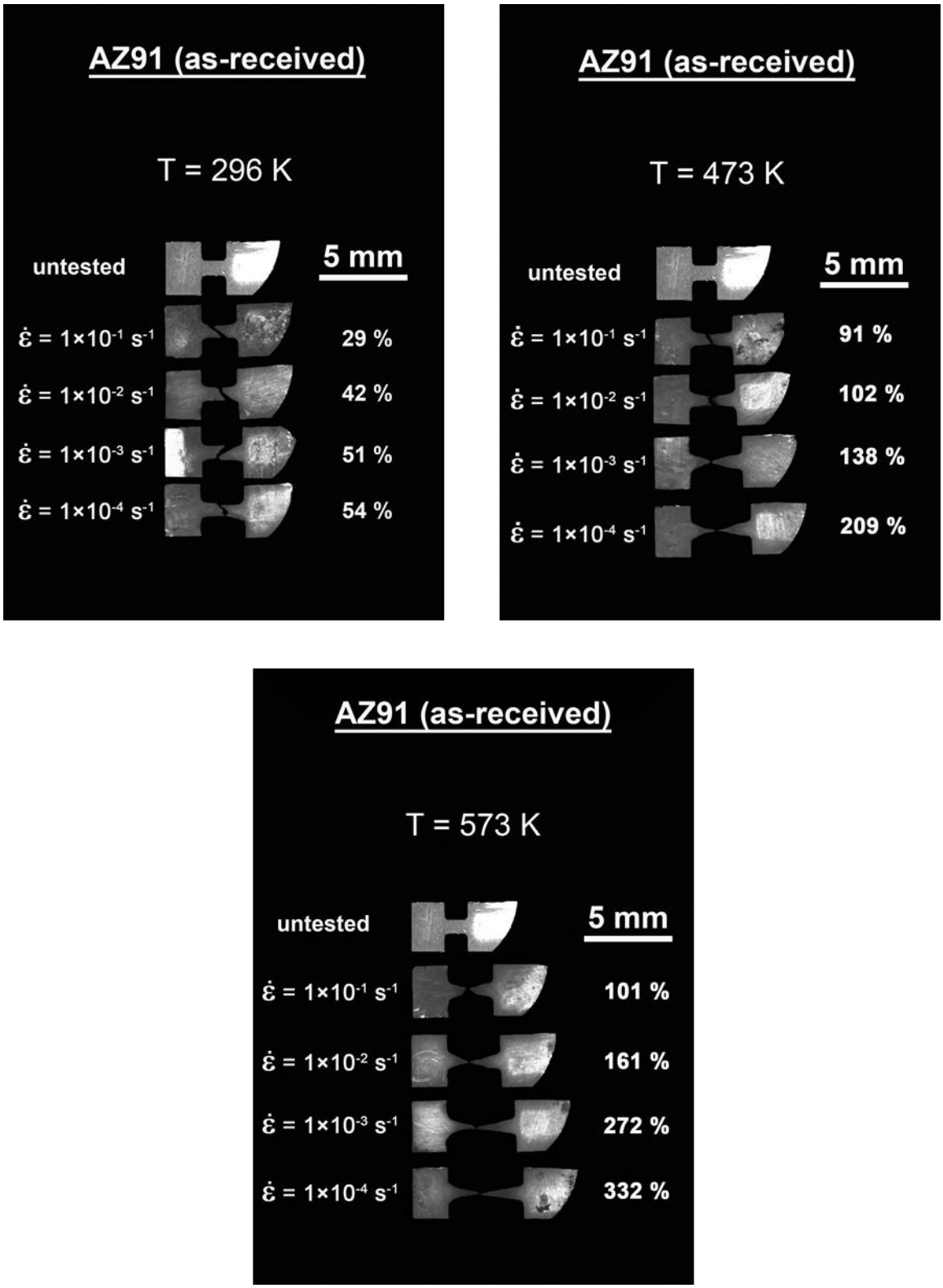

Figure 4.63: Appearance of the as–received AZ91 samples after tension to fracture at testing temperatures of 296 K, 473 K, and 573 K using different strain rates. The upper sample represents the untested case.

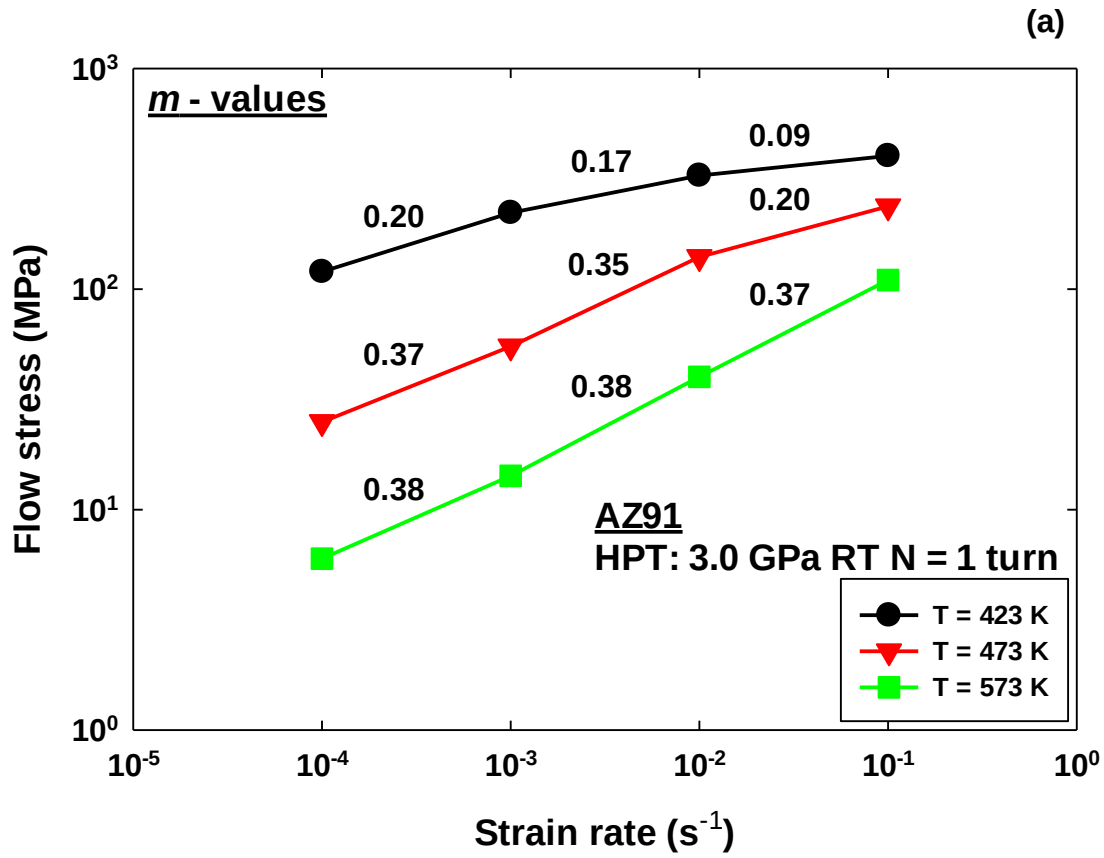
(a)
m - values
0.20
0.17
0.09
0.37
0.35
0.20
0.38
0.38
0.37
AZ91
HPT: 3.0 GPa RT N = 1 turn
T = 423 K
T = 473 K
T = 573 K
Flow stress (MPa)
Strain rate (s-1)

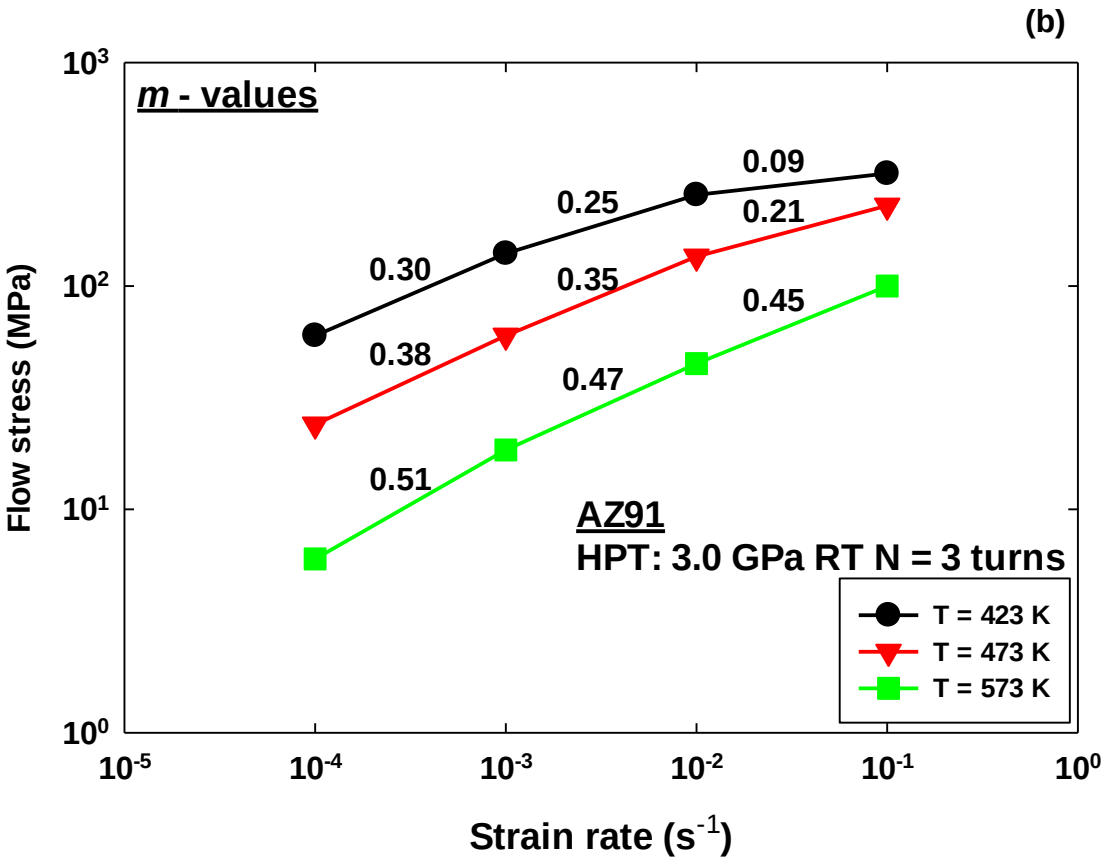
(b)
m - values
0.30
0.25
0.09
0.38
0.35
0.21
0.51
0.47
0.45
AZ91
HPT: 3.0 GPa RT N = 3 turns
T = 423 K
T = 473 K
T = 573 K
Flow stress (MPa)
Strain rate (s-1)

(c)

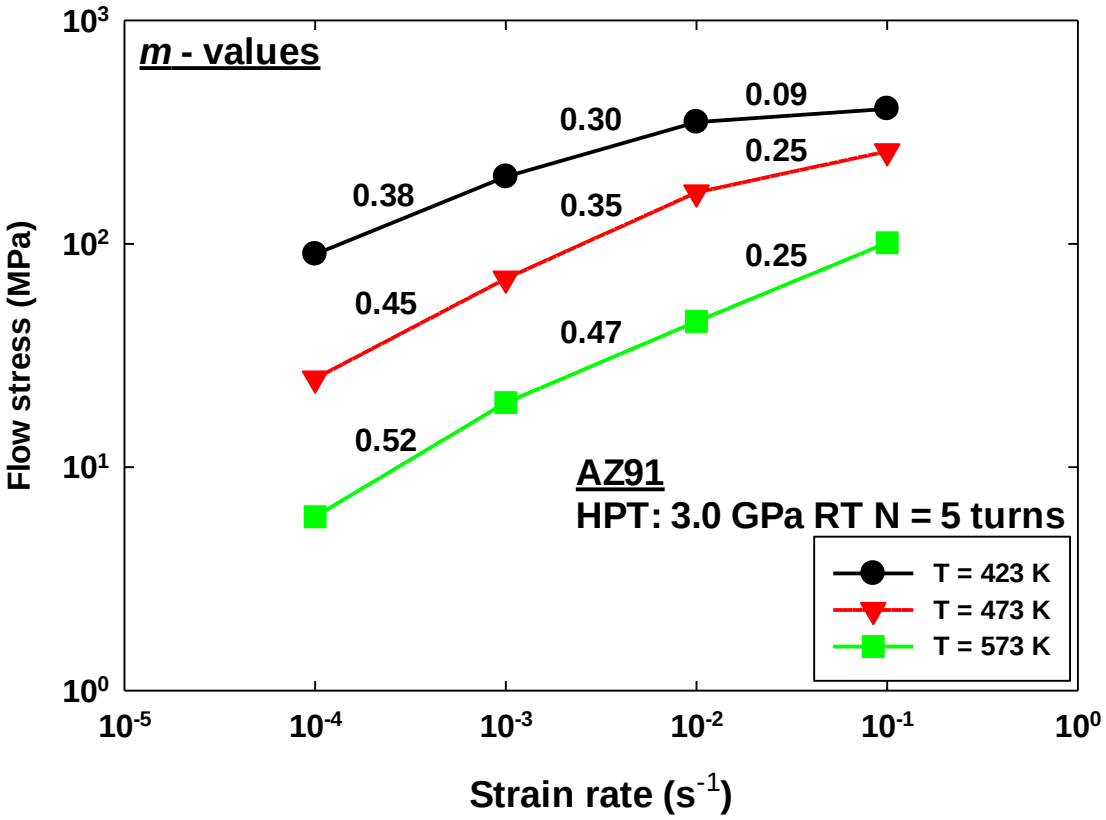
m - values
0.38
0.30
0.09
0.45
0.35
0.25
0.52
0.47
0.25
AZ91
HPT: 3.0 GPa RT N = 5 turns
T = 423 K
T = 473 K
T = 573 K
Flow stress (MPa)
Strain rate (s-1)

(d)

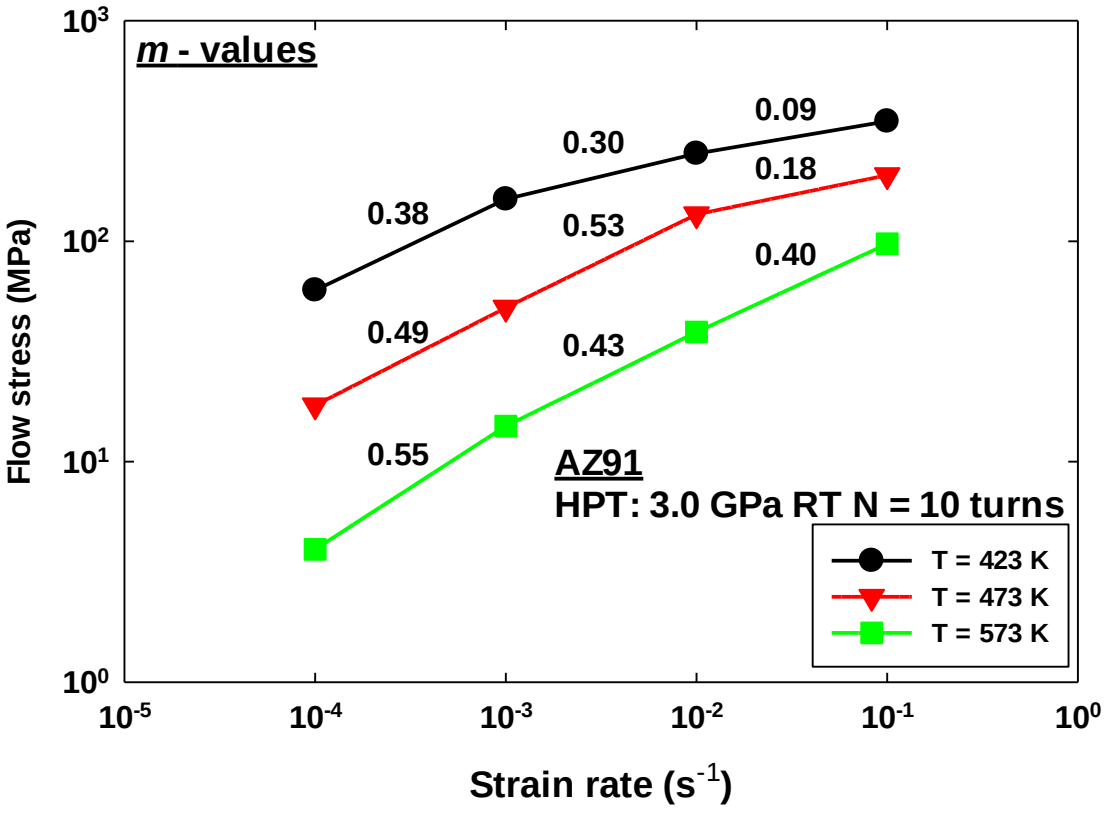
m - values
0.38
0.30
0.09
0.49
0.53
0.18
0.55
0.43
0.40
AZ91
HPT: 3.0 GPa RT N = 10 turns
T = 423 K
T = 473 K
T = 573 K
Flow stress (MPa)
Strain rate (s-1)

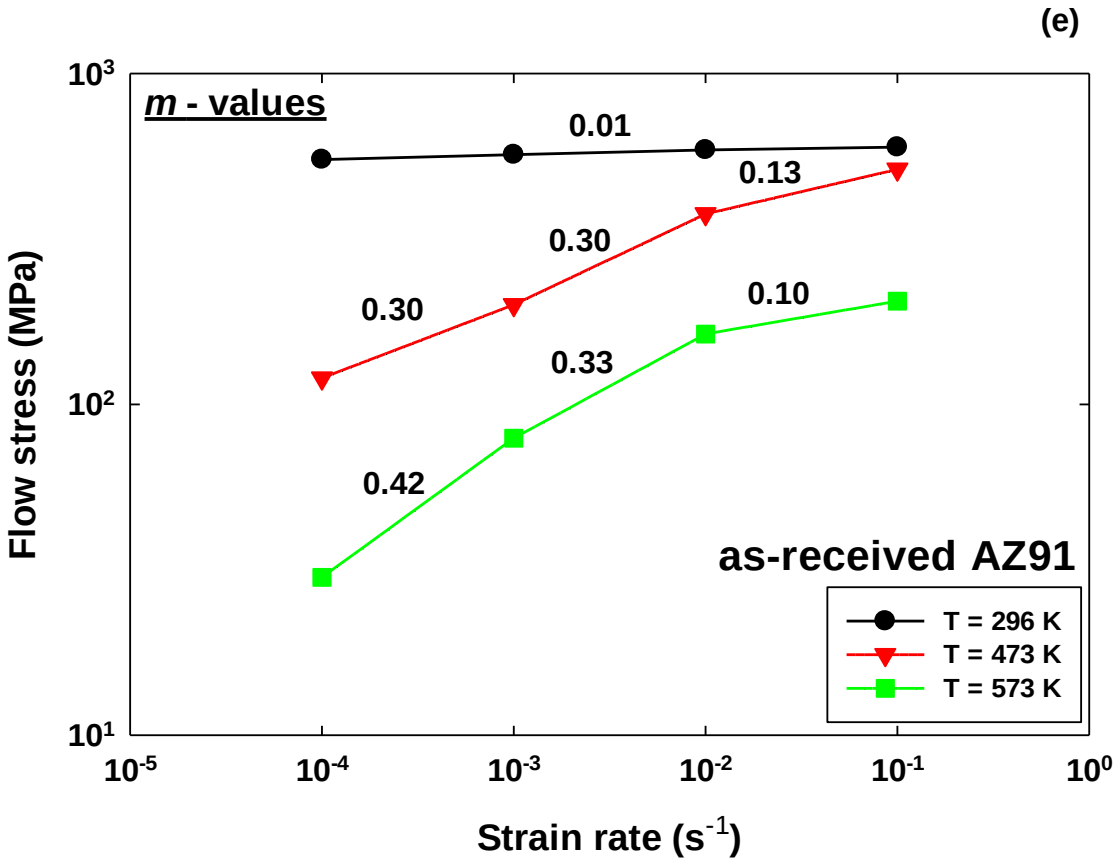

Figure 4.64: Flow stress–strain rate curves showing the values of strain–rate sensitivity (m) for the AZ91 alloy processed at room temperature in HPT using an applied pressure of 3.0 GPa for: (a) *N* = 1 turn, (b) *N* = 3 turns, (c) *N* = 5 turns, (d) *N* = 10 turns and (e) the as–received alloy tested in tension at different temperatures.

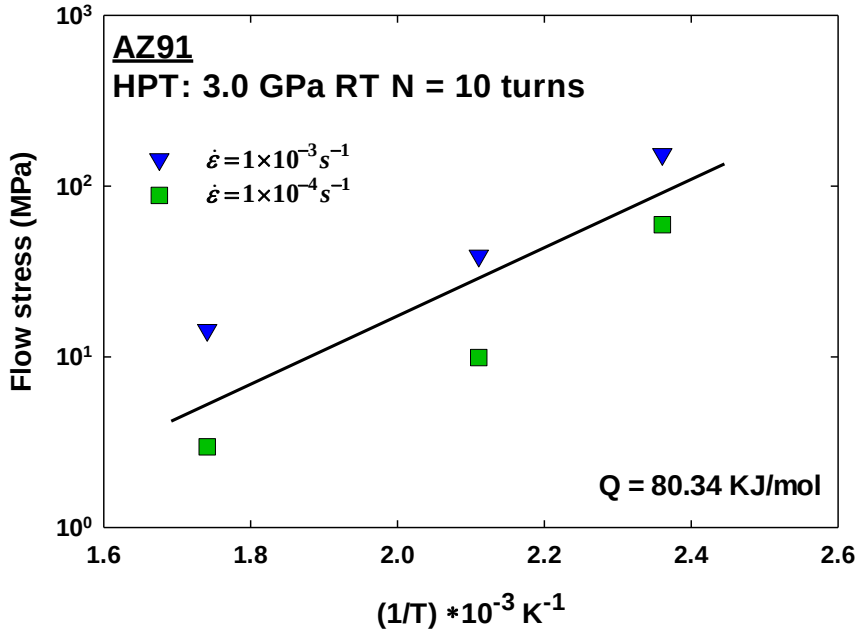

Figure 4.65: The variation in the flow stress with the reciprocal of the temperatures from 423 K to 573 K for determining the value of the activation energy (Q) for the tensile sample tested using strain rates of 1×10^{-3} s^{-1} and 1×10^{-4} s^{-1}. The straight line represents the fitting for the obtained data at 1×10^{-4} s^{-1} and its slope refers to the value of the activation energy. The plotted data are belonged to the AZ91 alloy processed in HPT for N = 10 turns at room temperature using an applied pressure of 3.0 GPa.

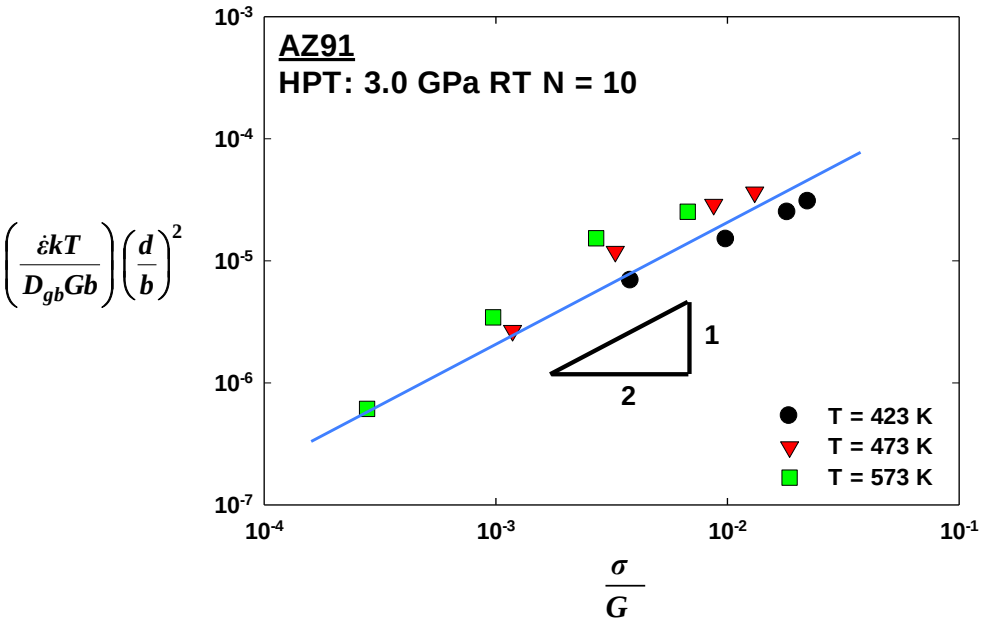

Figure 4.66: The temperature and grain size compensated strain rate versus normalised stress for the AZ91 alloy processed in HPT for N = 10 turns using an applied pressure of 3.0 GPa at room temperature and tested in tension at different temperatures and strain rates. The slope of the straight line has a value of the stress exponent of n = 2, and it represents the predicated superplastic strain rate.

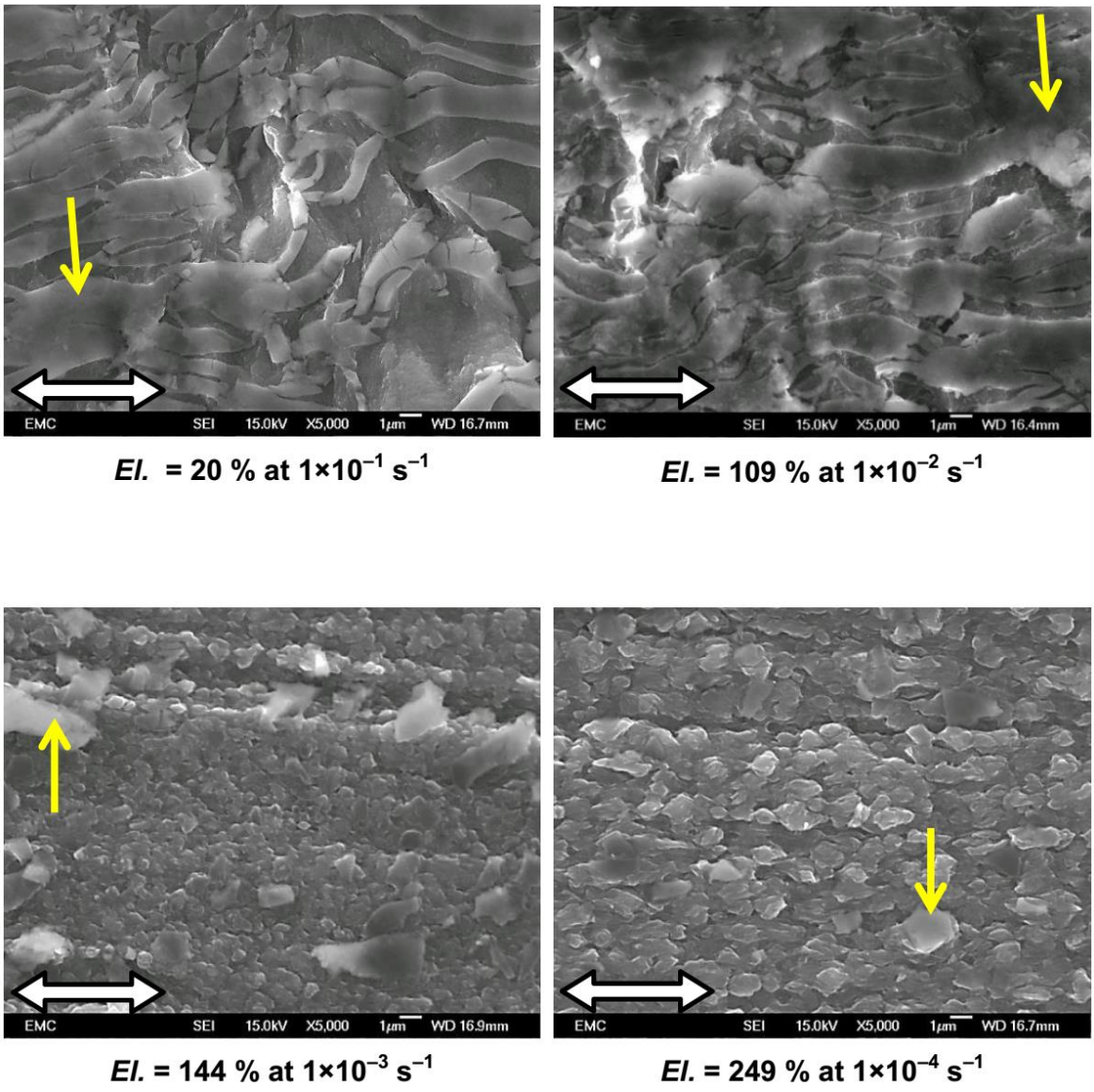

El. **= 20 % at 1×10^{-1} s^{-1}**

El. **= 109 % at 1×10^{-2} s^{-1}**

El. **= 144 % at 1×10^{-3} s^{-1}**

El. **= 249 % at 1×10^{-4} s^{-1}**

Figure 4.67: Magnified views of microstructures of the AZ91 alloy as observed by SEM at gauge lengths after the tensile test to fracture at 423 K. The samples above were processed by HPT using an applied pressure of 3.0 GPa for N = 1 turn at room temperature before tensile test. The yellow arrows refer to the fragmented particles of oxide. The white arrows refer to the direction of tension.

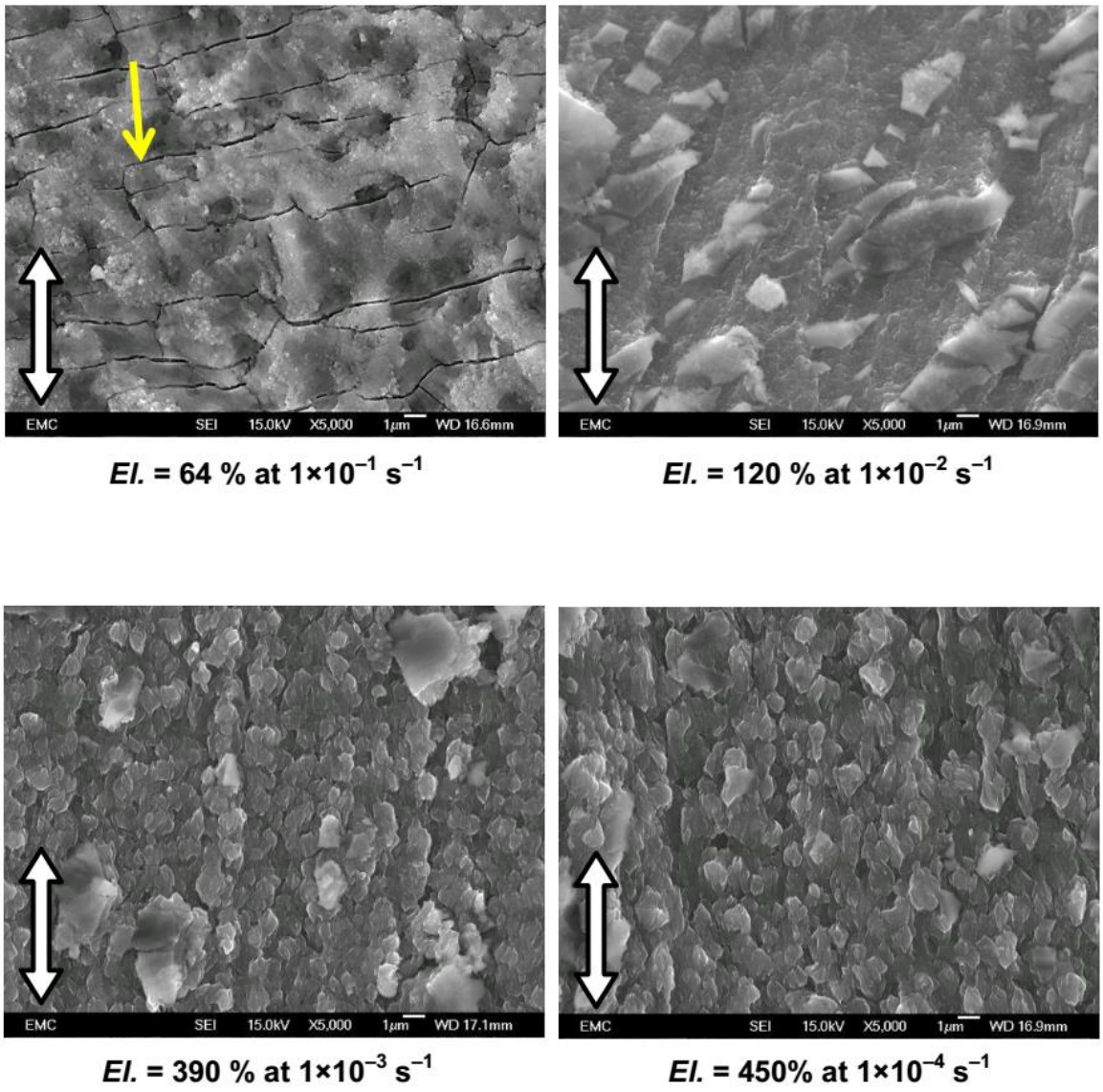

Figure 4.68: Magnified views of microstructures of the AZ91 alloy as observed by SEM at gauge lengths after the tensile test to fracture at 423 K. The samples above were processed by HPT using an applied pressure of 3.0 GPa for N = 3 turns at room temperature before tensile test. The yellow arrows refer to the fragmented particles of oxide. The white arrows refer to the direction of tension.

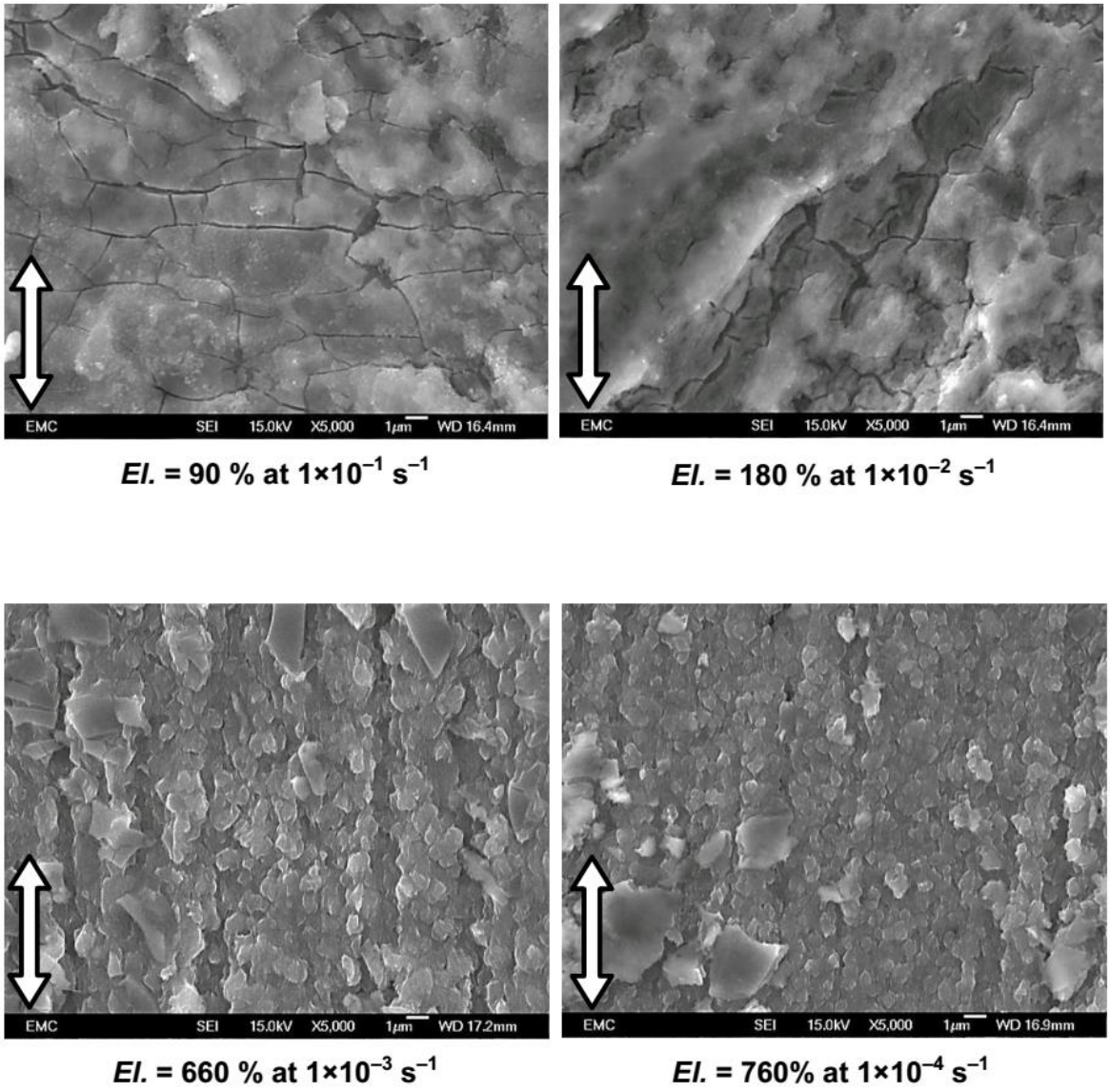

Figure 4.69: Magnified views of microstructures of the AZ91 alloy as observed by SEM at gauge lengths after the tensile test to fracture at 423 K. The samples above were processed by HPT using an applied pressure of 3.0 GPa for N = 10 turn at room temperature before tensile test. The yellow arrows refer to the fragmented particles of oxide. The white arrows refer to the direction of tension.

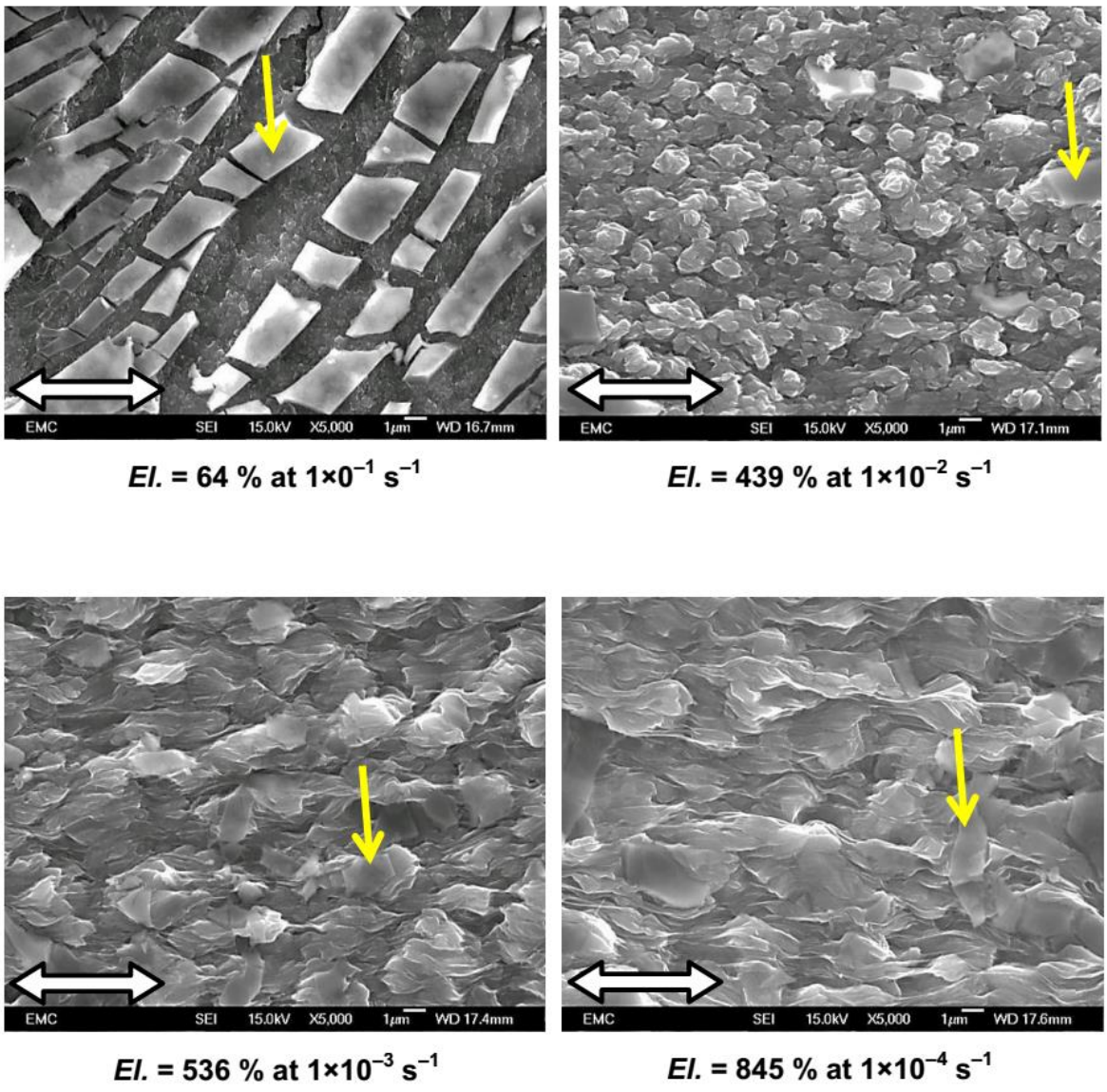

Figure 4.70: Magnified views of microstructures of the AZ91 alloy as observed by SEM at gauge lengths after the tensile test to fracture at 473 K. The samples above were processed by HPT using an applied pressure of 3.0 GPa for N = 1 turn at room temperature before tensile test. The yellow arrows refer to the fragmented particles of oxide. The white arrows refer to the direction of tension.

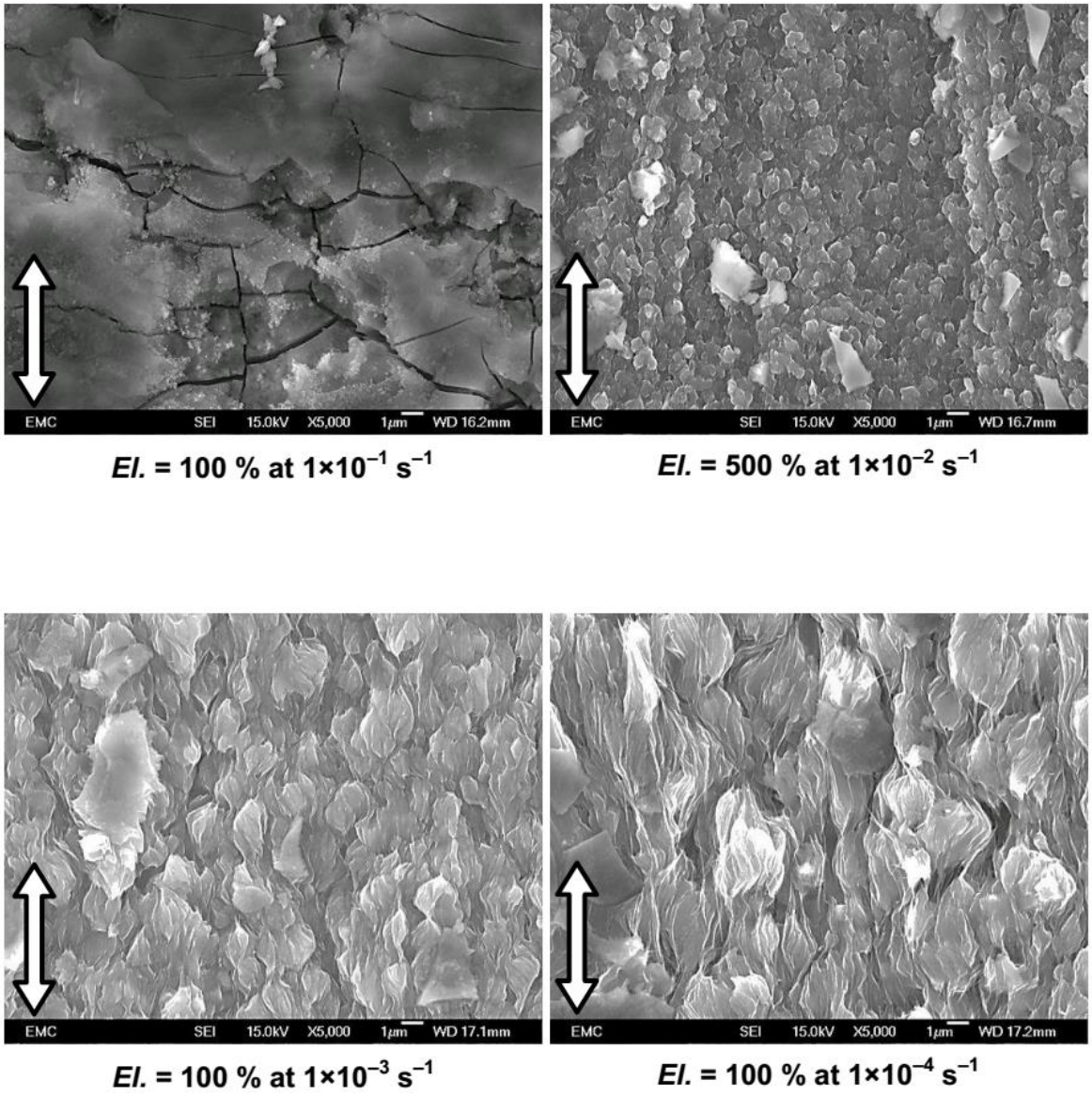

El. **= 100 % at 1×10^{-1} s^{-1}** ***El.*** **= 500 % at 1×10^{-2} s^{-1}**

El. **= 100 % at 1×10^{-3} s^{-1}** ***El.*** **= 100 % at 1×10^{-4} s^{-1}**

Figure 4.71: Magnified views of microstructures of the AZ91 alloy as observed by SEM at gauge lengths after the tensile test to fracture at 473 K. The samples above were processed by HPT using an applied pressure of 3.0 GPa for N = 3 turns at room temperature before tensile test. The white arrows refer to the direction of tension.

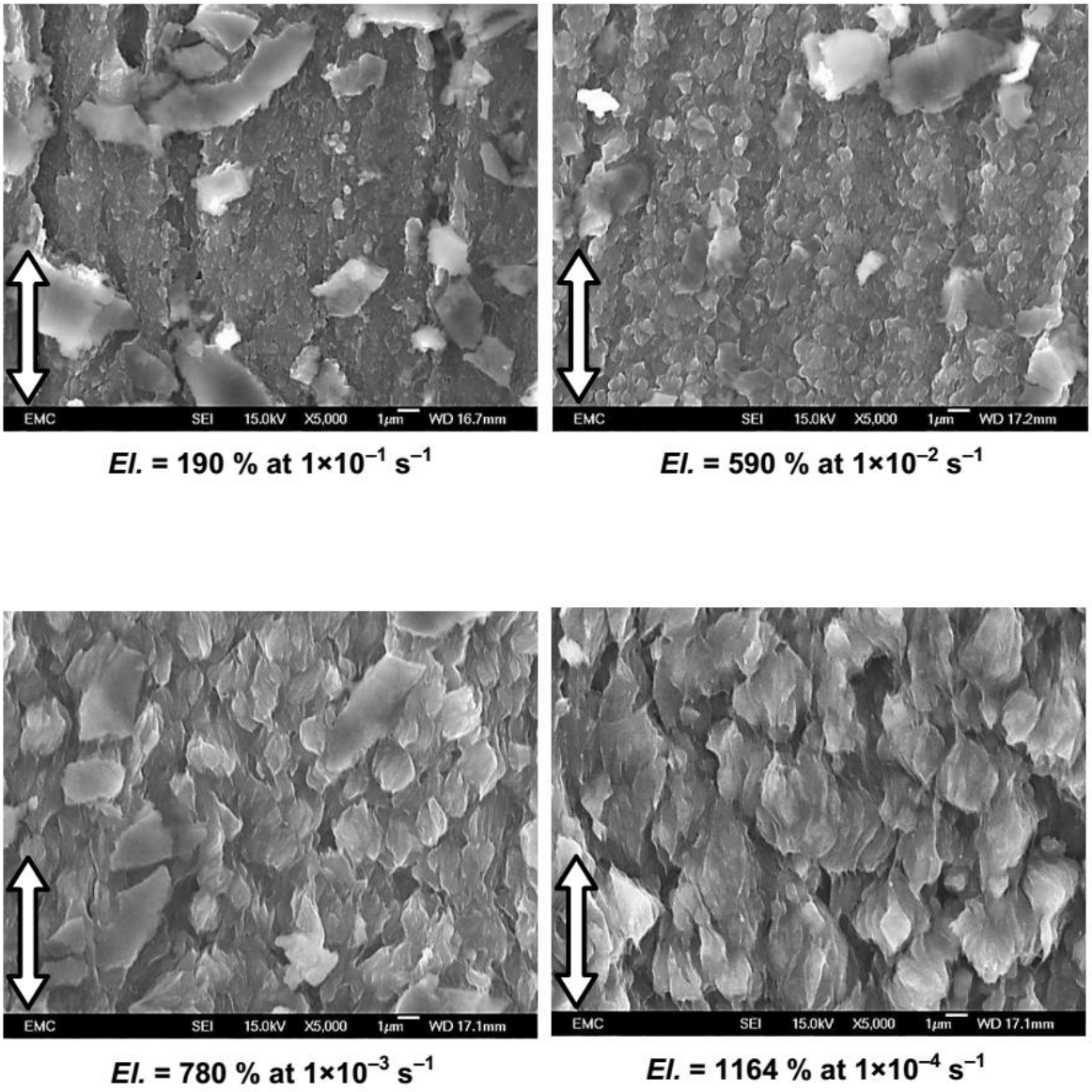

Figure 4.72: Magnified views of microstructures of the AZ91 alloy as observed by SEM at gauge lengths after the tensile test to fracture at 473 K. The samples above were processed by HPT using an applied pressure of 3.0 GPa for *N* = 10 turns at room temperature before tensile test. The white arrows refer to the direction of tension.

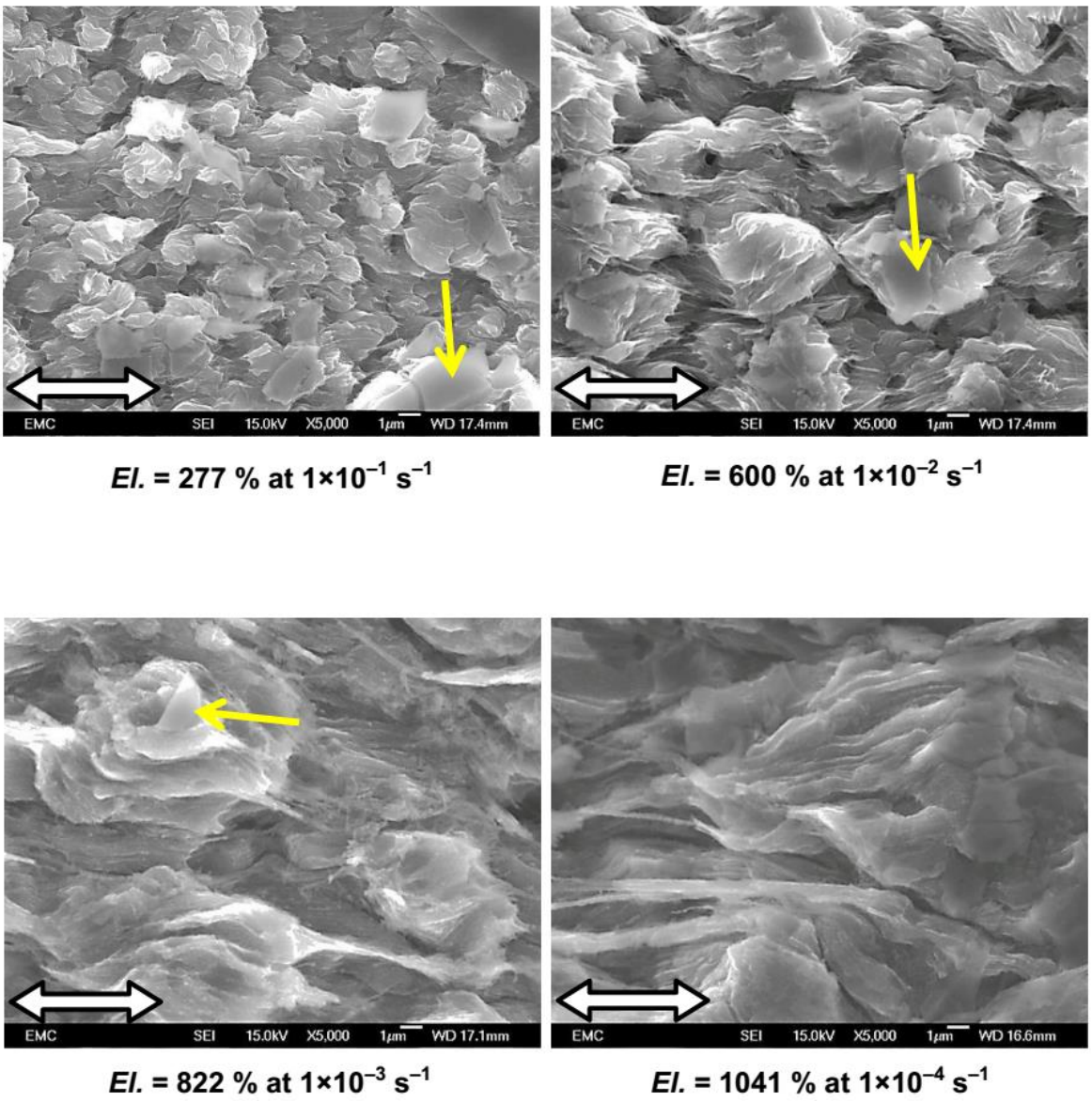

Figure 4.73: Magnified views of microstructures of the AZ91 alloy as observed by SEM at gauge lengths after the tensile test to fracture at 573 K. The samples above were processed by HPT using an applied pressure of 3.0 GPa for N = 1 turn at room temperature before tensile test. The yellow arrows refer to the fragmented particles of oxide. The white arrows refer to the direction of tension.

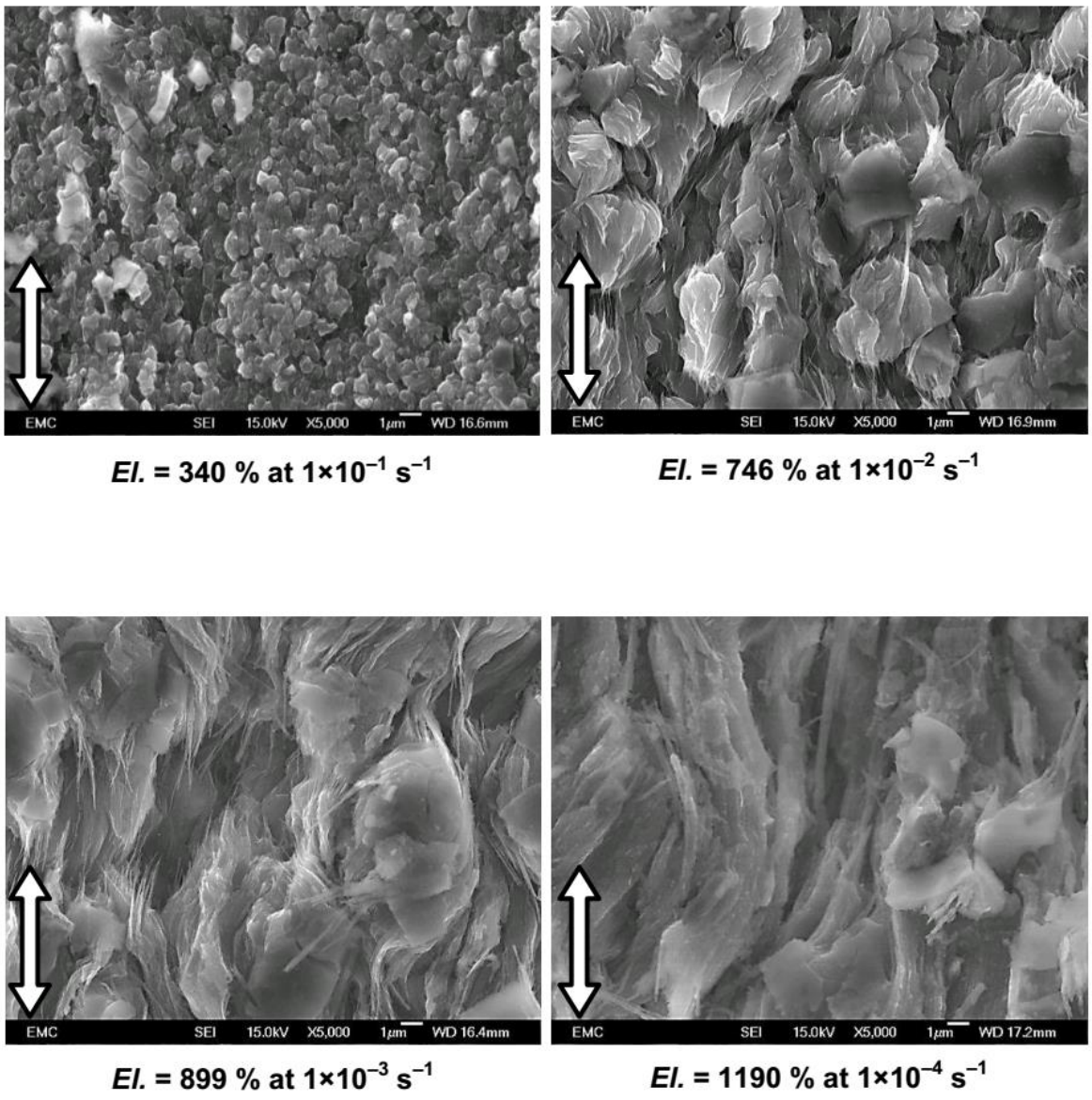

Figure 4.74: Magnified views of microstructures of the AZ91 alloy as observed by SEM at gauge lengths after the tensile test to fracture at 573 K. The samples above were processed by HPT using an applied pressure of 3.0 GPa for N = 3 turns at room temperature before tensile test. The white arrows refer to the direction of tension.

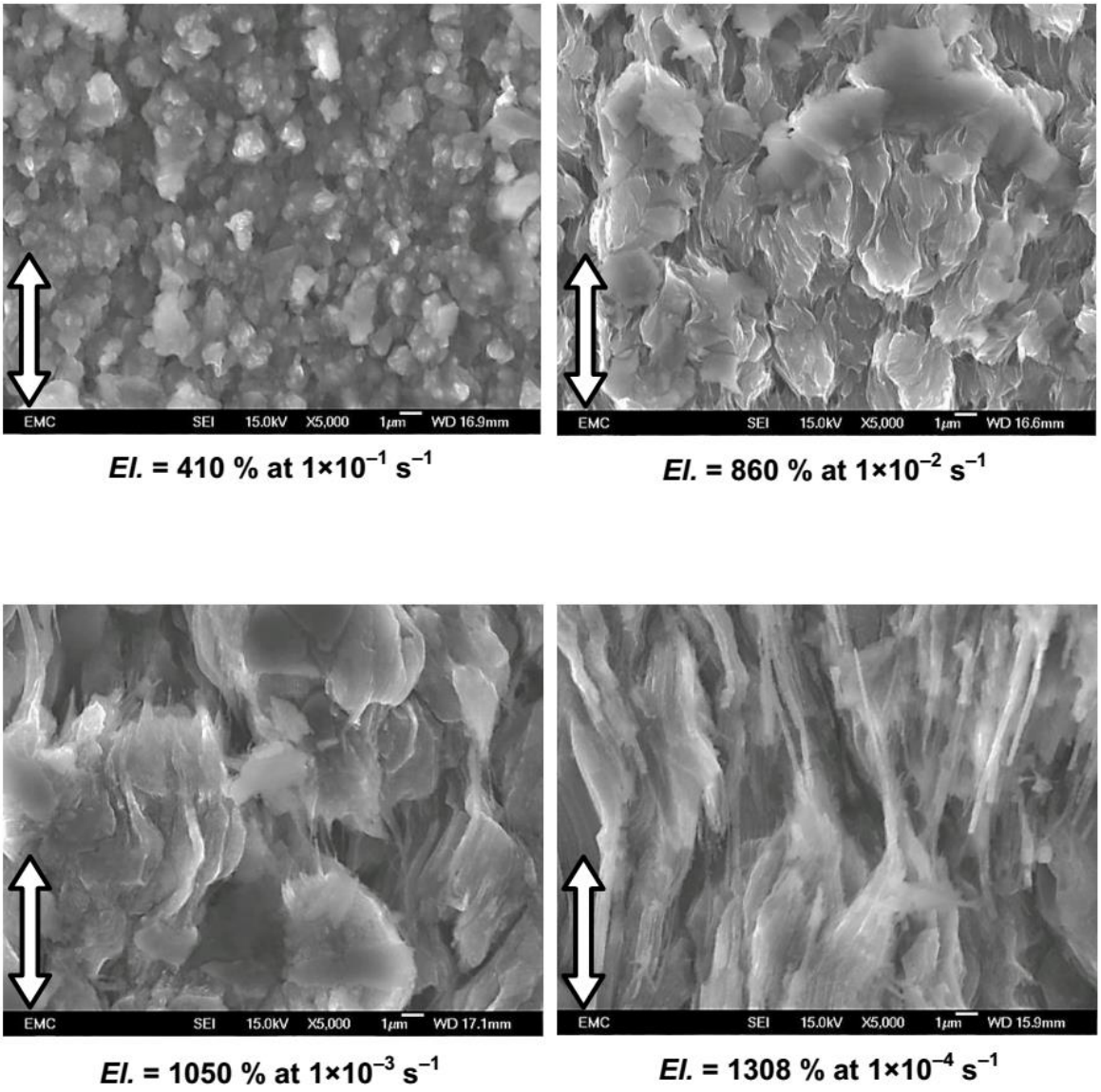

El. **= 410 % at 1×10^{-1} s^{-1}**

El. **= 860 % at 1×10^{-2} s^{-1}**

El. **= 1050 % at 1×10^{-3} s^{-1}**

El. **= 1308 % at 1×10^{-4} s^{-1}**

Figure 4.75: Magnified views of microstructures of the AZ91 alloy as observed by SEM at gauge lengths after the tensile test to fracture at 573 K. The samples above were processed by HPT using an applied pressure of 3.0 GPa for N = 10 turns at room temperature before tensile test. The white arrows refer to the direction of tension.

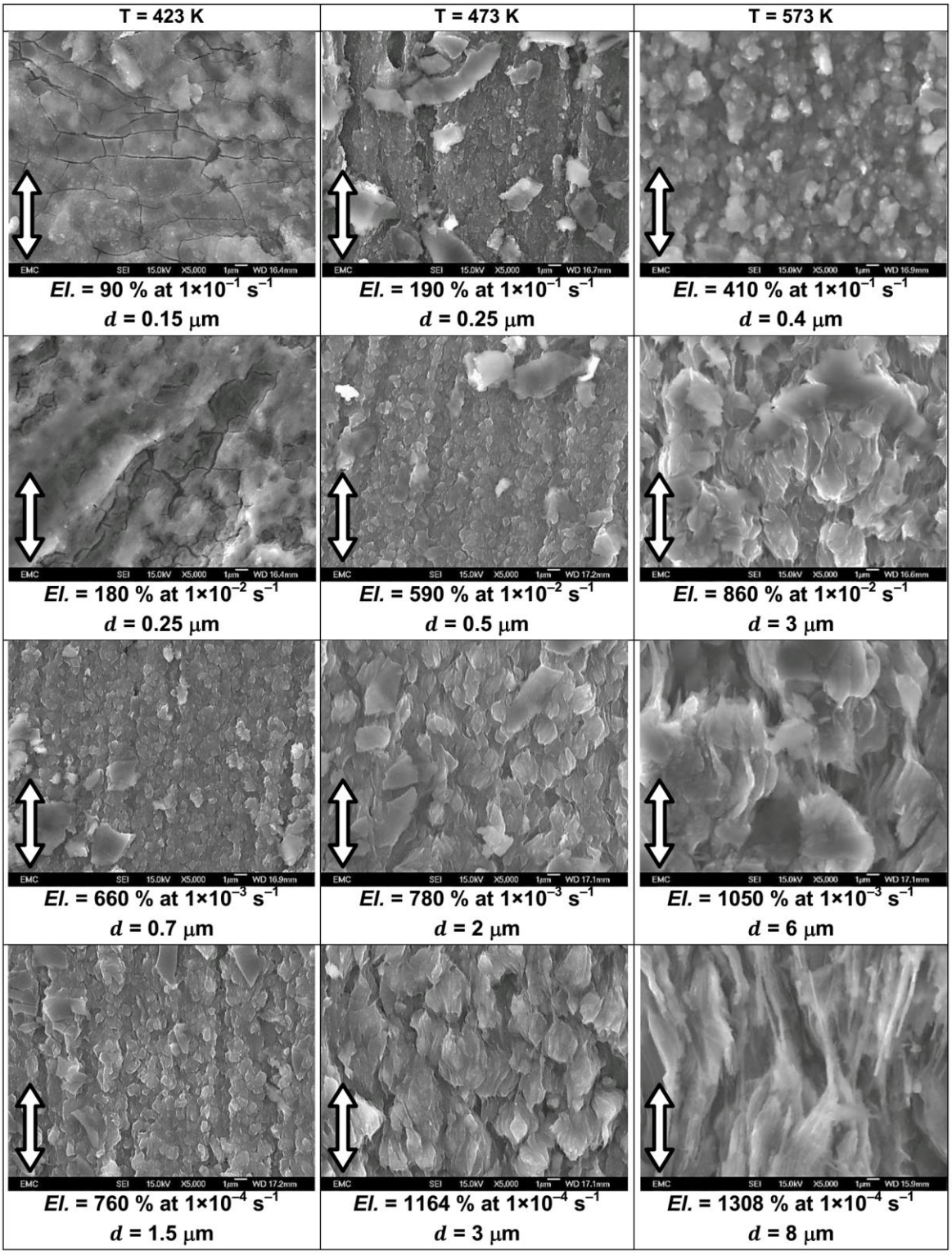

Figure 4.76: Magnified views of microstructures of the AZ91 alloy as observed by SEM at gauge lengths after the tensile test to fracture. The samples above were processed in HPT using an applied pressure of 3.0 GPa for N = 10 turns at room temperature before tensile test. All scales in micrographs are 1 μm. The white arrows refer to the direction of tension.

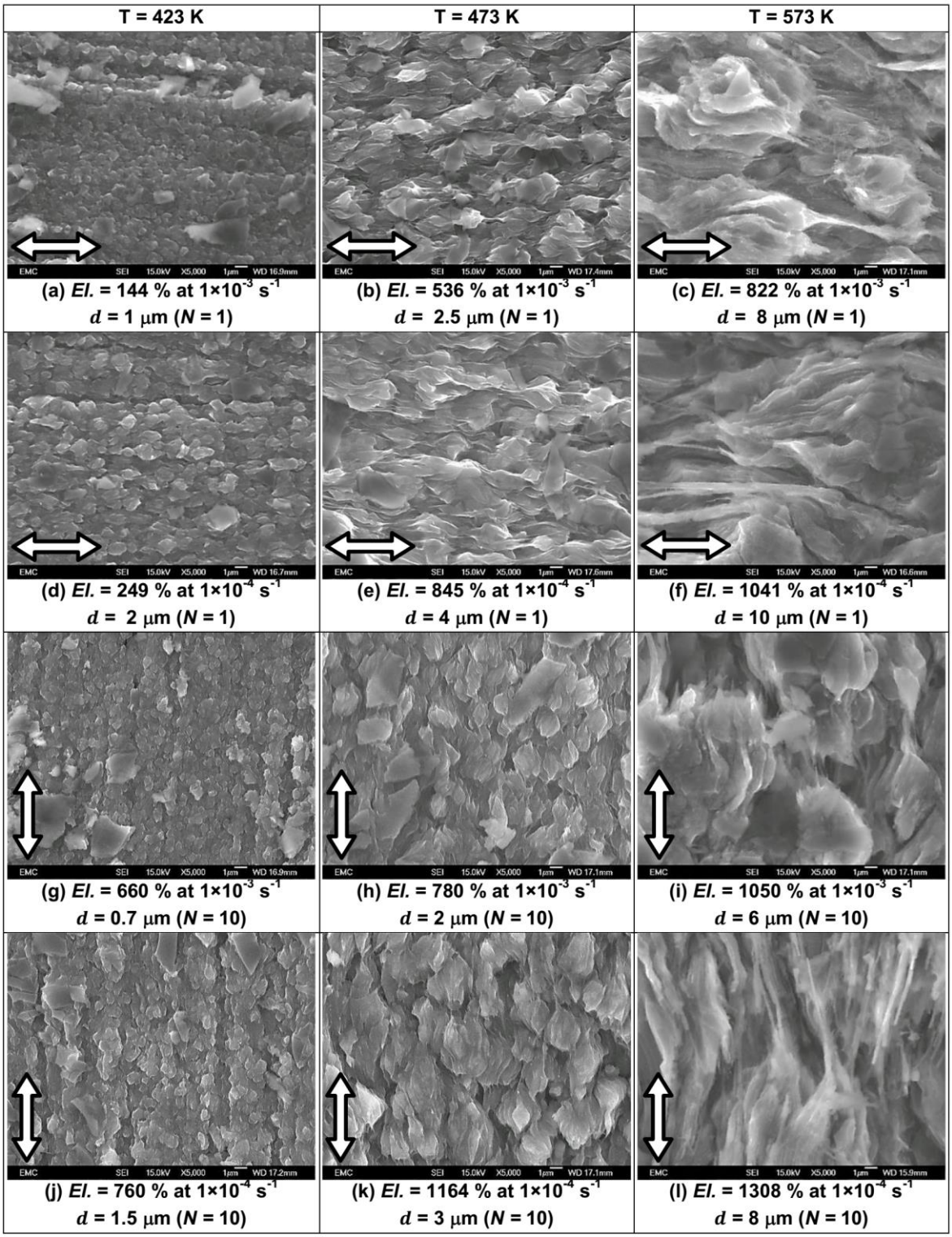

Figure 4.77: Magnified views of microstructures of the AZ91 alloy as observed by SEM at gauge lengths after the tensile test. The samples above were processed in HPT using an applied pressure of 3.0 GPa for N = 1 turn and N = 10 turns at room temperature before tensile test. The white arrows refer to the direction of tension.

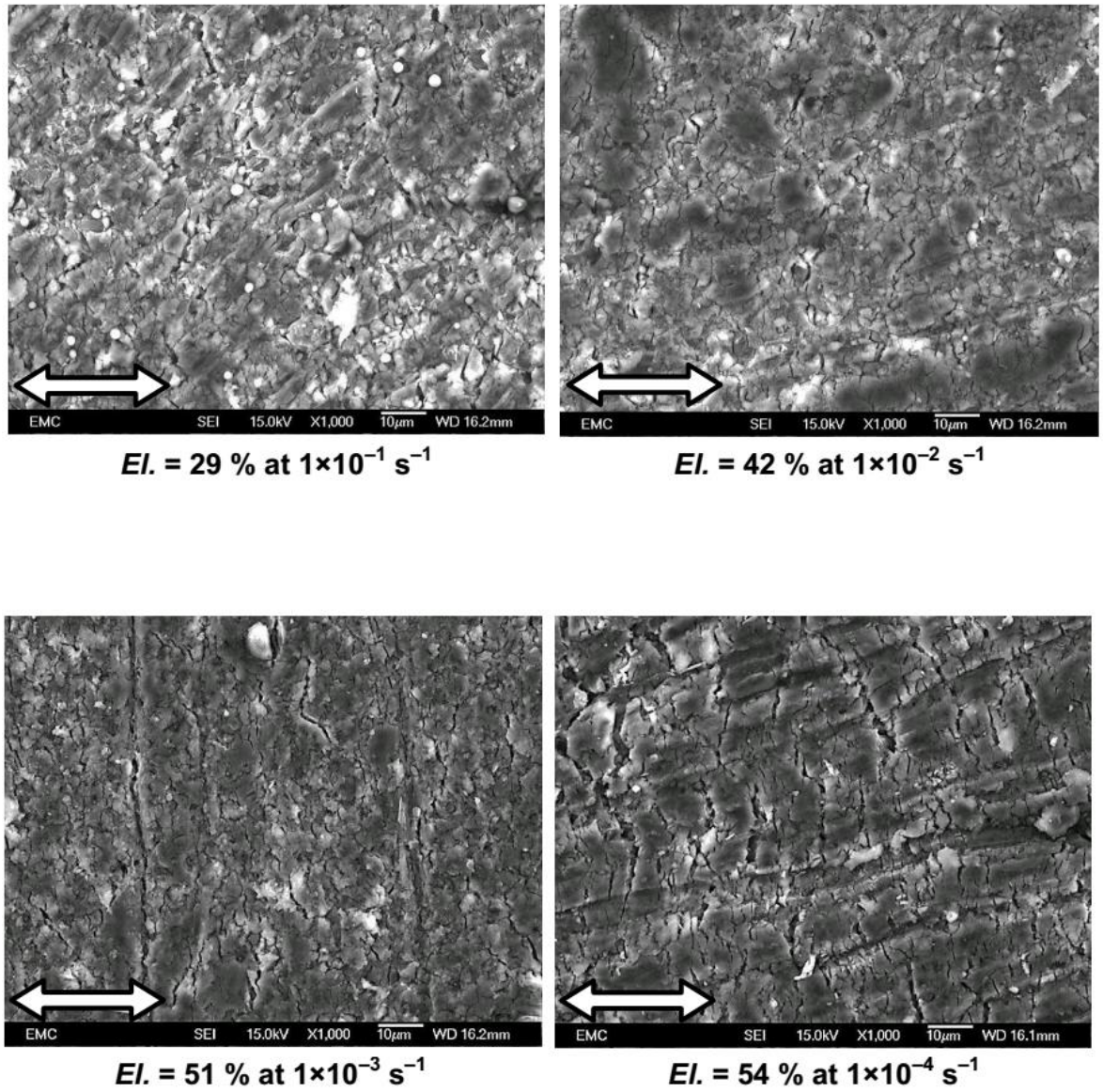

Figure 4.78: Magnified views of microstructures of the as–received AZ91 alloy as observed by SEM at gauge lengths after the tensile test to fracture at 296 K. The white arrows refer to the direction of tension.

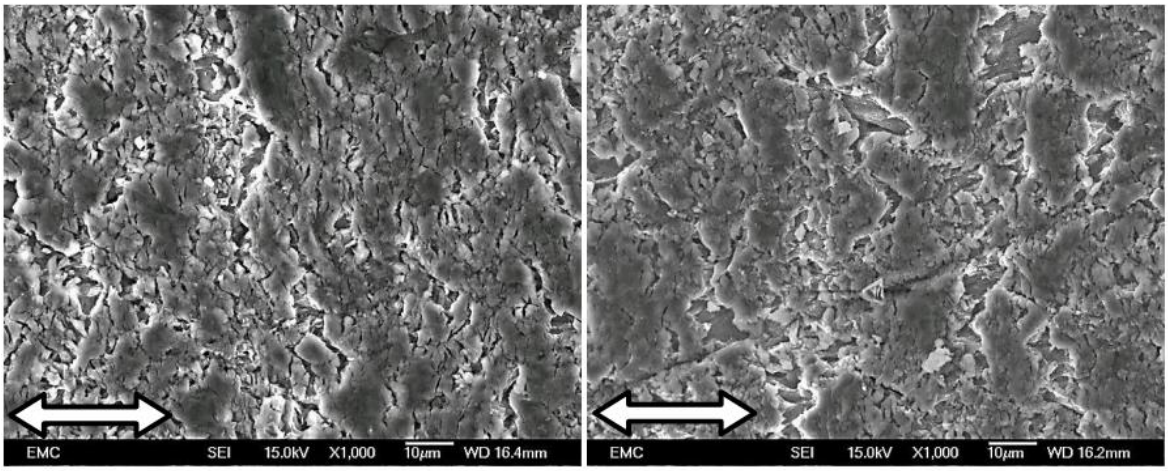

***El.* = 91% at 1×10^{-1} s^{-1}** **$El.$ = 102% at 1×10^{-2} s^{-1}**

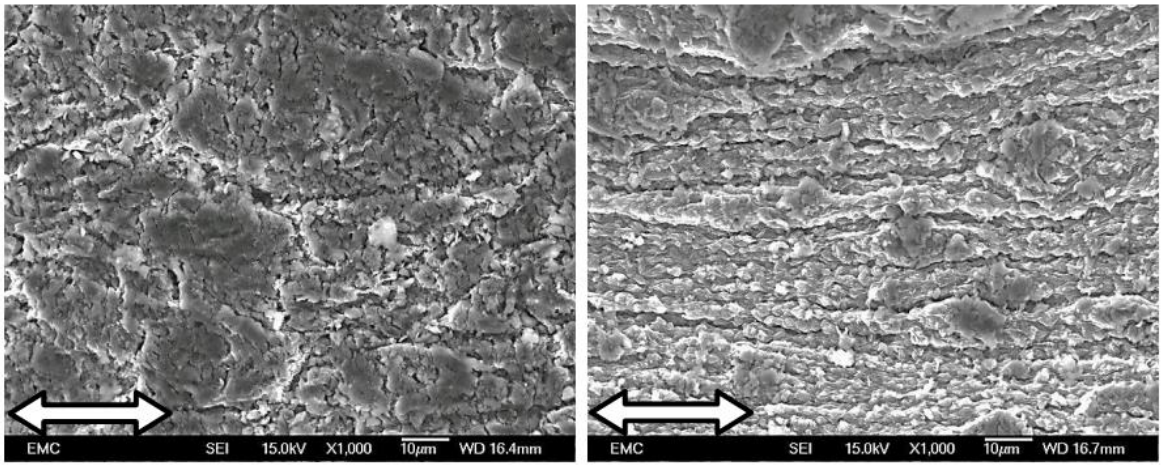

***El.* = 138% at 1×10^{-3} s^{-1}** **$El.$ = 209% at 1×10^{-4} s^{-1}**

Figure 4.79: Magnified views of microstructures of the as–received AZ91 alloy as observed by SEM at gauge lengths after the tensile test to fracture at 473 K. The white arrows refer to the direction of tension.

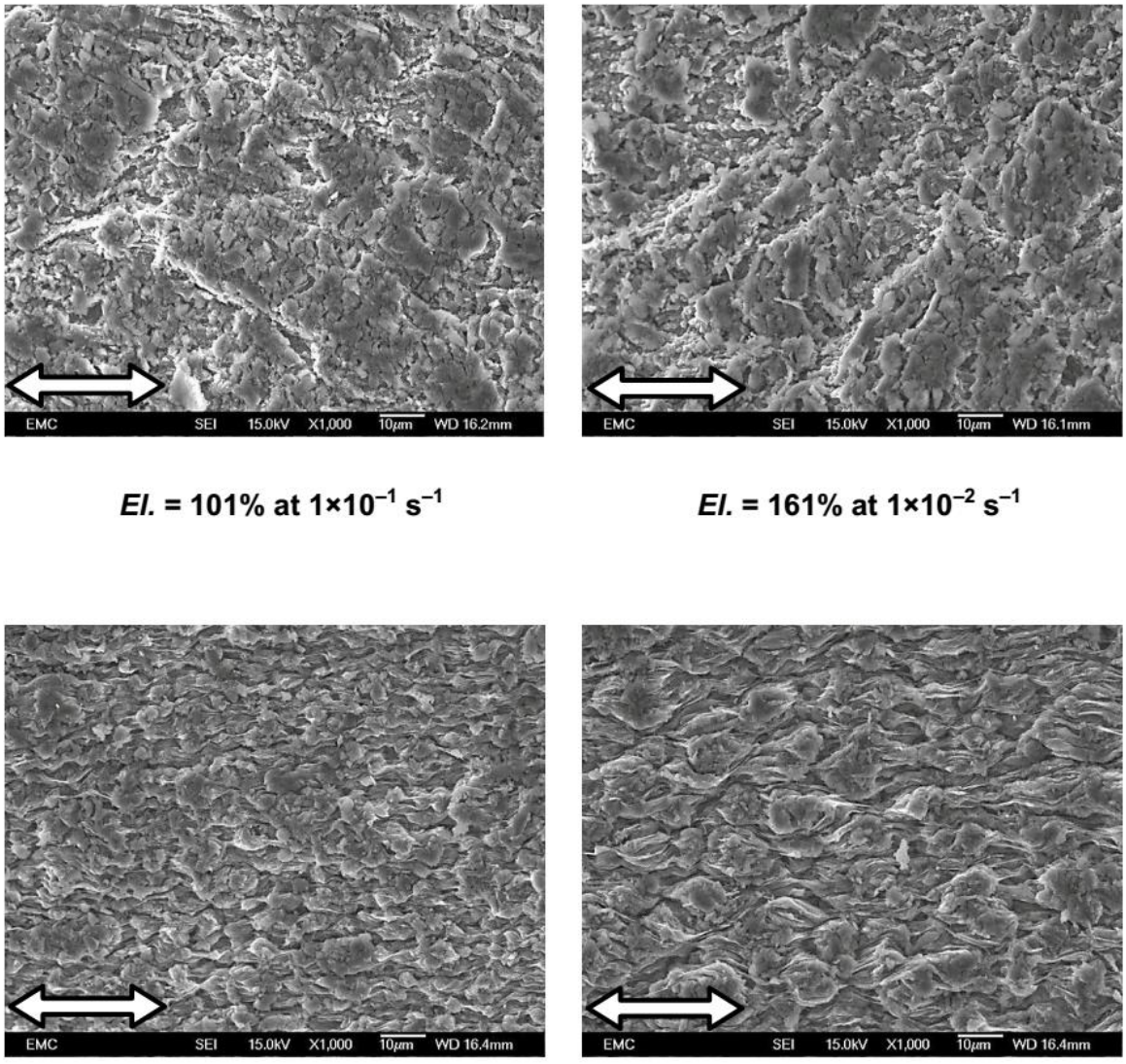

El. **= 101% at 1×10^{-1} s^{-1}** ***El.*** **= 161% at 1×10^{-2} s^{-1}**

El. **= 272% at 1×10^{-3} s^{-1}** ***El.*** **= 332% at 1×10^{-4} s^{-1}**

Figure 4.80: Magnified views of microstructures of the as–received AZ91 alloy as observed by SEM at gauge lengths after the tensile test to fracture at 573 K. The white arrows refer to the direction of tension.

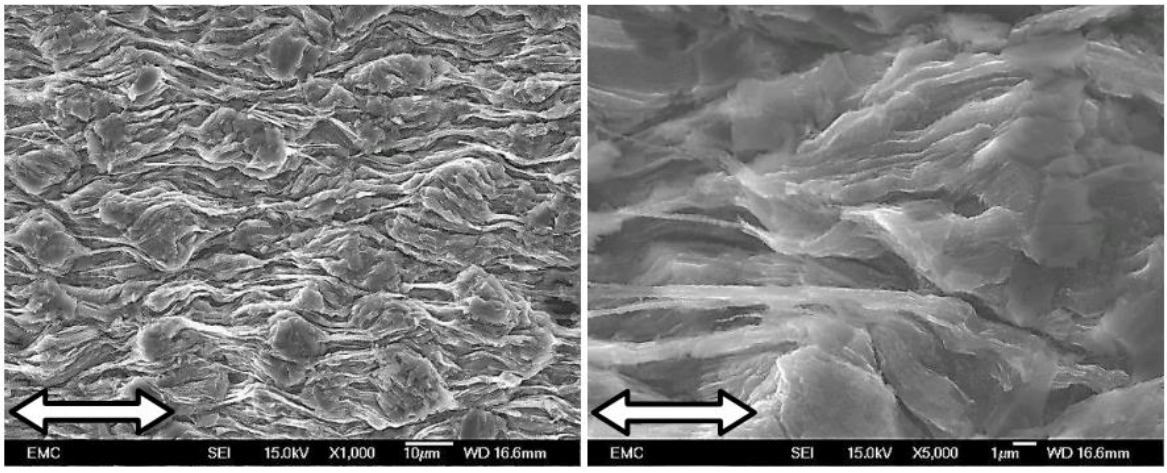

(a) *El.* = 1041% at 1×10^{-4} s^{-1}

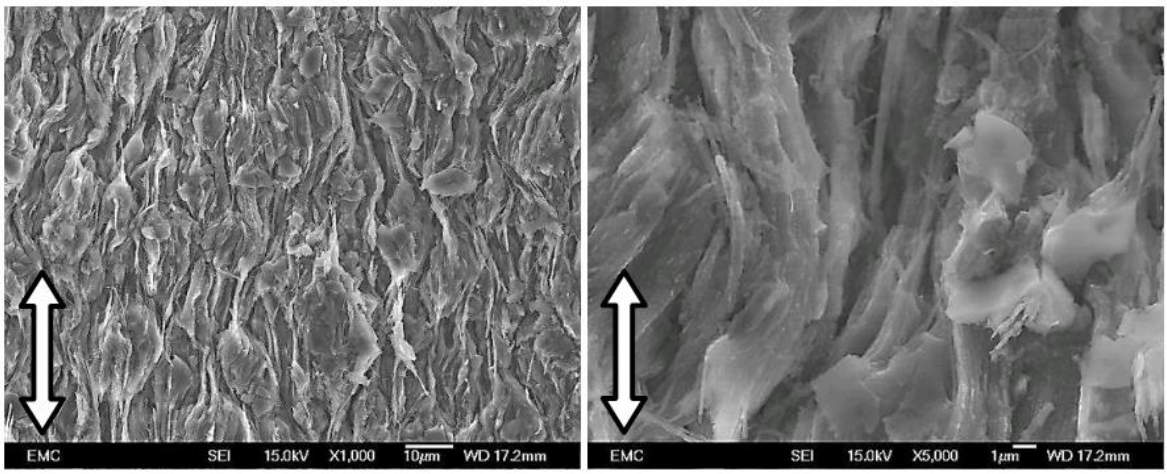

(b) *El.* = 1190% at 1×10^{-4} s^{-1}

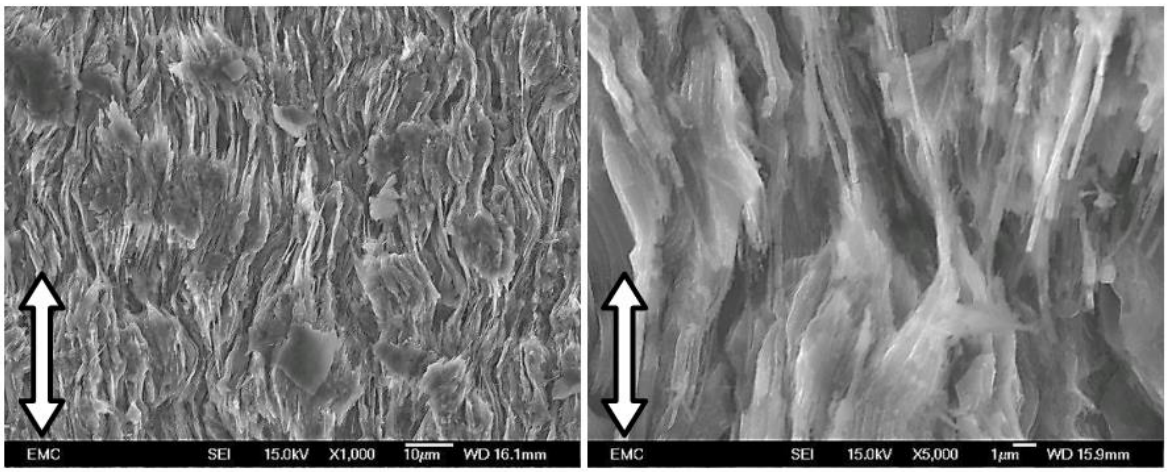

(c) *El.* = 1308% at 1×10^{-4} s^{-1}

Figure 4.81: Microstructures of the AZ91 alloy as observed by SEM at gauge lengths and the occurrence of fibrous morphologies after the tensile test to fracture at 573 K using a strain rate of 1×10^{-4} s^{-1}, for samples processed in HPT using an applied pressure of 3.0 GPa at room temperature for: (a) N = 1 turn, (b) N = 3 turns and (c) N = 10 turns. The white arrows refer to the direction of tension.

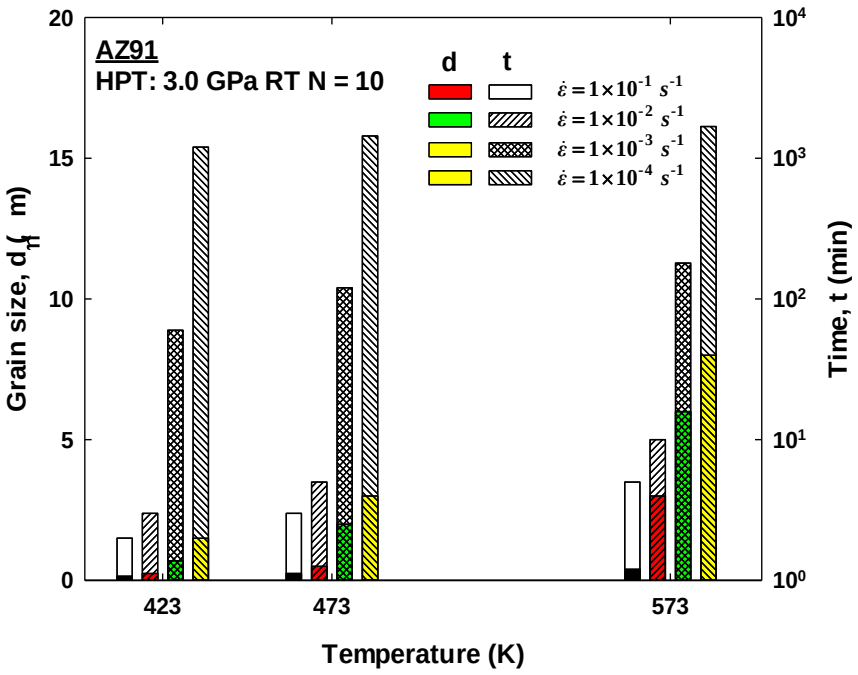

Figure 4.82: The variation in grain size and testing time with testing temperature and strain rate in tensile test for the AZ91 alloy processed in HPT *N* = 10 turns at room temperature using an applied pressure of 3.0 GPa.

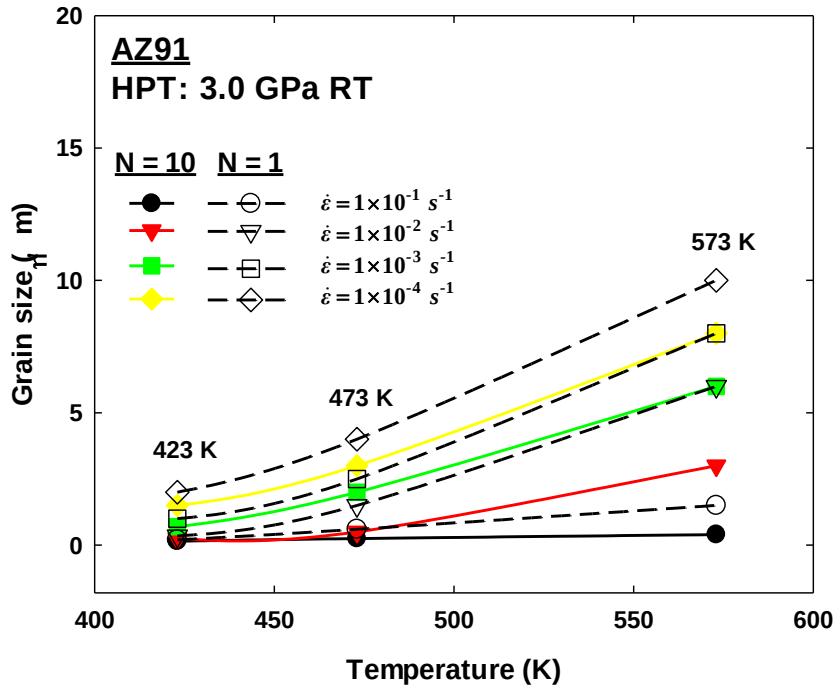

Figure 4.83: The variation in the grain size after the tensile test at different testing temperatures (423 K, 473 K, 573 K) and different strain rates for the AZ91 alloy processed in HPT for *N* = 1 and 10 turns at room temperature using an applied pressure of 3.0 GPa. The dashed and solid lines represent samples processed for *N* = 1 and 10 turns, respectively.

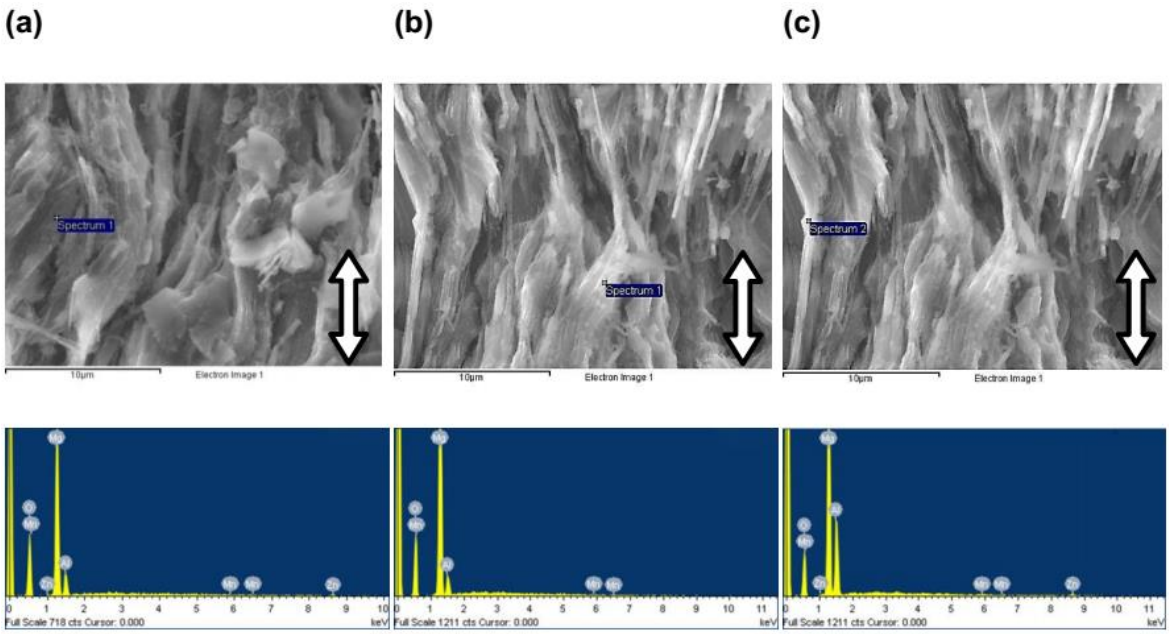

Element	wt.%
O	41.73
Mg	47.73
Al	9.97
Mn	0.40
Zn	0.17

Element	wt.%
O	31.14
Mg	60.80
Al	7.87
Mn	0.19
Zn	–

Element	wt.%
O	24.77
Mg	48.28
Al	26.13
Mn	0.16
Zn	0.65

Figure 4.84: EDS analyses with the weight fractions of the elements at: (a) grain, (b) grain boundary and (c) filament, for the sample processed in HPT for N = 10 turns at room temperature using an applied pressure of 3.0 GPa and tested in tension at testing temperature of 573 K using a strain rate of 1×10^{-4} s^{-1}. The white arrows refer to the direction of tension.

Chapter Five: Discussion

5. DISCUSSION

5.1 HPT processing of AZ91 magnesium alloy

Magnesium alloys are effective alternatives to replace the relatively denser materials, such as steel and aluminium alloys, with the objective to meet the requirements for saving fuel, and light weight / high strength parts [20]. The mechanisms of deformation in magnesium alloys at room temperature are basal slip and twinning, which result in a limitation in their workability at room temperature [13]. The limited ductility and workability of these alloys can be improved at higher temperatures by the activation of additional slip systems [20]. Thermo–mechanical processing is used to improve the workability of these alloys, although such processing is associated with grain growth and a greater consumption of energy [19][194].

The microstructure of the magnesium alloy is being optimised through variation in the processing conditions in order to overcome the difficulties of the low workability at low temperature and the grain growth at elevated temperatures [19]. Several processing routes have been introduced for microstructure refinement in magnesium alloys, and these routes include the dynamic recrystallization under high–temperatures in ECAP processing [10], hot rolling [194], HPT processing [18][155], ECAP processing at relatively low temperatures assisted by a back–pressure [15], or through the use of a higher channel angle of pressing die in ECAP processing [195]. The dynamic recrystallization is defined as a recrystallization process that occurs during hot working and involves the elimination of dislocations and the formation of new grains by means of the grain–boundary migration at temperatures above 0.6 T_m [196].

The presence of dynamic recrystallization results in the softening of the material under deformation, where ductility increases and microhardness decreases [197][198]. Therefore, the microhardness and then strengthening of the magnesium alloys that were processed at elevated temperatures, will be lower than those for alloys processed at low temperatures [199]. There is limited number of studies on the processing of magnesium alloys in HPT at room temperature, which are Mg–9wt.%Al alloy [18], AZ61 alloy [99] and AZ31 alloy [159]. These

studies have been investigated briefly the microhardness for samples processed at both 296 K and 423 K in HPT and the tensile behaviour for the samples processed at 423 K in HPT only. TEM investigation has been conducted for samples processed at both 296 K and 423 K in HPT and showed a significant grain refinement after processing up to high number of turns.

The current research has focused on the HPT processing at 296 K, 423 K and 473 K for the AZ91 alloy. The microstructure has investigated using the SEM, TEM and XRD for the alloy processed at 296 K. The distributions of microhardness along the horizontal and vertical cross–sections have broadly investigated for samples processed at the processing temperatures of at 296 K, 423 K and 473 K. The superplastic behaviour has extensively studied at a wide range of conditions for the alloy processed at 296 K. Therefore, this research can provide comprehensive information about the microstructure and mechanical behaviour of the AZ91 alloy processed in HPT at room temperature and elevated temperatures.

In the present research, a successful HPT processing of the AZ91 magnesium alloy at room temperature and an ultrafine microstructure has achieved, which was not applicable for the same alloy using ECAP processing at a temperature lower than 200 °C, due to the development of cracking with increasing number of passes [13]. The TEM and XRD revealed the occurrence of extensive grain refinement in the AZ91 magnesium alloy within the nanometre range as a result of imposing a very high plastic strain by HPT at 296 K after a relatively low number of turns. The processed alloy has been refined from 30 μm in the as–received alloy to about 1000 nm and 50 nm after processing for N = 1/2 turn and 1 turn, respectively as revealed by TEM. The measurements of the crystallite size of the processed alloy at 296 K exhibited a reduction in crystallite size (or subgrain sizes) from 60 nm to 35 nm with increasing the number of turns from N = 1/2 turn to N = 10 turns. In general, both TEM and XRD were inconsistent in regards of the refinement in the processed alloy at 296 K in HPT, but they confirm the significance of the processing temperature in HPT processing. However, the low values of the crystallite size (or subgrain sizes) that obtained by XRD was lower than the grain size measured by TEM.

This difference in the grain size measurements between the XRD and TEM analysis is expected in SPD–processed materials [170]. The grains in a heavily deformed material contain subgrains and / or dislocation cells. These structures are usually separated by low–angle grain boundaries or dislocation walls [25]. The coherent diffraction of the X–ray from these walls or subgrains corresponds to the coherent domains or the crystallites, and their sizes are therefore called the crystallite size rather than the grain size that can be obtained by TEM [200]. It is expected that the grain refinement for the current alloy continued gradually during HPT processing as indicated indirectly by microhardness measurements that have been carried out in previously reported work for the same alloy [201] and for AZ31 magnesium alloy also processed by other workers at room temperature [159].

The limitation in the processing of magnesium alloys with processing temperature arises from the availability of the operative slip systems in these alloys. The processing at higher temperature results in activation of the prismatic and pyramidal slip systems [38][202]. These additional slip systems enhance the plasticity under deformation and then permits the processing of magnesium alloys for a higher number of passes / turns [15][99]. Thus, the processing of these alloys at room temperature is difficult due to the limitation in workability due to the basal slip and twinning [36][203]. However, the current study showed the possibility of the successful HPT processing of AZ91 magnesium alloy at room temperature, although there were limited numbers of the deformation modes. The HPT processing at room temperature of this alloy can be attributed to the presence of hydrostatic pressure and the geometry of processing zone [15][18].

The hydrostatic pressure arises from the stress state by the interaction of the material under processing and the HPT anvils [25][204]. The development of the hydrostatic pressure during the HPT processing of AZ91 alloy influences the crack propagation by closing up, or confining of the alloy constituents during the HPT processing, thus preventing the propagation of fracture in such a relatively brittle alloy [25]. The brittleness of the magnesium alloy originates from the presence of HCP magnesium as the main constituent in the AZ91 alloy, and ductility was enhanced by the presence of hydrostatic compressive pressure during HPT processing. The enhanced deformability by the effect of the hydrostatic pressure

was noticed for Mg–9wt.%Al alloy [18], which has been processed by HPT at room temperature.

The geometry of the processing zone has a significant effect on the deformation of alloys of limited slip systems such as magnesium alloys. The configuration of the HPT cavity constrains the alloy within a volume as shown in Figure 3.2 [162], where the material is constrained by an outflow outside the processing zone and between the rims of the anvils [205]. The activation of twinning is induced by the shear state in the constrained deformation, which is caused by the reduction in the thickness–to–diameter ratio during processing. The latter results in an additional shear friction and hence induces the twinning formation [205] as shown in Figure 4.33, for the vertical cross sections of the processed disks. The formation of twinning during compression at room temperature was also found in AZ31 and AM30 magnesium alloys [206][207].

During the deformation of the polycrystalline material, each grain responses to the deformation in a relatively different way from the other grains; depending on the orientation of each grain in regards to the applied shear stress. Therefore, a constraint arises due to the presence of neighbouring grains, and the difference in the strain between the interior of the grain and the grain boundaries [25]. As the magnesium alloys have only two independent slip systems (basal slip systems) at room temperature, which are less than the five required systems for the homogeneous deformation. Therefore, the brittle behaviour and fracture are likely to take place under deformation at room temperature [37]. However, the lack of five independent slip systems results in a strain incompatibility between the grains of different orientation and across the grain boundaries. Therefore, additional stress is required to maintain a strain compatibility, leading to the activation of additional deformation modes under HPT processing [41].

It is believed that the unidirectional nature of straining during HPT processing may contribute to the re–orientation of the microstructure, including the α–Mg matrix and β–phase towards the easy slip [61]. As the critical resolved shear stress for twinning (3 MPa) is much lower than that required for the prismatic and pyramidal slip systems (40 MPa), then the twinning becomes the preferred mode for accompanying the basal slip in the magnesium alloy at room temperature

[36][208]. It was found that the increase of imposed strain through increasing the number of turns in the HPT processing leads to the re–orientation of the grains for twinning mode [209].

5.2 Microstructure over the *horizontal* cross–sections

It was shown by Figure 4.1 that the as–received microstructure of AZ91 magnesium alloy consists of α–Mg matrix, β–phase and Al_8Mn_5 particles. It is obvious that the microstructure has an average grain size of 30 μm with distinct grain boundaries. The β–phase is decorated along the grain boundaries as lamellar and agglomerate forms. The lamellar or discontinuous precipitates of β–phase resulted from the solution treatment and the aging of the as–cast alloy [210]; whereas the agglomerate precipitates of β–phase resulted from the non–uniform continuous precipitation [211]. It was found that the precipitation of β–phase at the grain boundaries results in an increase in the microhardness of alloy [212].

There was no significant alignment or configuration of the microstructures prior to the HPT processing along the horizontal cross–sections of the as–received sample, as shown in Figure 4.1. Following the HPT processing, considerable changes were found in the microstructures, as shown in Figures (4.4 – 4.29) for the horizontal cross–sections of the processed disks. In the stage of compression (N = 0), the β–phase fragmented into several segments due to the applied pressure, which resulted in breaking the lamellar and agglomerate β–phase into small pieces [213]. During the early stage of HPT processing, the fragmentation of this phase continued and it experienced more breaking–up due to an increase in the imposed strain by the HPT processing, up to N = 10 turns. The fragmented particles of the β–phase reached the nanometre sizes with the higher imposed strains, indicating a severe level of deformation of the alloy under processing [214].

It has found that the fragmentation of the β–phase was more intense at the edge regions than at the centre regions of the processed disks. The breaking–up of the β–phase reached almost the same level of fragmentation at the centre and edge regions at a higher number of turns, due to the high value of strain that was

imposed at the centre regions, which was comparable to the imposed strain at the edge regions at a high number of turns [145].

The deformation incompatibility between α–Mg matrix of HCP structure and β–phase of BCC structure may lead to the fragmentation of the β–phase under high strain in the HPT processing. The hard particles of the β–phase can obstruct the flow of the alloy under deformation [215]. A local strain gradient can be generated due to the plastic deformation of a matrix containing hard particles; therefore, these particles can result in heterogeneous structures and induce high local densities of dislocations in the areas around the matrix [149]. Since the β–phase is harder than the α–Mg matrix, which is relatively softer, then, the massive and agglomerate β–phase tend to fracture during HPT processing [25][216]. During the deformation, the fragmented particles of the β–phase separated from the original or pre–existing grain boundaries. The particle–matrix separation during the plastic deformation resulted from the stress concentration at the particles that are located at the grain boundaries, through the interaction of moving dislocations and these particles [217]. Increasing the scattering or spreading of the β–phase particles increased with the imposed strain, which emphasized the interaction between the β–phase particles and piled–up dislocations at the grain boundaries [25].

The alignment of the β–phase particles in the direction of straining was noticed to arise owing to mechanical fibering. The latter results in the alignment of these particles in the direction of mechanical straining during the HPT processing [218]. This alignment is common in the monotonic SPD processing, such as in HPT, ECAP (without rotation of billet) and ARB [219]. The alignment of the nano–particles of β–phase occurred at the edge regions and then moved to the centre regions with increasing the number of turns. Further straining resulted in the alignment of bands of the nano–particles, and these bands were elongated with regard to the direction of torsion, indicating a high level of imposed deformation during HPT processing [145].

It has found that the grain boundaries were obvious after the compression stage; however, they became ill–defined gradually with increasing the number of turns during the HPT processing. Some areas in the processed microstructures showed

the accumulation and alignment of the β–phase particles along specific directions over the horizontal cross–sections of the processed disks. It is assumed that this accumulation and alignment occurred due to flow localization or shear banding in these areas. The shear bands occur due to the limited active slip systems able to accommodate the high imposed strain in HPT processing of the AZ91 magnesium alloy [220]. The presence of the second phase particles in such areas provide sources for steep strain gradients resulting in occurrence of this flow localization [61][56]

The EDS analyses showed no significant changes in the chemical compositions of the α–Mg matrix and β–phase for the as–received alloy and processed one for *N* = 5 turns. Therefore, no dissolution was identified for Al in the matrix, which precludes the occurrence of the supersaturated alloy by the HPT processing. It has shown that the β–phase can precipitate along the grain boundaries during the ECAP processing [161] and compression [221] at elevated temperatures. In the current work, the HPT processing of AZ91 alloy was conducted at room temperature, which is much lower than that required for the precipitation of β–phase. Thus, the latter process was excluded during the HPT processing of this alloy at room temperature.

In addition, the size and shape of β–phase particles in the present research are significantly different form their counterparts that precipitate at elevated temperatures during the ECAP processing [161] and compression [221]. The current study showed that the nano–sized particles of β–phase with irregular shapes, has accumulated and aligned along the shear bands. The accumulated nano–sized particles were significantly finer than the micro–sized β–phase precipitates of rod–like and agglomerate shapes. Accordingly, such differences in the sizes and shapes of the β–phase also preclude the β–phase precipitation during the HPT processing of AZ91 in the current work.

It seems that the grain refinement in the alloy processed at 296 K has occurred by the extensive grain fragmentation or subdivision as shown by TEM investigation in Figure 4.31. The severe plastic deformation of the AZ91 alloy with low–stacking fault energy has resulted in bulk nanostructured alloy with nanometre grain sizes. The fragmentation of the old or original grains in the current alloy has been

achieved by the presence of twinning as shown in Figures (4.32, 4.33). The reduction in the stacking fault energy of the material leads to smaller grain sizes under SPD processing [50][222]. For instance, the effect of stacking fault energies of the pure Mg [20], AZ31 alloy, AZ61 alloy and AZ91 alloy [47] are 125, 27, 16 and 6 mJm^{-2}, respectively, and their average grain sizes after HPT at room temperature were 600 nm (*N* = 8 turns) [223], 200 nm (*N* = 15 turns) [159], 110 nm (*N* = 5 turns) [99] and 35 nm (*N* = 10 turns, the crystallite size in the current research), respectively.

The relatively high content of aluminium in the AZ91 magnesium alloy leads to a significant reduction in the stacking fault energy through the solute–dislocation interaction [224]. The solute atoms (aluminium) segregate preferentially to the stacking fault and hence the separation between the partial dislocations increases and the mobility of dislocations becomes harder [25]. In this case, the pile up of accumulated dislocations results in formation of planar structures at low strains and the occurrence of ultrafine microstructure by the formation of twinning and their fragmentation and formation of shear bands at higher strains [52]. The AZ91 microstructure developed from bimodal microstructure after processing at *N* = 1/2 turn to a fairly homogenous ultrafine one after *N* = 1 turn as observed by TEM as shown in Figure 4.31. As the alloy has been processed at room temperature, the effect of the dynamic recovery was slower and microstructural homogeneity observed after only *N* = 1 turn. It is anticipated that the homogeneity developed gradually with further straining at room temperature as mentioned by several investigators [17][99][159][225]. Therefore, an exceptional grain refinement has been found in the AZ91 alloy over the other aforementioned alloys after HPT processing at room temperature.

The occurrence of twinning in the alloy processed at room temperature during HPT processing as shown in Figures (4.32, 4.33) indicates the importance of twinning as a deformation mode in the AZ91 alloy with HCP structure and on the resultant microstructure after HPT processing at room temperature. XRD analysis has revealed the activation and domination of the compression twinning $(10\bar{1}1)$ and $(10\bar{1}3)$ and tension twinning $(10\bar{1}2)$ in the processed samples at all number of turns, whereas the prismatic plane $(10\bar{1}0)$ is the dominate one in the as–received alloy. Moreover, the basal plane (0002) was more pronounced in the processed

alloy than in the as–received alloy. These observations indicate the orientation of the processed microstructure towards twinning and basal deformation modes under HPT conditions at room temperature [226]. As discussed before, the existence of torsional straining, the geometry of anvils and the strain path during the HPT process produce a significant shearing on the alloy and thus the activation of twinning deformation at room temperature [25][61][205].

Electron back–scattered diffraction (EBSD) characterization is an effective technique that can provide crystallographic and microstructural information (e.g. grain size and orientation information) about various materials. This technique is a surface one, i.e., the information via diffraction patterns comes from the surface layer with depths of a few tens of nanometres. Therefore, low deformation and low contamination surfaces are required to gain good quality EBSD diffraction patterns [227]. EBSD was found to not be suitable for analysis of the AZ91 magnesium alloy processed in HPT. This is attributed to the rapid oxidation of the surfaces of the etched samples, where magnesium has a high reactivity with oxygen [9]. The heavily deformed surfaces (especially as deformation extended through the whole material) could not be removed by any available metallographic procedure; particularly since ion milling facilities was not available to this project. Many attempts were conducted during the course of the PhD but the resultant diffraction patterns were poorly indexed due to the surface oxide and severely distorted material.

The alloy processed at elevated temperatures (423 K and 473 K) showed a significant activity of twinning than for the alloy processed at 296 K. These twins are compression and tension twins along the c–axis. Microstructural observation for the alloy processed at 423 K and 473 K revealed that the twins were not completely found in all grains and the twinning developed gradually with increasing the number of turns. At the relatively lower number of turns, the grains were mainly orientated towards the basal slip plane and not pyramidal (twinning) plane. The CRSS for the basal slip is about 0.5 MPa which is smaller than 3.0 MPa for the twinning plane, thus the grains were likely tried to deform via basal plane [226]. However, due to the accommodation incompatibility for the plastic deformation on the basal slip plane in the alloy with the HCP structure, some grains have re–orientated themselves preferentially towards twinning as the CRSS reached to

enough value for initiation the deformation by twinning under the HPT loading conditions. Increasing the number of turns under such conditions was resulted in a gradual activation of twinning across the microstructure due to increase the preferential re–orientation for twinning to accommodate the further imposed deformation in HPT [228]. The massive shear produced by the combined compression and torsion in HPT at elevated temperatures may have lowered the CRSS required for the activation of twinning.

Despite the formation of twinning being normally observed at low temperature and or high strain rates [25][229][230], twins have been observed during hot compression of AZ91 at temperatures between 250 – 300 °C [231], in AM30 at a temperature of 450 °C [232] alloy and in AZ91 alloy processed by backward extrusion at a temperature of 450 °C [215]. The occurrence of twinning has been shown at a relatively lower processing temperature as in AZ31 magnesium alloy processed by HPT at 373 K [225]. The lack of sufficient slip systems for homogeneous deformation and the presence of fine particles of β–phase encourage deformation localization in the AZ91 magnesium alloy and thus promote formation of twins [61][56][206]. The high content of aluminium in the AZ91 alloy could promote the activation of twins at elevated temperatures due to pinning of dislocations by aluminium solute atmospheres [215][233].

Increasing the number of turns and processing temperature resulted in intersections of twins inside the grains and segmentation of the original grains into smaller grains. Microstructural observations revealed that the density of twinning at the centre regions of the processed samples are relatively lower than at the edge regions for alloy processed for N = 1/2 and 1 turn. It has found that the β–phase has fragmented into small pieces with some remaining clusters at the centre region, whereas fine particles of the β–phase have observed at the edge regions for the alloy processed for relatively low number of turns. Therefore, it is expected that migration of twin boundary has restricted by the relatively coarser particles of the β–phase that distributed at the centre region and this resulted in a lower distribution of twinning in the centre region [228]. The finer particles of the β–phase at the edge region have allowed to the twins to bypass them and hence a higher distribution of twinning has found in the edge region. However, increasing the number of turns to N = 5 turns resulted in a comparable values of twinning

density at the centre and edge regions, due to formation of nano–sized particles of the β–phase caused for further distribution of twins [234].

The grain refinement in the processed alloy at 423 K has developed efficiently by the twinning intersections as well as the grain subdivision mechanism. At this temperature the dynamic recrystallization was absent or had a minor effect on the refinement process compared to the twinning activity since the processing temperature only just at the beginning of the range for recrystallization temperature (420 – 600 K) in magnesium alloys [235]. It is likely that the dynamic recrystallization may have contributed to the grain refinement in the processed alloy at 473 K. It has been reported that the new recrystallized grains could form as necklace–like bands along the original grain boundaries and twin boundaries [236]. A limited grain growth has observed in the alloy processed at 473 K with increasing the number of turns up to N = 5 turns. The significant dispersion of nano–sized particles of the β–phase during HPT processing had pinning effect for the grain growth of the alloy at a higher number of turns [17]. However, the formation and fragmentation of twinning were the dominant mechanism for refinement at 473 K. The accumulation of nano–sized particles of the β–phase along shear bands and twin boundaries retarded nucleation and dynamic recrystallization [237][238]. However, the alloy processed at 296 K showed a microstructural homogeneity with at the early stage of HPT processing rather than the heterogeneity that found in the alloy processed at 423 K and 473 K, which needed further processing turns and / or higher processing temperature for achieving a reasonable homogeneity as reported earlier using ECAP processing at elevated temperatures [13][239].

The sources for heterogeneity and homogeneity in the materials processed by HPT are divided into two groups; the HPT process–related parameters and the material–related characters [1][205]. The HPT process–related parameters include: distribution of imposed strain over the sample, the applied pressure, the number of turns or value of imposed strain, the processing temperature, the sample dimensions, and the misalignment in HPT anvils [205]. The material–related characters include: the crystal structure, the value of stacking fault energy, and the presence of precipitates or second phases [1]. If it assumed that the HPT process–related parameters and the material–related characters were the same

for all processed samples, except the processing temperature that will be the crucial factor in achieving the homogeneity in the alloy.

It well–known that the temperature assists the activation of additional deformation modes in HCP magnesium alloys, and hence, increasing the temperature facilities the processing of these alloys [20]. In general, the processing of any material at elevated temperatures is time–dependent, thus, increasing processing time or the number of turns in HPT leads a microstructural homogeneity [235]. However, for the magnesium alloys the higher processing temperature and number of turns are associated with the dynamic recrystallization and grain growth during processing [194]. In the current research, an extensive twinning and grain growth have observed with increasing the temperature and number of turns for the alloy processed up to N = 5 turns at 473 K. The twinning activity seems has competed to the dynamic recrystallization even at higher processing temperature due to the existence of fine particles of the β–phase. This phase has melting point about 733 K (460 °C) [191]; therefore the grain growth of recrystallized grains and twinned grains under the highest temperature (473 K) has constricted by the pinning effect of this phase [240].

5.3 Microstructure over the *vertical* cross–sections

The current results reveal that the HPT processing produced inhomogeneous grain structures in the AZ91 magnesium alloy in the through–thickness directions of the disks processed for N = 1/4 and 5 turns at room temperature. It has observed that the applied pressure during HPT processing imposes a compressive stress state across the processing volume of HPT. According to the geometry of depression and the disk shape, the centre region of the disk is subjected to the highest compressive stresses due to friction, whereas the lower compressive stresses are induced at the edge regions [25]. It has found that the mean stress (the result of compressive load divided by circular area of the disk) decreases with increasing the number of turns as a result of the material outflow that occurs in quasi–constrained HPT. This outflow increases the effective cross–sectional area of the sample [241].

The microstructure of the AZ91 alloy reveals differences in the levels of inclination as shown in Figure 4.32, *N* = 1/4, 1 and 5 turns. The flow of plastic deformation can be traced through the configuration of the β–phase alignment, where any difference in the alignment through different locations along the axial direction of the processed disks, can reveal the variations in the plastic flow within the disks during the processing [25][216]. The shear bands decorated by β–phase has found near the top and bottom surfaces in the early stage of processing. The increase in straining resulted in a more shear bands and refined β–phase near these surfaces. It has found that the edge regions accommodated higher amounts of deformation than the centre regions at the early stage of processing, as shown in Figure 4.32, as a result of the proportionality of deformation with the distance from the centre as assumed by Eq. (1.10) [138].

Increasing the number of turns can spread the deformation progressively across the vertical cross–sections of the processed disks; however, this seems to be heterogeneous in nature especially for the β–phase relative to the α–matrix [155]. This phase is incompatible with α–matrix due to the difference in the crystal structures between them and thus it is more susceptible to the plastic deformation and flow under processing than the matrix [25][216]. As observed by TEM and XRD, it is highly expected that the grain refinement across the vertical cross–sections has attained within the nanometre range. The shear bands have occurred due to the concentration of deformation in specific areas, as shown by the red arrows in Figure 4.32, which reveals the heterogeneity of the deformation across the vertical cross–sections of the processed disks. The absence of sufficient slip systems for homogeneous deformation at room temperature, second phase particles and / or twins can lead to the shear localization and development of shear bands [61][56]. It has noticed that the presence of these bands increased with increasing the number of turns; however, their distribution was variable at different locations in the longitudinal directions in the disks processed through *N* = 1/4 to *N* = 5 turns. These bands appeared to be parallel to the surfaces of the disk, indicating the constraining of deformation relative to the plane of the theoretical maximum shear stress [155][201]. The shear bands have concentrated in the edge area, as shown in Figure 4.32, due to the high outflow of material during processing and the high imposed shear deformation in these regions [242][243].

It can be seen that the width of shear bands was directly proportional to the number of turns, as shown in Figure 4.32, which is attributed to an increase in the material outflow with increasing the straining. The back–pressure is generated due to the outflow between the anvils, and because of die geometry, which resulted in a heavily deformed microstructure, and a uniform distribution of shear banding in the edge region [205]. The heterogeneous deformation may occur due to the differences in the friction coefficients between the upper and lower anvils. The high friction coefficient leads to the material being stuck to the depression walls under the processing, whereas the low friction coefficient results in the sliding of the material over the depression walls [25]. Therefore, the high friction enforces the material to revolve as a rigid–body, whereas the low friction allows the material to flow plastically within the volume of processing. Thus, the difference in friction coefficient induces a gradient in the deformation over the axial direction [244].

The twins have induced, as shown in Figure 4.33, as a result of the shear deformation during the HPT processing. This twinning has induced by the stress concentrations and the reorientation of the grains during the HPT processing [40]. The nature of the HPT processing of the AZ91 alloy allows for occurrence of additional deformation mode at room temperature (twinning mode). During the early stage of HPT processing, the relatively coarse grains undergo slip across the basal slip plane. Piling–up of dislocations and existence of β–phase at areas that contain grains that are poorly orientated for the basal slip, can lead to the occurrence of stress concentrations at these areas [25]. Therefore, the poorly orientated grains will re–orientate themselves by means of torsion straining, and twinning will occur for accompanying the basal slip [226]. The generated twins include of both tension and compression types as shown by XRD analysis. The twinning activity has persisted in the processed alloy at 296 K with increasing the number of turns, which confirms its accommodation for the higher imposed strain by HPT.

5.4 Microhardness along the *diameter*

A considerable increment in the microhardness can be noticed for the as–pressed disk (N = 0), as shown in Figure 4.40. The increase in microhardness of the as–pressed alloy is attributed to the strain hardening by the compressive pressure [242], where the difference between the microhardness profiles for the as–received and as–pressed disks is obvious in Figure 4.40. The larger error bars that appear in the microhardness profile of the as–pressed disk indicate the presence of a local heterogeneity in the deformation during compression stage. The flow of the alloy laterally outward at the anvils during compression leads to the formation of frictional shear stresses at the edge regions. These stresses are directed towards the centre region of the alloy within the processing zone [25], which explains the increase in microhardness towards the edge regions of the disks under compression, and the associated local heterogeneity in deformation [205].

Many aspects can be concluded from Figure 4.40. First, the microhardness tends to increase with the increasing distance from the centre of the disk at the early stage of HPT processing. This behaviour can be explained using Eq. (1.10), which states that the strain imposed by HPT is proportional to the location from the centre of the disk [138]. Therefore, a gradient in the accumulated dislocations appears within the processed microstructure at the centre and edge regions at the early stage of HPT processing, which leads to finer and harder microstructures at the edge regions than those found at the centre region of lower hardness [245]. Second, a gradual development in the microhardness can be seen in the centre region of the processed disks with increasing the number of turns from N = 3 turns, up to N = 10 turns. This development in the achieved microhardness is a result of the finer and homogenous microstructures evolved at the centre regions for the processed disks after a large number of turns, resulting in a higher strengthening effect compared with its counterparts at the centre regions in the early stage of HPT processing [147]. Third, the microhardness profiles for the disks processed for N = 3, 5 and 10 turns are relatively similar in spite of the differences in the number of turns. The similarity in the distributions of microhardness after a high number of turns is assigned to the ultrafine–grained microstructures achieved gradually for the greater number of turns [140]. Fourth, no considerable difference was noticed between the profiles of microhardness for the disks processed using

the applied pressures of 3.0 GPa and 6.0 GPa for the same number of turns, except in the centre regions for N = 1/2, 1 and 3 turns. The saturation in the distributions of microhardness was found to be independent of the values of the applied pressures. This saturation can be attributed to the values of applied pressures used in HPT processing compared with the yield strength of the AZ91 alloy.

In HPT processing, there is a need for a minimum applied pressure in order to avoid the sliding of the sample within the anvils during the processing and to achieve enough frictional forces to deform the sample plastically. This pressure should be three times larger than the yield strength of the material under processing [205]. The AZ91 alloy has a yield strength of 170 MPa [28], that is significantly less than the pressures used in this work, which are 3.0 GPa and 6.0 GPa; thus the HPT processing at these pressures was clearly applicable for the AZ91 alloy. The first applied pressure (3.0 GPa) is much higher than the critical applied pressure for the HPT processing for AZ91 alloy, which value is close to the yield strength of the alloy [246]. Therefore, the HPT processing using an applied pressure of 6.0 GPa had no significant effect on the obtained microhardness. Moreover, it was found that there were no chemical changes in the microstructure of the AZ91 alloy after HPT processing with an applied pressure of 3.0 GPa in the current study, as shown by the EDS analysis in Table 4.2. The results of EDS analysis eliminate any possible increase in the microhardness of the processed alloy under the applied pressures of 3.0 GPa and 6.0 GPa. No new phase of higher microhardness was found during the HPT processing [246] such as that found for the pure Ti, which transformed from α–phase to ω–phase at higher applied pressures during the HPT processing, causing a significant increase in microhardness [247].

The values of the error bars have recorded and tabulated as shown in Table 4.3 for the distribution of microhardness along the diameter for alloy processed at 296 K. The highest values of error bars at the centre regions of the processed disks at the early stage of HPT processing, indicate the initial heterogeneity in the deformation and microstructure of the alloy at this stage. The further straining resulted in a gradual decrease in these bars due to the gradual evolution in microstructure towards homogeneity with increasing the number of turns [139].

The low values of the error bars at the edge regions can be attributed to the development of homogeneity in microstructure, where the microhardness at these regions was increased earlier than that for the centre regions, due to the high imposed strain in the edge regions [140].

5.5 Effect of the equivalent strain on the Hall–Petch relationship and dislocation density

A correlation of the microhardness values has constructed relative to the imposed equivalent strain during HPT processing as shown in Figure 4.42 (b), where the microhardness results were obtained from Figure 4.40 (b). This correlation for the obtained microhardness has been adopted in many studies [137][138]. The results shown in Figure 4.42 (b) have represented by a fitting line as shown in the plot, which highlights the increase and saturation in the measured microhardness with increasing the imposed strain. A schematic illustration of the variation in hardness with the equivalent strain is shown in Figure 5.1, which is based on the measurement shown in Figure 4.42 (b).

A significant increase in the microhardness found in the initial stages of deformation, where the increase appeared gradually at equivalent strains higher than ~20. The increase of microhardness can be explained by the accumulation of dislocations at the initial stage of the HPT processing, thus leading to the formation of subgrains within the original grains in the alloy as illustrated in stage I in Figure 5.1 [248]. Increasing the equivalent strain up to ~50, results in a continuous increase in microhardness, but at a slow rate. It was found that the further straining reduces the sizes of the subgrains, increases the clarity of the subgrain boundaries and increases the misorientation. The former evolution in microstructure leads to a slow rate in the progress of the microhardness [248]. A limited increase in the microhardness was found by increasing the equivalent strain in the range of 50 – 250, which reveals saturation in the measured microhardness using a high number of turns. The relative saturation in the measured microhardness can be attributed to the balance between the generation of dislocations during the HPT processing and the absorption of the dislocations

by the grain boundaries, which results in a lower rate of strain hardening as illustrated in the stage II in Figure 5.1 [131].

Increasing the number of turns in HPT at room temperature resulted in strengthening of the alloy through the grain reduction as shown in Figure 4.42 (a,b). The strength of alloy (in term of its microhardness) improved significantly with grain refinement at room temperature as illustrated in Figure 4.42 (a). This proportionality has expressed by the Hall–Petch relationship for the hardness measurement ($Hv = H_0 + k_H\, d^{-1/2}$) [249] as shown in Figure 4.42 (b). The effect of grain refinement on the strength of the processed alloy at room temperature showed a significant consistency with the Hall–Petch relationship. The linear relationship between the Vickers microhardness and the grain size after HPT processing gave a value of the parameter k_H (233 MPa.μm$^{1/2}$) and the AZ91 alloy showed a relatively higher level of hardness than for the AZ31 alloy [159]. The value of the parameter k in the Hall–Petch relationship indicates the ability of dislocations to extend from one grain to another during deformation [250][251][252], and it describes the contribution of strengthening by the grain boundaries [25]. The value of the parameter k is affected by the temperature, strain rate, texture and impurities [25][253]. The both aforementioned alloys processed at the same temperature and strain rate, as well as identical X–ray patterns have observed after processing.

This difference can be attributed to the difference in alloying constituents in both alloys. The AZ91 alloy contains a higher aluminium content (9 wt.%) than in the AZ31 alloy (3 wt.%). The alloying of a pure metal with impurity atoms results in occurrence of lattice strains that interact with the moving dislocation during the deformation causing hardening. The lattice strains arise from the change in the lattice constants of the pure metal after alloying with atoms of different atomic radii. For the pure magnesium, the lattice constants are a = 0.320 and c = 0.520 nm, whereas their values in the as–received AZ91 alloy as obtained by XRD were a = 0.317 and c = 0.550 nm. It is clearly that the lattice in the AZ91 alloy has contracted and extended along the a and c axes due to the presence of different alloying elements. The atomic size difference is about 15 % and 10 % between the magnesium atom and aluminium and zinc atoms, respectively, which results in a

noticeable change in the lattice dimensions and thus introduces strengthening. The strengthening effect in magnesium alloy depends on the concentration of the alloying elements as expressed by the following relation [254]: $\sigma_{ss} \cong k_s c^{2/3}$, where k_s is a constant and c is the atomic concentration of solute. It has noticed that hardness increased from Hv = 32 [223] to 55 [14] and 65 (the current work), for the pure Mg, AZ31 alloy and AZ91 alloy, respectively, which reveals the influence of alloying elements (Al and Zn) on the strength of the magnesium.

A significant strengthening has achieved after HPT processing at 296 K in the AZ91 alloy, which was higher than for the pure Mg [223] and AZ31 alloy [159] processed at the 296 K in HPT. The hardness improved considerably in the AZ91 alloy to an average value of Hv = 135 after processing for *N* = 10 turns, whereas the hardness reached to about Hv = 50 and 110 in the pure Mg processed for *N* = 16 turns and in the AZ31 alloy processed for *N* = 15 turns, respectively [159][223]. It can be seen that the rate of strain hardening has evolved earlier in the AZ91 alloy than in the pure Mg and AZ31 alloy, where the highest level of hardness has achieved at a relatively low number of turns for the AZ91 alloy. The evolution in dislocation density with increasing of imposed strain in HPT has a major effect on the achieved strengthening in the AZ91 alloy. The dislocation density has developed significantly with increasing the number of turns for samples processed at 296 K and this evolution was associated by extensive grain refinement as illustrated in Figure 4.42 (a). The measured microhardness for samples processed at different number of turns revealed the gradual development of strengthening with increasing the dislocation density as shown in Figure 4.43 (b) and Figure 4.44 (a). The calculated dislocation density and crystallite size for the AZ91 alloy were higher than for the AZ31 alloy [223] at all number of turns. The difference in dislocation density between both alloys is attributed to the difference in the contents of alloy elements, area fractions of β–phase, values of applied pressure in HPT and values of stacking fault energies in both alloys.

The increase in the content of alloying element in the AZ91 alloy resulted in finer microstructure than in the AZ31 alloy and therefore a higher dislocation density inside the refined grains and along the new grain boundary. Therefore, a higher level of strengthening has observed in the AZ91 alloy compared to that in the AZ31 alloy. A similar behaviour of the effect of alloying element on the grain

refinement dislocation density and hardness has been reported for the aluminium alloys with different Mg concentrations after ECAP processing at 296 K [255]. The higher content of aluminium atoms in the α–Mg solid solution leads to a significant obstruction for the dislocation mobility by the means of solute atmosphere [231].

The distribution and sizes of β–phase altered significantly during HPT and these changes could affect the evolution of dislocation density in the processed alloy. The area fraction of the fine particles of β–phase increased with increasing the number of turns and this increase associated with a significant refinement of the β–phase down to nanometre sizes. These fine particles act as barriers for the mobile dislocations during deformation as these particles are harder than the α–Mg matrix and they dispersed overall the matrix with significant alignment of these particles especially at the edge areas. The increase in the applied pressure used in HPT processing resulted in a higher value of dislocation density [256][257]. The applied pressure of 3.0 GPa used in this research for processing the AZ91 was higher than its counterpart used in processing AZ31 (2.5 GPa) [223]. The higher value of applied pressure enhances the obstruction of defect migration in the processed material and then promotes the suppression of lattice defect annihilation [257][258]. This results in a continuous accumulation of generated lattice defects by shear torsional deformation and thus a high density of lattice defects is expected [259][260].

As the value of stacking fault of the AZ91 is much lower than for the other magnesium alloys in the AZ alloy series such as AZ31 and AZ61 alloys [47]. Therefore, the dissociated dislocations are separated by wider distances in the AZ91 alloy than in the other alloys, which lead to a significant inhibition of dislocation cross–slip and formation of high density of planar arrays of dislocations [43]. During the deformation, the moving dislocations will be blocked effectively by the wide stacking faults and then hindering their movements. The possible segmentation of stacking faults by the moving dislocations could provide additional sources for dislocation accumulation and obstruction [261]. The continuous accumulation of dislocations at the stacking faults with increasing the imposed strain in HPT improved the strength of the alloy as indicated by microhardness measurements [159]. In general, the high concentration of grain boundaries, stacking faults, area fraction of the β–phase in the ultrafine-grained microstructure

are effective sources for obstruction of dislocations and thus enhance the strength of the material [261].

However, a comparison between strengthening by grain boundaries (Hall– Petch strengthening) and strengthening by dislocation activity (Taylor strengthening) has been illustrated in Figure 4.44 (b). It seems that the estimated values of microhardness using the Hall– Petch relation are closer to the measured values of the microhardness than by using the Taylor relation. It seems then that the grain boundaries have a more significant effect on the strength of ultrafine–grained AZ91 alloy rather than the dislocation density. This difference however should also be considered in terms of the potential errors in the measurements of the crystallite size (grain sizes should be used) and dislocation density [184][192].

However, the increase in processing temperature resulted in a minor increase in the crystallite size at 423 K and 473 K as shown in Figure 4.51 (a), which was associated by a significant decrease in the microhardness of processed alloy especially at 473 K for N = 10 turns as shown in Figure 4.51 (b). This behaviour can be attributed to the variation in the dislocation density with processing temperature and number of turns as shown in Figure 4.51 (c). It is clear that the processing temperature has a minor effect on the microhardness especially at the initial stages of HPT processing (N = 1/2 and 1 turn), where the times of processing are significantly low and thus the microstructures did not undergo any significant grain growth as observed in Figures (4.34 – 4.37, 4.51) for the alloy processed at 423 K and 473 K [225]. As the processing times increased for N = 5 and 10 turns the crystallite sizes increased clearly but they still within the nanometre range and the microhardness showed a significant decrease. The gradual decrease in the dislocation density with increasing the processing times at a given processing temperature has considerable effect on the values of microhardness of the alloy due to recovery at elevated temperatures [170][262].

The values of parameters in Hall–Petch relationship depend also on the texture after processing [263]. The XRD analysis showed a domination of the basal slip and pyramidal modes after processing. It has been reported that the basal textured microstructure in a magnesium alloy leads to domination of basal slip and then feasible transportation of gliding over the surrounding grains [263]. Therefore,

less resistance from the grain boundaries would appear and hence low value of the parameter k in the Hall–Petch relationship and low strength are highly expected. Activation of the non–basal deformation modes would enhance the obstruction of slip by grain boundaries and increase the value of parameter k and strength as observed in the processed alloy [251][264].

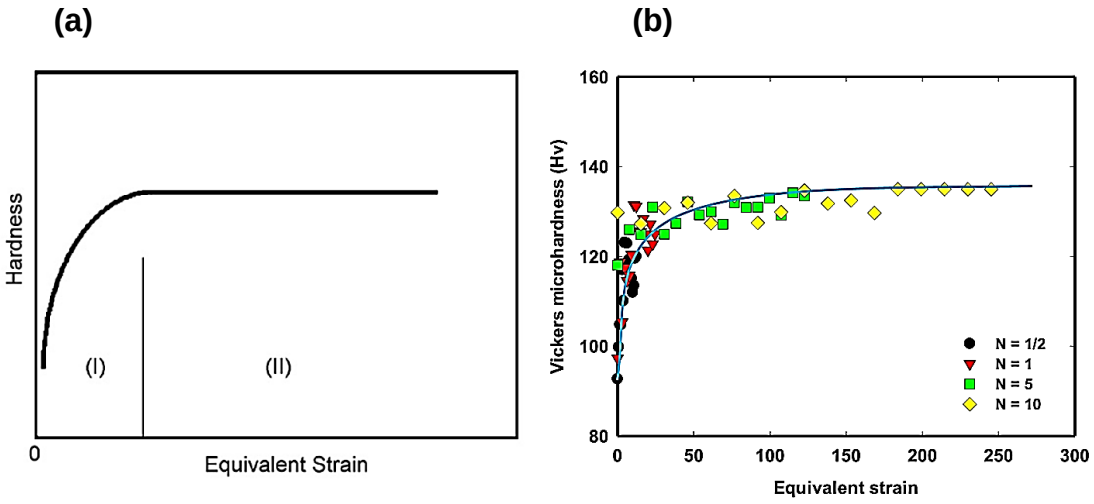

Figure 5.1: (a): A schematic illustration for correlation of the measured microhardness with the equivalent strain [248] and (b): A correlation of the microhardness (recorded along the diameter) with the equivalent strain for the AZ91 alloy processed in HPT at room temperature and using an applied pressure of 3.0 GPa.

5.6 Microhardness over the *horizontal* cross–sections

The distribution of microhardness for the AZ91 disks processed by HPT processing at temperatures of 296 K, 423 K and 473 K are shown in Figures (4.45 – 4.47). These graphical maps exhibit the evolution in the distributions of microhardness over the horizontal cross–sections with increasing the number of turns. A significant evolution has achieved in the microhardness of the alloy during HPT processing compared to its values in the as–received alloy. This increase in the microhardness is associated with the evolution in the microstructure during HPT processing with increasing the number of turns up to *N* = 10 turns [136]. The HPT processed disks showed an earlier increment in the microhardness at the edge regions compared with the counterpart values at the centre regions for *N* = 1/2 and 1 turn. At the initial stage of HPT processing, a relatively higher strain

imposed into the edge regions of the disk as predicted by Eq. (1.10), resulting in an earlier evolution in the microstructure and an increase in the microhardness in these areas. At the same time, the centre region experienced a lower value of the imposed strain, leading to a relatively lower deformation and then a lower microhardness at this area [136].

However, the centre region of the processed disk for N = 1/2 turn showed a higher microhardness than for the as–received alloy. The increase in the microhardness may be caused by the first stage of the compressive deformation that introduced by the applied pressure prior to the HPT processing, and to the second stage of the compressive deformation that appeared during the torsional deformation during the HPT processing [138]. The further straining resulted in a considerable increment in the microhardness in the centre regions for the disk processed for N = 5 turns with a minor increase in the microhardness in the edge regions. The increase in microhardness at the centre regions associated with the evolution in the microstructure during HPT processing, where fine and homogeneous microstructure has achieved due to the gradual spreading of the torsional deformation from the edges to the centre regions during HPT processing [18]. A relative saturation in the distributions of microhardness achieved both at the edge and centre regions of the disk processed for N = 5 and 10 turns. This behaviour attributes to fine and homogeneous that evolved at these regions [147].

The development of microhardness in the processed alloy can be explained through the evolution of microstructure during HPT processing. At the early stage of HPT processing, the average grain size at the edge regions was assumed smaller than that at the centre region, resulting in a non–uniform microstructure at the initial stage of HPT processing. Thus, a bimodal microstructure of relatively coarse and fine grains is expected to develop during the HPT processing for a low number of turns as shown in Figure 4.31 (a) [265]. The initial heterogeneity of microstructures leads to an initial heterogeneity in the distribution of microhardness [6]. Increasing the number of turns resulted in the spreading of deformation towards the interior regions of the processed disks. At the initial stage of HPT processing, i.e. at a small number of turns, and according to Eq. (1.10), the value of strain imposed by HPT is low at the centre region where the radius theoretically equals zero; thus, the expected imposed deformation is low at this

region. The high imposed strain is expected to be at the edge regions according to the above mentioned equation, where the radius is significantly larger than zero. The difference in grain sizes at the centre and edge regions was diminished by further straining, where a gradual evolution towards homogeneity has found in the microstructure and microhardness at both centre and edge regions of the processed disks for N = 5 and 10 turns.

This behaviour is anticipated at a higher number of turns according to Eq. (1.10), although the value of the radius equals zero at the centre region. The development of homogeneity can be explained according to three approaches. The first approach is called a repetitive undulating manner that has been proposed by Zhilyaev *et.al.* [136], where the shear deformation expands towards the centre region with increasing the number of turns as shown in Figure 4.45, where the areas of the higher microhardness covered the edge regions initially, and then moved to the centre regions. Increasing the number of turns resulted in the significant spreading of the deformation to cover the whole cross–section of the processed disks as shown in Figure 4.45, indicating a gradual homogeneity in the processed microstructure and then the microhardness.

The second approach has been proposed by Estrin *et.al.* [148] and related to the strain gradient phenomenon [149] across the material under deformation. It has been found that the high strain accumulates at the edge regions and the low strain accumulates at the centre regions at the initial stage of processing. Thus, the high and low rates of strain hardening appear at the edge and centre regions, respectively. This accumulation results in the occurrence of grain refinement significantly at the edge regions rather than at the centre region. This behaviour resulted in a higher and lower distributions of the microhardness at the edge and centre regions, respectively as shown in Figure 4.45. It was also found that the increasing number of turns led to an increase in the accumulated plastic strain in the centre region, resulting in an increase in the refined areas at this region of the processed disks, and further increase in the homogeneity of the microstructures and microhardness [148] as shown in Figure 4.45.

The third approach is related to the misalignment of HPT anvils, which plays an important role in reducing the un–deformed regions in the centres of processed

disks and then achieving a reasonable homogeneity after a high number of turns [138]. It has been found that the misalignment of the anvils increases with increasing the number of turns. This misalignment results by the reduction in the thickness of the disk under HPT processing, subsequently causing a friction between the two rims of the anvil and between the material's outflow and these rims [205]. The existence of misalignment between the anvils at high number of turns causes an additional deformation at the centre region of the processed disk, which appeared as an increase in the measured microhardness [138].

It has been reported that the development of microhardness after the HPT processing depends on the stacking fault energy of the alloy [139]. The AZ91 with low stacking fault energy (6 mJm^{-2}) [47] shows a slow rate of the dynamic recovery during the HPT processing, thus the strain hardening occurs at a fast rate during the processing [43]. Therefore, the microstructural homogeneity and progress in the microhardness (see Figure 4.45) requires a higher imposed strain or an increase in the number of turns [147][144]. The behaviour of strain hardening and dynamic recovery in magnesium alloys are in contrast to that for a material with high stacking fault energy such as pure aluminium (200 mJm^{-2}) [48]. A high rate of dynamic recovery has been observed during the HPT processing of pure aluminium, which means that the microhardness increases at the initial stage of processing then drops with further straining or by increasing the number of turns as shown in Figure 2.36 [139]. A schematic illustration for the development of Vickers microhardness for materials with low and high stacking fault energies after HPT or ECAP processing in Figure 5.2 [139]. It is clearly that the strain hardening and saturation in the microhardness for the AZ91 alloy with low stacking fault energy follows the behaviour as illustrated schematically in shown in Figure 5.2.

The development of microhardness can be explained in term of the stacking fault energy of the processed material. The AZ91 alloy processed in HPT for N = 5 turns showed an earlier saturation in the microhardness distribution than for the AZ31 alloy [159] processed at the same number of turns in HPT at room temperature. The stacking fault energy of the AZ91 alloy (6 mJm^{-2}) is smaller than for the AZ31 alloy (27 mJm^{-2}) [47]. Therefore, the evolution of grain refinement and strain hardening occurred at faster rates in the AZ91 alloy than for the AZ31 alloy. Furthermore, the area fraction of β–phase is higher than in the AZ31 alloy due to

higher amount of aluminium in the AZ91 alloy than for the AZ31 alloy. Therefore, the solute–dislocation interactions would be more intense in the AZ91 alloy than in the AZ31 alloy, which results in more obstruction of the motion of dislocations and then a higher strain hardening in the AZ91 alloy [25][266].

The effect of processing temperature on the development of microhardness can be seen in the coloured–coded maps in Figures (4.46 – 4.47). These maps represent the distribution of Vickers microhardness on the horizontal cross–sections of the AZ91 alloy processed at 423 K and 473 K. It is obviously that the overall microhardness for the alloy processed at 423 K is relatively similar to it counterpart for the alloy processed at 296 K, where the behaviour of strain hardening at both processing temperatures developed with increasing the number of turns. However, the rate of strain hardening and then the development of microhardness were slower at 423 K than at 296 K. The overall microhardness and rate of strain hardening for the alloy processed at 473 K were significantly lower than their counterparts at 296 K and 423 K. This can be explained according to the variation in dislocation density with processing temperature.

It has been stated that the dislocation density decreases significantly at higher processing temperatures [170]. Existence of the grain growth at such higher temperature (i.e., 473 K) had a detrimental influence on the strength of the alloy especially at high number of turns (N = 10 turns). Processing of the AZ91 alloy at lower temperatures (i.e., 296 K and 423 K) did not show any significant grain growth [156]. However, the rate of strain hardening in the alloy processed at 296 K was significantly faster and higher than at 423 K due to higher dislocation density that accumulated in the alloy at 296 K than at 423 K. Increasing the number of turns up to N = 10 turns resulted in development of the microhardness for the alloy processed at 423 K due to increase the dislocation density at high number of turns.

It has been reported that the processing of magnesium alloys at temperatures lower than 400 K leads to no grain growth [235]. Therefore, the limited grain growth that observed in the alloy processed at 473 K resulted in a lower overall microhardness compared to their counterparts obtained after processing at 296 K and 423 K [225]. The reduction in microhardness has been reported in the AZ31

alloy after processing at 473 K especially at high number of turns [267]. However, the overall microhardness for the AZ91 alloy processed at 473 K was higher than for the AZ31 at all number of turns. This difference can be attributed to the higher area fraction of the β–phase in the AZ91 alloy than in the AZ31 alloy. After the HPT processing this phase fragments into fine particles that have pinning effect for the accumulated dislocations and then influence the strengthening of the alloy [25][266].

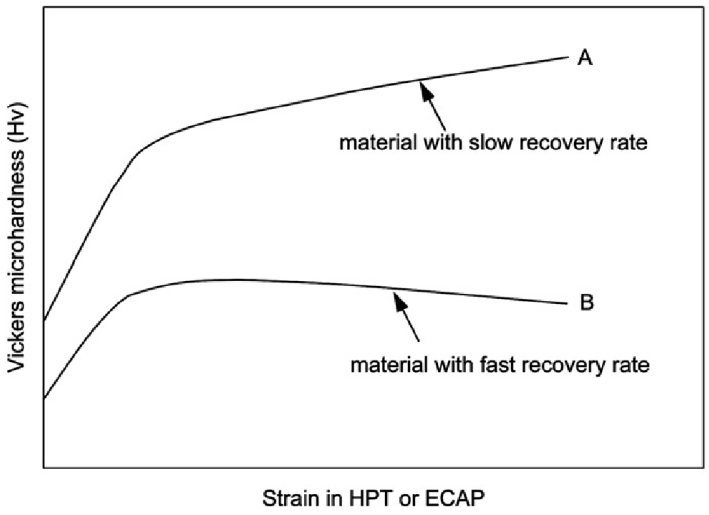

Figure 5.2: Schematic illustration of the distributions of Vickers microhardness for two materials with low and high rates of recovery processed by HPT or ECAP, for the materials of the low and high stacking fault energies, respectively [139].

5.7 Microhardness over the *vertical* cross–sections

The current results have shown that the microhardness distributions in the AZ91 alloy are heterogeneous along the through–thickness directions at the initial stage of deformation. This is supported by the differences in microstructural observations in the along this direction, as shown in Figures (4.48 – 4.50), and confirms the occurrence of plastic flow localisation. The results show that the microhardness developed by increasing the number of turns relative to the increase of the distance from the centre. These results are symmetric with the microstructural inspections on the vertical cross–sections of the processed disks. The evolution of deformed microstructure that elongated along the mid–plane of the processed disks for N = 1/2, 1, 5 and 10 turns contributed in the increase of microhardness

across the vertical cross–sectional planes. Increasing the imposed strain by HPT resulted in increasing the values of microhardness, especially in the mid–radius and edge regions of the disks processed for N = 1/2 and 1 turn. The initial heterogeneity in the deformation of AZ91 alloy at the initial stage of HPT processing has been shown reported for the AZ31 alloy [199] processed by HPT at 296 K and using an applied pressure of 6.0 GPa for N = 1/4, 1 and 5 turns.

This initial heterogeneity is a result of the lack of sufficient slip systems for a homogenous deformation in the magnesium alloy [20], which results in the occurrence of the localized plastic flow. The presence of shear bands along the vertical cross–sections gives an indication of this flow. The high friction coefficient leads to the rotation of the alloy within the volume of the centre region of the disk, whereas low friction coefficient results in the flow of the alloy across the volume at the edge region of the disk. Therefore, the difference in the friction coefficients leads to a heterogeneous distribution of the deformation in the through–thickness direction [268].

A significant saturation in the microhardness achieved after N = 5 and 10 turns, which indicates the development of homogeneity in the microstructure and measured microhardness. The development of homogeneity by increasing the number of turns can be explained by the presence of higher imposed strains under the hydrostatic pressure, which enforce the poorly orientated grains to re–orientate themselves towards the basal slip through the activation of twinning, and the latter increases the deformation homogeneity [61]. It is assumed that the sufficiently high number of turns may reduce the effect of the difference in the friction coefficients, due to the alloy being filled between the anvils and achieving a significant sticking condition [205][269]. The high processing temperature (423 K and 473 K) resulted in low and heterogeneous distribution of microhardness at initial stages of HPT processing and relatively homogeneous distribution of microhardness with increasing the number of turns. The effect of processing temperature on the average microhardness illustrated in Figure 4.51.

The alloy processed at 296 K shows a significant strengthening up to high number of turns, whereas the alloy processed at 423 K and 473 K exhibits a lower level of strengthening that becomes even lower with increasing the number of turns at 473

K indicating the loss of accumulated dislocation density and occurrence of grain growth. The distribution of microhardness along the vertical and horizontal cross–sections showed a considerable consistency for the alloy processed at each specific processing temperature, which indicates the development of microstructural homogeneity with increasing the imposed strain at each condition [245]. This consistency in the AZ91 alloy has not been observed in the AZ31 alloy processed at both ambient and elevated temperatures due to difference in the aluminium content and stacking fault energy in both alloys, which control the extent of grain refinement, dislocation density, achieved homogeneity and resultant mechanical properties [25] [47][224][266].

5.8 Flow behaviour during hot deformation

The discussion in this section and the following sections are based on the author's paper published on [270]. The stress–elongation curves in Figures (4.52 – 4.55) for the fine–grained AZ91 magnesium alloy reveal significant superplastic elongation and relative thermal stability of the alloy under tensile loading at temperatures up to 573 K for up to 1680 minutes using a strain rate of 1×10^{-4} s^{-1}. The achieved elongations varied with microstructure, strain rate and testing temperature as shown in Figures (4.57 – 4.58) and summaries in Table 4.4. For the alloy processed for N = 10 turns in HPT and then pulled in tension at a testing temperature of 573 K using a strain rate of 1×10^{-4} s^{-1}, the maximum elongation reached 1308 %; which (to the authors' knowledge) is the highest value of elongation reported to date in this alloy. The elongation results in the current research are significantly higher than data that have been published earlier. For instance, the maximum elongation previously published was 810 % at 473 K using at a strain rate of 5×10^{-4} s^{-1} for the Mg–9%Al alloy processed in HPT for N = 5 turns at 423 K [18], whereas in the present work, the maximum elongation was 1090 % at a testing temperature of 473 K using a strain rate of 1×10^{-4} s^{-1}, for the AZ91 alloy processed at room temperature in HPT for N = 5 turns.

In addition, the tensile elongations in this investigation are also higher than observed for alloy processed at high temperatures in ECAP as reported earlier

[17], where the maximum elongation was 840 % at a testing temperature of 473 K using a strain rate of 3.3×10^{-4} s^{-1} for samples processed for 2 passes in ECAP at a processing temperature of 473 K; whereas the current AZ91 alloy processed by HPT for *N* = 1 and 3 turns at room temperature showed maximum elongations of 845 % and 977 % at a testing temperature of 473 K using a strain rate of 1×10^{-4} s^{-1}.

This difference in the elongation can be attributed to the processing temperature in HPT and ECAP. For magnesium alloys, it is well documented that a much finer microstructure can be produced by SPD processes at room temperature rather than at elevated temperatures [17][99][159][225]. The current alloy has refined efficiently from 30 μm in the as–received alloy to about 35 nm in the alloy processed at room temperature for *N* = 10 turns in HPT. Furthermore, the level of grain refinement that achieved after HPT at room temperature is much finer than that after ECAP. The minimum grain sizes in AZ91 alloy were 1 μm in ECAP at 448 [10], 17 μm after 2 passes in ECAP at 473 K [13], 0.7 μm after 2 passes in EX–ECAP at 473 K [17] and 2 μm after 4 passes in two–step ECAP at 498 K and then 453 K [161]. The aforementioned grain sizes are significantly larger than the grain size in the current alloy after HPT; especially the grain growth has taken place with increasing the number of passes in ECAP at elevated temperatures. Thus, the observed higher elongations are expected from a finer microstructure during the subsequent hot deformation as the presence of fine grains is one of the prerequisites for achieving superplasticity in polycrystalline materials [88]. The increase in elongation with finer microstructure can be seen in Figures (4.57 – 4.58) and depicted in Figures (4.59 – 4.62), where the higher elongations towards the superplastic range were achieved with increasing the number of turns up to *N* = 10 turns.

For the as–received alloy, the elongations varied with strain rate and testing temperature as shown in Figures (4.57, 4.58, 4.63) and summarised in Table 4.5. The elongation has increased as the temperature increased and strain rate decreased in the as–received alloy. At a testing temperature of 296 K, the alloy showed the highest strain hardening among the tested samples and the lowest elongations, where the microstructure has not shown any changes at this

temperature. The strain hardening in the as–received samples is attributed to the high density of dislocations that accumulated in the samples tested at 296 K where slow recovery and no recrystallization occurred. The limited ductility at 296 K is attributed to the restricted number of slip systems in the AZ91 magnesium alloy. The magnesium and its alloys deform by the basal slip and twining at room temperature and thus the limited ductility results [20]. The moderate increase in elongation for the as–received alloy has influenced by the decreasing in the strain rate, where the microstructure could re–orientated its grains for the basal slip under tensile loading [226][271]. However, the presence of non–basal deformation modes such as prismatic and pyramidal planes as shown in Figure 4.38 has retained the high values of strain hardening even at low strain rates due to the obstruction of slip in the basal plane with its counterpart in the non–basal planes [251][264]. Increasing the temperature up to 473 K and 573 K resulted in lower values of strain hardening and significant improvement in the elongation for the as–received alloy at all strain rates due to softening of the microstructure by the dynamic recrystallization as shown in Figures (4.79, 4.80). The grain sizes were 3 μm and 5 μm after testing at 473 K and 573 K, respectively using a strain rate of 1×10^{-4} s^{-1}, which corresponding to elongations of 209 % and 332 % as illustrated in Figure 4.63.

5.9 Occurrence of the superplastic behaviour

The microstructural inspections along the gauge lengths of tensile samples after tension as shown in Figures (4.67 – 4.77), reveal that the apparent grains remained equiaxed (as revealed by SEM from the surface morphology of the tested samples [187][188][189]) with fine sizes until fracture at all temperatures and strain rates. The presence of these apparent equiaxed grains was associated with superplastic elongations, which indicated that the main deformation mechanism was grain–boundary sliding (GBS). The retention of an equiaxed microstructure at elevated temperature under tension is necessary for superplastic elongations through grain–boundary sliding [106][272]. In addition, the retention of equiaxed grains after the tensile test reveals the migration of grain boundaries during superplastic deformation at elevated temperatures. The stress

concentration at grain boundary discontinuities can be reduced by the migration of grain boundaries during deformation, and thus grain–boundary sliding continues as the main deformation mechanism [91].

The measurements of strain–rate sensitivity (m) confirm that grain–boundary sliding is the dominant deformation mechanism, where the m–values were 0.3 – 0.5 as illustrated in Figure 4.64. It is well known that high values of strain–rate sensitivity indicate a higher resistance to failure by necking and thus high elongations are expected [272]. The uniform appearances in the gauge lengths of tested samples that showed high elongations as depicted in Figures (4.59 – 4.62) reveal the absence of necking after hot deformation that indicates the occurrence of superplastic flow [273]. However, this necking has noticed in the samples with relatively lower elongations using the faster strain rate (1×10^{-1} s^{-1}) at relatively testing temperatures 423 K and 473 K, where these samples has fractured by the localized necking and the lower elongations have observed. At above–mentioned conditions, the test has conducted rapidly so there was no chance for strain softening and fine–grained microstructures were retained. At these rapid rates of deformation, the activation of twinning is anticipated for accommodation the deformation and re–orientation of the grains for the direction of tensile stress. Subsequently, the twins tend to re–orientation also in the direction of tensile stress [274], and the localized deformation appears at sites when twins intersect with each other while they are orientating towards the tensile stress leading to crack initiation at these sites and thus high strain hardening and low elongation are resulted [275].

The current results reveal an excellent high–strain rate superplasticity (HSRSP) for the AZ91 alloy processed by HPT at room temperature compared to those found previously for Mg–9%Al alloy processed by EX–ECAP (360 %, 1×10^{-2} s^{-1}, 498 K) [17], Mg–9%Al alloy processed by HPT (325 %, 1×10^{-2} s^{-1}, 473 K) [18], hot extruded AZ91 alloy (300 %, 1×10^{-2} s^{-1}, 548 K) [276], and hot rolled AZ91 alloy (275 %, 1×10^{-2} s^{-1}, 698 K) [277]. It has been assumed that an improvement in microstructural stability at elevated temperature and additional grain refinement are possible ways to achieve high–strain rate superplasticity in magnesium alloys [98]. In the present work, the AZ91 alloy was processed in HPT at room temperature, which was not the case reported by those using other processing

techniques such as equal channel angular pressing [17]. A more extreme grain refinement is expected after processing at room temperature than at elevated temperatures as reported in previous HPT studies [17][99][159][225]. Thus, the room temperature processed alloy with a finer microstructure exhibits better thermal stability and thus superior superplasticity under faster strain rates in hot deformation [278].

It can be seen in Figure 4.77 (g – l), for the sample processed for *N* = 10 turns in HPT, that high–strain rate superplasticity to elongations of 590 %, 410 % and 860 % using strain rates of 1×10^{-2} s^{-1} at 473 K, 1×10^{-1} s^{-1} and 1×10^{-2} s^{-1} at 573 K, respectively, and the grain growth was insignificant at testing temperatures of 473 K (for 2 – 3 minutes) and 573 K (for 5 – 10 minutes). In addition, it is obvious from Figures (4.54, 4.61), that the maximum high–strain rate superplasticity achieved for Mg–9%Al processed in HPT for *N* = 5 turns at 423 K [18], was significantly lower than its counterpart for the alloy in the present investigation that was processed in HPT for the same number of turns but at 296 K. This can also be attributed to the effect of processing temperature on the grain refinement of magnesium alloys as discussed previously.

Low–temperature superplasticity (LTSP) was also noticed in the AZ91 alloy during tensile testing at a low temperature of 423 K using strain rates of 1×10^{-3} s^{-1} and 1×10^{-4} s^{-1} as illustrated in Figure 4.57. The lower testing temperature is equivalent to 0.55 T_m, where T_m for the AZ91 alloy is 768 K (495 °C) as illustrated in the phase diagram of the alloy [33]. The current performance in the low–temperature superplasticity regime is better than previous data obtained for the AZ91 magnesium alloy [10][18]. It has been found that finer grain sizes are preferable for achieving low–temperature superplasticity as well as for achieving high–strain rate superplasticity [10]. It can be seen that the grain sizes were retained to within 1 μm and 4 μm for samples tested at 423 K and 473 K, respectively, using strain rates of 1×10^{-3} s^{-1} and 1×10^{-4} s^{-1} as observed in Figures (4.76 – 4.77). The current results for low–temperature superplasticity reveal the potential for superplastic forming of magnesium alloys at lower possible temperatures to overcome their poor workability at room temperature and excessive oxidation at elevated temperatures [279].

A small difference was observed in the maximum values of the low–temperature elongations, for samples processed by EX–ECAP (800 %, 1×10^{-4} s^{-1}, 423 K) [17], and its counterpart obtained in the current study (760 %, 1×10^{-4} s^{-1}, 423 K). This can be attributed to the difference in dimensions of tensile samples for ECAP and HPT. The ECAP tensile sample was cut from a cylindrical billet with a gauge length of 5 mm and gauge cross–section area of (3×2) mm^2 [17], whereas in this study, the HPT tensile sample was cut from a circular disk with a gauge length of 1.0 mm and gauge cross–section area of (0.9×0.6) mm^2. Therefore, the small difference in the calculated elongations can be attributed to the difference between the relatively large–scale and micro–scale tensile samples produced in ECAP and HPT, respectively [280][281]. Moreover, the direction of cutting for tensile samples from ECAP billets and HPT disks has a further impact. The tensile samples after EX–ECAP were cut parallel to the longitudinal axes after the extrusion step and after the ECAP [17], whereas the disk–shaped samples were cut firstly from an extruded rod perpendicular to the extrusion direction; then after HPT processing, the tensile samples were cut parallel to the shear–plane direction [99]. Therefore, occurrence of a strong texture is anticipated due to the extrusion and subsequent ECAP for 2 passes through the route B_c, and alignment of the basal planes parallel to the extrusion direction [282]. The ECAP processing for 2 passes does not lead to a redundant strain process and thus an significant alignment and texturing of the microstructure towards the direction of pressing is expected rather than after processing for 4 passes [283]. This leads to easy slip in tension at a testing temperature of 423 K and the occurrence of low–temperature superplasticity for the alloy processed in extrusion and ECAP for 2 passes [22]. In contrast, the monotonic HPT mode was used in the processing of the AZ91 alloy in this investigation, which leads to a more random texture with equiaxed grains at a high number of turns [284].

Therefore, at temperatures of 423 K, a relatively lower elongation is expected in the alloy processed by HPT compared to its counterpart processed by EX–ECAP. The average strain sensitivity of 0.3 and the equiaxed grains were found for all samples tested at a testing temperature of 423 K using a strain rate of 1×10^{-4} s^{-1}, which suggests that grain boundary sliding is the deformation mechanism at low temperature [10]. Lower elongations were found at a low temperature of 423 K

using high strain rates of 1×10^{-1} s^{-1} and 1×10^{-2} s^{-1}, and these elongations were associated with low values of strain–rate sensitivity with an average of 0.25. Thus, glide–dislocation creep is assumed as the deformation mechanism accommodated with grain–boundary sliding as the grains retained their equiaxed shapes and did not elongate as in the case of dislocation creep only [277][285].

5.10 Mechanisms of the deformation

The activation energy was calculated at a fixed strain rate using the following equation [193][286]: $Q = nR(\partial(ln\sigma)/\partial(1/T))$, where Q is the activation energy, n is stress exponent ($n = 1/m$), R is the gas constant, and $(\partial(ln\sigma)/\partial(1/T)$ is the slope of plot in Figure 4.65. For the AZ91 alloy, the activation energy was obtained for a sample processed in HPT for *N* = 10 turns then tensile tested using a strain rate of 1×10^{-4} s^{-1} over the temperature range (423 – 573) K as shown in Figure 4.76. It was found that the activation energy equals 80.34 KJ/mol that is close to the activation energy of grain boundary diffusion of pure magnesium (92 KJ/mol). Therefore, grain–boundary sliding is the dominant deformation mechanism, which is consistent with the observed microstructures as shown in Figure 4.76. The grain–boundary sliding mechanism was accommodated with diffusional flow at temperatures of 473 K and 573 K using a strain rate of 1×10^{-4} s^{-1} as shown in Figure 4.77 (c, f, i, l). It can be seen that the shapes of grains under these conditions were changed from equiaxed to elongated and oriented towards the tension axis and thus the highest level of superplasticity produced [287]. The relative difference in the obtained activation energy and its counterpart for pure magnesium is attributed to the presence of β–phase in the AZ91 alloy, where this phase has an activation energy for grain boundary diffusion of 65 KJ/mol, which reduces the overall activation energy for the present alloy [288][289].

The steady–state strain rate for the superplastic flow at high temperatures is expressed by [45]: $\dot{\varepsilon} = (ADGb/kT)(b/d)^p(\sigma/G)^n$, where D is the appropriate diffusion coefficient $D = D_o exp(-Q/RT)$, D_o is the pre–exponential complex constant, A is a dimensionless constant, G is the dynamic shear modulus, b is the Burgers vector, d is the grain size, σ is the applied stress, p and n are the

exponents of the inverse grain size and normalized stress, respectively. Using the following values of $p = 2$, $n = 2$, $A = 10$, $D = D_{gb}$ [272], $D_o = 7.8 \times 10^{-3}\ \mathrm{m^2 s^{-1}}$, $G = 1.92 \times 10^4 - 8.6 \times T\ (\mathrm{MPa})$, and $\boldsymbol{b} = 3.2 \times 10^{-10}\ \mathrm{m}$ [290] in the former equation for the grain–boundary sliding mechanism results in Figure 5.3, which represents the temperature and grain size compensated strain rate versus the normalized stress for the alloy processed for *N* = 10 turns and tested in tension at different temperatures and strain rates. The solid line represents the predicted strain rate for superplasticity with a slope of $n = 2$ ($m = 0.5$).

Good agreement was obtained between the observed experimental data for the current alloy and similar work in a series of magnesium alloys [291][292] and the constitutive equation of superplastic flow based on the assumption that grain–boundary sliding is the dominant deformation mechanism over these testing temperatures and strain rates. It is important to note that the values of apparent grain sizes were collected from the SEM micrographs of the gauge lengths of the tensile test as indicated in Figure 4.76 and these values were used in the constitutive equation. The glide–dislocation creep was assumed as the deformation mechanism accommodated with grain–boundary sliding at 423 K and fast strain rates $1\times10^{-1}\ \mathrm{s^{-1}}$ and $1\times10^{-2}\ \mathrm{s^{-1}}$, where the low values of strain–rate sensitivity were about 0.25 and the obtained elongations were significantly lower than at higher testing temperatures and slower strain rates. The microstructures at these conditions showed no elongated and equiaxed grains indicating the occurrence of dislocation creep [277][285].

For the as–received alloy, the glide–dislocation creep was assumed to be occurred at testing temperatures of 296 K using all strain rates, at 473 K using strain rates of $1\times10^{-1}\ \mathrm{s^{-1}}$ to $1\times10^{-3}\ \mathrm{s^{-1}}$ and 573 K using strain rates of $1\times10^{-1}\ \mathrm{s^{-1}}$ to $1\times10^{-2}\ \mathrm{s^{-1}}$. The mechanism of glide–dislocation creep assisted by grain–boundary sliding would assume at the lowest strain rates at testing temperatures of 473 K and 573 K, where the values of strain–rate sensitivity were about 0.3 – 0.4 and the fine–grained microstructures have observed due to the dynamic recrystallization at these temperatures [277][285].

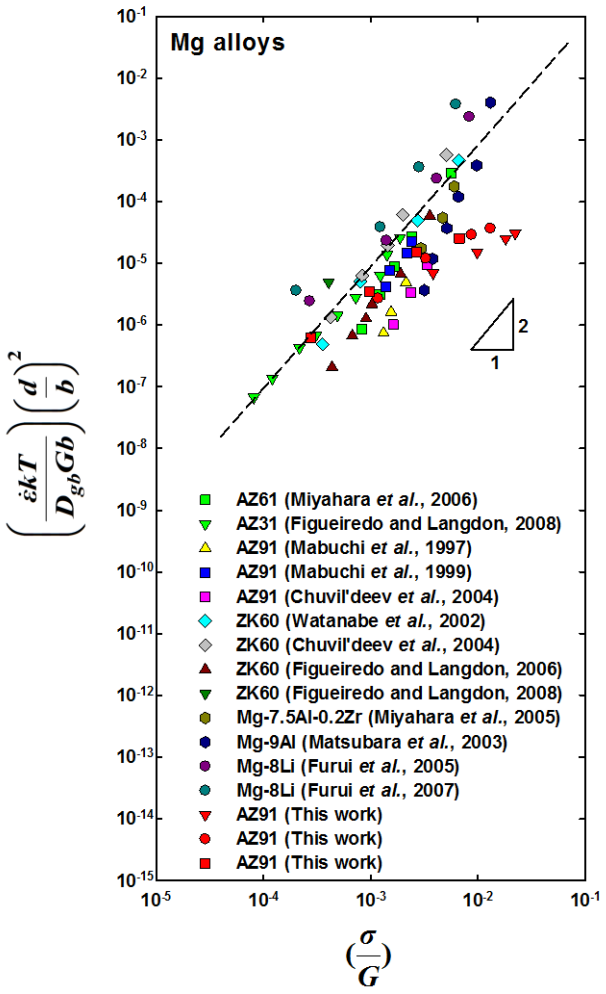

Figure 5.3: The temperature and grain size compensated strain rate versus normalised stress for the AZ91 alloy processed in HPT compared with a series of magnesium alloys. The slope of the straight line has a value of the stress exponent of 2, and represents the predicted superplastic strain rate.

5.11 Thermal stability during hot deformation

The thermal stability of the AZ91 alloy was enhanced by the presence of fine particles of the β–phase ($Mg_{17}Al_{12}$). Prior to HPT processing, the β–phase exists normally along the grain boundaries as lamellar and agglomerate forms in the unprocessed alloy as shown in Figure 4.1. After HPT processing, this phase fragmented into fine particles with nanometre sizes due to the high value of the imposed strain by HPT and these nano–sized particles were dispersed in the matrix (α–Mg solid solution) as shown in Figures (4.16, 4.29) for the alloy processed for N = 1 and 10 turns.

It was found that the morphology of the second phase significantly affects the mechanical behaviour of the metallic materials at room temperature and elevated temperatures [293]. The existence of well–dispersed particles of the β–phase inhibited significant grain growth during superplastic deformation at elevated temperature and then enhanced the extent of superplasticity. The β–phase has a melting point of about 733 K (460 °C) which is relatively lower than 768 K (495 °C) for the AZ91 alloy [191]; thus, the β–phase along the grain boundaries may glide relatively earlier than the grains during hot deformation.

For samples processed in HPT for a low number of turns (*N* = 1), it was noticed that the distribution and area fraction of the fine particles of the β–phase are relatively lower as shown in Figure 4.16 than in samples processed for a high number of turns (*N* = 10) as shown in Figure 4.29. Therefore, during tensile testing at elevated temperature, with a low fraction volume of the fine particles of β–phase, where the β–phase is located mainly near and / or on the grain boundaries, it acts as pinning phase and the sliding of grains is probably accommodated with limited sliding of the fine particles of β–phase. Increasing the distribution and area fraction of the fine particles of the β–phase leads to a more significant sliding of the β–phase particles, which can be expected in samples tested at a temperature of 573 K, which represents 0.78 T_m of the β–phase. It has been proposed that the β–phase acts as a lubricant for matrix sliding during tension [189]. Therefore, the highest elongations were obtained at all strain rates at a temperature of 573 K for samples processed in HPT for *N* = 10 as illustrated in Figures (4.55, 4.58, 4.62). The effect of area fraction of β–phase on the superplasticity has been reported earlier for Mg–15%Al–1%Zn alloy [189], Mg–33%Al alloy [94] where elongations have been improved considerably with increasing the amount of aluminium (or the area fraction of the β–phase).

As the strain rate decreased to 1×10^{-4} s^{-1} and testing temperature increased to 473 K and 573 K, the microstructure showed filaments and surface cavities as shown in Figure 4.77 (c, f, i, l) and Figure 4.81. The formation of filaments has been reported for AZ91 alloy in the temperature range of (623 – 698) K [277], Mg–15%Al–1%Zn alloy in the temperature range of (548 – 598) K [189] and in AZ61 alloy in the temperature range of (573 – 673) K [294]. The filaments appear to have reconnected the disconnected grains and grain boundaries and relinked the

cavities at the final stage of superplastic deformation. These fibres were formed and aligned in the direction of tension, and their lengths increased with decreasing strain rate and increasing temperature. Thus, the superplastic elongations were enhanced and maintained by the continuous fibrous structures at the slowest strain rate and elevated temperatures [189][277][294]. The micro–superplasticity of filaments in superplastic materials has been proposed to explain the superplastic elongations [189][295] as shown in Figures 4.77 (c, f, i, l) and Figure 4.81.

EDS analysis was conducted on matrix, grain boundary and filament as shown in Figure 4.84, for a sample processed in HPT for N = 10 turns and then tested at a temperature of 573 K using a strain rate of 1×10^{-4} s^{-1}. It can be seen that the alloy has oxidized since the testing was conducted in the air, as the chemical analysis revealed the presence of oxygen on the grain and grain boundary. The filaments were oxidized also but showed the presence of a higher aluminium level, 26.13 %, than in the structures of the grains and grain boundaries (9.97 % and 7.87 %, respectively). Therefore, it can be concluded that the filaments were composed mainly of the β–phase as shown in previous work [189].

The variation in the average grain size as observed using SEM is illustrated in Figures (4.82, 4.83) for tensile samples with increasing testing temperature using different strain rates. It can be seen that the processed alloy with fine particles of β–phase retained its grain size below 10 μm over the range of subsequent testing temperatures, strain rates and times. The alloy exhibited only modest grain growth at lower temperature and / or high strain rates (lower times), and a limited grain growth at higher temperature and slow strain rates (higher times at temperature). Moreover, it was found that presence of a high area fraction of these fine particles retarded cavity formation at elevated temperatures and slow strain rates due to softening of these particles at temperatures over 573 K [296].

Chapter Six: Conclusions

6. CONCLUSIONS

1. The AZ91 magnesium alloy has effectively processed by HPT at room temperature up to 10 turns, which was not applicable using ECAP at room temperature. The capability of HPT processing of AZ91 magnesium alloy at room temperature can be attributed to the presence of the hydrostatic pressure, the geometry of the processing zone and the unidirectional nature of torsional straining during the HPT processing.

2. An ultrafine–grained microstructure of the α–Mg solid solution and nano–sized particles of β–phase has developed during HPT processing with increasing the number of turns up to 10 turns. The extensive grain refinement with average crystallite size (subgrain size) of 35 nm was found in the alloy processed at 296 K, where the processing at 423 K and 473 K has been refined by twinning segmentation of the original grains into smaller grains with average crystallite size (subgrain size) of 60 nm.

3. The twins have observed at all processing temperatures. The occurrence of twinning during processing at 296 K has induced by the need for re–orientation of the microstructure towards the slip and for accommodating the severe plastic deformation.

4. The chemical composition of the alloy before and after the HPT processing has been unaltered indicating no chemical changes by the processing at room temperature.

5. Fragmentation and alignment of the β–phase in the direction of torsional strain have observed during the processing. This phase has refined into nano–sized particles with average sizes of 200 nm indicating the very high level of plastic deformation that imposed into the alloy during the HPT. The area fraction of the β–phase particles has increased throughout the processed alloy with increasing the number of turns.

6. Limited grain growth has found at the higher processing temperatures and number of turns, where this growth has been retarded by the high fraction of nano–sized particles of the β–phase.

7. The microstructural homogeneity has developed gradually at relatively low number of turns using the lower processing temperature and it continues with increasing the number of turns as indicated by microhardness measurements, TEM and XRD across horizontal and vertical cross–sections of the processed samples. A local heterogeneity was found along the vertical cross–sections of the processed samples due to the difference in friction coefficients between the upper and lower anvils.

8. The development in microhardness towards the homogeneity across the horizontal and vertical cross–sections of the processed samples with increasing the number of turns has achieved earlier in the alloy processed at 296 K rather than at 423 K and 473 K as revealed by the microstructural observations and microhardness measurements. A significant improvement in the strength of the alloy has been found after the HPT processing at all processing temperatures as shown by microhardness measurements. The different values of the applied pressure in the HPT processing had no significant differences in the distributions of microhardness.

9. The dislocation density has remarkably developed for the alloy processed at 296 K as the number of turns increased rather than alloy processed at 423 K and 473 K. The gradual increase in the dislocation density has been associated by an extensive grain refinement and has resulted in a gradual development in microhardness. The values of dislocation densities were significantly higher than their counterparts after ECAP due to the very higher value of the imposed strain during HPT than in ECAP for the same alloy, the processing at room temperature, and high fraction of β–phase particles. A linear proportion for experimental Hall–Petch relationship has achieved for the alloy processed at 296 K that emphasizes the significant dependence of the strength on grain size.

10. High–strain rate superplasticity was obtained with excellent elongations of 590 % at a testing temperature of 473 K using a strain rate of 1×10^{-2} s^{-1}, 410 % and 860 % at a testing temperature of 573 K using strain rates of 1×10^{-1} s^{-1} and 1×10^{-2} s^{-1}, respectively. Significant low–temperature superplasticity was achieved with maximum elongations of 660 % and 760 % at a testing temperature of 423 K and using strain rates of 1×10^{-3} s^{-1} and 1×10^{-4} s^{-1}, respectively.

11. The samples processed by HPT at room temperature revealed fine equiaxed grains with significant thermal stability at all testing temperatures and strain rates. The thermal stability of the processed alloy was attributed to the ultrafine grains produced by HPT at room temperature and to the high fraction of nano–sized β–phase particles.

12. Equiaxed microstructures and high values of strain–rate sensitivity indicate that grain–boundary sliding was the main deformation mechanism during the high–strain rate superplasticity regime. Glide–dislocation creep accommodated with grain–boundary sliding is suggested as the deformation mechanisms operating during the low–temperature superplasticity regime. At high temperature and slow strain rate the grain–boundary sliding accommodated with a diffusion creep mechanism.

13. The fibrous structures were mainly composed of β–phase and they enhanced the superplasticity at high temperatures and low strain rates through resisting the cavitation and relinking the disconnected grains.

Chapter Seven: Future Work

7. FUTURE WORK

1. Investigation of the microstructural evolution of the alloy at different processing temperatures and number of turns using TEM techniques. This would allow better definition of the mechanisms and stages of the grain refinement at different processing conditions, revealing in detail the role of twinning and stacking faults on development of the ultrafine–grained microstructure, the presence of dislocations in matrix and β–phase and matrix/β–phase interface, inspection of the interaction of matrix \ nano–particles of β–phase and twin \ nano–particles of β–phase and their influence on the strengthening and tensile behaviour of the processed alloy.

2. Using EBSD techniques to study the microstructural evolution of the alloy under different processing conditions. This analysis can be used to investigate the dynamic recrystallization, twin density, population of high–angle grain boundaries, and development of grain refinement with regards to dynamically recrystallized grains, twin subdivision and dynamic precipitation of the β–phase and its nano–sized particles. All these observations would be used to correlate the resultant mechanical properties with the observed microstructural evolution.

3. Investigation of the tensile properties of the alloy processed at 423 K and 473 K in HPT including the microstructure observations after the tensile test. This would show the effect of dynamic recrystallization of microstructure and dynamic participation of β–phase of the resultant properties and thermal stability of the alloy during the tensile test.

4. A model for strengthening in the alloy processed in HPT at different temperatures, including the effect of grain refinement, the nano–sized particles of the β–phase, and the twins.

REFERENCES

[1] A. P. Zhilyaev and T. G. Langdon, *Using high-pressure torsion for metal processing: Fundamentals and applications,* Progress in Materials Science, vol. 53, no. 6, pp. 893–979, 2008.

[2] E. O. HALL, *The Deformation and Ageing of Mild Steel: III Discussion of Results,* Proc. Phys. Soc. B, vol. 64, pp. 747–753, 1951.

[3] N. J. Petch, *The cleavage strength of polycrystals,* I. Iron Steel Inst., vol. 174, pp. 25–28, 1953.

[4] R. Armstrong, I. Codd, R. M. Douthwaite, and N. J. Petch, *The plastic deformation of polycrystalline aggregates,* Philosophical Magazine, vol. 7, no. 73, pp. 45–58, 1962.

[5] R. W. Armstrong, *The influence of polycrystal grain size on several mechanical properties of materials,* Metallurgical and Materials Transactions, vol. 1, no. 5, pp. 1169–1176, 1970.

[6] R. Z. Valiev, R. K. Islamgaliev, and I. V. Alexandrov, *Bulk nanostructured materials from severe plastic deformation,* vol. 45, no. 2. 2000.

[7] R. Z. Valiev, *Nanostructuring of metals by severe plastic deformation for advanced properties,* Nature materials, vol. 3, pp. 511–516, 2004.

[8] V. M. Segal, *Materials processing by simple shear,* Materials Science and Engineering: A, vol. 197, no. 2, pp. 157–164, 1995.

[9] T. V. Padfield, *Metallography of Magnesium and its Alloys,* in *ASM Handbook,* vol. 9, USA: ASM International, 2004, pp. 801–815.

[10] M. Mabuchi, H. Iwasaki, K. Yanase, and K. Higashi, *Low temperature superplasticity in an AZ91 magnesium alloy processed by ECAE,* Scripta Materialia, vol. 36, pp. 681–686, 1997.

[11] B. L. Mordike and T. Ebert, *Magnesium Properties — applications — potential,* vol. 302, pp. 37–45, 2001.

[12] H. Friedrich and S. Schumann, *Research for a "new age of magnesium" in the automotive industry,* Journal of Materials Processing Technology, vol. 117, no. 3, pp. 276–281, 2001.

[13] A. Yamashita, Z. Horita, and T. G. Langdon, *Improving the mechanical properties of magnesium and a magnesium alloy through severe plastic deformation,* Materials Science and Engineering A, vol. 300, no. 1–2, pp. 142–147, 2001.

[14] P. Serre, R. B. Figueiredo, N. Gao, and T. G. Langdon, *Influence of strain rate on the characteristics of a magnesium alloy processed by high-pressure torsion,* Materials Science and Engineering: A, vol. 528, no. 10–11, pp. 3601–3608, 2011.

[15] K. Xia, J. T. Wang, X. Wu, G. Chen, and M. Gurvan, *Equal channel angular pressing of magnesium alloy AZ31,* Materials Science and Engineering: A, vol. 410–411, pp. 324–327, 2005.

[16] K. U. Kainer, *Magnesium– Alloys and Technology*. Germany: Wiley-VCH Verlag GmbH & Co. KGaA, 2003.

[17] K. Matsubara, Y. Miyahara, Z. Horita, and T. G. Langdon, *Developing superplasticity in a magnesium alloy through a combination of extrusion and ECAP,* Acta Materialia, vol. 51, pp. 3073–3084, 2003.

[18] M. Kai, Z. Horita, and T. G. Langdon, *Developing grain refinement and superplasticity in a magnesium alloy processed by high-pressure torsion,* Materials Science and Engineering: A, vol. 488, pp. 117–124, 2008.

[19] K. Kubota, M. Mabuchi, and K. Higashi, *Processing and mechanical properties of fine-grained magnesium alloys,* Journal of Materials Science, vol. 4, pp. 2255–2262, 1999.

[20] N. V. Ravi Kumar, J. J. Blandin, C. Desrayaud, F. Montheillet, and M. Suéry, *Grain refinement in AZ91 magnesium alloy during thermomechanical processing,* Materials Science and Engineering: A, vol. 359, no. 1–2, pp. 150–157, 2003.

[21] E. A. Brandes and G. B. Brook, *Smithells Light Metals Handbook*. UK: Butterworth-Heinemann, 1998.

[22] H. K. Lin, J. C. Huang, and T. G. Langdon, *Relationship between texture and low temperature superplasticity in an extruded AZ31 Mg alloy processed by ECAP,* Materials Science and Engineering: A, vol. 402, no. 1–2, pp. 250–257, 2005.

[23] I. J. Polmear, *Magnesium alloys and applications,* Materials Science and Technology, vol. 10, no. 1, pp. 1–16, 1994.

[24] W. D. Callister and D. Rethwisch, *Materials science and engineering: an introduction*. USA: John Wiley & Sons, Inc., 2007.

[25] G. E. Dieter and D. Bacon, *Mechanical Metallurgy*. UK: McGraw-Hill Book Company Limited, 1988.

[26] R. E. Smallman and A. H. W. Ngan, *Physical Metallurgy and Advanced Materials*. India: Butterworth-Heinemann, 2007.

[27] F. Czerwinski, *Magnesium and Its Alloys,* in *Magnesium Injection Molding*, USA: Springer Science and Business Media LLC, 2007, pp. 1–79.

[28] *Magnesium Elektron Comapny UK - Elektron AZ91-Data sheet,* UK, 2011.

[29] K. Braszczynska, *Precipitates of γ –Mg17Al12 Phase in AZ91 Alloy,* Magnesium Alloys - Design, Processing and Properties, pp. 95–112, 2011.

[30] S. Housh, M. Mikucki, and A. Stevenson, *Selection and Application of Magnesium and Magnesium Alloys,* in *ASM Handbook: Properties and Selection: Nonferrous Alloys and Special-Purpose Materials*, USA: ASM International, 2004, pp. 1424–1589.

[31] A. Kiełbus, M. Sozańska, and L. Ciżek, *Microstructural Characterisation of AZ91 Magnesium Alloy,* in *Magnesium: Proceedings of the 6th International Conference Magnesium Alloys and Their Applications*, K. U. Kainer, Ed. Germany: WILEY-VCH Verlag GmbH & Co. KG aA, Weinheim, 2004, pp. 190–195.

[32] B. L. Mordike and P. Lukác, *Physical Metallurgy,* in *Magnesium Technology: Metallurgy, Design Data, Applications*, H. E. Friedrich and B. L. Mordike, Eds. Germany, 2006, pp. 63–107.

[33] T. J. Chen, R. Q. Wang, Y. Ma, and Y. Hao, *Semisolid microstructure evolution of AZ91D magnesium alloy refined by Al-Ti-B,* Materials Research, vol. 14, no. 4, pp. 532–540, 2011.

[34] N. Hort, Y. Huang, and K. U. Kainer, *Intermetallics in Magnesium Alloys,* Advanced Engineering Materials, vol. 8, no. 4, pp. 235–240, 2006.

[35] S. T. Niknejad, L. Liu, T. Nguyen, M.-Y. Lee, S. Esmaeili, and N. Y. Zhou, *Effects of Heat Treatment on Grain-Boundary β-Mg17Al12 and Fracture Properties of Resistance Spot-Welded AZ80 Mg Alloy,* Metallurgical and Materials Transactions A, vol. 44, no. 8, pp. 3747–3756, 2013.

[36] P. G. Partridge, *The crystallography and deformation modes of hexagonal close-packed metals,* International Materials Reviews, vol. 12, no. 1, pp. 169–194, 1967.

[37] D. R. Thornburg and H. R. Piehler, *An analysis of constrained deformation by slip and twinning in hexagonal close packed metals and alloys,* Metallurgical Transactions A, vol. 6, no. 8, pp. 1511–1523, 1975.

[38] S. Balasubramanian and L. Anand, *Plasticity of initially textured hexagonal polycrystals at high homologous temperatures: application to titanium,* Acta Materialia, vol. 50, no. 1, pp. 133–148, 2002.

[39] A. Staroselsky and L. Anand, *A constitutive model for hcp materials deforming by slip and twinning: Application to magnesium alloy AZ31B,* International Journal of Plasticity, vol. 19, no. 10, pp. 1843–1864, 2003.

[40] A. Luque, M. Ghazisaeidi, and W. A. Curtin, *Deformation modes in magnesium (0 0 0 1) and (01-11) single crystals: simulations versus experiments,* Modelling and Simulation in Materials Science and Engineering, vol. 21, no. 4, p. 045010, 2013.

[41] J. Koike, *Enhanced deformation mechanisms by anisotropic plasticity in polycrystalline Mg alloys at room temperature,* Metallurgical and Materials Transactions A, vol. 36, no. 7, pp. 1689–1696, 2005.

[42] S. Sandlöbes, M. Friák, S. Zaefferer, A. Dick, S. Yi, D. Letzig, Z. Pei, L.-F. Zhu, J. Neugebauer, and D. Raabe, *The relation between ductility and stacking fault energies in Mg and Mg–Y alloys,* Acta Materialia, vol. 60, no. 6–7, pp. 3011–3021, 2012.

[43] A. Rohatgi, K. S. Vecchio, and G. T. Gray, *The influence of stacking fault energy on the mechanical behavior of Cu and Cu-Al alloys: Deformation twinning, work hardening, and dynamic recovery,* Metallurgical and Materials Transactions A, vol. 32, pp. 135–145, 2001.

[44] M. Ahlers, *Stacking fault energy and mechanical properties,* Metallurgical Transactions, vol. 1, no. 9, pp. 2415–2428, 1970.

[45] Q. M. Hu and R. Yang, *Basal-plane stacking fault energy of hexagonal close-packed metals based on the Ising model,* Acta Materialia, vol. 61, no. 4, pp. 1136–1145, 2013.

[46] K. Hazeli, A. Sadeghi, M. O. Pekguleryuz, and A. Kontsos, *Damping and dynamic recovery in magnesium alloys containing strontium,* Materials Science and Engineering A, vol. 589, pp. 275–279, 2014.

[47] H. Somekawa, K. Hirai, H. Watanabe, Y. Takigawa, and K. Higashi, *Dislocation creep behavior in Mg–Al–Zn alloys,* Materials Science and Engineering: A, vol. 407, pp. 53–61, 2005.

[48] M. Muzyk, Z. Pakiela, and K. J. Kurzydlowski, *Ab initio calculations of the generalized stacking fault energy in aluminium alloys,* Scripta Materialia, vol. 64, no. 9, pp. 916–918, 2011.

[49] M. S. Soliman, *The high-temperature creep behaviour of an Al-1wt%Cu solid-solution alloy,* Journal of Materials Science, vol. 28, pp. 4483–4488, 1993.

[50] Y. H. Zhao, X. Z. Liao, Y. T. Zhu, Z. Horita, and T. G. Langdon, *Influence of stacking fault energy on nanostructure formation under high pressure torsion,* Materials Science and Engineering: A, vol. 410–411, pp. 188–193, 2005.

[51] C. X. Huang, W. Hu, G. Yang, Z. F. Zhang, S. D. Wu, Q. Y. Wang, and G. Gottstein, *The effect of stacking fault energy on equilibrium grain size and tensile properties of nanostructured copper and copper-aluminum alloys processed by equal channel angular pressing,* Materials Science and Engineering A, vol. 556, pp. 638–647, 2012.

[52] S. Qu, X. H. An, H. J. Yang, C. X. Huang, G. Yang, Q. S. Zang, Z. G. Wang, S. D. Wu, and Z. F. Zhang, *Microstructural evolution and mechanical properties of Cu-Al alloys subjected to equal channel angular pressing,* Acta Materialia, vol. 57, no. 5, pp. 1586–1601, 2009.

[53] E. J. Mittemeijer, *Fundamentals of materials science: The microstructure-property relationship using metals as model systems*. Germany: Springer Berlin Heidelberg, 2011.

[54] R. Abbaschian, L. Abbaschian, and R. E. Reed-Hill, *Physical Metallurgy Principles*, 4th ed. USA: Cengage Learning, 2009.

[55] F. J. Humphreys and M. Hatherly, *Recrystallization and related annealing phenomena*, 2nd ed. Netherlands: Elsevier, 2004.

[56] B. Verlinden, J. Driver, I. Samajdar, and R. Doherty, *Thermo-mechanical processing of metallic materials*, First edit. UK: Elsevier, 2007.

[57] C. Liao, H. Wu, S. Lee, F. Zhu, H. Liu, and C. Wu, *Strain-dependent constitutive analysis of extruded AZ61 Mg alloy under hot compression,* Materials Science and Engineering: A, vol. 565, pp. 1–8, 2013.

[58] Y. T. Zhu and T. G. Langdon, *The fundamentals of nanostructured materials processed by severe plastic deformation,* Journal of Metals, vol. 56, no. 10, pp. 58–63, 2004.

[59] Y. T. Zhu, T. C. Lowe, and T. G. Langdon, *Performance and applications of nanostructured materials produced by severe plastic deformation,* Scripta Materialia, vol. 51, no. 8, pp. 825–830, 2004.

[60] M. J. Zehetbauer and Y. T. Zhu, *Bulk Nanostructured Materials*. USA: John Wiley & Sons, Inc., 2009.

[61] P. B. Prangnell, J. R. Bowen, and P. J. Apps, *Ultra-fine grain structures in aluminium alloys by severe deformation processing,* Materials Science and Engineering: A, vol. 375–377, no. 1–2, pp. 178–185, 2004.

[62] N. Hansen, *Microstructural evolution during forming of metals,* Journal of Materials Science and Technology, vol. 17, no. 4, pp. 409–412, 2001.

[63] D. A. Hughes and N. Hansen, *High angle boundaries formed by grain subdivision*

mechanisms, Acta Materialia, vol. 45, no. 9, pp. 3871–3886, 1997.

[64] N. Hansen, X. Huang, and D. A. Hughes, *Microstructural evolution and hardening parameters,* Materials Science and Engineering A, vol. 317, no. 1–2, pp. 3–11, 2001.

[65] A. Gholinia, P. B. Prangnell, and M. V. Markushev, *The effect of strain path on the development of deformation structures in severely deformed aluminium alloys processed by ECAE,* Acta Materialia, vol. 48, no. 5, pp. 1115–1130, 2000.

[66] Y. Todaka, M. Umemoto, A. Yamazaki, J. Sasaki, and K. Tsuchiya, *Effect of Strain Path in High-Pressure Torsion Process on Hardening in Commercial Purity Titanium,* Materials Transactions, vol. 49, no. 1, pp. 47–53, 2008.

[67] J. Zhang, N. Gao, and M. J. Starink, *Microstructure development and hardening during high pressure torsion of commercially pure aluminium: Strain reversal experiments and a dislocation based model,* Materials Science and Engineering A, vol. 528, no. 6, pp. 2581–2591, 2011.

[68] F. J. Humphreys, P. B. Prangnell, J. R. Bowen, A. Gholinia, and C. Harris, *Developing stable fine-grain microstructures by large strain deformation,* Philosophical Transactions of the Royal Society A: Mathematical, Physical and Engineering Sciences, vol. 357, no. 1756, pp. 1663–1681, 1999.

[69] Y. T. Zhu and T. C. Lowe, *Observations and issues on mechanisms of grain refinement during ECAP process,* Materials Science and Engineering A, vol. 291, no. 1, pp. 46–53, 2000.

[70] V. M. Segal, *Equal channel angular extrusion: from macromechanics to structure formation,* Materials Science and Engineering A, vol. 271, no. 1–2, pp. 322–333, 1999.

[71] K. Nakashima, Z. Horita, M. Nemoto, and T. G. Langdon, *Influence of channel angle on the development of ultrafine grains in equal-channel angular pressing,* Acta Materialia, vol. 46, no. 5, pp. 1589–1599, 1998.

[72] R. Z. Valiev and T. G. Langdon, *Principles of equal-channel angular pressing as a processing tool for grain refinement,* Progress in Materials Science, vol. 51, no. 7, pp. 881–981, 2006.

[73] Y. Iwahashi, J. Wang, Z. Horita, M. Nemoto, and T. G. Langdon, *Principle of equal-channel angular pressing for the processing of ultra-fine grained materials,* Scripta Materialia, vol. 35, no. 2, pp. 143–146, 1996.

[74] K. Nakashima, Z. Horita, M. Nemoto, and T. G. Langdon, *Development of a multi-pass facility for equal-channel angular processing to high total strains,* Materials Science and Engineering A, vol. 281, pp. 82–87, 2000.

[75] N. Tsuji, Y. Saito, H. Utsunomiya, and S. Tanigawa, *Ultra-fine grained bulk steel produced by accumulative roll-bonding (ARB) process,* Scripta Materialia, vol. 40, no. 7, pp. 795–800, 1999.

[76] Y. Saito, H. Utsunomiya, N. Tsuji, and T. Sakai, *Novel ultra-high straining process for bulk materials—development of the accumulative roll-bonding (ARB) process,* Acta Materialia, vol. 47, no. 2, pp. 579–583, 1999.

[77] Y. Beygelzimer, V. Varyukhin, S. Synkov, and D. Orlov, *Useful properties of twist*

extrusion, Materials Science and Engineering A, vol. 503, no. 1–2, pp. 14–17, 2009.

[78] V. V. Stolyarov, Y. E. Beigel, D. V. Orlov, and R. Z. Valiev, *Refinement of Microstructure and Mechanical Properties of Titanium Processed by Twist Extrusion and Subsequent Rolling*, Physics of Metals, vol. 99, no. 2, pp. 204–211, 2005.

[79] M. Berta, D. Orlov, and P. B. Prangnell, *Grain refinement response during twist extrusion of an Al-0.13 % Mg alloy*, International Journal of Materials Research, vol. 98, no. 3, pp. 200–204, 2007.

[80] R. Z. Valiev, *Structure and mechanical properties of ultrafine-grained metals*, Materials Science and Engineering: A, vol. 234–236, pp. 59–66, 1997.

[81] R. Z. Valiev, N. A. Enikeev, M. Y. Murashkin, V. U. Kazykhanov, and X. Sauvage, *On the origin of the extremely high strength of ultrafine-grained Al alloys produced by severe plastic deformation*, Scripta Materialia, vol. 63, no. 9, pp. 949–952, 2010.

[82] A. V. Sergueeva, V. V. Stolyarov, R. Z. Valiev, and A. K. Mukherjee, *Advanced mechanical properties of pure titanium with ultrafine grained structure*, Scripta Materialia, vol. 45, pp. 747–752, 2001.

[83] V. A. Moskalenko and A. R. Smirnov, *Temperature effect on formation of reorientation bands in α-Ti*, Materials Science and Engineering: A, vol. 246, no. 1–2, pp. 282–288, 1998.

[84] D. A. Konstantinidis and E. C. Aifantis, *On the "anomalous" hardness of nanocrystalline materials*, Nanostructured Materials, vol. 10, no. 7, pp. 1111–1118, 1998.

[85] G. A. Salishchev, R. M. Galeyev, S. P. Malysheva, and M. M. Myshlyaev, *Structure and density of submicrocrystalline titanium produced by severe plastic deformation*, Nanostructured Materials, vol. 11, no. 3, pp. 407–414, 1999.

[86] V. V. Stolyarov, Y. T. Zhu, I. V. Alexandrov, T. C. Lowe, and R. Z. Valiev, *Influence of ECAP routes on the microstructure and properties of pure Ti*, Materials Science and Engineering: A, vol. 299, no. 1–2, pp. 59–67, 2001.

[87] V. V. Stolyarov, Y. T. Zhu, T. C. Lowe, and R. Z. Valiev, *Microstructure and properties of pure Ti processed by ECAP and cold extrusion*, Materials Science and Engineering A, vol. 303, no. 1–2, pp. 82–89, 2001.

[88] G. J. Davies, J. W. Edington, C. P. Cutler, and K. a. Padmanabhan, *Superplasticity: A review*, Journal of Materials Science, vol. 5, no. 12, pp. 1091–1102, 1970.

[89] T. G. Langdon, *Achieving superplasticity in ultrafine-grained metals*, Mechanics of Materials, vol. 67, pp. 2–8, 2013.

[90] I. Charit and R. S. Mishra, *Superplasticity and Superplastic Forming*, in *Materials Processing Handbook*, M. Powers, E. Lavernia, J. Groza, and J. Shackelford, Eds. CRC Press, 2007, pp. 1–35.

[91] T. G. Nieh, J. Wadsworth, and O. D. Sherby, *Superplasticity in Metals and Ceramics*. UK: Cambridge University Press, 2005.

[92] N. Ridley, *Superplastic microstructures*, Materials Science and Technology, vol. 6, no. 11, pp. 1145–1156, 1990.

[93] D. M. R. Taplin, G. L. Dunlop, and T. G. Langdon, *Flow and Failure of Superplastic Materials,* Annual Review of Materials Science, vol. 9, no. 1, pp. 151–189, 1979.

[94] D. Lee, *On the nature of superplastic deformation in the Mg-Al eutectic alloy, Acta Metallurgica*, vol. 17. pp. 1057–1069, 1969.

[95] A. K. Mukherjee, *Deformation Mechanisms in Superplasticity,* Annual Review of Materials Science, vol. 9, no. 1, pp. 191–217, 1979.

[96] F. A. Mohamed, M. M. I. Ahmed, and T. G. Langdon, *Factors influencing ductility in the superplastic Zn-22 Pct Al eutectoid,* Metallurgical Transactions A, vol. 8, no. 6, pp. 933–938, 1977.

[97] T. G. Langdon, *The mechanical properties of superplastic materials,* Metallurgical Transactions A, vol. 13, pp. 689–701, 1982.

[98] R. B. Figueiredo and T. G. Langdon, *Strategies for achieving high strain rate superplasticity in magnesium alloys processed by equal-channel angular pressing,* Scripta Materialia, vol. 61, no. 1, pp. 84–87, 2009.

[99] Y. Harai, M. Kai, K. Kaneko, Z. Horita, and T. G. Langdon, *Microstructural and Mechanical Characteristics of AZ61 Magnesium Alloy Processed by High-Pressure Torsion,* Materials Transactions, vol. 49, pp. 76–83, 2008.

[100] H. Hasegawa, S. Komura, A. Utsunomiya, and Z. Horita, *Thermal stability of ultrafine-grained aluminum in the presence of Mg and Zr additions,* Materials Science and Engineering A, vol. 265, pp. 188–196, 1999.

[101] P. B. Berbon, S. Komura, A. Utsunomiya, Z. Horita, M. Furukawa, M. Nemoto, and T. G. Langdon, *An Evaluation of Superplasticity in Aluminum-Scandium Alloys Processed by Equal-Channel Angular Pressing,* Materials Transactions JIM, vol. 40, pp. 772–778, 1999.

[102] S. Lee, M. Furukawa, Z. Horita, and T. G. Langdon, *Developing a superplastic forming capability in a commercial aluminum alloy without scandium or zirconium additions,* Materials Science and Engineering A, vol. 342, pp. 294–301, 2003.

[103] C. Xu, M. Furukawa, Z. Horita, and T. G. Langdon, *Using ECAP to achieve grain refinement, precipitate fragmentation and high strain rate superplasticity in a spray-cast aluminum alloy,* Acta Materialia, vol. 51, no. 20, pp. 6139–6149, 2003.

[104] R. I. Todd, *Critical review of mechanism of superplastic deformation in fine grained metallic materials,* Materials Science and Technology, vol. 16, no. 11, pp. 1287–1294, 2000.

[105] J. Pilling and N. Ridley, *Superplasticity in Crystalline Solids*. UK: Institute of Metals, 1989.

[106] K. S. Raghavan, *Superplasticity,* Bulletin of Materials Science, vol. 6, no. 4, pp. 689–698, 1984.

[107] T. G. Langdon, *An Analysis of Flow Mechanisms in High Temperature Creep and Superplasticity,* Materials Transactions, vol. 46, pp. 1951–1956, 2005.

[108] C. Herring, *Diffusional Viscosity of a Polycrystalline Solid,* Journal of Applied Physics, vol. 21, pp. 437–445, 1950.

[109] J. Friedel, *Dislocations*. USA: Pergamon, 1964.

[110] R. Coble, *Model for boundary diffusion-controlled creep in polycrystalline materials*, Journal of Applied Physics, vol. 34, no. 6, pp. 1679–1682, 1963.

[111] W. Rosenhain and D. Ewen, *The intercrystalline cohesion of metals*, Journal of the Institute of Metals, vol. 8, pp. 149–173, 1912.

[112] W. Rosenhain and D. Ewen, *The intercrystalline cohesion of metals (Second paper)*, Journal of the Institute of Metals, vol. 10, pp. 119–141, 1913.

[113] R. L. Bell and T. G. Langdon, *An investigation of grain-boundary sliding during creep*, Journal of Materials Science, vol. 2, no. 4, pp. 313–323, 1967.

[114] R. Gifkins, *Grain-boundary sliding and its accommodation during creep and superplasticity*, Metallurgical Transactions A, vol. 7, pp. 1225–1232, 1976.

[115] T. Johannesson and A. Thölén, *The Role of Grain Boundaries in Creep Deformation*, Metal Science, vol. 6, no. 1, pp. 189–194, 1972.

[116] I. M. Lifshitz, *On The Theory Of Diffusion-Viscous Flow Of Polycrystalline Bodies*, Soviet Physics Jetp-Ussr, vol. 17, no. 4, pp. 909–920, 1963.

[117] T. G. Langdon, *Grain boundary sliding revisited: Developments in sliding over four decades*, Journal of Materials Science, vol. 41, no. 3, pp. 597–609, 2006.

[118] A. Ball and M. M. Hutchinson, *Superplasticity in the aluminum-zinc eutectoid*, Metal Science Journal, vol. 3, pp. 1–7, 1969.

[119] M. E. Kassner and M. T. Perez-Prado, *Fundamentals of creep in metals and alloys*. UK: Elsevier Ltd., 2004.

[120] A. K. Mukherjee, *The rate controlling mechanism in superplasticity*, Materials Science and Engineering, vol. 8, no. 2, pp. 83–89, 1971.

[121] R. C. Gifkins, *Grain rearrangements during superplastic deformation*, Journal of Materials Science, vol. 13, no. 9, pp. 1926–1936, 1978.

[122] R. C. Gifkins, *Grain-boundary participation in high-temperature deformation: An historical review*, Materials Characterization, vol. 32, pp. 59–77, 1994.

[123] M. F. Ashby and R. A. Verrall, *Diffusion-accommodated flow and superplasticity, Acta Metallurgica*, vol. 21. pp. 149–163, 1973.

[124] R. J. Arsenault, *Plastic Deformation of Materials: Treatise on Materials Science and Technology*. UK: Elsevier Science, 2013.

[125] T. H. Courtney, *Mechanical Behavior of Materials*, 2nd ed. USA: Waveland Press, 2005.

[126] J. Weertman, *Steady-State Creep through Dislocation Climb*, Journal of Applied Physics, vol. 28, no. 3, p. 362, 1957.

[127] J. Pelleg, *Mechanical properties of materials*. Netherlands: Springer Netherlands, 2013.

[128] G. Sakai, Z. Horita, and T. G. Langdon, *Grain refinement and superplastic flow in an aluminum alloy processed by high-pressure torsion,* Materials Science and Engineering A, vol. 393, pp. 344–351, 2005.

[129] C. Xu, Z. Horita, and T. G. Langdon, *The evolution of homogeneity in an aluminum alloy processed using high-pressure torsion,* Acta Materialia, vol. 56, no. 18, pp. 5168–5176, 2008.

[130] Y. Ivanisenko, W. Lojkowski, R. Z. Valiev, and H.-J. Fecht, *The mechanism of formation of nanostructure and dissolution of cementite in a pearlitic steel during high pressure torsion,* Acta Materialia, vol. 51, no. 18, pp. 5555–5570, 2003.

[131] R. Z. Valiev, Y. V. Ivanisenko, E. F. Rauch, and B. Baudelet, *Structure and deformaton behaviour of Armco iron subjected to severe plastic deformation,* Acta Materialia, vol. 44, no. 12, pp. 4705–4712, 1996.

[132] J. Zhang, N. Gao, and M. J. Starink, *Al-Mg-Cu based alloys and pure Al processed by high pressure torsion: The influence of alloying additions on strengthening,* Materials Science and Engineering A, vol. 527, no. 15, pp. 3472–3479, 2010.

[133] J. Zhang, M. J. Starink, N. Gao, and W. Zhou, *Effect of Mg addition on strengthening of aluminium alloys subjected to different strain paths in high pressure torsion,* Materials Science and Engineering A, vol. 528, no. 4–5, pp. 2093–2099, 2011.

[134] M. V. Degtyarev, T. I. Chashchukhina, L. M. Voronova, A. M. Patselov, and V. P. Pilyugin, *Influence of the relaxation processes on the structure formation in pure metals and alloys under high-pressure torsion,* Acta Materialia, vol. 55, no. 18, pp. 6039–6050, 2007.

[135] A. P. Zhilyaev, T. R. McNelley, and T. G. Langdon, *Evolution of microstructure and microtexture in fcc metals during high-pressure torsion,* Journal of Materials Science, vol. 42, no. 5, pp. 1517–1528, 2007.

[136] A. P. Zhilyaev, G. V. Nurislamova, B. K. Kim, M. D. Baró, J. A. Szpunar, and T. G. Langdon, *Experimental parameters influencing grain refinement and microstructural evolution during high-pressure torsion,* Acta Materialia, vol. 51, no. 3, pp. 753–765, 2003.

[137] M. Kawasaki, R. B. Figueiredo, and T. G. Langdon, *An investigation of hardness homogeneity throughout disks processed by high-pressure torsion,* Acta Materialia, vol. 59, no. 1, pp. 308–316, 2011.

[138] A. Vorhauer and R. Pippan, *On the homogeneity of deformation by high pressure torsion,* Scripta Materialia, vol. 51, pp. 921–925, 2004.

[139] C. Xu, Z. Horita, and T. Langdon, *The evolution of homogeneity in processing by high-pressure torsion,* Acta Materialia, vol. 55, no. 1, pp. 203–212, 2007.

[140] A. P. Zhilyaev, K. Oh-ishi, T. G. Langdon, and T. R. McNelley, *Microstructural evolution in commercial purity aluminum during high-pressure torsion,* Materials Science and Engineering: A, vol. 410–411, pp. 277–280, 2005.

[141] A. P. Zhilyaev, S. Lee, G. V. Nurislamova, R. Z. Valiev, and T. G. Langdon, *Microhardness and microstructural evolution in pure nickel during high-pressure torsion,* Scripta Materialia, vol. 44, no. 12, pp. 2753–2758, 2001.

[142] G. Sakai, Z. Horita, and T. G. Langdon, *Grain refinement and superplasticity in an*

aluminum alloy processed by high-pressure torsion, Materials Science and Engineering A, vol. 393, no. 1–2, pp. 344–351, 2005.

[143] M. Kawasaki and T. G. Langdon, *The significance of strain reversals during processing by high-pressure torsion,* Materials Science and Engineering: A, vol. 498, no. 1–2, pp. 341–348, 2008.

[144] M. Kawasaki, S. N. Alhajeri, C. Xu, and T. G. Langdon, *The development of hardness homogeneity in pure aluminum and aluminum alloy disks processed by high-pressure torsion,* Materials Science and Engineering: A, vol. 529, pp. 345–351, 2011.

[145] M. Kawasaki, B. Ahn, and T. G. Langdon, *Microstructural evolution in a two-phase alloy processed by high-pressure torsion,* Acta Materialia, vol. 58, no. 3, pp. 919–930, 2010.

[146] Z. C. Duan, X. Z. Liao, M. Kawasaki, R. B. Figueiredo, and T. G. Langdon, *Influence of high-pressure torsion on microstructural evolution in an Al-Zn-Mg-Cu alloy,* Journal of Materials Science, vol. 45, no. 17, pp. 4621–4630, 2010.

[147] J. Wongsa-Ngam, M. Kawasaki, Y. Zhao, and T. G. Langdon, *Microstructural evolution and mechanical properties of a Cu–Zr alloy processed by high-pressure torsion,* Materials Science and Engineering: A, vol. 528, no. 25–26, pp. 7715–7722, 2011.

[148] Y. Estrin, A. Molotnikov, C. H. J. Davies, and R. Lapovok, *Strain gradient plasticity modelling of high-pressure torsion,* Journal of the Mechanics and Physics of Solids, vol. 56, no. 4, pp. 1186–1202, 2008.

[149] N. A. Fleck, G. M. Muller, M. F. Ashby, and J. W. Hutchinson, *Strain gradient plasticity: Theory and experiment,* Acta Metallurgica et Materialia, vol. 42, no. 2, pp. 475–487, 1994.

[150] A. Arsenlis and D. M. Parks, *Crystallographic aspects of geometrically-necessary and statistically-stored dislocation density,* Acta Materialia, vol. 47, no. 5, pp. 1597–1611, 1999.

[151] H. Jiang, Y. T. Zhu, D. P. Butt, I. V. Alexandrov, and T. C. Lowe, *Microstructural evolution, microhardness and thermal stability of HPT-processed Cu,* Materials Science and Engineering: A, vol. 290, no. 1–2, pp. 128–138, 2000.

[152] C. W. Su, B. W. Chua, L. Lu, and M. O. Lai, *Properties of severe plastically deformed Mg alloys,* Materials Science and Engineering A, vol. 402, no. 1–2, pp. 163–169, 2005.

[153] H. K. Kim and W. J. Kim, *Microstructural instability and strength of an AZ31 Mg alloy after severe plastic deformation,* Materials Science and Engineering A, vol. 385, no. 1–2, pp. 300–308, 2004.

[154] R. Lapovok, Y. Estrin, M. V. Popov, and T. G. Langdon, *Enhanced superplasticity in a magnesium alloy processed by equal-channel angular pressing with a back-pressure,* Advanced Engineering Materials, vol. 10, no. 5, pp. 429–433, 2008.

[155] R. B. Figueiredo and T. G. Langdon, *Development of structural heterogeneities in a magnesium alloy processed by high-pressure torsion,* Materials Science and Engineering: A, vol. 528, pp. 4500–4506, 2011.

[156] Y. Huang, R. B. Figueiredo, and T. G. Langdon, *Effect of HPT processing temperature on strength of a Mg-Al-Zn alloy,* Reviews on Advanced Materials Science, vol. 31, no. 2, pp. 129–137, 2012.

[157] J. Xu, M. Shirooyeh, J. Wongsa-Ngam, D. Shan, B. Guo, and T. G. Langdon, *Hardness homogeneity and micro-tensile behavior in a magnesium AZ31 alloy processed by equal-channel angular pressing*, Materials Science and Engineering A, vol. 586, pp. 108–114, 2013.

[158] R. B. Figueiredo and T. G. Langdon, *Evaluating the Superplastic Flow of a Magnesium AZ31 Alloy Processed by Equal-Channel Angular Pressing*, Metallurgical and Materials Transactions A, vol. 45, no. 8, pp. 3197–3204, 2013.

[159] J. Stráská, M. Janeček, J. Gubicza, T. Krajňák, E. Y. Yoon, and H. S. Kim, *Evolution of microstructure and hardness in AZ31 alloy processed by high pressure torsion*, Materials Science and Engineering: A, vol. 625, pp. 98–106, 2015.

[160] Z. Li, J. Dong, X. Q. Zeng, C. Lu, and W. J. Ding, *Influence of Mg17Al12 intermetallic compounds on the hot extruded microstructures and mechanical properties of Mg-9Al-1Zn alloy*, Materials Science and Engineering A, vol. 466, no. 1–2, pp. 134–139, 2007.

[161] B. Chen, D.-L. Lin, L. Jin, X.-Q. Zeng, and C. Lu, *Equal-channel angular pressing of magnesium alloy AZ91 and its effects on microstructure and mechanical properties*, Materials Science and Engineering: A, vol. 483–484, pp. 113–116, 2008.

[162] Y. Huang, M. Kawasaki, and T. G. Langdon, *Influence of Anvil Alignment on Shearing Patterns in High-Pressure Torsion*, Advanced Engineering Materials, vol. 15, no. 8, pp. 747–755, 2013.

[163] G. F. Vander Voort, Ed., *Metallography : An Introduction,* in *Metals Handbook: Metallography and Microstructures*, vol. 9, USA: ASM International, 2004, pp. 3–20.

[164] C. G. Derry and J. D. Robson, *Characterisation and modelling of toughness in 6013-T6 aerospace aluminium alloy friction stir welds*, Materials Science and Engineering A, vol. 490, no. 1–2, pp. 328–334, 2008.

[165] B. Mansoor and A. K. Ghosh, *Microstructure and tensile behavior of a friction stir processed magnesium alloy*, Acta Materialia, vol. 60, no. 13–14, pp. 5079–5088, 2012.

[166] K. Venkateswarlu, V. Rajinikanth, A. K. Ray, C. Xu, and T. G. Langdon, *The characteristics of aluminum–scandium alloys processed by ECAP*, Materials Science and Engineering: A, vol. 527, no. 6, pp. 1448–1452, 2010.

[167] T. Zhu, Z. W. Chen, and W. Gao, *Dissolution of Eutectic β-Mg17Al12 Phase in Magnesium AZ91 Cast Alloy at Temperatures Close to Eutectic Temperature*, Journal of Materials Engineering and Performance, vol. 19, no. 6, pp. 860–867, 2010.

[168] H. Mughrabi, *Dual role of deformation-induced geometrically necessary dislocations with respect to lattice plane misorientations and/or long-range internal stresses*, Acta Materialia, vol. 54, no. 13, pp. 3417–3427, 2006.

[169] A. K. Singh, *Advanced X-ray Techniques in Research and Industry*. India: IOS Press, 2005.

[170] K. Máthis, J. Gubicza, and N. H. Nam, *Microstructure and mechanical behavior of AZ91 Mg alloy processed by equal channel angular pressing*, Journal of Alloys and Compounds, vol. 394, pp. 194–199, 2005.

[171] P. Barnes, S. Jacques, and M. Vickers, *Crystallite Size and Strain*, 2006. [Online]. Available: http://pd.chem.ucl.ac.uk/pdnn/peaks/size.htm.

[172] T. Ungár, *Microstructural parameters from X-ray diffraction peak broadening*, Scripta Materialia, vol. 51, no. 8, pp. 777–781, 2004.

[173] T. Ungár, Á. Révész, and A. Borbély, *Dislocations and Grain Size in Electrodeposited Nanocrystalline Ni Determined by the Modified Williamson–Hall and Warren–Averbach Procedures*, Journal of Applied Crystallography, vol. 31, no. 4, pp. 554–558, 1998.

[174] J. Gubicza, *X-Ray Line Profile Analysis in Materials Science*. USA: IGI Global, 2014.

[175] A. L. Hannam and P. T. B. Shaffer, *Revised X-ray diffraction line intensities for silicon carbide polytypes*, Journal of Applied Crystallography, vol. 2, no. 2, pp. 45–48, 1969.

[176] A. L. Ortiz and L. Shaw, *X-ray diffraction analysis of a severely plastically deformed aluminum alloy*, Acta Materialia, vol. 52, no. 8, pp. 2185–2197, 2004.

[177] G. Ribárik and T. Ungár, *Characterization of the microstructure in random and textured polycrystals and single crystals by diffraction line profile analysis*, Materials Science and Engineering: A, vol. 528, no. 1, pp. 112–121, 2010.

[178] *MAUD-Materials Analysis Using Diffraction.* [Online]. Available: http://maud.radiographema.com/.

[179] S. J. Chipera and D. L. Bish, *Fitting Full X-Ray Diffraction Patterns for Quantitative Analysis : A Method for Readily Quantifying Crystalline and Disordered Phases,* Advances in Materials Physics and Chemistry, vol. 3, pp. 47–53, 2013.

[180] H.-J. Lee, B. Ahn, M. Kawasaki, and T. G. Langdon, *Evolution in hardness and microstructure of ZK60A magnesium alloy processed by high-pressure torsion*, Journal of Materials Research and Technology, vol. 4, no. 1, pp. 18–25, 2015.

[181] Y. Chen, N. Gao, G. Sha, S. P. Ringer, and M. J. Starink, *Strengthening of an Al–Cu–Mg alloy processed by high-pressure torsion due to clusters, defects and defect–cluster complexes*, Materials Science and Engineering: A, vol. 627, pp. 10–20, 2015.

[182] J. I. Langford, D. Louër, and P. Scardi, *Effect of a crystallite size distribution on X-ray diffraction line profiles and whole-powder-pattern fitting*, Journal of Applied Crystallography, vol. 33, no. 3, pp. 964–974, 2000.

[183] J. Gubicza, G. Ribárik, G. R. Goren-Muginstein, A. R. Rosen, and T. Ungár, *The density and the character of dislocations in cubic and hexagonal polycrystals determined by X-ray diffraction*, Materials Science and Engineering: A, vol. 309–310, pp. 60–63, 2001.

[184] G. Ribárik, J. Gubicza, and T. Ungár, *Correlation between strength and microstructure of ball-milled Al–Mg alloys determined by X-ray diffraction*, Materials Science and Engineering: A, vol. 387–389, pp. 343–347, 2004.

[185] A. W. Thompson, *Calculation of true volume grain diameter*, Metallography, vol. 5, pp. 366–369, 1972.

[186] J. C. Tan and M. J. Tan, *Superplasticity and grain boundary sliding characteristics in two stage deformation of Mg-3Al-1Zn alloy sheet*, Materials Science and Engineering A, vol. 339, no. 1–2, pp. 81–89, 2003.

[187] F. Chai, D. Zhang, W. Zhang, and Y. Li, *Microstructure evolution during high strain rate*

tensile deformation of a fine-grained AZ91 magnesium alloy, Materials Science and Engineering A, vol. 590, pp. 80–87, 2014.

[188] A. Mohan, W. Yuan, and R. S. Mishra, *High strain rate superplasticity in friction stir processed ultrafine grained Mg–Al–Zn alloys*, Materials Science and Engineering: A, vol. 562, pp. 69–76, 2013.

[189] S. W. Lee, Y. L. Chen, H. Y. Wang, C. F. Yang, and J. W. Yeh, *On mechanical properties and superplasticity of Mg-15Al-1Zn alloys processed by reciprocating extrusion*, Materials Science and Engineering A, vol. 464, no. 1–2, pp. 76–84, 2007.

[190] B. D. Cullity and R. S. Stuart, *Elements of X Ray Diffraction*. USA: Prentice Hall, 2001.

[191] M. M. Avadesian and H. Baker, *ASM Specialty Handbook-Magnesium and Magnesium Alloys*. USA: ASM International, 1999.

[192] L. Balogh, T. Ungár, Y. Zhao, Y. T. T. Zhu, Z. Horita, C. Xu, and T. G. Langdon, *Influence of stacking-fault energy on microstructural characteristics of ultrafine-grain copper and copper-zinc alloys*, Acta Materialia, vol. 56, no. 4, pp. 809–820, 2008.

[193] H. J. Frost and M. F. Ashby, *Deformation-mechanism maps (the plasticity and creep of metals and ceramics)*. UK: Pergamon Press, 1982.

[194] J. A. Valle, M. T. Perez-Prado, J. R. Bartolome, F. Peñalba, and O. A. Ruano, *Grain Refinement in a Mg AZ91 Alloy via Large Strain Hot Rolling*, Materials Transactions, vol. 44, no. 12, pp. 2625–2630, 2003.

[195] R. B. Figueiredo, P. R. Cetlin, and T. G. Langdon, *The processing of difficult-to-work alloys by ECAP with an emphasis on magnesium alloys*, Acta Materialia, vol. 55, no. 14, pp. 4769–4779, 2007.

[196] H. J. McQueen, *Dynamic Recovery and Recrystallization*, Encyclopedia of Materials: Science and Technology, pp. 1–7, 2001.

[197] T. Al-Samman, K. D. Molodov, D. A. Molodov, G. Gottstein, and S. Suwas, *Softening and dynamic recrystallization in magnesium single crystals during c-axis compression*, Acta Materialia, vol. 60, no. 2, pp. 537–545, 2012.

[198] K. Edalati and Z. Horita, *Significance of homologous temperature in softening behavior and grain size of pure metals processed by high-pressure torsion*, Materials Science and Engineering: A, vol. 528, no. 25–26, pp. 7514–7523, 2011.

[199] M. Kawasaki, R. B. Figueiredo, and T. G. Langdon, *Twenty-five years of severe plastic deformation: Recent developments in evaluating the degree of homogeneity through the thickness of disks processed by high-pressure torsion*, Journal of Materials Science, vol. 47, pp. 7719–7725, 2012.

[200] L. Balogh, R. B. Figueiredo, T. Ungár, and T. G. Langdon, *The contributions of grain size, dislocation density and twinning to the strength of a magnesium alloy processed by ECAP*, Materials Science and Engineering A, vol. 528, no. 1, pp. 533–538, 2010.

[201] A. Al-Zubaydi, R. B. Figueiredo, Y. Huang, and T. G. Langdon, *Structural and hardness inhomogeneities in Mg-Al-Zn alloys processed by high-pressure torsion*, Journal of Materials Science, vol. 48, pp. 4661–4670, 2013.

[202] Z. Horita, K. Matsubara, K. Makii, and T. G. Langdon, *A two-step processing route for achieving a superplastic forming capability in dilute magnesium alloys,* Scripta Materialia, vol. 47, no. 4, pp. 255–260, 2002.

[203] F. Pilehva, A. Zarei-Hanzaki, and S. M. Fatemi-Varzaneh, *The influence of initial microstructure and temperature on the deformation behavior of AZ91 magnesium alloy,* Materials & Design, vol. 42, pp. 411–417, 2012.

[204] R. Pippan, *High-Pressure Torsion - Features and Applications,* in *Bulk Nanostructured Materials*, M. J. Zehetbauer and Y. T. Zhu, Eds. Germany: WILEY-VCH Verlag GmbH & Co. KGaA, 2009, pp. 217–233.

[205] A. Hohenwarter, A. Bachmaier, B. Gludovatz, S. Scheriau, and R. Pippan, *Technical parameters affecting grain refinement by high pressure torsion,* International Journal of Materials Research, vol. 100, pp. 1653–1661, 2009.

[206] M. Eskandari, A. Zarei-Hanzaki, F. Pilehva, H. R. Abedi, S. M. Fatemi-Varzaneh, and A. R. Khalesian, *Ductility improvement in AZ31 magnesium alloy using constrained compression testing technique,* Materials Science and Engineering: A, vol. 576, pp. 74–81, 2013.

[207] L. Jiang, J. J. Jonas, R. K. Mishra, A. A. Luo, A. K. Sachdev, and S. Godet, *Twinning and texture development in two Mg alloys subjected to loading along three different strain paths,* Acta Materialia, vol. 55, no. 11, pp. 3899–3910, 2007.

[208] H. Q. Sun, Y. N. Shi, M. X. Zhang, and K. Lu, *Plastic strain-induced grain refinement in the nanometer scale in a Mg alloy,* Acta Materialia, vol. 55, no. 3, pp. 975–982, 2007.

[209] S. M. Fatemi-Varzaneh, A. Zarei-Hanzaki, and J. M. Cabrera, *Shear banding phenomenon during severe plastic deformation of an AZ31 magnesium alloy,* Journal of Alloys and Compounds, vol. 509, no. 9, pp. 3806–3810, 2011.

[210] J.-F. Nie, *Precipitation and Hardening in Magnesium Alloys,* Metallurgical and Materials Transactions A, vol. 43, no. 11, pp. 3891–3939, 2012.

[211] Y. Tamura, Y. Kida, A. Suzuki, H. Soda, and A. McLean, *Effects of Solute Segregation on Precipitation Phenomena and Age Hardening Response of High-Purity and Commercial AZ91 Magnesium Alloys,* Materials Transactions, vol. 50, no. 3, pp. 579–587, 2009.

[212] A. Kiełbus, C. Lubomir, and L. Pawlica, *Microstructural Changes of AZ91 Magnesium Alloy After Heat,* in *Magnesium: Proceedings of the 6th International Conference Magnesium Alloys and Their Applications*, Germany: WILEY-VCH Verlag GmbH & Co. KG aA, Weinheim, 2004, pp. 196–201.

[213] S. W. Xu, S. Kamado, N. Matsumoto, T. Honma, and Y. Kojima, *Recrystallization mechanism of as-cast AZ91 magnesium alloy during hot compressive deformation,* Materials Science and Engineering A, vol. 527, no. 1–2, pp. 52–60, 2009.

[214] W. J. Kim, S. I. Hong, and Y. H. Kim, *Enhancement of the strain hardening ability in ultrafine grained Mg alloys with high strength,* Scripta Materialia, vol. 67, pp. 689–692, 2012.

[215] A. Chalay-Amoly, A. Zarei-Hanzaki, P. Changizian, S. M. Fatemi-Varzaneh, and M. H. Maghsoudi, *An investigation into the microstructure/strain pattern relationship in backward extruded AZ91 magnesium alloy,* Materials and Design, vol. 47, pp. 820–827, 2013.

[216] G. Faraji, M. M. Mashhadi, and H. S. Kim, *Microstructure inhomogeneity in ultra-fine grained bulk AZ91 produced by accumulative back extrusion (ABE),* Materials Science and Engineering A, vol. 528, pp. 4312–4317, 2011.

[217] H. J. Yang, X. H. An, X. H. Shao, X. M. Yang, S. X. Li, S. D. Wu, and Z. F. Zhang, *Enhancing strength and ductility of Mg–12Gd–3Y–0.5Zr alloy by forming a bi-ultrafine microstructure,* Materials Science and Engineering: A, vol. 528, no. 13–14, pp. 4300–4311, 2011.

[218] M. A. Meyers and K. K. Chawla, *Mechanical Behavior of Materials*. UK: Cambridge University Press, 2009.

[219] R. Pippan, S. Scheriau, A. Taylor, M. Hafok, A. Hohenwarter, and A. Bachmaier, *Saturation of Fragmentation During Severe Plastic Deformation,* Annual Review of Materials Research, vol. 40, no. 1, pp. 319–343, 2010.

[220] P. Changizian, a. Zarei-Hanzaki, M. Ghambari, and a. Imandoust, *Flow localization during severe plastic deformation of AZ81 magnesium alloy: Micro-shear banding phenomenon,* Materials Science and Engineering A, vol. 582, pp. 8–14, 2013.

[221] S. W. Xu, N. Matsumoto, S. Kamado, T. Honma, and Y. Kojima, *Effect of Mg17Al12 precipitates on the microstructural changes and mechanical properties of hot compressed AZ91 magnesium alloy,* Materials Science and Engineering: A, vol. 523, no. 1–2, pp. 47–52, 2009.

[222] Y. H. Zhao, Y. T. Zhu, X. Z. Liao, Z. Horita, and T. G. Langdon, *Influence of stacking fault energy on the minimum grain size achieved in severe plastic deformation,* Materials Science and Engineering A, vol. 463, no. 1–2, pp. 22–26, 2007.

[223] X. G. Qiao, Y. W. Zhao, W. M. Gan, Y. Chen, M. Y. Zheng, K. Wu, N. Gao, and M. J. Starink, *Hardening mechanism of commercially pure Mg processed by high pressure torsion at room temperature,* Materials Science and Engineering: A, vol. 619, pp. 95–106, 2014.

[224] L. Rémy, A. Pineau, and B. Thomas, *Temperature dependence of stacking fault energy in close-packed metals and alloys,* Materials Science and Engineering, vol. 36, no. 1, pp. 47–63, 1978.

[225] Y. Huang, R. B. Figueiredo, T. Baudin, A. L. Helbert, F. Brisset, and T. G. Langdon, *Effect of temperature on the processing of a magnesium alloy by high-pressure torsion,* Journal of Materials Science, vol. 47, no. 22, pp. 7796–7806, 2012.

[226] M. M. Myshlyaev, H. J. McQueen, A. Mwembela, and E. Konopleva, *Twinning, dynamic recovery and recrystallization in hot worked Mg–Al–Zn alloy,* Materials Science and Engineering: A, vol. 337, pp. 121–133, 2002.

[227] D. P. F. Adam J. Schwartz, Mukul Kumar, Brent L. Adams, *Electron Backscatter Diffraction in Materials Science*. Boston, MA: Springer US, 2009.

[228] N. Tahreen, D. L. Chen, M. Nouri, and D. Y. Li, *Influence of aluminum content on twinning and texture development of cast Mg–Al–Zn alloy during compression,* Journal of Alloys and Compounds, vol. 623, pp. 15–23, 2015.

[229] M. H. Yoo, *Slip, twinning, and fracture in hexagonal close-packed metals,* Metallurgical Transactions A, vol. 12, no. 3, pp. 409–418, 1981.

[230] J. W. Christian and S. Mahajan, *Deformation twinning,* Progress in Materials Science, vol. 39, no. 1–2, pp. 1–157, 1995.

[231] L. Liu and H. Ding, *Study of the plastic flow behaviors of AZ91 magnesium alloy during thermomechanical processes,* Journal of Alloys and Compounds, vol. 484, no. 1–2, pp. 949–956, 2009.

[232] Q. Ma, B. Li, A. L. Oppedal, W. R. Whittington, S. J. Horstemeyer, E. B. Marin, P. T. Wang, and M. F. Horstemeyer, *Strain rate dependence of twinning at 450°C and its effect on microstructure of an extruded magnesium alloy,* Materials Science and Engineering: A, vol. 559, pp. 314–318, 2013.

[233] P. Changizian, A. Zarei-Hanzaki, and H. R. Abedi, *On the recrystallization behavior of homogenized AZ81 magnesium alloy: The effect of mechanical twins and γ precipitates,* Materials Science and Engineering: A, vol. 558, pp. 44–51, 2012.

[234] Y. T. Zhu, X. Z. Liao, X. L. Wu, and J. Narayan, *Grain size effect on deformation twinning and detwinning,* Journal of Materials Science, vol. 48, no. 13, pp. 4467–4475, 2013.

[235] R. B. Figueiredo and T. G. Langdon, *Grain refinement and mechanical behavior of a magnesium alloy processed by ECAP,* Journal of Materials Science, vol. 45, no. 17, pp. 4827–4836, 2010.

[236] A. Galiyev, R. Kaibyshev, and G. Gottstein, *Correlation of plastic deformation and dynamic recrystallization in magnesium alloy ZK60,* Acta Materialia, vol. 49, no. 7, pp. 1199–1207, 2001.

[237] R. D. Doherty, D. A. Hughes, F. J. Humphreys, J. J. Jonas, D. J. Jensen, M. E. Kassner, W. E. King, T. R. McNelley, H. J. McQueen, and A. D. Rollett, *Current issues in recrystallization: a review,* Materials Science and Engineering: A, vol. 238, no. 2, pp. 219–274, 1997.

[238] M. Hakamada, A. Watazu, N. Saito, and H. Iwasaki, *Dynamic recrystallization during hot compression of as-cast and homogenized noncombustible Mg–9Al–1Zn–1Ca (in mass%) alloys,* Materials Science and Engineering: A, vol. 527, no. 26, pp. 7143–7146, 2010.

[239] K. Máthis and Z. Heged, *Inhomogeneous evolution of microstructure in AZ91 Mg-alloy during high temperature equal-channel angular pressing,* Journal of Alloys and Compounds, vol. 492, pp. 166–172, 2010.

[240] F. Guo, D. Zhang, X. Yang, L. Jiang, and F. Pan, *Strain-induced dynamic precipitation of Mg17Al12 phases in Mg–8Al alloys sheets rolled at 748K,* Materials Science and Engineering: A, vol. 636, pp. 516–521, 2015.

[241] R. B. Figueiredo, P. R. Cetlin, and T. G. Langdon, *Using finite element modeling to examine the flow processes in quasi-constrained high-pressure torsion,* Materials Science and Engineering: A, vol. 528, no. 28, pp. 8198–8204, 2011.

[242] C. Xu, Z. Horita, and T. G. Langdon, *Evaluating the influence of pressure and torsional strain on processing by high-pressure torsion,* Journal of Materials Science, vol. 43, pp. 7286–7292, 2008.

[243] R. B. Figueiredo and T. G. Langdon, *Using severe plastic deformation for the processing of advanced engineering materials,* Materials Transactions, vol. 50, no. 7, pp. 1613–1619, 2009.

[244] R. B. Figueiredo, M. T. P. Aguilar, P. R. Cetlin, and T. G. Langdon, *Deformation heterogeneity on the cross-sectional planes of a magnesium alloy processed by high-pressure torsion,* Metallurgical and Materials Transactions A, vol. 42, no. 10, pp. 3013–3021, 2011.

[245] M. Kawasaki, *Different models of hardness evolution in ultrafine-grained materials processed by high-pressure torsion,* Journal of Materials Science, vol. 49, no. 1, pp. 18–34, 2014.

[246] K. Edalati and Z. Horita, *Universal Plot for Hardness Variation in Pure Metals Processed by High-Pressure Torsion,* Materials Transactions, vol. 51, no. 5, pp. 1051–1054, 2010.

[247] K. Edalati, E. Matsubara, and Z. Horita, *Processing pure Ti by high-pressure torsion in wide ranges of pressures and strain,* Metallurgical and Materials Transactions A: Physical Metallurgy and Materials Science, vol. 40, no. 9, pp. 2079–2086, 2009.

[248] K. Edalati, T. Fujioka, and Z. Horita, *Microstructure and mechanical properties of pure Cu processed by high-pressure torsion,* Materials Science and Engineering A, vol. 497, no. 1–2, pp. 168–173, 2008.

[249] M. Furukawa, Z. Horita, M. Nemoto, R. Z. Valiev, and T. G. Langdon, *Microhardness measurements and the Hall-Petch relationship in an Al-Mg alloy with submicrometer grain size,* Acta Materialia, vol. 44, pp. 4619–4629, 1996.

[250] T. Shanmugasundaram, M. Heilmaier, B. S. Murty, and V. S. Sarma, *On the Hall-Petch relationship in a nanostructured Al-Cu alloy*, Materials Science and Engineering A, vol. 527, no. 29–30, pp. 7821–7825, 2010.

[251] W. Yuan, S. K. Panigrahi, J.-Q. Su, and R. S. Mishra, *Influence of grain size and texture on Hall–Petch relationship for a magnesium alloy,* Scripta Materialia, vol. 65, no. 11, pp. 994–997, 2011.

[252] Y. S. Sato, M. Urata, H. Kokawa, and K. Ikeda, *Hall-Petch relationship in friction stir welds of equal channel angular-pressed aluminium alloys,* Materials Science and Engineering A, vol. 354, no. 1–2, pp. 298–305, 2003.

[253] N. Hansen, *Hall–Petch relation and boundary strengthening,* Scripta Materialia, vol. 51, no. 8, pp. 801–806, 2004.

[254] C. H. Cáceres, W. J. Poole, A. L. Bowles, and C. J. Davidson, *Section thickness, macrohardness and yield strength in high-pressure diecast magnesium alloy AZ91*, Materials Science and Engineering: A, vol. 402, no. 1–2, pp. 269–277, 2005.

[255] J. May, M. Dinkel, D. Amberger, H. W. Höppel, and M. Göken, *Mechanical properties, dislocation density and grain structure of ultrafine-grained aluminum and aluminum-magnesium alloys,* Metallurgical and Materials Transactions A, vol. 38, no. 9, pp. 1941–1945, 2007.

[256] D. Setman, E. Schafler, E. Korznikova, and M. J. Zehetbauer, *The presence and nature of vacancy type defects in nanometals detained by severe plastic deformation,* Materials Science and Engineering: A, vol. 493, pp. 116–122, 2008.

[257] M. J. Zehetbauer, H. P. Stüwe, A. Vorhauer, E. Schafler, and J. Kohout, *The Role of Hydrostatic Pressure in Severe Plastic Deformation,* in *Nanomaterials by Severe Plastic Deformation*, M. Zehetbauer and R. Z. Valiev, Eds. Germany: Wiley-VCH Verlag GmbH &

Co. KGaA, 2004, pp. 436–446.

[258] J. Gubicza, S. V. Dobatkin, E. Khosravi, A. A. Kuznetsov, and J. L. Lábár, *Microstructural stability of Cu processed by different routes of severe plastic deformation*, Materials Science and Engineering: A, vol. 528, pp. 1828–1832, 2011.

[259] M. J. Zehetbauer, J. Kohout, E. Schafler, F. Sachslehner, and A. Dubravina, *Plastic deformation of nickel under high hydrostatic pressure*, Journal of Alloys and Compounds, vol. 378, no. 1–2, pp. 329–334, 2004.

[260] Z. Hegedűs, J. Gubicza, M. Kawasaki, N. Q. Chinh, Z. Fogarassy, and T. G. Langdon, *Microstructure of low stacking fault energy silver processed by different routes of severe plastic deformation*, Journal of Alloys and Compounds, vol. 536, pp. S190–S193, 2012.

[261] W. W. Jian, G. M. Cheng, W. Z. Xu, H. Yuan, M. H. Tsai, Q. D. Wang, C. C. Koch, Y. T. Zhu, and S. N. Mathaudhu, *Ultrastrong Mg Alloy via Nano-spaced Stacking Faults*, Materials Research Letters, vol. 1, no. 2, pp. 61–66, 2013.

[262] S.-Y. Chang, S.-W. Lee, K. M. Kang, S. Kamado, and Y. Kojima, *Improvement of Mechanical Characteristics in Severely Plastic-deformed Mg Alloys*, Materials Transactions, vol. 45, pp. 488–492, 2004.

[263] Y. Wang and H. Choo, *Influence of texture on Hall–Petch relationships in an Mg alloy*, Acta Materialia, vol. 81, pp. 83–97, 2014.

[264] Y. N. Wang, C. I. Chang, C. J. Lee, H. K. Lin, and J. C. Huang, *Texture and weak grain size dependence in friction stir processed Mg-Al-Zn alloy*, Scripta Materialia, vol. 55, no. 7, pp. 637–640, 2006.

[265] R. B. Figueiredo and T. G. Langdon, *Principles of grain refinement and superplastic flow in magnesium alloys processed by ECAP*, Materials Science and Engineering A, vol. 501, no. 1–2, pp. 105–114, 2009.

[266] K. Edalati, D. Akama, A. Nishio, S. Lee, Y. Yonenaga, J. M. Cubero-Sesin, and Z. Horita, *Influence of dislocation–solute atom interactions and stacking fault energy on grain size of single-phase alloys after severe plastic deformation using high-pressure torsion*, Acta Materialia, vol. 69, pp. 68–77, 2014.

[267] Y. Huang, R. B. Figueiredo, T. Baudin, F. Brisset, and T. G. Langdon, *Evolution of strength and homogeneity in a magnesium AZ31 alloy processed by high-pressure torsion at different temperatures*, Advanced Engineering Materials, vol. 14, no. 11, pp. 1018–1026, 2012.

[268] R. B. Figueiredo, M. T. P. Aguilar, P. R. Cetlin, and T. G. Langdon, *Analysis of plastic flow during high-pressure torsion*, Journal of Materials Science, vol. 47, no. 22, pp. 7807–7814, 2012.

[269] D. J. Lee, E. Y. Yoon, L. J. Park, and H. S. Kim, *The dead metal zone in high-pressure torsion*, Scripta Materialia, vol. 67, no. 4, pp. 384–387, 2012.

[270] A. S. J. Al-Zubaydi, A. P. Zhilyaev, S. C. Wang, and P. A. S. Reed, *Superplastic behaviour of AZ91 magnesium alloy processed by high-pressure torsion*, Materials Science and Engineering: A, vol. 637, pp. 1–11, 2015.

[271] B. Srinivasarao, A. P. Zhilyaev, T. G. Langdon, and M. T. Pérez-Prado, *On the relation*

between the microstructure and the mechanical behavior of pure Zn processed by high pressure torsion, Materials Science and Engineering: A, vol. 562, pp. 196–202, 2013.

[272] T. G. Langdon, *A unified approach to grain boundary sliding in creep and superplasticity*, Acta Metallurgica et Materialia, vol. 42, no. 7, pp. 2437–2443, 1994.

[273] F. A. Mohamed and T. G. Langdon, *Flow localization and neck formation in a superplastic metal*, Acta Metallurgica, vol. 29, no. 5, pp. 911–920, 1981.

[274] R. Ohyama, J. Koike, T. Kobayashi, M. Suzuki, and K. Maruyama, *Enhanced Grain-Boundary Sliding at Room Temperature in AZ31 Magnesium Alloy*, Materials Science Forum, vol. 419–422, no. 4, pp. 237–242, 2003.

[275] D. Ando, J. Koike, and Y. Sutou, *The role of deformation twinning in the fracture behavior and mechanism of basal textured magnesium alloys*, Materials Science and Engineering A, vol. 600, pp. 145–152, 2014.

[276] H. Watanabe, T. Mukai, K. Ishikawa, and K. Higashi, *High-Strain-Rate Superplasticity in an AZ91 Magnesium Alloy Processed by Ingot Metallurgy Route*, Materials Transactions, vol. 43, pp. 78–80, 2002.

[277] Y. H. Wei, Q. D. Wang, Y. P. Zhu, H. T. Zhou, W. J. Ding, Y. Chino, and M. Mabuchi, *Superplasticity and grain boundary sliding in rolled AZ91 magnesium alloy at high strain rates*, Materials Science and Engineering A, vol. 360, no. 1–2, pp. 107–115, 2003.

[278] Y. Ma, M. Furukawa, Z. Horita, M. Nemoto, R. Z. Valiev, and T. G. Langdon, *Significance of microstructural control for superplastic deformation and forming*, Materials Transactions, JIM, vol. 37, pp. 336–339, 1996.

[279] H. Watanabe, T. Mukai, K. Ishikawa, and M. Mabuchi, *Realization of high-strain-rate superplasticity at low temperatures in a Mg – Zn – Zr alloy*, Materials Science and Engineering A, vol. 307, pp. 119–128, 2001.

[280] Y. H. Zhao, Y. Z. Guo, Q. Wei, T. D. Topping, A. M. Dangelewicz, Y. T. Zhu, T. G. Langdon, and E. J. Lavernia, *Influence of specimen dimensions and strain measurement methods on tensile stress-strain curves*, Materials Science and Engineering A, vol. 525, no. 1–2, pp. 68–77, 2009.

[281] Y. H. Zhao, Y. Z. Guo, Q. Wei, A. M. Dangelewicz, C. Xu, Y. T. Zhu, T. G. Langdon, Y. Z. Zhou, and E. J. Lavernia, *Influence of specimen dimensions on the tensile behavior of ultrafine-grained Cu*, Scripta Materialia, vol. 59, no. 6, pp. 627–630, 2008.

[282] S. R. Agnew, J. A. Horton, T. M. Lillo, and D. W. Brown, *Enhanced ductility in strongly textured magnesium produced by equal channel angular processing*, Scripta Materialia, vol. 50, no. 3, pp. 377–381, 2004.

[283] M. Berta, P. J. Apps, and P. B. Prangnell, *Effect of processing route and second phase particles on grain refinement during equal-channel angular extrusion*, Materials Science and Engineering A, vol. 410–411, pp. 381–385, 2005.

[284] D. Orlov, P. P. Bhattacharjee, Y. Todaka, M. Umemoto, and N. Tsuji, *Texture evolution in pure aluminum subjected to monotonous and reversal straining in high-pressure torsion*, Scripta Materialia, vol. 60, no. 10, pp. 893–896, 2009.

[285] R. Panicker, A. H. Chokshi, R. K. Mishra, R. Verma, and P. E. Krajewski, *Microstructural*

evolution and grain boundary sliding in a superplastic magnesium AZ31 alloy, Acta Materialia, vol. 57, no. 13, pp. 3683–3693, 2009.

[286] X. Wu and Y. Liu, *Superplasticity of coarse-grained magnesium alloy*, Scripta Materialia, vol. 46, no. 4, pp. 269–274, 2002.

[287] T. J. Lee, Y. B. Park, and W. J. Kim, *Importance of diffusional creep in fine grained Mg–3Al–1Zn alloys*, Materials Science and Engineering: A, vol. 580, pp. 133–141, 2013.

[288] M. Kawasaki, K. Kubota, K. Higashi, and T. G. Langdon, *Flow and cavitation in a quasi-superplastic two-phase magnesium–lithium alloy*, Materials Science and Engineering: A, vol. 429, no. 1–2, pp. 334–340, 2006.

[289] W. J. Kim, M. J. Kim, and J. Y. Wang, *Ultrafine-grained Mg–9Li–1Zn alloy sheets exhibiting low temperature superplasticity*, Materials Science and Engineering: A, vol. 516, no. 1–2, pp. 17–22, 2009.

[290] S. S. Vagarali and T. G. Langdon, *Deformation mechanisms in h.c.p. metals at elevated temperatures—II. Creep behavior of a Mg-0.8% Al solid solution alloy*, Acta Metallurgica, vol. 30, pp. 1157–1170, 1982.

[291] M. Kawasaki, N. Balasubramanian, and T. G. Langdon, *Flow mechanisms in ultrafine-grained metals with an emphasis on superplasticity*, Materials Science and Engineering A, vol. 528, no. 21, pp. 6624–6629, 2011.

[292] M. Kawasaki and T. G. Langdon, *Review: Achieving superplasticity in metals processed by high-pressure torsion*, Journal of Materials Science, vol. 49, no. 19, pp. 6487–6496, 2014.

[293] D. Zhang, S. Wang, C. Qiu, and W. Zhang, *Superplastic tensile behavior of a fine-grained AZ91 magnesium alloy prepared by friction stir processing*, Materials Science & Engineering A, vol. 556, pp. 100–106, 2012.

[294] Y. N. Wang and J. C. Huang, *Comparison of grain boundary sliding in fine grained Mg and Al alloys during superplastic deformation*, Scripta Materialia, vol. 48, no. 8, pp. 1117–1122, 2003.

[295] M. G. Zelin, *On micro-superplasticity*, Acta Materialia, vol. 45, pp. 3533–3542, 1997.

[296] A. Mussi, J. J. Blandin, L. Salvo, and E. F. Rauch, *Resistance to strain-induced damage of an ultrafine-grained magnesium alloy deformed in superplastic conditions*, Acta Materialia, vol. 54, no. 14, pp. 3801–3809, 2006.

APPENDIX

The following papers have been published during the course of the PhD study:

- **Structural and hardness inhomogeneities in Mg–Al–Zn alloys processed by high-pressure torsion**. A. Al-Zubaydi, R.B. Figueiredo, Y. Huang, T.G. Langdon, *Journal of Materials Science*, 48 (2013) 4661–4670.
- **An overview of flow patterns development on disc lower surfaces when processing by high-pressure**. Y. Huang, A. Al-Zubaydi, M. Kawasaki, T.G. Langdon, *Journal of Materials Research and Technology*, 3 (2014) 303–310.
- **Effect of anvil roughness on the flow patterns and hardness development in high-pressure torsion**. Y. Huang, M. Kawasaki, A. Al-Zubaydi, T.G. Langdon, *Journal of Materials Science*, 49 (2014) 6517–6528.
- **Superplastic behaviour of AZ91 magnesium alloy processed by high–pressure torsion**. Ahmed S.J. Al–Zubaydi, Alexander P. Zhilyaev, Shun C. Wang, Philippa A.S. Reed, *Materials Science and Engineering A*, 637 (2015) 1 – 11.
- **Evolution of microstructure in AZ91 alloy processed by high-pressure torsion**. Al-Zubaydi, Ahmed S.J. Al–Zubaydi, Alexander P. Zhilyaev, Shun C. Wang, Pawee Kucita, Philippa A.S. Reed, *Journal of Materials Science*, 51 (2016) 3380–3389.

J Mater Sci (2013) 48:4661–4670
DOI 10.1007/s10853-013-7176-1

NANOSTRUCTURED MATERIALS

Structural and hardness inhomogeneities in Mg–Al–Zn alloys processed by high-pressure torsion

Ahmed Al-Zubaydi · Roberto B. Figueiredo · Yi Huang · Terence G. Langdon

Received: 2 November 2012 / Accepted: 18 January 2013 / Published online: 31 January 2013

Abstract Experiments were conducted to evaluate the evolution of structure and hardness in processing by high-pressure torsion (HPT) of the magnesium AZ91 and AZ31 alloys. Both alloys were processed by HPT at room temperature for 1/4, 1, and 5 turns using a rotation speed of 1 rpm. Structure observations and microhardness measurements were undertaken on vertical cross-sectional planes cut through the HPT disks. The results demonstrate that the deformation is heterogeneous across the vertical cross sections but with a gradual evolution toward homogeneity with increasing numbers of revolutions.

Introduction

Mg–Al–Zn alloys have become one of the most important light alloys with widespread applications in the automotive industry [1]. However, magnesium alloys typically have low formability near room temperature due to their hexagonal close-packed (hcp) crystal structure and the limited number of slip systems that operate at lower temperatures.

A. Al-Zubaydi (✉) · Y. Huang · T. G. Langdon
Materials Research Group, Faculty of Engineering and the Environment, University of Southampton, Southampton SO17 1BJ, UK
e-mail: asaz1e11@soton.ac.uk

R. B. Figueiredo
Department of Materials Engineering and Civil Construction, Federal University of Minas Gerais, Belo Horizonte, MG 31270-901, Brazil

T. G. Langdon
Departments of Aerospace & Mechanical Engineering and Materials Science, University of Southern California, Los Angeles, CA 90089-1453, USA

Processing to produce grain refinement is an effective procedure for achieving both high strength and reasonable ductility at room temperature. It is now well established that ultrafine-grained microstructures can be produced in metals using severe plastic deformation (SPD) techniques. One of the most common SPD methods is equal-channel angular pressing (ECAP) which permits the fabrication of submicrometer microstructures without any reduction in the cross-sectional dimensions of the billets [2, 3]. More recently, high-pressure torsion (HPT), where a disk is subjected to a high pressure and concurrent torsional straining [4], has become a popular and important SPD technique. Most published results on the ECAP processing of Mg alloys describe experiments in which the processing was conducted at a relatively high temperature, typically at or above 423 K, because ECAP processing at lower temperatures generally leads to severe segmentation and cracking of the samples [5–9]. A detailed description of the characteristics of this unstable flow in ECAP was given in earlier reports [10, 11]. Alternatively, by using HPT it is possible to process Mg alloys at much lower temperatures, and even at room temperature, because of the presence of a high hydrostatic pressure that prevents segmentation and cracking during the straining process. To date, there are only very limited reports describing the room temperature processing of Mg–Al–Zn alloys by HPT [12, 13].

Moreover, the majority of papers focus on the structure and properties achieved after SPD processing and only a few on the processing characteristics. In addition, there are very few papers evaluating the homogeneity of deformation. The occurrence of heterogeneity in deformation in ECAP was reported in an early investigation when flow localization was observed in copper and an "end effect" was shown in a billet of aluminum processed by multiple passes [14]. Experiments using plasticine also revealed the

occurrence of heterogeneity of deformation in the regions of the billet in contact with the die walls [15] and finite element modeling showed the occurrence of heterogeneous plastic deformation in ECAP [16–18].

The occurrence of heterogeneity of deformation in HPT is not well understood at the present time. The principle of torsion deformation predicts a heterogeneous distribution of strain along the diameter of the disks since the center is assumed to be subjected to a lower strain and the edge to a larger strain. Thus, early investigations documented the distance from the disk center at which the experiments, such as microhardness measurements and structure characterization, were carried out in samples processed by HPT [19–22]. Later, a theoretical study showed that the variation in deformation along the whole surface of the disk tends to decrease with increasing numbers of rotations [23]. The tendency toward a homogenization of deformation was confirmed by microhardness measurements taken over the whole surfaces of disks processed by HPT to large numbers of turns [19, 24, 25]. Thus, the development of heterogeneity in the deformation imposed at different distances from centers of samples processed by HPT is now widely known. It is noteworthy that an early report suggested that microhardness measurements taken at different distances from the centers in individual HPT samples processed to different numbers of turns were well correlated through the use of the shear strain [21].

Nevertheless, heterogeneity of deformation along the through-thickness direction was not well studied in the earlier reports. It is only in very recent investigations that measurements have been taken to characterize the structure and microhardness distributions on vertical planes cut through the disks [26–35]. Accordingly, the present investigation was initiated in order to study and compare plastic flow and hardness homogeneities on two representative Mg–Al–Zn alloys. Specifically, tests were conducted on the AZ91 and AZ31 alloys having nominal aluminum contents of 9 and 3 wt%, respectively. These alloys were selected because they are the most common and most widely used within the AZ magnesium series.

Experimental materials and procedures

The materials used in this study were an AZ91 (Mg–9Al–1Zn) alloy supplied by Magnesium Elektron Co. (Manchester, UK) and an AZ31 (Mg–3Al–1Zn) alloy supplied by Timminco Co. (Aurora, CO, USA). Both alloys were supplied in the form of extruded rods having diameters of 10 mm. In the unprocessed condition, the average grain sizes and values of the Vickers microhardness, Hv, were ~30 μm and 70 Hv for the AZ91 alloy and ~9.4 μm and 68 Hv for the AZ31 alloy. The extruded rods were sliced into thin disks with thicknesses of about 1.5 mm and ground with abrasive papers to final thicknesses of ~0.85 mm for the AZ91 alloy disks and ~0.80 mm for the AZ31 alloy disks. Inspection showed that the distributions of grain size and hardness were homogeneous throughout the thicknesses of the unprocessed samples.

All disks were processed by HPT under quasi-constrained conditions [36–38] in which the disks are held in shallow depressions on the inner surfaces of the upper and lower anvils and there is a small outflow of material between the two anvils during the processing operation. The HPT processing was conducted at room temperature (296 K) at a rotational speed of 1 rpm using imposed pressures of 3.0 and 6.0 GPa for the AZ91 and AZ31 alloys, respectively. All disks were processed through totals of 1/4, 1, and 5 turns. The top and bottom surfaces of each disk were clearly marked prior to HPT processing.

After processing, the disks were sectioned vertically along their diameters in planes perpendicular to the radial direction and mounted in resin. These longitudinal sections were ground with abrasive papers, polished to a mirror-like finish, and etched to reveal the phase boundaries using optical microscopy (OM) in the AZ91 alloy and the grain boundaries in the AZ31 alloy. Following observations of the microstructure, the etched surfaces were re-polished and Vickers microhardness measurements were taken at selected locations. These measurements used an applied load of 100 gf and a dwell time of 10 s. The minimum distance between consecutive indentations was 100 μm in order to avoid any interference between the measurements. The values of hardness were determined as the average of five indentations and these values were then plotted as a function of the distance from the bottom of the disk. Separate measurements were carried out at points located at fractions of 0.1, 0.5, and 0.9 of the disk radius. Color-coded contour maps were constructed in which the individual hardness values were displayed using a color scale and these values were plotted as a function of the locations on the longitudinal sections of the disks.

Experimental results

Structural features of AZ91 after HPT

One-half cross sections of the three disks of the AZ91 alloy are shown in Fig. 1 after processing by HPT. It is readily apparent that the etching leads to variations in the contrast in different regions of the samples. A general and overall impression from the cross sections shown in Fig. 1 is that there is a more pronounced variation of structure in the through-thickness direction than in the radial direction. It is also evident that the sample processed to 5 turns cracked near the bottom corner.

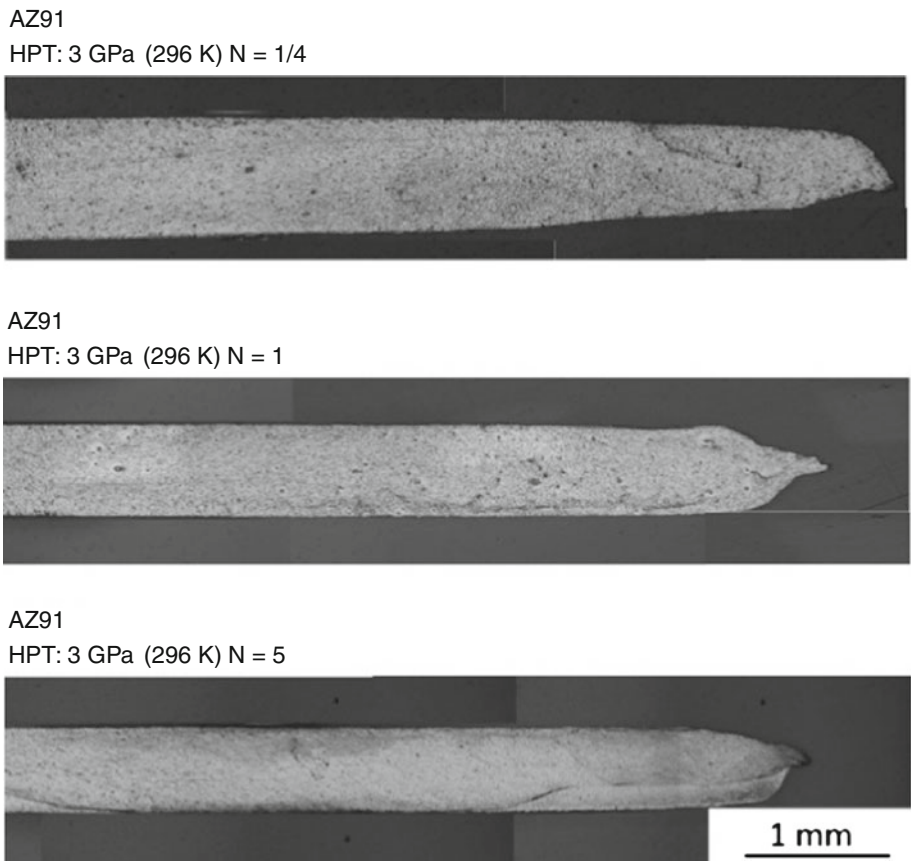

Fig. 1 Appearance of the one-half cross sections of disks of the AZ91 alloy after HPT processing to different numbers of turns

The AZ91 alloy has a two-phase microstructure consisting typically of a matrix of α grains with a β phase (intermetallic $Mg_{17}Al_{12}$) along the α grain boundaries. Etching reveals structural features of the dual phase AZ91 alloy, and Fig. 2 shows representative micrographs in the alloy in areas located ~3 mm from the center of each disk: these disks were processed through (a) 1/4 turn, (b) 1 turn, and (c) 5 turns, respectively. The presence of two phases in this alloy facilitates the observation of the plastic flow during deformation. The sample exhibited no major alignment of the darker phase before processing. Thus, any alignment observed after processing indicates plastic flow during processing. It is apparent that the phases near the top and bottom in Fig. 2a appear distorted and tend to align to a horizontal direction whereas the phases in the central region appear coarser and do not exhibit any major alignment. This suggests that there are differences in the plastic flow in these two areas. In Fig. 2b and c, it is also evident that different structural features are present at different distances from the bottom of the disks. Thus it is readily apparent, even when using optical microscopy, that the structure after HPT varies along the through-thickness direction. Generally, finer phases are observed near the surfaces of the disk processed to 1 turn in Fig. 2b while coarser phases are present near the mid-plane. In the sample processed to 5 turns in Fig. 2c, there is a clear difference in alignment of the phases near the bottom and near the mid-plane of the disk.

In addition, shear bands developed in the AZ91 alloy after HPT processing and these bands were visible at various locations in the three processed disks: two examples are shown in Fig. 3 marked with red arrows. Inspection showed these shear band extended over lengths of several hundreds of microns but their thicknesses were less than one micron. Figure 3a shows a shear band at a radius, *r*, of 3.5 mm in the disk processed to 1/4 turn and Fig. 3b shows a shear band at a radius of 4.5 mm in the disk processed to 1 turn. It is apparent that these shear bands are approximately parallel to the disk surfaces. However, they are not entirely linear and at some locations they are not parallel to the disk surfaces. These perturbations indicate that the processing deformation is not confined exclusively to the plane of the theoretical maximum shear stress.

Structural features of AZ31 after HPT

The longitudinal sections of disks of the AZ31 alloy processed by HPT to different numbers of turns are shown in Fig. 4. Again, it is readily apparent that the structural features vary in the through-thickness direction and, as for

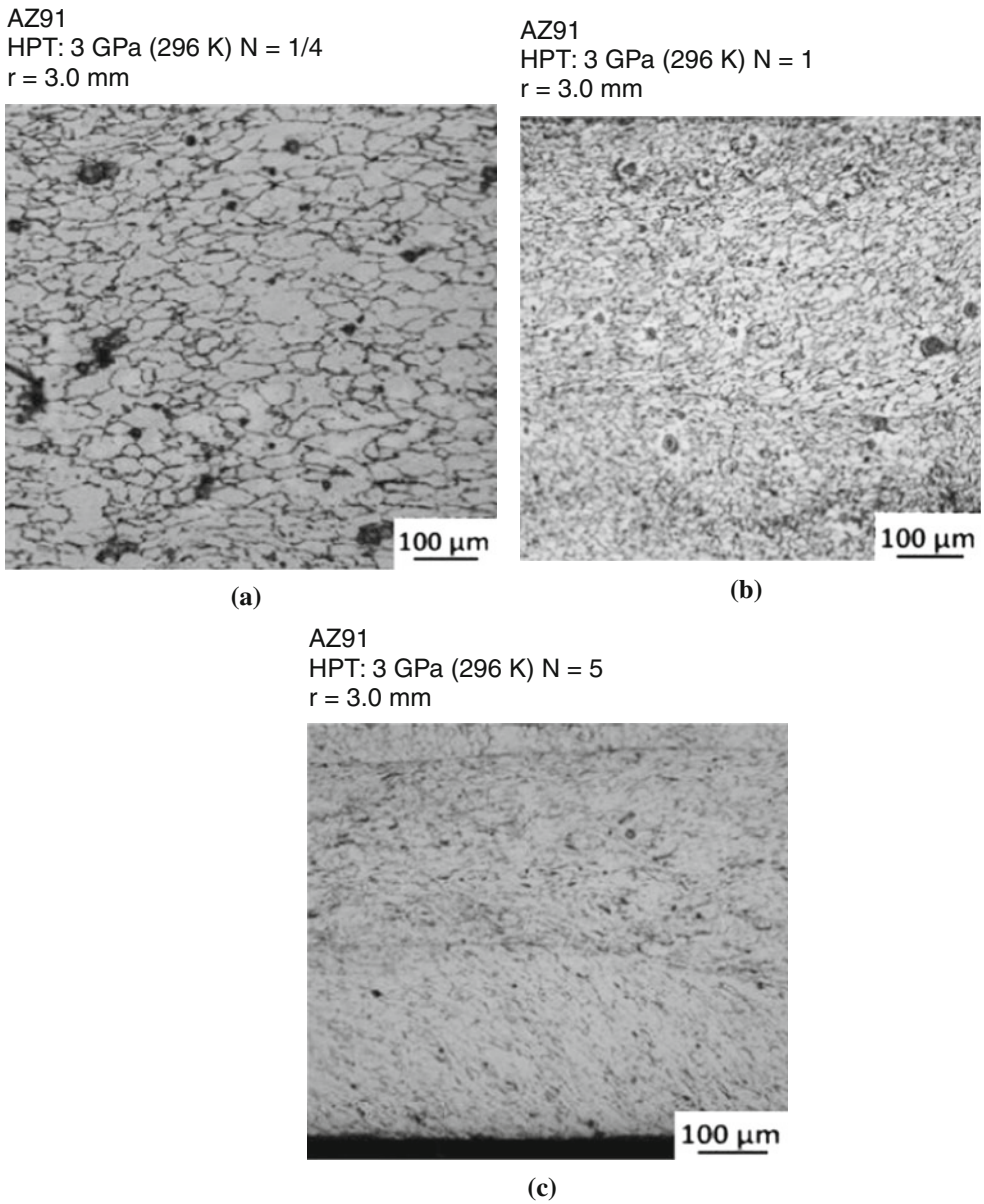

Fig. 2 Grain structures in the AZ91 alloy at a radius of 3.0 mm after HPT processing through different numbers of turns **a** $N = 1/4$ turn, **b** $N = 1$ turn, and **c** $N = 5$ turns

the AZ91 alloy, the variations in the through-thickness direction are clearer than along the radial direction.

Details of the flow lines are displayed at a higher magnification in Fig. 5 for selected areas of the disks processed for different numbers of turns. The area near the center of the disk processed to 1/4 turn is shown in the upper left image in Fig. 5. In this image in the early stages of processing, the flow lines are clearly aligned perpendicular to the disk surface. In fact, they are aligned parallel to the sample axial direction and this is caused by extrusion of the rod prior to the HPT processing. Thus, the material was received as extruded rods so that the initial flow lines are oriented parallel to the axial directions of the disks. It is also apparent from the image at upper right, corresponding to the edge of the sample after 1/4 turn, that the flow lines are not aligned perpendicular to the disk surface throughout the thickness in this region. Thus, some regions retain the original alignment (at the top and bottom corners) but there is no clear alignment in the area near the mid-plane. This suggests that the mid-plane area at the edge of the disk after 1/4 turn was subjected to higher deformation than the top and bottom corners.

The alignment of the flow lines becomes inclined at the edge of the disk after 1 turn of HPT as shown at the bottom left in Fig. 5, thereby suggesting high deformation by torsional shear parallel to the disk surface. At the edge of the sample processed to 5 turns, shown at the bottom right in

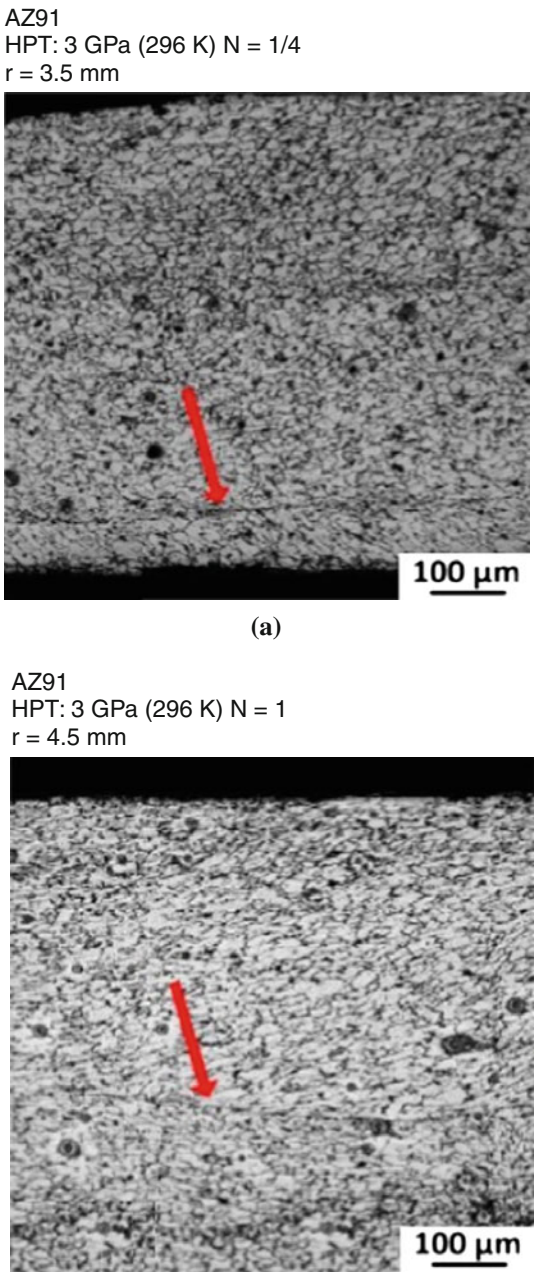

Fig. 3 Shear bands (marked by *red arrows*) in the AZ91 alloy after HPT processing through **a** $N = 1/4$ turn and **b** $N = 1$ turn (Color figure online)

Fig. 5, there is a clear alignment of the flow lines parallel to the surface of the disk between the mid-plane and the bottom surface. This alignment is due to the severe torsional shear taking place parallel to the disk surface during HPT. However, there is also a region with flow lines perpendicular to the disk surface near the upper surface of the sample processed to 5 turns. This demonstrates an inhomogeneity in the flow processing since it appears that this area retains the original flow alignment and, therefore, it was not subjected to the same level of severe deformation.

Microhardness distributions in AZ91 after HPT

Color-coded contour mapping was used to reveal changes in the microhardness on the longitudinal sections of AZ91 disks processed by HPT. Figure 6 shows plots of the hardness distributions as a function of location on one-half of the vertical cross sections of the disks processed by HPT through 1/4 turn (upper), 1 turn (center), and 5 turns (lower), respectively: the central positions in each disk are labeled 0 on the lower axes and the edges lie at the points labeled 5. It is apparent that there are significant differences in the levels of hardness at different radial positions in the disks processed to 1/4 and 1 turn and these differences occur especially in the vicinity of the centers of the disks. By contrast, there is a high degree of homogeneity in the disk processed through 5 turns such that there is little variation in the hardness values either in the radial or the axial directions. These results confirm, therefore, the gradual evolution into a homogeneous hardness distribution with increasing numbers of torsional revolutions. Furthermore, this evolution is consistent with the analytical treatment of homogeneity in HPT processing using strain gradient plasticity theory [23].

Microhardness distributions in AZ31 after HPT

Similar color-coded contour mapping was also used for the AZ31 alloy and the results for the one-half longitudinal sections are shown in Fig. 7 for disks processed through 1/4, 1, and 5 turns of HPT, respectively. Again it is observed that the hardness tends to increase with increasing distance from the center in the samples processed through 1/4 and 1 turn of HPT but after 5 turns there is a higher level of homogeneity although the AZ31 alloy is less homogeneous than the AZ91 alloy. After 1/4 and 1 turn the hardness varies significantly in the through-thickness direction in both samples and after 5 turns there is greater homogeneity but there remains a narrow region of lower hardness along the upper surface. This suggests that the AZ31 alloy requires more than 5 turns in HPT processing in order to attain a fully homogeneous structure. It should be noted that earlier experiments on the AZ31 alloy showed a much higher level of inhomogeneity after processing by HPT through 5 turns at a temperature of 463 K [29] and a comparison of these two processing temperatures confirms the advantage of performing HPT at the lowest possible temperature.

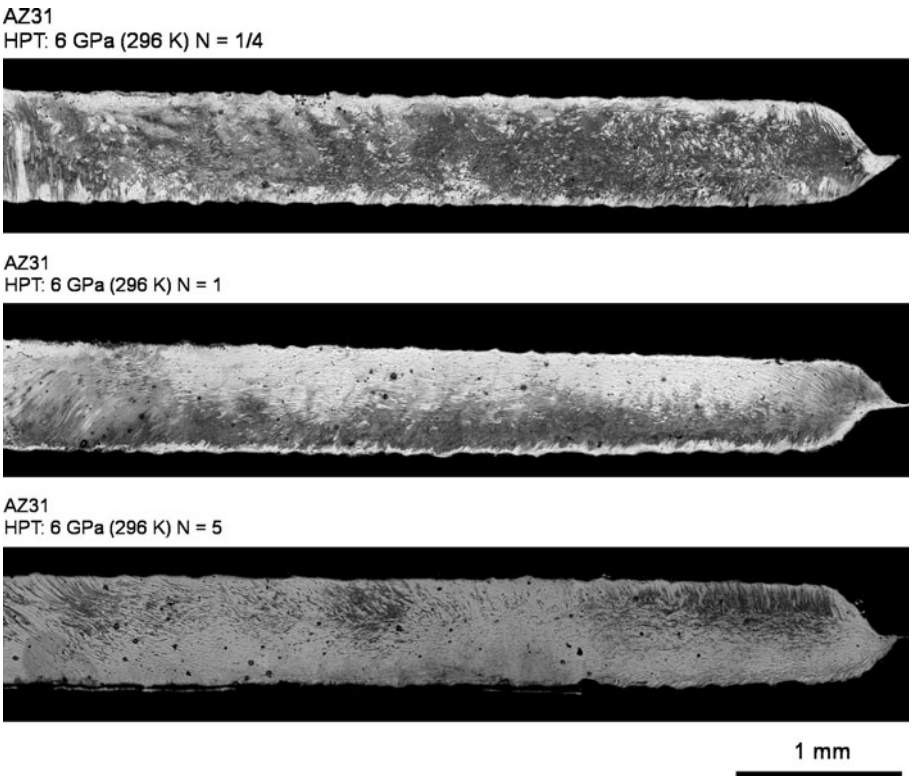

Fig. 4 Appearance of the one-half cross sections of disks of the AZ31 alloy after HPT processing to different numbers of turns

Discussion

The present results demonstrate that HPT processing produces inhomogeneous hardness distributions, and, therefore, inhomogeneous grain structures, in the AZ91 magnesium alloy in the through-thickness directions of disks processed by HPT for 1/4 or 1 turn. However, the alloy achieves a reasonable level of hardness homogeneity after processing through 5 turns. Similar results were obtained also for the AZ31 alloy although there was slightly less homogeneity in the flow patterns after 5 turns.

Significance of any rise in temperature during HPT

The present experiments were carried out at room temperature. However, the large amount of plastic deformation imposed to a small sample may produce a temperature rise in the disk. A recent report examined the temperature rise in the anvils during processing of different materials by HPT under different conditions [39] and finite element modeling was used to estimate the maximum temperature rise in the samples [37, 39]. Specifically, a graphical solution was developed in order to estimate the maximum temperature rise in a disk processed under quasi-constrained HPT conditions [37].

Using this graphical solution, it is possible to distinguish three regimes during HPT processing. There is an early stage when a continuous increase in temperature is observed in the sample, an intermediate stage where the rate of temperature rise decreases continuously due to heat lost to the environment, and a final stage where an essentially steady-state condition is attained and the heat generated is similar to the heat lost. The temperature rise in these three stages may be approximately calculated using the following three equations which are derived directly using the data in the earlier report [37]:

Stage 1 ($t < 300$ s)

$$\Delta T = (16 + 0.04t)\left\{(\omega\sigma)\left[1 + \left(0.025\frac{P}{\sigma}\right)\right]\right\} \quad (1)$$

Stage 2 ($300\text{ s} < t < 1500$ s)

$$\Delta T = [6.6\ln(t) - 9.5]\left\{(\omega\sigma)\left[1 + \left(0.025\frac{P}{\sigma}\right)\right]\right\} \quad (2)$$

Stage 3 ($t > 1500$ s)

$$\Delta T = (39)\left\{(\omega\sigma)\left[1 + \left(0.025\frac{P}{\sigma}\right)\right]\right\} \quad (3)$$

where ΔT is the maximum temperature rise in °C, t is the processing time in seconds, ω is the rotation rate in rpm, σ is the average flow stress of the material in GPa, and P is the applied pressure.

Noting that $\sigma \approx 0.4$ GPa from the hardness tests, it follows that the maximum temperature rises at 5 turns ($t = 300$ s at $\omega = 1$ rpm) for the two magnesium alloys are estimated as $\Delta T \approx 15$ °C for AZ31 where

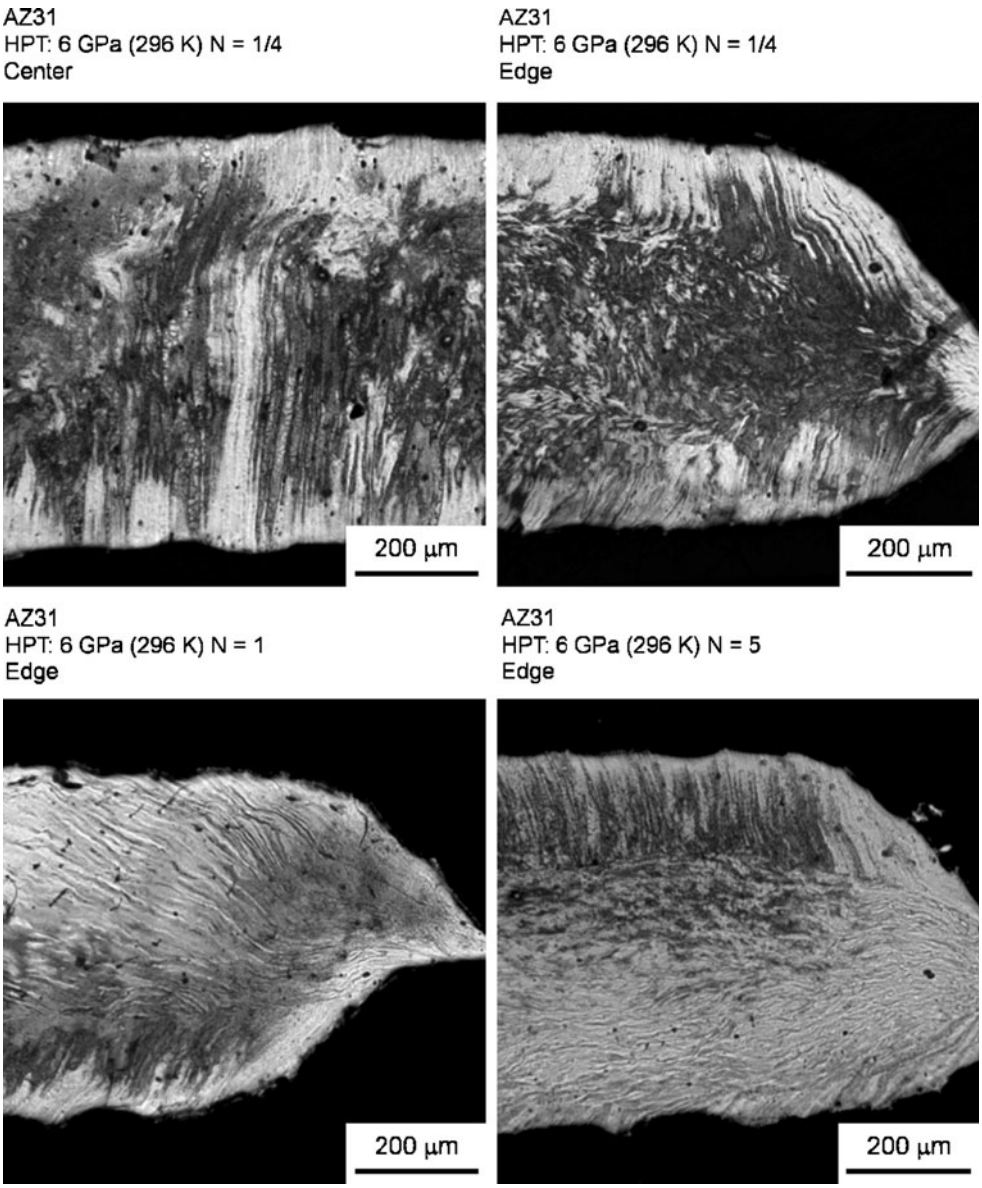

Fig. 5 Structures of the AZ31 alloy after HPT processing to different numbers of turns

$P = 6.0$ GPa and $\Delta T \approx 13$ °C for AZ91 where $P = 3.0$ GPa. Thus, these estimated values are low because of the low rotation rate and the reduced strength of the magnesium alloys. As a consequence, it is reasonable to conclude from these calculations that the temperature rise is of negligible importance and it cannot account for the occurrence of any recrystallization during processing.

Structural inhomogeneity

Magnesium has a hexagonal close-packed (hcp) structure and a limited number of slip planes so that it is generally characterized by limited ductility and a poor formability at room temperature [40, 41]. This inherent brittleness of magnesium alloys is a consequence both of the limited number of slip systems and the failure to fulfill von Mises criterion of five independent slip systems for general homogeneous polycrystalline deformation [42].

It is possible to process magnesium by HPT at room temperature because of the presence of a large hydrostatic pressure that prevents cracking within the sample. However, the sectional displays presented in Fig. 1 show the possibility of introducing cracking in the AZ91 alloy after processing through 5 turns under an applied pressure of 3.0 GPa. This pressure is calculated as the force applied by the anvils divided by the initial area of the sample. It was shown recently, using finite element modeling, that the real hydrostatic stress (or mean stress) is not constant across the cross section of the samples in HPT [36]. Larger compressive stresses are observed near the center and lower stresses are observed at the edge. Moreover, it was shown that the mean stresses decrease with increasing numbers of

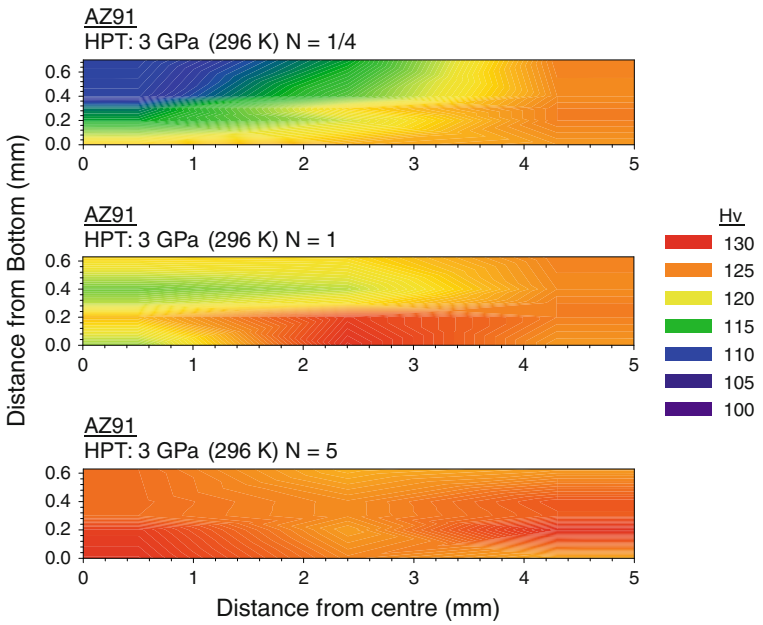

Fig. 6 Color-coded contour mapping for the AZ91 alloy showing the hardness distributions on one-half of the cross-sectional planes after HPT processing through 1/4 turn (*upper*), 1 turn (*center*), and 5 turns (*lower*)

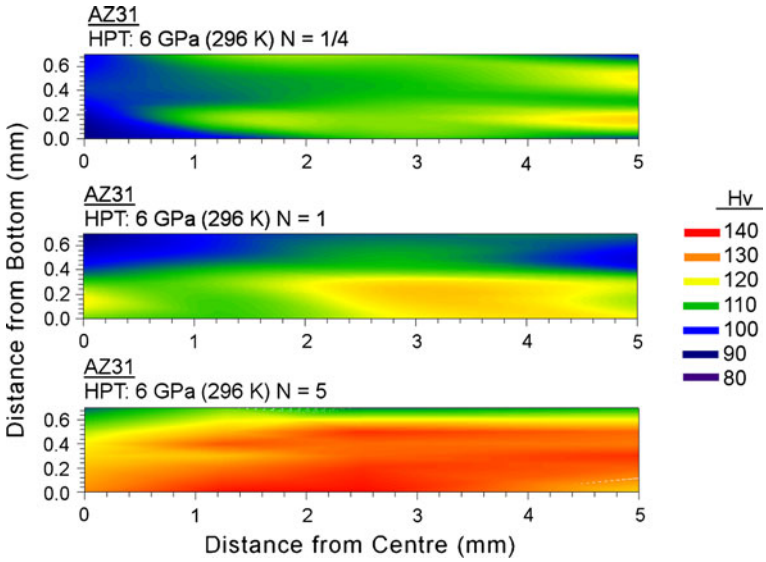

Fig. 7 Color-coded contour mapping for the AZ31 alloy showing the hardness distributions on one-half of the cross-sectional planes after HPT processing through 1/4 turn (*upper*), 1 turn (*center*), and 5 turns (*lower*)

rotations due to the material outflow which occurs in quasi-constrained HPT between the upper and lower anvils. In practice, this outflow increases the effective cross-sectional area of the sample.

The present results show different structural features along the through-thickness directions of the samples after processing by HPT. Furthermore, differences in the levels of inclination of the grain structures in the AZ91 alloy are readily apparent in Fig. 2 after 1/4, 1, and 5 turns. The alignment of grains is expected to reveal the traces of plastic flow during HPT and, therefore, differences in grain alignment at different distances from the disk surfaces demonstrate the development of variations in the plastic flow within the disks. In Fig. 2, the elongated areas of the grain structures lie mainly parallel to the disk surfaces, thereby revealing concentrations of deformation in these areas that are smaller in thickness than the size of the samples. This deformation appears to be concentrated essentially near the bottom and top surfaces of the disk processed to 1/4 turn but thereafter it spreads gradually throughout the vertical planes of disks processed through 1 and 5 turns.

It should be noted that these differences are not predicted by the theory of torsional deformation. However, computer modeling of plastic flow in HPT has shown the occurrence of heterogeneities along the through-thickness directions after processing [38]. These heterogeneities may be caused by the overall material behavior as in an absence

of strain hardening, by the sample aspect ratio and/or by the frictional forces between the samples and the lateral walls of the depressions in the anvils. It is noted that the present results in Fig. 3 show the occurrence of shear banding in the magnesium AZ91 alloy and this demonstrates a high propensity for flow localization in this material.

Hardness inhomogeneity

The present results provide a clear demonstration that in the Mg–Al–Zn alloys the hardness distributions are generally, at least initially, not homogeneous along the through-thickness directions. This supports the observations of differences in structure along this direction, as in Fig. 2, and confirms the occurrence of plastic flow localization. Moreover, the present results show an overall increase in hardness with increasing distance from the centers of the samples and with increasing numbers of rotations. Similar trends are observed in both alloys.

It was shown in early experiments using HPT processing that the measured hardness values vary with the distance from the center of each disk, but a reasonable correlation may be achieved by plotting hardness measurements against the calculated equivalent strains [21]. A similar approach was adopted in the present experiments in order to evaluate the effect of the alloying content on the evolution of hardness in these two magnesium alloys. In HPT processing, the equivalent von Mises strain, ε_{eq}, is given by a relationship of the form [43–45].

$$\varepsilon_{eq} = \frac{2\pi Nr}{h\sqrt{3}} \tag{4}$$

where N is the number of turns, r is the distance measured from the center, and h is the initial height (or thickness) of the sample. It is noteworthy that simulations of HPT by finite element modeling show a general consistency between the imposed strain and the values calculated by Eq. (4) [28, 35, 36]. Figure 8 shows the variation of hardness with equivalent strain where the hardness values were obtained by taking the average hardness values at selected points along the through-thickness directions. It is readily apparent from Fig. 8 that the alloy with the higher aluminum content (AZ91 with 9 wt% Al) exhibits a higher hardness in the initial stages of deformation but the other alloy (AZ31 with 3 wt% Al) exhibits an initial higher rate of hardening. In practice, both alloys exhibit similar values of hardness at the highest levels of strain where this corresponds reasonably with the saturation values.

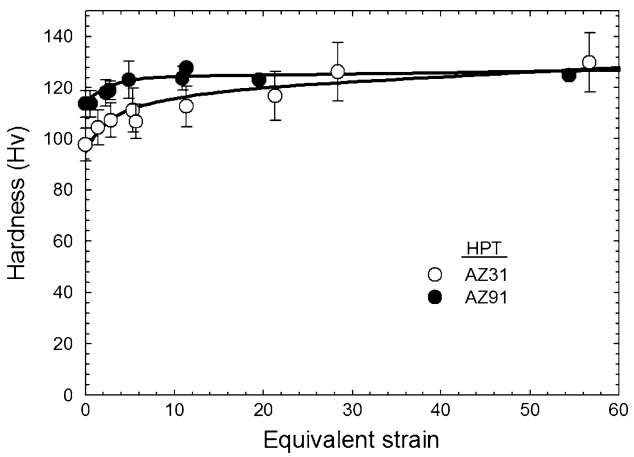

Fig. 8 Values of the Vickers microhardness plotted as a function of the equivalent strain for the AZ91 and AZ31 alloys after HPT processing

Summary and conclusions

(1) Samples of two magnesium alloys with different levels of alloying content (AZ91 and AZ31) were processed by HPT at room temperature for up to 5 turns. The structures were characterized and the hardness distributions were measured on vertical cross-sectional planes cut through the disks.

(2) Under quasi-constrained HPT processing, both alloys exhibit heterogeneous flow in the through-thickness directions. This heterogeneity is confirmed through variations in the flow pattern in the structures, the presence of shear bands, and variations in the microhardness along the longitudinal sections.

(3) The alloy with the higher content of aluminum (AZ91) exhibits higher hardness at lower levels of strain compared with its counterpart with a lower content of aluminum (AZ31). However, AZ31 exhibits increasing hardness with increasing strain and both alloys show similar saturation levels of hardness after large amounts of deformation.

Acknowledgements One of the authors is grateful for support from The Higher Committee for Education Development (HCED) of the Government of Iraq (AA-Z). This work was supported by the European Research Council under ERC Grant Agreement No. 267464-SPDMETALS.

References

1. Avedesian MM, Baker H (eds) (1999) ASM specialty handbook: magnesium and magnesium alloys. The Materials Information Society, Materials Park
2. Segal VM (1995) Mater Sci Eng A 197:157
3. Valiev RZ, Langdon TG (2006) Prog Mater Sci 51:881
4. Zhilyaev AP, Langdon TG (2008) Prog Mater Sci 53:893
5. Eddahbi M, del Valle JA, Perez-Prado MT, Ruano OA (2005) Mater Sci Eng A 410-411:308

6. Lapovok R, Estrin Y, Popov MV, Rundell S, Williams T (2008) J Mater Sci 43:7372. doi:10.1007/s10853-008-2685-z
7. Figueiredo RB, Langdon TG (2010) J Mater Sci 45:4827. doi:10.1007/s10853-010-4589-y
8. Figueiredo RB, Száraz Z, Trojanová Z, Lukáč P, Langdon TG (2010) Scripta Mater 63:504
9. Kang F, Liu JQ, Wang JT, Zhao X (2010) Adv Eng Mater 12:730
10. Figueiredo RB, Cetlin PR, Langdon TG (2009) Mater Sci Eng A 518:124
11. Figueiredo RB, Cetlin PR, Langdon TG (2010) Metall Mater Trans A 41A:778
12. Huang Y, Figuiredo RB, Baudin T, Helbert AL, Brisset F, Langdon TG (2012) J Mater Sci 47:7796. doi:10.1007/s10853-012-6578-9
13. Huang Y, Figuiredo RB, Baudin T, Brisset F, Langdon TG (2012) Adv Eng Mater 14:1018
14. Segal VM (1999) Mater Sci Eng A 271:322
15. Wu Y, Baker I (1997) Scripta Mater 37:437
16. Prangnell PB, Harris C, Roberts SM (1997) Scripta Mater 37:983
17. Semiatin SL, Delo DP, Shell EB (2000) Acta Mater 48:1841
18. Figueiredo RB, Aguilar MTP, Cetlin PR (2006) Mater Sci Eng A 430:179
19. Zhilyaev AP, Nurislamova GV, Kim BK, Baró MD, Szpunar JA, Langdon TG (2003) Acta Mater 51:753
20. Ivanisenko Y, Lojkowski W, Valiev RZ, Fecht HJ (2003) Acta Mater 51:5555
21. Vorhauer A, Pippan R (2004) Scripta Mater 51:921
22. Ivanisenko Y, Valiev RZ, Fecht HJ (2005) Mater Sci Eng A 390:159
23. Estrin Y, Molotnikov A, Davies CHJ, Lapovok R (2008) J Mech Phys Solids 56:1186
24. Xu C, Langdon TG (2009) Mater Sci Eng A 503:71
25. Kawasaki M, Ahn B, Langdon TG (2010) Acta Mater 58:919
26. Arpacay D, Yi S, Janecek M, Bakkaloglu A, Wagner L (2008) Mater Sci Forum 584–586:300
27. Hohenwarter A, Bachmaier A, Gludovatz B, Scheriau S, Pippan R (2009) Int J Mater Res 100:1653
28. Lapovok R, Pougis A, Lemiale V, Orlov D, Toth LS, Estrin Y (2010) J Mater Sci 45:4554. doi:10.1007/s10853-010-4403-x
29. Figueiredo RB, Langdon TG (2011) Mater Sci Eng A 528:4500
30. Geist D, Rentenberger C, Karnthaler HP (2011) Acta Mater 59:4578
31. Figueiredo RB, Aguilar MTP, Cetlin PR, Langdon TG (2011) Metall Mater Trans A 42A:3013
32. Jeong HJ, Yoon EY, Lee DJ, Kim NJ, Lee S, Kim HS (2012) J Mater Sci 47:7828. doi:10.1007/s10853-012-6540-x
33. Figueiredo RB, Kawasaki M, Langdon TG (2012) Acta Phys Pol A 122:425
34. Yilmazer H, Niinomi M, Nakai M, Hieda J, Todaka Y, Akahori T, Miyazaki T (2012) J Mech Behav Biomed Mater 10:235
35. Lee DJ, Yoon EY, Park LJ, Kim HS (2012) Scripta Mater 67:384
36. Figueiredo RB, Cetlin PR, Langdon TG (2011) Mater Sci Eng A 528:8198
37. Figueiredo RB, Pereira PHR, Aguilar MTP, Cetlin PR, Langdon TG (2012) Acta Mater 60:3190
38. Figueiredo RB, Aguilar MTP, Cetlin PR, Langdon TG (2012) J Mater Sci 47:7807. doi:10.1007/s10853-012-6506-z
39. Edalati K, Miresmaeili R, Horita Z, Kanayama H, Pippan R (2011) Mater Sci Eng A 528:7301
40. Mabuchi M, Iwasaki H, Yanase K, Higashi K (1997) Scripta Mater 36:681
41. Yamashita A, Horita Z, Langdon TG (2001) Mater Sci Eng A 300:142
42. Kubota K, Mabuchi M, Higashi K (1999) J Mater Sci 34:2255. doi:10.1023/A:1004561205627
43. Valiev RZ, Ivanisenko YV, Rauch EF, Baudelet B (1996) Acta Mater 44:4705
44. Wetscher F, Vorhauer A, Stock R, Pippan R (2004) Mater Sci Eng A 387–389:809
45. Wetscher F, Pippan R, Sturm S, Kauffmann F, Scheu C, Dehm G (2006) Metall Mater Trans A 37A:1963

J Mater Sci (2014) 49:6517–6528
DOI 10.1007/s10853-014-8203-6

ULTRAFINEGRAINED MATERIALS

Effect of anvil roughness on the flow patterns and hardness development in high-pressure torsion

Yi Huang · Megumi Kawasaki · Ahmed Al-Zubaydi · Terence G. Langdon

Received: 31 January 2014 / Accepted: 26 March 2014 / Published online: 16 April 2014

Abstract Two sets of anvils having different surface roughness were used to systematically investigate the flow patterns developed on the top and bottom surfaces of stainless steel discs with an anvil misalignment of 100 μm during high-pressure torsion. It is shown that the flow patterns on the disc surfaces have different variation tendencies depending on whether the anvils have rough or smooth surfaces. Double-swirl flow patterns were observed on the top and bottom surfaces of discs after 1 and 5 turns when using an anvil with a smooth surface. In contrast, when using an anvil with a rough surface the double-swirl flow patterns appeared only on the top surface after 1 turn and a single swirl appeared on both surfaces after 5 turns. Hardness measurements on the top surfaces showed that discs processed using an anvil with a rough surface have greater hardness than discs processed using an anvil with a smooth surface. There was no obvious hardness difference on the bottom surfaces for discs processed using anvils with rough or smooth surfaces.

Y. Huang (✉) · A. Al-Zubaydi · T. G. Langdon
Materials Research Group, Faculty of Engineering and the Environment, University of Southampton, Southampton SO17 1BJ, UK
e-mail: y.huang@soton.ac.uk

M. Kawasaki · T. G. Langdon
Departments of Aerospace & Mechanical Engineering and Materials Science, University of Southern California, Los Angeles, CA 90089-1453, USA

M. Kawasaki
Division of Materials Science and Engineering, Hanyang University, 17 Haengdang-dong, Seongdong-gu, Seoul 133-791, South Korea

Introduction

High-pressure torsion (HPT) is a mature severe plastic deformation technique which is regularly used to achieve significant grain refinement [1]. There are many published results on HPT processing of various metals and alloys [2] and recently HPT techniques were applied to the processing of metal powders [3, 4] and machining chips [5]. The uses of HPT also include mechanical mixing [6], investigations of amorphization [7, 8] and phase transformations [9–11], evaluations of the hydrogen storage capabilities of magnesium [12, 13], and examinations of the structural modifications and the mechanical properties of bulk metallic glasses [14, 15].

In the idealized HPT process, the deformation procedure can be considered as a simple shear process (rigid-body analysis) where the shear strain, γ, is evaluated using the equation [16]:

$$\gamma = \frac{2\pi Nr}{h} \tag{1}$$

where r and h are the radius and height (or thickness) of the disc, respectively, and N is the number of revolutions. In the idealized unconstrained HPT, the disc is placed between two flat anvils and the lateral flow of the material is not restricted under the applied pressure. However, this unconstrained HPT is technically difficult to implement as there is a continuous decrease in the sample thickness. In constrained HPT, the disc is placed within a cavity in the lower anvil so that the lateral flow of the material is totally restricted under the applied hydrostatic pressure. In this condition, the specimen deforms under torsional straining and under the imposed hydrostatic pressure without changes in the geometry if there is no friction force at the outer cylinder wall. However, because friction is unavoidable, a

homogenous shear deformation process cannot occur in constrained HPT. In practice, quasi-constrained HPT can overcome the drawbacks and problems associated with idealized unconstrained and constrained HPT. Most HPT processing is now conducted under quasi-constrained conditions where the disc is contained within shallow depressions on the lower and upper anvils, and there is some limited outflow of material between the two anvils during the straining operation [17, 18].

It follows from Eq. (1) that the shear strain should increase linearly with the radius of the disc. Therefore, based on the rigid-body assumption in Eq. (1), it is reasonable to anticipate that the microstructure and mechanical properties remain inhomogeneous across the disc. However, there is an additional strain on the HPT disc due to the applied compressive stress introduced in quasi-constrained HPT processing and this is not considered in Eq. (1). In practice, there is an evolution towards microstructural homogeneity in HPT and this has been effectively predicted by making use of strain gradient plasticity modelling [19]. In fact, a fully homogeneous microstructure and mechanical properties have been reported in many materials after HPT processing [13, 20–25].

Some recent experiments were conducted on a duplex stainless steel to observe visual displays of the flow patterns produced by the HPT processing [26–28]. The results were unexpected because there was evidence for the formation of significant local turbulence including the presence of double-swirl patterns and local shear strain vortices. Furthermore, double-swirl flow patterns were also observed in a Cu-28 % Ag alloy after HPT processing [29]. It is possible that the presence of double-swirl flow patterns may arise in HPT discs from a misalignment of the axes of the anvils prior to conducting the HPT processing. However, no specific information on the initial anvil alignment was available in these earlier reports, and no checks were undertaken to determine whether the anvils were in alignment [26–29]. Therefore, it is not possible to obtain a correlation between the appearance of double-swirl patterns on the disc surfaces and the inherent anvil misalignments.

The effect of a misalignment of the axes of the anvils was first considered in several reports of HPT in order to explain the reasons for attaining a fully-homogenized microstructure and hardness distribution [30, 31] but this possibility was never examined experimentally. Recently, a series of experiments were conducted to investigate the effect of different amounts of anvil misalignment on the flow patterns and hardness distributions on the top surfaces of discs in HPT processing [32–34]. These experiments showed that the presence of double-swirls on the disc top surfaces was a feature of HPT processing when the anvils had a small initial lateral misalignment.

Friction is an important factor which is needed in order to achieve the torsional straining. Therefore, the anvil surfaces are generally initially treated by sandblasting or spark erosion in order to generate a distinctive surface micro-roughness. Through this surface roughness, combined with the hydrostatic pressure, it is feasible to develop the high frictional forces that are required for rotational straining. To date, there has been no investigation to determine whether the initial anvil surface roughness has any effect on the flow patterns and the hardness distributions. Accordingly, the present research was initiated to investigate the influence of the anvil roughness on the flow patterns generated on both the top and bottom surfaces of the discs when processing by HPT.

Experimental material and procedures

A commercial F53 super duplex stainless steel was received in the form of a rolled plate having a thickness of 3 mm. This material was supplied by Castle Metals UK Ltd. (Blackburn, Lancashire. UK), and has a high yield strength up to ~570 MPa, good ductility and outstanding corrosion resistance. The chemical composition of the as-received material is given in Table 1 and the microstructure is shown in Fig. 1. The material consists of essentially equal proportions, and similar volume fractions, of the lighter-contrast austenitic (γ) and the darker-contrast ferritic (α) phases. The widths of these two phases varied between ~5 and ~50 μm.

Discs having diameters of 9.8 mm and thicknesses of ~1.2 mm were cut from the steel plate, and then ground to a uniform thickness of ~0.82 mm. The HPT processing was conducted at room temperature under quasi-constrained conditions [17, 18] using two massive anvils each machined with a central depression having a diameter of 10 mm and a depth of 0.25 mm. The term anvil misalignment is used to denote a parallel displacement of the rotation axis of the upper anvil with respect to the lower anvil, and the basic principles of anvil alignment were given in earlier reports [32–34]. In the present experiments, the anvils were set up with an initial misalignment of 100 μm.

Table 1 Chemical composition of the super duplex stainless steel

Element	C	Cr	Mn	Mo	N	Ni	P	S	Si
wt. (%)	<0.030	24.0–26.0	<1.20	3.0–5.0	0.24–0.32	6.0–8.0	<0.035	<0.020	<0.8

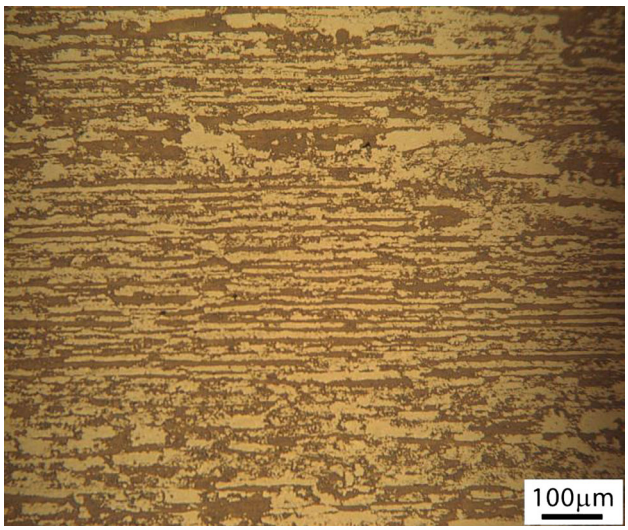

Fig. 1 Microstructure of the as-received duplex stainless steel

The surface roughness of the anvils was measured using Alicona Infinite Focus. Two sets of anvils having different surface roughness were used to investigate the flow patterns on the disc top and bottom surfaces after HPT. Figure 2 shows the anvil surface profile measurements on the two anvils which are nominally designated (a) smooth and (b) rough. For each anvil, the upper image is the anvil surface morphology as represented by a set of unique colours shown by the colour key on the right, and the lower image is the result of surface roughness measurements along the anvil surface shown in the upper image. The measured average surface roughness values of the smooth and rough anvils, R_a, were equal to 5 and 15 μm, respectively. Henceforth, these initial anvil surface conditions are named smooth with $R_a = 5$ μm and rough with $R_a = 15$ μm.

A set of discs was prepared for both of these anvil surface conditions with the discs processed at room temperature with a pressure 6.0 GPa and a rotation speed of 1 rpm through totals of $N = 1$ and 5 turns. To avoid any problems with slippage, all of the HPT processing was conducted using new anvils so that the surfaces within the depressions were in perfect condition. In addition, and following standard practice [35], some preliminary tests were conducted using discs with marker lines scribed on the top and bottom surfaces and these tests revealed no evidence for any slippage under the present experimental conditions.

After processing through 1 and 5 turns, the discs were mounted in bakelite for top and bottom surface observations. The mounted samples were mechanically polished, and then electro-etched using an electrolyte of 40 % NaOH solution at 25 °C. After etching, the γ-phase appeared bright and the α-phase appeared dark. The local flow patterns were examined using an Olympus BX51 microscope.

The values of the Vickers microhardness, Hv, were measured on the polished surfaces with separations of 0.3 mm between each consecutive point along the disc diameter. An FM300 hardness tester equipped with a Vickers indenter was used with a load of 300 gf and a dwell time of 15 s.

Experimental results

Flow pattern observations on disc top and bottom surfaces using the smooth anvil

Figure 3 shows the flow patterns developed on the disc top surface when using smooth anvils where the rows of black dots correspond to the marks from the hardness mapping indentations. The appearance of the disc top surface shows a clearly defined curvature of the phase domains for both 1 turn in Fig. 3 (a) and 5 turns in Fig. 3 (b). Close inspection shows there are pairs of curvatures for both conditions and these pairs correspond to double-swirls with each swirl having a unique swirl centre. Earlier reports demonstrated similar observations, and it was found that the double-swirl configurations decrease in size with increasing numbers of turns on the disc top surface [32–34].

Figure 4 displays the flow patterns on the disc bottom surface when using smooth anvils for (a) 1 turn and (b) 5 turns. The bottom surfaces also display well-defined curvature of the phase domains for both 1 and 5 turns. It is obvious that there are double-swirl flow patterns on the bottom surfaces and the distance between the two swirl centres is reduced with increasing numbers of rotations. The current observations on the disc bottom surfaces are different from those reported earlier where no double-swirls patterns were visible at the bottom [28]. However, the present observations are for samples processed with smooth anvils and with a measured anvil misalignment of 100 μm, whereas no information is available on either the smoothness of the anvils or the extent of the initial anvil misalignment in the earlier report.

Ideally, the flow patterns on the disc top and bottom surfaces should be identical but with the flow visible in opposite directions. Figs. 3 and 4 demonstrate this ideal symmetry because both top and bottom surfaces show the appearance of double-swirls and, as the numbers of rotations increase from 1 to 5 turns, the configuration size of the double-swirls becomes smaller on both the top and bottom surfaces.

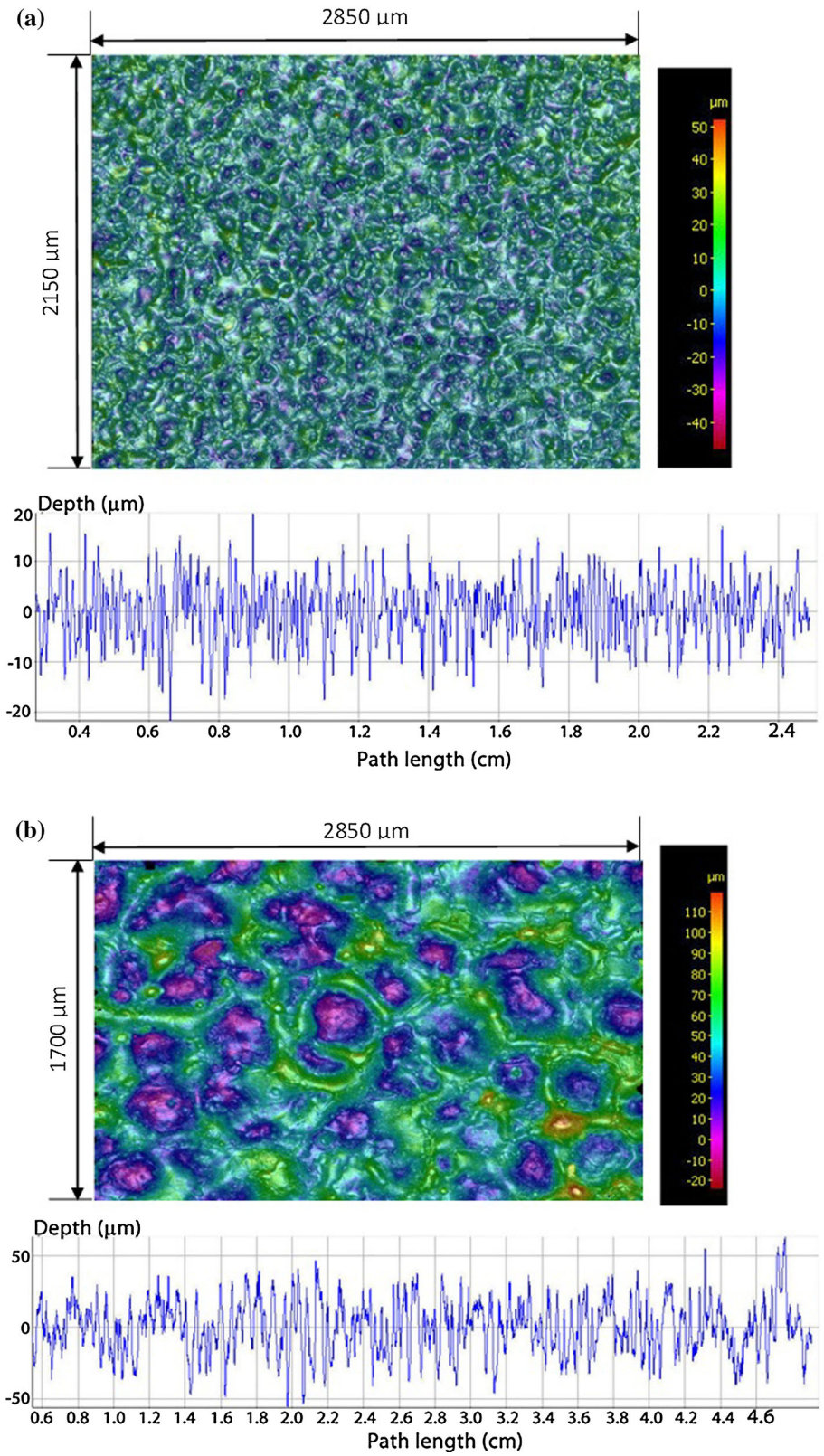

Fig. 2 Anvil surface profile measurements on **a** the smooth anvil and **b** the rough anvil: for each anvil, the *upper image* shows the surface morphology with the colour key on the right and the *lower image* shows the measurements of the surface roughness taken on the anvil surface shown in the upper image

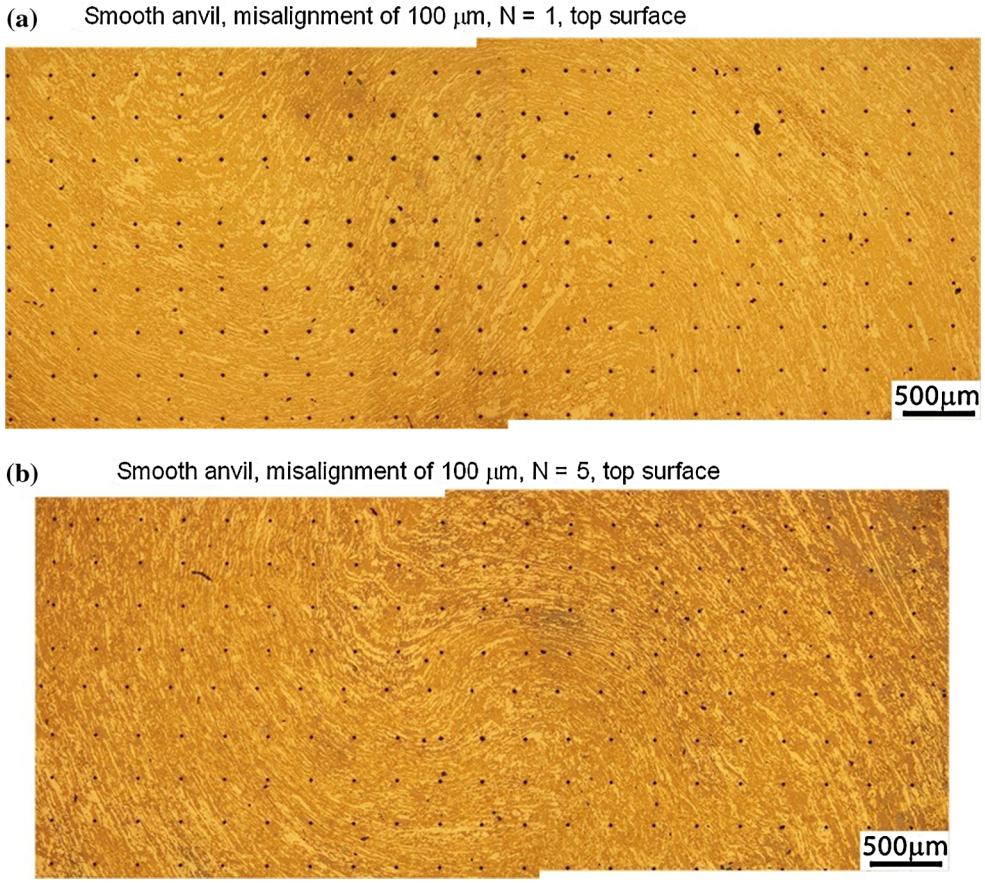

Fig. 3 The flow pattern appearance on the disc top surface while using smooth anvils ($R_a = 5$ μm) with an anvil misalignment of 100 μm for **a** $N = 1$ turn and **b** $N = 5$ turns

Flow pattern observations on disc top and bottom surfaces using the rough anvil

Figure 5 shows the flow patterns developed on the disc top surfaces when using the rough anvils. In Fig. 5 (a) and (b), the top row shows low magnification images of the phase domains along the disc diameter and the two lower rows show high magnification images of the areas in the red squares in the upper images. From the top row image in Fig. 5 (a), a double-swirl flow pattern can be recognised on the disc top surface after 1 turn, but the double-swirl is not clearly defined as on the top surface when using smooth anvils in Fig. 3 (a). Thus, in Fig. 3 (a) the austenitic (γ) and the ferritic (α) phases are clearly distinguished and the curvature of the phase domains is smooth, whereas in the top image in Fig. 5 (a) the overall curvature of the phase domains is not smooth so that some areas show clear two phase contrast and other areas display unclear phase contrast. The bottom images corresponding to the areas marked with the red squares in the top row show that the left red square contains many local vortices, whereas the right red square, which is an area showing unclear two phase contrast at the low magnification, has two phases with the widths of the austenitic (γ) and the ferritic (α) phases reduced significantly.

These observations suggest that local deformation, such as local vortices and local variations in the widths of the austenitic (γ) and ferritic (α) phase refinement, leads to a non-uniform appearance for the phase domains. After 5 turns, the disc top surface shows an overall single swirl appearance in the top row image in Fig. 5 (b). There appears to be a clear phase contrast and some local vortices, but the magnified image of the red square of the single swirl area shows that the widths of the austenitic (γ) and the ferritic (α) phases are significantly refined. Again, these observations confirm the occurrence of non-uniform deformation on the disc top surface.

The appearance of the flow patterns on the disc bottom surfaces when using a rough anvil is shown in Fig. 6 after (a) 1 turn and (b) 5 turns. After 1 turn, the domains for the austenitic γ and ferritic α phases are easily recognised in Fig. 6 (a) and the phase domains remain reasonably straight in the centres of the discs with an appearance that is generally similar to the initial as-received material shown in Fig. 1. These straight patterns continued throughout the disc bottom surface except for small

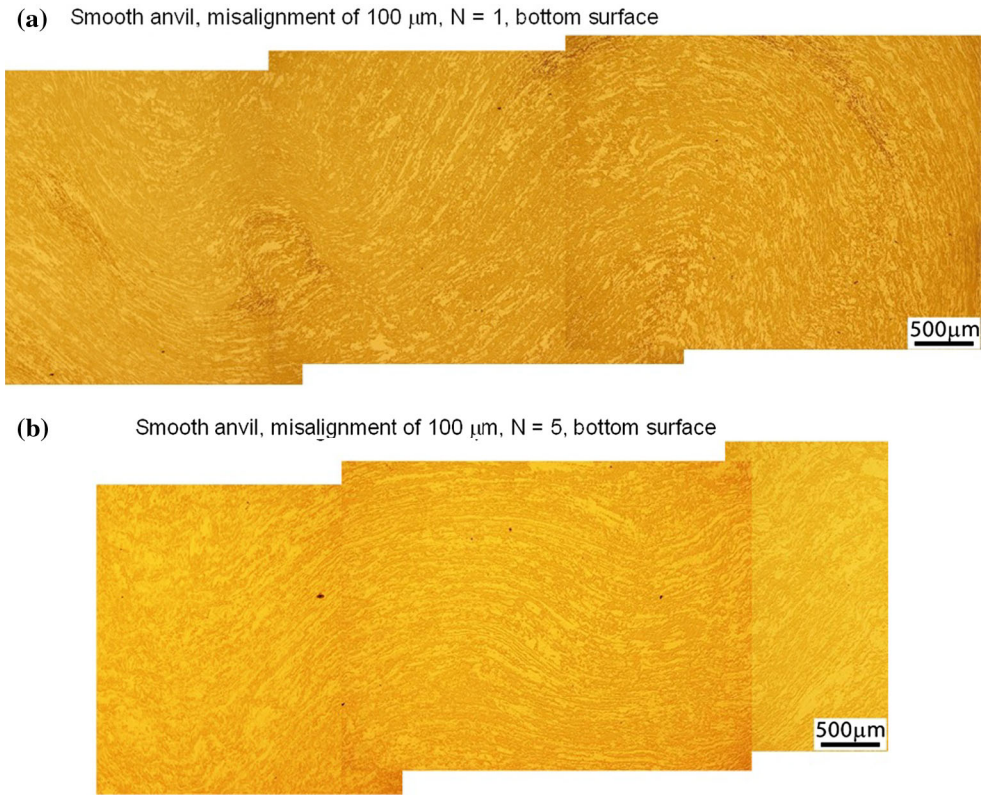

Fig. 4 The flow pattern appearance on the disc bottom surface, while using smooth anvils ($R_a = 5$ μm) with an anvil misalignment of 100 μm for **a** $N = 1$ turn and **b** $N = 5$ turns

deviations at the edges of the discs. In Fig. 6 (b), the top row shows low magnification images of the phase domains along the disc diameter and the bottom row shows high magnification images of the areas contained within the red squares in the upper images. A single swirl is clearly identified on the disc bottom surface after 5 turns as shown in the top row image of Fig. 6 (b) but in the right red square the domains of the austenitic γ and ferritic α phases cannot be identified clearly and this is similar to the single swirl observed on the disc top surface with the rough anvil after 5 turns as shown in Fig. 5 (b). The high magnification images in the bottom row of Fig. 6 (b) show the refined austenitic (γ) and the ferritic (α) phases in the right red square area and local vortices that have developed in the left red square area.

It is concluded from these observations that a rough anvil in HPT leads to different flow patterns on the disc top and bottom surfaces after 1 turn. Thus, the disc top surface shows double-swirl flow patterns in Fig. 5 (a), whereas the disc bottom surface displays straight phase domains in Fig. 6 (a). Figures 5 (b) and 6 (b) demonstrate the occurrence of ideal symmetry on the top and bottom surfaces after 5 turns because these surfaces show the same single swirl flow pattern.

A comparison of hardness evolution on the top surfaces with smooth and rough anvils

To compare the influence of smooth and rough anvils on the mechanical characteristics of the top surfaces, the hardness distributions were recorded after 1 and 5 turns as presented in Fig. 7 for (a) 1 and (b) 5 turns.

After 1 turn, the use of smooth anvils introduces double-swirl flow patterns on the disc top surface, whereas rough anvils lead to the appearance of double-swirls with non-uniform phase domain contrast. As shown in Fig. 7 (a), the hardness values on the top surface using the rough anvil are larger than with the smooth anvil. Nevertheless, the hardness distributions from the smooth and rough anvils display similar variations across the discs with a minimum hardness in the centre, higher values towards the edges and with evidence for a saturation condition at the edge of the disc over an outer ring having a width of about 2 mm.

After 5 turns, the smooth anvil generates double-swirl flow patterns on the top surface, whereas the rough anvil produces the appearance of a single swirl with a non-uniform phase domain contrast in the swirl area. In Fig. 7 (b)

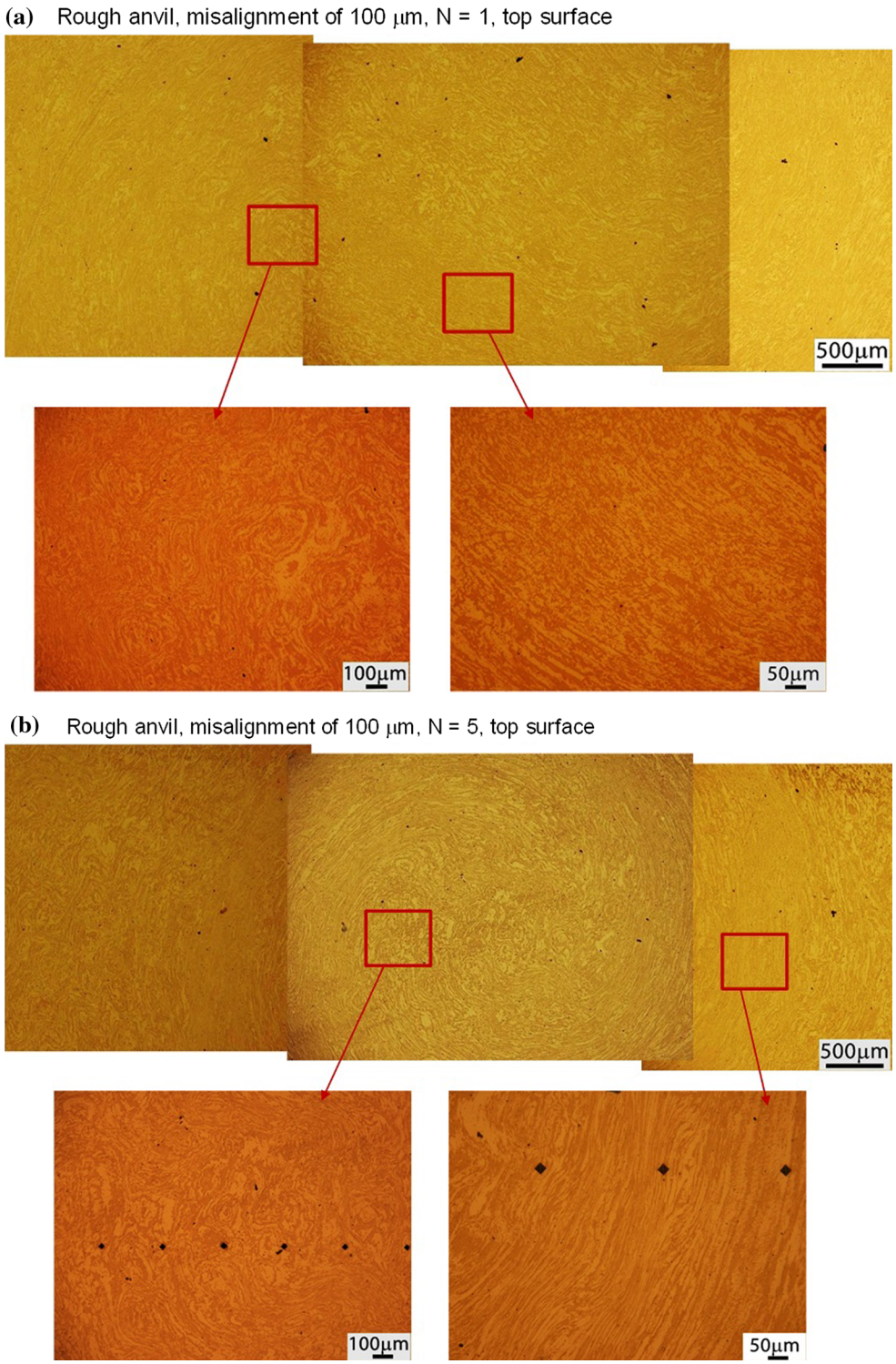

Fig. 5 The flow pattern appearance on the disc top surface while using rough anvils ($R_a = 15$ μm) with an anvil misalignment of 100 μm for **a** $N = 1$ turn and **b** $N = 5$ turns

the microhardness values after 5 turns are again larger for the rough anvil. Furthermore, after 5 turns the position of the minimum hardness is displaced from the disc centre for the smooth anvil, but it remains essentially in the centre position for the rough anvil.

A comparison of hardness evolution on the bottom surfaces with smooth and rough anvils

To compare the influence of smooth and rough anvils on the mechanical characteristics for the disc bottom surfaces,

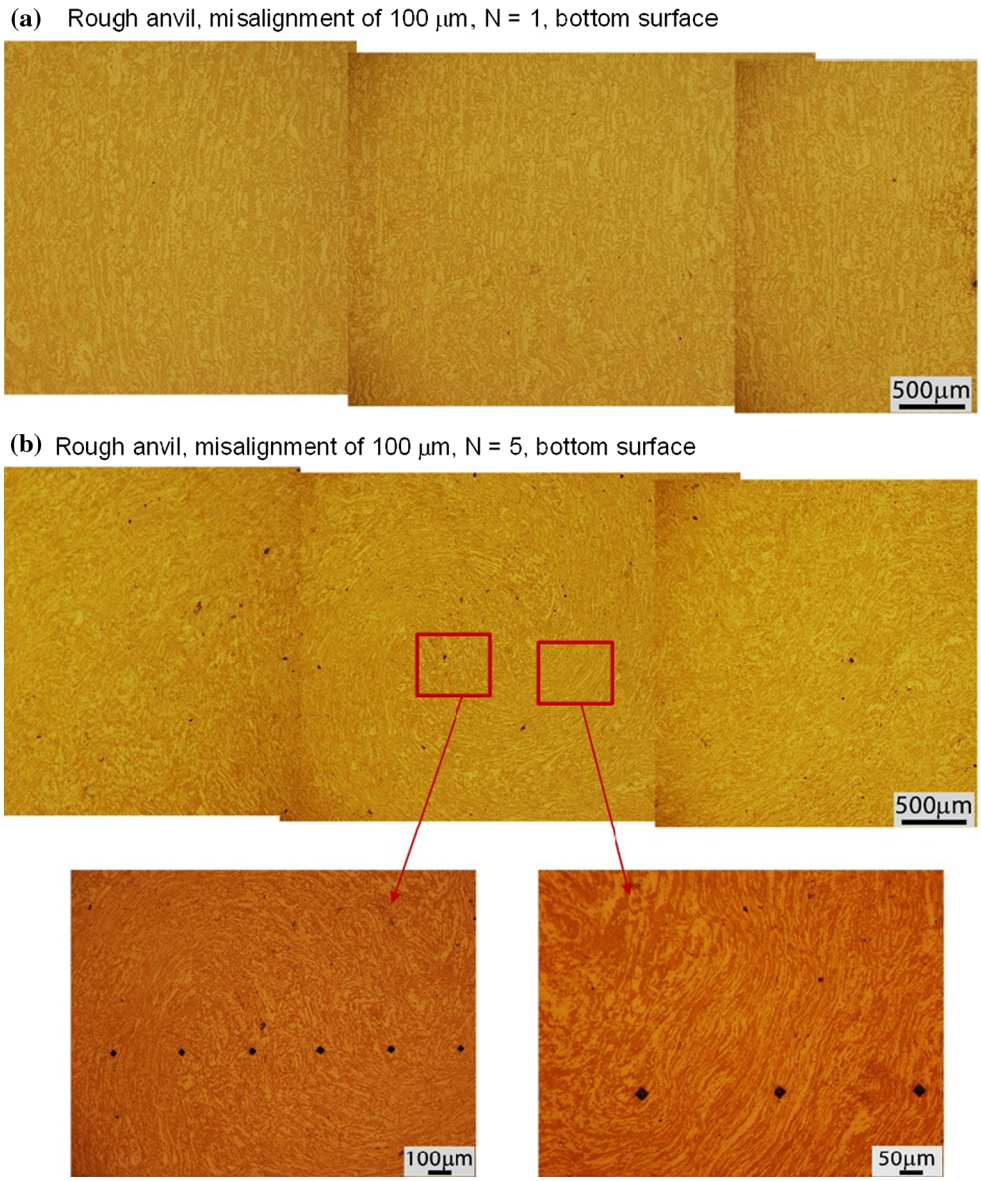

Fig. 6 The flow pattern appearance on the disc bottom surface while using rough anvils ($R_a = 15$ μm) with an anvil misalignment of 100 μm for **a** $N = 1$ turn and **b** $N = 5$ turns

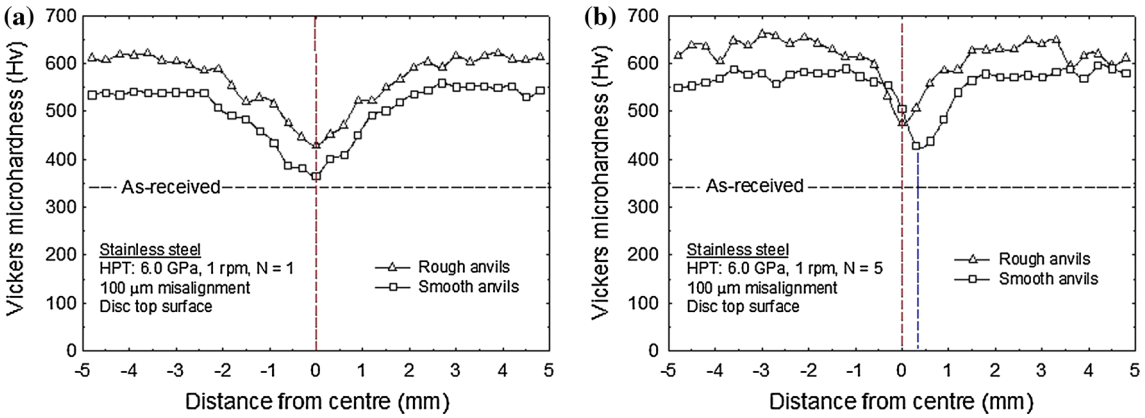

Fig. 7 Hardness distributions on the disc top surface after **a** 1 and **b** 5 turns using smooth and rough anvils

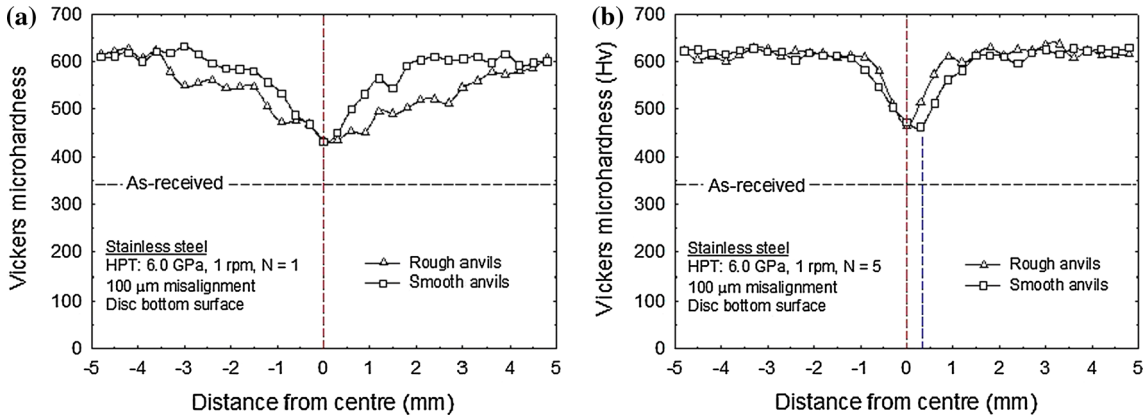

Fig. 8 Hardness distributions on the disc bottom surface after **a** 1 and **b** 5 turns using smooth and rough anvils

hardness distributions were recorded on the bottom surfaces as shown in Fig. 8 after (a) 1 and (b) 5 turns.

After 1 turn, double-swirl flow patterns are visible on the bottom surfaces with the smooth anvil, whereas the phase domains have a straight appearance with the rough anvil. Due to these different flow patterns, the hardness distributions for the smooth and rough anvils have different variations. As shown in Fig. 8 (a), with the smooth anvil the hardness distribution displays a two-stage behaviour which includes an initial linear variation between hardness and distance around the centre of the disc and then a saturation plateau. With rough anvils, the hardness values increase almost linearly with the disc radius from the centre to the edge. The linear variations of hardness on the bottom surface with the rough anvil demonstrate that the shear strain at the disc bottom is very close to the ideal rigid-body assumption. Overall, the hardness values at the bottom surface tend to be larger with the smooth anvil than with the rough anvil.

After 5 turns, smooth anvils produce double-swirl flown patterns on the disc bottom surface, whereas rough anvils generate the appearance of a single swirl with a non-uniform phase domain contrast. Figure 8 (b) shows the overall microhardness values at the disc bottom surface using the rough and smooth anvils. In Fig. 8 (b), both sets of data have similar values after processing through 5 turns of rotation, but for the smooth anvil; the minimum hardness position is again displaced from the centre position while the minimum hardness remains at the centre for the rough anvil.

Discussion

Comparing the surface morphology images of the depressions within the smooth and rough anvils in Fig. 2, it is readily apparent that the smooth anvil has not only a smaller value of R_a but also a smaller area for each pit. Overall, the smooth anvil surface in Fig. 2 (a) has shallow pits and a reasonably uniform pit distribution, whereas the rough anvil surface in Fig. 2 (b) has deeper and larger pits with a fairly non-uniform distribution. During HPT processing, the hydrostatic pressure which is imposed initially leads to a plastic flow of the sample material into the micro-asperities on the anvil surfaces within the depressions, and this provides an excellent fit between the sample and the anvil for subsequent rotational straining. Thus, shear deformation occurs in the interior of the disc sample.

With the rough anvil, the pit area and pit depth are large and the pit distribution is non-uniform so that the local frictional forces change from place to place during the HPT processing. These variations in the local frictional forces affect the flow patterns of the deformed materials. With the smooth anvil, the pit area and pit depth are relatively small and the pit distribution is reasonably uniform so that the local frictional force is reasonably uniform from place to place during the HPT processing. Due to the different surface roughness characteristics of the smooth and rough anvils, it is readily apparent that samples processed to the same numbers of rotations will have different flow patterns and hardness distributions depending on the precise nature of the anvil surfaces. Both the flow patterns and the refinement in width of the austenitic (γ) and the ferritic (α) phases make contributions to the hardness distributions on the top and bottom surfaces of the disc.

After 1 turn of rotation on the disc top surface, there are clear double-swirl flow patterns on samples processed with the smooth anvil, whereas the double-swirls are less easy to identify on the sample processed using the rough anvil. It is important to define and make a meaningful distinction between the terms *clear double-swirl flow patterns* and *recognisable double-swirl flow patterns*. The former have smooth and well-defined phase domains in low magnification images as shown in Fig. 3 (a) whereas the latter have

many local vortices and locally there is significantly refined austenitic γ and ferritic α phases as shown in Fig. 5 (a). It is reasonable to assume that variations in the local frictional forces introduced by the rough anvil contribute to the so-called recognisable double-swirl flow patterns. Furthermore, although the disc top surface shows a double-swirl flow pattern after 1 turn when using smooth or rough anvils, because of the obvious refinement in the widths of the austenitic γ and ferritic α phases with the rough anvil, as shown in Fig. 7 (a), the sample processed by 1 turn on the rough anvil has higher hardness values on the disc top surface than for the smooth anvil.

After 5 turns of rotation on the disc bottom surface, there are clear double-swirl flow patterns but with a smaller configuration when using the smooth anvil, whereas there is a single swirl flow pattern on the sample processed using the rough anvil. The double-swirl flow pattern has smooth and well-defined phase domains in the low magnification image shown in Fig. 4 (b), whereas the single swirl has local vortices in the swirl centre area and local austenitic γ and ferritic α phases which are significantly refined as shown in Fig. 6 (b). It is reasonable to assume that the local friction force variation introduced by the rough anvil leads to the single swirl flow pattern. With the smooth anvil, the disc bottom surface has double-swirl flow patterns, whereas with the rough anvil a single-swirl flow pattern accompanied by a refinement in the width of the austenitic (γ) and the ferritic (α) phases appears on the bottom surface. It is assumed the hardness value should be higher when using a rough anvil than when using a smooth anvil on the disc bottom surface but, as shown in Fig. 8 (b), the disc bottom surface of the sample processed by 5 turns with the rough anvil has similar hardness values as with the sample processed by the smooth anvil. Thus, the difference in flow patterns on the disc bottom surface failed to make a major contribution to the hardness values after 5 turns.

It should be noted that in the as-received stainless steel the widths of the austenitic (γ) and the ferritic (α) phases do not have a uniform size distribution, as shown in Fig. 1, but instead the widths vary from ~5 to ~50 μm. When using smooth anvils, *clear double-swirl flow patterns* and well-defined phase domains are present on the top and bottom surface and there are no significant refinements in the widths of the austenitic (γ) and the ferritic (α) phases. When using rough anvils, after 1 turn the disc top surface shows *a recognizable double-swirl flow pattern* with local refined austenitic (γ) and ferritic (α) phases. After 5 turns, the disc top and bottom surfaces show single-swirl flow patterns with local significantly refined austenitic (γ) and ferritic (α) phases. In these local refined phase domain areas, the measured widths of the austenitic (γ) and the ferritic (α) phases vary between ~1 and ~20 μm after 1 and 5 turns, where these values are significantly refined by comparison with the range from ~5 to ~50 μm for the austenitic (γ) and ferritic (α) phases in the as-received condition.

Finally, it is important to note that, although the strain varies significantly across the discs in HPT processing as documented in Eq. (1), there is a gradual evolution towards microstructural homogeneity with increasing numbers of revolutions and this evolution has been reported experimentally [22, 36–42] and predicted theoretically using strain gradient plasticity modelling [19].

Summary and conclusions

[1] Experiments were undertaken using a super duplex stainless steel to evaluate the influence of anvil surface roughness on the flow patterns and hardness evolution on the disc top and bottom surfaces using a fixed anvil misalignment of 100 μm during HPT processing. The experiments were conducted using smooth and rough anvils with roughness values of $R_a = 5$ μm and $R_a = 15$ μm, respectively.

[2] The results show that the same double-swirl flow patterns develop on the disc top and bottom surfaces when using a smooth anvil and the double-swirl configuration decreases with increasing numbers of rotations. When using a rough anvil, the disc top and bottom surfaces have the same single swirl flow patterns for 5 turns, whereas for 1 turn the disc top surface has a recognisable double-swirl flow pattern and the disc bottom surface has straight phase domains.

[3] While using rough anvils, there are two common features in the disc surface flow patterns. First, there are non-uniform phase domains with some areas having significantly refined austenitic γ and ferritic α phases. Second, there are some areas having local vortices. These features are attributed to variations in the local frictional forces which cause unstable flow and non-uniform structural refinement.

[4] Due to the local refinement of the austenitic γ and ferritic α phases when using the rough anvil, the disc top surface has larger hardness values than when using a smooth anvil. By contrast, there are no significant hardness differences at the bottom surface when using rough and smooth anvils.

Acknowledgements The authors thank Dr Liam Goodes for assistance during the anvil surface roughness measurements. This work was supported by the European Research Council under ERC Grant Agreement No. 267464-SPDMETALS.

References

1. Zhilyaev AP, Langdon TG (2008) Using high-pressure torsion for metal processing: fundamentals and applications. Prog Mater Sci 53:893–979
2. Kawasaki M, Figueiredo RB, Langdon TG (2012) Twenty-five years of severe plastic deformation: recent developments in evaluating the degree of homogeneity through the thickness of disks processed by high-pressure torsion. J Mater Sci 47:7719–7725. doi:10.1007/s10853-012-6507-y
3. Korznikov AV, Safarov IM, Laptionok DV, Valiev RZ (1991) Structure and properties of superfine-grained iron compacted out of ultradisperse powder. Acta Metall Mater 39:3193–3197
4. Edalati K, Horita Z, Fujiwara H, Ameyama K (2010) Cold consolidation of ball-milled titanium powders using high-pressure torsion. Metall Mater Trans A 41A:3308–3317
5. Zhilyaev AP, Gimazov AA, Raab GI, Langdon TG (2008) Using high-pressure torsion for the cold-consolidation of copper chips produced by machining. Mater Sci Eng, A 486:123–126
6. Miyazaki T, Terada D, Miyajima Y, Suryanarayana C, Murao R, Yokoyama Y, Sugiyama K, Umemoto M, Todaka Y, Tsuji N (2011) Synthesis of non-equilibrium phases in immiscible metals mechanically mixed by high pressure torsion. J Mater Sci 46:4296–4301. doi:10.1007/s10853-010-5240-7
7. Waitz T, Kazykhanov V, Karnthaler HP (2004) Martensitic phase transformations in nanocrystalline NiTi studied by TEM. Acta Mater 52:137–147
8. Révész Á, Hóbor S, Lábár JL, Zhilyaev AP, Kovács Z (2006) Partial amorphization of a Cu–Zr–Ti alloy by high pressure torsion. J Appl Phys 100:103522 (1–7)
9. Ivanisenko Y, Kilmametov A, Rösner H, Valiev RZ (2008) Evidence of alpha → omega phase transition in titanium after high pressure torsion. Int J Mater Res 99:36–41
10. Pérez-Prado MT, Zhilyaev AP (2009) First experimental observation of shear induced hcp to bcc transformation in pure Zr. Phys Rev Lett 102:175504 (1–4)
11. Wang YB, Zhao YH, Lian Q, Liao XZ, Valiev RZ, Ringer SP, Zhu YT, Lavernia EJ (2010) Grain size and reversible beta-to-omega phase transformation in a Ti alloy. Scr Mater 63:613–616
12. Leiva DR, Jorge AM, Ishikawa TT, Huot J, Fruchart D, Miraglia S, Kiminami CS, Botta WJ (2010) Nanoscale grain refinement and H-sorption properties of MgH_2 processed by high-pressure torsion and other mechanical routes. Adv Eng Mater 12:786–792
13. Edalati K, Yamamoto A, Horita Z, Ishihara T (2011) High-pressure torsion of pure magnesium: evolution of mechanical properties, microstructures and hydrogen storage capacity with equivalent strain. Scr Mater 64:880–883
14. Wang XD, Cao QP, Jiang JZ, Franz H, Schroers J, Valiev RZ, Ivanisenko Y, Gleiter H, Fecht H-J (2011) Atomic-level structural modifications induced by severe plastic shear deformation in bulk metallic glasses. Scr Mater 64:81–84
15. Wang YB, Qu DD, Wang XH, Cao Y, Liao XZ, Kawasaki M, Ringer SP, Shan ZW, Langdon TG, Shen J (2012) Introducing a strain-hardening capability to improve the ductility of bulk metallic glasses via severe plastic deformation. Acta Mater 60:253–260
16. Valiev RZ, Ivanisenko YuV, Rauch EF, Baudelet B (1996) Structure and deformation behaviour of Armco iron subjected to severe plastic deformation. Acta Mater 44:4705–4712
17. Figueiredo RB, Cetlin PR, Langdon TG (2011) Using finite element modeling to examine the flow processes in quasi-constrained high-pressure torsion. Mater Sci Eng, A 528:8198–8204
18. Figueiredo RB, Pereira PHR, Aguilar MTP, Cetlin PR, Langdon TG (2012) Using finite element modeling to examine the temperature distribution in quasi-constrained high-pressure torsion. Acta Mater 60:3190–3198
19. Estrin Y, Molotnikov A, Davies CHJ, Lapovok R (2008) Strain gradient plasticity modelling of high-pressure torsion. J Mech Phys Solids 56:1186–1202
20. Xu C, Horita Z, Langdon TG (2007) The evolution of homogeneity in processing by high-pressure torsion. Acta Mater 55:203–212
21. Wongsa-Ngam J, Kawasaki M, Zhao Y, Langdon TG (2011) Microstructural evolution and mechanical properties of a Cu–Zr alloy processed by high-pressure torsion. Mater Sci Eng, A 528:7715–7722
22. Kawasaki M, Figueiredo RB, Langdon TG (2011) An investigation of hardness homogeneity throughout disks processed by high-pressure torsion. Acta Mater 59:308–316
23. Loucif A, Figueiredo RB, Baudin T, Brisset F, Chemam R, Langdon TG (2012) Ultrafine grains and the Hall-Petch relationship in an Al–Mg–Si alloy processed by high-pressure torsion. Mater Sci Eng, A 532:139–145
24. Wongsa-Ngam J, Kawasaki M, Langdon TG (2012) Achieving homogeneity in a Cu–Zr alloy processed by high-pressure torsion. J Mater Sci 47:7782–7788. doi:10.1007/s10853-012-6587-8
25. Sabbaghianrad S, Kawasaki M, Langdon TG (2012) Microstructural evolution and the mechanical properties of an aluminum alloy processed by high-pressure torsion. J Mater Sci 47:7789–7795. doi:10.1007/s10853-012-6524-x
26. Cao Y, Wang YB, Alhajeri SN, Liao XZ, Zheng WL, Ringer SP, Langdon TG, Zhu YT (2010) A visualization of shear strain in processing by high-pressure torsion. J Mater Sci 45:765–770. doi:10.1007/s10853-009-3998-2
27. Cao Y, Kawasaki M, Wang YB, Alhajeri SN, Liao XZ, Zheng WL, Ringer SP, Zhu YT, Langdon TG (2010) Unusual macroscopic shearing patterns observed in metals processed by high-pressure torsion. J Mater Sci 45:4545–4553. doi:10.1007/s10853-010-4485-5
28. Cao Y, Wang YB, Figueiredo RB, Chang L, Liao XZ, Kawasaki M, Zheng WL, Ringer SP, Langdon TG, Zhu YT (2011) Three-dimensional shear-strain patterns induced by high-pressure torsion and their impact on hardness evolution. Acta Mater 59:3903–3914
29. Tian YZ, An XH, Wu SD, Zhang ZF, Figueiredo RB, Gao N, Langdon TG (2010) Direct observations of microstructural evolution in a two-phase Cu-Ag alloy processed by high-pressure torsion. Scr Mater 63:65–68
30. Vorhauer A, Pippan R (2004) On the homogeneity of deformation by high pressure torsion. Scr Mater 51:921–925
31. Hohenwarter A, Bachmaier A, Gludovatz B, Scheriau S, Pippan R (2009) Technical parameters affecting grain refinement by high pressure torsion. Int J Mater Res 100:1653–1661
32. Huang Y, Kawasaki M, Langdon TG (2013) An investigation of flow patterns and hardness distributions using different anvil alignments in high-pressure torsion. J Mater Sci 48:4533–4542. doi:10.1007/s10853-012-7015-9
33. Huang Y, Kawasaki M, Langdon TG (2013) Influence of anvil alignment on shearing patterns in high-pressure torsion. Adv Eng Mater 15:747–755
34. Huang Y, Kawasaki M, Langdon TG (2014) An evaluation of the shearing patterns introduced by different anvil alignments in high-pressure torsion. J Mater Sci 49:3146–3157. doi:10.1007/s10853-014-8015-8
35. Edalati K, Horita Z, Langdon TG (2009) The significance of slippage in processing by high-pressure torsion. Scr Mater 60:9–12
36. Zhilyaev AP, Lee S, Nurislamova GV, Valiev RZ, Langdon TG (2001) Microhardness and microstructural evolution in pure nickel during high-pressure torsion. Scr Mater 44:2753–2758
37. Zhilyaev AP, Nurislamova GV, Kim BK, Baró MD, Szpunar JA, Langdon TG (2003) Experimental parameters influencing grain

refinement and microstructural evolution during high-pressure torsion. Acta Mater 51:753–765
38. An XH, Wu SD, Zhang ZF, Figueiredo RB, Gao N, Langdon TG (2010) Evolution of microstructural homogeneity in copper processed by high-pressure torsion. Scr Mater 63:560–563
39. An XH, Lin QY, Wu SD, Zhang ZF, Figueiredo RB, Gao N, Langdon TG (2011) The influence of stacking fault energy on the mechanical properties of nanostructured Cu and Cu-Al alloys processed by high-pressure torsion. Scr Mater 64:954–957
40. An XH, Lin QY, Wu SD, Zhang ZF, Figueiredo RB, Gao N, Langdon TG (2011) Significance of stacking fault energy on microstructural evolution in Cu and Cu-Al alloys processed by high-pressure torsion. Philos Mag 91:3307–3326
41. Langdon TG (2013) Twenty-five years of ultrafine-grained materials: achieving exceptional properties through grain refinement. Acta Mater 61:7035–7059
42. Kawasaki M (2014) Different models of hardness evolution in ultrafine-grained materials processed by high-pressure torsion. J Mater Sci 49:18–34. doi:10.1007/s10853-013-7687-9

Available online at www.sciencedirect.com

jmr&t Journal of Materials Research and Technology

www.jmrt.com.br

Original Article

An overview of flow patterns development on disc lower surfaces when processing by high-pressure torsion☆

Yi Huang[a,*], Ahmed Al-Zubaydi[a], Megumi Kawasaki[b,c], Terence G. Langdon[a,c]

[a] Materials Research Group, Faculty of Engineering and the Environment, University of Southampton, Southampton, United Kingdom
[b] Division of Materials Science and Engineering, Hanyang University, Seoul, South Korea
[c] Departments of Aerospace & Mechanical Engineering and Materials Science, University of Southern California, Los Angeles, United States

ARTICLE INFO

Article history:
Received 12 May 2014
Accepted 20 June 2014
Available online 20 July 2014

Keywords:
Double-swirl
Flow pattern
High-pressure torsion
Stainless steel

ABSTRACT

Stainless steel was selected to study the flow patterns developed with anvil misalignments of 100, 200 and 300 μm on the disc lower surfaces during processing by high-pressure torsion (HPT) through totals of up to 16 turns. A pair of anvils having a roughness of Ra ≈ 15 μm was utilized to investigate the flow pattern development. Discs subjected to only compression in HPT exhibit similar characteristics to the as-received material in the phase domains and there were no overall curvatures of the austenitic (γ) and ferritic (α) phases. Double-swirl flow patterns were not observed in the 1 turn sample but they appeared on the disc lower surfaces after 5 and 16 turns with all three-anvil alignment conditions. There was no significant difference in the double-swirl configuration size for the 5 and 16 turns samples with different amounts of anvil misalignments. These results have important implications for processing metals by HPT.

1. Introduction

High-pressure torsion (HPT) is now recognized as the most effective severe plastic deformation (SPD) technique for producing ultrafine-grained and nanocrystalline metallic materials having superior mechanical properties including high strength [1–3]. During HPT processing, a disc is placed between two anvils and a torsional strain is imposed on the disc by applying a very high pressure (normally several GPa) to the upper anvil and simultaneously rotating the lower anvil. The shear strain imposed on the disc is estimated by the following equation based on the conventional rigid-body analysis [4]:

$$\gamma = \frac{2\pi Nr}{h} \quad (1)$$

☆ Paper presented in the form of an abstract as part of the proceedings of the Pan American Materials Conference, São Paulo, Brazil, July 21st to 25th 2014.

* *Corresponding author.*
E-mail: y.huang@soton.ac.uk (Y. Huang).

http://dx.doi.org/10.1016/j.jmrt.2014.06.005

where r and h are the radius and height (or thickness) of the disc, respectively, and N is the number of revolutions. Based on the rigid-body assumption in Eq. (1), it is reasonable to anticipate that the strain is inhomogeneous in HPT and varies linearly from zero strain at the disc centre to a maximum at the outer edge of the disc. However, there is an additional strain on the HPT disc due to the applied compressive stress introduced in HPT processing and this compression stress is not considered in Eq. (1). This means that the real shear strain distribution during HPT processing is not well described.

Experiments show that a fully homogeneous microstructure and mechanical properties may be achieved in many materials after HPT processing [5–11]. The evolution towards microstructural homogeneity in HPT has been explained successfully by making use of strain gradient plasticity modelling [12]. Attempts have been made to understand the shear process and shear strain distribution during HPT processing through microstructural observations on a duplex stainless steel [13–15] and a two-phase Cu-Ag alloy [16]. Evidence of unusual flow patterns, including the occurrence of double-swirls and local vortices, provide a clear demonstration that flow within the disc is not always consistent with the anticipated rigid-body analysis. A possible explanation for these effects may lie in an initial misalignment of the anvils in the HPT facility prior to conducting the HPT processing [17,18]. However, no specific information on the initial anvil alignment was available in these earlier reports and no checks were undertaken to determine whether the anvils were in full alignment [13–16].

Later, the flow pattern development on the disc upper surfaces was studied systematically while using smooth anvils (with roughness of Ra $\approx$ 5 μm) under different amounts of anvil misalignment (specifically, 100 and 200 μm misalignment) [19–22]. It was found that double-swirls develop on the disc upper surfaces when processing by HPT with a controlled amount of misalignment of either 100 or 200 μm in the anvil positions but there were no double-swirls when processing with essentially perfect alignment. Measurements showed the separations between the centres of the double-swirls both increased with increasing anvil misalignment and decreased with increasing numbers of turns [19]. Furthermore, if the straining was continued to a sufficiently large number of turns, as with 16 turns for an anvil misalignment of 100 μm, the double-swirl pattern disappeared [19,22].

Recently there was the first report on the effect of the initial anvil roughness on the flow patterns [23]. By comparing the flow patterns developed on the disc upper and lower surfaces using both rough and smooth anvils with a fixed anvil misalignment of 100 μm, it was shown that there were some differences in the flow patterns, which were dependent upon the initial surface roughness. However, there was no systematic investigation of the flow pattern development while using the rough anvils under different amounts of anvil misalignment. Therefore, the present research was undertaken in order to study the flow patterns generated on the disc lower surfaces when using rough anvils with a series of initial anvil misalignments of 100, 200 and 300 μm.

2. Experimental material and procedures

A commercial F53 super duplex stainless steel was obtained from Castle Metals UK Ltd. (Blackburn, Lancashire, UK) with a chemical composition consisting of C < 0.030, Si < 0.80, Mn < 1.20, P < 0.035, S < 0.020, Ni 6.0–8.0, Cr 24.0–26.0, Mo 3.0–5.0 and N 0.24–0.32 (wt.%). Fig. 1 shows the as-received microstructure which consists of essentially equal proportions, and similar volume fractions, of the lighter-contrast austenitic (γ) and the darker-contrast ferritic (α) phases. The widths of these two phases varied between ~5 and ~50 μm. Since the two phases exhibit good contrast, this material provides an excellent opportunity to reveal the flow patterns that are introduced during processing by HPT.

The as-received material was in the form of a rolled plate having a thickness of 3 mm. Disks having diameters of ~9.8 mm and thicknesses of ~1.2 mm were cut from the plate and then ground carefully to give a uniform thickness of ~0.82 mm. Processing by HPT was conducted at room temperature under quasi-constrained conditions in which a small amount of material flows outwards around the periphery during the processing operation [24,25]. During HPT processing, the upper anvil is in a fixed position and the lower anvil rotates in a single direction. Any parallel shift between the axis of the upper anvil and the axis of the lower anvil is designated as a measure of the anvil misalignment between the upper and lower anvils. The present experiments were conducted by making changes in the anvil alignment prior to HPT processing. Three different anvil alignment conditions were utilized in these experiments by making a deliberate parallel shifting of the upper anvil: the anvil misalignments were (1) about 100 μm, (2) about 200 μm and (3) about 300 μm. Normally the anvil alignment would fall within <100 μm when processing materials in a conventional manner. Therefore, an anvil misalignment of ~300 μm is rather large and is almost visible by eye observations. Nevertheless, an anvil misalignment of 300 μm was included in order to have systematic observations

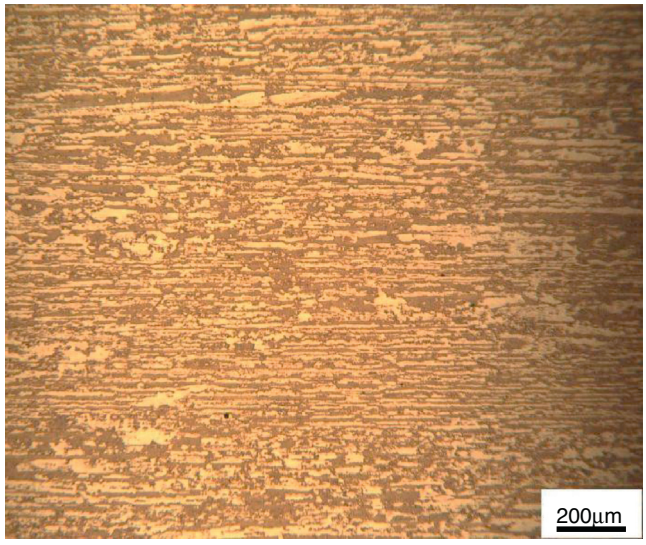

Fig. 1 – Microstructure of the as-received duplex stainless steel.

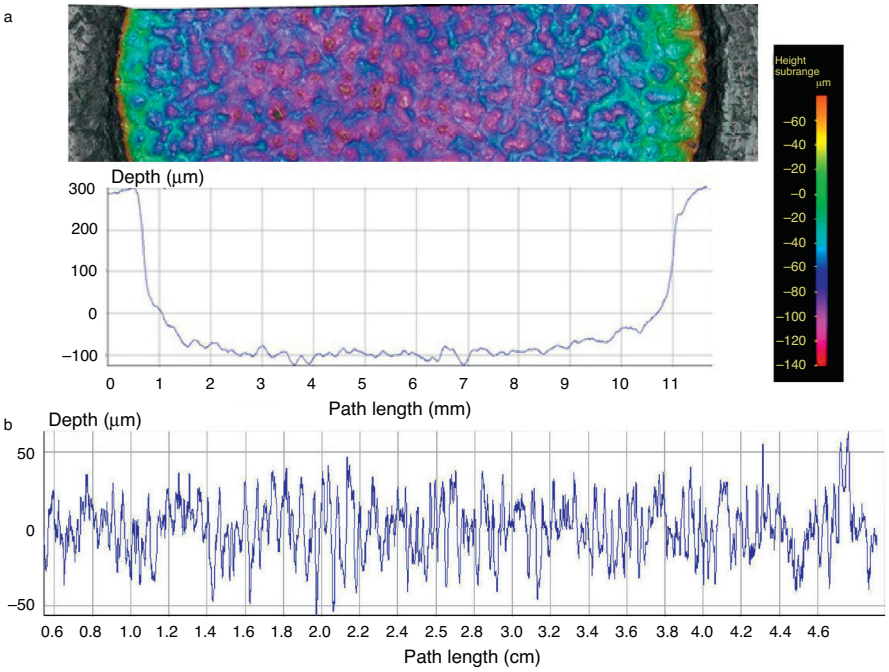

Fig. 2 – Anvil surface morphology and surface roughness showing (a) surface morphology and a line profile from one side of the anvil cavity to the other, and (b) the surface roughness measurements.

and investigations on the flow pattern development with various amounts of misalignment.

In order to avoid any problems associated with slippage during the processing operation, all of the HPT processing was conducted using new anvils so that the surfaces within the depressions were in perfect condition to have enough friction force to hold discs during rotation. In addition, and following standard practice [26], some preliminary tests were conducted using discs with marker lines scribed on the top and bottom surfaces and these tests revealed no evidence for any slippage under the present experimental conditions.

A set of discs was prepared for each of these three anvil misalignment conditions and HPT was conducted at room temperature using an applied pressure of 6.0 GPa and a rotation speed of 1 rpm through total numbers, N, of 1, 5 and 16 turns. In order to investigate whether the compressive stress makes any contribution to the flow pattern development, for each anvil misalignment condition one sample was processed using only an applied pressure of 6.0 GPa for 10 s but without anvil rotation. These compressed samples are designated as $N=0$ samples.

A set of relatively rough HPT anvils was used to investigate the flow patterns on the disc lower surfaces after processing. The surface roughness within the depression on the anvil was measured using Alicona Infinite Focus. Fig. 2 shows the surface morphology of the anvil depression and the profile measurements. The image in Fig. 2(a) shows the surface morphology within the depression as represented by a set of unique colours defined by the colour key on the right and with a line profile from one side of the anvil cavity to the other. The image in Fig. 2(b) is the result of surface roughness measurements along the anvil surface within the cavity area. The measured average surface roughness value, Ra, was equal to ~15 μm.

After processing through 0, 1, 5 and 16 turns, these discs were mounted and polished for surface observations within ~100 μm of the bottom surfaces of the discs. Samples were prepared by mechanically polishing and then electro-etching using an electrolyte of 40% NaOH solution at 25 °C. After etching, the γ-phase appeared bright and the α-phase appeared dark. The local microstructures and flow patterns were examined along the disc diameters using an Olympus BX51 microscope.

3. Experimental results

With an anvil misalignment of 100 μm, Fig. 3 shows the flow pattern development from one side to the other side of discs processed by HPT through $N=0$, 1, 5 and 16 turns. For the disc which was only compressed under 6.0 GPa pressure for 10 seconds but without rotation ($N=0$), Fig. 3(a) shows the phase domains remain straight in the majority area of the disc but in the area very close to the edge of the disc there are some local curvatures of the austenitic γ phase and ferrite α phases which are probably due to the anvil side wall constraint on the disc. It can be seen that the microstructures in Fig. 3(a) are very close to the microstructure of the as-received material as shown in Fig. 1. After HPT processing to 1 turn in Fig. 3(b) where the disc was subjected to combined compression and shear deformation, the disc lower surface shows no overall curvatures but with reasonably straight phase domains, although a slight local curvature of the austenitic γ phase and ferrite α phase can be identified in the disc centre area. No double-swirl flow pattern developed on the disc lower surface for the 1 turn sample. Comparing Fig. 3(b) with Fig. 3(a) it is apparent that the phase domains in the $N=1$ disc are not as straight as

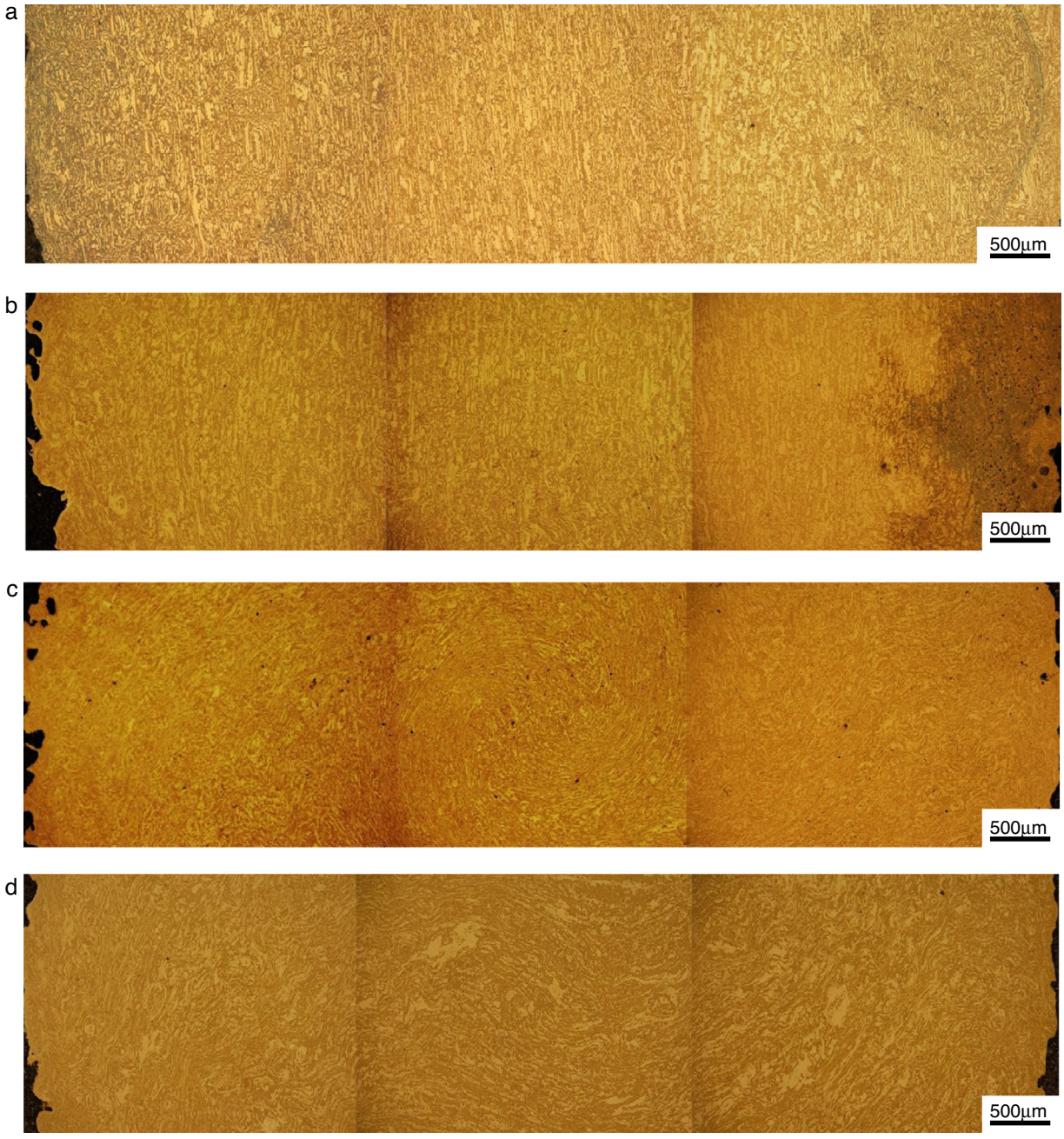

Fig. 3 – Flow pattern development on the lower surfaces after (a) $N = 0$, (b) $N = 1$, (c) $N = 5$ and (d) $N = 16$ turns across the disc diameters with an anvil misalignment of 100 μm.

the phase domains in the $N = 0$ disc. A single swirl is clearly identified on the disc lower surface after 5 turns as shown in the image of Fig. 3(c) although there are some areas with clear phase domain contrast and other areas where the phase domain contrast cannot be identified clearly. Earlier results demonstrated that these areas of unclear phase domain contrast, as in Fig. 3(c), are refined austenitic γ phase and ferrite α phase as revealed in higher magnification observations [23]. For the disc processed to 16 turns, clearly defined curvatures of the phase domains and overall double-swirl flow patterns are clearly visible as shown in Fig. 3(d).

With an anvil misalignment of 200 μm, the overviews of the flow pattern development across the diameters of discs after HPT processing to $N = 0$, 1, 5 and 16 turns are presented in Fig. 4. For the $N = 0$ sample, there are clearly defined and very straight phase domains in Fig. 4(a). After 1 turn, as shown in Fig. 4(b), the disc lower surface shows no signs of any overall curvature of the phase domains and there are no double-swirls or single swirl flow patterns, but there are local slight curvatures of the austenitic γ phase and ferrite α phase. Fig. 4(c) shows the recognizable double-swirl flow pattern develops on the disc lower surface after 5 rotations. In Fig. 4 (c), the phase domain

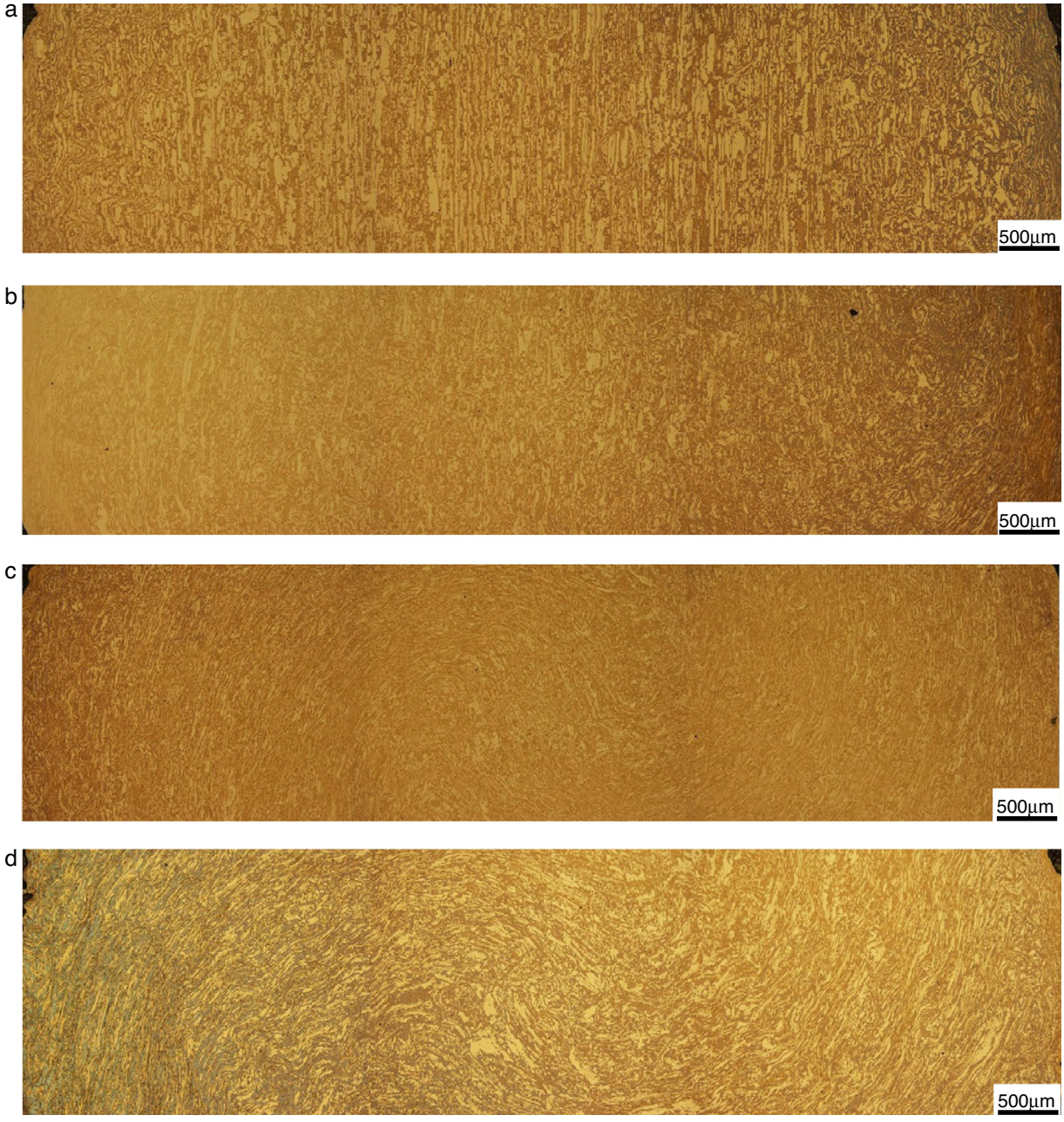

Fig. 4 – Flow pattern development on the lower surfaces after (a) N = 0, (b) N = 1, (c) N = 5 and (d) N = 16 turns across the disc diameters with an anvil misalignment of 200 μm.

contrast is not as well defined as in Fig. 4(a) and (b) and this is again due to the microstructural refinement of the austenitic γ phase and ferrite α phase. Further HPT processing to 16 turns as in Fig. 4(d) leads to a disc lower surface showing a clearly defined double-swirl flow pattern.

For the relatively large anvil misalignment of 300 μm, the flow patterns produced during HPT processing to N = 0, 1, 5 and 16 turns are displayed in Fig. 5. Again the N = 0 sample has clear straight phase domains in Fig. 5 (a). After 1 turn, the disc lower surface shows no overall curvature of the phase domains so that there is no double-swirl or single swirl flow pattern but there are local slightly curved austenitic γ and ferrite α phases in Fig. 5(b). In Fig. 5(c) after 5 turns, the HPT processing produces a recognizable double-swirl flow pattern with a phase domain contrast which is less clear as in Fig. 5(a) and (b) due to the microstructural refinement of the austenitic γ and ferrite α phases. With further HPT processing to 16 turns in Fig. 5(d), the disc lower surface shows a clearly defined double-swirl flow pattern and good contrast of the austenitic γ phase and the ferrite α phase.

4. Discussion

Based on the observations of flow pattern development from 0 turn to 1, 3, 5 and 16 turns with anvil misalignments of 100,

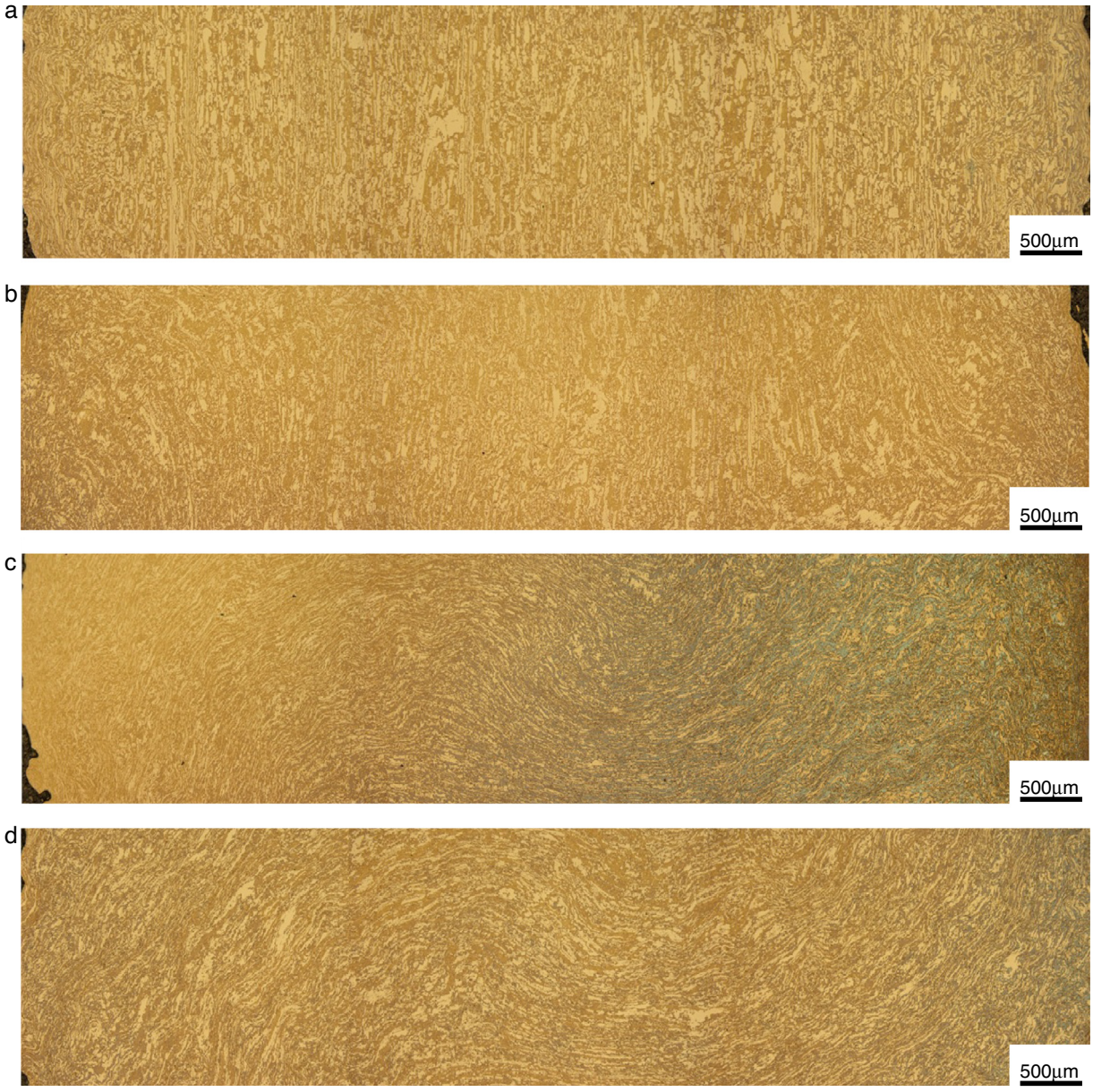

Fig. 5 – Flow pattern development on the lower surfaces after (a) N = 0, (b) N = 1, (c) N = 5 and (d) N = 16 turns across the disc diameters with an anvil misalignment of 300 μm.

200 and 300 μm in Figs. 3–5, there are some common features in the flow pattern evolution. First, with three anvil alignment conditions, samples subjected to only compression but without rotation have clear straight phase domains as shown in Figs. 3(a), 4(a) and 5(a) and they are very similar to the microstructure of the as-received material in Fig. 1. Therefore, this feature clarifies that the compression stress makes no contribution to any overall curvature in the phase domain development and it is not responsible for the double-swirl and single swirl flow patterns. Second, after introducing shear deformation to the low number of rotations of $N = 1$, the disc lower surfaces for the three anvil misalignment conditions all have a similar appearance with no overall curvature of the phase domains in Figs. 3(b), 4(b) and 5(b). Nevertheless, the phase domains are not as straight as in Figs. 3(a), 4(a) and 5(a). These observations show that with a low number of rotations, as in $N = 1$, the shear deformation begins to generate some changes in the appearance of the local phase morphology although shear deformation remains insufficient to produce an overall curvature of the phase domains. Third, as the deformation evolves to higher numbers of rotations, as in $N = 5$, the disc surfaces for the three anvil misalignment conditions all show microstructural refinement of the austenitic γ and ferrite α phases and there are also unclear phase domain contrasts at the present magnifications used for the images in Figs. 3(c), 4(c) and 5(c). Furthermore, all disc surfaces show an overall curvature of the phase domains although with an anvil misalignment of 100 μm the disc has a single swirl appearance in Fig. 3(c) whereas with 200 and 300 μm anvil misalignment the discs have double-swirl flow patterns in Figs. 4(c) and 5(c).

Fourth, the double-swirl flow patterns are retained in the samples processed to 16 rotations with the three anvil misalignments as shown in Figs. 3(d), 4(d) and 5(d).

Ideally, the flow patterns on the disc top and bottom surfaces should be identical but with the flow visible in opposite directions. When using smooth anvils and with an anvil misalignment of 100 μm used to process stainless steel, observations on the disc upper and lower surfaces confirm this type of symmetry [23]. Thus, the disc upper and lower surfaces all have double-swirl flow patterns after 1 and 5 turns and the configuration size of the double-swirls becomes smaller on both the upper and lower surfaces as the numbers of rotations increase from 1 to 5. More systematic results [19,22] on HPT processing of stainless steel using smooth anvils, which include anvil misalignments of 100 and 200 μm to rotation numbers of 1, 5 and 16 turns, show that the separations between the centres of the double-swirls both increase with increasing anvil misalignment and decrease with increasing numbers of turns.

There are some different tendencies concerning the double-swirl flow pattern development and the configuration size of the double-swirls when examining the earlier observations using smooth anvils [19–23] and the present observations when using rough anvils. With the use of rough anvils, the double-swirl flow patterns do not appear on the disc lower surface after 1 turn but they appear on the lower surface after 5 and 16 turns with the three anvil misalignment conditions. There are no size reductions for the configuration size of the double-swirls as the numbers of rotations increase from 5 to 16 with the three anvil misalignments. Therefore, it is readily apparent that these different tendencies should correlate directly with the anvil roughness.

The anvil surfaces are generally treated by sandblasting or spark erosion in order to generate a distinctive surface micro-roughness. Through this surface roughness, combined with the hydrostatic pressure, it is feasible to develop the high frictional forces that are a necessary prerequisite for rotational straining. During HPT processing, the hydrostatic pressure which is imposed initially leads to plastic flow of the sample material into these micro-asperities on the anvil surfaces within the depressions and this provides an excellent fit between the sample and the anvil for subsequent rotational straining. Thus, shear deformation in fact occurs in the interior of the disc sample, i.e. in the area that is below the micro-asperities layers on the disc top and bottom surface. The rough anvil surface shown in Fig. 2 has relatively deep and large pits, which have a fairly non-uniform distribution. Overall, the smooth anvil surface used in earlier research has shallow pits and a reasonably uniform pit distribution [23]. Normally, the disc thickness is ~0.78 mm after HPT processing, considering a smooth anvil has a roughness Ra ≈ 5 μm [23] and a rough anvil has a roughness Ra ≈ 15 μm, therefore, the real thickness for shear deformation in the interiors of the discs will be about 0.77 mm when using smooth anvils and 0.73 mm when using rough anvils. Thus, because of the use of rough anvils, the real thickness for shear deformation in the interior of the disc samples is reduced and, according to Eq. (1), the shear strain applied on each disc is larger when using rough anvils than when using smooth anvils. The calculated shear strain difference at the edge of the disc between a rough anvil and a smooth anvil is about 5.4%. It should be noted that, for the strain hardening metals including the stainless steel, an earlier FEM analysis demonstrated that differences in disc thicknesses leads to minor variations in the distribution of strain along the through-thickness [27]. Therefore, the shear strain difference at the edge of the disc between a rough anvil and a smooth anvil will lead to larger unsymmetrical shear and compression stresses when using anvil misalignment and this will produce more instability based on conventional buckling theory [21]. This difference provides an explanation for the double-swirl flow patterns, which are present in all 5 and 16 turns samples with the three anvil misalignment conditions and thus there is no tendency for the size of these double-swirl configurations to reduce as the rotation number increases from 5 to 16.

Therefore, the major factors contributing to double swirl flow pattern should arise from the anvil surface roughness.

With the use of rough anvils as in the present investigation, the pit area and pit depth are large and the pit distribution is non-uniform as shown in Fig. 2 so that the local frictional forces may change from place to place on the disc surface during HPT processing. In practice, these variations in the local frictional forces would also affect the flow patterns of the deformed materials.

5. Summary and conclusions

Experiments were conducted using a stainless steel to investigate the development of flow patterns near the surfaces of discs processed by high-pressure torsion (HPT) using anvils having relatively rough surfaces.

The absence of any double-swirls on discs processed only with compression but without rotation confirms that the unusual double-swirl flow patterns are not introduced by the compressive deformation. On the contrary, the presence of double-swirls is specifically a feature of the HPT shear deformation.

When using rough anvils and with anvil misalignments of 100, 200 and 300 μm, no double-swirls flow patterns develop for 1 turn samples but double-swirl flow patterns are produced by HPT for samples processed through 5 and 16 turns.

There are no obvious changes in the sizes of the double-swirl configurations for samples processed through 5 and 16 turns.

Conflicts of interest

The authors declare no conflicts of interest.

Acknowledgements

The authors thank Dr Liam Goodes for assistance during the anvil surface roughness measurements. This work was supported by the European Research Council under ERC Grant Agreement No. 267464-SPDMETALS.

REFERENCES

[1] Valiev RZ, Islamgaliev RK, Alexandrov IV. Bulk nanostructured materials from severe plastic deformation. Prog Mater Sci 2000;45:103–89.
[2] Zhilyaev AP, Langdon TG. Using high-pressure torsion for metal processing: fundamentals and applications. Prog Mater Sci 2008;53:893–979.
[3] Langdon TG. Twenty-five years of ultrafine-grained materials: achieving exceptional properties through grain refinement. Acta Mater 2013;61:7035–59.
[4] Valiev RZ, Ivanisenko Yu V, Rauch EF, Baudelet B. Structure and deformation behaviour of Armco iron subjected to severe plastic deformation. Acta Mater 1996;44:4705–12.
[5] Xu C, Horita Z, Langdon TG. The evolution of homogeneity in processing by high-pressure torsion. Acta Mater 2007;55:203–12.
[6] Wongsa-Ngam J, Kawasaki M, Zhao Y, Langdon TG. Microstructural evolution and mechanical properties of a Cu–Zr alloy processed by high-pressure torsion. Mater Sci Eng A 2011;528:7715–22.
[7] Edalati K, Yamamoto A, Horita Z, Ishihara T. High-pressure torsion of pure magnesium: evolution of mechanical properties, microstructures and hydrogen storage capacity with equivalent strain. Scr Mater 2011;64:880–3.
[8] Kawasaki M, Figueiredo RB, Langdon TG. An investigation of hardness homogeneity throughout disks processed by high-pressure torsion. Acta Mater 2011;59:308–16.
[9] Loucif A, Figueiredo RB, Baudin T, Brisset F, Chemam R, Langdon TG. Ultrafine grains and the Hall–Petch relationship in an Al–Mg–Si alloy processed by high-pressure torsion. Mater Sci Eng A 2012;532:139–45.
[10] Wongsa-Ngam J, Kawasaki M, Langdon TG. Achieving homogeneity in a Cu–Zr alloy processed by high-pressure torsion. J Mater Sci 2012;47:7782–8.
[11] Sabbaghianrad S, Kawasaki M, Langdon TG. Microstructural evolution and the mechanical properties of an aluminum alloy processed by high-pressure torsion. J Mater Sci 2012;47:7789–95.
[12] Estrin Y, Molotnikov A, Davies CHJ, Lapovok R. Strain gradient plasticity modelling of high-pressure torsion. J Mech Phys Solids 2008;56:1186–202.
[13] Cao Y, Wang YB, Alhajeri SN, Liao XZ, Zheng WL, Ringer SP, et al. A visualization of shear strain in processing by high-pressure torsion. J Mater Sci 2010;45:765–70.
[14] Cao Y, Kawasaki M, Wang YB, Alhajeri SN, Liao XZ, Zheng WL, et al. Unusual macroscopic shearing patterns observed in metals processed by high-pressure torsion. J Mater Sci 2010;45:4545–53.
[15] Cao Y, Wang YB, Figueiredo RB, Chang L, Liao XZ, Kawasaki M, et al. Three-dimensional shear-strain patterns induced by high-pressure torsion and their impact on hardness evolution. Acta Mater 2011;59:3903–14.
[16] Tian YZ, An XH, Wu SD, Zhang ZF, Figueiredo RB, Gao N, et al. Direct observations of microstructural evolution in a two-phase Cu-Ag alloy processed by high-pressure torsion. Scr Mater 2010;63:65–8.
[17] Vorhauer A, Pippan R. On the homogeneity of deformation by high pressure torsion. Scr Mater 2004;51:921–5.
[18] Hohenwarter A, Bachmaier A, Gludovatz B, Scheriau S, Pippan R. Technical parameters affecting grain refinement by high pressure torsion. Int J Mater Res 2009;100:1653–61.
[19] Huang Y, Kawasaki M, Langdon TG. Influence of anvil alignment on shearing patterns in high-pressure torsion. Adv Eng Mater 2013;15:747–55.
[20] Huang Y, Kawasaki M, Langdon TG. An investigation of flow patterns and hardness distributions using different anvil alignments in high-pressure torsion. J Mater Sci 2013;48:4533–42.
[21] Huang Y, Kawasaki M, Langdon TG. An evaluation of the shearing patterns introduced by different anvil alignments in high-pressure torsion. J Mater Sci 2014;49:3146–57.
[22] Huang Y, Kawasaki M, Langdon TG. Factors influencing the shearing patterns in high-pressure torsion. Mater Sci Forum 2014:783–6, 45–50.
[23] Huang Y, Kawasaki M, Al-Zubaydi A, Langdon TG. Effect of anvil roughness on the flow patterns and hardness development in high-pressure torsion. J Mater Sci 2014;49:6517–28.
[24] Figueiredo RB, Cetlin PR, Langdon TG. Using finite element modeling to examine the flow processes in quasi-constrained high-pressure torsion. Mater Sci Eng A 2011;528:8198–204.
[25] Figueiredo RB, Pereira PHR, Aguilar MTP, Cetlin PR, Langdon TG. Using finite element modeling to examine the temperature distribution in quasi-constrained high-pressure torsion. Acta Mater 2012;60:3190–8.
[26] Edalati K, Horita Z, Langdon TG. The significance of slippage in processing by high-pressure torsion. Scr Mater 2009;60:9–12.
[27] Figueiredo RB, Aguilar MT, Celtin PR, Langdon TG. Analysis of plastic flow during high-pressure torsion. J Mater Sci 2012;47:7807–14.

Materials Science & Engineering A 637 (2015) 1–11

Contents lists available at ScienceDirect

Materials Science & Engineering A

journal homepage: www.elsevier.com/locate/msea

Superplastic behaviour of AZ91 magnesium alloy processed by high-pressure torsion

Ahmed S.J. Al-Zubaydi [a,b,*], Alexander P. Zhilyaev [c], Shun C. Wang [a], Philippa A.S. Reed [a]

[a] Materials Research Group, Faculty of Engineering and the Environment, University of Southampton, Southampton SO17 1BJ, UK
[b] Branch of Materials Science, Department of Applied Sciences, University of Technology, Baghdad, Iraq
[c] Institute for Problems of Metals Superplasticity, Russian Academy of Sciences, Khalturina 39, Ufa 450001, Russia

ARTICLE INFO

Article history:
Received 10 February 2015
Received in revised form
4 April 2015
Accepted 6 April 2015
Available online 13 April 2015

Keywords:
AZ91 magnesium alloy
High pressure torsion
Microstructure
Superplasticity

ABSTRACT

An investigation has been conducted on the tensile properties of a fine-grained AZ91 magnesium alloy processed at room temperature by high pressure torsion (HPT). Tensile testing was carried out at 423 K, 473 K and 573 K using strain rates from $1\times10^{-1}\,s^{-1}$ to $1\times10^{-4}\,s^{-1}$ for samples processed in HPT for $N=1$, 3, 5 and 10 turns. After testing was completed, the microstructures were investigated by scanning electron microscopy and energy dispersive spectroscopy. The alloy processed at *room temperature* in HPT exhibited excellent superplastic behaviour with elongations higher than elongations reported previously for fine-grained AZ91 alloy produced by other severe plastic deformation processes, e.g. HPT, ECAP and EX-ECAP. A maximum elongation of 1308% was achieved at a testing temperature of 573 K using a strain rate of $1\times10^{-4}\,s^{-1}$, which is the highest value of elongation reported to date in this alloy. Excellent high-strain rate superplasticity (HSRSP) was achieved with maximum elongations of 590% and 860% at temperatures of 473 K and 573 K, respectively, using a strain rate of $1\times10^{-2}\,s^{-1}$. The alloy exhibited low-temperature superplasticity (LTSP) with maximum elongations of 660% and 760% at a temperature of 423 K and using strain rates of $1\times10^{-3}\,s^{-1}$ and $1\times10^{-4}\,s^{-1}$, respectively. Grain-boundary sliding (GBS) was identified as the deformation mechanism during HSRSP, and the glide-dislocation creep accommodated by GBS dominated during LTSP. Grain-boundary sliding accommodated with diffusion creep was the deformation mechanism at high test temperature and slow strain rates. An enhanced thermal stability of the microstructure consisting of fine equiaxed grains during deformation at elevated temperature was attributed to the extremely fine grains produced in HPT at room temperature, a high volume fraction of nano β-particles, and the formation of β-phase filaments.

1. Introduction

Magnesium alloys are widely used in many applications such as transportation, materials-handling, and commercial equipment due to their low density compared to other structural alloys such as steel and aluminium alloys [1]. However, the main limitation in the use of these alloys is their poor workability at room temperature, which makes mechanical processing difficult. The low ductility of magnesium alloys is a result of the hexagonal crystal structure of magnesium [2]. It has been found that severe plastic deformation can improve the strength and ductility of many materials including magnesium alloys [3]. Hence, several attempts have been made to enhance their mechanical properties via these processes, but the majority of these experiments have been conducted at elevated temperature, where dynamic recrystallization and grain growth take place [2,4–6]. Ultrafine-grained magnesium alloys have the potential to be used in automotive and aerospace applications due to their lightweight, a high ratio of strength-to-weight, and consequently, reduced fuel consumption [7,8]. The development of superplastic behaviour of ultrafine-grained magnesium alloys has been attracting significant attention in the last decade. Among magnesium alloys, the AZ91 alloy is widely used in industry. This alloy has a good machinability and castability, high strength-to-density ratio, and good corrosion resistance [7,9]. Fine-grained AZ91 alloy has been produced through several severe plastic deformation (SPD) techniques, such as ECAP [2,4], EX-ECAP [10] and HPT [11]. Superplasticity behaviour in any material requires a fine grain size ($\leq$ 10 μm), and typically a high temperature ($T > 0.5\,T_m$, where T_m is the absolute melting point of the material). Fine-grained AZ91 magnesium alloys have shown a wide range of superplasticity depending on strain rate and testing temperature. ECAP processing at 448 K in AZ91 alloy resulted in a superplastic elongation of 661% at a

* Corresponding author at: Materials Research Group, Faculty of Engineering and the Environment, University of Southampton, Southampton SO17 1BJ, UK.
E-mail address: asaz1e11@soton.ac.uk (A.S.J. Al-Zubaydi).

http://dx.doi.org/10.1016/j.msea.2015.04.004
0921-5093/

temperature of 473 K using a strain rate of $6\times10^{-5}\,s^{-1}$ [2]. Superplasticity behaviour was found in the same alloy processed by EX-ECAP at 473 K with elongation of 800% at temperature of 423 K using a strain rate of $6\times10^{-4}\,s^{-1}$ [2]. HPT processing at 423 K of a Mg–9%Al alloy resulted in elongation of 810% at a temperature of 473 K using a strain rate of $5\times10^{-4}\,s^{-1}$[11]. It can be seen then that earlier work on superplasticity in SPD processed AZ91 alloy has been based on processing of the AZ91 alloy at high temperatures, where the limited ductility and workability of the alloy has been improved by the activation of additional slip systems and dynamic recrystallization [12]. So far, no experiment has been reported which investigates the superplastic behaviour of the AZ91 alloy processed by HPT at *room temperature*. The current investigation focuses on superplastic behaviour and the thermal stability of the AZ91 magnesium alloy that have been processed at room temperature, and tested over different temperatures and strain rates.

2. Experimental procedure

An extruded 10 mm rod of AZ91 magnesium alloy (Mg–9%Al–1%Zn) was used in this study, which was supplied by Magnesium Elektron Co. (Manchester, UK). Thin disks were made of the extruded rod with thicknesses of 1.5 mm and then ground to final thicknesses of 0.85 mm using abrasive paper. The HPT processing was conducted at room temperature using a HPT facility that has been previously discussed in detail elsewhere [13]. This facility consists of upper and lower anvils and a circular depression of 0.25 mm in depth and 10 mm in diameter that is located centrally in both anvils. The HPT processing was conducted under a quasi-constrained condition at room temperature and at a speed of 1 rpm using an applied pressure of 3.0 GPa for differing numbers of turns (N): 1, 3, 5, and 10 turns. The peripheries of both anvils were coated with a lubricant containing MoS_2 to avoid any possible damage to these areas during processing. The as-received and the processed alloys were carefully ground, polished and etched in acetic-glycol solution (20 ml acetic acid + 19 ml water + 1 ml nitric acid + 60 ethylene glycol) then the microstructures observed using scanning electron microscopy (SEM, JEOL JSM-6500F, Japan). Small disks of 3 mm diameter were punched from the processed HPT disks and these small disks were ground to a thickness of 150 μm and then thinned using a twin-jet electropolishing facility (Struers Tenupol-3) with a solution of 15 ml perchloric acid, 15 ml glycerol, and 70 ml ethanol. Subsequently a transmission electron microscope (TEM, JEOL JEM-3010) was used for microstructural observation of the alloy after HPT processing. For tensile tests, the processed disks were carefully ground to thicknesses of 0.6 mm using an abrasive paper to prepare them for cutting into micro-tensile samples as previously reported elsewhere [14]. The method of cutting these micro-tensile samples from the HPT disks is known as the off-centre position method and it is used to avoid the central region in an HPT disk where structural heterogeneity is anticipated after HPT. This allows production of two miniature tensile samples per HPT disk with dimensions of $(1.0\times0.9\times0.6)\ mm^3$ as measured by the optical microscope (OLYMPUS-BX51, Japan). The tensile test was conducted at initial strain rates between $1\times10^{-1}\,s^{-1}$ and $1\times10^{-4}\,s^{-1}$ at each testing temperature of 423, 473, and 573 K, and for tensile samples produced from disks processed for $N=1$, 3, 5 and 10 turns. For better accuracy, each tensile test evaluation of a particular processing condition was conducted using two tensile samples and hence 96 tensile samples were used in this investigation. Tensile testing was carried out using a Zwick/Roell tension (Z030, Germany) machine operating at a constant rate of cross-head displacement. The load and displacement were gathered using testIIXpert testing software in a computer-acquisition system. Curves of engineering stress versus elongation and elongation-to-fracture versus strain rate were plotted. The flow stress versus strain rate curves were plotted to measure the values of strain-rate sensitivity (m). The microstructures of tensile samples after tests were observed at the gauge section surfaces using scanning electron microscopy. In order to investigate the surface morphology in detail, the as-tested samples were observed without any further metallographic preparation. The average grain size was measured from these SEM images using a linear intercept method and then corrected by a factor of *1.74*. The variation in grain size versus temperature and time at test temperature was assessed for samples processed in HPT for $N=1$ and 10 turns and tested in tension at different strain rates. The chemical composition of the matrix and the secondary phase were analysed using energy dispersive spectroscopy (EDS). To calculate the values of elongations, the final lengths of the tensile samples after the test were measured under the optical microscope. Representative images of the untested and fractured tensile samples were produced using a low-magnification optical microscope (Wild Herrbrugg, Switzerland), and these images show the testing temperature and strain rate used in tensile testing and the resultant percentages of elongations.

3. Results

The microstructure of the AZ91 magnesium alloy prior to and after HPT processing is shown in Fig. 1 as observed using SEM and TEM. The chemical analysis with weight fractions of alloying elements in the as-received alloy as obtained by EDS is shown in Fig. 2. The microstructure of the as-received alloy shows an average grain size of 30 μm as shown in Fig. 1(a), where the microstructure consists of two main phases: α-Mg matrix; and lamellar and agglomerate forms of β-phase with the presence of Al_8Mn_5 particles as confirmed by EDS analysis and illustrated by the weight fractions found in Fig. 2. It is obvious from Fig. 1(a) that the grain boundaries between α-Mg grains are covered with the β-phase. The magnesium matrix appears darker than the β-phase, which appears brighter as shown in Fig. 1(a). After HPT processing, the microstructure altered noticeably with significant grain refinement and the original decoration of the grain boundaries by β-phase disappeared with increasing number of turns (up to $N=10$ turns) as shown in Fig. 1(b and c). The β-phase fragmented into fine particles and aligned along the direction of the torsional straining. The microstructure shows a significant level of grain refinement even at the beginning of HPT processing with grain sizes down to nanometre scale as observed using TEM as shown in Fig. 1(d). It is expected that the grain refinement for the current alloy continued gradually during HPT processing as indicated indirectly by microhardness measurements that have been done in previously reported work for the same alloy [15] and for AZ31 magnesium alloy also processed by other workers at *room temperature* [16]. The engineering stress–strain behaviour of fine-grained AZ91 magnesium alloy is shown in Fig. 3, where samples have been processed in HPT for $N=10$ turns and then pulled to fracture at different testing temperatures of 423 K, 473 K, and 573 K using initial strain rates of $1\times10^{-1}-1\times10^{-4}\,s^{-1}$. The testing temperatures used in this investigation corresponded to $0.55T_m$ (423 K), $0.61T_m$ (473 K), and $0.74T_m$ (573 K), where the absolute melting point of the AZ91 alloy is 768 K (495 °C) [1]. These curves show the occurrence of superplastic elongation: with increasing number of turns in HPT, at slower tensile rates, as well as at higher testing temperatures, as illustrated in Fig. 3. The strain hardening behaviour of the alloy decreased and elongation-to-fracture increased with decreasing strain rate from 1×10^{-1} to

$1 \times 10^{-4}\ s^{-1}$ as shown in these curves. The effect of strain rate on elongation during hot deformation can be seen in (Figs. 3 and.4). The samples tested at the slowest strain rate, i.e., $1 \times 10^{-4}\ s^{-1}$, resulted in the highest elongations for all numbers of turns in HPT processing and at all testing temperatures used in tensile testing as shown in Fig. 5(a), e.g., for the sample processed in HPT for $N=1$

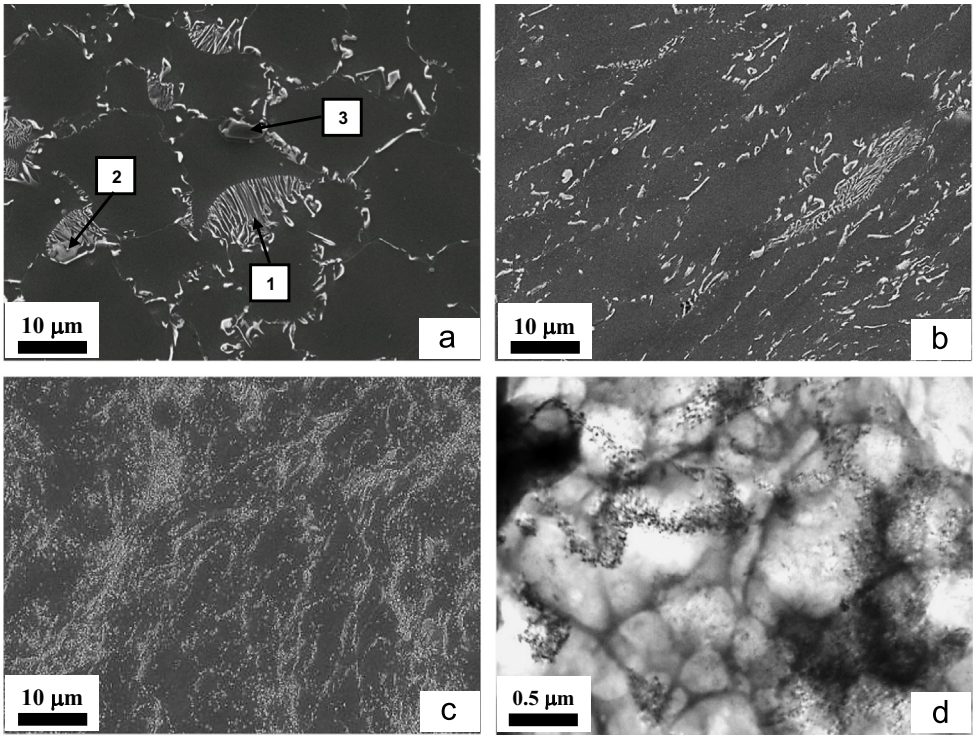

Fig. 1. SEM observations of microstructure for (a) the as-received AZ91 alloy, (b) the processed alloy for $N=1$ turn, (c) the processed alloy for $N=10$ turns and (d) TEM observation of the processed alloy for $N=1/2$ turn. The corresponding numbers (1,2,3) in the micrograph (a) represent the lamellar, agglomerate forms of the β-phase ($Mg_{17}Al_{12}$) and Al_8Mn_5, respectively.

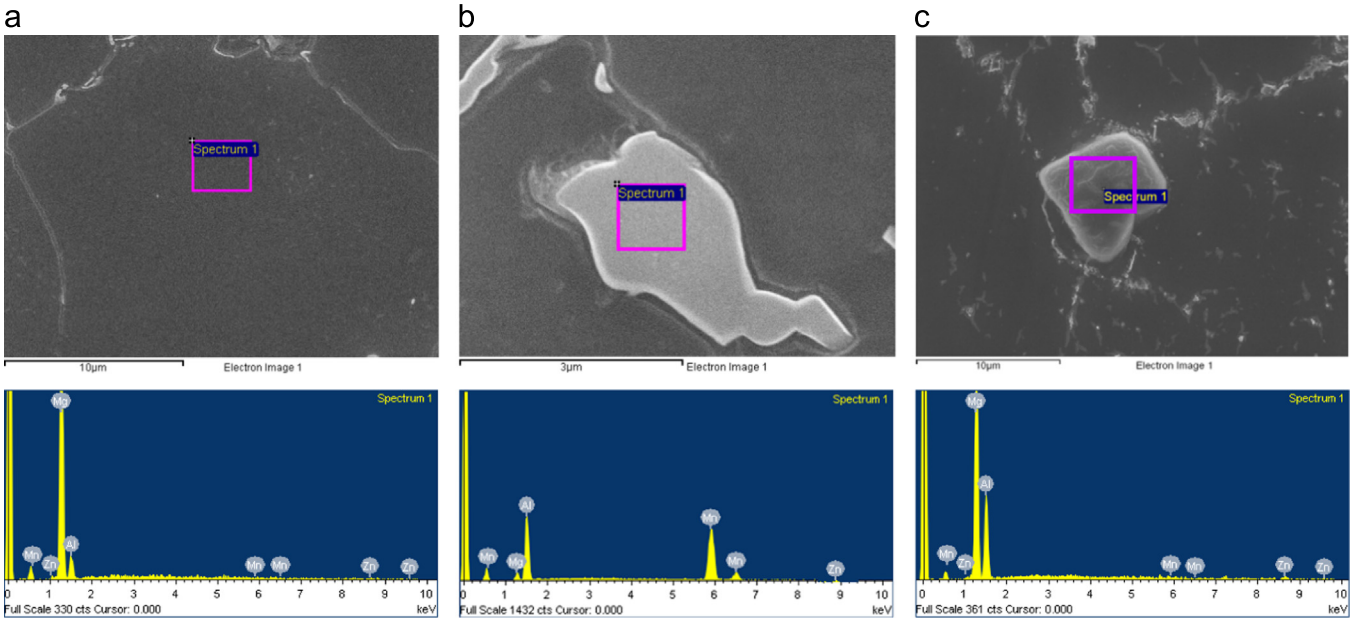

Element	wt.%
Mg	88.74
Al	9.57
Zn	1.11
Mn	0.58

Element	wt.%
Mg	55.14
Al	43.13
Zn	0.94
Mn	0.79

Element	wt.%
Mg	4.50
Al	43.10
Zn	0.45
Mn	51.95

Fig. 2. The chemical analysis with weight fractions of the as-received alloy showing: (a) α-Mg matrix, (b) β-phase ($Mg_{17}Al_{12}$), (c) Al_8Mn_5 compound.

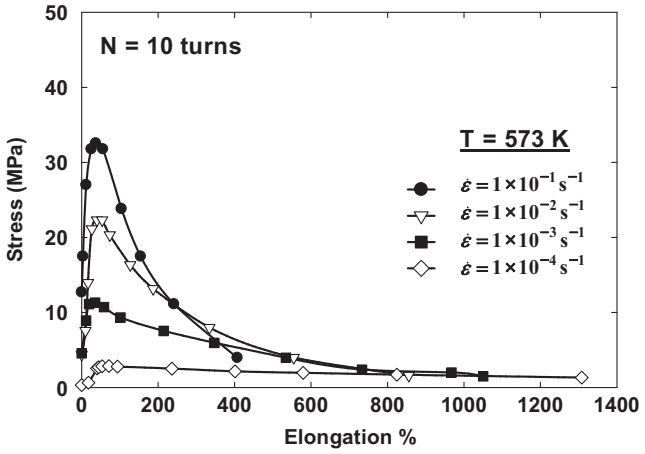

Fig. 3. The engineering stress–strain behaviour at a testing temperature of 573 K using different strain rates for AZ91 samples processed in HPT for $N=10$ turns.

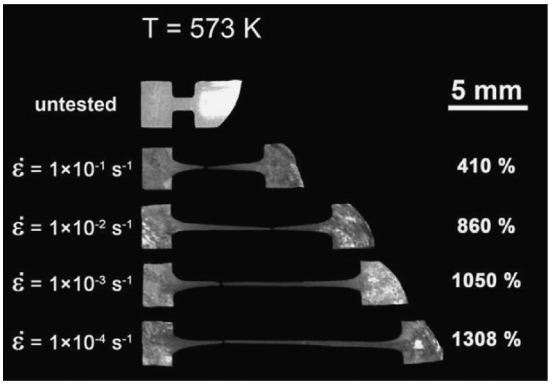

Fig. 4. Appearance of samples processed by HPT for $N=10$ turns after tension to fracture at a testing temperature of 573 K at different strain rates. The upper sample represents the untested case.

turn, the maximum elongations were 249%, 845% and 1041%, at testing temperatures of 423 K, 473 K and 573 K, respectively. The maximum elongations for the sample processed for $N=10$ turns were 760%, 1164% and 1308% using testing temperatures of 423 K, 473 K and 573 K, respectively. Significant elongations were achieved at all strain rates with increasing number of turns used in the HPT processing of the AZ91 alloy, where the highest values of the elongation using a strain rate of $1\times10^{-4}\,s^{-1}$ were 760%, 1164% and 1308% at testing temperatures of 423 K, 473 K and 573 K, respectively. These highest elongations were obtained for the alloy processed in HPT for $N=10$ turns as demonstrated in (Figs. 3–5(a)), where a homogeneous ultrafine microstructure is expected after HPT processing at room temperature as mentioned by several investigators [10,14,16,17]. Increasing the testing temperature resulted in increasing elongation at all numbers of turns in HPT processing, where the maximum elongations were 1041%, 1190%, 1234% and 1308% found in the alloy processed through $N=1$, 3, 5 and 10 turns, respectively at a testing temperature of 573 K, as illustrated in Fig. 5(a) and illustrated in Fig. 3 for samples processed for $N=10$ turns in HPT. Increasing the testing temperature resulted in the occurrence of significant elongations at even the fast strain rates, i.e., 1×10^{-1} and $1\times10^{-2}\,s^{-1}$ at temperatures of 473 K and 573 K, respectively as illustrated in (Figs. 3 and 5(a)). This indicates the presence of excellent high-strain rate superplasticity (HSRSP) at these strain rates and temperatures for the current alloy compared to earlier results obtained after processing in EX-ECAP [10], HPT [11], hot extrusion [18] and hot rolling [19]. Tensile testing at a lower temperature, i.e., 423 K, resulted in significant elongations using strain rates of 1×10^{-3} and $1\times10^{-4}\,s^{-1}$. These elongations increased with increasing the number of turns in the HPT process as shown in Fig. 5(a), where the maximum elongations were 660% and 760% using strain rates of $1\times10^{-3}\,s^{-1}$ and $1\times10^{-4}\,s^{-1}$, respectively at a temperature of 423 K. These data confirm the occurrence of low-temperature superplasticity (LTSP) for the AZ91 alloy. The values of strain-rate sensitivity (m) were obtained from the slopes of the log–log format plots of the variation in flow stress versus strain rate for samples tested at different testing temperatures as shown in Fig. 5(b). The values of sensitivity increased with decreasing the strain rate from 1×10^{-1} to $1\times10^{-4}\,s^{-1}$ at all testing temperatures, and are associated with an increase in the elongation-to-fracture for the slower strain rates as illustrated in the elongation–strain rate curves in Fig. 5(a). Increasing the testing temperature resulted in an increase in the values of sensitivity over the strain rate range as illustrated in Fig. 5(b). For a given number of turns for the sample processed in HPT and then pulled in tension, the flow stress decreased with decreasing strain rate and increasing testing temperature, which is reflected in the values of the sensitivity and in the extent of the elongation-to-fracture. The microstructures of tensile samples after tensile testing to fracture were observed along the gauge lengths by SEM as shown in Fig. 6. These samples were processed in HPT for $N=1$ and 10 turns and then tested at different testing temperatures and strain rates. The grain sizes in Fig. 6(a–f) for samples processed for $N=1$ are larger than for samples processed for $N=10$ turns as shown in Fig. 6(g–l) over the range of strain rates and testing temperature. The samples processed for $N=10$ turns in HPT exhibited significant microstructural stability with fine grains of an average size of 1.5 μm ± 0.2 μm after testing at 423 K (for 2–1200 min) over the strain rate range. After testing at 473 K (for 3–1440 min), the subsequent microstructures also showed fine grains with only modest grain growth to an average grain size of 3 μm ± 0.3 μm. Tensile testing at 573 K (for 5–1680 min) resulted in maintenance of a fairly fine microstructures with limited grain growth up to about 8 μm ± 0.5 μm as shown in Fig. 6. The grains remained equiaxed after testing at 423 K, 473 K and 573 K at different strain rates as observed in Fig. 6; where some individual grains have developed into fibrous morphologies at temperatures of 473 K and 573 K at strain rates of $1\times10^{-3}\,s^{-1}$ and $1\times10^{-4}vs^{-1}$ as shown in Fig. 6(b, c, e and f), and at a temperature of 573 K using strain rates of $1\times10^{-3}\,s^{-1}$ and $1\times10^{-4}\,s^{-1}$ as shown in Fig. 6 (k and l). The fibrous or filament structures were observed at the slower strain rates and higher temperatures, and they connect the grains, which appear to have separated during the superplastic elongation regimes as observed in Fig. 7. The EDS analysis of these fibrous structures revealed their composition as shown in Fig. 7, and the analysis was conducted at three locations: grain, grain boundary and filament. It was found that the composition of these filaments consists mostly of β-phase ($Mg_{17}Al_{12}$) as indicated by the relative estimation of the weights of the constituents. It is noticeable from (Figs. 6 and 8) that the existence of fine equiaxed grains and their relative thermal stability was seen in all samples tested at all temperatures and strain rates despite the differences in the number of turns in HPT processing. This indicates the level of the considerable grain refinement obtained in HPT processing and its impact on the superplastic elongations obtained at elevated temperatures.

4. Discussion

In the present investigation, a successful HPT processing of the AZ91 magnesium alloy at room temperature with an ultrafine microstructure was achieved, which was not produced for the same alloy using ECAP processing at a temperature lower than

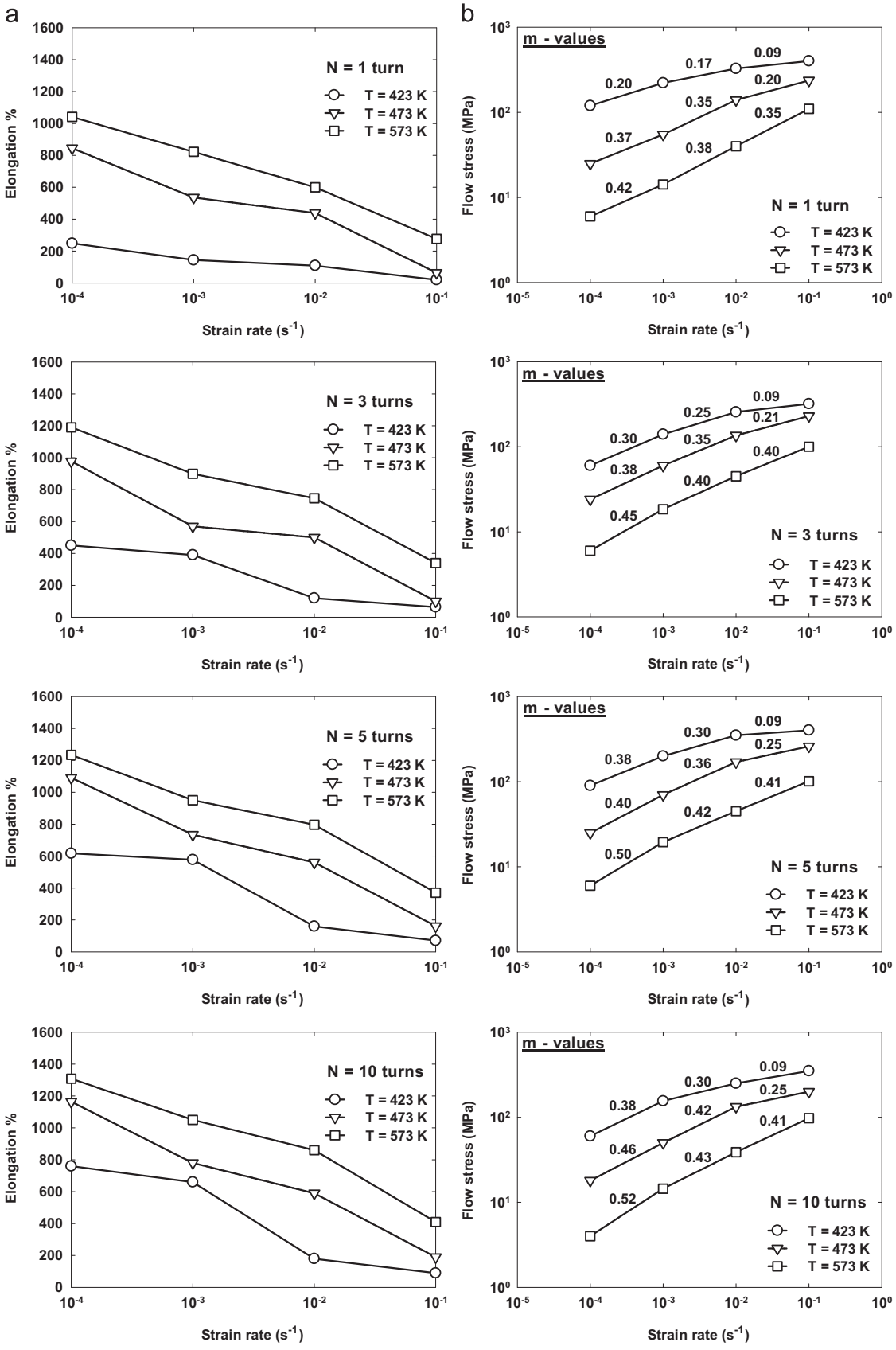

Fig. 5. (a) Elongation-to-fracture versus strain rate at different testing temperatures for alloy processed by HPT through $N=1$, 3, 5 and 10 turns. (b) log–log plot of the variation of flow stress as a function of strain rate shows the strain-rate sensitivity values (m) at different testing temperatures for the samples processed in HPT for $N=1$, 3, 5 and 10 turns.

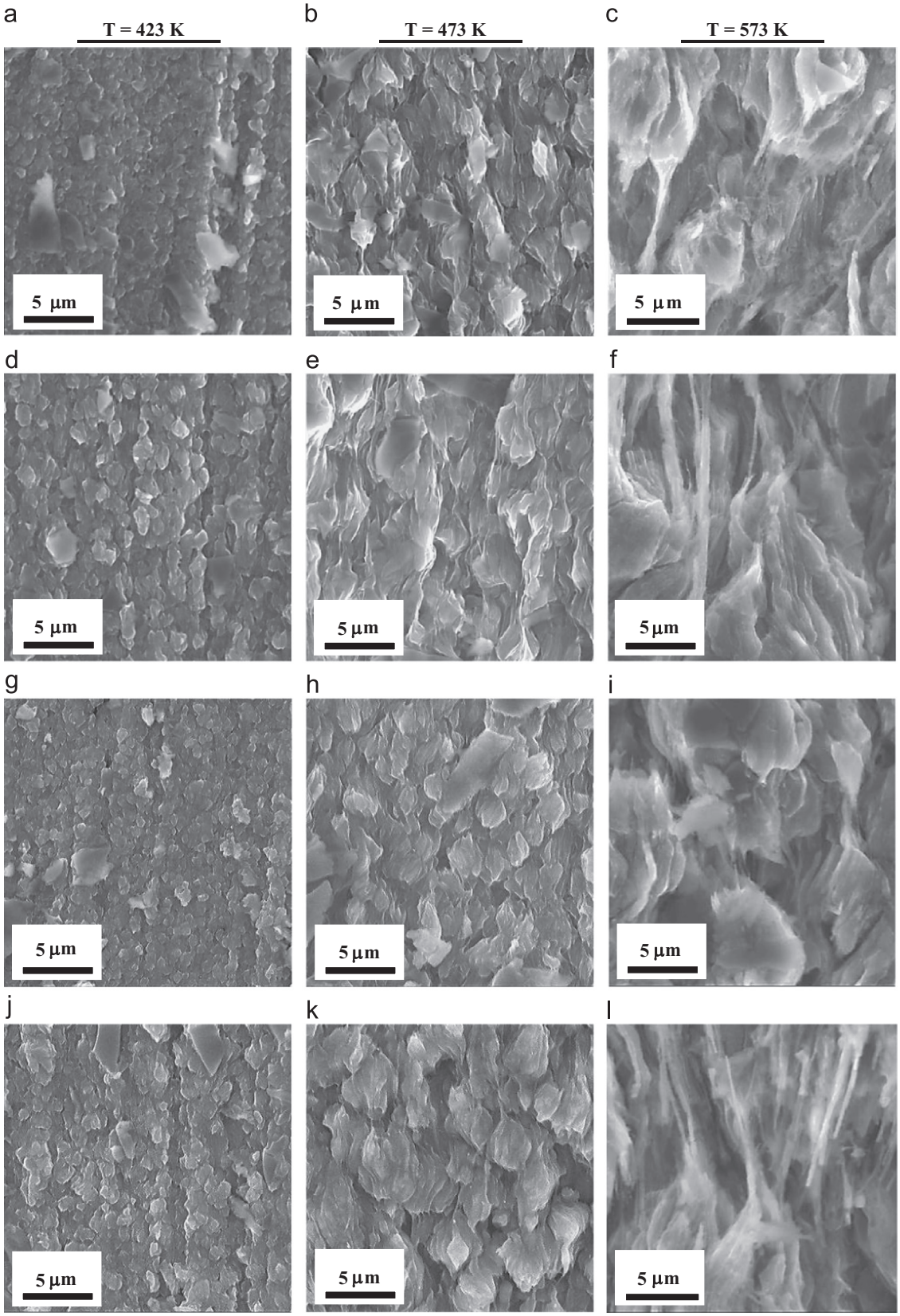

Fig. 6. Magnified views of the microstructures of the AZ91 alloy as observed by SEM on the gauge lengths after the tensile test. The samples above were processed by HPT for $N=1$ turn (a–f) and $N=10$ turns (g–l) before tensile testing. The tested samples showed fibrous morphologies as shown in (c, f, i and l).

200 °C, where development of cracking with increasing number of passes was observed [4]. It is believed that the grain refinement in the current work was achieved within the nanometre range due to the imposition of a high plastic strain by HPT. This is indicated by a comparison between: Mg–9 wt%Al alloy [11], AZ31 alloy [15] and the alloy in this study, in terms of: the HPT processing conditions,

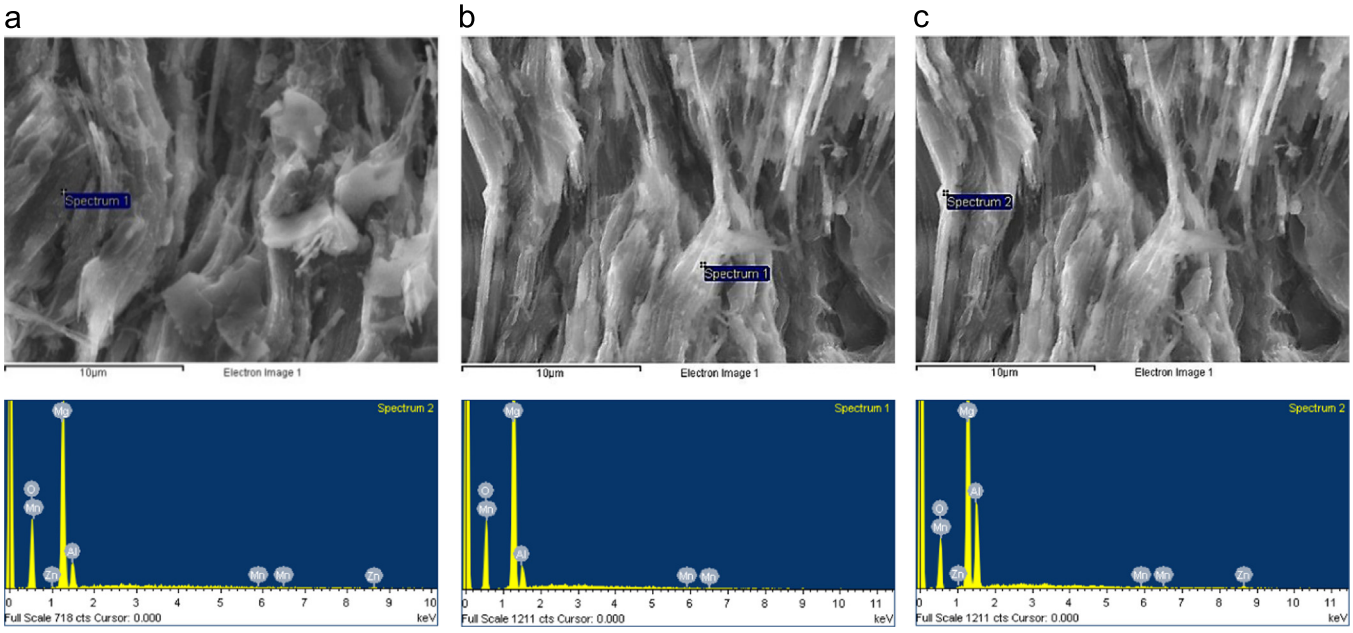

Element	wt.%
O	41.73
Mg	47.73
Al	9.97
Zn	0.17
Mn	0.40

Element	wt.%
O	31.14
Mg	60.80
Al	7.87
Zn	–
Mn	0.19

Elemen t	wt.%
O	24.77
Mg	48.28
Al	26.13
Zn	0.65
Mn	0.16

Fig. 7. EDS analyses with the weight fractions of the elements at: (a) grain, (b) grain boundary and (c) filament, for the sample processed in HPT for $N=10$ turns and tested in tension at a testing temperature of 573 K using a strain rate of $1\times10^{-4}\,s^{-1}$.

the achieved refinement, and the obtained microhardness [16]. Increasingly ultrafine-grained AZ91 alloy (albeit with indistinct grain boundaries) developed with increasing number of HPT turns as shown in Fig. 1. The morphology and distribution of the β-phase also altered after HPT processing. The β-phase separated from the grain boundaries and fragmented into fine particles. Increasing the number of turns resulted in a refinement of β-phase down to nano-sized particles. These nano-sized particles aligned in the form of bands in the direction of the torsional straining with a relatively homogeneous distribution within α-Mg grains, and in part this is what makes direct observation of the grain sizes after multiple HPT turns via TEM techniques challenging. The stress–elongation curves in Fig. 3 for the fine-grained AZ91 magnesium alloy reveal significant superplastic elongation and relative thermal stability of the alloy under tensile loading at temperatures up to 573 K for up to 1680 min using a strain rate of $1\times10^{-4}\,s^{-1}$. The achieved elongations varied with microstructure, strain rate and testing temperature as shown in (Figs. 3–6). For the alloy processed for $N=10$ turns in HPT and then pulled in tension at a testing temperature of 573 K using a strain rate of $1\times10^{-4}\,s^{-1}$, the maximum elongation reached 1308%; which (to the authors' knowledge) is the highest value of elongation reported to date in this alloy. The elongation results in the current study are significantly higher than data that have been published earlier. For instance, the maximum elongation previously published was 810% at 473 K using at a strain rate of $5\times10^{-4}\,s^{-1}$ for the Mg–9%Al alloy processed in HPT for $N=5$ turns at 423 K [11], whereas in the present study, the maximum elongation was 1090% at a testing temperature of 473 K using a strain rate of $1\times10^{-4}\,s^{-1}$, for an alloy processed at room temperature in HPT for $N=5$ turns. In addition, the tensile elongations in this investigation are also higher than observed for alloy processed at high temperatures in ECAP as shown earlier [10], where the maximum elongation was 840% at a testing temperature of 473 K using a strain rate of $3.3\times10^{-4}\,s^{-1}$ for samples processed with 2 passes in ECAP at a processing temperature of 473 K; whereas our alloy processed by HPT for $N=1$ and 3 turns at room temperature showed maximum elongations of 845% and 977% at a testing temperature of 473 K using a strain rate of $1\times10^{-4}\,s^{-1}$. This difference in the elongation can be attributed to the processing temperature in HPT and ECAP. For magnesium alloys, it is well documented that a much finer microstructure can be produced by SPD processes at room temperature rather than at elevated temperatures [10,14,16,17]. Thus, the observed higher elongations are expected from a finer microstructure during the subsequent hot deformation as the presence of fine grains is one of the prerequisites for achieving superplasticity in polycrystalline materials [20]. The increase in elongation with finer microstructure can be seen in Fig. 5(a), where the higher elongations towards the superplastic range were achieved with increasing the number of turns up to $N=10$ turns. The microstructural inspections along the gauge lengths of tensile samples after tension reveal that the grains remained equiaxed with fine sizes until fracture at all temperatures and strain rates. The presence of equiaxed grains was associated with superplastic elongations, which indicated that the main deformation mechanism was grain-boundary sliding (GBS). The retention of an equiaxed microstructure at elevated temperature under tension is necessary for superplastic elongations through grain-boundary sliding [21,22]. In addition, the retention of equiaxed grains after the tensile test as shown in Fig. 6 reveals the migration of grain boundaries during superplastic deformation at elevated temperatures. It was found that the stress concentration at grain boundary discontinuities can be reduced by the migration of grain boundaries during deformation, and thus grain-boundary sliding

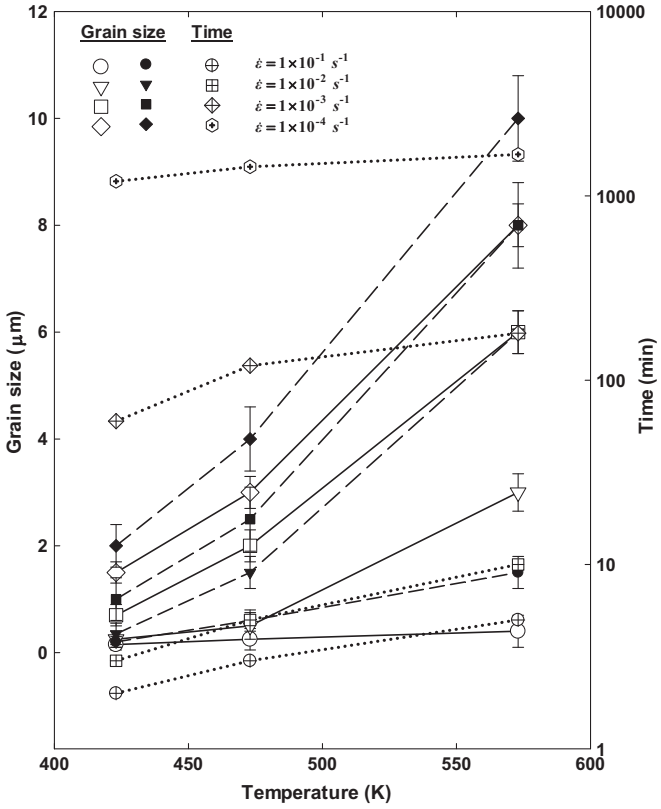

Fig. 8. The variation in the grain size after tensile testing at different testing temperatures (423 K, 473 K, 573 K) and different strain rates and testing times (dotted lines) for the AZ91 alloy processed in HPT for $N=1$ (dashed lines) and $N=10$ turns (solid lines).

continues as the main deformation mechanism [23]. The measurements of strain-rate sensitivity (m) confirm that grain-boundary sliding is the dominant deformation mechanism, where the m-values were 0.3–0.5 as illustrated in Fig. 5(b). It is well known that high values of strain-rate sensitivity indicate a higher resistance to failure by necking and thus high elongations are expected [21,22]. The current superplastic elongations were obtained as strain rate decreased and temperature increased, where m-values increased to 0.5. The tested samples showed excellent elongations using a strain rate of $1\times10^{-2}\,s^{-1}$ at testing temperature of 473 K; and using strain rates of $1\times10^{-1}\,s^{-1}$ and $1\times10^{-2}\,s^{-1}$ at testing temperature of 573 K as illustrated in (Figs. 3 and 5(a)). The current results reveal an excellent high-strain rate superplasticity (HSRSP) for the AZ91 alloy processed by HPT at room temperature compared to those found previously for Mg–9%Al alloy processed by EX-ECAP (360%, $1\times10^{-2}\,s^{-1}$, 498 K) [10], Mg–9%Al alloy processed by HPT (325%, $1\times10^{-2}\,s^{-1}$, 473 K) [11], hot extruded AZ91 alloy (300%, $1\times10^{-2}\,s^{-1}$, 548 K) [18], and hot rolled AZ91 alloy (275%, $1\times10^{-2}\,s^{-1}$, 698 K) [19]. It has been assumed that an improvement in microstructural stability at elevated temperature and additional grain refinement are possible ways to achieve high-strain rate superplasticity in magnesium alloys [24]. In the present work, the AZ91 alloy was processed in HPT *at room temperature*, which was not the case reported by those using other processing techniques such as equal channel angular pressing [10]. A more extreme grain refinement is expected after processing at room temperature than at elevated temperatures as reported in previous HPT studies [10,14,16,17]. Thus, the room temperature processed alloy with a finer microstructure exhibits better thermal stability and thus superior superplasticity under faster strain rates in hot deformation [25]. It can be seen in Fig. 6(g–l), for the sample processed for $N=10$ turns in HPT, that high-strain rate superplasticity to elongations of 590%, 410% and 860% using strain rates of $1\times10^{-2}\,s^{-1}$ at 473 K, $1\times10^{-1}\,s^{-1}$ and $1\times10^{-2}\,s^{-1}$ at 573 K, respectively, and the grain growth was insignificant at testing temperatures of 473 K (for 2–3 min) and 573 K (for 5–10 min). In addition, it is obvious from Fig. 5, that the maximum high-strain rate superplasticity achieved for Mg–9%Al processed in HPT for $N=5$ turns at 423 K [11], was significantly lower than its counterpart for the alloy in the present investigation that was processed in HPT for the same number of turns but at 296 K. This can also be attributed to the effect of processing temperature on the grain refinement of magnesium alloys as discussed previously. The thermal stability of the AZ91 alloy was enhanced by the presence of fine particles of the β-phase ($Mg_{17}Al_{12}$). Prior to HPT processing, the β-phase exists normally along the grain boundaries as lamellar and agglomerate forms in the unprocessed alloy as shown in Fig. 1(a). After HPT processing, this phase fragmented into fine particles with nanometre sizes due to the high value of the imposed strain by HPT and these nano particles were dispersed in the matrix (α-Mg solid solution) as shown in Fig. 1 (b and c). It was found that the morphology of the second phase significantly affects the mechanical behaviour of the metallic materials at room temperature and elevated temperatures [26]. The existence of well-dispersed particles of the β-phase inhibited significant grain growth during superplastic deformation at elevated temperature and then enhanced the extent of superplasticity. The β-phase has a melting point of about 733 K (460 °C) which is relatively lower than 768 K (495 °C) for the AZ91 alloy [1]; thus, the β-phase along the grain boundaries may glide relatively earlier than the grains during hot deformation. For samples processed in HPT for a low number of turns ($N=1$), it was noticed that the distribution and volume fraction of the fine particles of the β-phase are relatively lower as shown in Fig. 1 (b) than in samples processed for a high number of turns ($N=10$) as shown in Fig. 1(c). Therefore, during tensile testing at elevated temperature, with a low fraction volume of the fine particles of β-phase, where the β-phase is located mainly near and/or on the grain boundaries, it acts as pinning phase and the sliding of grains is probably accommodated with limited sliding of the fine particles of β-phase. Increasing the distribution and volume fraction of the fine particles of the β-phase leads to a more significant sliding of the β-phase particles, which can be expected in samples tested at a temperature of 573 K, which represents 0.78 T_m of the β-phase. It has been proposed that the β-phase acts as a lubricant for matrix sliding during tension [27]. Therefore, the highest elongations were obtained at all strain rates at a temperature of 573 K for samples processed in HPT for $N=10$ as illustrated in (Figs. 5(a) and 6). The effect of volume fraction of β-phase on the superplasticity has been reported earlier for Mg–15%Al–1%Zn alloy [27], Mg–33% Al alloy [28] where elongations have been improved considerably with increasing the amount of aluminium (or the volume fraction of the β-phase). As the strain rate decreased to $1\times10^{-4}\,s^{-1}$ and testing temperature increased to 473 K and 573 K, the microstructure showed filaments and surface cavities as shown in (Figs. 6(c, f, i and l), 7). The formation of filaments has been reported for AZ91 alloy in the temperature range of (623–698) K [19], Mg–15%Al–1% Zn alloy in the temperature range of (548–598) K [27] and in AZ61 alloy in the temperature range of (573–673) K [29]. The filaments appear to have reconnected the disconnected grains and grain boundaries and relinked the cavities at the final stage of superplastic deformation. These fibres were formed and aligned in the direction of tension, and their lengths increased with decreasing strain rate and increasing temperature. Thus, the superplastic elongations were enhanced and maintained by the continuous fibrous structures at the slowest strain rate and elevated temperatures [19,27,29]. The micro-superplasticity of filaments in superplastic materials has been proposed to explain the superplastic

elongations [27,30] as shown in (Figs. 6 (c, f, i and l), 7). EDS analysis was conducted on matrix, grain boundary and filament as shown in Fig. 7, for a sample processed in HPT for $N=10$ turns and then tested at a temperature of 573 K using a strain rate of $1\times10^{-4}\,s^{-1}$. It can be seen that the alloy has oxidized since the testing was conducted in the air, as the chemical analysis revealed the presence of oxygen on the grain and grain boundary. The filaments were oxidized also but showed the presence of a higher aluminium level, 26.13%, than in the structures of the grains and grain boundaries (9.97% and 7.87%, respectively). Therefore, it can be concluded that the filaments were composed mainly of β-phase as shown in previous work [27]. The variation in the average grain size as observed using SEM is illustrated in Fig. 8 for tensile samples with increasing testing temperature using different strain rates. It can be seen that the processed alloy with fine particles of β-phase retained its grain size below 10 μm over the range of subsequent testing temperatures, strain rates and times. The alloy exhibited only modest grain growth at lower temperature and/or high strain rates (lower times), and a limited grain growth at higher temperature and slow strain rates (higher times at temperature). Moreover, it was found that presence of a high volume fraction of these fine particles retarded cavity formation at elevated temperatures and slow strain rates due to softening of these particles at temperatures over 573 K [31]. Low-temperature superplasticity (LTSP) was also noticed in the AZ91 alloy during tensile testing at a low temperature of 423 K using strain rates of $1\times10^{-3}\,s^{-1}$ and $1\times10^{-4}\,s^{-1}$ as illustrated in Fig. 5(a). The lower testing temperature is equivalent to $0.55T_m$, where T_m for the AZ91 alloy is 768 K (495 °C) as illustrated in the phase diagram of the alloy [32]. The current performance in the low-temperature superplasticity regime is better than previous data obtained for the AZ91 magnesium alloy [2,11]. It has been found that finer grain sizes are preferable for achieving low-temperature superplasticity as well as for achieving high-strain rate superplasticity [2]. It can be seen that the grain sizes were retained to within 1 μm and 4 μm for samples tested at 423 K and 473 K, respectively, using strain rates of $1\times10^{-3}\,s^{-1}$ and $1\times10^{-4}\,s^{-1}$ as observed in Fig. 6 and illustrated in Fig. 8. The current results for low-temperature superplasticity reveal the potential for superplastic forming of magnesium alloys at lower possible temperatures to overcome their poor workability at room temperature and excessive oxidation at elevated temperatures [33]. A small difference was observed in the maximum values of the low-temperature elongations, for samples processed by EX-ECAP (800%, $1\times10^{-4}\,s^{-1}$, 423 K) [10], and its counterpart obtained in the current study (760%, $1\times10^{-4}\,s^{-1}$, 423 K). This can be attributed to the difference in dimensions of tensile samples for ECAP and HPT. The ECAP tensile sample was cut from a cylindrical billet with a gauge length of 5 mm and gauge cross-section area of $(3\times2)\,mm^2$ [10], whereas in this study, the HPT tensile sample was cut from a circular disk with a gauge length of 1.0 mm and gauge cross-section area of $(0.9\times0.6)\,mm^2$. Therefore, the small difference in the calculated elongations can be attributed to the difference between the relatively large-scale and micro-scale tensile samples produced in ECAP and HPT, respectively [34,35]. Moreover, the direction of cutting for tensile samples from ECAP billets and HPT disks has a further impact. The tensile samples after EX-ECAP were cut parallel to the longitudinal axes after the extrusion step and after the ECAP [10], whereas the disk-shaped samples were cut firstly from an extruded rod perpendicular to the extrusion direction; then after HPT processing, the tensile samples were cut parallel to the shear-plane direction [14]. Therefore, occurrence of a strong texture is anticipated due to the extrusion and subsequent ECAP through the route B_c, and alignment of the basal planes parallel to the extrusion direction [36], which leads to easy slip in tension at a testing temperature of 423 K and the occurrence of low-temperature superplasticity [37]. In contrast, the monotonic HPT mode was used in the processing of the AZ91 alloy in this investigation, which leads to a more random texture with equiaxed grains at a high number of turns [38]. Therefore, at temperatures of 423 K, a relatively lower elongation is expected in the alloy processed by HPT compared to its counterpart processed by EX-ECAP. The average strain sensitivity of 0.3 and the equiaxed grains were found for all samples tested at a testing temperature of 423 K using a strain rate of $1\times10^{-4}\,s^{-1}$, which suggests that grain boundary sliding is the deformation mechanism at low temperature [2]. Lower elongations were found at a low temperature of 423 K using high strain rates of $1\times10^{-1}\,s^{-1}$ and $1\times10^{-2}\,s^{-1}$, and these elongations were associated with low values of strain-rate sensitivity with an average of 0.25. Thus, glide-dislocation creep is assumed as the deformation mechanism accommodated with grain-boundary sliding as the grains retained their equiaxed shapes and did not elongate as in the case of dislocation creep only [19,39]. The activation energy was calculated at a fixed strain rate using the following equation [40,41]: $Q=nR(\partial(\ln\sigma)/\partial(1/T))$, where Q is the activation energy, n is stress exponent ($n=1/m$), R is the gas constant, and $(\partial(\ln\sigma)/\partial(1/T)$ is the slope of plot in Fig. 9. For the AZ91 alloy, the activation energy was obtained for a sample processed in HPT for $N=10$ turns then tensile tested using a strain rate of $1\times10^{-4}\,s^{-1}$ over the temperature range (423–573) K as shown in Fig. 9. It was found that the activation energy equals 80.34 KJ/mol that is close to the activation energy of grain boundary diffusion of pure magnesium (92 KJ/mol). Therefore, grain-boundary sliding is the dominant deformation mechanism, which is consistent with the observed microstructures as shown in Fig. 6. The grain-boundary sliding mechanism was accommodated with diffusional flow at temperatures of 473 K and 573 K using a strain rate of $1\times10^{-4}\,s^{-1}$as shown in Fig. 6 (c, f, i and l). It can be seen that the shapes of grains under these conditions were changed from equiaxed to elongated and oriented towards the tension axis and thus the highest level of superplasticity produced [42]. The relative difference in the obtained activation energy and its counterpart for pure magnesium is attributed to the presence of β-phase in the AZ91 alloy [27], where this phase has an activation energy for grain boundary diffusion of 65 KJ/mol, which reduces the overall activation energy for the present alloy [43,44]. The steady-state strain rate for the superplastic flow at high temperatures is expressed by [45]:

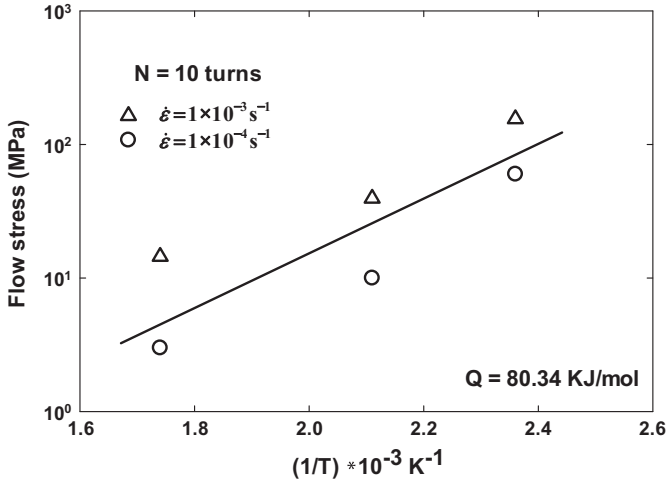

Fig. 9. The variation in the flow stress with the reciprocal of the temperatures from 423 K to 573 K to determine the value of the activation energy (Q) for the tensile samples tested using strain rates of $1\times10^{-3}\,s^{-1}$ and $1\times10^{-4}\,s^{-1}$. The straight line represents the linear least squares fit for the obtained data and its slope then refers to the value of the activation energy.

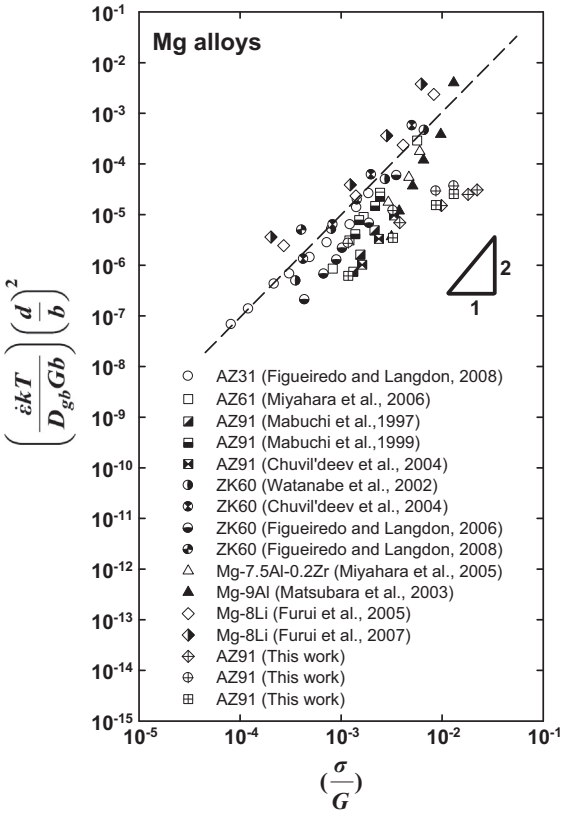

Fig. 10. The temperature and grain size compensated strain rate versus normalised stress for the AZ91 alloy processed in HPT compared with a series of magnesium alloys. The slope of the straight line has a value of the stress exponent of 2, and represents the predicted superplastic strain rate.

$\dot{\varepsilon} = (ADG\boldsymbol{b}/kT)(\boldsymbol{b}/d)^p(\sigma/G)^n$, where D is the appropriate diffusion coefficient $D = D_o\exp(-Q/RT)$, D_o is the pre-exponential complex constant, A is a dimensionless constant, G is the dynamic shear modulus, $\boldsymbol{b}$ is the Burgers vector, d is the grain size, σ is the applied stress, p and n are the exponents of the inverse grain size and normalized stress, respectively. Using the following values of $p = 2$, $n = 2$, $A = 10$, $D = D_{gb}$ [22], $D_o = 7.8 \times 10^{-3}$ m^2s^{-1}, $G = 1.92 \times 10^4 - 8.6T$ (MPa), and $\boldsymbol{b} = 3.2 \times 10^{-10}$ m [45] in the former equation for the grain-boundary sliding mechanism results in Fig. 10, which represents the temperature and grain size compensated strain rate versus the normalized stress for the alloy processed for $N = 10$ turns and tested in tension at different temperatures and strain rates. The solid line represents the predicted strain rate for superplasticity with a slope of $n = 2$ ($m = 0.5$). Good agreement was obtained between the observed experimental data for the current alloy and similar work in a series of magnesium alloys [46,47] and the constitutive equation of superplastic flow based on the assumption that grain-boundary sliding is the dominant deformation mechanism over these testing temperatures and strain rates. It is important to note that that the values of grain sizes were collected from the SEM micrographs of the gauge lengths of the tensile test as indicated in Fig. 6 and these values were used in the constitutive equation.

5. Conclusions

1. The HPT processing at room temperature for the AZ91 magnesium alloy resulted in excellent superplastic elongations that were higher than their counterparts obtained in earlier work through HPT, ECAP and EX-ECAP.
2. High-strain rate superplasticity (HSRSP) was obtained with excellent elongations of 590% at a testing temperature of 473 K using a strain rate of 1×10^{-2} s^{-1}, 410% and 860% at a testing temperature of 573 K using strain rates of 1×10^{-1} s^{-1} and 1×10^{-2} s^{-1}, respectively.
3. Significant low-temperature superplasticity (LTSP) was achieved with maximum elongations of 660% and 760% at a testing temperature of 423 K and using strain rates of 1×10^{-3} s^{-1} and 1×10^{-4} s^{-1}, respectively.
4. The samples processed by HPT at *room temperature* revealed fine equiaxed grains with significant thermal stability at all testing temperatures and strain rates.
5. Equiaxed microstructures and high values of strain-rate sensitivity indicate that grain-boundary sliding was the main deformation mechanism during the high-strain rate superplasticity regime. Glide-dislocation creep accommodated with grain-boundary sliding is suggested as the deformation mechanisms operating during the low-temperature superplasticity regime. At high temperature and slow strain rate the grain-boundary sliding accommodated with a diffusion creep mechanism.
6. Considerable thermal stability of the processed alloy was attributed to the ultrafine grains produced by HPT at room temperature and to the high volume fraction of fine, nano-sized β-phase particles.

   The fibrous structures were mainly composed of β-phase and they enhanced the superplasticity at high temperatures and low strain rates through resisting the cavitation and relinking the disconnected grains.

Acknowledgements

One of the authors (Ahmed S.J. Al-Zubaydi) is grateful to The Higher Committee for Education Development (HCED) of the Government of Iraq for the provision of PhD scholarship. This work was supported in part by the Russian Science Foundation under Grant no. 14-29-00199 (APZ).

References

[1] T.V. Padfield, Z.F. Sachs, Metallography and Microstructures of Magnesium and Its Alloys, ASM International, USA, 2004.
[2] M. Mabuchi, H. Iwasaki, K. Yanase, K. Higashi, Scr. Mater. 36 (1997) 681–686.
[3] A.P. Zhilyaev, T.G. Langdon, Prog. Mater. Sci. 53 (2008) 893–979.
[4] A. Yamashita, Z. Horita, T.G. Langdon, Mater. Sci. Eng. A 300 (2001) 142–147.
[5] P. Serre, R.B. Figueiredo, N. Gao, T.G. Langdon, Mater. Sci. Eng. A 528 (2011) 3601–3608.
[6] K. Xia, J.T. Wang, X. Wu, G. Chen, M. Gurvan, Mater. Sci. Eng. A 410 – 411 (2005) 324–327.
[7] B.L. Mordike, T. Ebert, Mater. Sci. Eng. A 302 (2001) 37–45.
[8] H. Friedrich, S. Schumann, J. Mater. Process. Technol. 117 (2001) 276–281.
[9] K.U. Kainer, Magnesium-Alloys and Technology 2003.
[10] K. Matsubara, Y. Miyahara, Z. Horita, T.G. Langdon, Acta Mater. 51 (2003) 3073–3084.
[11] M. Kai, Z. Horita, T.G. Langdon, Mater. Sci. Eng. A 488 (2008) 117–124.
[12] N.V. Ravi Kumar, J.J. Blandin, C. Desrayaud, F. Montheillet, M. Suéry, Mater. Sci. Eng. A 359 (2003) 150–157.
[13] G. Sakai, Z. Horita, T.G. Langdon, Mater. Sci. Eng. A 393 (2005) 344–351.
[14] Y. Harai, M. Kai, K. Kaneko, Z. Horita, T.G. Langdon, Mater. Trans. 49 (2008) 76–83.
[15] A. Al-Zubaydi, R.B. Figueiredo, Y. Huang, T.G. Langdon, J. Mater. Sci. 48 (2013) 4661–4670.
[16] J. Stráská, M. Janeček, J. Gubicza, T. Krajňák, E.Y. Yoon, H.S. Kim, Mater. Sci. Eng. A 625 (2015) 98–106.
[17] Y. Huang, R.B. Figueiredo, T. Baudin, A.-L. Helbert, F. Brisset, T.G. Langdon, J. Mater. Sci. 47 (2012) 7796–7806.
[18] H. Watanabe, T. Mukai, K. Ishikawa, K. Higashi, Mater. Trans. 43 (2002) 78–80.

[19] Y.H. Wei, Q.D. Wang, Y.P. Zhu, H.T. Zhou, W.J. Ding, Y. Chino, et al., Mater. Sci. Eng. A 360 (2003) 107–115.
[20] G.J. Davies, J.W. Edington, C.P. Cutler, K.A. Padmanabhan, J. Mater. Sci. 5 (1970) 1091–1102.
[21] K.S. Raghavan, Bull. Mater. Sci. 6 (1984) 689–698.
[22] T.G. Langdon, Acta Metall. Mater 42 (1994) 2437–2443.
[23] T.G. Nieh, J. Wadsworth, O.D. Sherby, Superplasticity in Metals and Ceramics 1997.
[24] R.B. Figueiredo, T.G. Langdon, Scr. Mater. 61 (2009) 84–87.
[25] Y. Ma, M. Furukawa, Z. Horita, M. Nemoto, R.Z. Valiev, T.G. Langdon, Mater. Trans. JIM. 37 (1996) 336–339.
[26] D. Zhang, S. Wang, C. Qiu, W. Zhang, Mater. Sci. Eng. A 556 (2012) 100–106.
[27] S.-W. Lee, Y.-L. Chen, H.-Y. Wang, C.-F. Yang, J.-W. Yeh, Mater. Sci. Eng. A 464 (2007) 76–84.
[28] D. Lee, Acta Metall. 17 (1969) 1057–1069.
[29] Y.N. Wang, J.C. Huang, Scr. Mater. 48 (2003) 1117–1122.
[30] M.G. Zelin, Acta Mater. 45 (1997) 3533–3542.
[31] A. Mussi, J.J. Blandin, L. Salvo, E.F. Rauch, Acta Mater. 54 (2006) 3801–3809.
[32] T.J. Chen, R.Q. Wang, Y. Ma, Y. Hao, Mater. Res. 14 (2011) 532–540.
[33] H. Watanabe, T. Mukai, K. Ishikawa, M. Mabuchi, Mater. Sci. Eng. A 307 (2001) 119–128.
[34] Y.H. Zhao, Y.Z. Guo, Q. Wei, T.D. Topping, A.M. Dangelewicz, Y. Zhu, et al., Mater. Sci. Eng. A 525 (2009) 68–77.
[35] Y.H. Zhao, Y.Z. Guo, Q. Wei, A.M. Dangelewicz, C. Xu, Y.T. Zhu, et al., Scr. Mater. 59 (2008) 627–630.
[36] S.R. Agnew, J.A. Horton, T.M. Lillo, D.W. Brown, Scr. Mater. 50 (2004) 377–381.
[37] H.K. Lin, J.C. Huang, T.G. Langdon, Mater. Sci. Eng. A 402 (2005) 250–257.
[38] D. Orlov, P.P. Bhattacharjee, Y. Todaka, M. Umemoto, N. Tsuji, Scr. Mater. 60 (2009) 893–896.
[39] R. Panicker, A.H. Chokshi, R.K. Mishra, R. Verma, P.E. Krajewski, Acta Mater. 57 (2009) 3683–3693.
[40] X. Wu, Y. Liu, Scr. Mater. 46 (2002) 269–274.
[41] H.J. Frost, M.F. Ashby, Deformation-Mechanism Maps: The Plasticity and Creep of Metals and Ceramics 1982.
[42] T.J. Lee, Y.B. Park, W.J. Kim, Mater. Sci. Eng. A 580 (2013) 133–141.
[43] W.J. Kim, M.J. Kim, J.Y. Wang, Mater. Sci. Eng. A 516 (2009) 17–22.
[44] M. Kawasaki, K. Kubota, K. Higashi, T.G. Langdon, Mater. Sci. Eng. A 429 (2006) 334–340.
[45] S.S. Vagarali, T.G. Langdon, Acta Metall. 30 (1982) 1157–1170.
[46] M. Kawasaki, N. Balasubramanian, T.G. Langdon, Mater. Sci. Eng. A 528 (2011) 6624–6629.
[47] M. Kawasaki, T.G. Langdon, J. Mater. Sci. 49 (2014) 6487–6496.

J Mater Sci (2016) 51:3380–3389
DOI 10.1007/s10853-015-9652-2

Evolution of microstructure in AZ91 alloy processed by high-pressure torsion

Ahmed S. J. Al-Zubaydi[1,2] · Alexander P. Zhilyaev[3,4] · Shun C. Wang[1] · P. Kucita[1] · Philippa A. S. Reed[1]

Received: 25 September 2015 / Accepted: 6 December 2015 / Published online: 21 December 2015

Abstract An investigation has been conducted on AZ91 magnesium alloy processed in high-pressure torsion (HPT) at 296, 423 and 473 K for different numbers of turns. The microstructure has altered significantly after processing at all processing temperatures. Extensive grain refinement has been observed in the alloy processed at 296 K with apparent grain sizes reduced down to 35 nm. Segmentation of coarse grains by twinning has been observed in the alloy processed at 423 K and 473 K with average apparent grain sizes of 180 nm and 250 nm. Substantial homogeneity in microhardness has been observed in the alloy processed at 296 K compared to that found at 423 K and 473 K. The ultrafine-grained AZ91 alloy exhibited a significant dependence of the yield strength on grain size as shown by the microhardness measurements, and it obeys the expected Hall–Petch relationship. The alloying elements, fraction of nano-sized particles of β-phase, and the dominance of basal slip and pyramidal modes have additional effects on the strengthening of the alloy processed at 296 K.

✉ Ahmed S. J. Al-Zubaydi
asaz1e11@soton.ac.uk

Alexander P. Zhilyaev
alexz@anrb.ru

Shun C. Wang
wangs@soton.ac.uk

P. Kucita
pk4v07@soton.ac.uk

Philippa A. S. Reed
p.a.reed@soton.ac.uk

[1] Materials Research Group, Faculty of Engineering and the Environment, University of Southampton, Southampton SO17 1BJ, UK

[2] Branch of Materials Science, Department of Applied Sciences, University of Technology, Baghdad, Iraq

[3] Institute for Problems of Metals Superplasticity, Russian Academy of Sciences, Khalturina 39, Ufa, Russia 450001

[4] Research Laboratory for Mechanics of New Nanomaterials, St. Petersburg State Polytechnical University, St. Petersburg, Russia 195251

Introduction

Magnesium alloys are promising alternatives to replace denser materials, such as steel and aluminium alloys, with the objective of meeting requirements to save fuel by manufacturing light weight/high strength parts [1]. The mechanisms of deformation in magnesium alloys at room temperature are basal slip and twinning, which result in a limitation in their workability at room temperature [2]. The limited ductility and workability of these alloys can be improved at higher temperatures by the activation of additional slip systems [1]. Thermo-mechanical processing is used to improve the workability of these alloys, although such processing is associated with grain growth and a greater consumption of energy [3]. Several processing routes have been introduced to achieve optimization of the microstructure, and these routes include dynamic recrystallization under high-temperatures in ECAP processing [4], HPT processing [5, 6], ECAP processing at relatively low temperatures assisted by a back-pressure [7], or through the use of a higher channel angle of pressing die in ECAP processing [8]. The majority of the earlier work in SPD processing of magnesium alloys, especially for AZ91 alloy, has been conducted using ECAP at elevated temperatures (≥473 K) [2, 4, 9] with resultant grain refinement being achieved in the micrometre range. The AZ91 alloy (Mg–9wt%Al–1wt%Zn–0.3wt%Mn) is a common alloy in

the Mg–Al–Zn family. This alloy has a good strength-to-density ratio, good corrosion resistance and ease of production and machining [3]. To date, only one investigation has been conducted on Mg–9wt%Al alloy [6] using HPT at room temperature. The development of microstructure and microhardness across horizontal and vertical cross-sections of AZ91 samples processed by HPT has not been reported to date. This research describes the microstructural homogeneity and development of microhardness in AZ91 alloy after processing by HPT at different processing temperatures. The dislocation density, distribution of β-phase and Hall–Petch relationship have also been investigated.

Experimental materials and procedures

AZ91 alloy (Mg–9 %Al–1 %Zn) in the form of an extruded rod was used in this work, the alloy was supplied by Magnesium Elektron Co. (Manchester, UK). Thin discs were made of the extruded rod with thicknesses of 1.5 mm and final thicknesses of 0.85 mm. The HPT processing was conducted at 296, 423 and 473 K using a HPT facility that has been previously discussed in detail elsewhere [10]. The HPT processing was conducted under a quasi-constrained condition at a speed of 1 rpm using an applied pressure of 3.0 GPa for differing numbers of turns: $N = 1/2$, 1, 5 and 10 turns. The as-received and processed microstructures were observed using optical microscopy (OM, OLYMPUS-BX51, Japan) and scanning electron microscopy (SEM, JEOL JSM-6500F, Japan). Subsequently, a transmission electron microscope (TEM, JEOL JEM-3010) was used for microstructural observation of the alloy after HPT processing. The chemical compositions of the as-received and processed alloy were analysed using energy-dispersive spectroscopy (EDS). The area fraction and average size of the β-phase particles in the as-received alloy and processed alloy were determined by ImageJ software using a point count technique [11]. X-ray diffraction was used to determine the crystallite size and dislocation density in the processed alloy using an XRD facility (D2 Phaser, Germany). The diffraction data were analysed using Rietveld refinement based software program (MAUD). Microstructural observations and microhardness testing were conducted over the horizontal and vertical cross-sections that are illustrated schematically in Fig. 1a, b. The microhardness measurements of the processed disc were conducted using a Vickers microhardness tester (FM-300, Japan) and using an applied load of 100 gf and a dwell time of 15 s. The microhardness data were recorded at separation distances of 0.3 and 0.1 mm throughout the entire horizontal and vertical cross-sections, as reported earlier [5, 12].

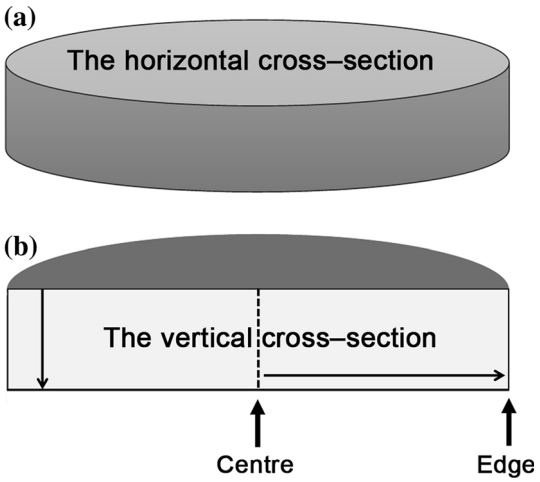

Fig. 1 An illustration of a HPT disc shows **a** the horizontal cross-section, and **b** The vertical cross-section. These cross-sections were used in the microstructural and microhardness observations. The *arrow* from the centre to the edge refers to the longitudinal (*radial*) direction, whereas the *arrow* from the upper surface to lower surface refers to the through-thickness (*vertical*) direction

Experimental results

The microstructure of the AZ91 magnesium alloy prior to and after HPT processing is shown in Fig. 2. The as-received AZ91 alloy has an average grain size of 30 μm and an average value of Vickers microhardness of 70 ± 5. The initial and processed microstructures consist of two main phases: α-Mg matrix, β-phase and Al_8Mn_5 particles as shown in Fig. 2a, b. The chemical analysis obtained by EDS of alloying elements in the alloy processed at 296 K for $N = 5$ turns is shown in Fig. 3. The alloy constituents were identical before and after HPT as shown earlier [13]. The processed microstructure at 296 K showed extensive grain refinement, and the original decoration of the grain boundaries by β-phase disappeared with increasing number of turns as shown in Fig. 2b, c. The β-phase fragmented into nano-sized particles as observed in Fig. 2b–d and appears aligned along the direction of torsional straining. A strong degree of grain refinement after processing at 296 K was observed with an apparent grain size down to 500 and 50 nm observed after $N = 1/2$ and 1 turn, respectively, as shown in Fig. 2e, f. A reduction in the crystallite size from 60 to 35 nm was found with increasing number of turns up to $N = 10$ turns. The processed microstructures at 296 K across the vertical cross-sections are shown in Fig. 4. The microstructure seems slightly deformed with the presence of twinning as shown in Fig. 4a. Shear bands decorated by the β-phase were observed aligned parallel to the radial direction across the vertical cross-section as observed in Fig. 4b. Recorded peaks by XRD as shown in Fig. 5 are

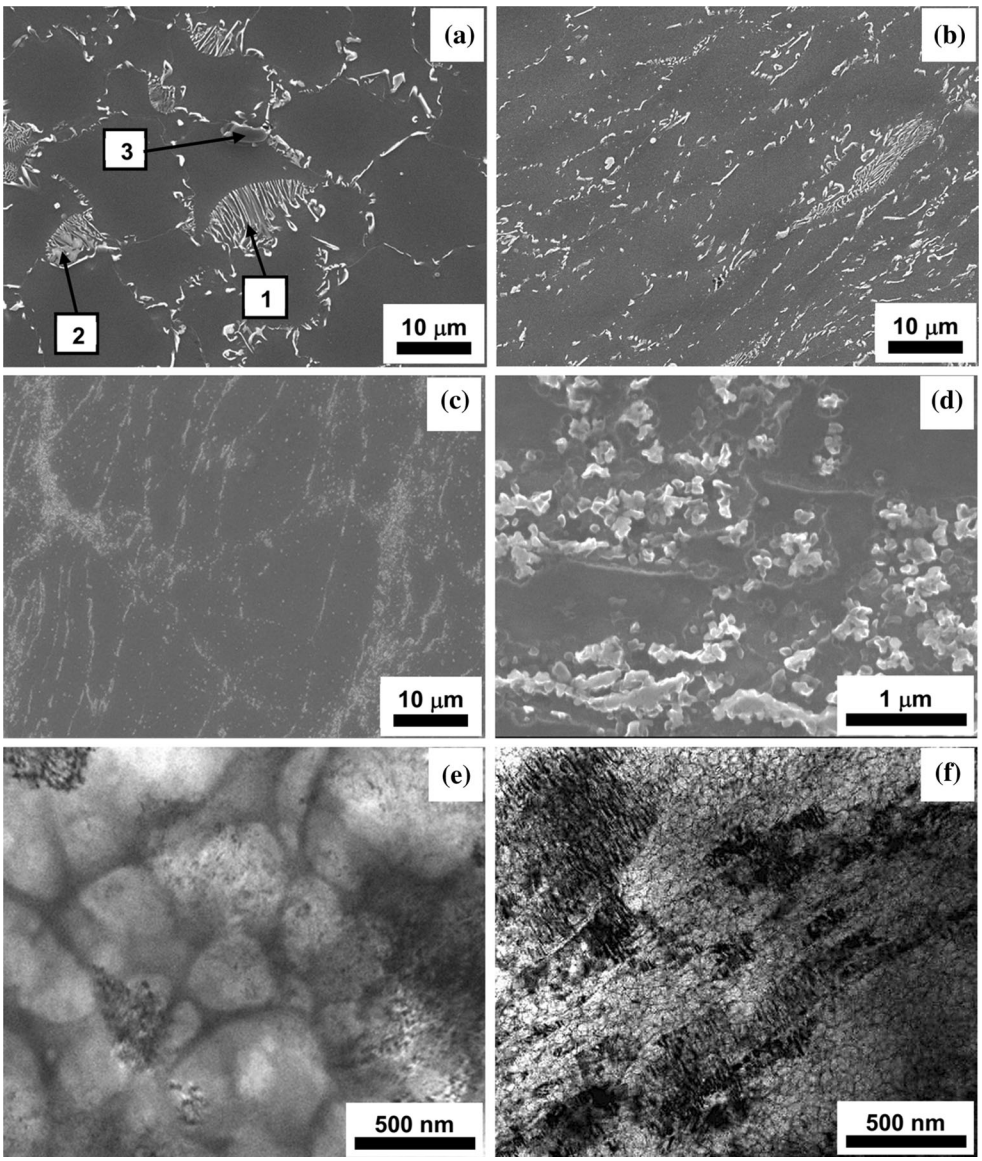

Fig. 2 Microstructural observations using SEM for **a** the as-received alloy, **b** the alloy processed for $N = 1$ turn (296 K), **c** the alloy processed for $N = 10$ turns (296 K) and **d** the nano-sized particles of β-phase in the alloy processed for $N = 10$ turns (296 K), and TEM observation of the alloy processed for **e** $N = 1/2$ turn (296 K) and **f** $N = 1$ turn (296 K). The corresponding numbers (*1*, *2*, *3*) in the micrograph **a** represent the lamellar, agglomerate forms of the β-phase ($Mg_{17}Al_{12}$) and Al_8Mn_5 particle, respectively

prismatic planes $(10\bar{1}0)$, $(11\bar{2}0)$, $(20\bar{2}0)$, basal plane (0002) and pyramidal planes $(10\bar{1}1)$, $(10\bar{1}2)$, $(10\bar{1}3)$. The microstructures of the alloy processed at 423 and 473 K are shown in Fig. 6. The samples showed twinning, and the distribution of twinning increased and spread gradually with increasing number of turns. The microstructures were effectively refined by the segmentation of the coarse grains by twinning as observed in Fig. 6a, b. However, grain growth has been observed at 473 K with increasing number of turns up to $N = 5$ turns as shown in Fig. 6b. The apparent area fraction has increased (which may reflect a sampling effect once the second phase is more homogeneously distributed), and the average size of the β-phase particles has been refined down to 200 nm in the processed alloy compared to the as-received alloy as shown in Fig. 7. A gradual development in the microhardness over the horizontal and vertical cross-sections has been achieved with increasing number of turns up to $N = 10$ turns as shown in Figs. 8 and 9. The distributions of microhardness were relatively lower for the alloy processed at 423 and 473 K than at 296 K. A significant increase in the microhardness has been observed as shown

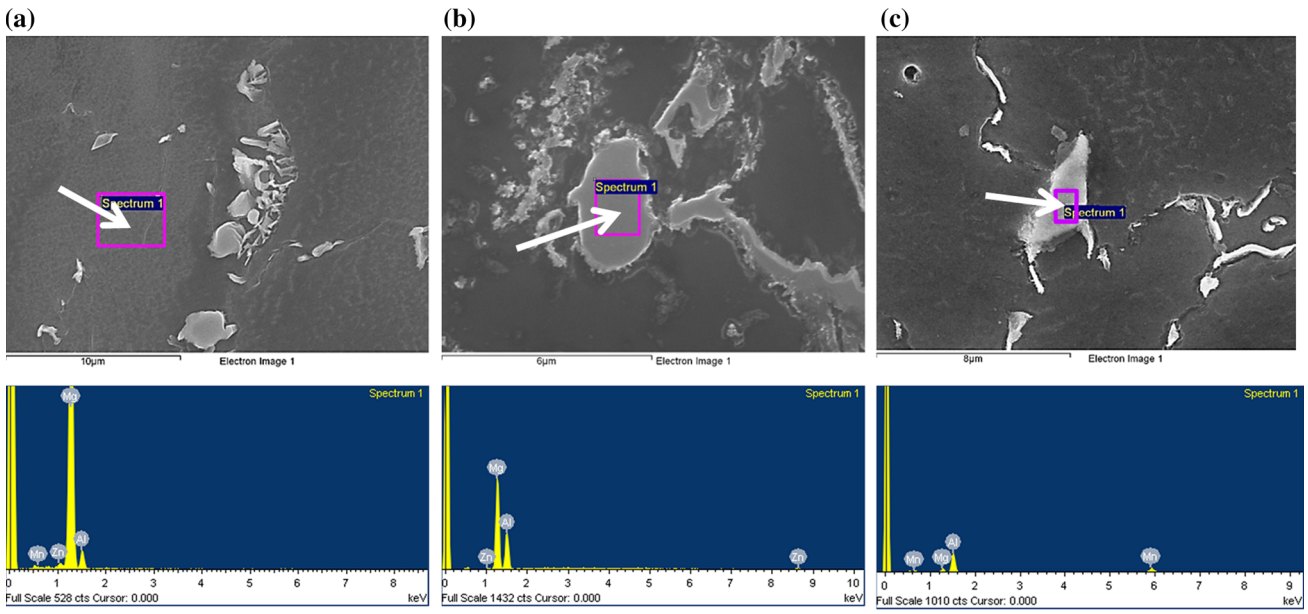

Element	wt.%
Mg	87.74
Al	10.53
Zn	1.31
Mn	0.42

Element	wt.%
Mg	58.22
Al	40.20
Zn	0.91
Mn	0.67

Element	wt.%
Mg	6.10
Al	42.10
Zn	0.65
Mn	51.15

Fig. 3 The chemical analysis with weight fractions of the alloy processed at 296 K for $N = 5$ turns showing **a** α-Mg matrix, **b** β-phase ($Mg_{17}Al_{12}$), **c** Al_8Mn_5 particle

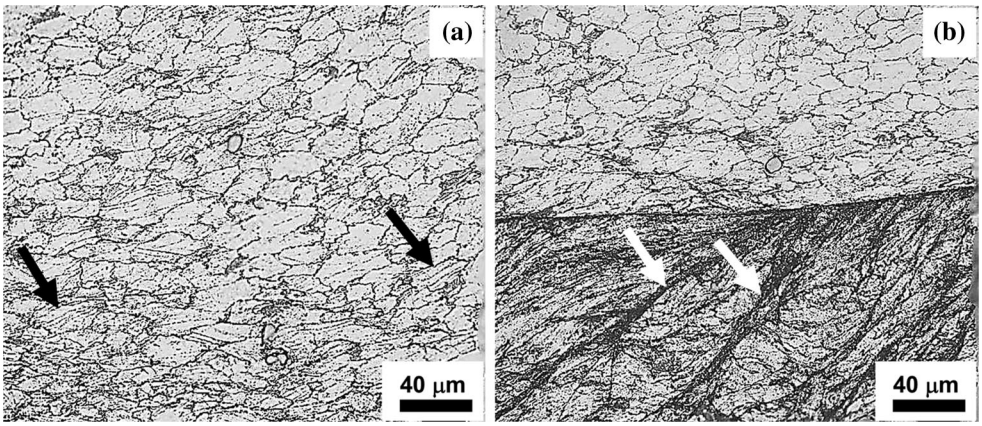

Fig. 4 The microstructures of the alloy processed at 296 K as observed along the vertical cross-sections for **a** $N = 1$ turn and **b** $N = 5$ turns. The *black* and *white arrows* refer to the twinning and shear bands decorated by the β-phase, respectively

in Fig. 10, with increasing equivalent strain imposed during HPT for the alloy processed at 296 K. A significant dependency of the microhardness on the crystallite size of the AZ91 alloy processed at 296 K is shown in Fig. 11. The lower processing temperature leads to finer crystallite size, higher microhardness and dislocation density, and at elevated temperatures, these outcomes decreased significantly as the number of turns increased as shown in Fig. 12.

Discussion

Feasibility of HPT processing of AZ91 magnesium alloy

The TEM and XRD revealed the occurrence of extensive grain refinement in the AZ91 alloy due to the imposition of a very high plastic strain by HPT at 296 K. However, for the sample processed for $N = 1/2$ turn, it is noteworthy that the

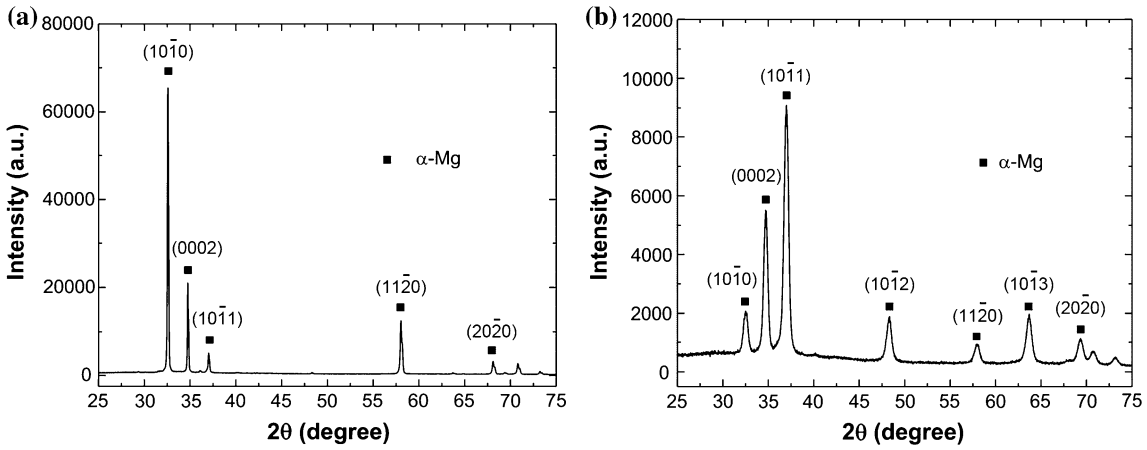

Fig. 5 XRD diffraction patterns for **a** the as-received alloy and **b** the alloy processed at 296 K for $N = 10$ turns

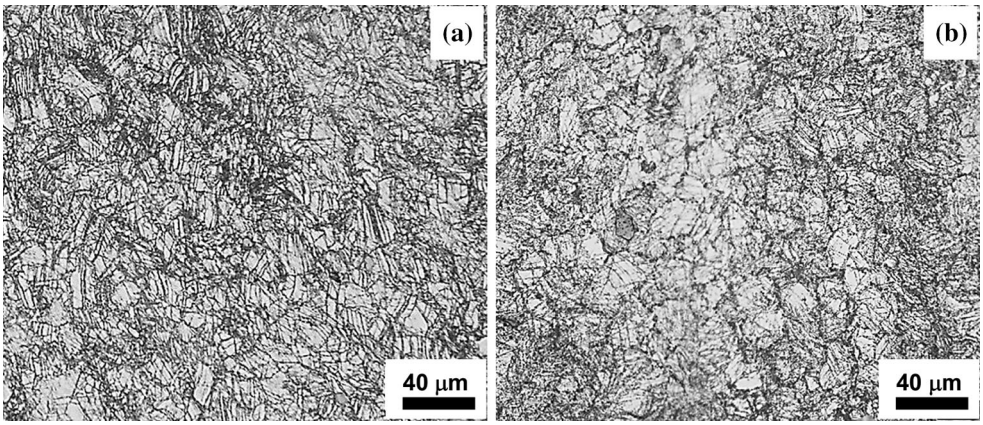

Fig. 6 The microstructures of the alloy as observed across the horizontal cross-sections after HPT processing at **a** 423 K ($N = 5$ turns) and **b** 473 K ($N = 5$ turns)

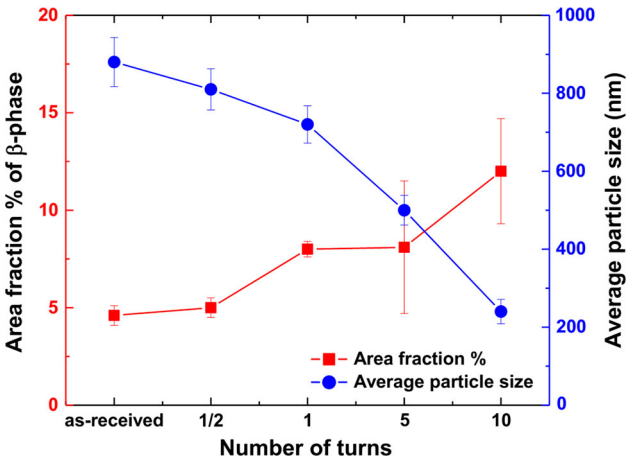

Fig. 7 The area fraction and average size of the β-phase particles in the as-received alloy and processed alloy at 296 K for different number of turns

value of the crystallite size obtained by XRD was significantly lower than the apparent grain size measured by TEM. This difference between the measurements via XRD and TEM is expected in SPD-processed materials, because the grains in these materials are made of subgrains and/or dislocation cells. Thus, coherent scattering of the X-ray from these substructures represents the (smaller) mean crystallite size rather than grains which can be more easily observed in TEM [14]. The feasibility of HPT processing at 296 K for the AZ91 magnesium alloy can be attributed to the presence of hydrostatic pressure, which prevents propagation of fracture during processing [6–8]. Furthermore, the geometry of the processing zone constrains the alloy within a specific volume as illustrated earlier and thus activation of twinning [8, 15, 16]. The XRD observations indicate the orientation of the processed microstructure towards twinning and basal deformation modes under HPT conditions that facilitate processing at room temperature [16]. The unidirectional nature of straining during HPT processing may have contributed to re-orientation of the microstructure towards easy slip [17]. The twinning activity has persisted in the processed alloy at 296 K with increasing number of turns, which confirms its accommodation for the higher imposed strain produced by HPT [18].

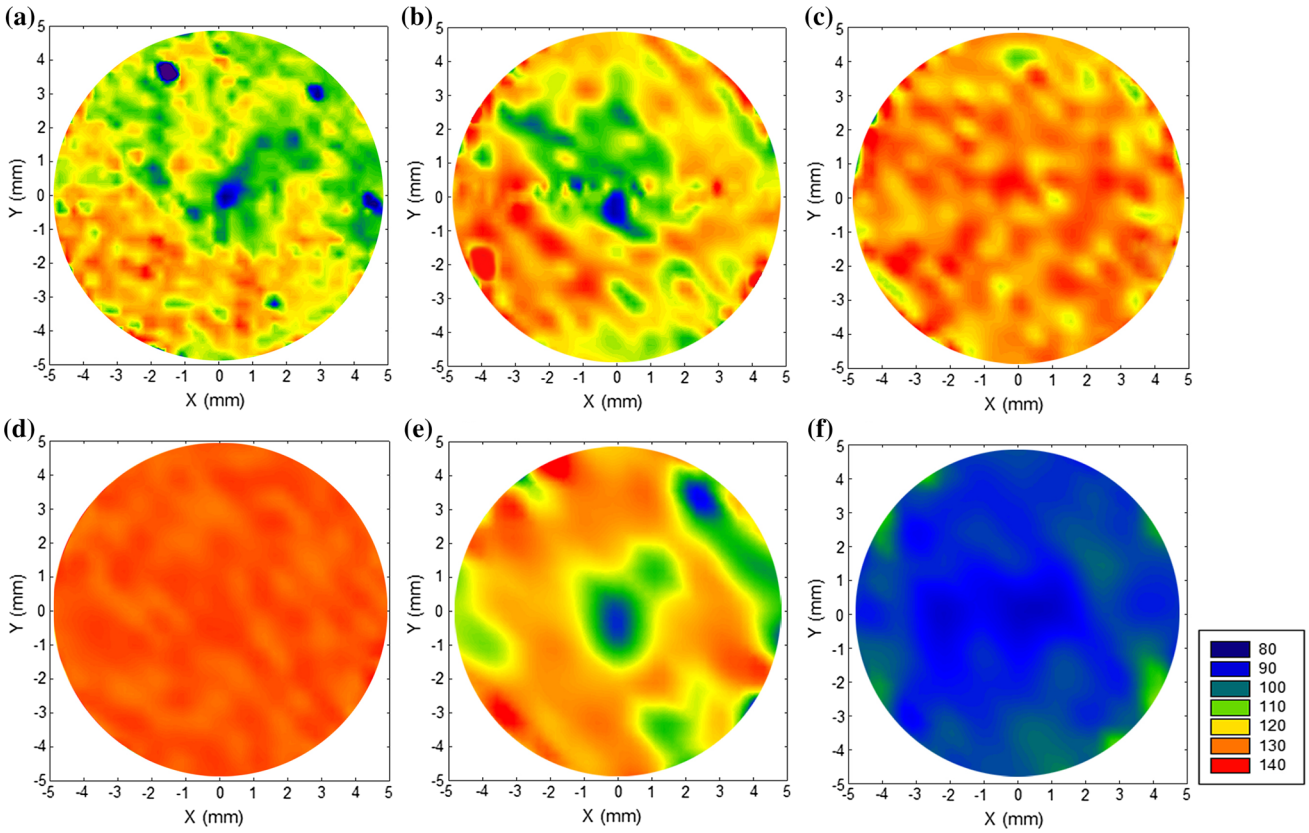

Fig. 8 The *colour*-coded maps of the microhardness over the horizontal cross-sections of the AZ91 discs processed forf **a** $N = 1/2$ turn (296 K), **b** $N = 1$ turn (296 K), **c** $N = 5$ turns (296 K), **d** $N = 10$ turns (296 K), **e** $N = 10$ turns (423 K) and **f** $N = 10$ turns (473 K). The *small inset* in the figure shows the scale of the microhardness with regard to each *colour* (Color figure online)

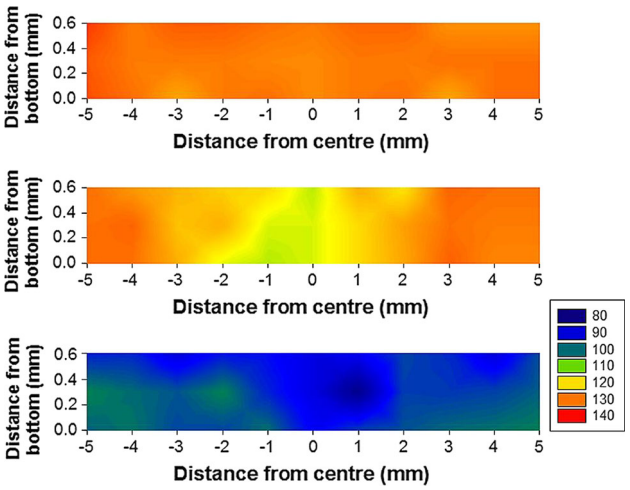

Fig. 9 The *colour*-coded maps of the microhardness distributions over the vertical cross-sections of the AZ91 discs processed for $N = 10$ turns at 296 K (*upper*), 423 K (*centre*) and 473 K (*lower*). The *small inset* in the figure shows the scale of the microhardness with regard to each *colour* (Color figure online)

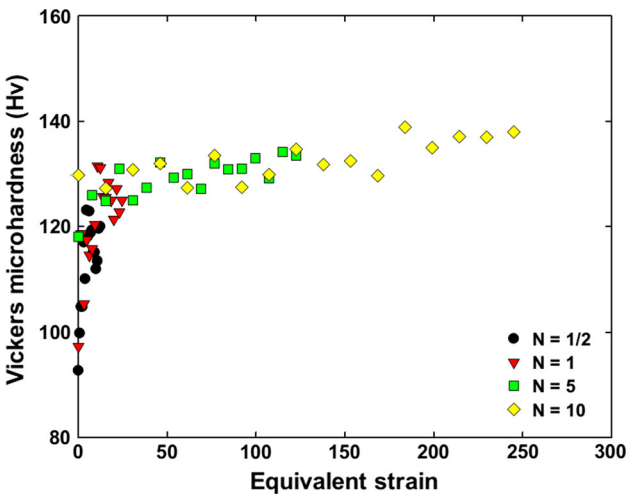

Fig. 10 Correlation of the measured microhardness with the equivalent strain imposed by HPT processing for the alloy processed at 296 K for different number of turns

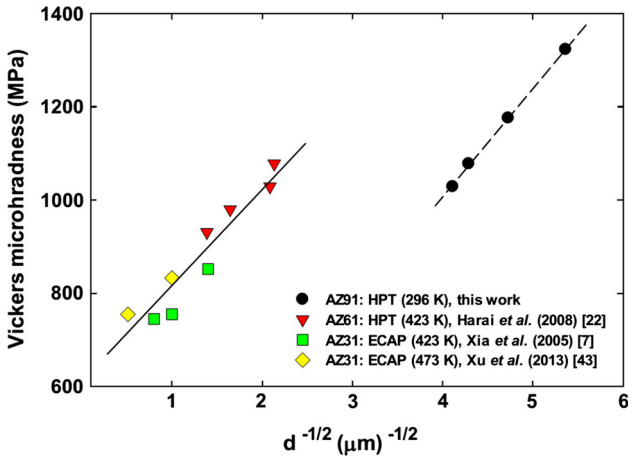

Fig. 11 The Hall–Petch relationship for the ultrafine-grained AZ91 alloy in the current work and for AZ31 and AZ61 alloys processed by HPT and ECAP

Grain refinement in AZ91 alloy

The relatively high content of aluminium in the AZ91 magnesium alloy leads to a significant reduction in the stacking fault energy through the solute–dislocation interaction and results in smaller grain sizes under SPD processing [19]. The effect of dynamic recovery was absent as the alloy has been processed at room temperature. It is anticipated that the homogeneity developed gradually with further straining at room temperature as mentioned by several investigators [20–23]. The grain refinement in the processed alloy at 423 K has developed efficiently by twinning intersections and the grain subdivision mechanism. At this temperature, dynamic recrystallization was absent or had a minor effect on the refinement process compared to the twinning activity. It is likely that dynamic recrystallization may have contributed to grain refinement in the processed alloy at 473 K. However, the formation and fragmentation of twinning appears to be the dominant mechanism for refinement at 473 K. The HPT-processed alloy at 423 and 473 K has significantly refined apparent grain sizes of 180 and 250 nm, respectively, which are finer than in the previously reported ECAP [20, 24–26], FSP [27] and ARB-processed alloys [28]. In the aforementioned SPD techniques, grain refinement occurs mainly by dynamic recrystallization with resultant microstructures of micrometre size grains. The severe levels of deformation in the alloy and the deformation incompatibility between α-Mg matrix and β-phase have resulted in fragmentation of the β-phase [29]. The significant dispersion of nano-sized particles of the β-phase during processing had a pinning effect on grain growth at a higher number of turns and elevated temperatures [23]. The alloy processed at 296 K showed microstructural homogeneity at the initial stage of

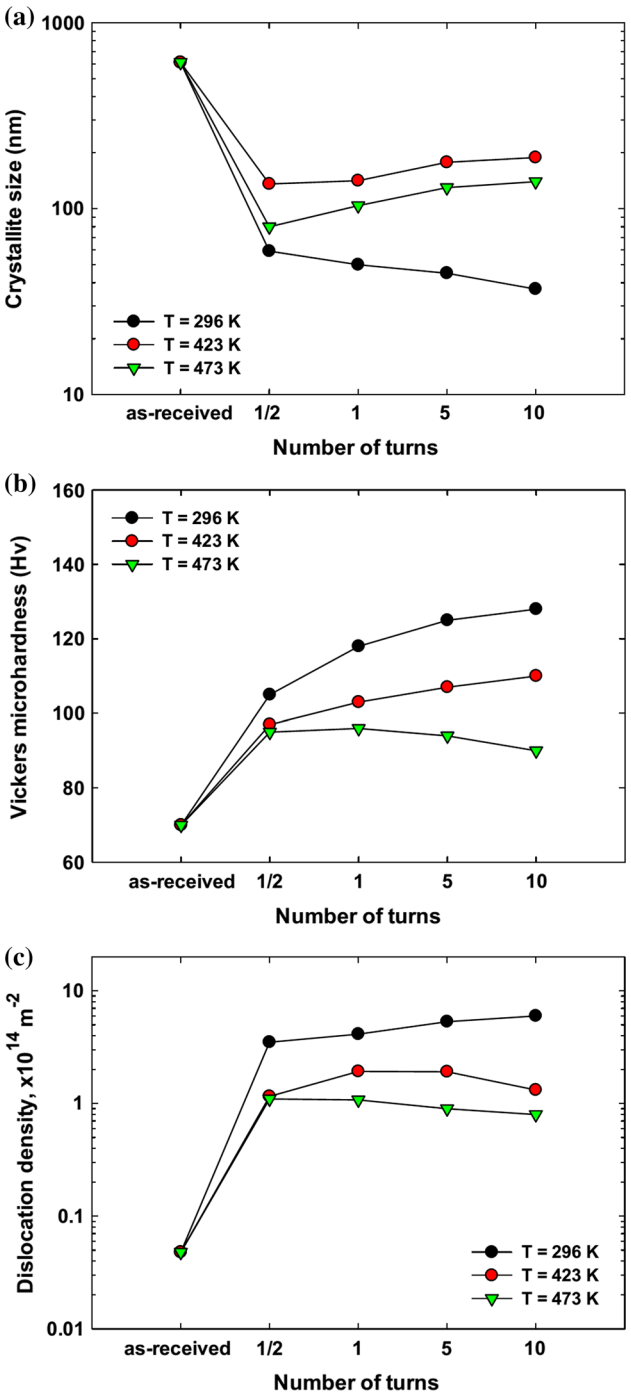

Fig. 12 The overall variation in the average **a** crystallite size, **b** dislocation density and **c** microhardness for the AZ91 alloy after HPT at different processing temperatures

HPT processing rather than the heterogeneity observed in the alloy processed at 423 and 473 K, which required further processing turns and/or higher processing temperature to achieve a reasonable homogeneity [10]. The temperature rise expected during HPT processing at room temperature does not exceed 293 K for samples processed

at 296 K for $N = 10$ turns. This value of temperature rise has been calculated using the equation stated in [30], and is similar to the experimental value (290 K) measured directly from the thermocouple located in the upper anvil. The low value of temperature rise can be attributed to (1) the heat loss from relatively small samples in contact with the much larger HPT anvils and (2) due to the low strain rates of deformation in HPT processing [31]. A further factor, making the heat generated low, is the lower friction expected between the relatively lower strength magnesium alloy and the high strength (high speed tool steel) anvils [15, 31]. As a result, any temperature rise due to processing is considered negligible and unlikely to produce any occurrence of recrystallization or grain growth during processing at room temperature [32].

Development of microhardness

The initial heterogeneity of microstructures leads to an initial heterogeneity in the distribution of microhardness [10, 33, 34]. The difference in grain sizes at the centre and edge regions was diminished by further straining, where a gradual evolution towards homogeneity was found in the observed microstructure and microhardness at both centre and edge regions at a higher number of turns [10, 35]. The existence of misalignment between the anvils at a high number of turns causes an additional deformation at the centre region of the processed disc, which appears as an increase in the measured microhardness [36, 37]. The development of microhardness after HPT processing depends on the stacking fault energy of the alloy [10, 19]. The AZ91 alloy with a low stacking fault energy [38] shows a slow rate of dynamic recovery during processing at room temperature, thus strain hardening occurs at a fast rate during processing [20, 32]. The AZ91 alloy processed in HPT showed an earlier saturation in the microhardness distribution than for the AZ31 alloy [21] processed in HPT at room temperature. The stacking fault energy is lower, and the fraction of particles of β-phase is higher in the AZ91 alloy than for the AZ31 alloy [38, 39]. Therefore, the evolution of grain refinement and strain hardening occurred at faster rates in the AZ91 alloy than for the AZ31 alloy. The overall microhardness values for the alloy processed at 473 K were significantly lower than for their counterparts processed at 296 and 423 K, due to the variation in dislocation density with processing temperature [14]. However, the level and homogeneity of strengthening are still higher when processing by HPT at elevated temperatures than observed in ECAP [26], and FSP [27], where strengthening has been lowered by dynamic recrystallization, over-ageing and precipitate coarsening [26, 27]. The microhardness distributions in the AZ91 alloy are heterogeneous along the through-thickness directions in the initial stage of deformation. This is supported by the differences in microstructural observations along this direction. A sufficient high number of turns may reduce heterogeneity, by filling the alloy in-between the anvils and achieving a significant sticking condition which then increases the deformation and microstructural homogeneity [5, 12, 15, 40, 41]. The distribution of microhardness along the vertical and horizontal cross-sections showed considerable consistency for the current alloy processed at each specific processing temperature. This indicates the development of microstructural homogeneity with increasing imposed strain at each condition [8]. This consistency in the AZ91 alloy has not been observed in the AZ31 alloy or AZ91 alloy processed by ECAP [26] and FSP [27]. This is attributed to the difference in the aluminium content and stacking fault energy in both alloys, which control the extent of grain refinement, dislocation density, achieved homogeneity and resultant mechanical properties [14, 21, 38]. The behaviour of strain hardening and homogeneity of microhardness in the AZ91 alloy follows a standard model of hardness evolution with increasing equivalent strain reported in earlier work [20].

The effect of the equivalent strain on the Hall–Petch relation and dislocation density

The increase in the equivalent strain resulted in an evolution in microstructure and a gradual development in the microhardness [10]. The strength of the alloy in terms of its microhardness improved significantly with grain refinement at room temperature. This proportionality has been expressed by the Hall–Petch relationship for hardness measurements: $Hv = H_0 + k_H d^{-1/2}$ [42]. The effect of grain refinement on the strength of the ultrafine-grained alloy AZ91 alloy showed a significant consistency with this Hall–Petch relationship. The material constants are $H_0 = 76$ MPa and $k_H = 233$ MPa $\mu m^{1/2}$, which is relatively higher than those found for AZ31 and AZ61 alloys ($H_0 = 647$–697 MPa and $k_H = 118$–170 MPa $\mu m^{1/2}$) [7, 22, 43]. Thus, the ultrafine-grained AZ91 alloy shows a relatively higher level of hardness than for AZ31 and AZ61 alloys processed by HPT and ECAP processing at room temperature and elevated temperatures [21, 22, 44]. The difference in k_H can be attributed to the difference in alloying constituents in the mentioned alloys, where the high content of alloying element in the AZ91 alloy resulted in a lowering of its stacking fault and thus a finer microstructure and a higher dislocation density in the AZ91 alloy after processing than in the AZ61 and AZ31 alloy [19, 21, 22]. The evolution in dislocation density with increase of imposed strain in HPT has a major effect on the

achieved strengthening in the AZ91 alloy. The evolution of dislocation density is affected by the fraction of nano-sized particles of β-phase, value of applied pressure in HPT, and value of stacking fault energy. The widely distributed β-phase fine particles are reported as acting as barriers for mobile dislocations during deformation [39]. The high value of applied pressure has also been reported to enhance the obstruction of defect migration in the processed material and then promotes the suppression of dislocation annihilation [45, 46]. The low stacking fault energy in the AZ91 alloy leads to a significant inhibition of dislocation cross-slip, and formation of a high density of planar arrays of dislocations has also been reported [10, 38].

Conclusions

1. AZ91 magnesium alloy has been effectively processed in HPT processing at room temperature with an ultrafine-grained microstructure down to 35 nm. The alloy processed at 423 and 473 K has been significantly refined by twinning segmentation of the original grains into fine grains with average apparent grain sizes of 180 and 250 nm, respectively.
2. Fragmentation and alignment of the β-phase in the direction of torsional strain have been observed during processing. This phase has been refined down to nanometre sizes with a higher fraction as the number of turns increased, indicating the very high level of plastic deformation that is imparted to the alloy during HPT.
3. Existence of twins at all processing temperatures and their distribution was proportional to processing temperature and the number of turns. The occurrence of twinning has been induced by the need for re-orientation of the microstructure towards the slip direction and to accommodate severe plastic deformation.
4. Lower processing temperature has resulted in homogenous microstructure and significant development of strength. Higher processing temperatures have resulted in heterogeneous microstructures especially in the initial stages of HPT and this heterogeneity decreased gradually at higher numbers of turns.
5. A considerable dislocation density has developed with increasing the number of turns at lower processing temperature rather than at higher processing temperatures. The values of dislocation density after HPT were higher than earlier reported data for the same alloy.
6. The ultrafine-grained AZ91 alloy follows the Hall–Petch relationship, and this emphasizes the significant dependence of strength on grain size. The higher alloying content, fraction of nano-sized particles of β-phase and the dominance of basal slip and pyramidal modes after processing also have a significant effect on the strengthening of the alloy processed at 296 K.

Acknowledgements One of the authors (Ahmed S. J. Al-Zubaydi) is grateful to The Higher Committee for Education Development (HCED) of the Government of Iraq for the provision of Ph.D. scholarship.

Funding This work was supported in part by the Russian Science Foundation under Grant No. 14-29-00199 (APZ).

Compliance with ethical standards

Conflict of Interest The authors declare that they have no conflict of interest.

References

1. Ravi Kumar NV, Blandin JJ, Desrayaud C, Montheillet F, Suéry M (2003) Grain refinement in AZ91 magnesium alloy during thermomechanical processing. Mater Sci Eng A 359:150–157
2. Yamashita A, Horita Z, Langdon TG (2001) Improving the mechanical properties of magnesium and a magnesium alloy through severe plastic deformation. Mater Sci Eng A 300:142–147
3. Kubota K, Mabuchi M, Higashi K (1999) Processing and mechanical properties of fine-grained magnesium alloys. J Mater Sci 34:2255–2262. doi:10.1023/A:1004561205627
4. Mabuchi M, Iwasaki H, Yanase K, Higashi K (1997) Low temperature superplasticity in an AZ91 magnesium alloy processed by ECAE. Scr Mater 36:681–686
5. Figueiredo RB, Langdon TG (2011) Development of structural heterogeneities in a magnesium alloy processed by high-pressure torsion. Mater Sci Eng A 528:4500–4506
6. Kai M, Horita Z, Langdon TG (2008) Developing grain refinement and superplasticity in a magnesium alloy processed by high-pressure torsion. Mater Sci Eng A 488:117–124
7. Xia K, Wang JT, Wu X, Chen G, Gurvan M (2005) Equal channel angular pressing of magnesium alloy AZ31. Mater Sci Eng A 410–411:324–327
8. Valiev RZ, Zhilyaev AP, Langdon TG (2013) Bulk nanostructured materials: fundamentals and applications. Wiley, New Jersey
9. Gubicza J, Máthis K, Hegedűs Z, Ribárik G, Tóth AL (2010) Inhomogeneous evolution of microstructure in AZ91 Mg-alloy during high temperature equal-channel angular pressing. J Alloy Compd 492:166–172
10. Zhilyaev AP, Langdon TG (2008) Using high-pressure torsion for metal processing: fundamentals and applications. Prog Mater Sci 53:893–979
11. Vander Voort GF (2004) Metals handbook: metallography and microstructures, vol 9. ASM International, Cleveland
12. Kawasaki M, Figueiredo RB, Langdon TG (2011) An investigation of hardness homogeneity throughout disks processed by high-pressure torsion. Acta Mater 59:308–316

13. Al-Zubaydi ASJ, Zhilyaev AP, Wang SC, Reed PAS (2015) Superplastic behaviour of AZ91 magnesium alloy processed by high-pressure torsion. Mater Sci Eng A 637:1–11
14. Máthis K, Gubicza J, Nam NH (2005) Microstructure and mechanical behavior of AZ91 Mg alloy processed by equal channel angular pressing. J Alloy Compd 394:194–199
15. Hohenwarter A, Bachmaier A, Gludovatz B, Scheriau S, Pippan R (2009) Technical parameters affecting grain refinement by high pressure torsion. Int J Mater Res 100:1653–1661
16. Myshlyaev MM, McQueen HJ, Mwembela A, Konopleva E (2002) Twinning, dynamic recovery and recrystallization in hot worked Mg–Al–Zn alloy. Mater Sci Eng A 337:121–133
17. del Valle JA, Pérez-Prado MT, Ruano OA (2003) Texture evolution during large-strain hot rolling of the Mg AZ61 alloy. Mater Sci Eng A 355:68–78
18. Al-Samman T, Gottstein G (2008) Room temperature formability of a magnesium AZ31 alloy: examining the role of texture on the deformation mechanisms. Mater Sci Eng A 488:406–414
19. Zhao YH, Liao XZ, Zhu YT, Horita Z, Langdon TG (2005) Influence of stacking fault energy on nanostructure formation under high pressure torsion. Mater Sci Eng A 410–411:188–193
20. Kawasaki M, Figueiredo RB, Huang Y, Langdon TG (2014) Interpretation of hardness evolution in metals processed by high-pressure torsion. J Mater Sci 49:6586–6596. doi:10.1007/s10853-014-8262-8
21. Stráská J, Janeček M, Gubicza J, Krajňák T, Yoon EY, Kim HS (2015) Evolution of microstructure and hardness in AZ31 alloy processed by high pressure torsion. Mater Sci Eng A 625:98–106
22. Harai Y, Kai M, Kaneko K, Horita Z, Langdon TG (2008) Microstructural and mechanical characteristics of AZ61 magnesium alloy processed by high-pressure torsion. Mater Trans 49:76–83
23. Matsubara K, Miyahara Y, Horita Z, Langdon TG (2003) Developing superplasticity in a magnesium alloy through a combination of extrusion and ECAP. Acta Mater 51:3073–3084
24. Braszczyńska-Malik KN, Froyen L (2005) Microstructure of AZ91 alloy deformed by equal channel angular pressing. Int J Mater Res (former: Zeitschrift für Metallkunde) 96:913–917
25. Braszczyńska-Malik KN (2009) Spherical shape of γ-Mg17Al12 precipitates in AZ91 magnesium alloy processed by equal-channel angular pressing. J Alloy Compd 487:263–268
26. Zhao Z, Chen Q, Hu C, Shu D (2009) Microstructure and mechanical properties of SPD-processed an as-cast AZ91D + Y magnesium alloy by equal channel angular extrusion and multi-axial forging. Mater Des 30:4557–4561
27. Cavaliere P, De Marco PP (2007) Superplastic behaviour of friction stir processed AZ91 magnesium alloy produced by high pressure die cast. J Mater Process Technol 184:77–83
28. Pérez-Prado MT, Valle D, Ruano OA (2004) Grain refinement of Mg–Al–Zn alloys via accumulative roll bonding. Scr Mater 51:1093–1097
29. Kim WJ, Hong SI, Kim YH (2012) Enhancement of the strain hardening ability in ultrafine grained Mg alloys with high strength. Scr Mater 67:689–692
30. Figueiredo RB, Pereira PHR, Aguilar MTP, Cetlin PR, Langdon TG (2012) Using finite element modeling to examine the temperature distribution in quasi-constrained high-pressure torsion. Acta Mater 60:3190–3198
31. Edalati K, Miresmaeili R, Horita Z, Kanayama H, Pippan R (2011) Significance of temperature increase in processing by high-pressure torsion. Mater Sci Eng A 528:7301–7305
32. Al-Zubaydi A, Figueiredo RB, Huang Y, Langdon TG (2013) Structural and hardness inhomogeneities in Mg-Al-Zn alloys processed by high-pressure torsion. J Mater Sci 48:4661–4670. doi:10.1007/s10853-013-7176-1
33. Zhilyaev AP, Nurislamova GV, Kim B-K, Baró MD, Szpunar JA, Langdon TG (2003) Experimental parameters influencing grain refinement and microstructural evolution during high-pressure torsion. Acta Mater 51:753–765
34. Zhilyaev AP, Oh-ishi K, Langdon TG, McNelley TR (2005) Microstructural evolution in commercial purity aluminum during high-pressure torsion. Mater Sci Eng A 410–411:277–280
35. Zhilyaev AP, Lee S, Nurislamova GV, Valiev RZ, Langdon TG (2001) Microhardness and microstructural evolution in pure nickel during high-pressure torsion. Scr Mater 44:2753–2758
36. Vorhauer A, Pippan R (2004) On the homogeneity of deformation by high pressure torsion. Scr Mater 51:921–925
37. Huang Y, Kawasaki M, Langdon TG (2013) Influence of anvil alignment on shearing patterns in high-pressure torsion. Adv Eng Mater 15:1–755
38. Somekawa H, Hirai K, Watanabe H, Takigawa Y, Higashi K (2005) Dislocation creep behavior in Mg–Al–Zn alloys. Mater Sci Eng A 407:53–61
39. Tahreen N, Chen DL, Nouri M, Li DY (2014) Effects of aluminum content and strain rate on strain hardening behavior of cast magnesium alloys during compression. Mater Sci Eng A 594:235–245
40. Figueiredo RB, Aguilar MTP, Cetlin PR, Langdon TG (2012) Analysis of plastic flow during high-pressure torsion. J Mater Sci 47:7807–7814. doi:10.1007/s10853-012-6506-z
41. Kawasaki M, Figueiredo RB, Langdon TG (2012) Twenty-five years of severe plastic deformation: recent developments in evaluating the degree of homogeneity through the thickness of disks processed by high-pressure torsion. J Mater Sci 47:7719–7725. doi:10.1007/s10853-012-6507-y
42. Furukawa M, Horita Z, Nemoto M, Valiev RZ, Langdon TG (1996) Microhardness measurements and the Hall-Petch relationship in an Al-Mg alloy with submicrometer grain size. Acta Mater 44:4619–4629
43. Xu J, Shirooyeh M, Wongsa-Ngam J, Shan D, Guo B, Langdon TG (2013) Hardness homogeneity and micro-tensile behavior in a magnesium AZ31 alloy processed by equal-channel angular pressing. Mater Sci Eng A 586:108–114
44. Chang S-Y, Lee S-W, Kang KM, Kamado S, Kojima Y (2004) Improvement of mechanical characteristics in severely plastic-deformed Mg alloys. Mater Trans 45:488–492
45. Setman D, Schafler E, Korznikova E, Zehetbauer MJ (2008) The presence and nature of vacancy type defects in nanometals detained by severe plastic deformation. Mater Sci Eng A 493:116–122
46. Gubicza J, Dobatkin SV, Khosravi E, Kuznetsov AA, Lábár JL (2011) Microstructural stability of Cu processed by different routes of severe plastic deformation. Mater Sci Eng A 528:1828–1832